Transactions of the ASME®

Transactions of the ASME, Journal of Turbomachinery (ISSN 0889-504X) is published quarterly (Jan., Apr., July, Oct.) for $130.00 per year by The American Society of Mechanical Engineers, 345 East 47th Street, New York, NY 10017. Second class postage paid at New York, NY and additional mailing offices. POSTMASTER: Send address change to Transactions of the ASME, Journal of Turbomachinery, c/o THE AMERICAN SOCIETY OF MECHANICAL ENGINEERS, 22 Law Drive, Box 2300, Fairfield, NJ 07007-2300.
CHANGES OF ADDRESS must be received at Society headquarters seven weeks before they are to be effective. Please send old label and new address.
PRICES: To members, $40.00, annually; to nonmembers, $130.00.
Add $24.00 for postage to countries outside the United States and Canada.
STATEMENT from By-Laws. The Society shall not be responsible for statements or opinions advanced in papers or . . . printed in its publications (B7.1, Par. 3).

INDEXED by Applied Mechanics Reviews and Engineering Information, Inc.
Canadian Goods & Services Tax Registration #126148048

Journal of Turbomachinery

Published Quarterly by The American Society of Mechanical Engineers

VOLUME 115 • NUMBER 2 • APRIL 1993

TECHNICAL PAPERS

ANNOUNCEMENTS

The Role of Laminar-Turbulent Transition in Gas Turbine Engines: A Discussion

G. J. Walker
University of Tasmania,
Hobart, Australia

An extended discussion of Mayle's (1991) critical study of transition phenomena in gas turbine engines is presented. Attention is focused on transition in decelerating flow regions, which are the major sources of loss production for axial turbomachine blades. The following points are examined in detail: (a) the physics of transition and its implications for the correlation of various transition phenomena; (b) the relative importance of pressure gradient and free-stream turbulence in controlling transition; (c) the influence of pressure gradient on periodic-unsteady transition; (d) the correlation of transition length under conditions of arbitrary pressure gradient and free-stream turbulence level; and (e) transition behavior in laminar separation bubbles. The discussion examines various differences in philosophy concerning the above phenomena and makes further suggestions for transition research, which may assist in resolving the issues raised.

Introduction

This paper has been written as an extended discussion of Mayle's (1991) critical study of the role of laminar-turbulent transition in gas turbine engines. In commencing, the present author congratulates Professor Mayle on his comprehensive survey of fundamental transition phenomena and the manner in which this has been placed in the practical context of engine design.

Designers have typically adopted different approaches to the analysis of flow in compressors and turbines because of the generally different nature of transition phenomena associated with these components. In compressors, the bulk relative flow is decelerating and transition tends to be completed very rapidly; here, simple integral techniques are widely employed for calculating boundary layer development and the crude assumption of point transition is often used. In turbines, the bulk relative flow is accelerating and transition is usually much more protracted; this has important consequences for heat transfer to the blade surfaces and prompts the use of differential calculation methods with more advanced turbulence models for predicting transitional flow development.

In view of these traditional differences, a notable feature of Mayle's review is the way in which it attempts a unified approach to the whole range of transition phenomena in compressors and turbines. This has been done by describing transitional flow in terms of turbulent intermittency and correlating the transition onset and turbulent spot production rate in terms of the various parameters affecting them. A significant aspect is the use of the "acceleration" parameter $K = (\nu/U^2)(dU/dx)$ to describe the effects of pressure gradient in decelerating as well as accelerating flow. The application of this parameter had hitherto been largely restricted to the turbine design field because of its relevance to the reverse transition phenomenon in strongly accelerating flow.

The present author approaches the problem of transition in gas turbine engines from a rather different perspective, reflecting a background more in the area of compressor design and the physics of transition in decelerating flow. This viewpoint leads to certain differences in philosophy, which will be expanded upon throughout the paper. The opportunity will also be taken to amplify several matters discussed in Mayle's review and to highlight some particular areas of disagreement regarding the interpretation of published results. In conclusion, some suggestions will be made for further research, which might assist in resolving the issues raised.

Modes of Transition

Mayle has adopted the conventional approach of classifying transition into "natural," "bypass," and "separated-flow" modes.

Natural Transition. "Natural" transition (observed at low levels of free-stream turbulence) is the classical process emanating from the appearance of two-dimensional Tollmien-Schlichting instability waves in the laminar boundary layer. This is followed by a three-dimensional instability leading to the development of streamwise vorticity through the formation of vortex loops. The final stage of transition involves the initiation of turbulent spots from regions of peak shear and their ultimate merging to form a continuously turbulent flow. The natural transition process may be modified by two-dimensional spatial or temporal disturbances such as surface waviness or

Contributed by the International Gas Turbine Institute and presented at the 37th International Gas Turbine and Aeroengine Congress and Exposition, Cologne, Germany, June 1-4, 1992. Manuscript received by the International Gas Turbine Institute February 24, 1992. Paper No. 92-GT-301. Associate Technical Editor: L. S. Langston.

free-stream fluctuations perturbing the boundary layer velocity profile and altering the Tollmien–Schlichting wave amplification.

Bypass Transition. "Bypass" transition, in the context of Mayle's review, has been defined as the direct production of turbulent spots within the boundary layer as a result of high free-stream turbulence levels. As the name indicates, the initial two-dimensional instability phase of natural transition is bypassed in this case. Similar effects may be induced by certain types of three-dimensional surface roughness.

It does not follow, however, that linear stability theory is irrelevant in the case of bypass transition because no Tollmien–Schlichting waves are observed. The passage of free-stream disturbances will excite eigenmodes of the relevant stability equations within the laminar boundary layer, and the scale of these perturbations will govern the ultimate production rate of turbulent spots. Thus stability theory and its related governing parameters should at least be of significance in relation to the length of transitional flow in the bypass mode.

Separated-Flow Transition. The use of a single mode to describe transition in a separated laminar shear layer is somewhat anomalous, in that both natural and bypass transition processes should also be expected in this case. One is tempted to ask whether the "separated-flow" mode should be abandoned in favor of developing a unified approach to transition in attached and separated shear layers for both natural and bypass phenomena.

It is true that there may be some physical phenomena peculiar to separated flow, such as an increased receptivity to free-stream disturbances at a separation point. It can also be said that existing correlations of separated-flow transition have produced results of considerable practical importance. There are nevertheless some significant limitations and problems associated with current techniques and these will be discussed later in more detail.

Effect of Pressure Gradient

Mayle has chosen to correlate the influence of pressure gradient on transition via the acceleration parameter $K = (\nu/U^2)dU/dx$ because of its importance in relation to reverse transition and its apparent relevance to bypass transition in favorable pressure gradients. He acknowledges the significance of the alternative (Pohlhausen) parameter $\lambda_\theta = (\theta^2/\nu)dU/dx$ in relation to natural transition, but suggests that the latter mode will only occur in highly decelerating flow with the high free-stream turbulence levels normally encountered in gas turbine engines.

The results of Gostelow and Dey (1991), however, indicate a strong correlation of dimensionless turbulent spot production rate $N = n\sigma\theta_t^3/\nu$ with $\lambda_{\theta t}$ over the whole range of positive pressure gradients up to laminar separation. The variation in N produced by changing $\lambda_{\theta t}$ from 0 to -0.08 is an order of magnitude greater than that achieved by increasing the turbulence level Tu from 0.3 to 5.4 percent, which changes only slowly with $\lambda_{\theta t}$ over this range. These results are in accordance with the changing physics of transition in decelerating flow reported by Walker and Gostelow (1990), which become evident at quite small negative values of λ_θ. The foregoing considerations leave it unclear, at this time, that K should be preferred over λ_θ for describing transition in a positive pressure gradient.

It is noted in conclusion that the use of local parameters to correlate transition onset is only likely to succeed for bypass transition modes. In the case of natural transition, it becomes

Nomenclature

c = airfoil chord
$f, f_1, f_2..$ = functions
l_1 = length of constant-pressure region
n = turbulent spot production rate
$\hat{n}$ = dimensionless spot production rate $= n\nu^2/U_t^3$
t = time
u = tangential velocity component
$\bar{u}$ = time-mean tangential velocity
x = streamwise distance
y = distance normal to surface
C = turbulent spot convection velocity
C_f = skin friction coefficient
C_R = propagation velocity of laminar instability wave
G = transition length parameter, Eq. (10)
$G_{\gamma tr}$ = arbitrary parameter replacing constant value 1200, Eq. (10)
K = acceleration parameter $= (\nu/U^2)dU/dx$
L = characteristic length for oscillating flow $= 2\pi U/\omega$
L_T = transition length $= (x_T - x_t)$
N = dimensionless spot production rate $= n\sigma\theta_t^3/\nu$
Re_c = chord Reynolds number $= U_\infty c/\nu$
Re_x = streamwise length Reynolds number $= Ux/\nu$
Re_{LT} = transition length Reynolds number $= UL_T/\nu$
Re_{NS} = non-steady Reynolds number $= L\Delta U/2\pi\nu$
Re_{δ^*} = displacement thickness Reynolds number $= U\delta^*/\nu$
Re_θ = momentum thickness Reynolds number $= U\theta/\nu$
Re_λ = transition length Reynolds number $= U\lambda/\nu$
Tu = free-stream turbulence intensity, percent
U = local free-stream velocity
U_∞ = reference free-stream velocity
γ, γ_{tr} = turbulent intermittency
δ = boundary layer thickness
δ^* = boundary layer displacement thickness
θ = boundary layer momentum thickness
λ = transition length parameter $= (x_{\gamma=0.75} - x_{\gamma=0.25})$
λ_θ = pressure gradient parameter $= (\theta^2/\nu)dU/dx$
ν = kinematic viscosity
σ = turbulent spot dependence area factor
τ^* = dimensionless time $= t\omega/2\pi$
ω = circular frequency of free-stream oscillation
ΔU = amplitude of free-stream velocity oscillation

Subscripts

min = minimum transition length value, defined in Eq. (13)
r = reattachment
s = laminar separation
t = start of transition
tw = start of wake-induced transition
u = upper surface
FP = zero pressure gradient value (flat plate)
LE = spot leading edge
RA = reattachment, Fig. 6
SL = laminar separation, Fig. 6
T = end of transition (attached flow); end of constant pressure region (separated flow)—Mayle
TE = spot trailing edge
$T1$ = start of transition, Fig. 6
$T2$ = end of transition, Fig. 6

necessary to use mean values of the relevant parameters to allow for variations in the amplification rate of two-dimensional disturbances over the region of unstable laminar flow.

Effect of Free-Stream Turbulence

Mayle has correctly stressed the importance of considering disturbance length scale as well as amplitude in relation to the influence of free-stream turbulence on transition. Further parameters are undoubtedly necessary in the general case, but the need for these remains unclear because of an incomplete understanding of the turbulent spot production process.

There are at least three mechanisms by which free-stream disturbances may influence transition, namely:

(*a*) the modification of natural transition processes through essentially two-dimensional perturbations in free-stream velocity or pressure gradient;
(*b*) bypass mechanisms resulting in the direct generation of streamwise vorticity within the boundary layer through localized three-dimensional disturbances; and
(*c*) the diffusion of turbulent energy or direct injection of turbulent fluid from the free-stream into the boundary layer.

Mechanism (*a*) may well be significant in relation to the production mechanism for wake-induced turbulent strips, due to the "jet-" or "sink-like" characteristics of wake disturbances that have been noted in Mayle's review. Whether this effect is considered here or under periodic-unsteady transition, its description will require at least the use of a non-steady Reynolds number based on the disturbance amplitude and wavelength (see Loehrke et al., 1975). This makes it rather improbable that simple correlations of transition onset in terms of K, Tu alone will be generally valid (although it is conceivable that they could be made to work over a limited range of conditions).

However, even granting the existence of such a correlation, one is left with the vital question of the effective value of the turbulence parameter to be used in its application. The disturbance field in a gas turbine engine can be decomposed into periodic and random components; the observations of Evans (1975) in an axial compressor indicated these to be comparable magnitude near the design point, with the random component becoming dominant near stall. The periodic component will also be influenced by axial blade row spacing and will be enhanced by the higher blade loadings employed in turbines.

The relative influence of periodic and random free-stream disturbances on transition in turbomachinery remains unclear. The random component might well be largely irrelevant in situations where transition is dominated by periodic disturbances.

This could provide an alternative explanation for Mayle's proposal of the ineffectiveness of wake turbulence beyond a certain "saturation" level.

Periodic-Unsteady Transition

Introduction. Transition in a gas turbine is periodically unsteady, in sympathy with the essentially unsteady nature of the energy transfer process in a turbomachinery. The wakes of upstream airfoils or obstructions usually provide the dominant source of unsteadiness, but the passage of trailing shock waves from transonic airfoils has also been known to generate periodic transition phenomena.

As indicated in Mayle's review, the mechanism by which free-stream disturbances cause the production of turbulent strips is still not completely understood. The balance of current opinion in the literature appears to favor the impingement of turbulent fluid as the mechanism for wake-induced transition, but no simple relation between transition Reynolds number and wake turbulence level has yet been identified.

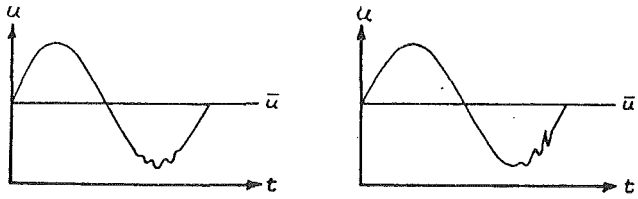

(a) Initial appearance (b) Subsequent development

Fig. 1 Schematic diagram of wave packet development during transition in oscillating flow

As discussed above in relation to the effective value of free-stream turbulence parameter, the relative importance of the periodic and random components of wake disturbances remains unclear. It is certainly possible to promote transition through free-stream oscillations unaccompanied by turbulence; this phenomenon could arise in the turbomachine context from the potential flow interactions produced by neighboring blade rows in relative motion. A brief summary of published results on transition in oscillating flow is therefore in order before attempting further interpretation of wake-induced transition observations.

Transition in Oscillating Flow. The transition behavior on a flat plate in a non-steady boundary layer flow induced by sinusoidal oscillations in the free-stream velocity under low-turbulence conditions was examined experimentally by Miller and Fejer (1964) and Obremski and Fejer (1967). A review of this work and related studies of transition in oscillating boundary layers has been given by Loehrke et al. (1975).

Fejer and co-workers found the manner in which transition occurred to depend on a "non-steady Reynolds number" $\mathrm{Re}_{NS} = L\Delta U/2\pi\nu$. Here $L = 2\pi U/\omega$ is a characteristic length equal to the distance traveled by a fluid particle in the free-stream during one cycle of the imposed oscillation (frequency $\omega/2\pi$ Hz). The characteristic velocity ΔU is the amplitude of the free-stream oscillation.

When Re_{NS} exceeded a certain critical value (about 26,000 for zero pressure gradient), transition began with turbulent bursts appearing periodically at the frequency of the free-stream oscillation. In this case, the transition Reynolds number depended only on the amplitude of the free-stream oscillations, to a first order, and not on their frequency. Breakdown to turbulence was preceded in space and time by a packet of disturbance waves resembling a Tollmien–Schlichting instability. For the range of conditions investigated, these waves appeared first in the trough of the boundary layer velocity trace as shown in Fig. 1(*a*); they subsequently increased in amplitude and moved into the accelerating part of the velocity trace as shown in Fig. 1(*b*).

In oscillating flow with Re_{NS} below the critical value described above, the transition Reynolds number became independent of both the amplitude and the frequency of the oscillation in the range tested. Transition was still preceded by the appearance of wave packets in the trough of the velocity trace, but the turbulent outbreak and development tended to occur somewhat later on the upper part of the free-stream waveform closer to the crest. The turbulent bursts lacked the strong periodicity observed at the supercritical Re_{NS} values, but because of their preferred outbreak location they could not be characterized as occurring randomly in time. Obremski and Fejer termed this behavior "aperiodic."

Oscillating flow transition with Re_{NS} exceeding its critical value results in the regular formation of two-dimensional spanwise turbulent strips similar to those observed in wake-induced transition. Figure 2 shows a typical time–space distribution of events during periodic transition on a flat plate in zero pressure gradient under low free-stream turbulence conditions, as pub-

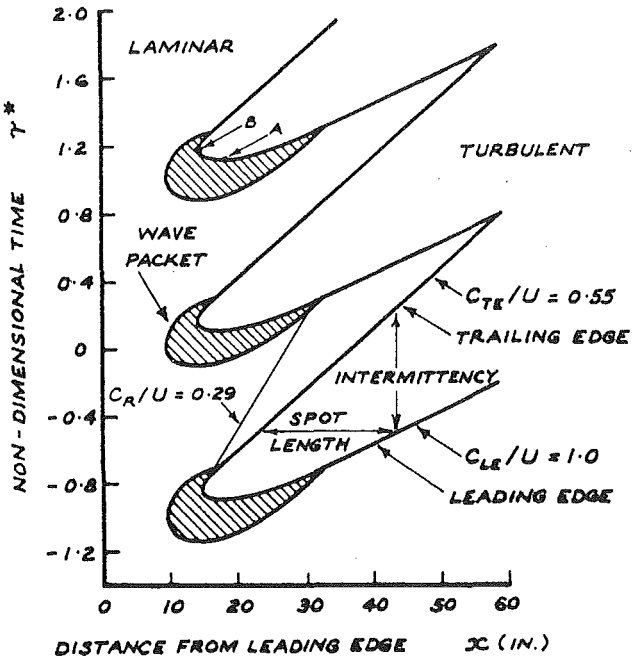

Fig. 2 Time-space distribution of turbulent spots during periodic transition in zero pressure gradient (predominantly convective mode development); run 15 from Obremski and Fejer (1967)

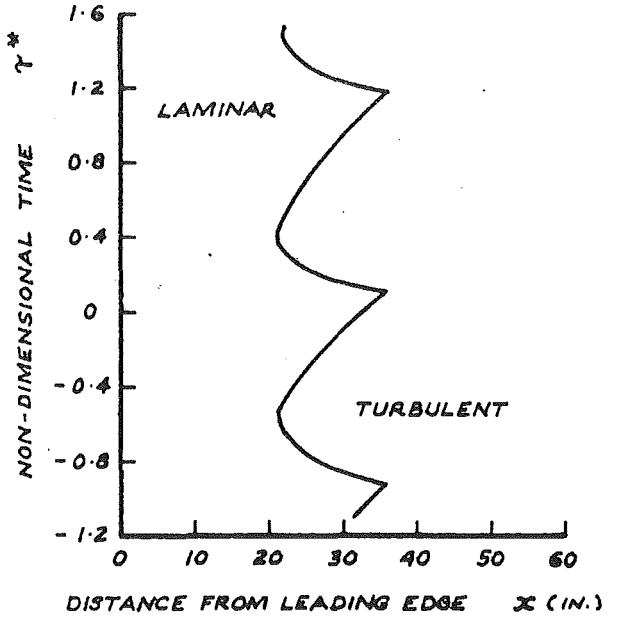

Fig. 3 Time-space distribution of turbulent spots during periodic transition in an adverse pressure gradient (predominantly creative mode development); run D-6 from Obremski and Fejer (1967)

lished by Obremski and Fejer (1967). These workers classified the development of turbulent spots during periodic transition as follows:

(*a*) the initial appearance of a turbulent spot from a point within the disturbance wave packet at a time slightly later than the occurrence of the minimum in the free-stream velocity;

(*b*) a "creative mode" during which large-amplitude instability waves are still present at the spot boundary and the growth rate of the turbulent spot varies with time. This occurs immediately after the formation of a turbulent spot, and is characterized by a rapid spreading of the spot boundary in both the upstream and downstream directions. Termination of creative mode development is apparently associated with the appearance of a calmed region caused by the trailing spot boundary moving faster than the following Tollmien–Schlichting waves;

(*c*) a "convective mode" in which laminar instability waves are absent from the spot boundary. The growth rate of the turbulent spot is constant due to its leading and trailing edges moving downstream at constant but different velocities;

(*d*) a region of continuously turbulent flow formed by the merging of turbulent spots created during successive oscillations of the free stream.

During periodic transition in an adverse pressure gradient, Obremski and Fejer found that a considerably larger proportion of the turbulent spot development occurred in the creative mode, as indicated by the greater curvature of the turbulent spot boundary shown in Fig. 3. This shortened the laminar tongues in the x–τ^* plane and so reduced the length of transitional flow significantly. The relative proportions of creative and convective mode development for the whole range of cases examined by Obremski and Fejer appeared somewhat dependent on properties of the imposed free-stream oscillation and were not a function of pressure gradient alone. The frequency parameter $\omega x/U$ is also significant here.

Unsteady Transition on Turbomachine Blades. The periodic-unsteady transition model of Mayle and Dullenkopf (1990) assumes that turbulent spots on turbomachine blades are produced by a combination of wake-induced transition and other transition modes. Passing wakes are assumed to result in the immediate formation of turbulent strips, which then propagate and grow at fixed rates; this corresponds to the convective mode of development as defined by Obremski and Fejer.

To commence the transitional flow calculation, it is first necessary to specify the point x_{tw} at which the wake-induced turbulent strips appear. This point may depend, in general, on both periodic (i.e., wake "jet" or "sink") fluctuations and turbulence associated with the passing wake, as Mayle has noted. Dong and Cumpsty (1990a, 1990b) and Addison and Hodson (1990a, 1990b), however, both discounted jet-wake fluctuations as having been significant in their experiments. These workers all found the appearance of a turbulent patch in the boundary layer to coincide with the wake passage and deduced that the wake turbulence alone was responsible for the initiation of turbulent spots. Addison and Hodson (1990b) used a quasi-steady model to predict transition onset from the instantaneous turbulence level in the passing wake.

A rather different picture is indicated by Walker's (1974) observations of transition on the suction surface of an axial compressor stator blade subject to passing rotor wakes. The set of observations reproduced in Fig. 4 indicates that the turbulent patch in the boundary layer occurs at the end of the wake passage and does not coincide with the expected region of peak turbulence within the wake. The periodic fluctuation associated with the wake passage is not considered to have had a significant influence on the transition location, as this differed little from that observed on a similar blade section, in cascade, at low free-stream turbulence (see Fig. 1 of Walker, 1987). However, the wake clearly produces organized behavior of the turbulent spots. It is suggested that this behavior might represent a case of the "aperiodic" mode of transition described by Obremski and Fejer for low Re_{NS}, in which free-stream oscillations cause fairly regular fluctuations in the laminar–turbulent interface without having any first-order influence on transition location.

Mayle (1991) discounted the observations of Walker (1974) by stating that this case involved the formation and collapse of separation bubbles (presumably at the blade leading edge as implied by following discussion). However, there is no evidence of leading edge breakdown occurring over the range investigated; at low incidence, the turbulent spots clearly orig-

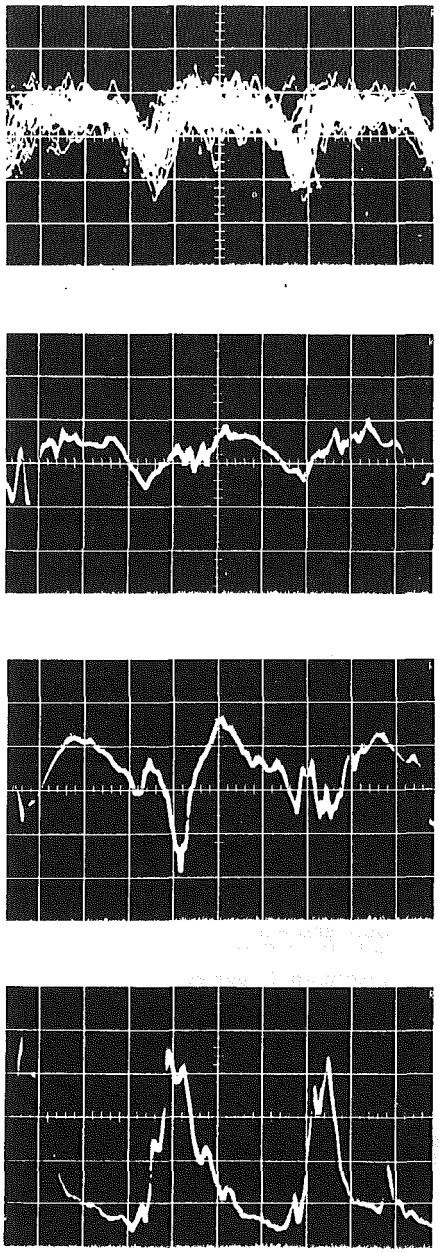

Fig. 4 Velocity fluctuations in transitional boundary layer on suction surface of compressor stator at 50 percent chord ($i = 0.5$ deg, $Re_c = 4.9 \times 10^4$) from Walker (1974); scale: 2 ms/div horiz

inated around midchord and the preceding flow appeared continuously laminar. The transition onset behavior observed by Walker was in fact closely similar to the turbine blade observations of Addison and Hodson (1990b) apart from the different phase of the wake passage at which breakdown occurred.

The turbulent spot development on Walker's compressor blade occurred predominantly in the creative mode, and transition was completed within 20 percent chord. This is an order of magnitude shorter than the length of around 200 percent chord, which would have occurred with the spot developing entirely in the convective mode. While transition could be completed earlier due to other transition modes, this example serves to emphasize Addison and Hodson's (1990b) comment that a constant spot spreading rate is too simplistic to be of general use. The author is therefore in full agreement with Mayle's (1991) proposal for further experimentation to determine appropriate design criteria for wake-induced transition.

Prediction of Transitional Flow

Introduction. Mayle (1991) has given an excellent survey of recent developments in the prediction of transitional flow using intermittency theory. The basis of this technique is the use of a suitable correlation to predict turbulent spot production rates, and four main approaches to this problem have been proposed:

(*a*) Mayle's correlation of spot production rate $\hat{n}\sigma$ in terms of acceleration parameter $K = \lambda_\theta / Re_\theta^2$ and free-stream turbulence level Tu, presented graphically in Fig. 15 of Mayle (1991);

(*b*) correlations of $N = \hat{n}\sigma Re_{\theta t}^3$ in terms of pressure gradient parameter λ_θ and Tu proposed by Gostelow and co-workers;

(*c*) correlations based on stability theory and a minimum transition length concept, as developed by Walker and co-workers;

(*d*) correlations of $N = \hat{n}\sigma Re_{\theta t}^3$ in terms of Tu developed by Narasimha and co-workers, which represent a subset of method (*b*).

Mayle is rather dismissive to the last two approaches, stating that "*correlations based on either Narasimha's parameter N or Walker's (1987) minimum transition length produce errors up to factors of three in the transition length over the complete range of pressure gradients and turbulence levels and are not recommended.*" This statement is strictly true if the models are applied in their original form, but it may give the misleading impression that there is some fundamental deficiency in the Narasimha and Walker methods.

The following discussion is undertaken to explain more fully the Walker and Narasimha transition length correlation techniques. It will be shown that all four approaches mentioned above are physically interrelated. Consideration of these relationships will show that extended versions of the Narasimha or Walker techniques (as earlier foreshadowed by Walker, 1989) are likely to be more generally applicable than Mayle's method.

Transition Length Correlations

(*a*) *Physical Basis.* The application of Emmons' (1951) turbulent spot theory together with a suitable assumption for the turbulent spot production function leads to an expression for the intermittency distribution that relates the length of the transition zone to the turbulent spot formation rate. Dhawan and Narasimha's (1958) assumption of turbulent spot inception occurring in a concentrated region around the start of the transition zone yields the relation[1]

$$Re_\lambda = 0.642(\hat{n}\sigma)_t^{-1/2}; \quad \hat{n} = n\nu^2/U_t^3 \tag{1}$$

Provided that some correlation can be identified between the transition length Reynolds number and the local conditions at the start of the transition zone, it is then possible to relate the turbulent spot production rate to the conditions at transition inception. Dhawan and Narasimha (1958) suggested the correlation

$$Re_\lambda \simeq 5\ Re_{xt}^{0.8} \tag{2}$$

on the basis of the data available to them. This data showed considerable scatter due to the influence of other factors such as free-stream turbulence level and Mach number. Narasimha (1978) later proposed the amended expression

$$Re_\lambda \simeq 9\ Re_{xt}^{0.75} \tag{3}$$

which is still consistent with Dhawan and Narasimha's data.

This indicates that the appropriate dimensionless parameter for breakdown rate should be

[1]Mayle's (1991) notation is followed here. Narasimha and co-workers define $\hat{n} = n\sigma\nu^2/U^3$.

$$N = n\sigma\theta_t^3/\nu = \mathrm{Re}_{\theta t}^3(\hat{n}\sigma) \tag{4}$$

As Narasimha (1985) has stated, this clearly suggests that the breakdown rate scales primarily with the boundary layer thickness δ_t and viscous diffusion time δ_t^2/ν—a physically appealing conclusion.

Further support for the validity of Narasimha's parameter N is provided by Walker's (1987) minimum transition length theory, which yields precisely the same functional relationship of Re_λ with Re_{xt} as Eq. (3). The underlying physical basis for this functional form is the correlation of dominant disturbance frequency with local boundary layer Reynolds number obtained from linearized stability theory for the laminar boundary layer.

(*b*) *Constant Pressure Flows* (*Arbitrary Turbulence*). On the basis of limited data, Dey and Narasimha (1984) and Narasimha (1985) suggested that the dimensionless breakdown rate N should take a constant value

$$N \simeq 0.7 \times 10^{-3} \tag{5}$$

for transition forced by free-stream turbulence in a constant pressure flow. Using more extensive data based on intermittency measurements, Gostelow and Dey (1991) and Gostelow et al. (1992) later suggested the modified relation

$$N = 0.86 \times 10^{-3} \exp(-0.564 \ln (Tu)) \tag{6}$$

which indicates that N should decrease monotonically with increasing free-stream turbulence.

These results may be compared with Mayle's (1991) proposal that the spot production rate in zero pressure gradient flow should be given by

$$\hat{n}\sigma = n\sigma\nu^2/U_t^3 = N/\mathrm{Re}_{\theta t}^3 = 1.5 \times 10^{-11} Tu^{7/4} \tag{7}$$

The latter result at first appears physically unreasonable in that the spot production rate n does not involve the local boundary layer thickness. However, this discrepancy is largely resolved by realizing that there is also a correlation between $\mathrm{Re}_{\theta t}$ and Tu for transition in zero pressure gradient flow, given by Mayle as

$$\mathrm{Re}_{\theta t} = 400\ Tu^{-5/8} \tag{8}$$

(*c*) *Arbitrary Pressure Gradient* (*Low Turbulence*). Chen and Thyson (1971) modeled the transition zone for arbitrary pressure gradient flows (under low-turbulence conditions) by assuming:

(*i*) spot propagation velocities at any given station are proportional to the local external velocity $U(x)$;

(*ii*) a spot grows at a constant angle relative to the local external streamline; and

(*iii*) the hypothesis of concentrated breakdown at x_t remains valid.

In accordance with this model, Cebeci and Smith (1974) proposed the intermittency distribution

$$\gamma = 1 - \exp\left[-G(x - x_t) \int_{x_t}^{x} (dx/U) \right] \tag{9}$$

where

$$G = (1/1200)(U^3/\nu^2)\mathrm{Re}_{xt}^{-1.34} \tag{10}$$

This model has been calibrated against constant-pressure flow data. For the case of zero pressure gradient, Eqs. (9) and (10) yield

$$\mathrm{Re}_\lambda = 22\ \mathrm{Re}_{xt}^{0.67} \tag{11}$$

which gives similar results to those of Eqs. (2) and (3).

The Chen–Thyson model may give useful results for accelerating flow, but it breaks down completely for decelerating flow because it does not comprehend the major influence of adverse pressure gradients on the physics of laminar instability and turbulent breakdown processes. Even a mild adverse pressure gradient greatly increases the turbulent spot production rate and causes an associated shortening of the transition zone. This is a most significant point, which is overlooked in Mayle's (1991) review.

It was the failure of the Chen–Thyson model to give reasonable results in low Reynolds number airfoil calculations that provided the stimulus for Walker's (1987) minimum transition length model. As described by Walker et al. (1988), these calculations failed completely because of excessive transitional flow lengths producing burst laminar separation bubbles in the computed flow. However, satisfactory results were obtained by using a transitional flow length comparable to that predicted by the minimum transition length model.

Walker's (1987) minimum transition length hypothesis was based on the assumption of continuous breakdown of laminar instability waves in a strong positive pressure gradient, together with a correlation for instability wave frequency in terms of local boundary layer parameters and a simple spot spreading model. The resulting theoretical minimum transition length was originally proposed as a limiting value, which could be useful in sensitivity analyses of transitional flow calculations. However, Walker and Gostelow (1990) later used this model as a theoretical basis for correlating transition length in adverse pressure gradients under low free-stream turbulence conditions. This correlation, given by

$$\frac{L_T}{L_{T\min}} = \frac{0.14 + 20 \exp(100\ \lambda_{\theta t})}{0.33 + 3 \exp(100\ \lambda_{\theta t})} \tag{12}$$

expresses the ratio of observed transition length L_T to the theoretical minimum value given by

$$L_{T\min} = 2.3\ \mathrm{Re}_{\delta^*t}^{3/4} \tag{13}$$

as a function of the pressure gradient parameter at transition inception $\lambda_{\theta t}$.

The experimental data of Walker and Gostelow also provided a calibration of the theoretical minimum transition length, which was found to be about twice the observed minimum. It is important to note that the minimum attainable transition length, achieved with a separating laminar boundary layer at the point of breakdown, differs from that predicted by the Dhawan–Narasimha constant pressure correlation by an order of magnitude. The Chen–Thyson model is similarly in error as the transition length is short and the effects of altered spot propagation velocity alone are relatively minor.

(*d*) *Arbitrary Pressure Gradient and Turbulence Level.* The Walker–Gostelow correlation, Eqs. (12) and (13) can be used to relate turbulent spot production rate to streamwise pressure gradient under conditions of low free-stream turbulence. The Narasimha correlation and later developments, Eqs. (5) and (6) are complementary in that they relate spot production rate to free-stream turbulence level without including the influence of pressure gradient.

Clearly, neither the Narasimha nor the Walker–Gostelow model can be expected to give accurate predictions of transition length for arbitrary values of both pressure gradient and turbulence level in their original forms. But both approaches are quite capable of being extended to make them generally applicable. The basic forms of these models are still important, however, because of the physical insight they provide. Taken together, they indicate that a correlation of bursting rate $\hat{n}\sigma$ valid for all pressure gradients and turbulence levels must involve both λ_θ and Re_θ.

The Walker model can be extended to the case of arbitrary turbulence level by writing

$$\mathrm{Re}_{LT}/\mathrm{Re}_{LT\min} = f_1(\lambda_{\theta t}, Tu) \tag{14}$$

which can be transformed to

$$f_2(\hat{n}\sigma)/f_3(\mathrm{Re}_{\theta t}, \lambda_{\theta t}) = f_1(\lambda_{\theta t}, Tu) \quad (15)$$

This approach was foreshadowed by Walker (1989) and some preliminary results were presented on the basis of data published by Gostelow (1989). The method has now been examined in more detail by Gostelow et al. (1992) using more extensive data; they propose the extended correlation

$$L_T/L_{T\min} = 9.412 \exp\{-3.121\,\lambda_{\theta t} \ln(Tu) + 33.69\,\lambda_{\theta t} + 0.248 \ln(Tu)\} \quad (16)$$

The Narasimha correlation may be extended to the case of arbitrary pressure gradient by writing

$$N = \hat{n}\sigma \mathrm{Re}_{\theta t}^3 = f_4(\lambda_{\theta t}, Tu) \quad (17)$$

Correlations of this form have now been reported by Gostelow and Dey (1991) and Gostelow et al. (1992) who give

$$N = 0.86 \times 10^{-3} \exp\{2.134\,\lambda_{\theta t} \ln(Tu) - 59.23\,\lambda_{\theta t} - 0.564 \ln(Tu)\} \quad (18)$$

A similar approach was suggested independently by Addison and Hodson (1992), although their data were too sparse to determine any particular trend with Tu.

The new transition length correlation presented graphically by Mayle (1991) is of the form

$$\hat{n}\sigma/\hat{n}\sigma_{FP} = f_5(K_t, Tu) \quad (19)$$

i.e.,

$$\hat{n}\sigma/f_6(Tu \text{ or } \mathrm{Re}_{\theta t}) = f_5(K_t, Tu) \quad (20)$$

There is a distinct analogy with Walker's approach, provided that the denominator on the left-hand side of Eq. (20) is evaluated in terms of $\mathrm{Re}_{\theta t}$ and not in terms of Tu as recommended by Mayle. The interchangeability of Tu and $\mathrm{Re}_{\theta t}$ as the argument of f_6 follows from Eq. (8).

Noting that $K = \lambda_\theta/\mathrm{Re}_\theta^2$, it could be said that the transition length correlations expressed by Eqs. (15), (17) and (20) all involve the same group of parameters $\hat{n}\sigma$, Re_θ, λ_θ, Tu. However, Mayle's relation, Eq. (20), excludes the independent explicit representation of λ_θ considered necessary to describe the spot production rate under arbitrary conditions. In addition, it is not obvious that functional forms can be chosen to allow an exact equivalence between the representations of $\hat{n}\sigma$ in Eqs. (17) and (20). Hence, while Mayle's model might be an improvement on the basic models of Narasimha and Walker, its application appears restricted at best to a particular class of surface pressure distributions in order to assure the implicit relationship between $\lambda_{\theta t}$ and $\mathrm{Re}_{\theta t}$ determined by a particular value of K. This situation could be further clarified if Mayle's correlation were made available in algebraic rather than graphic form.

The extended Narasimha and Walker transition length correlations proposed by Gostelow et al. (1992) appear at least as encouraging as that of Mayle (1991), but neither has been widely tested as yet. The foregoing discussion indicates that it is premature to judge the suitability of any of these models. Further studies should be carried out to determine the general applicability and accuracy of the spot production models corresponding to Eqs. (14), (17), and (19). These should preferably be based on transition onset and transition length observations determined from turbulent intermittency measurements and standardized data reduction techniques. It is particularly important to remove any bias from erroneous theoretical predictions or experimental observations of transition onset. A wide range of Reynolds number should be covered, with the parameters Tu, $\mathrm{Re}_{\theta t}$, $\lambda_{\theta t}$, and K_t being varied independently as far as possible to test their significance. The ultimate test of transition length predictions should lie in a quantitative assessment of their performance in practical situations, rather than in the goodness of fit of the basic correlation functions employed.

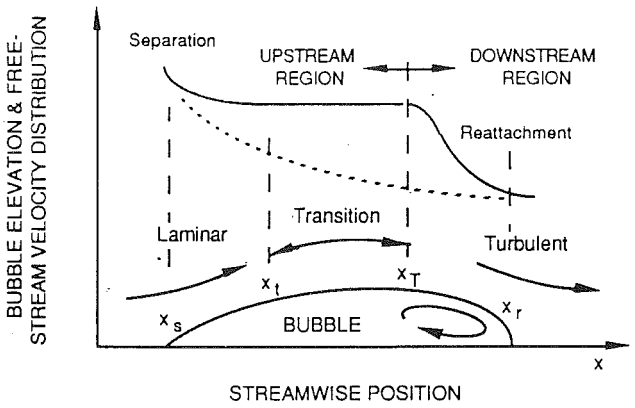

Fig. 5 Flow around a separation bubble and corresponding pressure distribution from Mayle (1991)

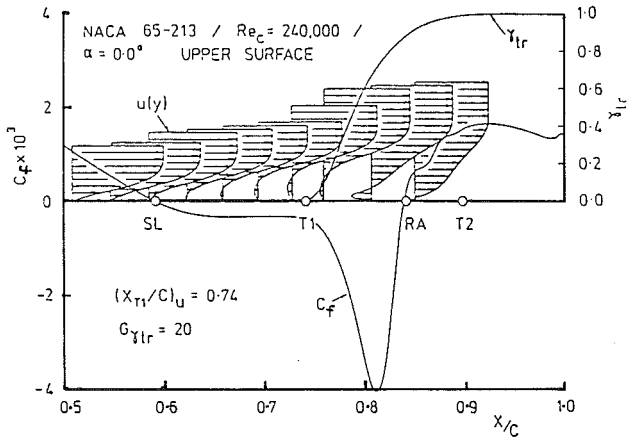

Fig. 6 Typical computed separation bubble flow from Walker et al. (1988)

Separated Flow Transition

Introduction. The author endorses the general thrust of Mayle's (1991) proposals to improve the modeling of transition in separated flow in order to allow the full application of modern numerical codes. However, there are some significant differences of opinion on matters of detail.

Mayle has presented a modified picture of the flow behavior in a short separation bubble, which is reproduced in Fig. 5. This differs from the simplified model of Horton (1969) and Roberts (1975, 1980) in two important respects:

(*a*) there is a transitional flow region of finite length; and

(*b*) the start of transition occurs in the region of constant pressure. (But transition is still assumed complete at the end of the constant pressure region so that, in common with the Horton–Roberts model, the shear layer is fully turbulent during pressure recovery and reattachment.)

There is ample evidence to justify the assumption of transition commencing prior to the start of pressure recovery, and this was also proposed by Walker (1975). However, the assumption that the end of transition x_T coincides with the start of pressure recovery in the time-mean flow cannot be supported. The experimental observations of Walker (1975) and the computational studies of Walker et al. (1988) strongly indicate that transitional flow may occur throughout the pressure recovery process; in some cases the end of transition may lie downstream of time-mean reattachment point, as shown in Fig. 6.

Further light is shed on this matter by the shear layer turbulence observations of Gaster, to which Mayle has usefully drawn attention. These have been employed as suggested by

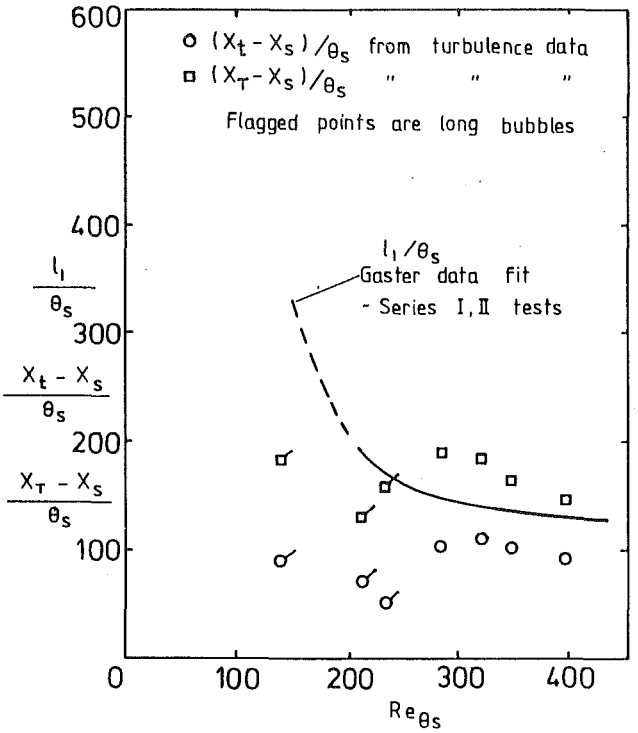

Fig. 7 Length of constant-pressure region in Series I and II laminar separation bubbles from Gaster (1967); comparison with limits of transition region from shear layer turbulence data for Series II tests

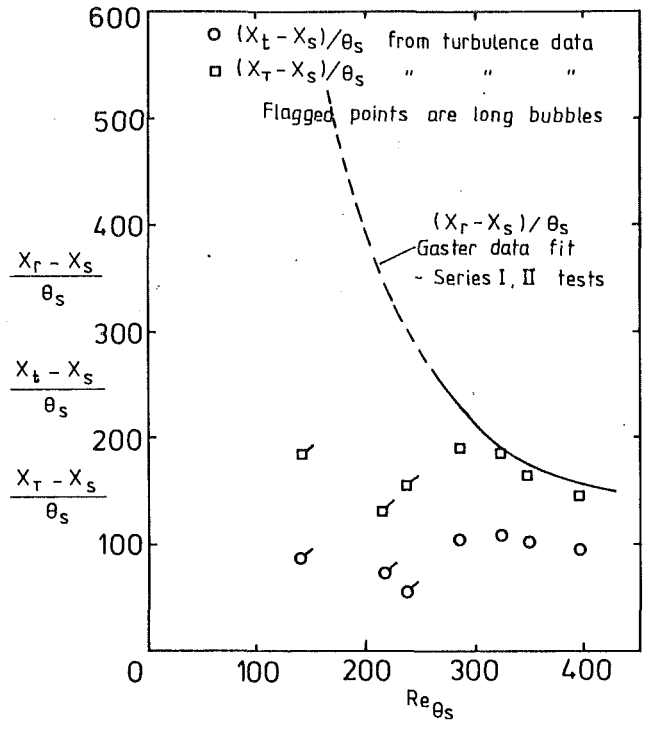

Fig. 8 Length of separated flow in Series I and II laminar separation bubbles from Gaster (1967); comparison with limits of transition region from shear layer turbulence data for Series II tests

Mayle to indicate the limits of transitional flow, x_t and x_T by following Mayle's assumption that $\gamma \simeq Tu/Tu_T$. The results are plotted in Figs. 7 and 8 where they are compared with Gaster's (1967) data. Transition onset was arbitrarily defined as corresponding to $Tu/Tu_T = 0.2$ because of the nonzero disturbance level upstream. It should be noted that some contribution to Tu may be generated by shear layer flapping (Strouhal vortex shedding) and associated oscillations of the instantaneous reattachment point. Thus Tu/Tu_T may not exactly represent the shear layer intermittency associated with transition.

Figure 7 indicates that for short bubbles the transitional flow region neatly straddles the end of the dead air region (i.e., region of constant pressure, length l_1, as defined by Gaster). For long bubbles, the transition process is completed well before the end of the constant pressure region. Comparison with Gaster's curve fit for the total length of separated flow in Fig. 8 indicates that the end of transition occurred close to reattachment for the short bubbles in his Series II tests. This result appears quite reasonable, considering that in an incipient short bubble only occasional turbulent mixing should suffice to ensure reattachment; in that case, the end of transition would be expected to lie downstream of the mean reattachment point.

These considerations do not invalidate the correlation for $(\mathrm{Re}_x)_{st}$ (Eq. (11) and Fig. 19 of Mayle, 1991), which has been based on turbulence data to determine x_t. However, as $(\mathrm{Re}_x)_{sT}$ has been determined from the extent of constant pressure in the bubble, it is clear that Mayle's Eq. (10)

$$(\mathrm{Re}_x)_{sT} = \mathrm{Re}_{xT} - \mathrm{Re}_{xs} = 700\ \mathrm{Re}_{\theta_s}^{0.7} \tag{21}$$

must significantly underestimate $(\mathrm{Re}_x)_{sT}$ for short bubble flows. Hence the value of transition length in separation bubbles, as indicated by Mayle's Eq. (12) for Re_{LT}

$$\mathrm{Re}_{LT} = 400\ \mathrm{Re}_{\theta_s}^{0.7} \tag{22}$$

will similarly be too low.

Mayle has commented that Eq. (21) for Re_{sT} "*is significantly different from that proposed by Walker (1989) based on stability considerations and a minimum turbulent spot merging distance.*" He is apparently referring to the relation

$$\mathrm{Re}_{LT} = 0.97\ \mathrm{Re}_{\delta^*_s}^{1.5} \tag{23}$$

This comparison is inappropriate, as Eq. (23) is strictly based on the length of transitional flow, not the length of the constant pressure region in a bubble. A more appropriate comparison is that between Eq. (23) and Eq. (22), although the latter equation underestimates the transition length as noted above.

Assuming $\delta^*/\theta = 3.7$ at separation, Eq. (23) transforms to

$$\mathrm{Re}_{LT} = 6.9\ \mathrm{Re}_{\theta_s}^{1.5} \tag{24}$$

The 1.5 power dependence on $\mathrm{Re}_{\theta s}$ results from estimation of the dominant disturbance frequency from laminar stability theory, utilizing the conditions at separation; this is supported by the limited data available. The functional dependence on $\mathrm{Re}_{\theta s}$ is significantly different from that in Eq. (22), but the two expressions nevertheless produce values of Re_{LT} of the same order for the range of $\mathrm{Re}_{\theta s}$ commonly encountered. Exact equivalence occurs for $\mathrm{Re}_{\theta s} \simeq 160$, but a higher value would be expected if the underestimate in Re_{LT} from Eq. (22) were corrected.

Should it be desirable to retain a point transition model ($\mathrm{Re}_{LT} = 0$) for engineering purposes, Fig. 7 indicates that the downstream limit of constant pressure is the most appropriate location in well-developed short bubbles. This is precisely the location adopted by Horton and Roberts in their semi-empirical models.

Prediction of Transition Onset. The accurate prediction of transition onset is a particularly important factor in the computation of separation bubble flows. Mayle has followed the conventional method of dealing with separated flow transition by correlating $(\mathrm{Re}_x)_{st}$ in terms of the local conditions at separation (Eq. (11) and Fig. 19 of Mayle, 1991).

A significant characteristic of this correlation (and similar

ones published in the literature[2]) is that a zero length of separated laminar shear layer is impossible for $Re_{\theta s} \neq 0$. This means that an incipient short bubble cannot grow continuously from zero length as Reynolds number is reduced and transition onset moves downstream of a laminar separation point. Nor can a short bubble disappear continuously as Reynolds number is increased. This phenomenon can cause instability in low Reynolds number airfoil flow calculations due to bubbles appearing and disappearing on successive iterations.

Such behavior would not be unexpected with long bubbles, for which large hysteresis effects are well known. For short bubbles, however, it does not seem to accord with observations of slow, continuous changes in deflection, drag, and surface pressure perturbations as separated flow regions appear or disappear on an airfoil.

The apparent incompatibility of transition criteria for attached and separated flow raises the further question of upstream influence on the transition process in separation bubbles. The conditions upstream of separation will certainly be of major importance in low free-stream turbulence cases. Here, transition will rather be dependent on some average condition for the region of unstable flow, and a correlation in terms of separation conditions must imply some similarity in the upstream surface pressure distribution. This could not possibly apply for such diverse cases as leading edge and midchord bubbles.

The situation regarding transition onset in the presence of both strong deceleration and high free-stream disturbance level is less clear. However, it is significant that in the cases of transition on a compressor stator with a midchord bubble reported by Walker (1975), lengths of unstable laminar flow up to 40 percent of chord existed prior to separation. Here it is inevitable that considerable development of instability waves would have occurred prior to separation and transition. Similar observations have been reported in cascade tests by Citavy and Norbury (1977), where an increase in turbulence level from 0.35 to 4.4 percent altered the total length of unstable flow by around 20 percent only. The latter result, which is quite typical of other published data, is suggestive of turbulence having only a secondary influence on transition in this situation. This contrasts with the impression gained by viewing movements in transition onset relative to the laminar separation point, which would suggest a relatively larger influence of free-stream turbulence on transition.

Another significant aspect of the Citavy and Norbury high-turbulence case ($Tu = 4.4$) is that the observed suction surface transition location of $x/c \simeq 0.60$ at $Re_c = 1.87 \times 10^5$ differs markedly from that of $x/c \simeq 0.35$ predicted by Mayle's flat plate correlation, Eq. (8) above. This is only an isolated case, but it casts further doubt on the simplified method of predicting transition onset presented in Fig. 16 of Mayle (1991). It also stresses the point that the most important consideration is the quantitative accuracy with which a procedure can predict transition onset, rather than the apparent closeness of data points on a correlation plot. These considerations add further weight to Mayle's call for experiments to investigate separated-flow transition at high turbulence levels.

Separation Bubble Bursting and Long Bubbles. As regards separation bubble bursting, it should be noted that this most probably results from separation of the reattaching turbulent flow downstream of the bubble. Gaster's (1967) bursting criterion

$$(\lambda_\theta)_{\text{crit}} = f(Re_{\theta s}) \tag{25}$$

can be approximated by the line

$$(\theta/U)\,(dU/dx) = \text{const} \tag{26}$$

where the velocity gradient is evaluated over the length of the bubble. Equation (26) is well known as a separation criterion for equilibrium turbulent flow.

If the surface pressure distribution remains unaltered (a reasonable approximation for a flow with a short bubble) the laminar separation point will not alter the chord Reynolds number, as the value of λ_θ at each point on the surface will be a constant. The value of $(\theta/U)\,(dU/dx)$ in the region of the bubble, however, will progressively become more negative as Re_c is reduced. For sufficiently low Re_c the turbulent separation criterion will be exceeded and the turbulent shear layer will fail to reattach.

The subsequent flow behavior, and whether a long bubble is possible, will depend very much on the airfoil geometry and incidence. The major interaction of the long bubble with the surface pressure distribution is the most probable explanation for the altered transition onset distance shown in Fig. 19 of Mayle (1991); this further emphasizes the possible influence of flow upstream of separation on the transition process.

The larger values of Re_{sT} for long bubbles shown in Fig. 18 of Mayle (1991) reflect not an increased length to the end of transition but rather a greater distance to the point where turbulent mixing is felt at the surface. This is a consequence of the transitioning shear layer having moved further from the surface in the long bubble situation. A universal correlation for lengths of the constant pressure region cannot be expected with the strong viscous–inviscid interactions typical of long bubbles.

This point is emphasized by considering the Gaster (1967) data shown in Fig. 8. The shear layer turbulence observations show a fairly constant dimensionless distance to the end of transition, while the dimensionless length of the constant pressure region progressively exceeds this value in long bubbles as $Re_{\theta s}$ is reduced.

Conclusions

While much work remains to be done, there has been very encouraging progress in understanding the problem of transition in gas turbine engines in recent years. Mayle (1991) has given an excellent overview of these developments and their application to the design of engine components.

The author strongly endorses the general thrust of Mayle's analysis on the basis of intermittency theory and his suggestions for future work. In carrying out further observations it is urged that investigators should use measurements of intermittency to provide accurate quantitative data on the progress of transition and to permit a direct comparison with the results of turbulent spot theory. Experiments should be conducted with turbulence level Tu, Reynolds number $Re_{\theta t}$, pressure gradient parameter $\lambda_{\theta t}$, and acceleration parameter K_t being varied independently over as wide a range as possible so that the individual roles of these factors in the transition process can be more clearly distinguished.

Despite the fact that free-stream turbulence may exert a dominating influence in some situations, the author cannot agree with Mayle that transition information obtained at low free-stream turbulence levels is virtually useless for the gas turbine designer. The author and co-workers have found observations at low turbulence to provide useful physical insights, which have been beneficial in developing a more general understanding of transition phenomena.

[2]Horton's (1969) correlation indicates that the Reynolds number based on the length of the constant pressure region, l_1, should remain constant regardless of the value of $Re_{\theta s}$. Roberts (1975, 1980) modified this result by incorporating a turbulence function that reduces l_1, as Tu increases; however, $l_1 = 0$ is strictly possible only for $Tu = \infty$.

Mayle's (1991) Eqs. (11) and (10) indicate Re_{st} and Re_{sT} both increasing with $Re_{\theta s}$. These relations do not include any allowance for free-stream turbulence effects as they were derived almost entirely from low-turbulence data; Mayle intended them to provide a framework for future investigations at higher turbulence levels.

Nor can it be agreed that the length of transition in gas turbines depends only on the free-stream turbulence and pressure gradient. The foregoing discussion has indicated that boundary layer Reynolds number should also be an important parameter.

In relation to transition length, it has also been stressed that even mild positive pressure gradients cause a major shortening of the transition zone. Under these conditions, which are relatively more extensive than envisaged by Mayle, the influence of free-stream turbulence becomes much less important.

The basis of transition length correlations has been examined in some detail. This study has indicated that Mayle's technique may be considered a development of the Narasimha and Walker approaches, but one that is subject to some lack of generality in that it does not permit independent variation of Reynolds number and pressure gradient parameters that influence natural transition modes. The latter parameter may be significant in relation to spot production rates, even in a highly turbulent stream where bypass modes predominate.

Mayle's attempt to improve separation bubble modeling by incorporating a finite transition length is supported, but it has been pointed out that his assumption of the end of transition coinciding with the limit of the constant pressure region is incorrect. The author has outlined several other limitations of current models.

The author supports Mayle's call for further study into the periodic-unsteady transition phenomenon. Neither Mayle's nor the present examination have revealed any clear criterion for the onset of wake-induced transition, and the author's observations of transition on a compressor blade differ significantly from those of other workers in some important respects. The compressor blade data suggested that the transition location was not greatly influenced by either periodic or random disturbances associated with passing rotor wakes.

Taken overall, such differences of opinion as have been identified above largely reflect the differing backgrounds of Mayle and the present author, which are mainly in the turbine and compressor fields, respectively. The most stimulating aspect of Mayle's review for the present author has been its general consideration of transition phenomena in gas turbines from the turbine engineer's perspective. The final conclusion, therefore, is that the promotion of even closer interaction between compressor and turbine designers could act as a catalyst for further useful progress in the boundary layer transition field.

Acknowledgments

The author expresses appreciation to the Australian Research Council and to Rolls-Royce plc for their financial support and encouragement.

References

Addison, J. S., and Hodson, H. P., 1990a, "Unsteady Transition in an Axial Flow Turbine: Part 1—Measurements on the Turbine Rotor," ASME JOURNAL OF TURBOMACHINERY, Vol. 112, pp. 206–214.

Addison, J. S., and Hodson, H. P., 1990b, "Unsteady Transition in an Axial Flow Turbine: Part 2—Cascade Measurements and Modeling," ASME JOURNAL OF TURBOMACHINERY, Vol. 112, pp. 215–221.

Addison, J. S., and Hodson, H. P., 1992, "Modeling of Unsteady Transitional Boundary Layers," ASME JOURNAL OF TURBOMACHINERY, Vol. 114, pp. 580–589.

Cebeci, T., and Smith, A. M. O., 1974, *Analysis of Turbulent Boundary Layers*, Academic Press, New York.

Chen, K. K., and Thyson, N. A., 1971, "Extension of Emmons' Spot Theory to Flows on Blunt Bodies," *AIAA J.*, Vol. 9, pp. 821–825.

Citavy, J., and Norbury, J. F., 1977, "The Effect of Reynolds Number and Turbulence Intensity on the Performance of a Compressor Cascade With Prescribed Velocity Distribution," *J. Mech. Eng. Sci.*, Vol. 19, pp. 93–100.

Dey, J., and Narasimha, R., 1984, "Spot Formation Rate in Incompressible Constant-Pressure Boundary Layers," Indian Inst. Sci. Dept. Aero. Eng., Report No. 84 FM 11.

Dhawan, S., and Narasimha, R., 1958, "Some Properties of Boundary Layer Flow During the Transition From Laminar to Turbulent Motion," *J. Fluid Mech.*, Vol. 3, pp. 418–436.

Dong, Y., and Cumpsty, N. A., 1990a, "Compressor Blade Boundary Layers: Part 1—Test Facility and Measurement With No Incident Wakes," ASME JOURNAL OF TURBOMACHINERY, Vol. 112, pp. 222–230.

Dong, Y., and Cumpsty, N. A., 1990b, "Compressor Blade Boundary Layers: Part 2—Measurements With Incident Wakes," ASME JOURNAL OF TURBOMACHINERY, Vol. 112, pp. 231–240.

Emmons, H. W., 1951, "The Laminar–Turbulent Transition in a Boundary Layer—Part 1," *J. Aero. Sci.*, Vol. 18, pp. 490–498.

Evans, R. L., 1975, "Turbulence and Unsteadiness Measurements Downstream of a Moving Blade Row," ASME *Journal of Engineering for Power*, Vol. 97, pp. 131–139.

Gaster, M., 1967, "The Structure and Behavior of Laminar Separation Bubbles," United Kingdom, National Physical Laboratory, Aero Report 1181 (revised); also ARC R & M 3595.

Gostelow, J. P., 1989, "Adverse Pressure Gradient Effects on Boundary Layer Transition in a Turbulent Free-Stream," *Proc. 9th Int. Symp. Air Breathing Engines*, Athens, pp. 1299–1306.

Gostelow, J. P., and Dey, J., 1991, "Spot-Formation Rates in Transitional Boundary Layers Under Zero and Adverse Pressure Gradients," *Proc. Boundary Layer Transition and Control Conference*, Cambridge, United Kingdom, pp. 29:1–29:7.

Gostelow, J. P., Blunden, A. R., and Walker, G. J., 1992, "Effects of Free-Stream Turbulence and Adverse Pressure Gradients on Boundary Layer Transition," ASME Paper No. 92-GT-380, accepted for publication in the ASME JOURNAL OF TURBOMACHINERY.

Horton, H. P., 1969, "A Semi-empirical Theory for the Growth and Bursting of Laminar Separation Bubbles," UK Aeronautical Research Council, CP 1073.

Loehrke, R. I., Morkovin, M. V., and Fejer, A. A., 1975, "REVIEW—Transition in Nonreversing Oscillating Boundary Layers," ASME *Journal of Fluids Engineering*, Vol. 97, pp. 534–549.

Mayle, R. E., and Dullenkopf, K., 1990, "A Theory for Wake-Induced Transition," ASME JOURNAL OF TURBOMACHINERY, Vol. 112, pp. 188–195.

Mayle, R. E., 1991, "The Role of Laminar–Turbulent Transition in Gas Turbine Engines," ASME JOURNAL OF TURBOMACHINERY, Vol. 113, pp. 509–537.

Miller, J. A., and Fejer, A. A., 1964, "Transition Phenomena in Oscillating Boundary Layer Flows," *J. Fluid Mech.*, Vol. 18, pp. 438–449.

Narasimha, R., 1978, "A Note on Certain Turbulent Spot and Burst Frequencies," Indian Inst. Sci., Dept. Aero. Eng., Report No. 78 FM 10.

Narasimha, R., 1985, "The Laminar–Turbulent Transition Zone in the Boundary Layer," *Prog. Aerospace Sci.*, Vol. 22, pp. 29–80.

Obremski, H. J., and Fejer, A. A., 1967, "Transition in Oscillating Boundary Layer Flows," *J. Fluid Mech.*, Vol. 29, pp. 93–111.

Roberts, W. B., 1975, "The Effect of Reynolds Number and Laminar Separation on Axial Cascade Performance," ASME *Journal of Engineering for Power*, Vol. 97, pp. 261–274.

Roberts, W. B., 1980, "Calculation of Laminar Separation Bubbles and Their Effect on Airfoil Performance," *AIAA J.*, Vol. 18, pp. 25–31.

Walker, G. J., 1974, "The Unsteady Nature of Boundary Layer Transition on an Axial-Flow Compressor Blade," ASME Paper No. 74-GT-135.

Walker, G. J., 1975, "Observations of Separated Laminar Flow on Axial Compressor Blading," ASME Paper No. 75-GT-63.

Walker, G. J., 1987, "Transitional Flow on Axial Turbomachine Blading," *AIAA J.*, Vol. 27, pp. 595–602.

Walker, G. J., Subroto, P. H., and Platzer, M. F., 1988, "Transition Modeling Effects on Viscous/Inviscid Interaction Analysis of Low Reynolds Number Airfoil Flows Involving Laminar Separation Bubbles," ASME Paper No. 88-GT-32.

Walker, G. J., 1989, "Modeling of Transitional Flow in Laminar Separation Bubbles," *Proc. 9th Int. Symp. Air Breathing Engines*, Athens, Greece, pp. 539–548.

Walker, G. J., and Gostelow, J. P., 1990, "Effects of Adverse Pressure Gradients on the Nature and Length of Boundary Layer Transition," ASME JOURNAL OF TURBOMACHINERY, Vol. 112, pp. 196–205.

Nor can it be agreed that the length of transition in gas turbines depends only on the free-stream turbulence and pressure gradient. The foregoing discussion has indicated that boundary layer Reynolds number should also be an important parameter.

In relation to transition length, it has also been stressed that even mild positive pressure gradients cause a major shortening of the transition zone. Under these conditions, which are relatively more extensive than envisaged by Mayle, the influence of free-stream turbulence becomes much less important.

The basis of transition length correlations has been examined in some detail. This study has indicated that Mayle's technique may be considered a development of the Narasimha and Walker approaches, but one that is subject to some lack of generality in that it does not permit independent variation of Reynolds number and pressure gradient parameters that influence natural transition modes. The latter parameter may be significant in relation to spot production rates, even in a highly turbulent stream where bypass modes predominate.

Mayle's attempt to improve separation bubble modeling by incorporating a finite transition length is supported, but it has been pointed out that his assumption of the end of transition coinciding with the limit of the constant pressure region is incorrect. The author has outlined several other limitations of current models.

The author supports Mayle's call for further study into the periodic-unsteady transition phenomenon. Neither Mayle's nor the present examination have revealed any clear criterion for the onset of wake-induced transition, and the author's observations of transition on a compressor blade differ significantly from those of other workers in some important respects. The compressor blade data suggested that the transition location was not greatly influenced by either periodic or random disturbances associated with passing rotor wakes.

Taken overall, such differences of opinion as have been identified above largely reflect the differing backgrounds of Mayle and the present author, which are mainly in the turbine and compressor fields, respectively. The most stimulating aspect of Mayle's review for the present author has been its general consideration of transition phenomena in gas turbines from the turbine engineer's perspective. The final conclusion, therefore, is that the promotion of even closer interaction between compressor and turbine designers could act as a catalyst for further useful progress in the boundary layer transition field.

Acknowledgments

The author expresses appreciation to the Australian Research Council and to Rolls-Royce plc for their financial support and encouragement.

References

Addison, J. S., and Hodson, H. P., 1990a, "Unsteady Transition in an Axial Flow Turbine: Part 1—Measurements on the Turbine Rotor," ASME JOURNAL OF TURBOMACHINERY, Vol. 112, pp. 206–214.

Addison, J. S., and Hodson, H. P., 1990b, "Unsteady Transition in an Axial Flow Turbine: Part 2—Cascade Measurements and Modeling," ASME JOURNAL OF TURBOMACHINERY, Vol. 112, pp. 215–221.

Addison, J. S., and Hodson, H. P., 1992, "Modeling of Unsteady Transitional Boundary Layers," ASME JOURNAL OF TURBOMACHINERY, Vol. 114, pp. 580–589.

Cebeci, T., and Smith, A. M. O., 1974, *Analysis of Turbulent Boundary Layers*, Academic Press, New York.

Chen, K. K., and Thyson, N. A., 1971, "Extension of Emmons' Spot Theory to Flows on Blunt Bodies," *AIAA J.*, Vol. 9, pp. 821–825.

Citavy, J., and Norbury, J. F., 1977, "The Effect of Reynolds Number and Turbulence Intensity on the Performance of a Compressor Cascade With Prescribed Velocity Distribution," *J. Mech. Eng. Sci.*, Vol. 19, pp. 93–100.

Dey, J., and Narasimha, R., 1984, "Spot Formation Rate in Incompressible Constant-Pressure Boundary Layers," Indian Inst. Sci. Dept. Aero. Eng., Report No. 84 FM 11.

Dhawan, S., and Narasimha, R., 1958, "Some Properties of Boundary Layer Flow During the Transition From Laminar to Turbulent Motion," *J. Fluid Mech.*, Vol. 3, pp. 418–436.

Dong, Y., and Cumpsty, N. A., 1990a, "Compressor Blade Boundary Layers: Part 1—Test Facility and Measurement With No Incident Wakes," ASME JOURNAL OF TURBOMACHINERY, Vol. 112, pp. 222–230.

Dong, Y., and Cumpsty, N. A., 1990b, "Compressor Blade Boundary Layers: Part 2—Measurements With Incident Wakes," ASME JOURNAL OF TURBOMACHINERY, Vol. 112, pp. 231–240.

Emmons, H. W., 1951, "The Laminar–Turbulent Transition in a Boundary Layer—Part 1," *J. Aero. Sci.*, Vol. 18, pp. 490–498.

Evans, R. L., 1975, "Turbulence and Unsteadiness Measurements Downstream of a Moving Blade Row," ASME *Journal of Engineering for Power*, Vol. 97, pp. 131–139.

Gaster, M., 1967, "The Structure and Behavior of Laminar Separation Bubbles," United Kingdom, National Physical Laboratory, Aero Report 1181 (revised); also ARC R & M 3595.

Gostelow, J. P., 1989, "Adverse Pressure Gradient Effects on Boundary Layer Transition in a Turbulent Free-Stream," *Proc. 9th Int. Symp. Air Breathing Engines*, Athens, pp. 1299–1306.

Gostelow, J. P., and Dey, J., 1991, "Spot-Formation Rates in Transitional Boundary Layers Under Zero and Adverse Pressure Gradients," *Proc. Boundary Layer Transition and Control Conference*, Cambridge, United Kingdom, pp. 29:1–29:7.

Gostelow, J. P., Blunden, A. R., and Walker, G. J., 1992, "Effects of Free-Stream Turbulence and Adverse Pressure Gradients on Boundary Layer Transition," ASME Paper No. 92-GT-380, accepted for publication in the ASME JOURNAL OF TURBOMACHINERY.

Horton, H. P., 1969, "A Semi-empirical Theory for the Growth and Bursting of Laminar Separation Bubbles," UK Aeronautical Research Council, CP 1073.

Loehrke, R. I., Morkovin, M. V., and Fejer, A. A., 1975, "REVIEW—Transition in Nonreversing Oscillating Boundary Layers," ASME *Journal of Fluids Engineering*, Vol. 97, pp. 534–549.

Mayle, R. E., and Dullenkopf, K., 1990, "A Theory for Wake-Induced Transition," ASME JOURNAL OF TURBOMACHINERY, Vol. 112, pp. 188–195.

Mayle, R. E., 1991, "The Role of Laminar–Turbulent Transition in Gas Turbine Engines," ASME JOURNAL OF TURBOMACHINERY, Vol. 113, pp. 509–537.

Miller, J. A., and Fejer, A. A., 1964, "Transition Phenomena in Oscillating Boundary Layer Flows," *J. Fluid Mech.*, Vol. 18, pp. 438–449.

Narasimha, R., 1978, "A Note on Certain Turbulent Spot and Burst Frequencies," Indian Inst. Sci., Dept. Aero. Eng., Report No. 78 FM 10.

Narasimha, R., 1985, "The Laminar–Turbulent Transition Zone in the Boundary Layer," *Prog. Aerospace Sci.*, Vol. 22, pp. 29–80.

Obremski, H. J., and Fejer, A. A., 1967, "Transition in Oscillating Boundary Layer Flows," *J. Fluid Mech.*, Vol. 29, pp. 93–111.

Roberts, W. B., 1975, "The Effect of Reynolds Number and Laminar Separation on Axial Cascade Performance," ASME *Journal of Engineering for Power*, Vol. 97, pp. 261–274.

Roberts, W. B., 1980, "Calculation of Laminar Separation Bubbles and Their Effect on Airfoil Performance," *AIAA J.*, Vol. 18, pp. 25–31.

Walker, G. J., 1974, "The Unsteady Nature of Boundary Layer Transition on an Axial-Flow Compressor Blade," ASME Paper No. 74-GT-135.

Walker, G. J., 1975, "Observations of Separated Laminar Flow on Axial Compressor Blading," ASME Paper No. 75-GT-63.

Walker, G. J., 1987, "Transitional Flow on Axial Turbomachine Blading," *AIAA J.*, Vol. 27, pp. 595–602.

Walker, G. J., Subroto, P. H., and Platzer, M. F., 1988, "Transition Modeling Effects on Viscous/Inviscid Interaction Analysis of Low Reynolds Number Airfoil Flows Involving Laminar Separation Bubbles," ASME Paper No. 88-GT-32.

Walker, G. J., 1989, "Modeling of Transitional Flow in Laminar Separation Bubbles," *Proc. 9th Int. Symp. Air Breathing Engines*, Athens, Greece, pp. 539–548.

Walker, G. J., and Gostelow, J. P., 1990, "Effects of Adverse Pressure Gradients on the Nature and Length of Boundary Layer Transition," ASME JOURNAL OF TURBOMACHINERY, Vol. 112, pp. 196–205.

DISCUSSION

N. A. Cumpsty[3]

We are fortunate to have the present discussion paper by G. J. Walker, who has done much to improve our understanding of transition in turbomachines, a topic that is now arguably the single biggest impediment to the improvement of numerical methods for the calculation of turbomachinery flows. In his IGTI Scholar Lecture R. E. Mayle did an excellent job of sifting and collating information and ideas on transition to make them useful to the turbomachine aerodynamicist. In

[3]Whittle Laboratory, Cambridge University, Cambridge, United Kingdom.

providing definite statements, and in simplifying the problem to make it more amenable, it would have been improbable if he had not made statements that others feel need refining or correcting. With Mayle's lecture as its focus Walker has produced an interesting and stimulating discussion, and it is to be hoped that this will spark further attention to the subject of transition.

I have two substantive points to make. The first relates to the inception of turbulence by the passage of wakes from upstream. Walker uses his results, shown here as Fig. 4, to claim that the wake turbulence is not initiating the boundary layer turbulence. He comes to the conclusion because at this chordwise position ($x/c = 0.50$) the boundary layer is turbulent at times where the rear part of the wake is over it and in the rear of the wake the turbulence is reduced. Actually this is just what one would expect if the wake turbulence were initiating the boundary layer turbulence at some position further upstream; because the wake is convected at the local free-stream velocity but the boundary layer spots travel at about 0.85 times free-stream velocity, the wake moves ahead of the boundary layer that turbulence initiates. This is demonstrated on compressor blades by, for example, Dong and Cumpsty (1990a, 1990b) and Li (1990). An aspect of this that remains a mystery is why the wake can initiate turbulence near the leading edge of the blade, where the Reynolds number is low, but then appears unable to do so farther back, but instead travels passively over the laminar boundary underneath.

The second point, which is directed at both the present paper by Walker and the earlier one by Mayle (1991), relates to transition taking place in separation bubbles. The discussion of this topic seems to take place in terms of a very limited group of papers, principally Gaster (1967), Horton (1969), and Roberts (1975). There are other papers it would be useful to involve in the discussion and in interpreting the behavior. I would particularly draw attention to the work of Arena and Mueller (1980), where flow visualization was used to determine explicitly the position of the start of transition and the mean position of reattachment.

Additional References

Arena, A. V., and Mueller, T. J., 1980, "Laminar Separation, Transition and Turbulent Reattachment Near the Leading Edge of Airfoils," *AIAA Journal*, Vol. 18, pp. 743–747.

Li, Y. S., 1990, "Mixing in Axial Compressors," PhD Dissertation, Cambridge University, United Kingdom.

Author's Closure

The author thanks N. A. Cumpsty for his comments and welcomes the opportunity to expand further on the two substantive points that have been raised.

The question of how the wake passage initiates turbulence is a critical one. There is no doubt that turbulent breakdown in the boundary layer may coincide with the passing wake disturbance, as many other authors (including Cumpsty and co-workers) have observed. It is a moot point, however, whether such breakdowns are due to the direct action of wake turbulence, the periodic unsteadiness associated with the wake, or interaction effects resulting from the wake passage over the blade (both potential flow and viscous–inviscid interactions).

Figure 4 of the paper (taken from Walker, 1974) was included to support the view that turbulence inception might be induced indirectly by the wake perturbations or associated interaction effects. Cumpsty correctly points out that this single figure cannot conclusively establish that the initial breakdown did not coincide with the wake passage at some point further upstream. Additional material from Walker (1974) was included in the presentation of the paper to indicate that the instant immediately following the wake passage was the favored time for turbulent breakdown. Stronger evidence for the existence of indirect mechanisms is provided by the more recent results of Orth (1992) and Walker and Solomon (1992).

Orth's (1992) observations are particularly interesting in that they seem to indicate the existence of both direct and indirect mechanisms in the same experiment. Here, the boundary layer on a flat plate was subjected to periodic disturbances from the wakes of a rotating cascade of bars. The stronger wakes of the nearer bars generated turbulent spots coincident with the wakes at a position close to the plate leading edge. The weaker wakes of bars in the far positions initiated transition much later, with breakdown definitely lagging behind the wake and no direct connection between the boundary layer and wake turbulence. Whether this breakdown resulted from periodic unsteadiness or from ingestion of wake turbulence into the boundary layer (as Orth argues), the mechanism is clearly indirect. Perhaps the most telling argument for an indirect mechanism is the mysterious phenomenon (noted by both Cumpsty and Orth) of the passing wake traveling passively over the laminar boundary layer after initiating turbulence near the leading edge of a blade or plate.

On the second discussion point, the author strongly agrees with Cumpsty on the need for a better physical understanding of transition phenomena in laminar separation bubbles. Combined flow visualization and hot-wire studies, such as that of Arena and Mueller (1980), have made an important contribution here. These workers note, however, that pinpointing transition onset from flow visualization observations is rather difficult, and the present author considers intermittency measurements a better tool for this purpose.

The main reason for focusing on the limited group of papers from Gaster (1967), Horton (1969), and Roberts (1975) was that, despite their known limitations, these semi-empirical models of laminar separation bubble behavior have been the mainstay of engineering calculation methods for around two decades. The paper of Arena and Mueller, for all its useful physical insights, did no more than agree with these existing prediction methods for short bubbles.

References

Orth, U., 1992, "Unsteady Boundary Layer Transition in Flow Periodically Disturbed by Wakes," ASME Paper No. 92-GT-283; ASME JOURNAL OF TURBOMACHINERY, in press.

Walker, G. J., and Solomon, W. J., 1992, "Turbulent Intermittency Measurement on an Axial Compressor Blade," *11th Australasian Fluid Mechanics Conference*, Hobart, Australia, Vol. II, pp. 1277–1280.

providing definite statements, and in simplifying the problem to make it more amenable, it would have been improbable if he had not made statements that others feel need refining or correcting. With Mayle's lecture as its focus Walker has produced an interesting and stimulating discussion, and it is to be hoped that this will spark further attention to the subject of transition.

I have two substantive points to make. The first relates to the inception of turbulence by the passage of wakes from upstream. Walker uses his results, shown here as Fig. 4, to claim that the wake turbulence is not initiating the boundary layer turbulence. He comes to the conclusion because at this chordwise position ($x/c = 0.50$) the boundary layer is turbulent at times where the rear part of the wake is over it and in the rear of the wake the turbulence is reduced. Actually this is just what one would expect if the wake turbulence were initiating the boundary layer turbulence at some position further upstream; because the wake is convected at the local free-stream velocity but the boundary layer spots travel at about 0.85 times free-stream velocity, the wake moves ahead of the boundary layer that turbulence initiates. This is demonstrated on compressor blades by, for example, Dong and Cumpsty (1990a, 1990b) and Li (1990). An aspect of this that remains a mystery is why the wake can initiate turbulence near the leading edge of the blade, where the Reynolds number is low, but then appears unable to do so farther back, but instead travels passively over the laminar boundary underneath.

The second point, which is directed at both the present paper by Walker and the earlier one by Mayle (1991), relates to transition taking place in separation bubbles. The discussion of this topic seems to take place in terms of a very limited group of papers, principally Gaster (1967), Horton (1969), and Roberts (1975). There are other papers it would be useful to involve in the discussion and in interpreting the behavior. I would particularly draw attention to the work of Arena and Mueller (1980), where flow visualization was used to determine explicitly the position of the start of transition and the mean position of reattachment.

Additional References

Arena, A. V., and Mueller, T. J., 1980, "Laminar Separation, Transition and Turbulent Reattachment Near the Leading Edge of Airfoils," *AIAA Journal*, Vol. 18, pp. 743–747.

Li, Y. S., 1990, "Mixing in Axial Compressors," PhD Dissertation, Cambridge University, United Kingdom.

Author's Closure

The author thanks N. A. Cumpsty for his comments and welcomes the opportunity to expand further on the two substantive points that have been raised.

The question of how the wake passage initiates turbulence is a critical one. There is no doubt that turbulent breakdown in the boundary layer may coincide with the passing wake disturbance, as many other authors (including Cumpsty and co-workers) have observed. It is a moot point, however, whether such breakdowns are due to the direct action of wake turbulence, the periodic unsteadiness associated with the wake, or interaction effects resulting from the wake passage over the blade (both potential flow and viscous–inviscid interactions).

Figure 4 of the paper (taken from Walker, 1974) was included to support the view that turbulence inception might be induced indirectly by the wake perturbations or associated interaction effects. Cumpsty correctly points out that this single figure cannot conclusively establish that the initial breakdown did not coincide with the wake passage at some point further upstream. Additional material from Walker (1974) was included in the presentation of the paper to indicate that the instant immediately following the wake passage was the favored time for turbulent breakdown. Stronger evidence for the existence of indirect mechanisms is provided by the more recent results of Orth (1992) and Walker and Solomon (1992).

Orth's (1992) observations are particularly interesting in that they seem to indicate the existence of both direct and indirect mechanisms in the same experiment. Here, the boundary layer on a flat plate was subjected to periodic disturbances from the wakes of a rotating cascade of bars. The stronger wakes of the nearer bars generated turbulent spots coincident with the wakes at a position close to the plate leading edge. The weaker wakes of bars in the far positions initiated transition much later, with breakdown definitely lagging behind the wake and no direct connection between the boundary layer and wake turbulence. Whether this breakdown resulted from periodic unsteadiness or from ingestion of wake turbulence into the boundary layer (as Orth argues), the mechanism is clearly indirect. Perhaps the most telling argument for an indirect mechanism is the mysterious phenomenon (noted by both Cumpsty and Orth) of the passing wake traveling passively over the laminar boundary layer after initiating turbulence near the leading edge of a blade or plate.

On the second discussion point, the author strongly agrees with Cumpsty on the need for a better physical understanding of transition phenomena in laminar separation bubbles. Combined flow visualization and hot-wire studies, such as that of Arena and Mueller (1980), have made an important contribution here. These workers note, however, that pinpointing transition onset from flow visualization observations is rather difficult, and the present author considers intermittency measurements a better tool for this purpose.

The main reason for focusing on the limited group of papers from Gaster (1967), Horton (1969), and Roberts (1975) was that, despite their known limitations, these semi-empirical models of laminar separation bubble behavior have been the mainstay of engineering calculation methods for around two decades. The paper of Arena and Mueller, for all its useful physical insights, did no more than agree with these existing prediction methods for short bubbles.

References

Orth, U., 1992, "Unsteady Boundary Layer Transition in Flow Periodically Disturbed by Wakes," ASME Paper No. 92-GT-283; ASME JOURNAL OF TURBOMACHINERY, in press.

Walker, G. J., and Solomon, W. J., 1992, "Turbulent Intermittency Measurement on an Axial Compressor Blade," *11th Australasian Fluid Mechanics Conference*, Hobart, Australia, Vol. II, pp. 1277–1280.

Low Aspect Ratio Transonic Rotors: Part 1—Baseline Design and Performance

C. H. Law
Wright Laboratory,
Wright-Patterson AFB, OH 45433

A. R. Wadia
GE Aircraft Engines,
Cincinnati, OH 45215

The analytical design and experimental test of a single-stage transonic axial-flow compressor are described. This design is the baseline of a compressor design study in which several blade design parameters have been systematically varied to determine their independent effects on compressor performance. The baseline design consisted of ruggedizing an existing compressor design that demonstrated outstanding aerodynamic performance, to correct some undesirable aeromechanical characteristics. The design study was performed by varying only one design parameter at a time, keeping the other design variables as close as possible to the baseline design. Specific design parameters of interest were those for which very few data were available to determine their sensitivity on compressor performance. This paper describes the baseline compressor design and its experimental performance. A detailed definition and flow analysis of the baseline design test point (used as the basis for all subsequent design variations) are provided.

Introduction

Recent trends in aircraft turbine engine design have led to significant reductions in the aspect ratios of fans and compressors. This has brought with it a greatly reduced engine weight, cost, and parts count with improved ruggedness and aeroelastic stability. The primary design objectives that contribute most to the reduction in aspect ratio are an increase in flow per frontal or annulus area and reducing the number of stages used to achieve a given pressure ratio. Reducing the number of stages to reduce the weight of the compressor inevitably means that each stage must do more work. Maximizing the work per stage while retaining acceptable overall performance has been the biggest challenge for the aircraft engine designer.

One way to increase work per stage is to increase wheel speed and swirl velocity and, therefore, the relative Mach number of the rotor. The relative Mach number may be increased by maximizing the throughflow velocity. The key to a successful design rests with efficient handling of the high relative Mach numbers to limit losses associated with shock waves. Adequate stall margin may be maintained by choosing appropriate blade shapes and surface contours.

In 1971, the Air Force Aero Propulsion Laboratory (now the Aero Propulsion and Power Directorate of the Wright Laboratory) initiated a program to develop an axial compressor for a turbo-jet-type aircraft turbine engine similar to a J-79. The compressor was designed with less than half the current number of stages and a higher flow per frontal area than had ever been achieved by any U.S. production engine. The original design objectives for the compressor were to produce a pressure ratio of 12:1 in five stages with an overall efficiency of 84 percent and reasonable surge margin. The first rotor tip speed was to be 1500 ft/s (457 m/s) and the flow rate to be achieved per unit frontal area was 39.7 lb/s/ft^2 (192.5 kg/s/m^2). A design philosophy was adopted that used more loading in the first stage and correspondingly less loading in the downstream stages. The design pressure ratio and efficiency for the first stage were 1.912 and 83 percent, respectively. Arbitrary blade and vane camber line specifications were optimized using the axial static pressure variations. Swept stator leading edges and variable blade-to-platform fillet radii were used to minimize losses. A detailed description of the design philosophy and characteristics of the original design was provided by Wennerstrom and Frost (1976).

The first-stage design had a constant rotor tip diameter of 17 in. (43.2 cm) and a corrected flow of 62.6 lb/sec (28.4 kg/s). No inlet guide vanes were employed and the stator vanes were fixed and designed as the load bearing structure that would support the front bearing in the real engine. The rotor structure was designed to be adequate to meet the design objectives, but not so rugged as to compromise the aerodynamic efficiency.

The original first-stage design was tested in the 2000-hp Compressor Aerodynamic Research Laboratory at Wright-Patterson Air Force Base, OH, in 1976. The map of stage performance from 40 to 100 percent corrected speed for the original compressor is shown in Fig. 1. At design speed and pressure ratio, the flow rate and efficiency exceeded the design values by 0.8 and 2.6 percent, respectively. At design speed, efficiency peaked at 88.2 percent (5.2 percentage points higher than design). At 90 percent corrected speed, efficiency peaked at 90.9 percent. At design speed, approximately 11 percent

Contributed by the International Gas Turbine Institute and presented at the 37th International Gas Turbine and Aeroengine Congress and Exposition, Cologne, Germany, June 1–4, 1992. Manuscript received by the International Gas Turbine Institute February 11, 1992. Paper No. 92-GT-185. Associate Technical Editor: L. S. Langston.

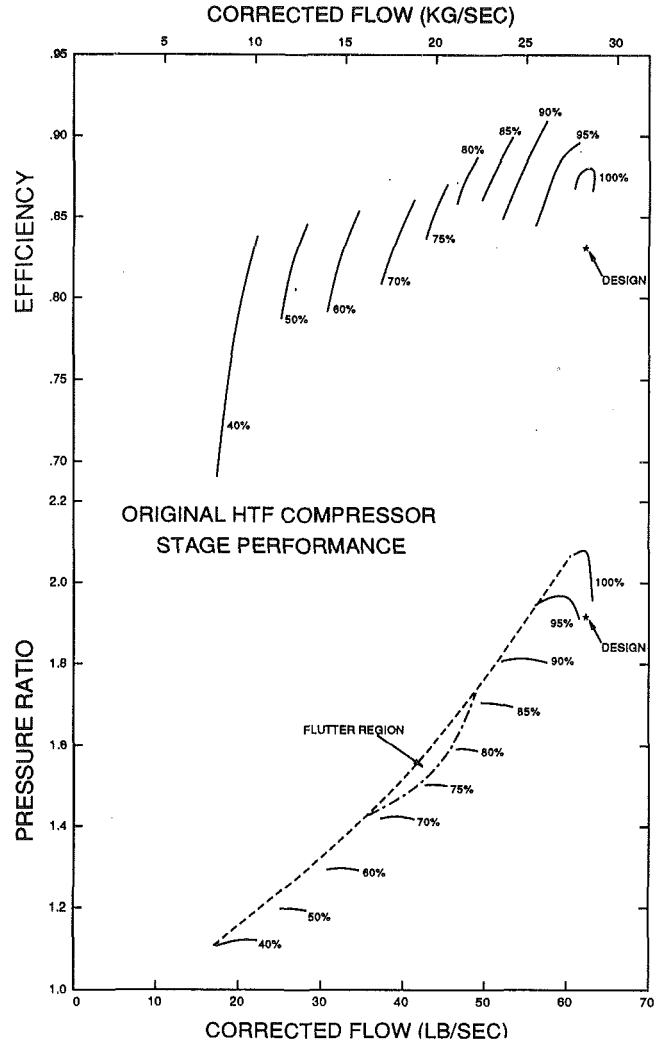

Fig. 1 Original high-throughflow compressor stage performance

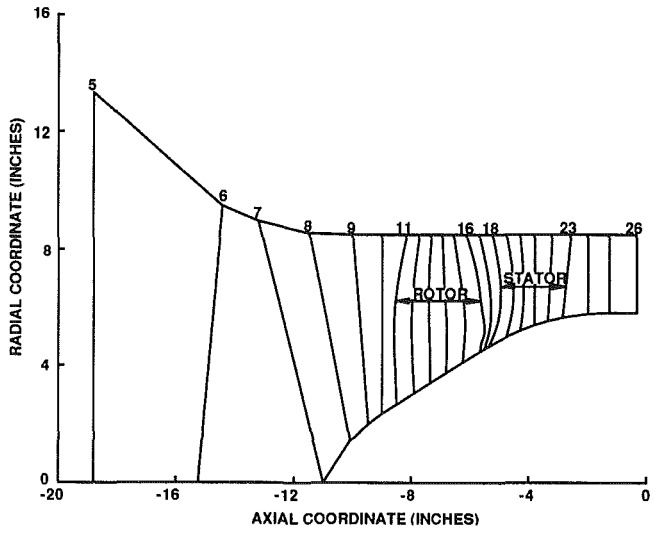

Fig. 2 Computational geometry and computing station definition

stall margin remained beyond design pressure ratio. A detailed description of these test results was presented by Wennerstrom et al. (1976).

During the original design tests, transonic stall flutter was experienced at the first bending frequency at 75–85 percent speed. At speeds above and below this, conventional stalls were experienced. This instability occurred in an operating speed range critical for supersonic fighter applications. Also, the rotor leading edge radii were judged by potential manufacturers as unrealistic relative to foreign object damage potential in many applications. For these reasons, a rotor redesign effort was initiated. This additional effort was considered worthwhile due to the outstanding aerodynamic performance characteristics demonstrated by the original design and the significant interest generated within the turbomachinery community toward several possible applications. It was considered highly feasible that the same procedures used to design the original rotor could be used to design a more rugged version with similar outstanding performance.

Aerodynamic Design

A rotor redesign effort was initiated with a goal of achieving a structurally enhanced rotor with improved foreign object damage resistance and decreased vibrational sensitivity. Minimum impact on the aerodynamic performance of the original design was desired. Specifically, the rotor leading and trailing edge thicknesses were doubled and the rotor maximum thickness-to-chord ratio distribution was varied. As little of the remaining original aerodynamic design was modified as possible. Only the meridional distribution of work internal to the rotor and the rotor hub contour were modified to compensate for the new rotor blade metal blockage distribution. The detailed aerodynamic redesign was accomplished using the same computer program used in the original design. A detailed description of the rotor redesign was provided by Wennerstrom and Buzzell (1979).

The detailed aerodynamic design was accomplished with an early version of the computer program described by Hearsey (1975), employing the streamline curvature method of computation. The computational mesh included curved computing stations, as illustrated in Fig. 2 (for simplicity, only the hub and case streamlines are shown). The computational mesh included 21 streamsurfaces and 26 computing stations: 10 stations in the compressor inlet, one station at each blade/vane edge, four stations internal to each blade/vane row, one station between the rotor and stator, and three stations in the stage exit.

The detailed design computer program obtains an aerodynamic solution through an iterative numerical procedure that simultaneously solves the equations of momentum, continuity, and energy at each computing station in sequence through the compressor. After each computational pass through the compressor, the streamline locations at each computing station are adjusted and the procedure is repeated until the changes occurring from one pass to the next fall within a specified tolerance. The analysis assumes the flow to be axisymmetric and described by a series of concentric streamsurfaces across which no mass or momentum is transferred. The full radial equilibrium version of the momentum equation is satisfied at each streamsurface/computing-station intersection and includes the effects of streamline curvature and entropy gradients. At computing stations located within blade/vane rows, blade force terms are included in the momentum equation as a body-force field assumed to act in a direction everywhere normal to the three-dimensional surface formed by the stacked camber lines of each blade/vane row.

The detailed design computational scheme used computing stations internal to the blade/vane rows. An optimization criterion was developed to select the best airfoil geometries capable of satisfying the same end conditions. A criterion was developed based on minimizing the airfoil losses. This was accomplished by minimizing the meridional gradient of static pressure in a circumferential average sense. The design objective was to generate a meridional gradient of static pressure that was approximately linear through the first three quarters of the blade/vane. The static pressure gradient tapered off

toward the trailing edge, because an airfoil cannot sustain loading all the way to its trailing edge. This approach was used for both the rotor and the stator, by specifying the meridional distributions of total enthalpy through the rotor and angular momentum through the stator.

Using the assumed work distributions, the aerodynamic flowfield analysis produces a set of relative flow angles to which, after correcting for the internal deviation angle distribution, the airfoils are matched. This procedure is iteratively repeated until the optimization criteria are met over the full span. Airfoil metal blockages used in the aerodynamic analysis are set to be consistent with those calculated by the blade/vane generation program during the iteration. The computing stations used to represent the blade/vane leading and trailing edges are closely matched to the envelope of the stacked airfoil. To avoid peculiarly shaped airfoils having undesirable mechanical and/or aerodynamic properties, the distributions of work vary smoothly both along streamsurfaces and along computing stations. Distributions that depart greatly from a linear distribution along streamsurfaces are not usually required.

The through-the-blade-row design technique described above requires several additional assumptions to be made within each blade/vane row. These are the spatial distributions of deviation angle, blockage, and loss, listed in decreasing order of importance. The assumption was made that the deviation angle should equal the incidence angle at the leading edge and the conventional deviation angle (predicted by empirical correlations) at the trailing edge. The deviation angle should be extremely small in the covered portion of the passage and have a rate of change approximately equal and opposite to the rate of change of the camber line angle at the trailing edge. The deviation angles were predicted at the trailing edges for blades/vanes according to the method described by Johnson et al. (1965) (Eqs. (269) and (271)). A shape correction factor of 1.0 was used for both the rotor and stator and all predicted values for the rotor were increased by 2.0 deg to match existing relevant experimental data better.

The final choice for leading edge incidence was based on results obtained from cascade experiments and inviscid time-dependent cascade plane analyses. The relative inlet Mach number to the rotor is supersonic over most of the span and flow through the rotor is controlled primarily by the wave pattern propagated upstream. To achieve the desired design flow, the final rotor design assumed a constant 2.0 deg of incidence with respect to the suction surface. A sonic absolute Mach number and high solidity at the hub of the stator were conducive to choking. A positive incidence of 5.0 deg with respect to the camber line was assumed for the stator hub. Highly cambered subsonic cascade sections favor low to negative incidence angles. High incidence angles were expected at the stator tip as the stage was throttled toward stall. For these reasons, zero degrees of incidence with respect to the camber line was assumed for the stator tip. The stator incidence angle was linearly varied from hub to tip in the final design.

The absolute level of blockage at each computing station was calculated according to a simplified formula for a turbulent boundary layer on a flat plate. Meridional velocity and length were substituted for absolute velocity and path length as described by Jansen (1967). Although the computation was originally conceived as an annulus wall blockage model, it was employed here as a wake blockage model. The blockage was linearly distributed from hub to tip in proportion to the spanwise solidity variation. Midspan blockage estimated in this manner rose from 1.0 percent at the rotor leading edge to 6.0 percent at the rotor trailing edge, and remained at 6.0 percent throughout the stator.

By using arbitrary camber line airfoils, the axial static pressure distribution could be largely controlled by specifying the work distributions through the rotor and stator. It was not necessary to make large adjustments to the annulus wall contour within the blade/vane passages to satisfy the optimization criteria. Consequently, a specific objective in laying out the annulus geometry of this design was to maximize the radii of curvature defining the hub and case flow paths. As a result, the spinner contour is a circular arc tangent to the rotor hub and the hub flow path from the rotor trailing edge to the exit plane is a single circular arc tangent to the rotor hub and to a cylinder about half a stator chord length downstream of the stator exit plane. The case flow path consisted of a circular-arc bellmouth tangent to a cylinder that extended past the stage exit plane.

The original rotor was designed to be minimally adequate structurally so as not to compromise the aerodynamics. A maximum rotor section thickness distribution of from 6.0 percent chord at the hub to 2.5 percent chord at the tip was selected. For the redesigned rotor, the maximum thickness-to-chord ratio at the hub was increased to 10.0 percent; the tip value was unchanged. This change in maximum thickness was approximately linearly distributed from hub to tip.

Rotor leading edge wedge angles near the tip were minimized to reduce shock losses by locating the position of maximum airfoil thickness relatively far aft. At the hub, wedge angles were minimized to prevent choking. The position of maximum airfoil thickness was linearly varied from 55 percent chord at the hub to 70 percent chord at the tip. The same distribution was used for both the original and redesigned rotors.

The original rotor leading edge radius was a constant 0.005 in. (0.13 mm) in the tip region flaring to 0.015 in. (0.38 mm) within the last 50 percent of span approaching the hub. Trailing edge thickness from one-third trailing edge span outward was equal to leading edge thickness on the same streamsurface. Trailing edge thickness inboard of that point was increased to a maximum at the hub two-thirds greater than at the leading edge. For the redesigned rotor, the leading and trailing edge thicknesses were doubled everywhere.

To enhance aerodynamic stability, a tip solidity high enough to capture a weak oblique passage shock, extending from the leading edge of one airfoil to the suction surface of another, within the passage was selected. A tip solidity of approximately 1.5 was chosen so that such a shock would intersect the suction surface at approximately 90 percent chord. This tip solidity plus the chord length set the number of rotor blades at 20. The resultant hub solidity was 3.2, with a nearly linear spanwise variation. The bowed appearance of the rotor blade in the meridional view shown in Fig. 2 resulted from the desirability of increasing the solidity (by increasing the chord length) near two-thirds span for aerodynamic reasons and to preserve the satisfactory, nearly linear area distribution.

The stator solidity distribution was defined based on aerodynamic considerations related to loading, operating range, and leading edge sweep. The stator leading edge was swept forward near the hub to reduce the normal component of Mach number to maximize incidence range and to minimize shock losses. The corresponding high solidity also reduced the diffusion factor. The stator leading edge was also swept forward at the tip to increase solidity and reduce stage length. Chord length was approximately fixed according to the considerations related to aspect ratio and hub flow path contour. A minimum solidity of approximately 1.6 was selected because of the high turning required of the stator (varying from 40 to 50 deg) and the high average Mach number level (varying from about 0.7 to 1.0). An odd number of vanes having no common divisor with the 20 rotor blades was desired to minimize the chance of exciting any resonant frequencies in the rotor through rotor–stator interaction. These conditions were satisfied by choosing the stator vane meridional envelope shown in Fig. 2 and by specifying 31 vanes. Maximum vane thickness was located at a constant 50 percent chord and varied in magnitude from 4.0 percent chord at the hub to 6.0 percent chord at the tip. Leading and trailing edge radii were held constant at 0.006 in. (0.15

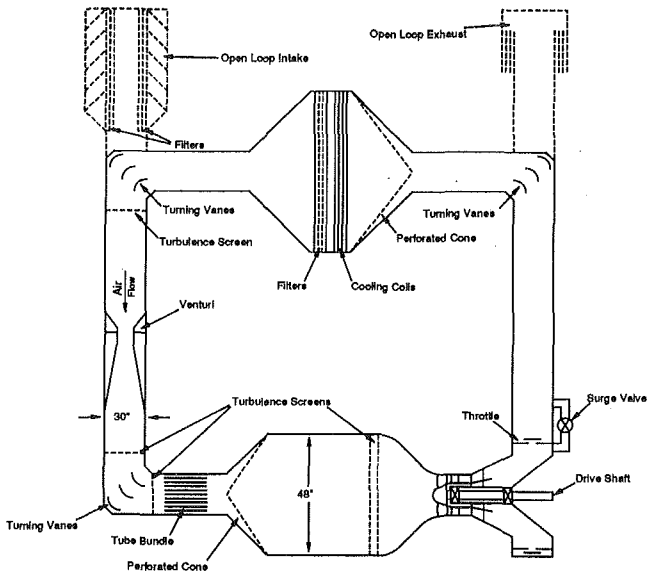

Fig. 3 2000-hp compressor aerodynamic research laboratory facility flow path

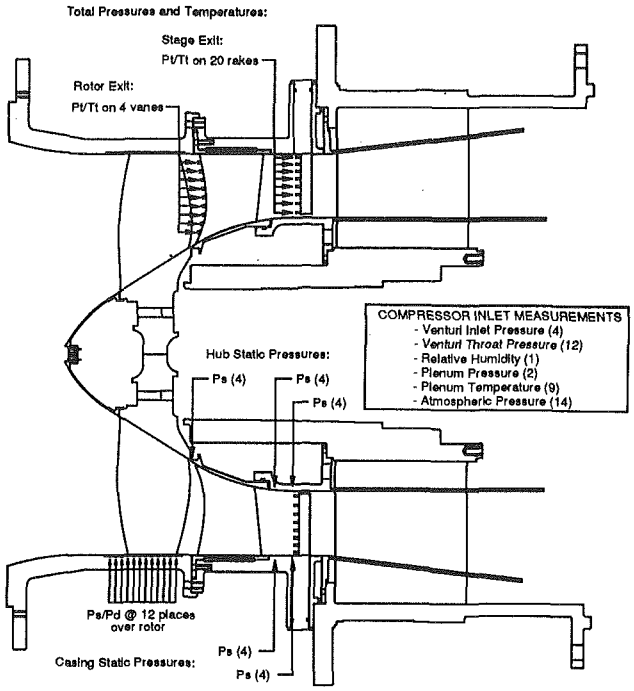

Fig. 4 Compressor test vehicle and instrumentation

mm) across the span. The same stator design was used for both the original and redesigned rotor investigations.

The fillet geometry chosen was patterned after the aircraft wing-fuselage juncture model to minimize interference drag and boundary layer growth (and the possibility of separation) in the corner. A fillet was chosen equal to approximately one-fourth of the average local blade/vane spacing. Then, over a distance equal to about 20 percent chord, the fillet was reduced to about one-fourth of its midchord value as the leading and trailing edges were approached. This fillet treatment was applied to the rotor hub and to both stator endwalls.

The final stage dimensional and design point characteristics obtained for the original and redesigned (ruggedized) rotor configurations were as follows:

	Original	Ruggedized
Stage outer diameter, in.	17.0	17.0
Rotor inlet hub/tip radius ratio	0.312	0.312
Number of blades/vanes	20/31	20/31
Rotor inlet hub/tip radius ratio	0.312	0.312
Mean rotor aspect ratio	1.320	1.320
Mean stator aspect ratio	1.255	1.255
Rotor mass averaged total pressure ratio	1.966	1.964
Stage mass averaged total pressure ratio	1.912	1.911
Rotor tip static pressure ratio	2.169	2.211
Rotor tip relative Mach number	1.658	1.675
Rotor isentropic efficiency	0.869	0.868
Stage isentropic efficiency	0.830	0.829

Test Apparatus and Procedure

Test Facility and Vehicle. The high-throughflow compressor (HTFC) with the original and ruggedized (redesigned) rotor configurations was tested in the 2000-hp Compressor Aerodynamic Research Laboratory shown schematically in Fig. 3. The compressor rig design employed a cantilevered rotor supported by four struts with leading edges located about two stator chord lengths downstream of the stator trailing edge plane. The rotors were of integral construction, the blades and disks being machined from single forgings of 6A14V titanium. The rotor tip diameter was nominally 17 in. (43.2 cm) with a designed running clearance at design speed of 0.025 in. (0.635 mm) or about 0.6 percent of the rotor tip chord. A typical compressor test vehicle and instrumentation layout are shown in Fig. 4.

Instrumentation and Data Reduction. Aerodynamic instrumentation in the compressor consisted of probes mounted in the stator leading edges to measure rotor exit total pressure and temperature, rakes downstream of the stators for measuring total pressure and temperature, static pressure taps on the inner and outer flow paths and on the surfaces of one adjacent pair of stator vanes, dynamic pressure measurements along the casing wall over the rotor tip, and dynamic strain gage measurements at several points on the rotor blades. Facility instrumentation consisted of probes to measure inlet total pressure and temperature and relative humidity, a Universal Venturi Tube to measure mass flow rate, a Bentley transducer to measure rotor driveshaft speed (rpm), and active Rotadata probes to measure rotor tip clearance at two axial planes.

Detailed aerodynamic analyses of all test points were performed using a complete radial equilibrium, streamline-curvature analysis comparable to that used for the design aerodynamic analysis. A computational grid similar to that shown in Fig. 2 was used, with the exception that not all data points were analyzed with computing stations located within the rotor blade row (computing stations located within the stator vane row were omitted for all data points). Although total temperatures and total pressures were measured both at the stator leading edge and the exit plane, exit plane data were considered to be more reliable and used for determining rotor performance. Rotor performance was calculated using total temperatures, circumferentially mass-averaged in the exit plane, and total pressures that were the peak values obtained from the exit plane circumferential distribution. The circumferentially mass-averaged exit plane total pressures and temperatures were used to determine stage performance. Boundary layer and wake blockages were determined within the analysis computer program by iteratively adjusting the throughflow solution until calculated and measured casing static pressures coincided, interpolating blockage between planes where the static pressure was measured. For selected data points of interest (the operating point, peak efficiency point, etc.) within-rotor computing stations were used and blockage and work

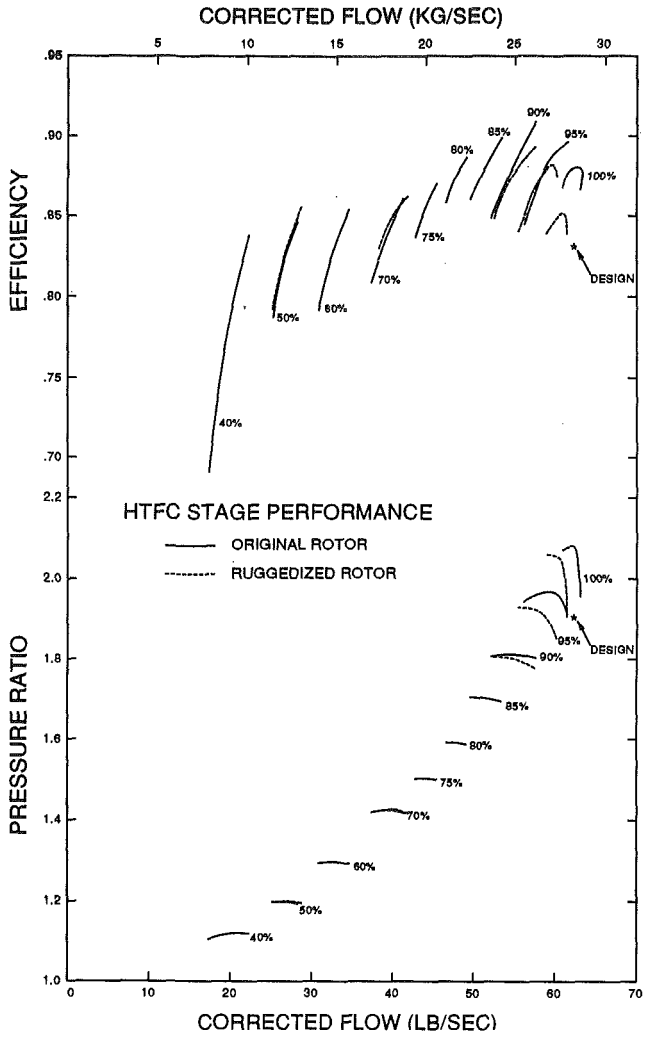

Fig. 5 High-throughflow compressor stage performance with original and ruggedized rotors

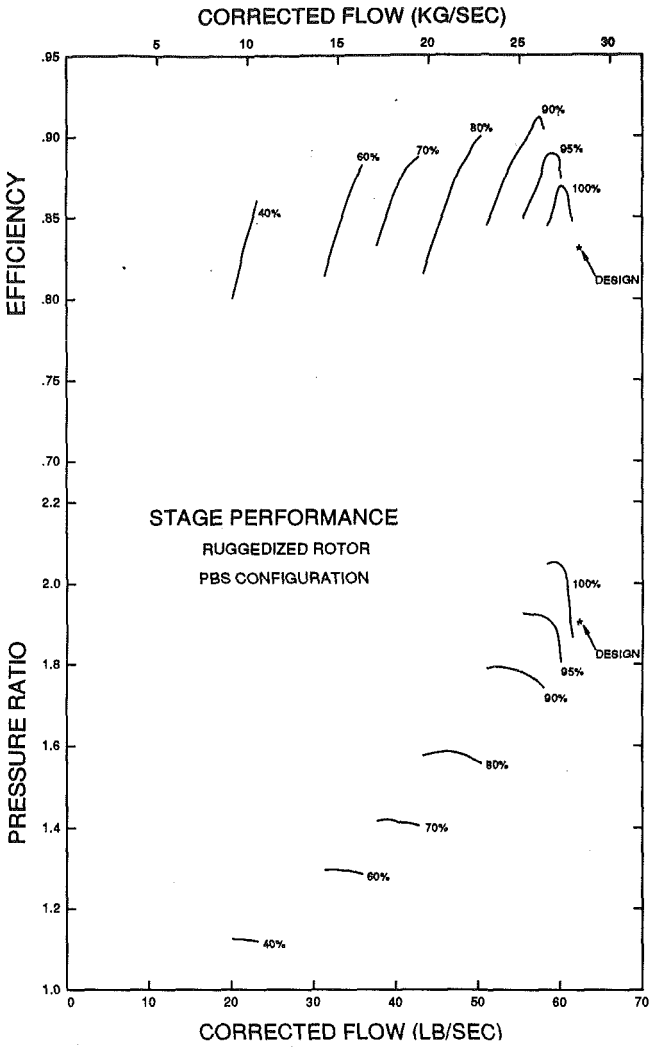

Fig. 6 High throughflow compressor stage performance with the ruggedized rotor in the PBS configuration

(total enthalpy) were adjusted to match the experimental values of static pressure measured on the casing across the rotor tip and to give a reasonable through-blade distribution of deviation angle.

Performance Results

The results from the tests of the HTFC with the original and ruggedized rotor configurations are shown in Fig. 5. The aerodynamic performance of the HTFC with the ruggedized rotor configuration was not as good as that with the original rotor configuration, but was still respectable. At design speed and peak efficiency, the flow rate was down approximately 2 percent from design at 61.36 lb/sec (27.84 kg/s, the stage pressure ratio was 0.4 percent higher than design at 1.93, and the peak stage efficiency was 2.4 percentage points higher than design at 85.4 percent. The aeromechanical instability demonstrated by the original rotor configuration was no longer present.

The ruggedized rotor configuration was tested later in the compressor test vehicle designed specifically for the Parametric Blade Design Study. The designation for the compressor configuration was changed from "HTFC" to "PBS." The HTFC test vehicle and facility were modified somewhat for the PBS and included conversion of the facility to run in the closed-loop mode as shown in Fig. 3, modifications to the facility data acquisition system to upgrade the pressure and temperature calibration and scanning systems, and test vehicle modifications to improve exit plane instrumentation and stator vane installation. Test vehicle modifications also included a new integrally machined stator (using the original aerodynamic design specifications) and new, higher density, exit plane instrumentation.

The results obtained from the PBS configuration were slightly different from those obtained from the original HTFC configuration (shown in Fig. 5). The differences are assumed (but cannot be proved) to be the result of improved exit flow field definition and the use of a higher manufacturing quality, one piece stator assembly. The map of stage performance for the PBS configuration with the ruggedized rotor from 40 to 100 percent corrected speed is shown in Fig. 6. Transonic stall flutter was not experienced anywhere in the operating range and conventional stalls were experienced at all speeds.

Design point performance can best be assessed by examining Fig. 7, which plots efficiency versus pressure ratio at design speed. At design pressure ratio (1.912), the flow achieved was 61.2 lb/sec (27.8 kg/s), or approximately 2.2 percent below design, and the efficiency was 0.856, or 2.6 points above design. The peak stage efficiency measured at design speed was 0.869, with a pressure ratio of 2.04. The peak stage efficiency measured was 0.912, with a pressure ratio of 1.752 at 90 percent speed.

Discussion of Results

Shock Loss Prediction. It is apparent that the design aero-

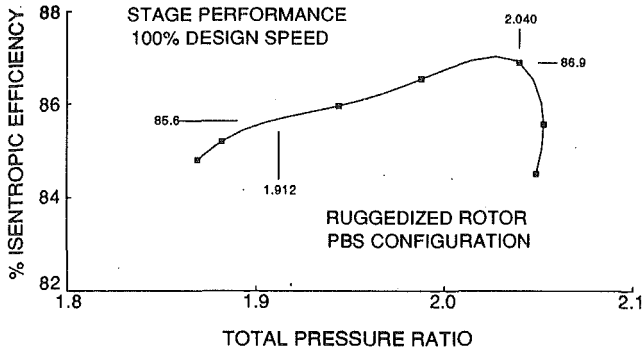

Fig. 7 Ruggedized rotor design speed performance

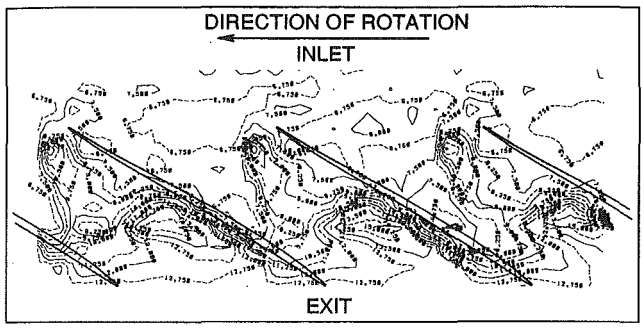

Fig. 8 Measured static pressure contours at design speed, choke condition

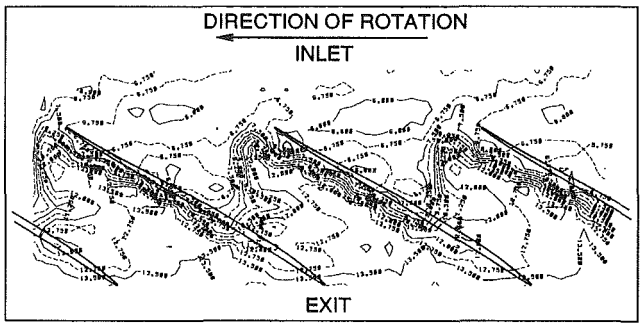

Fig. 9 Measured static pressure contours at design speed, peak efficiency condition

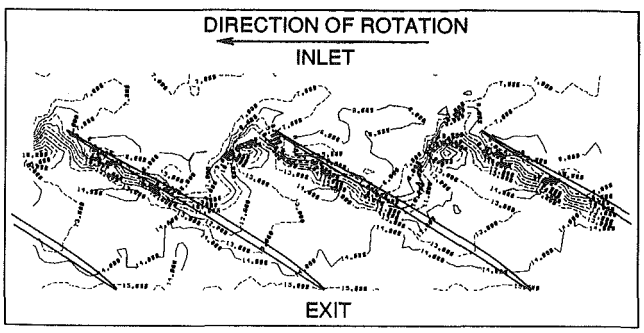

Fig. 10 Measured static pressure contours at design speed, stall condition

dynamic analysis has underestimated the efficiency potential of the HTFC with both the original and ruggedized rotors. One explanation for this fault is the inaccuracy of the shock loss prediction schemes for low aspect ratio blades. One aerodynamic design problem introduced by a move to lower aspect ratio blading is the increased three dimensionality of the flow. The normal shock loss model proposed by Miller et al. (1961) worked well for past designs with aspect ratios in excess of 2.0. However, as aspect ratio declines below 2.0, significant spanwise sweep of the shock surface results due to blade twist and solidity variations characteristic of blade rows of low hub/tip ratio.

An improved shock loss model was developed by Wennerstrom and Puterbaugh (1984) to take into account the substantial spanwise sweep of the shock surface near the blade suction surface. The shock model was incorporated into the axisymmetric, streamline-curvature-type computer program described by Hearsey (1975) used to design both the original and ruggedized HTFC rotors. The shock model was evaluated with several axial compressor designs that shared the common characteristics of low aspect ratio, tip relative Mach numbers in the range of 1.5 to 1.7, and higher than expected efficiency demonstrated at design speed. One test case chosen was the HTFC with the original rotor design. The following table presents a comparison of the stage performance predicted using the Miller–Lewis–Hartmann (M–L–H) shock loss model (used to design all HTFC configurations), using the new-oblique (N–O) shock loss model, and as experimentally measured at peak efficiency at design speed.

	M–L–H model	N-O model	Test results
Total pressure ratio	2.026	2.061	2.058
Isentropic efficiency, percent	86.96	89.07	88.90

The new oblique shock model predicted an isentropic efficiency 2.11 points higher than the Miller–Lewis–Hartmann model and only slightly higher (0.17 points) than the experimental test results. It should be pointed out, however, that this relatively successful prediction was primarily due to the use of the experimental data for calibration of the diffusion loss curves rather than the introduction of shock surface sweep effects.

To verify the validity of the new shock loss model, it was necessary to determine the actual shock surface shape. To this end, a complement of 12 high-frequency response Kulite pressure transducers was mounted in the outer casing over the rotor blade tips of the PBS compressor test vehicle. From these transducers, ensemble-averaged static pressure distributions were measured and the results for the ruggedized rotor at design speed are shown in Figs. 8–10 in the form of static pressure contours. At the choke condition, shown in Fig. 8, the passage shock is quite oblique to the inlet relative flow and a strong reflected shock is clearly present. At the peak efficiency condition, shown in Fig. 9, the passage shock has moved forward but is still oblique to the inlet relative flow and the reflected shock has nearly disappeared. At the stall condition, shown in Fig. 10, the passage shock becomes nearly normal to the inlet relative flow angle and the suction surface shock moves forward to approximately 55 percent of chord.

Although these results did not conclusively prove the validity of the new shock loss model, they did illustrate the potential of increasing efficiency prediction accuracy by including the shock surface obliquity in the shock loss calculations.

PBS Design Data Match. The intent of the parametric blade design study (PBS) was to vary specific rotor design parameters individually, keeping other design variables as close as practical to the baseline rotor. To accomplish this goal, an aerodynamic design point was established by a data match of a design speed data point for the baseline rotor located at a typically acceptable 15 percent constant stall margin from its measured stall line. The measured stage pressure ratio at this point was 1.92 with a measured corrected flow level of 61.36 lb/sec (27.87 kg/s) and an efficiency of 0.854.

The measured airflow, discharge pressures and temperatures, flow path geometry, and rotor and stator blading ge-

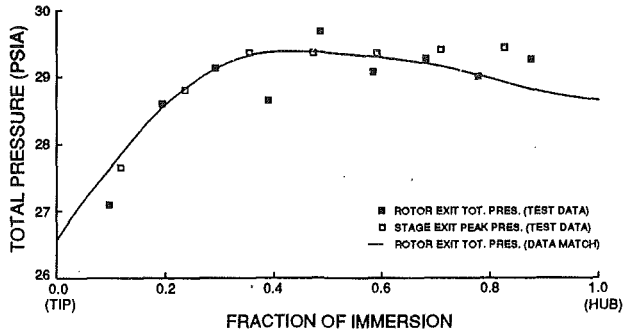

Fig. 11 Test data and data match rotor exit total pressure distributions

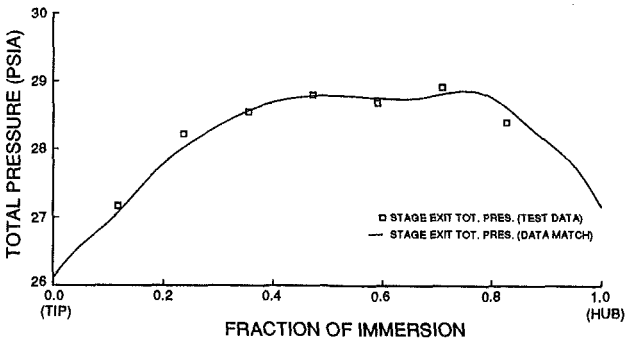

Fig. 12 Test data and data match stage exit total pressure distribution

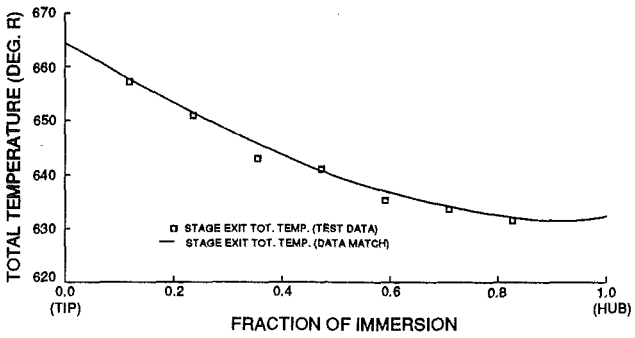

Fig. 13 Test data and data match stage exit total temperature distributions

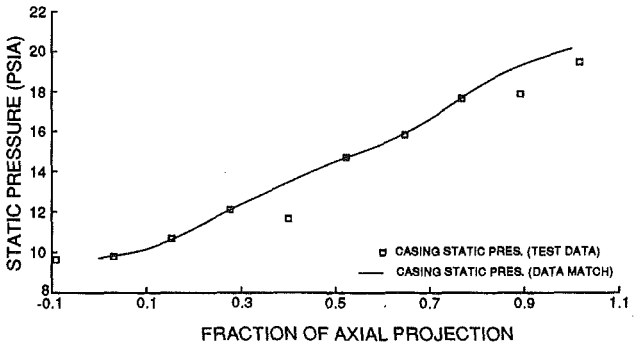

Fig. 14 Test data and data match casing static pressure distributions over the rotor

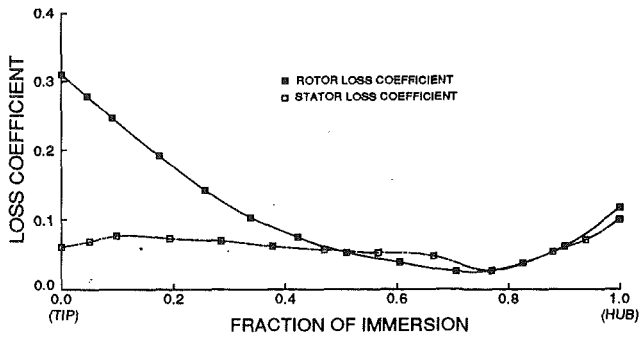

Fig. 15 Data match rotor and stator total pressure loss coefficient distributions

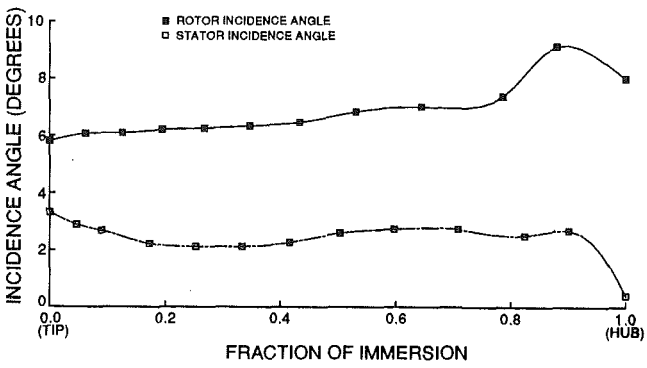

Fig. 16 Data match rotor and stator incidence angle distributions

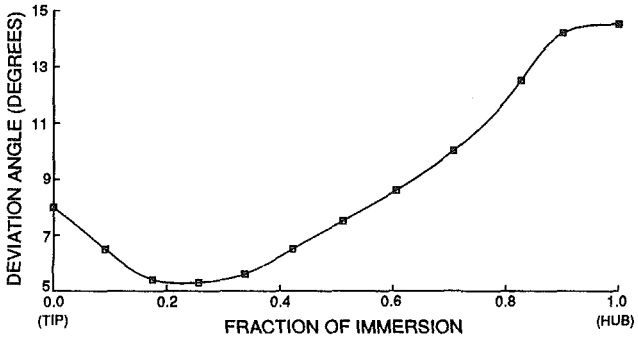

Fig. 17 Data match rotor deviation angle distributions

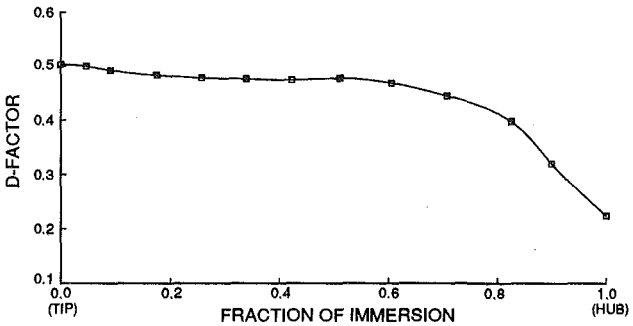

Fig. 18 Data match rotor diffusion factor distribution

ometries were used to calculate the circumferential average flow field through the stage. Figures 11–13 show the total pressure and total temperature distributions used in the throughflow analysis along with the test data at the rotor exit and stage exit stations. Some smoothing and extrapolation of the data at the endwalls were required. The assumed chordwise work distribution was adjusted at each streamline until a reasonable internal blade mean camber line deviation angle distribution and level and a good match of the measured static pressure over the rotor tip was obtained. Figure 14 shows both the measured and "data match" casing static pressures over the rotor tip. The overall agreement with test data is good.

The rotor and stator blade element total pressure loss coefficients are illustrated in Fig. 15. The calculated baseline in-

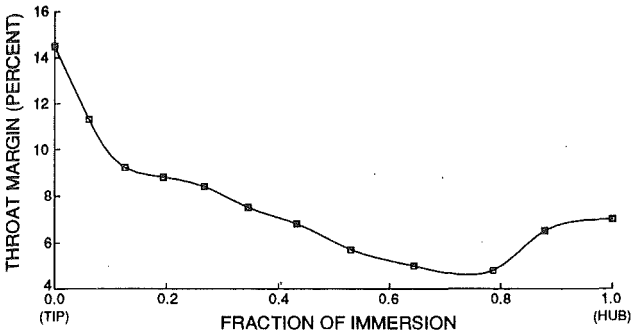

Fig. 19 Data match rotor throat margin distribution

cidences for the rotor and stator and the rotor deviation and diffusion factor are illustrated in Figs. 16–18. Since all PBS rotors were to be tested with the same baseline stator configuration, it was imperative that their implied stator incidence angle levels did not depart too greatly from that shown in Fig. 16. Further aerodynamic details of the data match calculations can be found in Parker and Simonson's (1982) report.

The streamsurface blade sections were analyzed to determine the various cascade aerodynamic parameters including several passage area ratios on each streamsurface. Figure 19 shows the resulting radial distribution in the rotor throat margin levels. The throat margin for a streamsurface section is defined as the percent excess throat area available over the minimum theoretical area required ($M_{throat} = 1.0$) to pass the streamtube flow assuming a total pressure loss equivalent to one normal shock at the upstream Mach number, and accounting for the effect of the radius change (between the leading edge and throat) on the relative total enthalpy and pressure.

Conclusions

The assumptions made during the design and some of the unusual features incorporated in the HTFC ruggedized rotor have led to an efficient, practical axial compressor stage design. Ruggedization of the original HTFC rotor has been successfully accomplished to eliminate an undesirable aeroelastic instability. Some design features that may have contributed to this success are as follows:

1 The high degree of sweep incorporated in the stator leading edge at the hub appeared to eliminate entirely the shock losses that otherwise might be appreciable in this region.

2 The optimization criteria based upon the meridional static pressure gradient appeared reasonably successful for both subsonic and supersonic sections.

3 Still open for discussion is the effect of the airfoil fillet geometry on performance: No direct conclusion can be reached because only one fillet geometry was tested.

The general conclusion can be reached that it has been proven feasible to obtain high efficiency at higher values of flow, Mach number, and loading than have heretofore been common. Further, a high level of performance has been demonstrated for a practical compressor design, one that is aeromechanically stable and robust enough for general application in military and commercial aircraft turbofan and turbojet engines.

To achieve further performance improvements in transonic compressor stages, it has been considered desirable to conduct a comprehensive experimental program aimed at exploring the sensitivity of compressor performance to variations in several common design parameters. The objectives of the program have been to perform the aerodynamic design and experimental analysis of a series of transonic compressor rotors, all parametrically related to a baseline design that has been well documented and demonstrated. Because of its excellent performance and robust characteristics, the HTFC stage with the ruggedized rotor configuration was chosen as the baseline for the Parametric Blade Study. Each of the design variations were to deviate from the baseline, insofar as practical, by a variation of one parameter only. The results of two of these design variations and their respective performance analyses are the subject of part two of this paper.

References

Hearsey, R. M., 1975, "A Revised Computer Program for Axial Compressor Design," ARL-TR-75-0001, Vols. I & II, A009273 and A009157, Aerospace Research Laboratories, Wright-Patterson AFB, OH.

Jansen, W., 1967, "The Application of End-Wall Boundary Layer Effects in the Performance Analysis of Axial Compressors," ASME Paper No. 67-WA/GT-11.

Johnson, I. A., Bullock, R. O., et al., 1965, "Aerodynamic Design of Axial Flow Compressors," NASA SP-36.

Miller, G. R., Lewis, G. W., and Hartmann, M. J., 1961, "Shock Losses in Transonic Compressor Blade Rows," *ASME Transactions*, Vol. 83, No. 3, pp. 235–242.

Parker, D. E., and Simonson, M. R., 1982, "Transonic Fan/Compressor Rotor Design Study, Vol. 1," AFWAL-TR-82-2017, Aero Propulsion Laboratory, Wright-Patterson AFB, OH.

Wennerstrom, A. J., et al., 1976, "Investigation of a 1500 ft/sec, Transonic, High-Through-Flow, Single-Stage, Axial-Flow Compressor with Low Hub/Tip Ratio," AFAPL-TR-76-92, ADB016506, Aero Propulsion Laboratory, Wright-Patterson AFB, OH.

Wennerstrom, A. J., and Frost, G. R., 1976, "Design of a 1500 ft/sec, Transonic, High-Through-Flow, Single-Stage, Axial-Flow Compressor With Low Hub/Tip Ratio," AFAPL-TR-76-59, ADB016386, Aero Propulsion Laboratory, Wright-Patterson AFB, OH.

Wennerstrom, A. J., and Buzzell, W. A., 1979, "Redesign of a Rotor for a 1500 ft/sec, Transonic, High-Through-Flow, Single-Stage Axial-Flow Compressor With Low Hub/Tip Ratio," AFAPL-TR-79-2078, ADB042609, Aero Propulsion Laboratory, Wright-Patterson AFB, OH.

Wennerstrom, A. J., and Puterbaugh, S. L., 1984, "A Three-Dimensional Model for the Prediction of Shock Losses in Compressor Blade Rows," ASME JOURNAL OF TURBOMACHINERY, Vol. 106, pp. 295–299.

Low Aspect Ratio Transonic Rotors: Part 2—Influence of Location of Maximum Thickness on Transonic Compressor Performance

A. R. Wadia
GE Aircraft Engines,
Cincinnati, OH 45215

C. H. Law
Wright Laboratory,
Wright-Patterson AFB, OH 45433

Transonic compressor rotor performance is sensitive to variations in several known design parameters. One such parameter is the chordwise location of maximum thickness. This article reports on the design and experimental evaluation of two versions of a low aspect ratio transonic rotor that had the location of the tip blade section maximum thickness moved forward in two increments from the nominal 70 percent to 55 and 40 percent chord length, respectively. The original hub characteristics were preserved and the maximum thickness location was adjusted proportionately along the span. Although designed to satisfy identical design speed requirements, the experimental results reveal significant variation in the performance of the rotors. At design speed, the rotor with its maximum thickness located at 55 percent chord length attains the highest peak efficiency among the three rotors but has lowest flow rollback relative to the other two versions. To focus on current ruggedization issues for transonic blading (e.g., bird and ice ingestion), detailed comparison of test data and analysis to characterize the aerodynamic flow details responsible for the measured performance differences were confined to the two rotors with the most forward location of maximum thickness. A three-dimensional viscous flow analysis was used to identify the performance-enhancing features of the higher efficiency rotor and to provide guidance in the interpretation of the experimental measurements. The computational results of the viscous analysis show that the difference in performance between the two rotors can be attributed to the higher shock losses that result from the increased leading edge "wedge angle" as the maximum thickness is moved closer to the leading edge. The test data and the three-dimensional viscous analysis also reveal that the higher efficiency rotor achieves the same static pressure rise potential and loading at a higher flow level than its less efficient counterpart and this is responsible for its resulting lower flow rollback and apparent loss in stall margin. Comparison of the peak efficiencies attained by the two rotors described in this article with the baseline ruggedized rotor performance presented in part 1 of this paper suggests the existence of an optimum maximum thickness location at 55 to 60 percent chord length for such low aspect ratio transonic rotors.

Introduction

In 1971, the Air Force Aero Propulsion Laboratory initiated a program to develop an axial compressor known to the turbomachinery community as the High-Through-Flow Compressor (HTFC) with the purpose of significantly reducing the number of stages to achieve a given pressure ratio. This meant higher pressure ratios per stage, requiring higher blade tip speeds/Mach numbers and lower airfoil aspect ratios relative to contemporary design technology.

During the preliminary design of the HTFC, it was concluded that the greatest aerodynamic challenge was to design an efficient first stage. The USAF designed the original first stage (Wennerstrom and Frost, 1976) with high specific flow, low aspect ratio custom tailored blading with swept leading edge stators and variable blade fillet radii. The original design was tested and the results have been reported by Wennerstrom et

Contributed by the International Gas Turbine Institute and presented at the 37th International Gas Turbine and Aeroengine Congress and Exposition, Cologne, Germany, June 1–4, 1992. Manuscript received by the International Gas Turbine Institute February 11, 1992. Paper No. 92-GT-186. Associate Technical Editor: L. A. Langston.

al. (1976). Good aerodynamic performance was achieved but the blade exhibited aeromechanical instability. The original rotor was ruggedized (Wennerstrom and Buzzell, 1979) and retested. The test results of this ruggedized rotor are reported in part 1 (Law and Wadia, 1992) of this two-part paper.

While significant improvement to turbomachinery aerodynamic design state of the art was accomplished by the design and test of this transonic compressor stage, it was felt that a new era would evolve in transonic fan design if a comprehensive experimental program aimed at exploring the sensitivity of compressor performance to variations in several common key design parameters could be initiated. This paper reports on some of the test results obtained during the course of this joint program by the Compressor Research Group, Technology Branch, Turbine Engine Division at Wright Patterson Air Force Base. The aerodynamic design of the rotors was performed by GE Aircraft Engines under an Air Force contract.

One of the parameters investigated in this experimental program was the chordwise location of maximum thickness. NACA research in the 1950s indicated that, in general, as the inlet relative Mach number increases, it is desirable to move the location of maximum thickness aft on an airfoil. However, the early work was done with airfoils having significant positive camber distributed on predefined mean camber line shapes. With the current design approach that uses custom tailored mean camber lines, the tip regions of transonic rotors have little overall relative turning, sometimes negative turning, and frequently high customized mean camber lines of S-shape, i.e., negative camber followed by some positive camber. For fans with stringent bird strike requirements, moving the location of maximum thickness forward becomes structurally mandatory and this study addresses the expected performance impact associated with this type of ruggedization for transonic blading.

Objectives and Scope

The objective of the work presented in this paper was to get definitive aerodynamic performance data comparing the effect of the location of airfoil maximum thickness on two transonic compressor rotors henceforth described as Rotor 1 and Rotor 2, parametrically related to the baseline ruggedized design whose test results have been presented in the companion paper (Law and Wadia, 1993). Rotor 1 was designed with the location of maximum thickness of the airfoil tip section at 40 percent of chord length, and Rotor 2 at 55 percent. The original hub characteristics of the baseline ruggedized rotor were preserved in both rotor designs. The distribution of the location of maximum thickness was adjusted proportionately along the span and is illustrated in Fig. 1.

The aerodynamic and cascade area quantities from the data match circumferential averaged flow solution presented in part 1 (Law and Wadia, 1993) are used to define the detailed geometric configuration of the two new rotors. The design of Rotors 1 and 2 is described first, followed by the comparison of the measured performance of the rotors. Three-dimensional viscous analysis results of Rotors 1 and 2 at the design speed

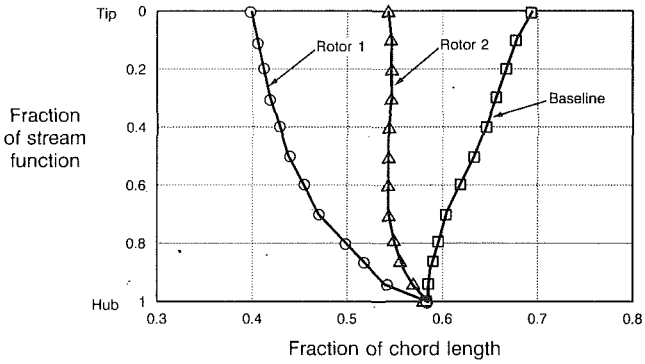

Fig. 1 Comparison of the distribution of the location of maximum thickness

peak efficiency condition are used to illustrate the details of the internal flow field that are responsible for the difference in performance between the two rotors. The three-dimensional calculations are also used to provide guidance in the interpretation of the test data at off-design conditions.

Design of Rotors 1 and 2

The aerodynamic synthesis of the baseline rotor described in part 1 served as the basis to perturb the baseline configuration to study the effect of the location of maximum thickness on transonic fan performance.

The thickness distribution as a function of distance along the meanline was described by two cubic equations. The first equation describes the thickness from the leading edge to the maximum thickness point, while the second defines the thickness between the point of maximum thickness and the trailing edge. The magnitude and chordwise location of maximum thickness and the leading and trailing edge thicknesses are specified by the designer. Slope and curvature are continuous at the maximum thickness location where the two equations meet. The comparison of the thickness distributions of the tip section calculated from the above procedure is presented in Fig. 2.

During the design of Rotors 1 and 2 the annulus blockage used in the internal blade calculation stations for the circumferential average throughflow analysis adjusted to be consistent with the forward shift of airfoil maximum thickness. The element loss coefficients were held fixed. There was no attempt made to adjust the local loss coefficient levels to reflect changes in the location of maximum thickness. The assumed chordwise work distribution was iteratively adjusted to obtain the calculated chordwise distribution of static pressure similar to that of the data match calculations of the baseline rotor. The blade mean camber line angles were adjusted to maintain the same throat area and flow induction capacity as the baseline blade.

To adjust for the increased blade blockage in the forward half of the blade, and to preserve the data match static pressure distribution in the hub, the hub contour internally within the

Nomenclature

D-Factor = diffusion factor
IMM = radial immersion (0 = tip and 1 = hub)
LE = leading edge
M_{isen} = isentroptic Mach number
P = pressure
PS = pressure surface
PSI = fraction of stream function (0 = tip and 1 = hub)
R = radial distance
SS = suction surface
T = temperature
TE = trailing edge
t_{le} = leading edge thickness
t_{max} = maximum thickness
t_{te} = trailing edge thickness
U_T = tip speed
Z = axial distance

Subscripts

In = blade-row inlet
s = static conditions
T = stagnation quantity (total conditions)

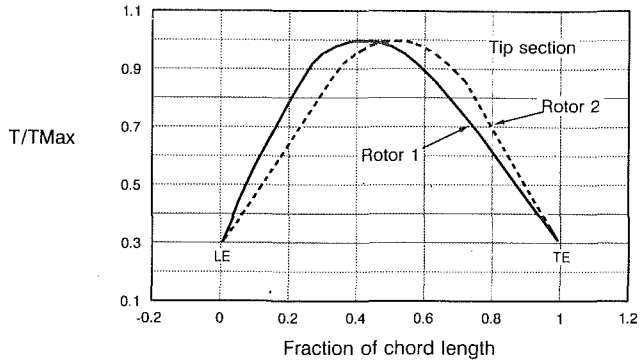

Fig. 2 Comparison of the chordwise distribution of the tip section airfoil thickness

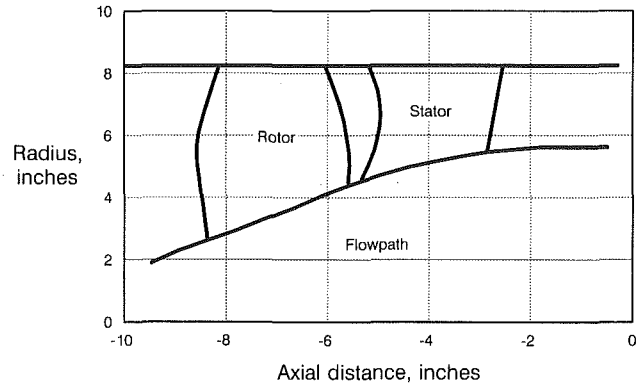

Fig. 3 Low aspect ratio rotor flowpath

rotor was "scalloped" slightly relative to the baseline rotor. Figure 3 shows the compressor flowpath and the blading in the meridional view. The rotor hub scalloping amounts to a 0.012 in. lower radius at 60 percent chord location, which then fairs smoothly into the baseline hub contour near the edge locations.

The rotor leading and trailing edges were kept at the same axial projection as the baseline rotor. Since the blade stagger angle in the outer portions changed slightly for the two different rotors, the blade chords differed a small amount relative to the reference blade. The radial distribution of maximum thickness was kept the same as the baseline. Since the chords for the two designs differed slightly, there were some minor variations in the maximum thickness to chord ratios. The radial distribution of the ratio of the leading edge and trailing edge thicknesses to maximum thickness was the same as the baseline ruggedized rotor (see Table 1).

The rotor exit radial distributions of total pressure and temperature were maintained the same as those used for the data match of the baseline rotor. To satisfy similar flow induction capacity as the baseline blade, it was necessary to use larger meanline incidence angles, especially for Rotor 1, as a result of the larger blade leading edge wedge angle resulting from the forward location of maximum thickness. The overall blade circulation between Rotors 1 and 2 relative to the baseline blade was maintained, taking into account the change in streamline radius and meridional velocity.

To evaluate the performance of the new rotor designs accurately by comparing overall stage performance, the stator had approximately the same inlet conditions in both cases.

Table 1 summarizes the salient geometric and aerodynamic features of Rotors 1 and 2. Further details of the blading geometry and design vector diagrams can be found from Parker and Simonson (1982). The streamsurface tip sections of Rotors

Table 1 Rotors 1 and 2 design parameters

Parameter	Rotor 1	Rotor 2
Inlet Corrected Flow	61.36 lb/sec	61.36 lb/sec
Corrected Tip Speed	1500 ft/sec	1500 ft/sec
Specific Flow	43.13 lbm/sec-ft²	43.13 lbm/sec-ft²
Pressure Ratio	1.92	1.92
Inlet Radius Ratio	0.311	0.311
Number of Blades/Vanes	20/31	20/31
Tip Diameter	17.0 inches	17.0 inches
Corrected RPM	20222 RPM	20222 RPM
Stage Exit Mach No. (Ae/A=0.95)	0.592	0.592
Avg. Aspect-Ratio Rotor/Stator	1.3/1.46	1.3/1.46
Avg. Solidity Rotor/Stator	2.3/1.68	2.3/1.68
Tip, Pitch and Hub Stagger (degrees)	57.80,42.06, 15.09	57.30,38.64, 14.82
Tip, Pitch and Hub Camber (degrees)	0.56,13.22, 61.95	2.96,18.76, 61.73
Tip, Pitch and Hub Chord (inches)	3.820,3.771, 2.933	3.768,3.809, 2.926
Tip t_{le}/t_{max}	0.19	0.19
Tip t_{te}/t_{max}	0.20	0.20
Location of tip t_{max} (% chord)	40	55
Tip, Pitch and Hub t_{max}/c	0.025,0.0624, 0.1216	0.025,0.0624, 0.1216

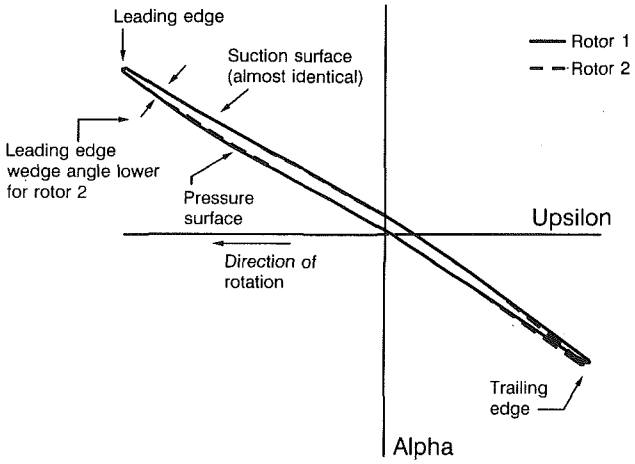

Fig. 4(*a*) Comparison of the tip sections of rotors 1 and 2

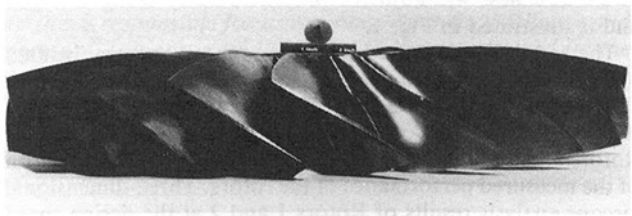

Fig. 4(*b*) Rotor 1 blisk

1 and 2 are shown in Fig. 4(*a*). The suction sides of both blades at the leading edge are almost identical by design intent to maintain the flow induction capability. The difference in the pressure side of the leading edge characterizes the increased leading edge "wedge-angle" on Rotor 1. The term "effective camber" is used to indicate approximately the circulation capacity of a cascade and the trailing edge variations between Rotors 1 and 2 are a direct consequence of keeping the effective camber level identical on both rotors. The manufactured blisk for Rotor 1 is shown in Fig. 4(*b*).

Test Setup and Instrumentation

This section briefly describes the compressor rig instrumentation that provided the experimental measurements for the performance of the two rotors. The single-stage test compressor rig is shown in part 1 (Law and Wadia, 1993) of this article. There are no inlet guide vanes in the experimental setup.

Aerodynamic instrumentation in the single-stage configuration consisted of vane-mounted leading edge total-pressure and temperature probes and rakes downstream of the stators for total-pressure and temperature measurements. The ten discharge-plane rakes each had eight sensors spaced at centers of equal area radially while the rakes were uniformly distributed around the circumference and spaced to divide a single exit vane passage into ten equal parts. The nine stator leading edge probes were distributed on two vanes and uniformly spaced to radially divide the area between the hub and the case into nine equal parts.

Static pressure taps were located on the inner and outer endwalls at the inlet and exit plane of the stator. Dynamic pressure measurements along the casing over the rotor tip, in conjunction with complimentary steady-state static pressure measurements, were acquired to determine the tip blade-to-blade flow field at key operating points. In addition, measurements of inlet total pressure, temperature, mass flow, and inlet relative humidity and rotor speed were also obtained. Further compressor instrumentation details are summarized in part 1 of this article.

During the test, the vane-mounted instrumentation ceased to work effectively and the "rotor-alone" performance was determined from the stage measurements of total pressure and total temperature. The three highest stator exit plane total pressures were used to determine the rotor exit total pressure distribution and the exit plane total temperatures were used as the rotor exit total temperature distribution. All test data were acquired with some degree of depressed inlet pressure and later corrected to standard inlet conditions as reported herein. Repeatability of the data was quite good and the overall quality of the measurements was judged to be excellent. Cold radial tip clearance was nominally 0.03 to 0.045 in. representing clearance-to-chord ratios of 0.8 to 1.2 percent, respectively, depending on the axial location. Running clearance was measured with an active nontouching spark-gap-type clearance measuring system at the rotor leading edge and midchord at two circumferential locations. The average running clearance at design speed was approximately 0.025 in. representing a tip clearance-to-chord ratio of approximately 0.67 percent.

Comparison of Rotor and Stage Performance

The measured rotor and stage performance for Rotors 1 and 2 is presented in Fig. 5. The design point target matching the baseline stage performance, is illustrated in Fig. 5(*b*). Rotor 2 exceeded its flow requirements by approximately 0.5 percent while Rotor 1 was slightly lower in flow by about 0.6 percent at design speed. Generally Rotor 2 has higher flow pumping capability relative to Rotor 1. Considering the complexity of transonic flows, the difficulty in maintaining all the key design parameters identical except for the variation of maximum thickness location, and deformation and manufacturing uncertainties, the similarity of flow levels achieved by both designs relative to the design point is gratifying.

The stage and rotor-alone peak efficiencies achieved by Rotor 2 are higher than those attained by Rotor 1 at all speeds, as shown in Fig. 5. At design speed, the stage efficiency with Rotor 2 is approximately 0.75 points and the "rotor-alone" efficiency is about 1.0 point better relative to Rotor 1. The peak efficiency trends are similar at part speed, although the slightly lower minimum operating line at 80 percent speed may be responsible for this. Since Fig. 4(*a*) shows identical suction side metal angles between both rotors, the higher flow pumping capability of Rotor 2 may be attributed to reduced leading edge region shock strength and the reduced blockage effects as a result of the improved performance at both design and off-design operating conditions.

While Rotor 2 has higher efficiency, Rotor 1 has considerably more flow rollback relative to Rotor 2 at the design and 95 percent speed conditions as illustrated in Fig. 5. At 90 percent speed Rotors 1 and 2 have approximately the same flow rollback while below 90 percent speed the flow rollback trend is reversed.

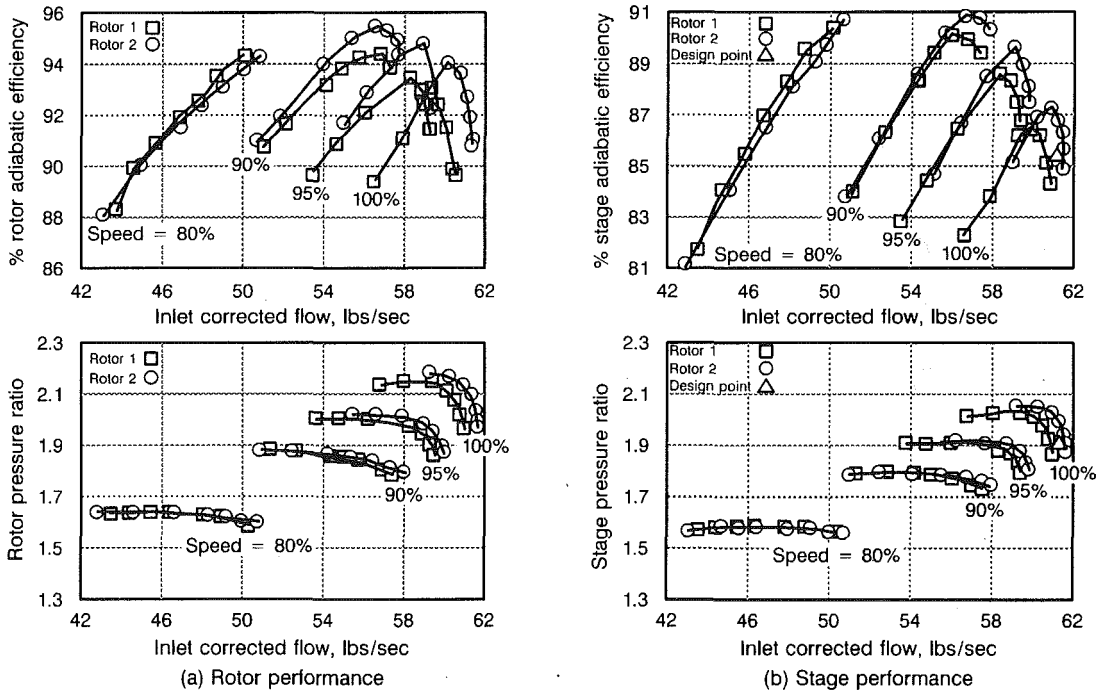

Fig. 5 Comparison of rotor and stage measured performance for Rotors 1 and 2

Similar to the flow trends, Rotors 1 and 2 do not stall at the same efficiency levels. Between 90 and 100 percent speeds Rotor 2's performance at stall is better than Rotor 1's. Rotor 2 appears to "let go" sooner as it is throttled up the speedline at design speed while Rotor 1, even with poorer performance than Rotor 2, seems to be able to be throttled much further. At 90 percent speed and below, where the inlet relative Mach numbers are lower and the shocks are weaker, Rotors 1 and 2 attain nearly identical performance levels at the near-stall condition. In later sections of this article the test data are analyzed with the help of a three-dimensional viscous analysis to further clarify the flow mechanism responsible for the above noted performance differences.

Comparison of Radial Profiles

Figure 6 shows the comparison of the radial profiles of total pressure, temperature and adiabatic efficiency for Rotors 1 and 2 at design speed and 90 percent speed. The effects of throttling are included in each figure.

At design speed near the intended aerodynamic design condition, the total pressure profiles for both rotors are very hub strong. The work input is almost identical in both rotors at this condition and the higher efficiencies in the tip region for Rotor 2 result in higher total pressure in its outer 60 percent span relative to Rotor 1. The hub element, however, indicates slightly lower efficiency for Rotor 2.

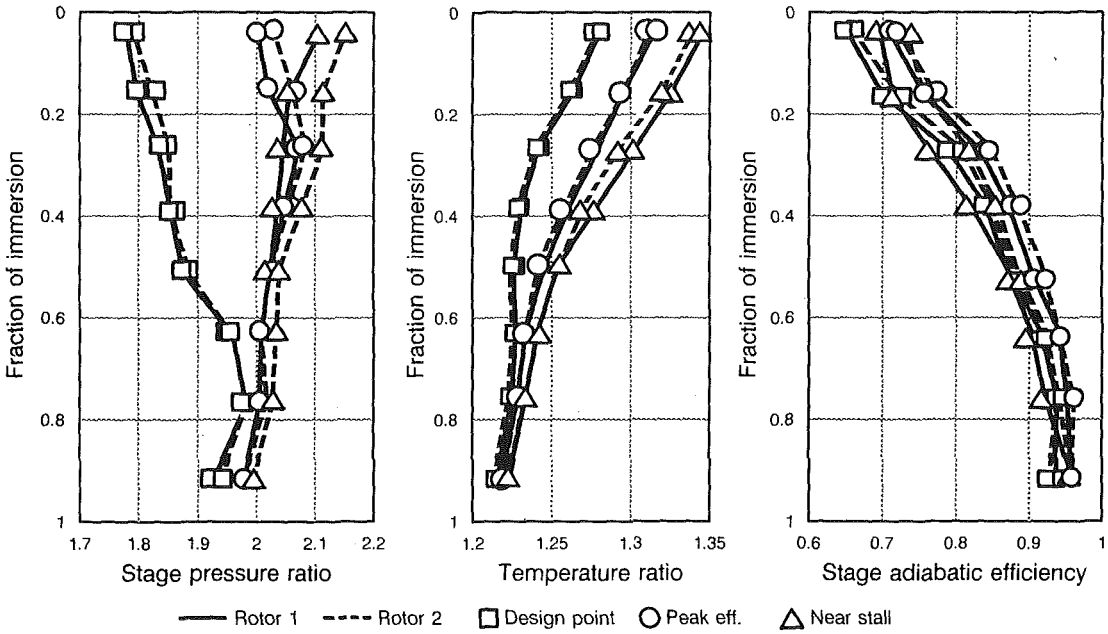

Fig. 6(*a*) Comparison of stage exit radial profiles of total pressure, total temperature, and adiabatic efficiency at design speed

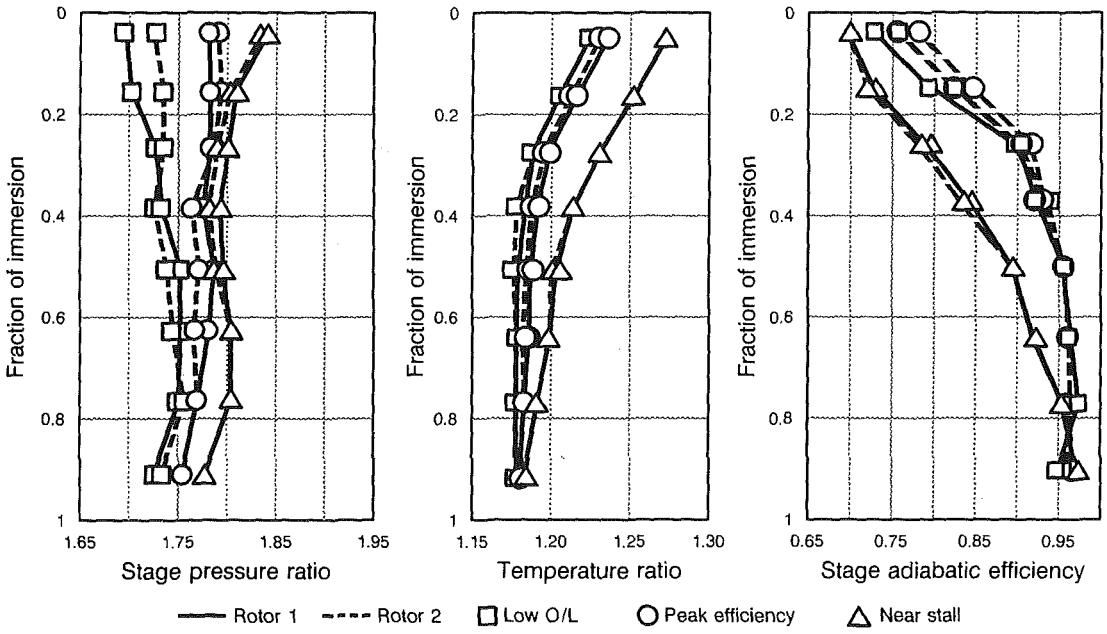

Fig. 6(*b*) Comparison of stage exit radial profiles of total pressure, total temperature, and adiabatic efficiency at 90 percent speed

As the stages are throttled up toward peak efficiency, the total pressure profile begins to flatten, with the third element from the tip reaching the highest total pressure for both rotors. Consistent with the much steeper characteristic slopes in the tip region, the tip element total pressure and work input increase significantly relative to the hub element. The efficiency profile shows significant improvement in the tip region for both rotors, with Rotor 2 being the better of the two in this region by 1.0 point. As expected with a transonic stage, the peak efficiency is reached at the "knee" of the speedline shown in Fig. 5 (pressure ratio versus flow characteristics) where the flow roll-back takes on a much quicker pace as the back pressure is increased.

As the stages are throttled up toward stall the profiles show markedly different characteristics between Rotors 1 and 2. For Rotor 1, the total pressure increases for the two tip elements and decreases elsewhere (pressure ratio for Rotor 1 begins to decrease, as seen in Fig. 6(*a*) whereas for Rotor 2 the total-pressure profile becomes significantly tip strong with a large increase in the tip element value. Consistent with the flat characteristics there is almost not increase in the hub total pressure for either rotor. With its added flow roll-back, Rotor 1 achieves a larger work input at the near-stall condition relative to Rotor 2, and unlike Rotor 2 its element efficiencies near stall are considerably lower relative to the peak efficiency point. Interestingly, Rotor 2 tip element efficiency attains its peak at the near-stall condition. Other Rotor 2 element efficiencies near stall are lower than their corresponding peak efficiency values but higher than those of Rotor 1 at the same condition.

At 90 percent speed the rotors achieve approximately identical work input distribution levels. Near the most unthrottled point achieved in the test rig, the Rotor 1 total pressure profile is more hub strong relative to that of Rotor 2 owing to its lower tip efficiencies. At peak efficiency both Rotors 1 and 2 have slightly tip strong total pressure profiles. At stall, Rotor 1 has a total pressure profile that is slightly more tip strong relative to Rotor 2, a reversal in trend from what was observed at design speed. At 90 percent speed the efficiency improvement measured with Rotor 2 relative to Rotor 1 appears to be in the supersonic part of the blade, i.e., from the tip to approximately 40 percent immersion. Comparison of the peak efficiency profiles at design and 90 percent speeds shows considerable improvement in the element efficiencies near the tip (about 8 points for the tip element), which in most part can be associated with reductions in shock strength and shock interaction with the endwall boundary layer.

Comparison of Casing Statics and Over-the-Tip Kulites

Figure 7 illustrates the shock structure and blade-to-blade

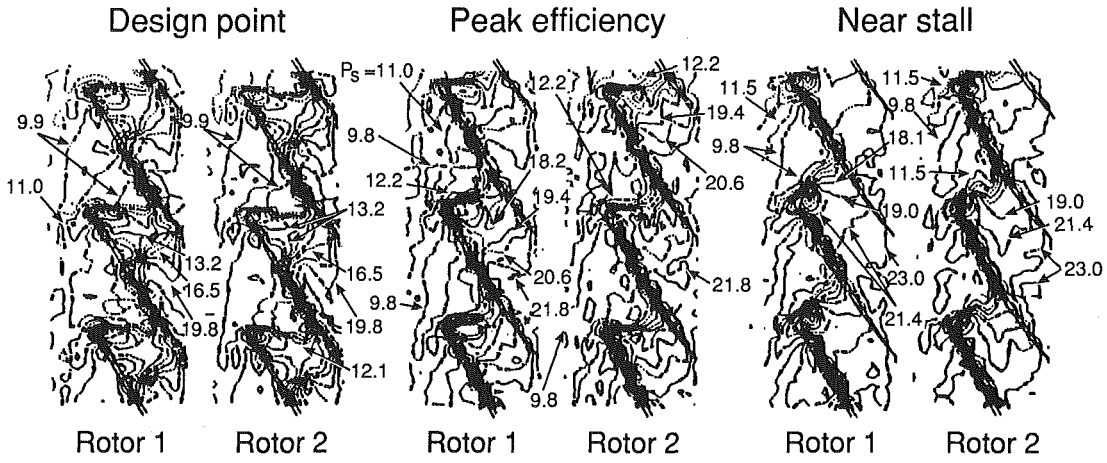

Fig. 7(*a*) Comparison of over-the-blade-tip kulites at design speed

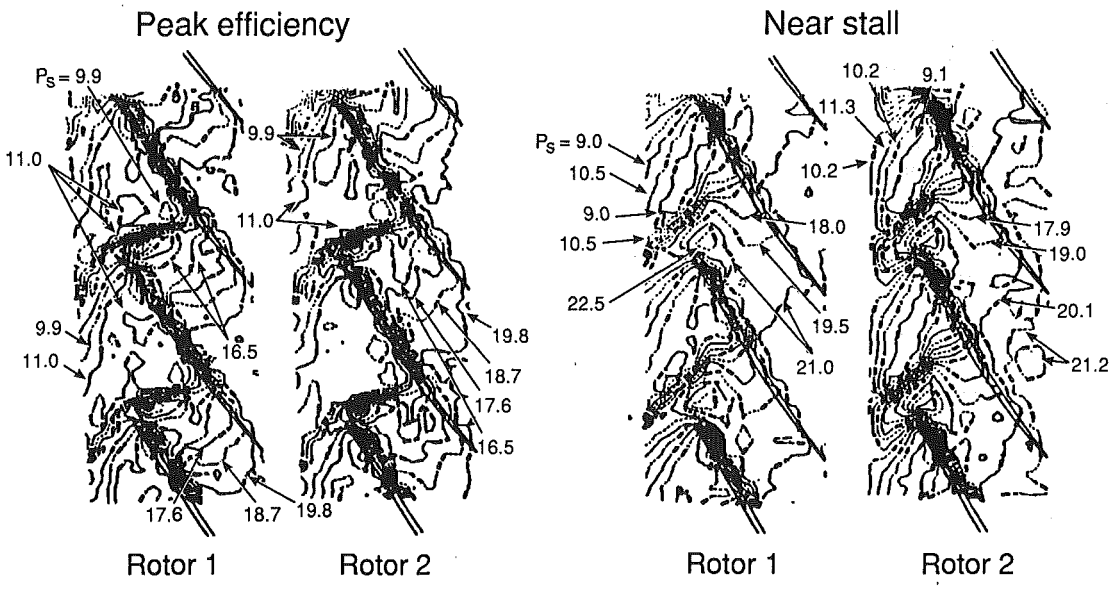

Fig. 7(*b*) Comparison of over-the-blade-tip kulites at 90 percent speed

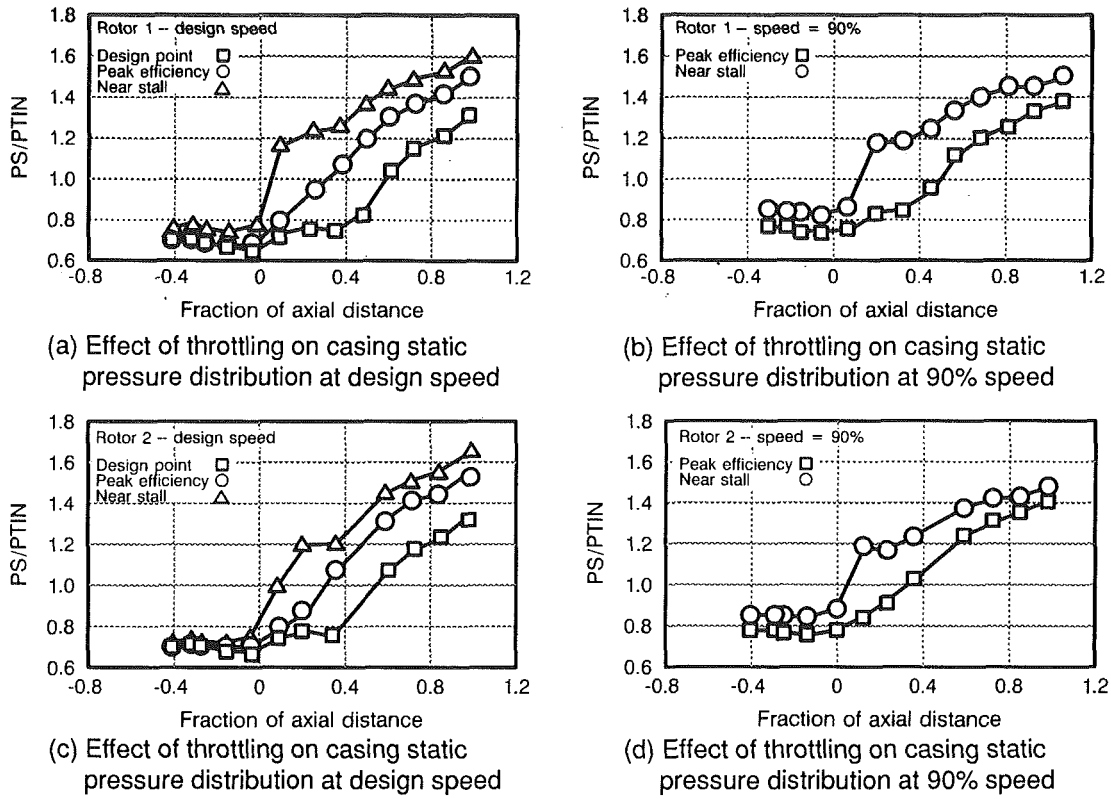

Fig. 8 Comparison of the measured casing static pressure distribution at key operating conditions at design and 90 percent speeds

flow field measured by the over-the-blade-tip dynamic pressure transducers for Rotors 1 and 2 at design and part speeds at the most unthrottled point near the aerodynamic design point, peak efficiency, and stall operating conditions. The corresponding measured casing static pressure distributions are presented in Figs. 8 and 9.

Casing Statics and Tip Kulite Comparisons at Design Speed

At 100 percent speed at design point (see Fig. 7*a*) there is a weak leading edge shock followed by a second stronger passage shock near the trailing edge for both rotors at the most unthrottled condition measured in the compressor rig. The static pressure rise across the passage shock (in both rotors) that intersects the pressure surface of the blade is more than the static pressure rise achieved through the leading edge shock resulting in lower leading edge loading and large trailing edge loading as illustrated by the casing static pressure distributions shown in Figs. 8(*a*) and 8(*c*). The larger leading edge wedge angle in Rotor 1 (relative to Rotor 2) results in higher leading edge loadings as seen by comparing the static pressure rise from the leading edge to 40 percent axial distance Figs. 8(*a*) 8(*c*), where, for example, the design point P_s/P_T, in at 25 percent axial distance is 0.8 for Rotor 2 (Fig. 8*c*).

Throttling up to peak efficiency at design speed results in the weakening of the second passage shock and the strengthening of the leading edge shock (see Fig. 7*a*), which remains attached to the leading edge. Again for Rotor 1, due to its larger leading edge wedge angle, higher leading edge loading is indicated (Fig. 9*c*) relative to Rotor 2. Both the over-the-blade-tip Kulites and the measured casing static pressure distributions in Figs. 8(*a*), 8(*b*), and 9(*c*) indicate a very weak second passage shock, especially in Rotor 2. The lower overall shock loss (leading edge shock + passage shock + bow wave shock) is most likely responsible for the higher efficiency of Rotor 2. This issue will be addressed in greater detail in the three-dimensional viscous analysis comparisons of Rotors 1 and 2 presented in later sections of this paper.

The over-the-blade-tip Kulites (Fig. 7*a*) show a single normal detached shock for both rotors at design speed near stall. This is of special significance in the case of Rotor 2 since it has a significantly lower flow roll-back at the stall condition. With the advent of the detached shock, the leading edge incidence and hence the leading edge loading increases on both rotors. This is evident in the casing static pressure distributions shown in Figs. 8(*a*) and 8(*c*) where the slope of the axial distribution of static pressure from the leading edge to approximately 28 percent has increased rapidly followed by almost no increase in static pressure for an additional 10 percent of axial distance. This region of almost no static pressure rise implies a very weak or even separated boundary layer region downstream of the shock as it impinges on the blade suction surface such that it cannot support any further increase in the downstream static pressure in a steady-state manner, and the stage stalls.

In Fig. 5 the measured performance at design speed near the stall condition indicated Rotor 2 to have lower flow back while its efficiency was considerably better relative to Rotor 1. The improved efficiency (hence lower loss) of Rotor 2 translates into lower endwall and blade surface displacement thicknesses, which enhances the static pressure rise across this rotor. This is illustrated in Figs. 9(*a*) and 9(*c*) where the static pressure at the trailing edge of Rotor 2 is measured to be higher than that for Rotor 1 at both the peak efficiency and the near-stall conditions. The enhanced static pressure rise across Rotor 2 will cause this rotor to be aerodynamically more loaded and have shock fronts that are more normal compared to Rotor 1 along a given throttle line. This is illustrated in Fig. 7(*a*) where the shocks on both Rotors 1 and 2 are at approximately the same location but the mass flow rate is considerably lower and

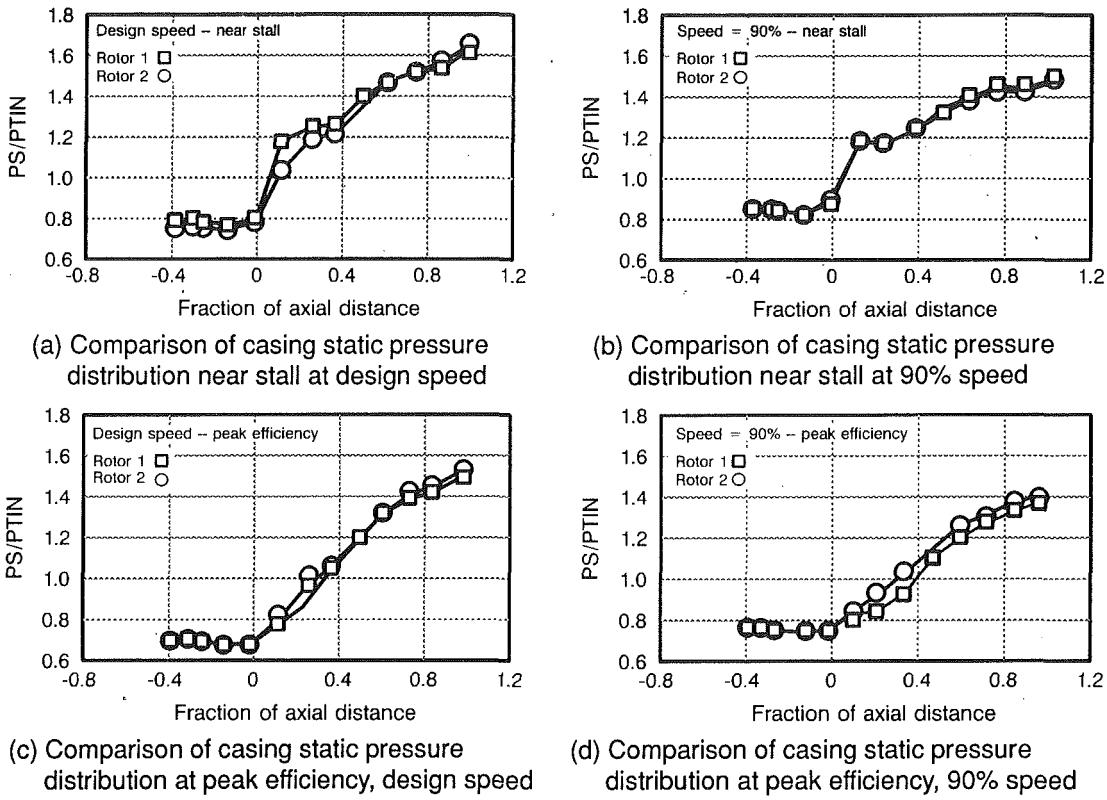

(a) Comparison of casing static pressure distribution near stall at design speed

(b) Comparison of casing static pressure distribution near stall at 90% speed

(c) Comparison of casing static pressure distribution at peak efficiency, design speed

(d) Comparison of casing static pressure distribution at peak efficiency, 90% speed

Fig. 9 Comparison of measured casing static pressure distribution between rotors 1 and 2 at similar operating conditions at design and 90 percent

the throttle line is higher for Rotor 1 with respect to Rotor 2. In addition, because of the higher inlet mass flow rate at this condition for Rotor 2, the static pressure at the leading edge of Rotor 2 is lower relative to Rotor 1 as shown in Fig. 9(*a*). The casing static pressure rise at stall normalized by the inlet dynamic head for Rotors 1 and 2 was calculated to be 0.38 and 0.40, respectively. This seems to suggest that for the specified flowpath, the maximum pressure rise potential of the blading remains the same. Consequently due to its better efficiency, Rotor 2 with its enhanced static pressure recovery reaches its static pressure loading limit at a lower flow rollback and stall margin level. This is in general agreement with the ideas suggested by Koch (1981) where the maximum pressure rise potential of individual stages was related with two-dimensional diffuser performance.

Casing Statics and Tip Kulite Comparisons at 90 Percent Speed

Figure 7(*b*) shows the over-the-tip Kulites for Rotors 1 and 2 at 90 percent speed at the peak efficiency and the near-stall conditions, respectively. Figures 8(*b*), 8(*d*), 9(*b*), and 9(*d*) show the corresponding comparison of the axial distribution of the casing static pressures at part speed for both rotors.

The tip Kulites at peak efficiency (Fig. 7*b*) show a strong leading edge shock for both rotors and also a weak second passage shock in Rotor 1. The single shock structure in Rotor 2 is illustrated by a uniform increase in the measured casing static pressure distribution presented in Figs. 8(*d*) and 9(*d*). The existence of a weak second passage shock in Rotor 1 illustrated by the tip Kulites is supported by the discontinuity in slope of the measured casing static pressure distribution for Rotor 1 at approximately 25 percent axial distance shown in Fig 2. 8(*d*) and 9(*d*). Figure 9(*d*) also shows the trailing edge casing static pressure at the peak efficiency condition to be higher on Rotor 2, resulting (as shown in Fig. 7(*b*) in the leading edge shock being pushed further forward from the leading edge relative to Rotor 1.

At 90 percent speed, near the stall condition, the leading edge shock is detached from the blade leading edge. The shocks are much farther upstream than at design speed near stall (Fig. 7*a*). The flow separation indicated by no increase in the casing static pressure in Figs. 8(*b*), 8(*d*) and 9(*b*) occurs between 10 and 25 percent axial distance from the leading edge where the shock intersects with the suction surface. The casing static pressure distributions near the stall condition for both rotors are almost identical and hence both rotors stall at the same static pressure loading level. Unlike the process at design speed, both rotors stall at similar pressure ratio and efficiency level at 90 percent speed as shown in Fig. 5.

The reduced shock losses due to lower inlet relative Mach number at 90 percent speed results in higher efficiencies for both rotors relative to design speed. However, once the shock detaches from the leading edge, bow waves become more predominant as can be seen in Fig. 7(*b*). As the shock detaches, the local leading edge loadings increase quite rapidly with the significant increase in the leading edge loss being responsible for the rapid drop in efficiency as the blades are throttled up to stall.

Three-Dimensional Viscous Analysis of Rotor 1 and Rotor 2

The details of the three-dimensional viscous analysis code used to study the flow field in the two transonic compressor rotors have been reported by Turner and Jennions (1991, 1993). The code has found wide usage within General Electric Company for compressor and turbine design and generally agrees well with test data.

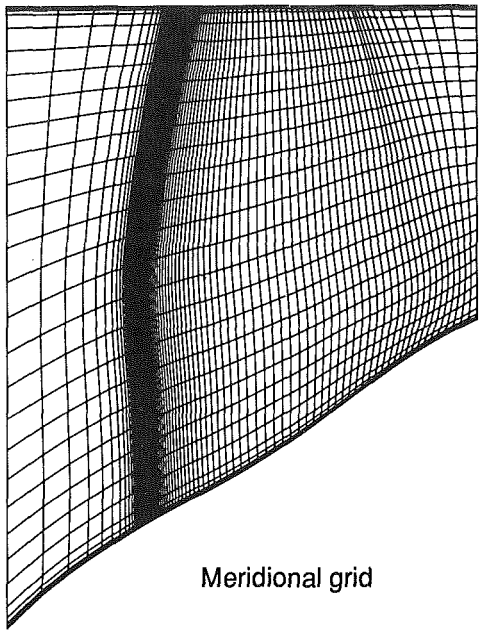

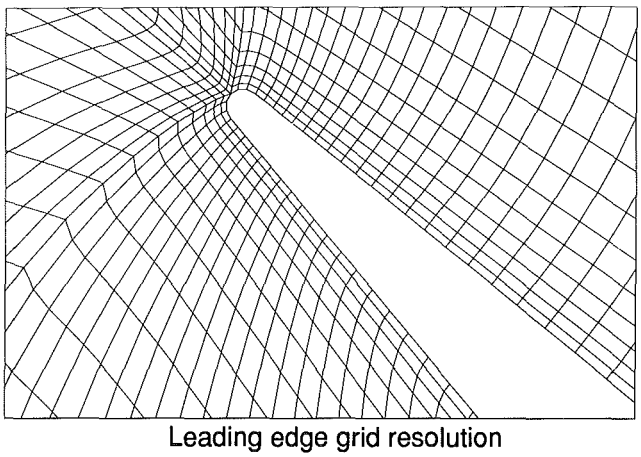

Fig. 10 Computational mesh for three-dimensional calculations

Grid Description

The three-dimensional calculations were performed using the grid shown in Fig. 10. The computations were performed with an attempt to resolve the details of the tip clearance flow. The grid consists of 93 nodes in the axial direction, of which 63 were subdivided nonuniformly from the leading edge to the trailing edge, 49 nodes in the blade-to-blade direction and 33 nodes in the spanwise direction. A stretching parameter between 1.0 and 1.2 was used in all three directions to model the gradients in the flow field near the endwalls and the blade surfaces. Special care was taken to model the leading edge region accurately to obtain the correct shock structure in the analysis. The tip clearance measured in the test was 0.025 in. (tip clearance to chord ratio = 0.67 percent) and five grid cells were used in the analysis within the tip gap. The rotating hub including the spinner was modeled in the three-dimensional analysis. Although the capability to account for the presence of the downstream stator exists, for our exploratory, comparative three-dimensional analysis it was not employed.

Boundary Conditions

The inlet boundary conditions for the three-dimensional viscous analysis consisted of the inlet total pressure and temperature and the tangential flow velocity. There is no inlet swirl, and the inlet total pressure and temperature were assumed to be uniform as it is believed that the compressor rig does not have any noticeable inlet pressure or temperature distortion present. The exit boundary condition consisted of prescribing the exit tip static pressure level such that the flow-pressure ratio characteristic calculated by the three-dimensional analysis would be on the same operating line as the measured data point. The data points selected for the three-dimensional analysis were the measured peak efficiency and the near-stall conditions at design speed for both rotors (Fig. 5).

Comparison of Three-Dimensional Calculations at Peak Efficiency and Design Speed

The calculated casing static pressure contours of the blade-to-blade flow field at the tip determined by the three-dimensional analysis for Rotor 1 and Rotor 2 are illustrated in Fig. 11. The measured shock structures at peak efficiency design speed for both rotors are also shown in Fig. 11. The static pressure contours are spaced at approximately the same interval as the measurements. Strong shocks at the leading edges were obtained in the three-dimensional analysis and agree well with the experimental data. The three-dimensional analysis and the over-the-blade-tip Kulites indicate the presence of an oblique passage shock near the pressure surface of both blades. In comparison, Fig. 12 shows the static pressure rise across the leading edge shock is more for Rotor 1 in both the analytical calculations and the over-the-blade tip casing static pressure measurements. The agreement between the measured casing static pressure distribution and the circumferential average static pressure distribution calculated from the three-dimensional flowfield is generally good with the relative trends predicted extremely well. Within the blade, Rotor 1 has higher static pressure near the leading edge and Rotor 2 has higher static pressure at the trailing edge.

Figures 13 and 14 show the isentropic Mach number contours in the meridional and blade-to-blade planes. In the meridional view, the shock front on both surfaces is swept back and is approximately parallel to the blade leading edge projection in the spanwise direction. At the blade tip a single well-resolved leading shock is formed. At 15 percent immersion a two-shock structure is observed with the leading edge oblique shock slightly stronger in Rotor 1 than Rotor 2. The suction surface Mach number just ahead of the shock is also calculated to be higher in Rotor 1. At 33 percent immersion a weak leading edge oblique shock with a nearly normal second shock was obtained in the analysis. The three-dimensional calculations also show that, while this second shock is eliminated at the blade tip, it is present at the inner immersions for this peak efficiency design speed condition.

Figure 15 compares the calculated blade surface isentropic Mach number distributions for Rotors 1 and 2. At the blade tip (Fig. 15*a*) the suction surface Mach numbers from the leading edge to 15 percent axial distance are almost identical for both rotors as per design intent. The pressure surface Mach number in this region is higher for Rotor 2 signifying the reduced wedge angle, which causes lower shock static pressure ratio (hence lower shock losses), resulting in a significantly lower leading edge loading. The suction surface shock on Rotor 2 is slightly aft of Rotor 1's shock, but this could be attributed to the higher operating line of Rotor 1 at the peak efficiency condition (see Fig. 5). Also, at 15 and 33 percent immersions, the higher leading edge wedge angle of Rotor 1 results in higher leading edge loadings on Rotor 1. The leading edge Mach numbers on the pressure surface at 15 and 34 percent immersions are higher for Rotor 2, but the peak pressure surface Mach number and the Mach number diffusion are lower and occur farther upstream relative to Rotor 1. The higher leading edge Mach number level and the lower Mach number diffusion indicate lower shock loss levels near the pressure side in the

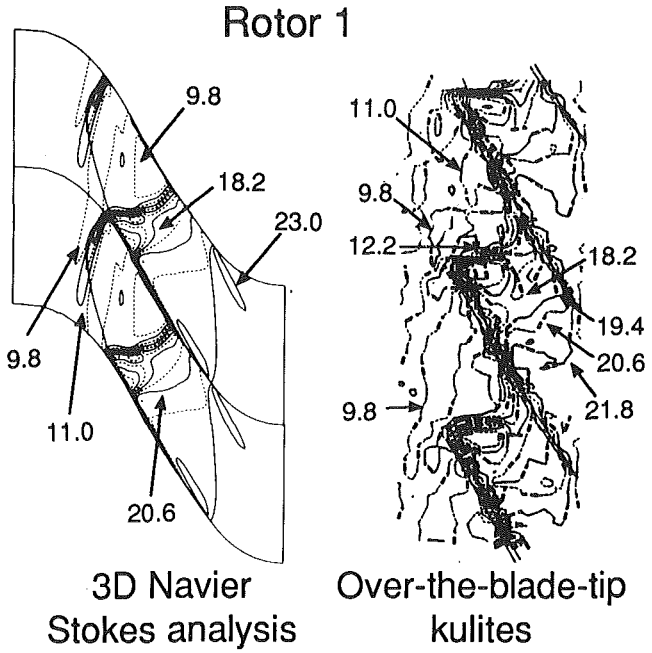

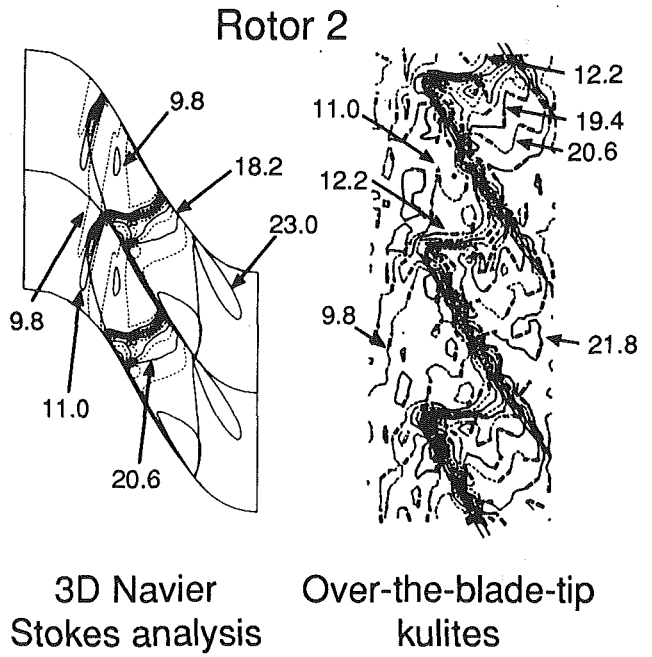

Fig. 11 Comparison of calculated casing static pressure contours with over-the-blade-tip Kulites at peak efficiency and design speed (static pressure contour interval = 1.2 psia)

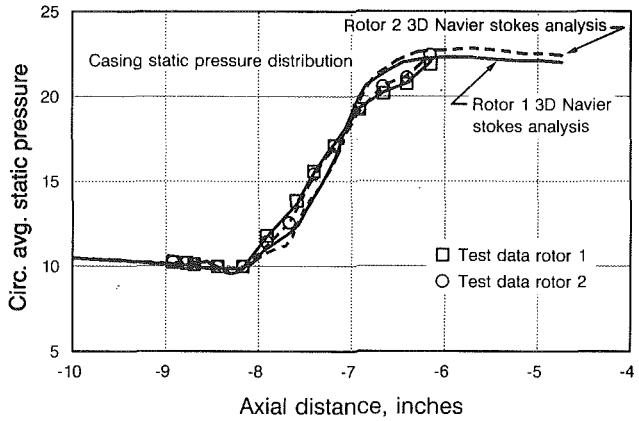

Fig. 12 Comparison of the casing static pressure distribution at peak efficiency and design speed

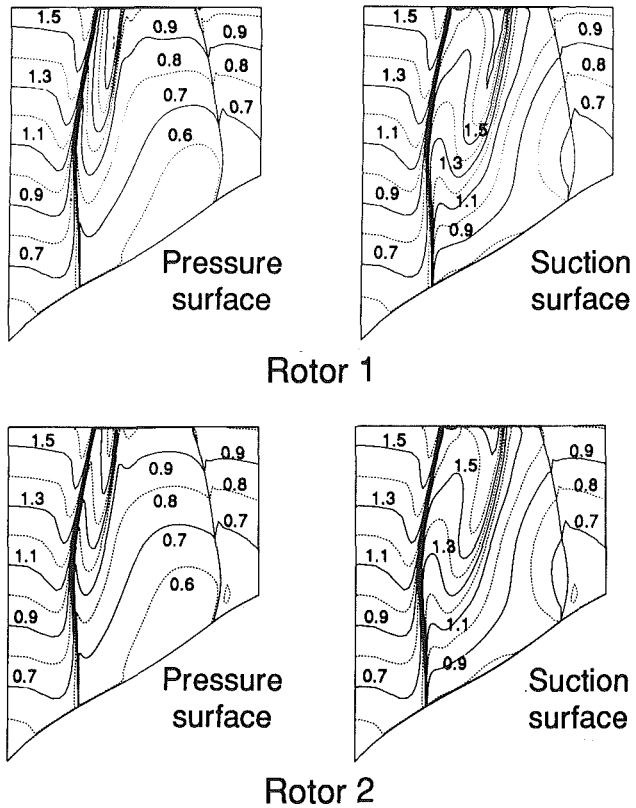

Fig. 13 Mach number contours calculated by the three-dimensional Navier–Stokes analysis (Mach number contour interval, M = 0.1)

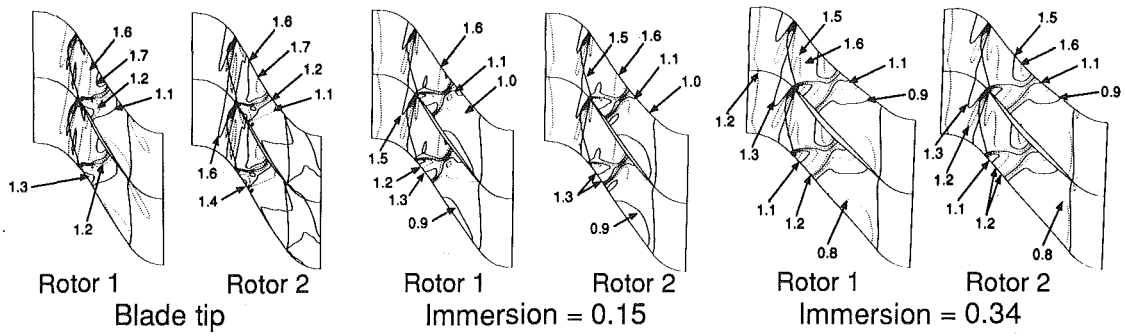

Fig. 14 Comparison of blade-to-blade Mach number contours at peak-efficiency and design speed (Mach number contour interval = 0.1)

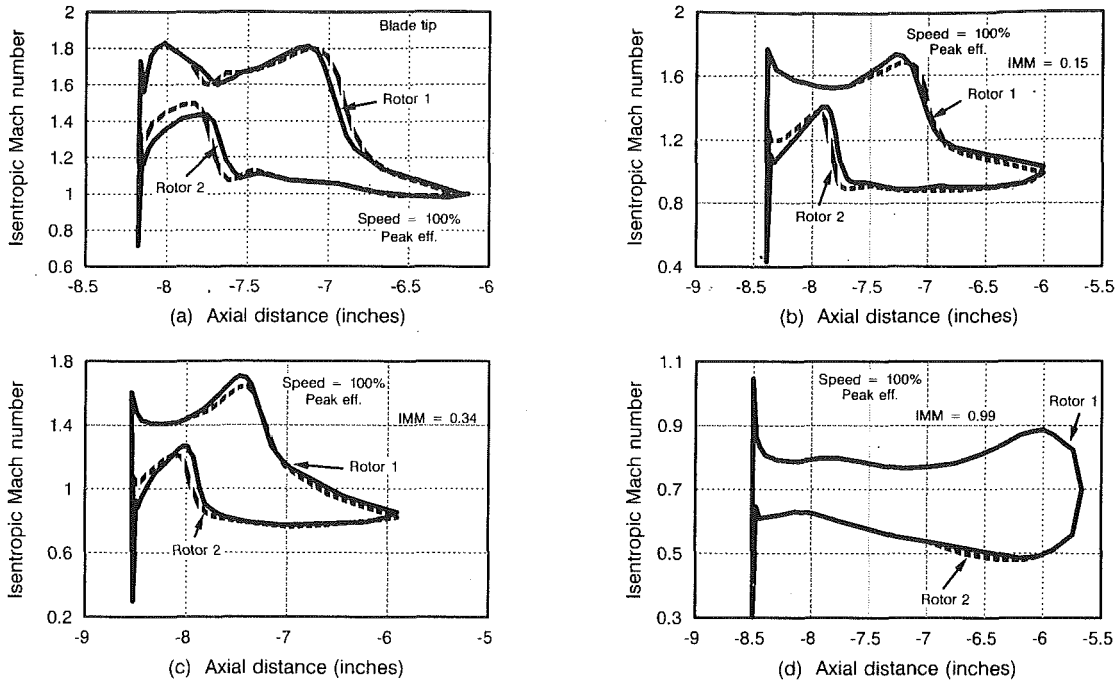

Fig. 15 Comparison of calculated blade surface isentropic Mach number distribution at peak efficiency and design speed

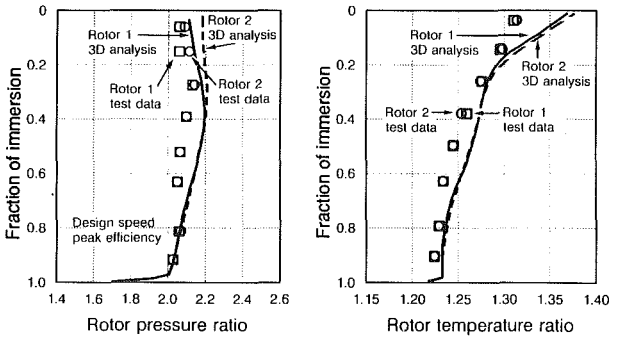

Fig. 16 Comparison of the measured and calculated radial profiles of total pressure and total temperature at peak efficiency and design speed

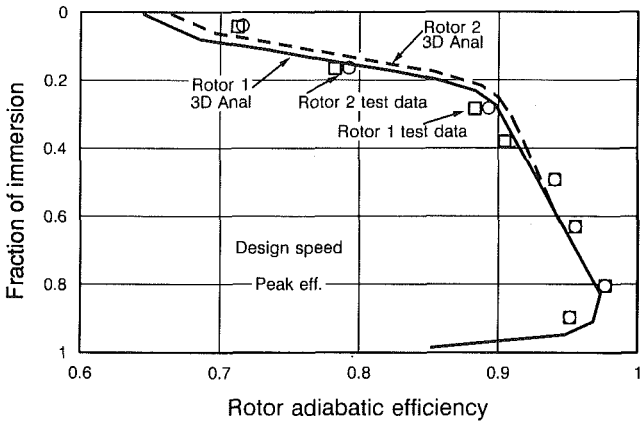

Fig. 17 Comparison of the measured and calculated radial profile of rotor adiabatic efficiency

tip region of Rotor 2. As a further benefit of the more aft location of its maximum thickness, the peak suction surface Mach number before the shock is also slightly lower on Rotor 2 relative to Rotor 1 at these immersions. Near the hub where the sections are identical for both rotors and the airfoils are aft loaded, the isentropic surface Mach number distributions (Fig. 15(*d*)) are similar.

Comparison of the radial profiles of total pressure and temperature calculated by the three-dimensional viscous analysis with the measurements are illustrated in Fig. 16. The calculated total pressure in the top 40 percent of Rotor 2 is higher than Rotor 1 with a corresponding minor increase in the calculated work input resulting in a better performance (efficiency) characteristic for Rotor 2. Some of the small differences observed between the measured and calculated radial profiles can be attributed to the following: (*a*) As stated before, measured rotor profiles were deduced from the stage exit measurements. The mixing through the stator and the unsteady, nonperiodic effects could not be isolated perfectly to provide the "rotor-alone" performance. (*b*) Also, the presence of the stator was not modeled in this comparative three-dimensional study. Figure 17 shows the comparison of the calculated adiabatic efficiency profiles relative to the measured values for both Rotors 1 and 2. While not identical in level, the proper trends in efficiency variations at different immersions are very well predicted by the three-dimensional analysis. The calculated performance levels from the three-dimensional analysis show Rotor 2 efficiency to be 0.67 point better than Rotor 1, which is in excellent agreement with the measured performance difference between the two rotors shown in Fig. 5.

Estimation of Efficiency Penalty Due to Shock Loss

With the three-dimensional flow mechanism in Rotors 1 and 2 established, we decided to investigate further the role that the shock losses have on the performance of the two rotors. The shock losses were calculated by isolating their entropy rise contribution according to the indicated static pressure ratio level.

The blade-to-blade static pressure contours were obtained from the three-dimensional viscous analysis at several immersions along the span. The blade passage between two adjacent blades (blade-to-blade plane) was circumferentially divided into ten equal parts. This blade-to-blade grid was superimposed on the plot of the contours of static pressure and the static pressure

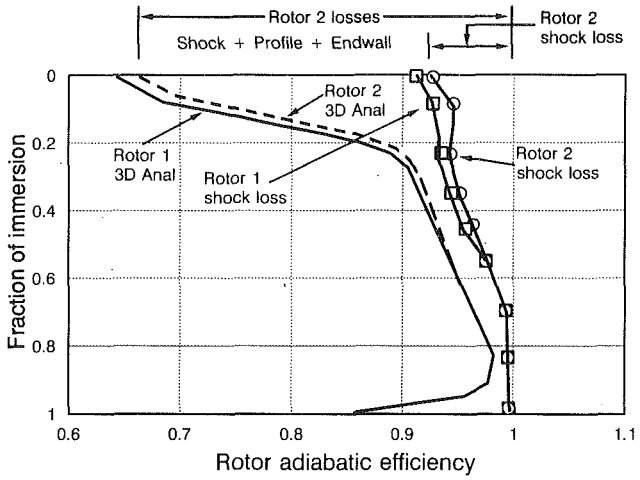

Fig. 18 Shock losses calculated from three-dimensional Navier-Stokes analysis

ratio across each component of the shock system (i.e., leading edge shock, bow waves, and second passage shock if one exists) was determined along these equidistant grid points. The entropy rise across the nodes was calculated (Equation (112), NACA Compressible Flow Tables, Ames Research Staff, 1953) and an area-averaged value of the entropy rise was calculated for that blade-to-blade plane. The efficiency loss due to the shock system at that immersion was then computed.

Figure 18 shows the comparison of the spanwise distributions of calculated efficiency loss for the three-dimensional calculated shocks for Rotors 1 and 2 with the overall calculated radial efficiency profile in the background. The difference in the shock loss efficiency levels between the two rotors corresponds to the difference in the overall efficiency predicted by the three-dimensional analysis, which as stated earlier is in close agreement with the measured efficiency difference. This result indicates that the performance impact on transonic blading due to the change in the chordwise location of maximum thickness stems from the alteration it causes in the structure of shock system. Even though the inlet relative Mach number is decreasing from the tip to 40 percent immersion, the shock loss calculated from the results of the three-dimensional analysis remains approximately the same for either rotor.

The profile loss can now be estimated from Fig. 18 as the difference between the total loss and the shock loss between 30 and 85 percent immersion. The profile losses between the two blades are approximately similar. The tip endwall loss consisting of tip leakage, scrubbing, shock and casing boundary layer interaction, and centrifugal blade surface boundary layers extends from 0 to 30 percent immersion. Similarly, at the hub, but to a much lesser spanwise penetration and level, added losses associated with the frictional drag of the inner wall materialize.

Three-Dimensional Viscous Analysis Near Stall at Design Speed

With the three-dimensional flow field established for Rotors 1 and 2 at peak efficiency, we extended our study to investigate the probable cause of lower flow rollback (less stall margin) for the higher efficiency Rotor 2. For this study the exit casing static pressure in the three-dimensional viscous analysis was increased to the measured stall casing static pressure. The inlet conditions were the same as for the previous analysis. In the "rotor-alone" three-dimensional analysis we assumed that the tip clearance and the blade deflection remained the same along the speedline with throttling. The calculated flow rollback from

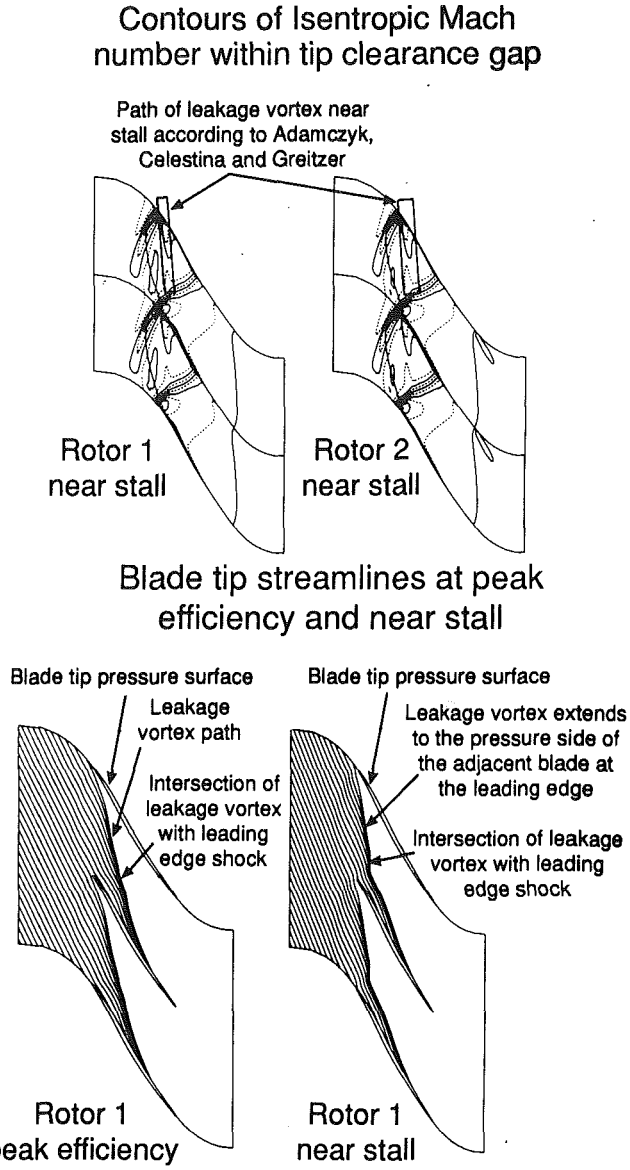

Fig. 19 Illustration of the leakage vortex path calculated by the three-dimensional Navier analysis at design speed

the peak efficiency condition for both rotors was similar to the measured flow rollbacks in Fig. 5.

Figure 19 shows the contours of isentropic Mach number within the clearance space. Adamczyk et al. (1991) have proposed from the results of a three-dimensional analysis of the NASA/Lewis Rotor 67 that a transonic blade reaches its maximum pressure rise potential when the tip leakage vortex reaches the pressure side of the adjacent blade near the leading edge. This criterion as illustrated in Fig. 19(*d*) seems to apply to both Rotors 1 and 2 in a similar manner in spite of the large difference in their corrected flow level at stall. The change in the streaklines at the blade tip of Rotor 1 as it is throttled from peak efficiency to stall shown in Figs. 19(*c*) and 19(*d*) illustrates how the tip leakage vortex reaches the pressure side of the adjacent blade near the leading edge at the stall condition.

Figures 20(*a*) and 20(*b*) show the comparison of the blade-tip surface isentropic Mach number distribution at peak efficiency and near stall for Rotors 1 and 2. The larger leading edge loadings, a precondition to stall, is evident in both rotors. While the overall shock strength appears to have been reduced near stall for both rotors, the subsequent incidence increase

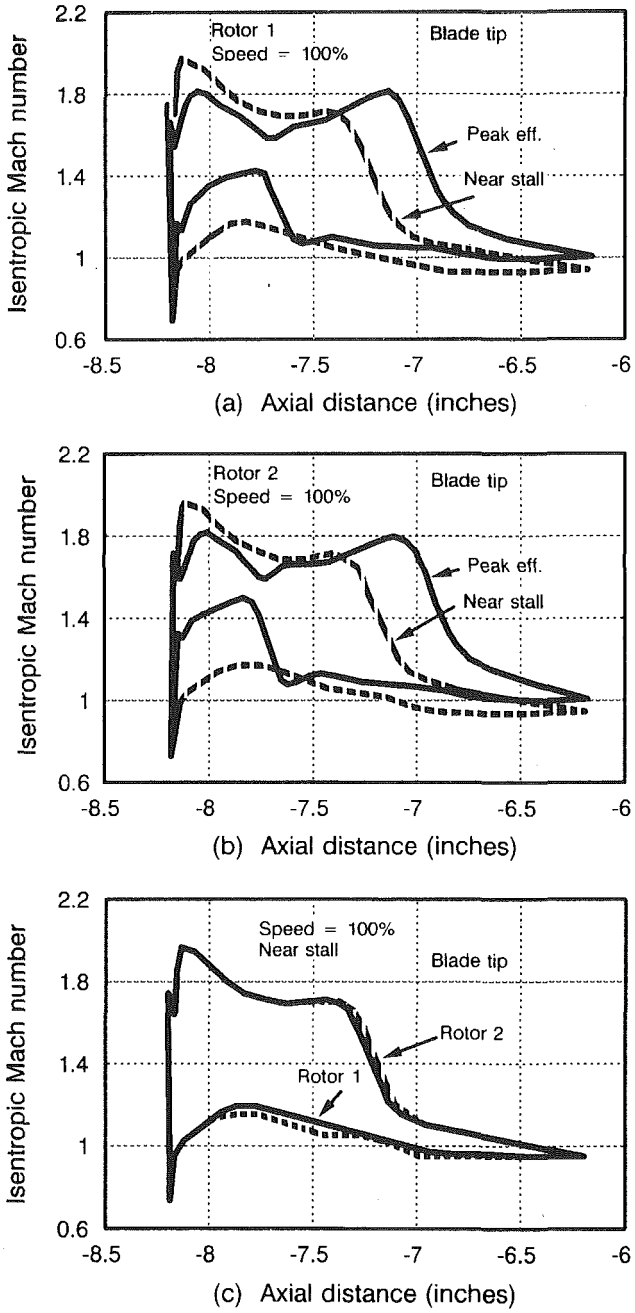

Fig. 20 Comparison of calculated blade surface isentropic Mach number distribution at peak efficiency and near stall at design speed

and the higher overall blade diffusion levels result in a decrease in performance near the stall operating condition.

Figure 20(*c*) shows the comparison of the calculated blade tip isentropic surface Mach number distribution for Rotors 1 and 2, near stall. At peak efficiency (see Fig. 15*a*) the leading edge loadings on Rotor 2 are considerably lower relative to Rotor 1. However, near stall both rotors have reached the same loading levels; Rotor 2 because of its better performance reaching a comparable normal shock condition with Rotor 1 at a higher flow than Rotor 1.

Comparison of Measured Performance With Baseline Rotor

The peak performance of the baseline rotor described in detail in Part 1 of this paper is compared with that of Rotors 1 and 2 in Fig. 21. Recall that the baseline rotor has its location

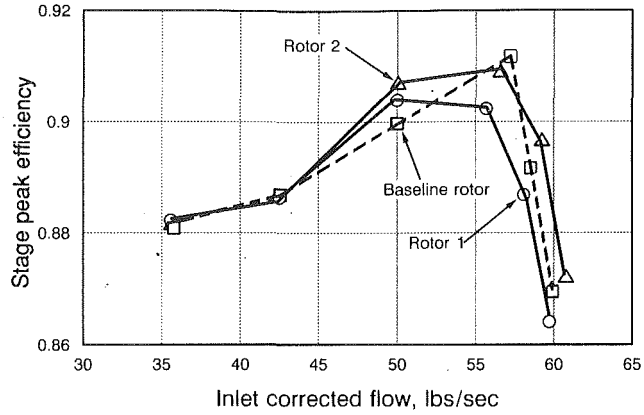

Fig. 21 Comparison of the efficiency at flow for baseline rotor, rotor 1 and rotor 2

of maximum thickness at 70 percent of chord length at the tip while Rotors 1 and 2 have their location of maximum thickness at 40 and 55 percent, respectively. The wedge angle at the leading edge is no longer critical for the baseline rotor as a smooth transition can be easily accomplished from the leading edge to the location of maximum thickness. The trailing edge wedge angle now appears to be larger, which can indirectly affect the blade trailing edge camber. Also, the throats for transonic blades are generally located between 60 and 75 percent of axial distance from the leading edge for tip sections and the location of maximum thickness in this region with a resulting larger trailing edge wedge angle could become a performance liability.

The efficiency at flow presented in Fig. 21 shows the high-speed performance of the baseline rotor to be between that of Rotors 1 and 2. This suggests the existence of an optimum thickness location, which could possibly be at 55 to 60 percent for such low aspect ratio transonic rotors.

Conclusions

Both analytical and detailed experimental results of an investigation of the influence of the location of maximum thickness on low aspect ratio transonic rotor performance have been presented. Comparison of the measured performance shows that the more aft position of maximum thickness (55 percent chord length versus 40 percent) is preferred for the best high-speed performance, keeping the edge and maximum thickness values the same. The better performance, as explained by the three-dimensional viscous analysis, is a by-product of lower shock front losses with the finer section that results when the location of the maximum thickness is moved aft. Experimental measurements on both rotors investigated verify the analytical results.

The penalty in the stall margin of Rotor 2, as determined in the compressor rig test, appears to be a direct consequence of its higher efficiency resulting in higher static pressure recovery. The blade loading limits for both Rotors 1 and 2 are almost identical at stall as illustrated by the three-dimensional calculations, but Rotor 2 reaches its static pressure diffusion limit at a higher flow relative to Rotor 1.

One implication of this study is that the designer can depend, to some extent, on leading edge loading (reduced shock strength) relief by positioning the location of maximum thickness aft on an airfoil with the 55–60 percent chord region being about adequate for good performance. It seems that some recognition of the possible penalty on flow rollback with the higher efficiency attained is desirable in the design process. The only reliable technique available to determine the loading consequences of this drawback of high-efficiency blading during the design process is to use three-dimensional analysis tools. Key

operating points must be analyzed with these advanced numerical techniques if the design is to meet all its performance goals.

Acknowledgments

The design of Rotors 1 and 2 was accomplished by the late Dave Parker and Ray Simonson under US Air Force Contract F33615-80-C-2059. The first author wishes to thank Roy Smith and Peter Szucs for the help, guidance and support during the course of this investigation and to GE Aircraft Engines and the United States Air Force for permission to publish this paper.

References

Adamczyk, J. J., Celestina, M. L., and Greitzer, E. M., 1991, "The Role of Tip Clearance in High-Speed Fan Stall," presented at the ASME Gas Turbine Conference, Orlando, FL, June 3–6.

Ames Research Staff, 1953, "Equations, Tables and Charts for Compressible Flow," NACA Report 1135.

Koch, C. C., 1981, "Stalling Pressure Rise Capability of Axial Flow Compressor Stages," ASME *Journal of Engineering for Power*, Vol. 103, pp. 645–656.

Jennions, I. K., and Turner, M. G., 1993, "Three-Dimensional Navier–Stokes Computations of Transonic Fan Flow Using and Explicit Flow Solver and an Implicit κ–ϵ Solver," ASME JOURNAL OF TURBOMACHINERY, Vol. 115, this issue, pp. 261–272.

Law, C. H., and Wadia, A. R., 1993, "Low Aspect Ratio Transonic Rotors: Part 1—Baseline Design and Performance," ASME JOURNAL OF TURBOMACHINERY, Vol. 115 this issue, pp. 218–225.

Parker, D. E., and Simonson, M. R., 1982, "Transonic Fan/Compressor Rotor Design Study," Vols. I, II, and III; Aero Propulsion Laboratory Report No. AFWAL-TR-82-2017.

Turner, M. G., and Jennions, I. K., 1991, "A Novel Implementation of an Implicit K–ϵ Turbulence Model Coupled With an Explicit Navier–Stokes Solver," presented at the AIAA CFD Conference, Honolulu, HI.

Turner, M. G., and Jennions, I. K., 1993, "An Investigation of Turbulence Modeling in Transonic Fans Including a Novel Implementation of an Implicit κ–ϵ Turbulence Model," ASME JOURNAL OF TURBOMACHINERY, Vol. 115, this issue, pp. 249–260.

Wennerstrom, A. J., and Frost, G. R., 1976, "Design of a 1500 ft/sec, Transonic, High-Through-Flow, Single-Stage, Axial-Flow Compressor With Low Hub/Tip Ratio," Air Force Aero Propulsion Laboratory Report No. AFAPL-TR-76-59.

Wennerstrom, A. J., Derose, R. D., Law, G. H. and Buzzell, W. A., 1976, "Investigation of a 1500 ft/sec, Transonic, High-Through-Flow, Single-Stage, Axial-Flow Compressor With Low Hub/Tip Ratio," Air Force Aero Propulsion Laboratory Report No. APAPL-TR-76-92.

Wennerstrom, A. J., and Buzzell, W. A., 1979, "Redesign of a Rotor for a 1500 ft/sec, Transonic, High-Through-Flow, Single-Stage Axial-Flow Compressor With Low Hub/Tip Ratio," Air Force Aero Propulsion Laboratory Report No. AFAPL-TR-79-2078.

Three-Dimensional Flow Phenomena in a Transonic, High-Throughflow, Axial-Flow Compressor Stage

W. W. Copenhaver
Wright Laboratory,
Wright-Patterson AFB, OH 45433

C. Hah
NASA Lewis Research Center,
Cleveland, OH 44135

S. L. Puterbaugh
Wright Laboratory,
Wright-Patterson AFB, OH 45433

A detailed aerodynamic study of a transonic, high-throughflow, single-stage compressor is presented. The compressor stage was comprised of a low-aspect-ratio rotor combined alternately with two different stator designs. Both experimental and numerical studies are conducted to understand the details of the complex flow field present in this stage. Aerodynamic measurements using high-frequency, Kulite pressure transducers and conventional probes are compared with results from a three-dimensional viscous flow analysis. A steady multiple blade row approach is used in the numerical technique to examine the detailed flow structure inside the rotor and the stator passages. The comparisons indicate that many flow field features are correctly captured by viscous flow analysis, and therefore unmeasured phenomena can be studied with some level of confidence.

Introduction

In the mid-1970s a transonic high-throughflow single-stage fan was designed and demonstrated as reported by Wennerstrom (1984). This rotor was subsequently redesigned to provide a more rugged geometry and yet maintain aerodynamic performance. These experimental results were reported by Law and Wadia (1993). The salient features of the stage performance were as follows:

Pressure ratio	1.92
Isentropic efficiency	85.4 percent
Specific flow rate	43.13 lbm/sec/ft^2 (210.5 kg/s/m^2)
Rotor tip relative Mach number	1.629

The success of this stage, particularly the rotor, and its state-of-the-art geometry (e.g., low aspect ratio, arbitrary airfoils, etc.) made it an ideal baseline for a parametric design investigation. The intent of this investigation was to quantify the effect of several design parameters by designing, fabricating, and testing a series of rotors, each differing as much as practical from the baseline by a single parameter. The parameters varied were those thought to be important to performance but that have not been included in the loss models of contemporary design systems. The specific parameters included chordwise location of maximum thickness, various cascade area ratios, and leading edge sweep. A total of seven rotors were designed and fabricated for the initial test program. The most successful unswept design was designated Rotor 4 and is the subject of the current numerical study.

Rotor 4 was designed to investigate the ability to control shock strength by tailoring the suction surface shape. The specific design parameter in this case was inlet-to-throat area ratio along with the suction surface contour (when considering the airfoil/passage in the cascade plane). Although this could be considered as two design variables, it is effectively one since a change in inlet-to-throat area ratio must be accompanied by some change of surface contour (except for a simple re-staggering). The rotor was designed with less throat margin than the baseline (due to a steeper suction surface angle ahead of the passage shock) and the suction surface shape was tailored to lessen the shock-boundary layer interaction. Further details of the Rotor 4 design are provided by Parker and Simonson (1982).

In addition to the rotor study, an investigation using two different stator designs was performed. The original stator design was described by Wennerstrom (1984). The redesign was accomplished using experimental data given by earlier efforts described by Law and Wadia (1993). The range of inlet air angles from choke to stall was considered, as well as the presence of severe overturning near the casing, which results from rotor tip clearance losses. The two stators were tested in back-to-back fashion with several rotors of the test series including Rotor 4. The original and redesigned stators shall be referred to as Stator 1 and Stator 2, respectively.

The flow field analysis of the full stage (for both Stator 1 and Stator 2) using a computational fluid dynamics (CFD) technique and comparison of the results with experiment are the subjects of the present paper. CFD technology for tur-

Contributed by the International Gas Turbine Institute and presented at the 37th International Gas Turbine and Aeroengine Congress and Exposition, Cologne, Germany, June 1-4, 1992. Manuscript received by the International Gas Turbine Institute February 11, 1992. Paper No. 92-GT-169. Associate Technical Editor: L. S. Langston.

bomachinery aerodynamics has been developed significantly over the last decade (Davis et al., 1988; Dawes, 1986; Denton, 1986; Giles, 1988; Hah, 1987; Moore and Moore, 1985; Rao and Delaney, 1990; etc.). Fully three-dimensional flow calculations based on the Reynolds-averaged Navier–Stokes equations are now relatively well established and applied routinely for the design analysis of many turbomachinery components. The maturation of numerical schemes to compute the flow field around isolated blade rows has led to various efforts to extend the techniques to multiple blade rows (Adamczyk, 1985; Arts, 1985; Dawes, 1986; Denton and Singh, 1979; Ni, 1989; etc.).

In this study, a numerical method based on the steady-state Reynolds-averaged Navier–Stokes equations is applied to investigate the flow field inside the subject transonic compressor stage. A relatively simple numerical procedure is employed to handle the full-stage computation. The method utilizes a mixing plane to transmit information between blade rows. This simple method does not attempt to model any unsteady effects on the steady flow field.

Measured casing static pressure distributions for several different stage operating conditions are compared with the numerical solutions. In addition, rotor exit efficiency profiles, determined from stage exit plane information using an axisymmetric throughflow experimental data match technique, are compared with rotor efficiency profiles obtained from the numerical solutions. Finally some discussion is given for interesting flow phenomena including the tip clearance region, shock geometry of the rotor, and stator aerodynamic performance.

Experiment

The compressor stage configurations (Rotor 4/Stator 1 and Rotor 4/Stator 2) were tested in the Wright Laboratory Compressor Aero Research Lab. This test facility is configured for closed-loop testing of high specific flow fans and compressors with a 2000 hp maximum power requirement. The test configuration and instrumentation were designed to define overall steady-state performance of the stage and time-resolved rotor tip static pressures. Details of the test facility and steady-state instrumentation are provided by Law and Wadia (1993).

Rotor tip time-resolved static pressure data were obtained from twelve high-frequency Kulite pressure transducers. These transducers were positioned at 12 uniformly spaced axial locations beginning 0.75 in. (19 mm) upstream of the rotor leading edge. The 0.25 in. (6.3 mm) spacing allowed for three measurements upstream of the rotor tip leading edge and nine along the chord of the blade tip. The time-resolved data were ensemble averaged to remove randomness. An ensemble consisted of 400 discrete points that, when spatially resolved, span approximately two and one half blade passages. Averaging was triggered such that the same two and one half blade passages were presented in the ensemble. Absolute static pressure levels were determined by combining dynamic pressures from the Kulites and steady pressures from steady-state casing pressures at the same axial locations.

Numerical Procedure

The Reynolds-averaged Navier–Stokes equations detailed by Hah and Wennerstrom (1991) are solved for the current problem. To close the system of equations, a closure model for the turbulence stress should be applied. Currently many turbulence models are available for large-scale three-dimensional flow calculations. Although none of the existing closure models represent all of the salient flow features accurately, major differences between the flow fields of different aerodynamic designs can be calculated with the existing models.

It is well known that neither the conventional mixing length type turbulence model nor any standard two-equation type turbulence model describes turbulence stresses properly in the region behind a shock wave or in the separated flow regions. Several recent studies indicate that significant improvement can be achieved when the standard two-equation model is modified to include the low Reynolds number effects. For the current study, a standard two-equation model is modified to include the low Reynolds number effects following the studies of Chien (1982). The following transport equations are solved for the turbulent shear stresses:

$$\frac{\partial(\rho U_i k)}{\partial x_i} = \frac{\partial}{\partial x_i}\left(\frac{\mu_{\text{eff}}}{\sigma_k}\frac{\partial k}{\partial x_i}\right) - \rho\overline{u_i u_j}\,U_{ij} - \rho\epsilon - \frac{2\mu k}{l^2} \tag{1}$$

$$\frac{\partial(\rho U_i \epsilon)}{\partial x_i} = \frac{\partial}{\partial x_i}\left(\frac{\mu_{\text{eff}}}{\sigma_\epsilon}\frac{\partial \epsilon}{\partial x_i}\right) + C_1\frac{\rho\epsilon}{k}\,(\overline{u_i u_j}\,U_{i,j}) - \frac{\rho\epsilon}{k}\left(C_2 f\epsilon + \frac{2\nu k\exp(-C_4 u^* l/\nu)}{l^2}\right) \tag{2}$$

$$\mu_{\text{eff}} = \mu + C_\mu(k^2/\epsilon)\{1-\exp[-(C_3 u^* l/\nu)]\} \tag{3}$$

$$f = 1 - \frac{0.4}{1.8}\exp-[(k^2/6\nu\epsilon)^2] \tag{4}$$

No attempt was made to optimize the constants of the turbulence transport equations for the current study. Therefore, standard values for the constants are used; these values are

$$C_\mu = 0.09,\ C_1 = 1.25,\ C_2 = 1.8,\ \sigma_k = 1.0,\ \sigma_\epsilon = 1.3,$$

$$C_3 = 0.0115,\ C_4 = 0.5.$$

The governing Reynolds-averaged Navier–Stokes equations are solved with a pressure-based implicit relaxation method using a fully conservative control volume approach described by Hah (1987) for isolated rotor configurations. A third-order accurate interpolation scheme is used for the discretization of the convection terms and central differencing is used for the diffusion terms. The numerical method is of second-order accuracy with smoothly varying grids. Details of the current method for applications to transonic flows are given by Hah and Wennerstrom (1991).

In this study, the numerical procedure is expanded to include the stator in a fan stage configuration. In order to maintain stability of the numerical method, sufficient domain upstream and downstream of the blade row is required. This fact, combined with the close coupling of the blade rows in this stage (15 percent of rotor blade chord at the hub), drove the development of a somewhat unconventional approach to interface the blade rows computationally. The complete blade free region is utilized for both the rotor exit and stator entrance computations by using the overlapping grid shown in Fig. 1. The computational domain of the rotor extends to the leading

Nomenclature

$C_1, C_2, C_3, C_4, C_\mu$ = constants in turbulence closure models
k = turbulent kinetic energy
l = characteristic length
U_i = mean velocity components
u_i = fluctuating velocity components
ϵ = turbulence dissipation rate
μ = viscosity
μ_{eff} = effective viscosity
ν = kinematic viscosity
ρ = density
$\sigma_k, \sigma_\epsilon$ = constants in turbulence closure models

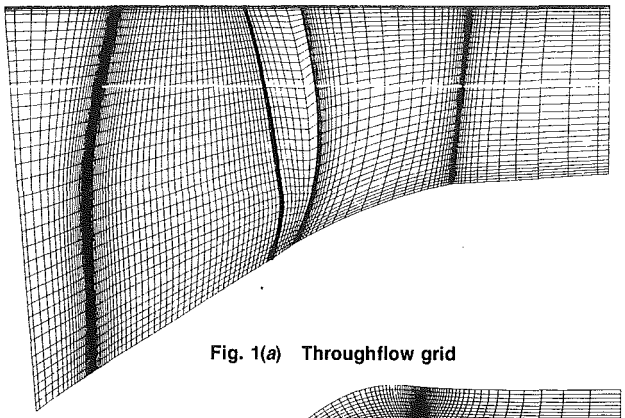

Fig. 1(*a*) Throughflow grid

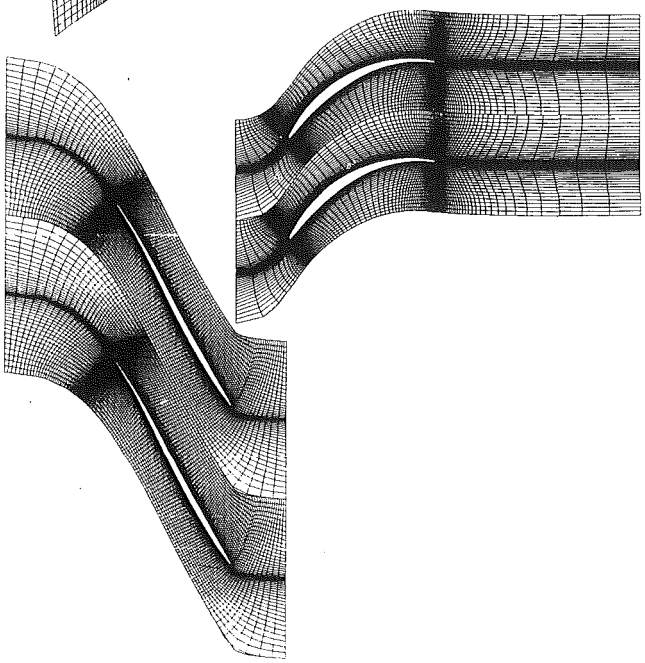

Fig. 1(*b*) Blade-to-blade grid

edge plane of the stator while the computational domain of the stator begins at the trailing edge plane of the rotor. Therefore, two interface planes are used to transmit information between blade rows. With the current steady-state multiple blade rows calculation, the flow field of the rotor and the flow field of the stator are computed iteratively.

For the rotor, the radial distribution of the static pressure at the exit of the computational domain is obtained from the stator flow field. At this plane, which is located at the leading edge plane of the stator, the circumferentially averaged static pressure distribution from the stator solution is used for the boundary condition of the rotor flow field. All the other variables at this boundary are extrapolated from the rotor inner solution.

For the stator, radial distributions of all the variables at the inlet of the computational domain are obtained from the rotor solution. At this mixing plane, which is located at the trailing edge plane of the rotor, a classical mixing analysis is performed at each radial location to obtain circumferentially uniform values of velocity and density. Since a shock wave does not cross the mixing planes for the present problem, this boundary condition does not cause any numerical instability. The mixing analysis, which is based on the work of Dring and Spear (1991), is necessary to obtain a steady inlet condition for the stator flow field. The overall mass flow rate across the stage is determined by the specified static pressure at the exit of the stator and the radial distribution of the total temperature and total pressure at the inlet of the rotor. As pointed out by Denton and Xu (1990), this calculation can also be performed by running two separate isolated blade row solutions. However, some human intervention during the solution can be eliminated with the current procedure.

The current computational grid was generated to give an orthogonal grid near the leading edge and near the blade surface where the most important flow phenomena occur (passage shock, shock-boundary layer interaction, etc.). Spatial periodicity at the periodic surfaces is not enforced for the grid; therefore the physical periodicity condition is handled inside the code using an interpolation function. The grid consists of 50 nodes in the blade-to-blade direction, 46 nodes in the spanwise direction, 152 nodes in the streamwise direction for the rotor, and 112 nodes in the streamwise direction for the stator. Six grid nodes in the spanwise direction are used to describe the tip-clearance region of the rotor. Inside the tip gap, the grid is closed in the blade-to-blade direction and the periodicity condition is applied. As indicated earlier, the rotor and stator flow fields are computed iteratively at each cycle of the computation with the information transmitted through the mixing planes. For the currently adopted grid (607,200 nodes), about four to five hours of Cray YMP single processor time is necessary to get a fully converged solution for each operating condition.

As is well known, the quality of the numerical solution can deteriorate due to numerical diffusion when insufficient grid size is used. For the current stage configuration type (low aspect ratio, transonic), computational grids with more than 200,000 grid nodes on each blade row seem to give grid-independent solutions for the total pressure and the aerodynamic loss. Residuals of each finite difference equation are integrated over the entire domain. The solution is considered converged when the integrated residuals of all the equations are reduced by four orders of the magnitude from the initial value.

Results and Discussion

The three-dimensional Navier–Stokes method previously described was applied to the Rotor 4 configuration. The intent was to evaluate the capability of the numerical method in predicting the detailed features of this complex flow field. The full-stage computation (with Stator 1 and Stator 2) was performed at 100 percent speed, peak efficiency point only. Isolated Rotor 4 computations were performed for 6 points from choke to stall at both 100 percent and 90 percent speeds. The Rotor 4 isolated and in-stage results were very similar at the peak efficiency point and this trend was expected to continue at other points. Comparisons of steady-state rotor performance are presented to support the use of the numerical technique for investigation of flow features that were not measured in the test program. The detailed flow features presented from the numerical method provide insight into how rotor designs may be altered for improved performance. In addition, stage performance comparisons are presented that indicate that the numerical scheme, chosen to accommodate rotor–stator interactions, can be used for stage investigations. In the following sections, the rotor flow fields at four operating conditions (two flow rates at two rotor speeds) are analyzed in detail first. The flow fields across the two stators are then compared for stage performance.

All the numerical solutions were performed using rotor hot, running geometry. Separate blade stress analyses were performed at 100 percent rotor speed and 90 percent rotor speed to determine the true running geometries for the numerical analysis. Flow fields at 12 different mass flow rates at these speeds have been numerically analyzed for comparison with rotor performance data. Detailed casing flow field results at the peak efficiency and near-stall points for each rotor speed are analyzed and compared with the measured data.

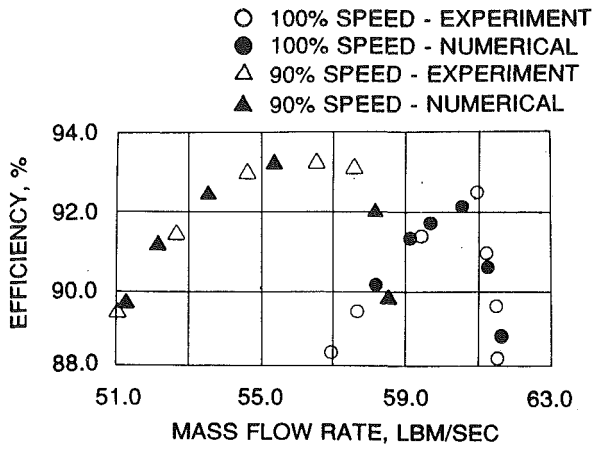

Fig. 2 Comparison of rotor efficiency map

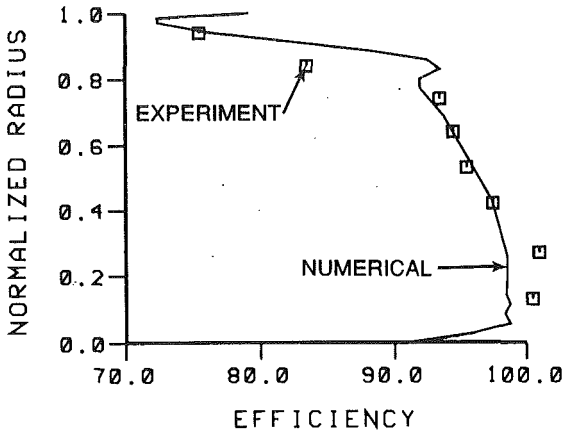

Fig. 3(*a*) Comparison of blade section efficiency at 90 percent rotor speed

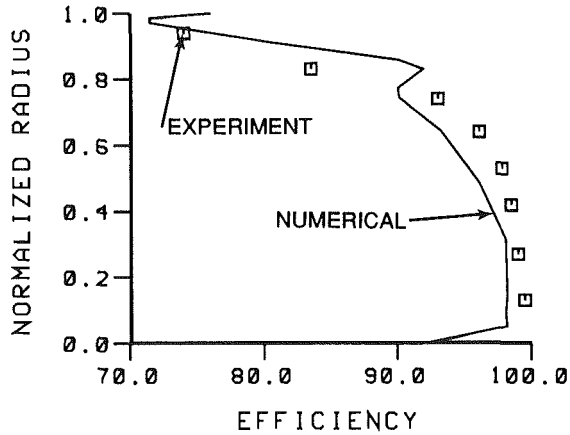

Fig. 3(*b*) Comparison of blade section efficiency at 100 percent rotor speed

Rotor Aerodynamic Performance. Experimental rotor performance presented here is computed using an axisymmetric inviscid throughflow data match analysis. As a part of this analysis, the stage exit data at a given radius are projected forward to the rotor exit along streamlines. No mixing model is used in the analysis. At a given radius the exit total temperatures used for this extrapolation are mass averages while the total pressures are the numerical average of the three highest exit plane circumferential values. The rotor exit comparisons presented in this section are between these extrapolated values (identified as experimental) and those determined by the current three-dimensional Navier–Stokes numerical procedure. No special adjustments were made to the numerical procedure, for this rotor, to obtain the results presented.

The rotor efficiency maps from the experimental data and the numerical results are compared in Fig. 2. The rotor performances at various flow conditions are properly calculated. Both the experimental and the numerical results show that the rotor has higher peak efficiency at 90 percent rotor speed than at 100 percent rotor speed. This may be due to a reduced shock strength at 90 percent speed and a resulting weaker shock–boundary layer interaction. This theory will be explored further when details of the three-dimensional flow field are described.

In Fig. 3, comparisons are made between the experimental and the numerical values of the blade section efficiency for two operating conditions. The efficiencies from the numerical method were determined from an area-weighted circumferential average of the nodal temperatures and pressures at the rotor exit for common spanwise locations.

The overall agreement is very good considering the complexity of the flow field. Although the absolute value of the loss is not calculated exactly for most spanwise locations, the spanwise variation is captured. Differences between the experimental and numerical results in Fig. 4 may be attributed to the lack of a mixing model in the data match procedure and possible numerical inaccuracies. Both results, experimental and numerical, indicate tip region efficiency levels are much lower than midspan and hub region levels. This suggests that understanding and controlling the flow near the endwall region is very important for improved efficiency over the range of operation for such a transonic, low-aspect-ratio fan. Details of the endwall flow will be discussed in the next section.

Rotor Flow Field. In Fig. 4, measured static pressure contours on the casing at 90 percent speed, at peak efficiency and near-stall operating conditions, are compared with the corresponding numerical solutions. At the peak efficiency condition (Fig. 4*a*), the shock, which is standing almost normal to the incoming flow, is clearly seen in both experimental and numerical presentations. The numerical solution also shows evidence of the tip-leakage vortex, which cannot be clearly seen in the measured data. At the near-stall condition (Fig. 4*b*) the shock is pushed farther upstream than at the peak efficiency operating condition. This also is clearly seen in both numerical and experimental presentations. The numerical solution indicates that the shock has been moved forward to a point where the tip-leakage vortex interacts with the shock and weakens it near midpassage. The weakening of the shock at midpassage is indicated in the measured pressure contours as well, but little evidence of the vortex can be seen.

The interaction of the shock structure and the tip-leakage vortex presented for 90 percent speed is also evident at 100 percent speed, as shown in Fig. 5, but is less pronounced because the shock is farther back in the passage. Figure 5 also shows a high gradient static pressure region on the suction surface just downstream of the shock. This is considered to represent a weak secondary shock. The influence of this weak secondary shock on the tip-leakage flows will be discussed later. To explore the evidence of the tip-leakage vortex in the experimental data, measured and calculated static pressure plots across the blade passage are presented in Fig. 6. The figure shows the static pressure variation across the passage at an axial location just downstream of the leading edge. The drop in static pressure near the blade suction surface due to the tip-clearance vortex is represented in both measured and calculated data. The static pressure measurement transducers were spaced too far apart to capture the high axial static pressure gradient in the vortex, but do indicate a drop in static pressure at this location. Figure 6 also demonstrates the excellent agreement in measured and calculated circumferential static pressure distribution.

Fig. 4(*a*) Comparison of casing static pressure at peak efficiency condition (90 percent rotor speed)

Fig. 4(*b*) Comparison of casing static pressure at stall condition (90 percent rotor speed)

The comparisons in Figs. 4, 5, and 6 show that the endwall shock structures and tip-leakage flows at various operating conditions are calculated very well with the current numerical procedure. Therefore, to gain an increased understanding of the interaction of these fluid structures, details of unmeasured three-dimensional flow phenomena predicted by the numerical procedure will be studied.

Calculated static pressure contours on the blade surfaces for 90 percent rotor speed and 100 percent rotor speed at peak efficiency operating conditions are shown in Figs. 7 and 8, respectively. Changes in the passage shock system due to the changes in rotor speed are clearly displayed in both Figs. 7 and 8. The shock system for both operating conditions in this unswept design is three dimensional and inclines forward away from the endwall. However, the shock becomes normal to the endwall near the casing due to the physical constraint. The impact of this shock structure on design assumptions was presented by Hah and Wennerstrom (1991). The figures suggest that the passage shock is weaker below the tip region at 90 percent rotor speed (Fig. 7) than at 100 percent speed (Fig. 8). This weaker shock system and resulting less severe shock-boundary layer interaction might imply why the rotor has the highest peak efficiency at 90 percent rotor speed as was presented in the performance results.

The influence of tip-leakage vortices on the shock system at the rotor casing was presented in Figs. 4, 5, and 6. Three-dimensional details of the tip-leakage vortex system present in the rotor passage, as determined from the numerical calculation, provide additional insight into their interactions with passage shocks and clearance flows. Figure 9 shows particle traces near the tip region for the peak efficiency condition at 100 percent rotor speed. The particles, which are released near the suction side of the blade tip, show the detailed structure of the tip-leakage vortex. The vortex emanating from the leading edge is clearly the dominating flow structure in the figure. It is formed almost at the leading edge and shows a clear swirling motion along the vortex core line. Particles released along the tip downstream of the leading edge and upstream of the shock eventually are influenced by the tip-leading-edge vortex and follow a vortex like behavior. As these fluid structures encounter the shock, they turn and the vortex becomes less organized. Downstream of the shock a third vortexlike structure is evident. It is formed behind the passage shock where a weak secondary shock appears, as was defined previously (Fig. 5). The static pressure gradient across this vortex like structure is much smaller than of the tip-leading-edge vortex and therefore it is difficult to identify this phenomenon clearly as a vortex.

The interrelationship of the tip-clearance vortex structure and the passage shock is important to understand, as the aerodynamic efficiency and the surge margin of the compressor rotor are closely associated to the tip-leakage flow. Control of this tip-leakage flow structure could improve the compressor efficiency and the operating range.

Steady-state numerical computations of the Rotor 4 flow field in an isolated environment have shown that good agreement with experimental data can be achieved, and many important flow field phenomena have been identified. The Rotor 4 geometry was then thought to provide a good opportunity to apply the multiple blade row modeling approach. Results from this approach will be discussed next.

Stator Flow Field. The original detailed stator design (Stator 1) was described by Wennerstrom (1984); a quick overview will be given here. The stator inlet Mach number ranged from 1.0 at the hub to 0.7 at the case. In an attempt to eliminate

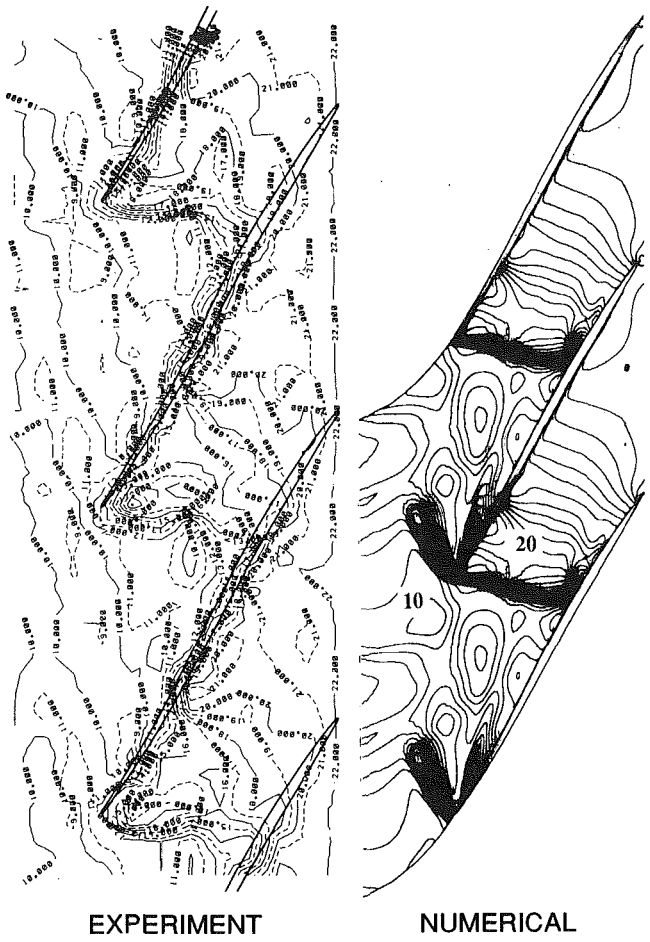

Fig. 5(*a*) Comparison of casing static pressure at peak efficiency condition (100 percent rotor speed)

Fig. 5(*b*) Comparison of casing static pressure at stall condition (100 percent rotor speed)

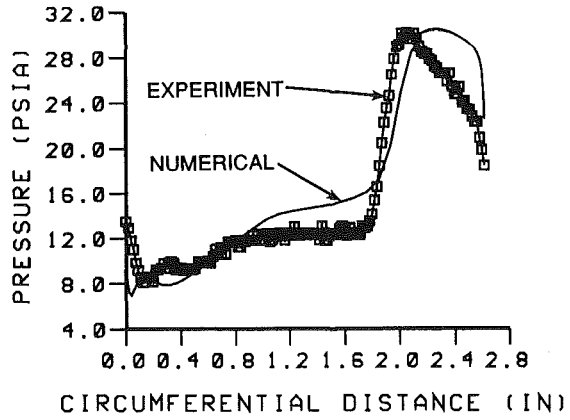

Fig. 6 Comparison of circumferential casing static pressure distribution 0.25 in. (6.4 mm) downstream of leading edge at stall condition (100 percent rotor speed)

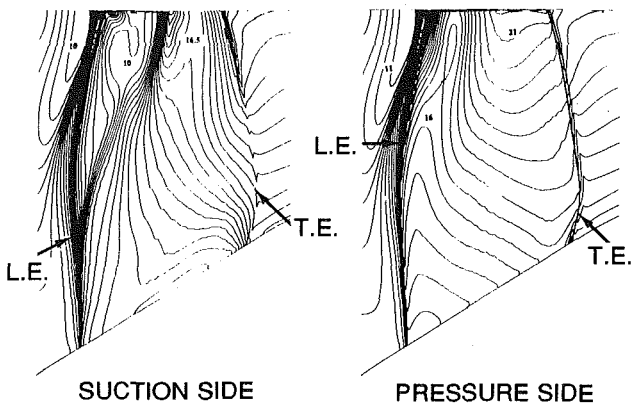

Fig. 7 Blade surface static pressure distribution at peak efficiency condition (90 percent rotor speed)

shock-related losses due to the high hub Mach number, the leading edge was swept near the hub. The inlet flow was turned to axial at the exit, requiring 40 to 50 deg of turning. This drove the selection of aspect ratio (1.255) and solidity (2.8 at the hub and 1.6 at the tip). The spanwise distribution of diffusion factor peaked at the hub at a value of 0.55. The experimental results showed that the stator performed very well, as indicated by the overall stage performance, as reported by Wennerstrom (1984).

The stator was redesigned (Stator 2) and tested. The motivation for the redesign was to evaluate an alternate design approach. The objectives of the new approach were to generate blade sections that were more tolerant to off-design incidence angles and produce a lower loss than the original. The inlet conditions as determined by experiment, at design and off-design points, were used in the redesign. Subsequent tests showed that at 100 percent rotor speed, peak efficiency operating point the Rotor 4/Stator 2 combination outperformed the Rotor 4/Stator 1 combination by 1.4 points in efficiency. The detailed flow features that existed in the stator were not measured directly; therefore, the numerical method was utilized to provide this information.

The subject multiple blade row calculation technique was

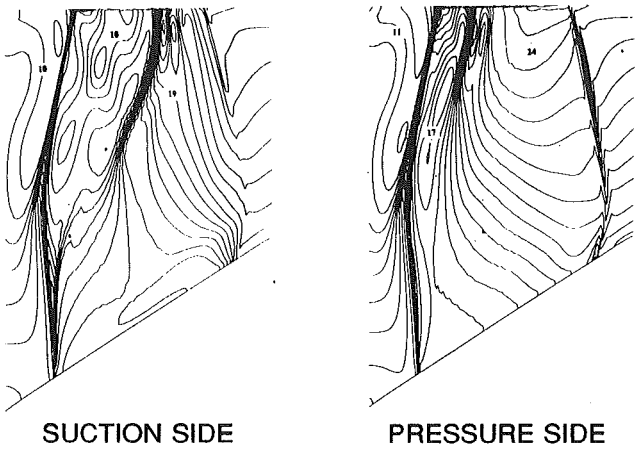

Fig. 8 Blade surface static pressure distribution at peak efficiency condition (100 percent rotor speed)

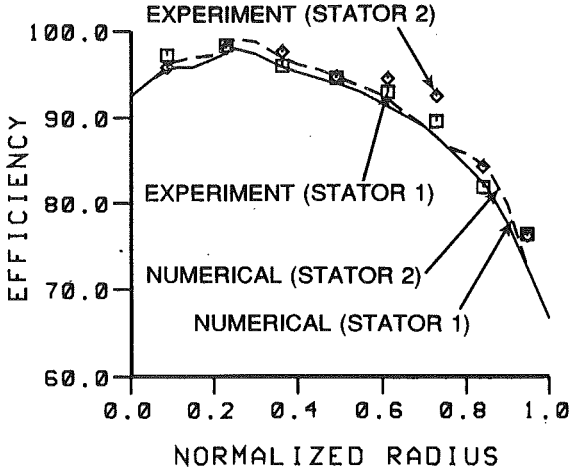

Fig. 10 Comparison of stage efficiencies with the two stators

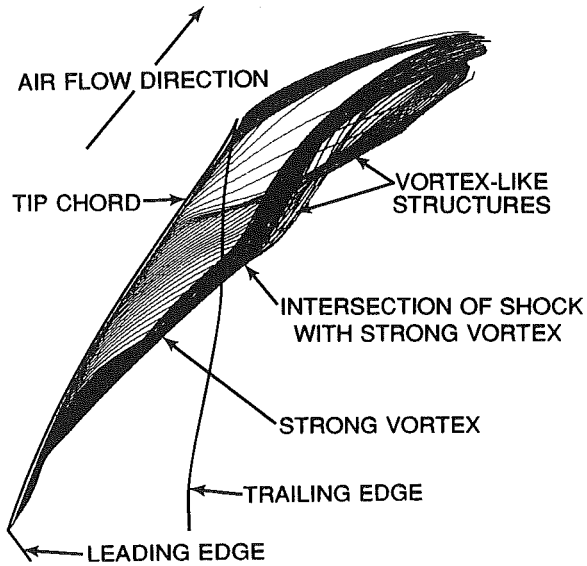

Fig. 9 Tip-leakage flow structure at peak efficiency condition (100 percent rotor speed)

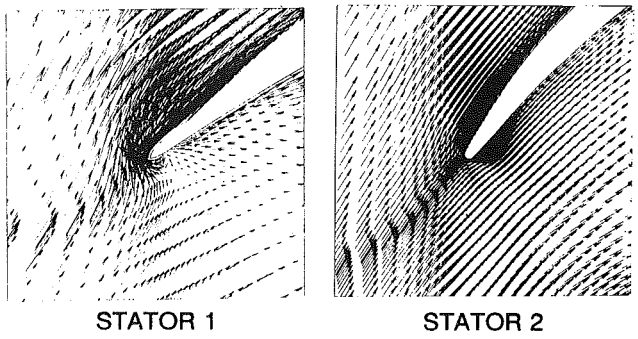

Fig. 11 Comparison of velocity vectors near the case

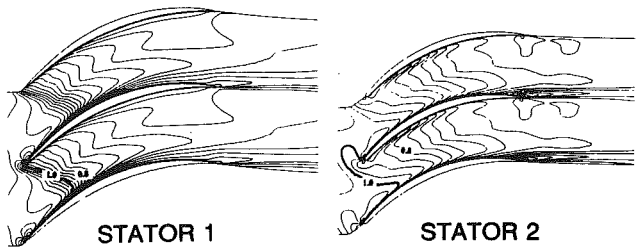

Fig. 12 Comparison of Mach number contours near the hub

applied to both rotor/stator combinations at the peak efficiency point. According to the numerical results, the rotor flow fields with Stator 1 and with Stator 2 are very similar. However, the stator flow fields are quite different. Some of the representative features of the two stator flow fields are compared in this section.

Spanwise distributions of stage efficiency are compared in Fig. 10. The numerical results indicate that the stage with Stator 2 installed performed more efficiently than the Stator 1 installation over most of the span. The experimental data show similar behavior except near the hub. The overall trend of the efficiency distribution is successfully captured by the numerical method. However, the distribution of the difference in efficiency between the two stator installations is less successfully captured. The difference in integrated stage efficiency for the two stator installations obtained from the numerical solutions was 0.6 percent, with the Stator 2 installation being higher. The measured difference was 1.4 percent, with the Stator 2 installation being higher. The magnitude of this variation is considered small and can be explained by lack of modeling of unsteady effects, experimental inaccuracies, and numerical error. Since the trend is correct and the absolute levels agree fairly well, flow field details that only computational fluid dynamics techniques can provide were studied.

Since the experimentally determined inlet flow conditions were available for the Stator 2 design, an improved incidence angle match was achieved. This was especially evident at the casing where Stator 2 was overcambered to accept the flow from the rotor tip. The flow in this region possessed a large tangential velocity component due to rotor tip clearance losses. Figure 11 compares velocity vectors near the case in the leading edge region from each solution. The stagnation point on the Stator 1 airfoil is located downstream of the leading edge of the pressure surface. This causes an expansion of the flow around the leading edge, onto the suction surface. The Stator 2 flow field shows a well-behaved velocity field, the stagnation point located near the leading edge with no expansion around the leading edge. Experimental results (not shown here) showed a slight increase in flow range while maintaining higher efficiency for the stage with Stator 2 installed.

Mach number contours are compared in Fig. 12 for the near-hub region. The Stator 1 hub flow field indicates a near-choke condition, while Stator 2 is clearly unchoked. Choked flow was not present at any other spanwise location. Also note that a shock is not found in either case (near sonic inlet Mach number), which may be evidence of the success of the swept

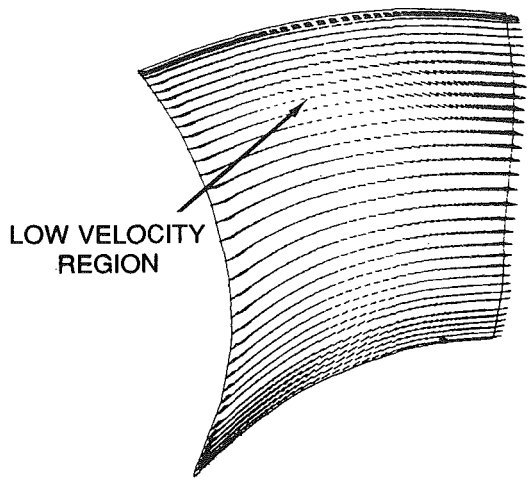

Fig. 13 Stator 2 velocity vectors near the pressure surface

leading edge, especially in the case of Stator 1. Stator 2 achieves less severe velocity gradients near the leading edge, due to the design of the suction surface contour, which would tend to reduce losses.

Figure 13 shows velocity vectors for Stator 2 in a nearly meridional plane close to the pressure surface. Radial secondary flow is indicated by the deviation of the velocity vector from the streamwise grid lines (these approximate streamlines from the axisymmetric solution). The magnitude of the secondary flow in other regions in both stators is less than indicated in this figure. As can be seen, the magnitude of the secondary flow is minimal. A feature peculiar to the region depicted in this figure (and peculiar to Stator 2 as well) is an area of low-velocity fluid at about 3/4 span. This flow deceleration is apparently due to the concavity of the blade surface in the streamwise direction. The presence of the low-velocity region would increase blockage and possibly reduce the diffusion potential of the blade row. The pressure surface concavity is more severe for Stator 2 than for Stator 1. No flow separation is evident, but a small degree of secondary flow around this region of low velocity is present. It is not clear whether this would be detrimental to efficiency. Flow separation was not observed on the suction surface of either stator for any spanwise location.

The computational results examined in this section give some interesting insight into details of the stator flow field. The solutions indicate that both stators are well behaved (at least at the operating point considered). One must keep in mind, however, that this was a steady-state computation and caution should be exercised when generalizing various findings. For example, it is reasonable to expect that unsteady effects, especially for this close-coupled stage, may induce a greater degree of secondary flow in the stator than what was seen here. The unsteady calculations may yield a greater variation in performance for the two stators, closer to the measured difference of 1.4. A follow-on effort to develop and demonstrate an unsteady rotor–stator computation is currently under way.

Concluding Remarks

An experimental and numerical study to investigate a transonic, high-throughflow, low aspect ratio fan stage has been conducted. The details of the flow structure and the aerodynamic performance of a state-of-the-art rotor were studied at 100 percent rotor speed and 90 percent rotor speed.

A multiple blade row calculation method based on a mixing plane approach is used to study the steady-state flow characteristics. To obtain stable and correct solutions for the current closely coupled blade rows, two interface planes are used for the transmission of information between the rotor and the stator. Comparisons between the numerical solution and the experimental data show that major time-averaged flow features inside the stage are properly calculated with the approach presented.

Both the experimental data and the numerical analysis indicate that the overall aerodynamic efficiency and the operating range of the stage are directly associated with the flow characteristics near the endwall. Interactions among the passage shock, tip-leakage vortex, and the boundary layers dominate the flow near the end wall. The numerical results imply that a leading edge vortex and two other vortexlike structures are generated by the tip-leakage flow.

The numerical results also confirm that Stator 2 has indeed better incidence tolerance without choking than Stator 1. The experimental data and the numerical results indicate that the stage with Stator 2 has better peak efficiency than the stage with Stator 1. This improvement comes from the reduced incidence and shock losses.

The excellent agreement between experimental and numerical performance suggests that the current three-dimensional Navier–Stokes numerical approach can be applied for parametric study of transonic compressor blades for improved fan/compressor stage design. Further improvement in physical modeling for strongly diffusing flow and further development of numerical techniques to shorten the turnaround time of the numerical analysis will certainly widen the application of the numerical method to fan/compressor stage design.

Acknowledgments

The authors would like to acknowledge G.E. Aircraft Engine Company for the design of Rotor 4 and Pratt & Whitney Aircraft Company for the design of Stator 2 under Air Force contracts. In addition, the authors would like to thank Dr. A. R. Wadia of the G.E. Aircraft Engine for his many useful discussions during the course of the current work.

References

Adamczyk, J. J., 1985, "Model Equation for Simulating Flows in Multistage Turbomachinery," ASME Paper No. 85-GT-226.

Arts, T., 1985, "Calculation of the Three-Dimensional, Steady, Inviscid Flow in a Transonic Axial Turbine Stage," ASME *Journal of Engineering for Gas Turbines and Power*, Vol. 107, pp. 286–292.

Chien, K. Y., 1982, "Prediction of Channel and Boundary-Layer Flows With a Low Reynolds Number Turbulence Model," *AIAA Journal*, Vol. 20, No. 1, pp. 33–38.

Davis, R. L., Hobbs, D. E., and Weingold, H. D., 1988, "Prediction of Compressor Cascade Performance Using a Navier–Stokes Technique," ASME JOURNAL OF TURBOMACHINERY, Vol. 110, pp. 520–531.

Dawes, W. N., 1986, "Development of a Three-Dimensional Navier–Stokes Solver for Application to All Types of Turbomachinery," ASME Paper No. 86-GT-70.

Denton, J. D., and Singh, U. K., 1979, "Time Marching Methods for Turbomachinery Flow Calculation," VKI Lecture Series, 1979-7.

Denton, J. D., 1986, "The Use of a Distributed Body Force to Simulate Viscous Flow in Three-Dimensional Flow Calculations," ASME Paper No. 86-GT-144.

Denton, J. D., and Xu, L., 1990, "The Trailing Edge Loss of Transonic Turbine Blades," ASME JOURNAL OF TURBOMACHINERY, Vol. 112, pp. 277–285.

Dring, R. P., and Spear, D. A., 1991, "The Effects of Wake Mixing on Compressor Aerodynamics," ASME JOURNAL OF TURBOMACHINERY, Vol. 113, pp. 600–607.

Giles, M. B., 1988, "Stator/Rotor Interaction in a Transonic Turbine," AIAA Paper No. 88-3093.

Hah, C., 1987, "Calculation of Three-Dimensional Viscous Flows in Turbomachinery With an Implicit Relaxation Method," *AIAA Journal of Propulsion and Power*, Vol. 3, No. 5, pp. 415–422.

Hah, C., and Wennerstrom, A. J., 1991, "Three-Dimensional Flowfields Inside a Transonic Compressor With Swept Blades," ASME JOURNAL OF TURBOMACHINERY, Vol. 113, pp. 241–251.

Law, C. H., and Wadia, A. R., 1993, "Low Aspect Ratio Transonic Rotors: Part 1—Baseline Design and Performance," ASME JOURNAL OF TURBOMACHINERY, Vol. 115, this issue, pp. 218–225.

Moore, J., and Moore, J. E., 1985, "Performance Evaluation of Linear Turbine Cascade Using Three-Dimensional Viscous Flow Calculations," ASME

Journal of Engineering for Gas Turbines and Power, Vol. 17, No. 1, pp. 969–975.

Ni, R. H., 1989, "Prediction of Three-Dimensional Multi-stage Turbine Flow Field Using a Multiple Grid Euler Solver," AIAA Paper No. 89-0203.

Parker, D. E., and Simonson, M. R., 1982, "Transonic Fan/Compressor Rotor Design Study, Vol. V," AFWAL-TR-82-2017.

Rao, K., and Delaney, R., 1990, "Investigation of Unsteady Flow Through Transonic Turbine Stage," AIAA Paper No. 90-2408.

Wennerstrom, A. J., 1991, "Experimental Study of a High-Through-Flow Transonic Axial Compressor Stage," ASME *Journal of Engineering for Gas Turbines and Power*, Vol. 106, pp. 552–560.

Journal of Engineering for Gas Turbines and Power, Vol. 17, No. 1, pp. 969–975.

Ni, R. H., 1989, "Prediction of Three-Dimensional Multi-stage Turbine Flow Field Using a Multiple Grid Euler Solver," AIAA Paper No. 89-0203.

Parker, D. E., and Simonson, M. R., 1982, "Transonic Fan/Compressor Rotor Design Study, Vol. V," AFWAL-TR-82-2017.

Rao, K., and Delaney, R., 1990, "Investigation of Unsteady Flow Through Transonic Turbine Stage," AIAA Paper No. 90-2408.

Wennerstrom, A. J., 1991, "Experimental Study of a High-Through-Flow Transonic Axial Compressor Stage," ASME *Journal of Engineering for Gas Turbines and Power*, Vol. 106, pp. 552–560.

DISCUSSION

N. A. Cumpsty[1]

There are not many data relating to high-performance turbomachinery in the open literature and it is very welcome to see some of the results of the highly successful program carried out at Wright-Patterson. It is also very welcome to see these compared with calculations. I have two principal observations to make.

A careless reader could get the impression that all the calculations performed for this paper were carried out using the procedure for the coupled stage, the procedure that uses the approach outlined in Figs. 1(*a*) and 1(*b*) of the paper. In fact the coupled calculation was only used to calculate the flow at peak efficiency. The results for the rotor treated as an isolated component and the results for the rotor when it was treated as part of a stage were found to be similar at peak efficiency, and it is stated that this trend was expected to continue at other operating points. This *may* be true, but it is not self-evident. Peak efficiency is probably close to the design point at which the actual flow is likely to follow fairly closely the axisymmetric streamsurfaces presumed in the design, without very large spanwise shifts associated with off-design operation or major regions of separation. Under such conditions the effect of a downstream blade row on the rotor may be expected to be small. At other flow conditions, particularly near stall, there may be large spanwise movements of the streamsurfaces and the downstream blade may have a substantial effect. Can the authors show how well the two calculations agree for a range of conditions, including comparisons of the mean meridional flow, from calculations with and without the downstream blade row at a range of conditions?

The second major point relates to the pressure distributions measured by Kulite pressure gages on the casing. In looking at such traces in the past I have always been surprised how smeared such results are, seeming to lack fine detail even when the transducers were very small compared to the blade pitch. This smearing is particularly clear when compared with the calculated distributions in Fig. 4 of the present paper. I feel fairly confident that the explanation for this smearing is the inherent unsteadiness of the shock and clearance vortex structure, since the measured pressure distributions invariably consist of ensemble averages. This means that in trying to understand the flow field one may perhaps obtain a better appreciation of the actual instantaneous pressure field and shock pattern from the calculations than the measurements.

Two additional small matters. Do the authors have explanations for the "ears" in the calculated efficiency at around 80 percent span shown in Figs. 3(*a*) and 3(*b*)? Can they please provide enlarged versions of Fig. 11 and Fig. 13 because in both cases the detail is lost?

[1]Whittle Laboratory, Cambridge University, Cambridge, United Kingdom.

Authors' Closure

Dr. Cumpsty's comment regarding in-stage rotor performance at various operating conditions is a good one and requires further discussion. We did not mean to imply that we had proven that the stator has minimal effects on the rotor, although it should be considered a possibility. We merely stated what was observed in the results of these particular computations. Several other operating points were investigated, and for all cases, the stator had minimal impact on the rotor. In other words, the solution of the isolated rotor computation and the solution of the in-stage rotor computation were virtually identical. This implies that the rotor downstream boundary conditions for the two cases (isolated and in-stage) were very similar and remained so as a function of operating point. This may be a result of the mixing plane technique, which was used to interface the two blade rows. This treatment (required for a steady calculation) may or may not be a true representation of the actual conditions; we, therefore, cannot be assured that all potential stator effects on the rotor are adequately modeled. We do not feel that including details of such results would provide any additional information.

With regard to Dr. Cumpsty's other point about smearing of the Kulite results, we agree that shock position unsteadiness is the likely cause, but to date, have not conducted any detailed investigation. Furthermore, we feel that although numerical results certainly provide a more detailed view of the flow physics, both measured and computed pressure distributions have merit, and in conjunction, can provide much knowledge about the flow field.

The presentations in Fig. 4 were provided to indicate that the code captures the significant structures in the flow field. When comparing contour plots with different numbers of contours, it is difficult to determine flow field details. We, therefore, provided a plot with a comparison of spatially resolved measured and calculated data in Fig. 6. We would note that for the axial location reported, the calculation indicates a more gradual rise in static pressure across the shock than the measured (ensemble-averaged) signals, thereby indicating greater smearing in the computation. We agree that the Kulite measurements have limitations and care must be used in interpretation, but they should not be discounted as they provide some valuable information. The shock unsteadiness can be determined from unaveraged data and we intend to review this.

With regard to the "ears" on the efficiency curves, we have not investigated their cause in detail but we presume it is a result of the complex interactions in the tip region of the shock, tip vortex, and blade surface boundary layers. Similar features have been observed in the results from other calculation techniques during informal presentations.

An Investigation of Turbulence Modeling in Transonic Fans Including a Novel Implementation of an Implicit k-ϵ Turbulence Model

M. G. Turner
Engineer, Computational Turbomachinery Aerodynamics.
Mem. ASME

I. K. Jennions
Manager, Computational Turbomachinery Aerodynamics.
Mem. ASME

GE Aircraft Engines,
Cincinnati, OH 45215

An explicit Navier–Stokes solver has been written with the option of using one of two types of turbulence model. One is the Baldwin–Lomax algebraic model and the other is an implicit k–ϵ *model which has been coupled with the explicit Navier–Stokes solver in a novel way. This type of coupling, which uses two different solution methods, is unique and combines the overall robustness of the implicit* k–ϵ *solver with the simplicity of the explicit solver. The resulting code has been applied to the solution of the flow in a transonic fan rotor, which has been experimentally investigated by Wennerstrom. Five separate solutions, each identical except for the turbulence modeling details, have been obtained and compared with the experimental results. The five different turbulence models run were: the standard Baldwin–Lomax model both with and without wall functions, the Baldwin–Lomax model with modified constants and wall functions, a standard* k–ϵ *model, and an extended* k–ϵ *model, which accounts for multiple time scales by adding an extra term to the dissipation equation. In general, as the model includes more of the physics, the computed shock position becomes closer to the experimental results.*

Introduction

The fan in a commercial or military turbofan engine is a component critical to the successful attainment of the performance and efficiency targets of the entire engine. As the pressure ratio and loading increase, it becomes more difficult to meet efficiency goals, stall margin, and mechanical constraints. The flow field is extremely complex and the geometry length scales span several orders of magnitude, from the span of the blade to the tip gap and leading edge radius. Current designs are already very efficient with relatively high pressure ratios. Designing more efficient fans requires better understanding of the fluid mechanics and more sophisticated analytical tools to predict the performance and efficiency accurately. Tip clearance effects, boundary layers with associated shear stress and blockage, turbulence effects, and shock loss must be accurately modeled to predict the shock position, the flow rate, and the overall loss and performance correctly. This requires a three-dimensional Navier–Stokes solution of the flow field.

Starting with the Navier–Stokes equations, which fully describe the flow field, one could perform a direct numerical simulation with a minimum number of assumptions. These have been obtained for simple geometries (Rai and Moin, 1991), but the approach has not yet been demonstrated for transonic flow and complex geometries. In addition, the current cost in computer time would make this approach prohibitive as a design tool. The first level of assumptions leads to the Reynolds-averaged Navier–Stokes equations. These are obtained by ensemble averaging the equations, which filters out the turbulent or random fluctuations of the flow field. The dependent variables in these equations then become the unsteady deterministic (non-random) velocity, density, and energy. Apparent stresses are produced by the averaging process due to the time unsteadiness of the actual flow field and the nonlinear terms in the equations. The problem with this system of equations is how to determine these apparent stresses and close the system. This is accomplished with a turbulence model.

One could solve the time-accurate equations or account for the deterministic unsteadiness by performing a time and passage average as proposed by Adamczyk (1985). The former is still too costly in computer time while the averaging operators lead to additional apparent stresses, which must be determined from empirical models. Rather than do this, one more level of assumptions can be introduced, namely, that the deterministic flow field is steady in a rotating frame of reference.

The explicit Euler code described by Holmes and Tong (1985)

Contributed by the International Gas Turbine Institute and presented at the 37th International Gas Turbine and Aeroengine Congress and Exposition, Cologne, Germany, June 1–4, 1992. Manuscript received by the International Gas Turbine Institute February 27, 1992. Paper No. 92-GT-308. Associate Technical Editor: L. S. Langston.

was extended by Cedar and Holmes (1989) to account for boundary layer blockage and solid bodies. This code has been further extended at GE Aircraft Engines to solve the Reynolds-averaged Navier–Stokes equations. The resulting code has the option of running inviscid, laminar, and turbulent with the Baldwin–Lomax model or the k–ϵ model. The numerical scheme for solving the k–ϵ equations is based on an implicit staggered grid method of solving convection-diffusion equations as described by Patankar (1980). An explicit k–ϵ solver was not pursued because the stability of this scheme was not well understood at the time. It was decided instead to modify extensively an existing implicit staggered grid k–ϵ solver and couple this with the Runge–Kutta explicit Navier–Stokes solver. The modifications included using the area projections contained in the explicit solver rather than the inverse Jacobian, modifying the data structures to those used by the explicit solver and vectorizing the entire code on the CRAY YMP. The details of the algorithm will be presented in this paper.

The coupling strategy is very simple. The density, velocity, and energy field is updated at each time step in the time marching solver. Using this velocity and density field, the turbulence model and law of the wall are applied with a resulting turbulent viscosity and wall shear stress calculated. For the algebraic Baldwin–Lomax model, the turbulent viscosity is simply calculated, whereas for the k–ϵ model, the finite volume forms of the k and ϵ equations are advanced one iteration, and the turbulent viscosity is calculated from the k and ϵ values. The turbulent viscosity and shear stress in turn are used by the viscous time marching solver.

A transonic fan rotor that has been experimentally investigated by Art Wennerstrom, formerly at Wright-Patterson AFB, has been used to validate and compare the Navier–Stokes code with five variations of the turbulence models. By using the same Navier–Stokes solver, the same grid and the same boundary conditions, the effect of the turbulence model on the quality of the flow field results can be quantified. Except for investigating the effect of the Baldwin–Lomax constants, which other researchers have made a function of pressure gradient, it has been the intent to keep the method general and not "tune" the constants based on the experimental results.

The Wennerstrom fan has also been run as a stage with the stator modeled as axisymmetric source terms. These results along with the results of two other fan geometries are described by Jennions and Turner (1993).

Background to Turbulence Modeling Efforts

Closing the Reynolds-averaged Navier–Stokes equations requires a model for the turbulent shear stresses. The Boussinesq hypothesis has been used, which says that the effective turbulent shear stress can be related to the strain times the turbulent viscosity.

The Baldwin–Lomax turbulence model (Baldwin and Lomax, 1978) is a two-layer algebraic model, which determines the turbulent viscosity in an inner and outer layer, which are subsequently matched. Dawes (1985), Adamczyk et al. (1989), and Rai (1989) have used this model for turbomachinery applications. Granville (1987) and York and Knight (1985) have investigated the effects of pressure gradients on the predictive capability of such a model, and have concluded that the model constants need to be modified in the presence of a pressure gradient.

The two-equation k–ϵ model, described by Launder and Spalding (1974), has been developed with fewer approximations than the Baldwin–Lomax model. The turbulent viscosity is a function of the k and ϵ values. This model is often associated with a pressure-correction solver, and the current code started with the k–ϵ model in a pressure-correction solver, which was modified to fit into the framework of the explicit time-marching solver.

Chen and Kim (1987) describe an extension to the k–ϵ model. Basically an attempt is made to model the physical process of the generation of large eddies, which break down into smaller eddies, and fine-scale eddies, which are then dissipated. This is done by using two time scales of the turbulent kinetic energy spectrum rather than just one, making a few assumptions, and adding an extra term to the dissipation rate equation. This additional term has the effect of decreasing the turbulent viscosity, which seems to be overpredicted using the standard model when the mean shear is large.

In order to overcome the extremely fine grids required to model boundary layers accurately down to the wall, both turbulence models use wall functions. This is an option when using the Baldwin–Lomax model. However, the k–ϵ solver is a high Reynolds number model, and the wall functions are always applied. It is a gridding requirement to keep the grid from becoming too fine.

The Navier–Stokes Equations

The compressible Navier–Stokes equations for a single blade

Nomenclature

C_μ, C_D = k–ϵ constants
C_1–C_3 = k–ϵ constants
C.V. = control volume
f, f^1, f^2 = functions of y^+
M = Mach number
R = added term in extended k–ϵ model, or ideal gas constant
s = surface of control volume, or entropy
TURBIN = inlet turbulence intensity
v_x, v_y, v_z = absolute velocity components
V = absolute velocity magnitude
$\overline{V}$ = absolute velocity vector
Vol = volume of control volume
w_x, w_y, w_z = relative velocity components
W = relative velocity magnitude
$\overline{W}$ = relative velocity vector
x, y, z = Cartesian position components; z is axial, y is also a generic distance from a wall
γ = ratio of specific heats $= C_p/C_v$
ϵ = turbulent dissipation rate
κ = thermal conductivity
ν = kinematic viscosity coefficient
ξ^1, ξ^2, ξ^3 = three-dimensional computational coordinates, ξ^1 is blade-to-blade, ξ^2 is hub-to-tip, and ξ^3 is streamwise
Π = work done due to viscous stresses
σ = k–ϵ constant
τ = shear stress
τ_w = wall shear stress magnitude
$\overline{\tau_w}$ = wall shear stress vector

Subscripts and Superscripts

$(\ )_c$ = cell center
$(\ )_{lw}$ = relates to law of the wall
$(\ )_P$ = local cell center (point)
$(\ )_V$ = viscous terms
$(\ )_x$ = x components
$(\ )_y$ = y component
$(\ )_z$ = z component
$(\ )_{xx}$–$(\ )_{zz}$ = tensor components
$(\ )_1$–$(\ )_6$ = refers to a node number
$(\ )^1$ $(\ )^2$ $(\ )^3$ = computational coordinates

row in three dimensions are cast in terms of absolute velocity but solved in a relative non-Newtonian reference frame rotating along with the blade about the z axis with angular velocity Ω. The equations are written in a conservative form in Cartesian coordinates (x, y, z). The equations in differential form are:

$$\frac{\partial \mathbf{U}}{\partial t}+\frac{\partial \mathbf{F}}{\partial x}+\frac{\partial \mathbf{G}}{\partial y}+\frac{\partial \mathbf{H}}{\partial z}=\mathbf{E}+\frac{\partial \mathbf{F_V}}{\partial \mathrm{x}}+\frac{\partial \mathbf{G_V}}{\partial \mathrm{y}}+\frac{\partial \mathbf{H_V}}{\partial \mathrm{z}}, \tag{1}$$

where the solution vector $\mathbf{U}$ is given by

$$\mathbf{U}=\begin{bmatrix}\rho\\ \rho v_x\\ \rho v_y\\ \rho v_z\\ \rho e\end{bmatrix} \tag{2}$$

in which ρ is the density and e is the total internal energy. The absolute velocity vector $\overrightarrow{V}=v_x\hat{i}+v_y\hat{j}+v_z\hat{k}$ and $\hat{i}$, $\hat{j}$, and $\hat{k}$ are the unit vectors in the x, y, and z directions. $\mathbf{E}$ accounts for terms due to rotation of the coordinate system:

$$\mathbf{E}=\begin{bmatrix}0\\ \Omega\rho v_y\\ -\Omega\rho v_x\\ 0\\ 0\end{bmatrix}, \tag{3}$$

and $\mathbf{F}$, $\mathbf{G}$, and $\mathbf{H}$ are the convective fluxes given by:

$$\mathbf{F}=\begin{bmatrix}\rho w_x\\ \rho w_x v_x+p\\ \rho w_x v_y\\ \rho w_x v_z\\ w_x(\rho e+p)-\Omega y p\end{bmatrix}, \tag{4}$$

$$\mathbf{G}=\begin{bmatrix}\rho w_y\\ \rho w_y v_x\\ \rho w_y v_y+p\\ \rho w_y v_z\\ w_y(\rho e+p)+\Omega x p\end{bmatrix}, \quad \mathbf{H}=\begin{bmatrix}\rho w_z\\ \rho w_z v_x\\ \rho w_z v_y\\ \rho w_z v_z+p\\ w_z(\rho e+p)\end{bmatrix}. \tag{5}$$

The pressure p is determined through an equation of state. The ideal gas law is assumed:

$$P=(\gamma-1)(\rho e-\rho V^2/2). \tag{6}$$

The static temperature T is determined by:

$$T=\frac{e-V^2/2}{C_v}, \tag{7}$$

where C_v is the specific heat at constant volume, which is a property of the fluid and is a constant if the gas is assumed to be perfect. The relative velocity vector $\overrightarrow{W}=w_x\hat{i}+w_y\hat{j}+w_z\hat{k}$ is related to the absolute velocity through the following equations:

$$w_x=v_x+\Omega y, \quad w_y=v_y-\Omega x, \quad w_z=v_z. \tag{8}$$

The viscous terms $\mathbf{F_V}$, $\mathbf{G_V}$, and $\mathbf{H_V}$ are given assuming no internal energy sources or radiation heat transfer:

$$\mathbf{F_V}=\begin{bmatrix}0\\ \tau_{xx}\\ \tau_{xy}\\ \tau_{xz}\\ \Pi_x-q_x\end{bmatrix}, \quad \mathbf{G_V}=\begin{bmatrix}0\\ \tau_{yx}\\ \tau_{yy}\\ \tau_{yz}\\ \Pi_y-q_y\end{bmatrix}, \quad \mathbf{H_V}=\begin{bmatrix}0\\ \tau_{zx}\\ \tau_{zy}\\ \tau_{zz}\\ \Pi_z-q_z\end{bmatrix}, \tag{9}$$

in which the shear stresses are related to the strains by the following linear relationships:

$$\tau_{xx}=\frac{2}{3}\mu\left(2\frac{\partial v_x}{\partial x}-\frac{\partial v_y}{\partial y}-\frac{\partial v_z}{\partial z}\right), \tag{10}$$

$$\tau_{xy}=\tau_{yx}=\mu\left(\frac{\partial v_x}{\partial y}+\frac{\partial v_y}{\partial x}\right), \tag{11}$$

where μ is the viscosity. The equations for τ_{yy} and τ_{zz} are similar to Eq. (10), and the equations for τ_{xz}, τ_{zx}, τ_{yz}, and τ_{zy} are similar to Eq. (11). The components of work done due to viscous stresses are:

$$\Pi_x=v_x\tau_{xx}+v_y\tau_{xy}+v_z\tau_{xz}, \tag{12}$$

$$\Pi_y=v_x\tau_{xy}+v_y\tau_{yy}+v_z\tau_{zy}, \tag{13}$$

$$\Pi_z=v_x\tau_{xz}+v_y\tau_{xz}+v_z\tau_{zz}, \tag{14}$$

and q accounts for the heat condition within the fluid:

$$q_x=-\kappa\frac{\partial T}{\partial x}, \quad q_y=-\kappa\frac{\partial T}{\partial y}, \quad q_z=-\kappa\frac{\partial T}{\partial z}, \tag{15}$$

with the thermal conductivity being given by:

$$\kappa=\frac{\mu C_p}{\mathrm{Pr}}, \tag{16}$$

in which C_p is the specific heat at constant pressure and Pr is the Prandtl number.

The unsteady Navier–Stokes equations have been presented. These equations fully describe the flow field including the turbulence, but to solve them numerically requires resolving very small spatial and temporal details. To obtain meaningful results with coarser grids, these equations can be averaged over relatively small time periods to produce the Reynolds-averaged form of these equations. This yields equations with apparent stresses due to the time unsteadiness. Boussinesq introduced a hypothesis that says that this apparent stress can be related to the strain times the turbulent viscosity. An effective viscosity, μ_{eff}, therefore has two distinct parts:

$$\mu_{\mathrm{eff}}=\mu_l+\mu_t, \tag{17}$$

and similarly:

$$\kappa_{\mathrm{eff}}=C_p\left(\frac{\mu_l}{\mathrm{Pr}_l}+\frac{\mu_t}{\mathrm{Pr}_t}\right) \tag{18}$$

where the l and t subscripts denote laminar and turbulent quantities, respectively. For air, $\mathrm{Pr}_l=0.74$ is a property and $\mathrm{Pr}_t=0.9$ has been applied. With μ_{eff} and κ_{eff} replacing μ and κ, the above Navier–Stokes equations remain unchanged in form. Conceptually these are now the deterministic velocities being calculated rather than instantaneous velocities. The laminar viscosity is modeled by Sutherland's law in which μ_l is a function of the local static temperature. The turbulent viscosity calculation, which is needed to close this system of equations, is discussed below for two turbulence models.

The Navier–Stokes Numerical Scheme

The equations above would reduce to the Euler equations if $\mathbf{F}_v$, $\mathbf{G}_v$, and $\mathbf{H}_v$ are set to zero. The code and solution method is then the same as described by Holmes and Tong (1985) and Cedar and Holmes (1989), both of which describe a turbomachinery version of the cell-centered Runge–Kutta algorithm described by Jameson et al. (1981). Essentially, the equations are integrated about a finite control volume and marched in time using a five-stage Runge–Kutta scheme. This scheme, on which the dissipation is evaluated on the first and second steps only, has dissipative properties that are particularly suited to the multigrid strategy employed to accelerate the solution. Both second and fourth-order smoothing are applied with the second-order smoothing being tripped by a pressure gradient switch. Because only a steady result is desired, local time stepping is used.

The current algorithm extends this basic strategy. Various

Runge-Kutta schemes have been coded to compare the schemes and aid in starting particularly difficult solutions. A two-stage scheme, similar to that of Dawes (1985) where the dissipation is calculated on each step, has proved particularly robust. Residual averaging has been added to enhance stability and robustness. Rather than increase the Courant number (CFL), the residual averaging has been used to stabilize solutions using the same CFL number. Essentially, the residuals are smoothed implicitly using an SLOR type strategy. The smoothing parameters used to obtain the results presented here are all unity.

To account for the viscous terms, velocity and temperature gradients are required. A Green's theorem approach is used similar to that used by Kallanderis (1987). The volume integral of the gradient can be converted into a surface integral using Green's theorem. The resulting integral can be expressed in terms of face areas and variable values as:

$$\text{Vol}\,\frac{\partial T}{\partial x} \approx \int\int\int_{\forall} \frac{\partial T}{\partial x}\, d\forall = \int\int_{s} T(\hat{i}\cdot\bar{n})\, ds \approx \sum_{\text{C.V.}} TA_x. \quad (19)$$

This is applied to a control volume that is offset from the other control volumes as shown in Fig. 1. Appropriate values and averages of these gradients are then used to obtain the viscous fluxes, $\mathbf{F}_v$, $\mathbf{G}_v$, and $\mathbf{H}_v$, about the flux balance control volume.

For a viscous calculation, the no-slip and adiabatic wall boundary conditions are applied. In order to utilize grid points most efficiently, a law of the wall model can be used to evaluate the shear stress and shear work terms at a wall boundary. This model is described below in more detail. At the inlet, the absolute total pressure and temperature profiles are specified as well as the absolute tangential velocity and flow angle in the r-z plane. At the exit, the static pressure is specified at one spanwise location and a simple radial equilibrium condition is used to determine the static pressure at the rest of the exit plane.

The Baldwin–Lomax Turbulence Model

The formulation of the Baldwin-Lomax model is identical to that described by Baldwin and Lomax (1978), but there is much contention as to how it should be coded in practice. Several assumptions or clarifications of the model were used:

- The equations are applied along grid lines rather than normals to solid surfaces. This avoids having to calculate all the normal distances and the interpolation of flow variables.
- Since a law of the wall approach is used in practice, the Van Driest damping terms are dropped.
- There is a limit placed on $y_{\text{crossover}}$ in order for it not to occur too far from the wall.
- Beyond the trailing edge, the turbulence model is essentially frozen. Average values of F_{max} and y_{max} are taken from the trailing edge suction and pressure surfaces and applied at downstream locations.
- The downstream running grid line from the blade trailing edge is assumed to be the wake centerline.
- F_{wake} has been formulated to be the smaller of two terms (Baldwin and Lomax, 1978). Only the term $F_{\text{wake}} = y_{\max} F_{\max}$ has been used.
- The turbulent viscosity is limited to 1000 times the laminar viscosity in order not to have spuriously high viscosities in the flow field. The number of nodes that are clipped in this fashion is kept track of in the code.

Granville (1987) has attempted to predict the behavior of two of the constants, C_{CP} and C_{KLEB}, for varying pressure gradients. The values used by Baldwin and Lomax are $C_{CP} = 1.6$, and $C_{\text{KLEB}} = 0.3$, which lie far outside the curve suggested by Granville. York and Knight (1985) have also suggested different values of these constants in their work. The effects these changes can have on a solution are demonstrated later in the paper.

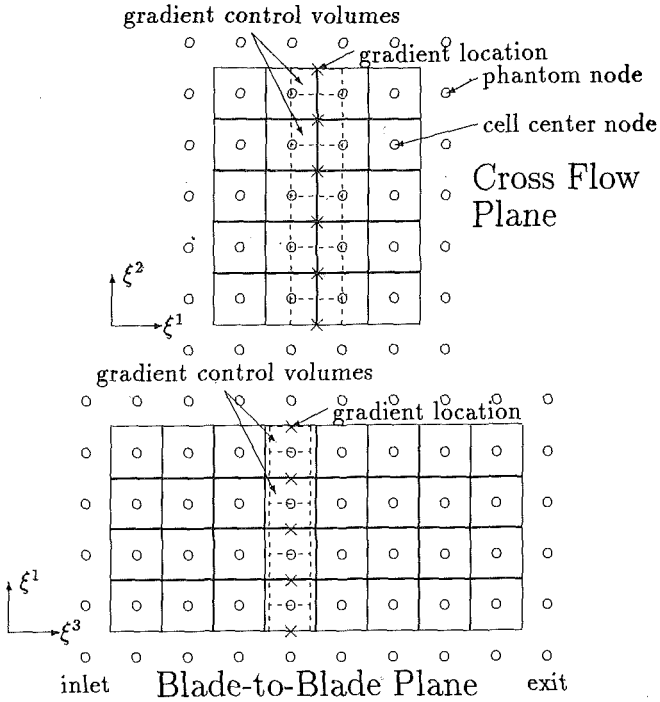

Fig. 1 Location of the cell center nodes, gradient calculation control volumes, and gradient location; the flux balance control volume sides are defined by, and are identical to, the grid

The k–ϵ Turbulence Model

The k-ϵ turbulence model is a two-equation model, which determines the turbulent kinetic energy k, and a macro length scale of the turbulence l from transport equations. The turbulent kinetic energy is defined as

$$k = \frac{1}{2}\overline{u_i' u_i'}, \quad (20)$$

where u_i' are the components of the unsteady velocity vector. The length scale can be related to k and the isotropic turbulent dissipation rate ϵ through the following relation:

$$l = \frac{C_D k^{3/2}}{\epsilon}, \quad (21)$$

where C_D is a constant. The dissipation rate is defined as:

$$\epsilon = \frac{\mu}{\rho}\overline{\frac{\partial u_i'}{\partial x_j}\frac{\partial u_i'}{\partial x_j}}. \quad (22)$$

The k-ϵ model for high Reynolds numbers is described by the following equation (Launder and Spalding, 1974) presented in the conservative differential form of Eq. (1). Subscripts of k-ϵ will indicate the vectors for these equations:

$$\mathbf{U}_{k-\epsilon} = \begin{bmatrix} \rho k \\ \rho \epsilon \end{bmatrix}, \quad (23)$$

$$\mathbf{E}_{k-\epsilon} = \begin{bmatrix} \text{Gen} - \rho\epsilon \\ \dfrac{C_1 \epsilon}{k}\,\text{Gen} - \dfrac{C_2 \rho \epsilon^2}{k} \end{bmatrix}, \quad (24)$$

$$\mathbf{F}_{k-\epsilon} = \begin{bmatrix} \rho w_x k \\ \rho w_x \epsilon \end{bmatrix}, \quad \mathbf{G}_{k-\epsilon} = \begin{bmatrix} \rho w_y k \\ \rho w_y \epsilon \end{bmatrix}, \quad \mathbf{H}_{k-\epsilon} = \begin{bmatrix} \rho w_z k \\ \rho w_z \epsilon \end{bmatrix}, \quad (25)$$

$$\mathbf{F}_{\mathbf{V}\,k-\epsilon}=\begin{bmatrix}\frac{\mu_t}{\sigma_k}\frac{\partial k}{\partial x}\\ \\ \frac{\mu_t}{\sigma_\epsilon}\frac{\partial \epsilon}{\partial x}\end{bmatrix},\quad \mathbf{G}_{\mathbf{V}\,k-\epsilon}=\begin{bmatrix}\frac{\mu_t}{\sigma_k}\frac{\partial k}{\partial y}\\ \\ \frac{\mu_t}{\sigma_\epsilon}\frac{\partial \epsilon}{\partial y}\end{bmatrix},\quad \mathbf{H}_{\mathbf{V}\,k-\epsilon}=\begin{bmatrix}\frac{\mu_t}{\sigma_k}\frac{\partial k}{\partial z}\\ \\ \frac{\mu_t}{\sigma_\epsilon}\frac{\partial \epsilon}{\partial z}\end{bmatrix}, \tag{26}$$

In Cartesian coordinates, the generation term, Gen, is:

$$\begin{aligned}\text{Gen}=\mu_t\Bigg(2\left(\left(\frac{\partial w_x}{\partial x}\right)^2+\left(\frac{\partial w_y}{\partial y}\right)^2+\left(\frac{\partial w_z}{\partial z}\right)^2\right)\\ +\left(\left(\frac{\partial w_x}{\partial y}\right)+\left(\frac{\partial w_y}{\partial x}\right)\right)^2+\left(\left(\frac{\partial w_y}{\partial z}\right)+\left(\frac{\partial w_z}{\partial y}\right)\right)^2\\ +\left(\left(\frac{\partial w_x}{\partial z}\right)+\left(\frac{\partial w_z}{\partial x}\right)\right)^2\Bigg).\end{aligned} \tag{27}$$

The turbulent viscosity is

$$\mu_t=\min\left(\frac{C_\mu\rho k^2}{\epsilon},\ \mu_{\text{limit}}\mu_l\right), \tag{28}$$

where the turbulent viscosity is clipped for numerical stability of the time marching solver. A value of $\mu_{\text{limit}}=1000$ is generally used in practice (for cases in which the inlet μ_t values would be clipped, larger values of μ_{limit} are used).

The constants applied are:

$$C_\mu=0.09,\quad C_1=1.44,\quad C_2=1.92,\quad \sigma_k=1.0,\quad \sigma_\epsilon=1.217. \tag{29}$$

Extended k–ϵ Model

Chen and Kim (1987) describe an extended turbulence model, which adds one term to the ϵ equation and uses a modified set of constants. This new term is in the source term

$$\mathbf{E}_{k-\epsilon}=\begin{bmatrix}\text{Gen}-\rho\epsilon\\ \\ \frac{\epsilon}{k}\,\text{Gen}\,(C_1+C_3R)-\frac{C_2\rho\epsilon^2}{k}\end{bmatrix}, \tag{30}$$

where

$$R=\min\left(3,\frac{\text{Gen}}{\rho\epsilon}\right). \tag{31}$$

C_3 is a new constant. The value of this constant and the suggested values of the other constants (Chen, 1991) are:

$$C_\mu=0.09,\quad C_1=1.15,\quad C_2=1.90,\quad C_3=0.25,$$
$$\sigma_k=0.75,\quad \sigma_\epsilon=1.05. \tag{32}$$

This extra term represents the energy transfer rate from large-scale turbulence to small-scale turbulence controlled by the production rate time scale and the dissipation rate time scale (two time scales as opposed to one in the standard model). If the generation term is large (i.e., the mean shear is strong), then this extra term will increase ϵ and suppress the overshoot of k (Chen and Kim, 1987). The resulting turbulent viscosity is also decreased.

k–ϵ Boundary Conditions. At the inlet, k and ϵ must be prescribed. For the results presented, these are specified as uniform for the entire inlet plane. The inlet turbulence intensity, TURBIN, defines the level of turbulent kinetic energy given an average relative velocity, W, as:

$$k_{\text{inlet}}=\frac{3}{2}\,(\text{TURBIN}\ W)^2, \tag{33}$$

where the factor of 3 is needed because there are three components of velocity. It is assumed that l is proportional to some characteristic length L of the problem (the inlet annular height for the fan solution) so

$$\epsilon_{\text{inlet}}=\frac{C_D k_{\text{inlet}}^{3/2}}{\lambda L} \tag{34}$$

where $C_D=1$ and $\lambda=0.05$ is the proportionality constant. The values of k and ϵ at the inlet can be specified to be nonuniform, but the variation of turbulence intensity and length scale is very difficult to predict. Consequently, k and ϵ assume uniform values at the inlet.

The boundary conditions for k and ϵ at the wall are based on the wall-function method discussed in the next section and more fully explained by Launder and Spalding (1974). A normalized distance, y^+, is defined by:

$$y^+=\frac{y\sqrt{\rho_w\tau_w}}{\mu_w}, \tag{35}$$

where the w subscript denotes values at the wall. At the node closest to the wall, the value of y^+ is determined from

$$y^+=\frac{\rho\sqrt{k}C_\mu^{1/4}\delta y}{\mu_l} \tag{36}$$

which is based on $\tau/\rho=C_\mu^{1/2}k=\text{const}$. The value of ϵ is proportional to $k^{3/2}/y$ so

$$\epsilon_{\text{wall}}=\frac{C_\mu^{3/4}}{\kappa_{lw}}\frac{k^{3/2}}{y}. \tag{37}$$

The value of k is determined from the transport equation applied at the near-wall point. However, several modifications of the equation need to be applied. First, there is no flux of k across the wall. Second, based on Eq. (37) the ϵ term in the k equation is applied as

$$\iiint_{\mathcal{V}}\rho\epsilon d\mathcal{V}=\begin{cases}\rho C_\mu^{3/4}k^{3/2}\dfrac{y^+}{\delta y}\,\text{Vol} & \text{if } y^+\le 11.63\\ \rho\dfrac{C_\mu^{3/4}k^{3/2}}{\kappa_{lw}\delta y}\ln(E_{lw}y^+)\text{Vol} & \text{if } y^+>11.63\end{cases} \tag{38}$$

where the constants $E_{lw}=9.793$ and $\kappa_{lw}=0.4187$ are the coefficient of roughness and the von Karman constant, respectively. Third, the generation term includes the stresses along the wall that are not related to the strains, but are determined from the law of the wall. The generation term for the faces parallel to the wall is

$$\text{Gen}=\tau_w\frac{\partial W}{\partial y}, \tag{39}$$

where τ_w is obtained from the law of the wall.

k–ϵ Discretization Approach and Solution Method. The k–ϵ model is discretized about the same flux balance control volumes used by the explicit solver (Fig. 1), and the k and ϵ values are stored at the cell center nodes. The approach is based on writing a general form of the transport equations as is common in a pressure-correction scheme, which involves the local cell center, P, plus the six neighbor cell centers N, S, E, W, D, and U:

$$a_P\phi_P=\sum_{i=N,S,E,W,D,U}a_i\phi_i+(S_\phi)_P. \tag{40}$$

The variable ϕ is either k or ϵ. The term $(S_\phi)_P$ includes the original source term in the equation plus any additional terms that are not made up from the seven grid points. As explained by Patankar (1980), the following condition must be satisfied to ensure stability:

$$|a_P|\ge\sum_{i=N,S,E,W,D,U}|a_i|. \tag{41}$$

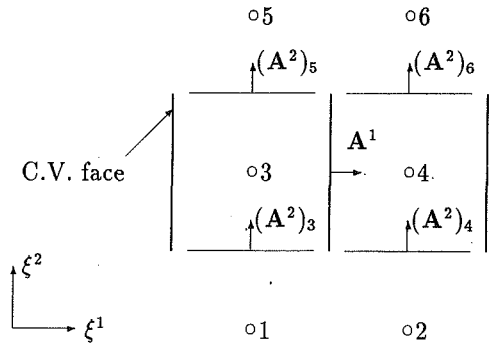

Fig. 2 Discretization stencil for the diffusion term in the k-ϵ equation for the face denoted by its outward normal A^1

This is achieved by using a hybrid scheme, which upwinds the convective terms if the diffusion terms are too small. The convective term is just the mass flux through a face times the average of the cell center values.

Equation (40) is solved using an ADI scheme on a crossflow plane. A tridiagonal solver couples the blade-to-blade direction and the spanwise direction. The equations are not solved implicitly in the streamwise direction. The equations are solved on a crossflow plane starting at the inlet and marching downstream to the exit.

The diffusion term discretization is based on summing $(\mu_t/\sigma_\phi)(\nabla\phi\cdot\bar{n})ds$ over the six faces of the control volume. This term can be related to the derivatives along the grid lines as follows:

$$(\nabla\phi\cdot\bar{n})ds = A_x\frac{\partial\phi}{\partial x}+A_y\frac{\partial\phi}{\partial y}+A_z\frac{\partial\phi}{\partial z} \tag{42}$$

$$=\left(A_x\frac{\partial\xi^1}{\partial x}+A_y\frac{\partial\xi^1}{\partial y}+A_z\frac{\partial\xi^1}{\partial z}\right)\frac{\partial\phi}{\partial\xi^1} \tag{43}$$

$$+\left(A_x\frac{\partial\xi^2}{\partial x}+A_y\frac{\partial\xi^2}{\partial y}+A_z\frac{\partial\xi^2}{\partial z}\right)\frac{\partial\phi}{\partial\xi^2} \tag{44}$$

$$+\left(A_x\frac{\partial\xi^3}{\partial x}+A_y\frac{\partial\xi^3}{\partial y}+A_z\frac{\partial\xi^3}{\partial z}\right)\frac{\partial\phi}{\partial\xi^3}. \tag{45}$$

If this face projection is in the ξ^1 direction as shown by $\mathbf{A}^1$ in Fig. 2, then the grid derivatives

$$\frac{\partial\xi^1}{\partial x}=\frac{A_x^1}{\text{Vol}};\quad \frac{\partial\xi^1}{\partial y}=\frac{A_y^1}{\text{Vol}};\quad \frac{\partial\xi^1}{\partial z}=\frac{A_z^1}{\text{Vol}}, \tag{46}$$

where

$$\mathbf{A}^1=A_x^1\hat{i}+A_y^1\hat{j}+A_z^1\hat{k}, \tag{47}$$

and the derivative $\partial\phi/\partial\xi^1$ is approximated by central differencing the nodes on either side of the face. This term is then

$$\left(A_x\frac{\partial\xi^1}{\partial x}+A_y\frac{\partial\xi^1}{\partial y}+A_z\frac{\partial\xi^1}{\partial z}\right)\frac{\partial\phi}{\partial\xi^1} =\frac{(A_x^1)^2+(A_y^1)^2+(A_z^1)^2}{\text{Vol}}(\phi_4-\phi_3) \tag{48}$$

and is contained in the coefficients of Eq. (40). The volume is the average of the two adjoining control volumes:

$$\text{Vol}=\frac{1}{2}(\text{Vol}_3+\text{Vol}_4). \tag{49}$$

For the other derivatives, the grid derivatives are obtained by averaging the surrounding area projections, and central differencing is again used. For example

$$\left(A_x\frac{\partial\xi^2}{\partial x}+A_y\frac{\partial\xi^2}{\partial y}+A_z\frac{\partial\xi^2}{\partial z}\right)\frac{\partial\phi}{\partial\xi^2}= \frac{((A_x^1)\overline{(A_x^2)}+(A_y^1)\overline{(A_y^2)}+(A_z^1)\overline{(A_z^2)})}{\text{Vol}}\left[\frac{(\phi_5+\phi_6)-(\phi_1+\phi_2)}{2}\right], \tag{50}$$

where

$$\overline{(A_x^2)}=\frac{1}{4}((A_x^2)_3+(A_x^2)_4+(A_x^2)_5+(A_x^2)_6), \tag{51}$$

and similar expressions can be written for $\overline{(A_y^2)}$ and $\overline{(A_z^2)}$. Terms such as this are made part of the source term $(S_\phi)_P$ in Eq. (40). The other terms for this face and the other faces are calculated similarly.

The use of the projected areas is very similar to using the inverse of the Jacobian matrix to obtain the grid derivatives, which is a more common approach (Anderson et al., 1984). It was used here because the areas had already been allocated memory storage for the explicit solver and the inverse of the Jacobian did not need to be calculated.

The Law of the Wall

The law of the wall model uses empirical data of how the wall shear stress relates to the distance away from the wall. White (1974) shows that these data collapse to a log-linear curve for $y^+>30$ when u^+ and y^+ are plotted. The inner-law velocity variable u^+ is defined as:

$$u^+=u/\sqrt{\tau_w/\rho}, \tag{52}$$

and y^+ is defined by Eq. (35). By using this u^+-y^+ relation, the grid does not have to be fine enough to resolve the entire boundary layer to get the correct shear stress. The grid does have to be fine enough to ensure the log-linear relation is valid, which depends on the pressure gradient. The maximum valid y^+ at the wall lies between 150 and 1000.

The force of the shear stress on the wall is applied parallel to the velocity vector and has a magnitude of the shear stress times the area magnitude.

Law of the Wall With the Baldwin and Lomax Model. The u^+-y^+ relation used with this model is a combination of Spalding's model presented by White (1974), blended with the following log-linear curve:

$$u^+=\frac{1}{0.435}\ln(1.01+9y^+). \tag{53}$$

The cell Reynolds number is

$$\text{Re}_c=\left(\frac{\rho u\delta y}{\mu_l}\right)_c. \tag{54}$$

At the wall $\delta y=y$ so $y^+=\text{Re}_c/u^+$. The u^+-y^+ relation defines $u^+=f(y^+)$ so the cell Reynolds number

$$\text{Re}_c=y^+u^+=f^1(y^+). \tag{55}$$

This relation has been curve fit to give

$$y^+=f^2(\text{Re}_c) \tag{56}$$

where the cell Reynolds number is known. Once y^+ is known, u^+ is determined from the u^+-y^+ relation and the wall shear stress is known.

Law of the Wall With the k-ϵ Model. The law of the wall has already been assumed in prescribing the boundary conditions for the k and ϵ equations. The y^+ values are calculated using Eq. (36), and the u^+-y^+ relation used is:

$$u^+=\begin{cases} y^+ & \text{if } y^+\le 11.63 \\ \dfrac{1}{\kappa_{lw}}\ln(E_{lw}y^+) & \text{if } y^+>11.63 \end{cases} \tag{57}$$

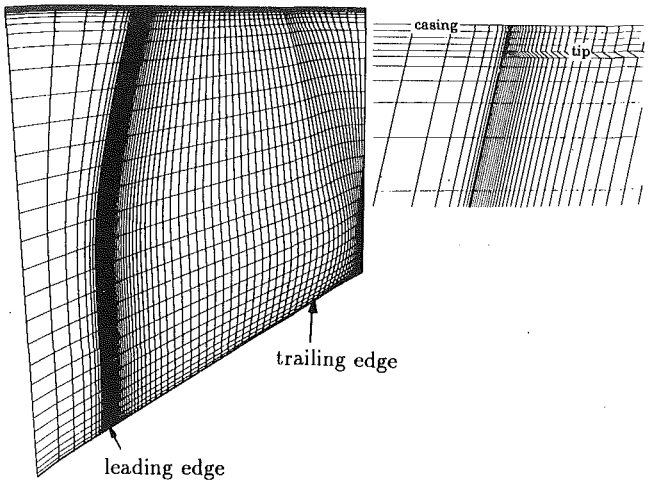

Fig. 3 Meridional view of the grid with a blowup of the tip gap

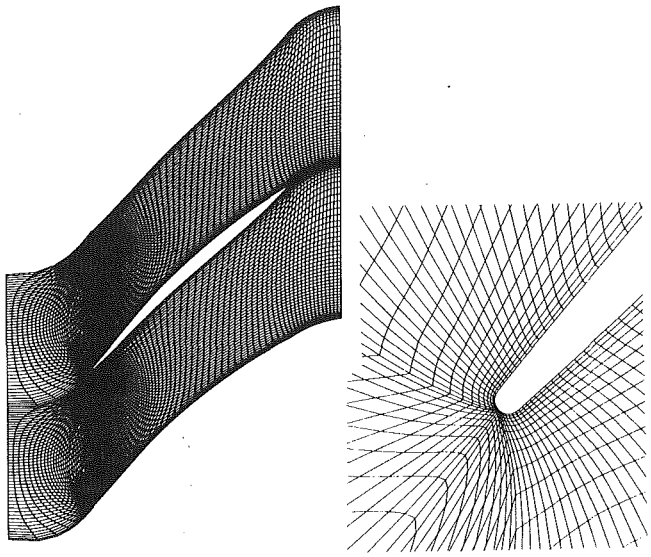

Fig. 4 Blade-to-blade view of the grid with a blowup of the leading edge

where $E_{lw}=9.793$ and $\kappa_{lw}=0.4187$. The way this equation is applied is that for $y^+ \le 11.63$,

$$\tau=\mu_l \frac{dW}{dy}; \quad \frac{\tau}{W}=\frac{\mu_l}{\delta y}. \tag{58}$$

For $y^+ > 11.63$,

$$\tau=\mu_t \frac{dW}{dy}. \tag{59}$$

From this equation, the equation for viscosity, Eq. (28), and the average dissipation over a control volume, Eq. (38), the shear stress equation is

$$\tau=\left[\frac{\rho C_\mu^{1/4} k^{1/2} \kappa_{lw} \delta y}{\ln(E_{lw} y^+)}\right] \frac{dW}{dy}. \tag{60}$$

Therefore,

$$\frac{\tau}{W}=\rho \frac{C_\mu^{1/4} k^{1/2} \kappa_{lw}}{\ln(E_{lw} y^+)}. \tag{61}$$

Results

The Navier–Stokes solver has been used to solve the flow field about a transonic fan rotor, which was designed at GE Aircraft Engines under a USAF contract and has been experimentally investigated by Wennerstrom at Wright Patterson AFB. This is the fourth rotor in a sequence of experimental fan rotors. Solutions have been obtained using three variations of the Baldwin–Lomax turbulence model and two variations of the k–ϵ model. Each of the five cases used the same grid, the same smoothing constants, and the same boundary conditions.

The grid used is shown in Figs. 3 and 4. The grid near the walls was spaced to be valid for a turbulence model with wall functions. It has 49 grid points within the blade passage and 37 grid points spanwise (5.855 in. span at the leading edge) of which 4 are within the tip gap (0.025 in.). Upstream of the leading edge, there are 16 axially spaced grid points; there are 65 grid points along the blade surface axially, and there are 16 grid points downstream of the trailing edge for a total of 97 axial grid points. This is a total of 175,861 grid points.

The inlet boundary conditions specified are a uniform absolute total pressure and total temperature. The test inlet total pressure and temperature were 9.85 psi and 545 R, respectively. All measurements have been corrected to standard conditions, so the calculation ran with an inlet total pressure of 14.696 psi and an inlet total temperature of 518.688 R. The tip speed is 1500 ft/sec at a tip radius of 8.5 in. The tangential velocity is zero, and the meridional flow angle, arctan (V_r/V_z), was determined from a throughflow calculation. The inlet turbulence intensity for the k–ϵ solutions have been specified as 2 percent. At the exit, the static pressure at the casing was specified, and simple radial equilibrium was applied to determine the static pressure at the rest of the span. The pressure at each radial grid line is treated to be uniform tangentially (i.e., $\partial p/\partial\theta=0$). At the wall, the shear stress is determined from the velocity gradient or from the wall function if the wall functions are used. These shear stresses are then multiplied by the velocity of the wall in the absolute frame to determine the shear work terms of Eqs. (12)–(14). This means there is a shear work contribution from the rotating hub and blade surfaces, but it is zero at the casing.

Solutions have been obtained using the following turbulence models:

1 The Baldwin–Lomax model with standard constants and no wall functions.
2 The Baldwin–Lomax model with standard constants and wall functions.
3 The Baldwin–Lomax model with a set of constants modified for pressure gradient ($C_{CP}=1.0$ and $C_{\mathrm{KLEB}}=0.64$) and wall functions. These were chosen to lie on the curve predicted by Granville (1987) in the adverse pressure gradient region.
4 The standard k–ϵ model.
5 The extended k–ϵ model.

The general procedure to run these complex solutions is to start using the more robust two-stage Runge–Kutta scheme and continue with the faster five-stage scheme. The k–ϵ solutions were run until a level of the residual was smaller than a convergence criterion (1000 iterations for case 4 and 915 iterations for case 5). The Baldwin–Lomax residuals, however, leveled off at a larger value than this convergence criterion, and would not reduce further. The solution was determined to be converged when the rms velocity in the flow field stopped changing (1300 iterations for case 1 and 1000 iterations for cases 2 and 3). This lack of continued convergence is attributed to the discrete maximum operator used in the Baldwin–Lomax model (Baldwin and Lomax, 1978). If the turbulent viscosities are frozen at a given iteration, the solution converges.

The solution time using the five-stage scheme, the k–ϵ model, three levels of multigrid and residual averaging was 3.67×10^{-5} sec/iter/grid point with all arrays in main memory on a CRAY YMP. The Baldwin–Lomax model with everything else identical takes about 10 percent longer for each iteration. Even

Table 1 Calculated mass flow compared to experiment

case	wall functions	calculated mass flow (difference from experiment)
Baldwin-Lomax standard consts.	no	+3.5%
Baldwin-Lomax standard consts.	yes	+2.5%
Baldwin-Lomax modified consts.	yes	+2.3%
k-ϵ standard	yes	+1.7%
extended k-ϵ	yes	+1.4%

The experimental mass flow is 1.372 kg/sec/blade passage with an accuracy of ±0.8%.

Table 2 y^+ statistics for the standard k-ϵ model solution

	min	max	avg	stand. dev.
hub	16.5	173.0	84.08	17.67
tip	16.2	73.10	44.56	10.28
pressure surface	8.36	384.0	86.17	67.06
suction surface	8.61	347.0	77.47	59.67

though the k-ϵ coding has been vectorized and modified to reduce redundant calculations, and the Baldwin-Lomax coding has not, it is still surprising that it is faster to update two partial differential equations than calculate a complex algebraic equation. Many people choose the Baldwin-Lomax model because it is supposedly more efficient. However, based on the speed difference demonstrated, the choice of using the Baldwin-Lomax turbulence model should be based on simplicity of coding and quality of results, but not efficiency. The time solving the k-ϵ equations could be reduced further if one iteration of the k-ϵ model is run every other or every fifth iteration of the time-marching procedure rather than every iteration.

The flow rates calculated using the different turbulence models are shown in Table 1 as a percentage greater than the experimentally measured flow rate. The extended k-ϵ model predicts the flow rate to be closest to the experimental value, but still outside the accuracy of the measurement, which is ±0.8 percent.

In Table 2, the near-wall y^+ statistics for the standard k-ϵ solution are presented. These are typical values for the other cases except the Baldwin-Lomax solution with no wall functions (case 1), which are approximately half those in Table 2. The statistical quantities of y^+ are useful because with current structured gridding techniques, one cannot *a priori* create a grid that satisfies the y^+ constraints. One can calculate an approximate distribution of y^+ prior to obtaining a solution that helps in the gridding process. The variation of y^+ at midspan for the standard k-ϵ solution is shown in Fig. 5. The average and standard deviation are convenient to determine whether the grid is appropriate for the given turbulence model. For the standard k-ϵ model presented (high Reynolds number and law of the wall), an average y^+ plus or minus the standard deviation with 35 to 300 is felt adequate. For a Baldwin-Lomax solution with wall functions, the average plus the standard deviation should be less than 300. The upper bound of 300 is valid for any pressure gradient as long as the flow is not separated; however, it can be as high as 1000 for a very favorable pressure gradient. With no wall functions, the y^+ values should all be near 1. The values for case 1 are much too large for the solution to be meaningful. It is presented to demonstrate that a quality solution is obtained only when the grid resolution matches the model being used.

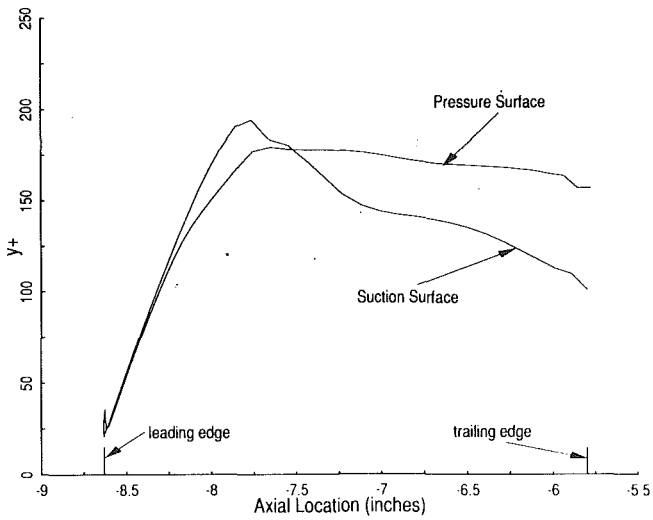

Fig. 5 The y^+ values on the blade surface at midspan for the standard k-ϵ solution

Figure 6 shows the contours of the casing static pressures for the five cases compared with the measured Kulite data contour plot. In Fig. 6(*b*), one can clearly see the bow shock. Other features are harder to distinguish, but with the help of Fig. 6(*a*), one can see a diffuse passage shock and the presence of a tip vortex originating near the leading edge. Clearly, the Baldwin-Lomax solution without wall functions in Fig. 6(*e*) predicts the passage shock to be too strong and too far aft like an inviscid solution. This is because the shear stress is underpredicted without the law of the wall and with the near-wall y^+ values too large. With the shear stress underpredicted, there is not enough blockage to move the shock forward. The Baldwin-Lomax solution with standard constants and wall functions in Fig. 6(*f*) still seems to predict the passage shock to be too strong; it is not spread out enough. Figures 6(*c*, *g*) (the standard k-ϵ solution and the solution using the Baldwin-Lomax model with modified constants) are remarkably similar, showing good agreement with the experimental results. The extended model in Fig. 6(*d*) is very similar to the experimental results also. In this solution, the tip vortex emanating near the leading edge appears tighter and stronger than in the other solutions.

Figure 7 compares the measured casing static pressure with the circumferentially averaged static pressure for each numerical solution. This essentially represents the tangential average of the pressures in Fig. 6. The pressure rise shown in this plot comes mainly from the bow and passage shocks. The pressure rise is wrong when wall functions are not used. The Baldwin-Lomax solution with standard constants and wall functions predict the pressure rise to be too far aft. Again the standard k-ϵ solution and the Baldwin-Lomax model with modified constants are very similar and close to the test data. The extended k-ϵ model moves the shock slightly forward compared with the standard k-ϵ model, and a little closer to the test data.

Figures 6 and 7 show that the modified constants chosen for case 3 do produce a change to the results that were expected based on the pressure gradient. However, the constants chosen for this Baldwin-Lomax run were somewhat arbitrary and may not be suitable in other flow situations. Also, it is difficult to generalize and code an algorithm that determines the values of the constants to use. The standard k-ϵ model, however, already contains this pressure gradient effect.

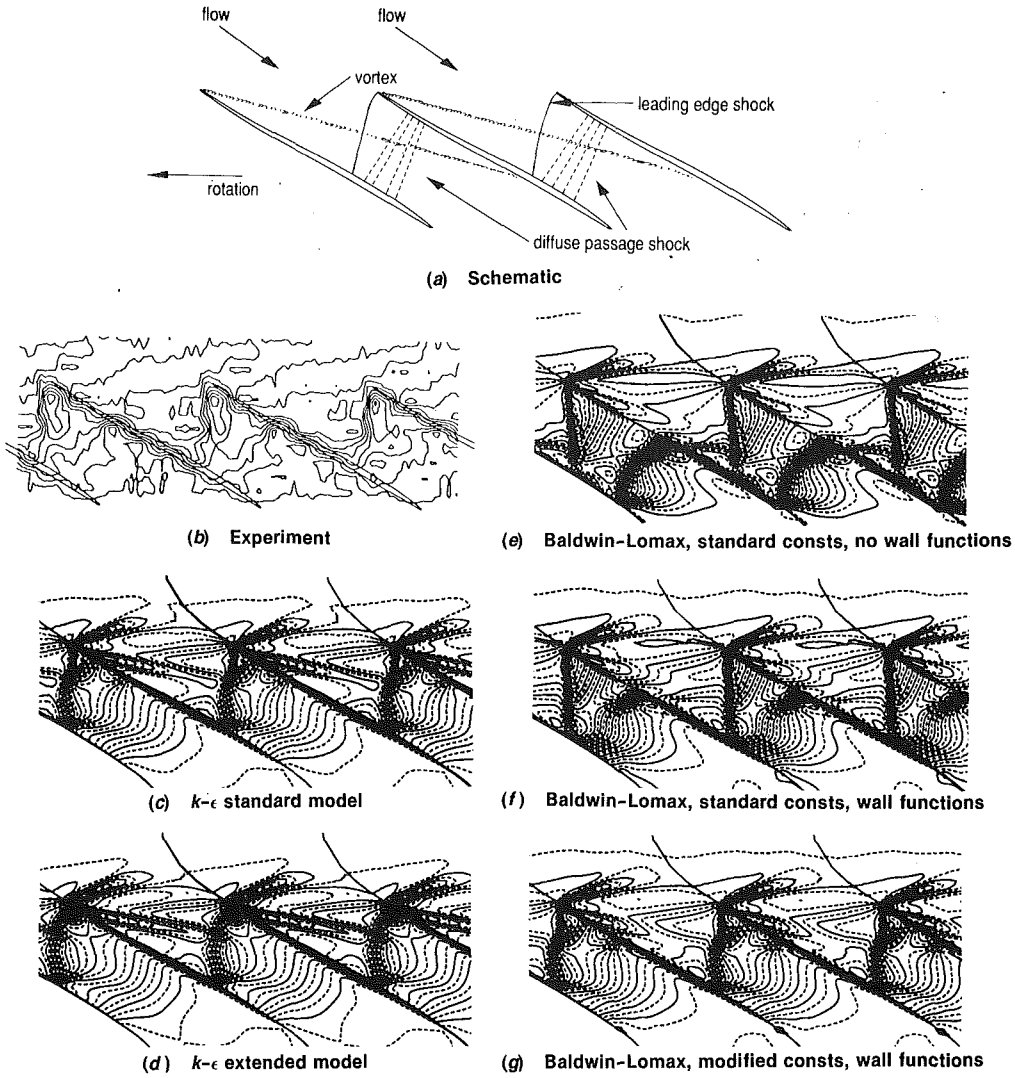

Fig. 6 Casing static pressure contours comparing five numerical results with experimental Kulite measurements; the numerical contour intervals are 0.5 psi

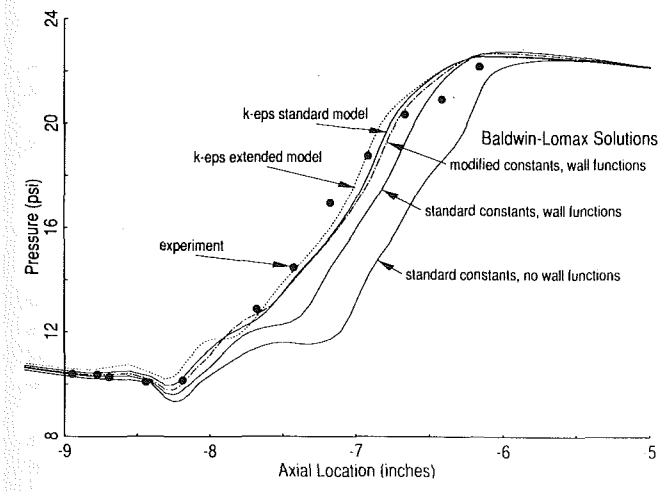

Fig. 7 Circumferentially averaged static pressures at the casing: comparison between experiment and five numerical results

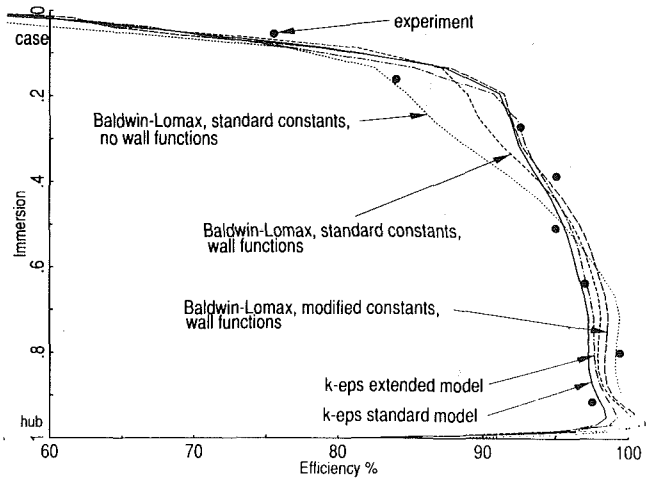

Fig. 8 Adiabatic efficiency hub-to-case profile at the trailing edge plane comparing the five numerical results with experimentally derived values

Figure 8 shows the hub-to-case efficiency profiles calculated at the trailing edge plane compared with experimentally derived data. The measurements were taken downstream of a stator, and a data-match has been used to separate out the stator losses. It can be seen that all but the Baldwin–Lomax solution without wall functions are in good mutual agreement and match the data reasonably.

The previous discussion focused mainly on the comparison of the casing static pressures. This is because the fan is being modeled as an isolated rotor, but was run as a stage (a stage

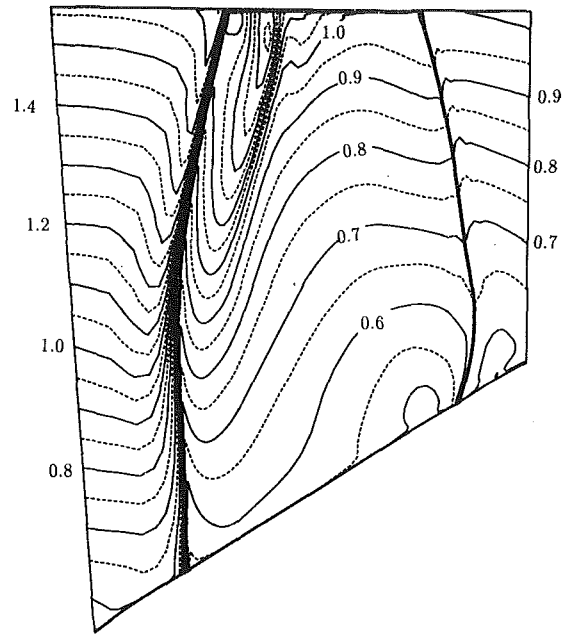

Fig. 9 Ideal Mach number on the pressure surface for the standard k-ϵ solution; contour intervals are 0.05

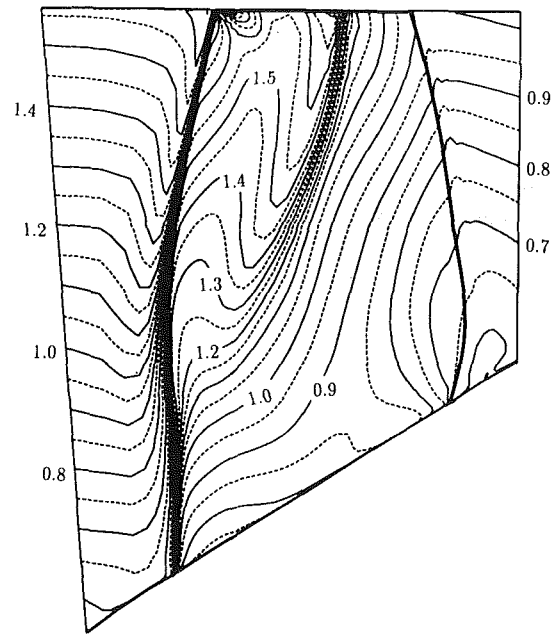

Fig. 10 Ideal Mach number on the suction surface for the standard k-ϵ solution; contour intervals are 0.05

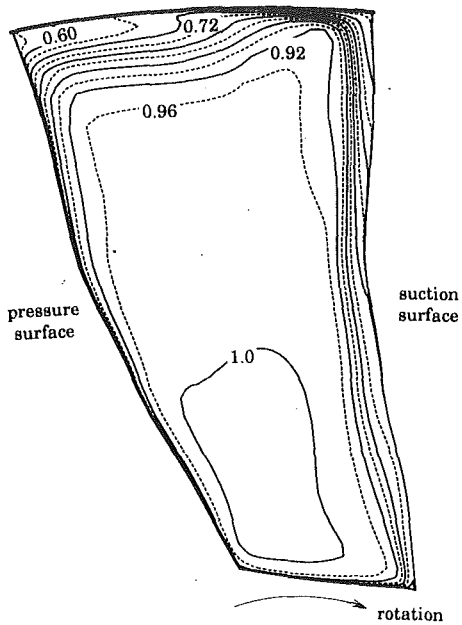

Fig. 11 Entropy function contours at the trailing edge grid surface for the standard k-ϵ solution; contours are of exp($-\Delta s/R$) with 0.04 intervals

simulation has been run by Jennions and Turner, 1993). The efficiency, therefore, has to be calculated assuming a stator loss. Also, the shock position is more sensitive for the different turbulence models. Getting the shock position correct using the experimental downstream static pressure means the flow rate, efficiency, and pressure rise should be correct and consistent. The comparison of shock position can therefore be a sensitive measure of the prediction capability of the code. The shock position compared well for the Baldwin–Lomax solution with the modified constants and both k–ϵ solutions. The flow rate for both the k–ϵ solutions was closer to experiment than any of the Baldwin–Lomax solutions.

Even with the k–ϵ models, the flow rates are still high relative to the accuracy of the measurement. There are several physical phenomena still missing in these solutions that might explain this. First, the inlet total pressure profile was specified to be flat because the incoming casing boundary layer was not measured. However, even though the experiment was set up to minimize the boundary layer thickness, it would still not be zero. Second, the fan was run as a coupled stage. The assumption that the relative deterministic flow is steady is not 100 percent valid. This effect could be modeled by adding the terms that Adamcyzk (1985) recommends or using a time accurate solver for both the rotor and stator. Third, the turbulence has been assumed to be locally isotropic. With such a complicated flow field, especially in the tip, this is probably not the case, although no detailed measurements of turbulence have been made in the tip region of a transonic fan. Fourth, the running tip clearance is not accurately known because it is very small and hard to measure, and the flow rate is very sensitive to the size of the tip clearance modeled.

The contours of ideal Mach number (a normalized static pressure assuming no loss) for the standard k–ϵ model solution are shown in Figs. 9 and 10 for the pressure and suction surfaces, respectively. These clearly show the calculated shock locations on the blade surfaces.

Contours of an entropy function (exp($-\Delta s/R$)) are shown in Fig. 11 at the trailing edge grid surface for the standard k–ϵ model solution. Entropy is a much better quantity for observing loss than total pressure because the system is rotating. Values of one indicate no loss. There are large losses associated with the tip clearance represented by the low level of this entropy function (0.60) associated with the tip clearance vortex. The losses are much larger on the suction surface than the pressure surface due to the higher shock losses.

To demonstrate how different the k–ϵ and Baldwin–Lomax models are, a contour plot of the quantity μ_t/μ_l is shown for the Baldwin–Lomax solution with standard constants and wall functions (Fig. 12) and the standard k–ϵ solution (Fig. 13) at midspan. In Fig. 12, the turbulent viscosity goes to zero in the middle of the passage, whereas in the standard k–ϵ model solution, the turbulent viscosity at the inlet is 400 times the laminar value based on the specified inlet turbulence intensity and length scale. Figure 14 shows how the turbulent viscosities are reduced using the extended model.

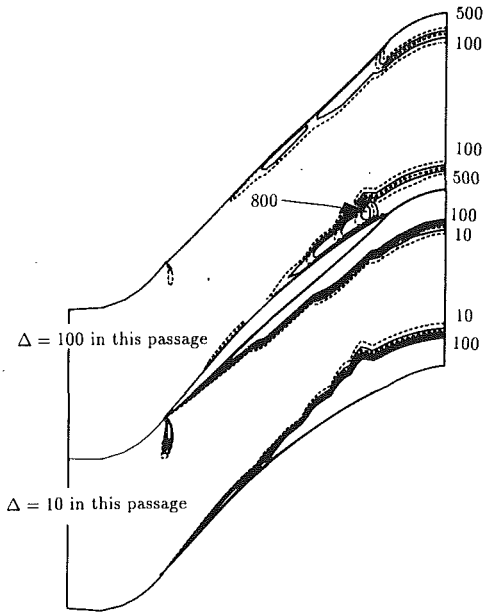

Fig. 12 Contour plot of μ_t/μ_l at the midspan of the blade for the Baldwin-Lomax solution using standard constants and wall functions; contour intervals are 10 in the lower passage and 100 in the upper passage

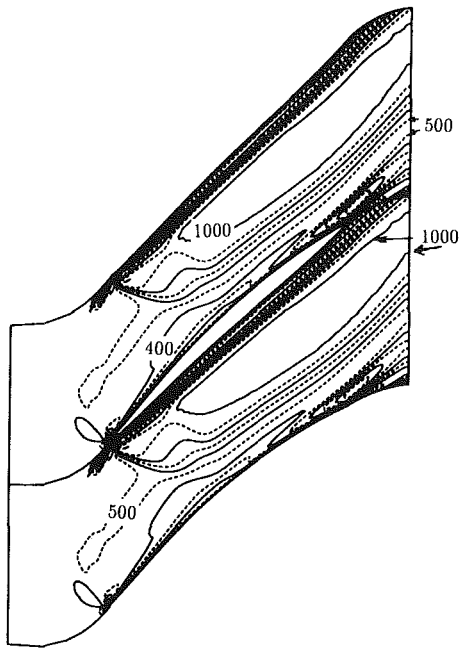

Fig. 13 Contour plot of μ_t/μ_l at the midspan of the blade for the standard k-ϵ solution; contour intervals are 100

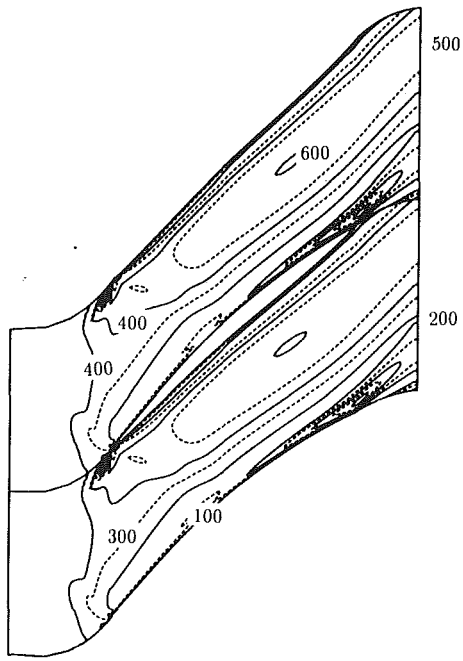

Fig. 14 Contour plot of μ_t/μ_l at the midspan of the blade for the extended k-ϵ solution; contour intervals are 100

Concluding Remarks

An explicit Navier-Stokes solver, which has the option of using either a Baldwin-Lomax algebraic turbulence model or an implicit k-ϵ turbulence model, has been written. Five solutions have been presented for a transonic fan rotor using modifications of these two turbulence models while keeping the grid, smoothing, and boundary conditions identical. Several conclusions can be drawn from the current work:

1 Coupling an implicit k-ϵ solver with the explicit Navier-Stokes solver has proven very successful.
2 Unless the Baldwin-Lomax constants are modified for the pressure gradient, the shock position does not compare as well with experiment as the k-ϵ solutions.
3 The flow rate for the k-ϵ solutions is closer to experiment than any of the Baldwin-Lomax solutions.
4 An extended k-ϵ model, which is a simple modification to the standard k-ϵ model, produces a shock position and mass flow rate that agree slightly better with experimental data than even the standard k-ϵ model. Further cases need to be run to determine the generality of the extended model.
5 The k-ϵ code, which solves two partial differential equations, actually runs faster than the algebraic Baldwin-Lomax code. Coupled with the k-ϵ solutions converging better than the Baldwin-Lomax solutions, the overall run times are less.
6 The k-ϵ equations are very stiff and the practical success of the model can be attributed to solving these equations implicitly. Using this approach to solve other stiff systems, such as the chemical reaction equations, might prove very useful.

Based on these conclusions, designers at GE Aircraft Engines are using this code with the k-ϵ turbulence model on a day-to-day basis. Many different turbomachinery components are being analyzed and designed with the help of this code at both design and off design conditions.

Additional solutions using this code with the standard k-ϵ model are presented by Jennions and Turner (1993) for two other fan geometries and the fan presented in this paper run as a stage. These results show similar agreement of shock position and flow rate with experimental results to those presented in this paper, and rotor operating characteristics are computed that include tip clearance effects.

Acknowledgments

The authors wish to thank Mark Braaten at GE CR & D for first suggesting the idea to use an existing k-ϵ solver to couple with the Navier-Stokes code. The help, advice, and support of the following people are also greatly appreciated: Chung Shin, Zee Moussa, Roy Smith, Art Wennerstrom, Aspi Wadia, and Chander Prakash.

References

Adamczyk, J. J., 1985, "Model Equation for Simulating Flows in Multistage Turbomachinery," ASME Paper No. 85-GT-226.

Adamczyk, J. J., Celestina, M. L., Beach, T. A., and Barnett, M., 1990, "Simulation of Three-Dimensional Viscous Flow Within a Multistage Turbine," ASME JOURNAL OF TURBOMACHINERY, Vol. 112, pp. 370–376.

Anderson, D. A., Tannehill, J. C., and Pletcher, R. H., 1984, *Computational Fluid Mechanics and Heat Transfer*, Hemisphere Publishing Corporation, New York.

Baldwin, B. S., and Lomax, H., 1978, "Thin Layer Approximation and Algebraic Model for Separated Turbulent Flows," AIAA Paper No. 78-257.

Cedar, R. D., and Holmes, D. G., 1989, "The Calculation of the Three-Dimensional Flow Through a Transonic Fan Including the Effects of Blade Surface Boundary Layers, Part-Span Shroud, Engine Splitter and Adjacent Blade Rows," ASME Paper No. 89-GT-325.

Chen, Y. S., and Kim, S. W., 1987, "Computation of Turbulent Flows Using an Extended k-ϵ Turbulence Closure Model," NASA-CR-179204.

Chen, Y. S., 1991, Personal Communication with C. Prakash at GE.

Dawes, W. N., 1985, "A Pre-processed Implicit Algorithm for 3D Viscous Compressible Flow," in: *6th GAMM Conference on Numerical Methods in Fluid Mechanics*, Gottingen, DFVLR, Sept.

Granville, P. S., 1987, "Baldwin-Lomax Factors for Turbulent Boundary Layers in Pressure Gradients," *AIAA Journal*, Vol. 25, No. 12, pp. 1624–1627.

Holmes, D. G., and Tong, S. S., 1985, "A Three-Dimensional Euler Solver for Turbomachinery Blade Rows," ASME *Journal of Engineering for Gas Turbines and Power*, Vol. 107, pp. 258–264.

Jameson, A., Schmidt, W., and Turkel, E., 1981, "Numerical Solutions of the Euler Equations by Finite Volume Methods Using Runge-Kutta Time-Stepping Schemes," Paper No. AIAA-81-1259.

Jennions, I. K., and Turner, M. G., 1993, "Three-Dimensional Navier-Stokes Computations of Transonic Fan Flow Using an Explicit Flow Solver and Implicit k-ϵ Solver," ASME JOURNAL OF TURBOMACHINERY, Vol. 115, this issue, pp. 261–272.

Kallinderis, J. G., and Baron, J. R., 1987, "Adaptation Methods for a New Navier-Stokes Algorithm," Paper AIAA 87-1167.

Launder, B. E., and Spalding, D. B., 1974, "The Numerical Computation of Turbulent Flows," in: *Computer Methods in Applied Mechanics and Engineering 3*, North-Holland Publishing Company, pp. 269–289.

Patankar, S. V., 1980, *Numerical Heat Transfer and Fluid Flow*, Hemisphere Publishing Co., New York.

Rai, M. M., 1989, "Three-Dimensional Navier-Stokes Simulations of Turbine Rotor-Stator Interaction: Part 1—Methodology," *Journal of Propulsion*, Vol. 5, No. 3, p. 305.

Rai, M., and Moin, P., 1991, "Direct Numerical Simulation of Transition and Turbulence in a Spatially Evolving Boundary Layer," Paper No. AIAA-91-1607.

White, F. M., 1974, *Viscous Fluid Flow*, McGraw-Hill, New York.

York, B., and Knight, D., 1985, "Calculation of Two-Dimensional Turbulent Boundary Layers Using the Baldwin–Lomax Model," *AIAA Journal*, Vol. 23, No. 12, pp. 1849–1850.

Three-Dimensional Navier-Stokes Computations of Transonic Fan Flow Using an Explicit Flow Solver and an Implicit $\kappa - \epsilon$ Solver

I. K. Jennions
Manager,
Computational Turbomachinery
Aerodynamics.
Mem. ASME

M. G. Turner
Engineer,
Computational Turbomachinery
Aerodynamics.
Mem. ASME

GE Aircraft Engines,
Cincinnati, OH 45215

Computational fluid dynamics (CFD) has become a powerful ally of the experimental test facility in revealing the flow physics of some highly complex flows. For certain classes of flow, CFD has reached maturity and is therefore being increasingly used in industry by designers. This paper is intended to show current transonic prediction capability at GE Aircraft Engines in terms of a recently developed three-dimensional Navier–Stokes code. The flow simulations addressed are concerned with transonic fan design and illustrate those issues that are important to designers such as tip leakage flow, shock boundary layer interaction, boundary layer growth, and account of internal solid bodies such as part-span shrouds and engine splitters. In this respect, three successively more complex Navier–Stokes simulations representative of modern fans—NASA Rotor 67, GE/Wennerstrom Rotor 4, and the GE/NASA E^3 fan—are considered in this paper.

Introduction

The long-range goal of CFD code developers is to produce computer programs that can be used accurately to optimize aerodynamic designs, aid understanding of fluid flow phenomena, and to supplement experimental testing. As this is a long-range goal, the users of such codes work with a list of assumptions inherent in their codes and relinquish these assumptions as the next layer of modeling is validated for their use. Much progress has been made recently and three-dimensional Navier–Stokes solutions are now used routinely by aerodynamic designers in a number of industries. Issues of solution accuracy, geometric complexity, speed (cost), unsteadiness, turbulence (in particular near-wall modeling), and overall time to analyze a design still exist, but use of the currently available methods can lead to significant insight into the physical flow that is being studied.

The flow in the transonic fan of modern commercial engines is perhaps the most physically complex of all turbomachinery flows. Shock position is governed by blade profile and endwall boundary layer blockage, tip clearance, part-span shroud placement, adjacent blade row effects, and the influence of core to bypass flow split. Important physical length scales vary from the large span and chord to the small tip gap and leading edge radii, a range of several orders of magnitude. Coupled with this, the overall efficiency is very high (around 90 percent) and so each contribution has to be modeled accurately before the shock position and hence the associated flow field is revealed.

Contributed by the International Gas Turbine Institute and presented at the 37th International Gas Turbine and Aeroengine Congress and Exposition, Cologne, Germany, June 1–4, 1992. Manuscript received by the International Gas Turbine Institute February 27, 1992. Paper No. 92-GT-309. Associate Technical Editor: L. S. Langston.

Early three-dimensional solutions with Euler solvers (Denton, 1983; Singh, 1982) showed the shock system to be placed very firmly at the blade trailing edge. With compensation for boundary layer blockage via a coupled inviscid/viscous approach utilizing either a quasi-three-dimensional (Calvert and Ginder, 1985) or three-dimensional (Wood et al., 1988) method, reasonable agreement with experimental data was achieved. Full three-dimensional Navier–Stokes solutions have likewise progressed to the point at which good agreement with experimental data is possible (Dawes, 1987; Von Backstrom, 1990; Hah and Reid, 1992). Such an approach offers an attractive hands-off operation for a designer with less built-in empiricism than previous methods.

The challenge that is faced in industry today is to bring these CFD codes into use in a design system. Miranda (1982) suggested the *Effectiveness* of a code for general use by technical (non-CFD) personnel be defined by:

$$Effectiveness = Quality * Acceptance$$

with *Quality* being demonstrated through a series of validation studies against acceptable data bases (experimental, analytical, etc.). *Acceptance* is defined in terms of criteria such as: user-friendliness, robustness, and affordability. Although this formula is shown as linear, experience indicates that the *Acceptance* has a much stronger influence outside the CFD community and provides a good reason for any company to build on its previous CFD successes. This has been the line pursued in the development of the current Navier–Stokes solver.

In 1985 an Euler code was written for GE Aircraft Engines by Holmes and Tong and subsequently used in the design of the unducted fan (Smith, 1987). The code was then further

enhanced (Cedar and Holmes, 1989) to account for boundary layers, solid bodies such as part-span shrouds and engine splitters, and the presence of adjacent blade rows. It was used extensively in transonic fan design. Next, the viscous stress terms, viscous boundary conditions, and Baldwin–Lomax turbulence model were added, followed by a novel implementation of the k–ϵ turbulence model as discussed by Turner and Jennions (1992). These progressive steps allowed for code development inside a common framework, both from a CFD code developer's and a designer's point of view, and consequently have increased designer productivity.

As it is difficult to show actual commerical designs, this paper illustrates our current capability by presenting three-dimensional Navier–Stokes flow results for three different fan geometries representative of modern transonic fan design from the open literature. Results from the code are also shown in a paper by Wadia and Law (1993) who used it to identify performance enhancing features and aid interpretation of experimental data for transonic rotors. This paper is divided broadly into three sections. The first section describes the equations solved and the numerical scheme employed, followed by a short look at the preprocessing and postprocessing system inside which the code operates. Lastly the results from the fan simulations are presented and discussed.

The Three Dimensional Navier–Stokes Code

The papers cited above describe the individual parts of the present code and an accompanying paper (Turner and Jennions, 1993) describes the viscous numerics in some detail. Thus we restrict ourselves here to a brief description, emphasizing the main attributes of the solver, in order to provide background for the numerical simulations.

The Reynolds-averaged form of the full three-dimensional Navier–Stokes equations including the energy equation written in Cartesian coordinates are solved. The flow is assumed to be compressible with adiabatic walls; supersonic and transonic solutions are allowed. The equations are cast in terms of absolute velocity, but are solved in a relative non-Newtonian reference frame rotating with the blade. All that is needed to close this system of equations are models for the laminar and turbulent viscosity.

The laminar viscosity is modeled by Sutherland's law and a choice of turbulence models is provided. The Baldwin–Lomax model (Baldwin and Lomax, 1978) implemented as a nearest wall model for three-dimensional flows was coded first. This model unfortunately contains very little physics, especially in accounting for pressure gradient effects (Dawes, 1990), which we believe to be important in fans. As a consequence, the k–ϵ turbulence model (Launder and Spalding, 1974) was also coded and used as the default model in all runs. In order to achieve engineering solutions in acceptable times, both models use optional wall functions, which yield the shear stress and shear work terms at wall boundaries. It is interesting to observe that as the Baldwin–Lomax model is not highly vectorized, as is the case with all Baldwin–Lomax models the authors have seen, both turbulence models take approximately the same computer time to execute.

The equations of motion are integrated to produce a cell-centered finite volume flux balance, which, with the addition of the usual second and fourth-order smoothing terms, is solved using the explicit Runge–Kutta scheme of Jameson et al. (1981). Various stage schemes are available in the code with the default being the five-stage scheme described by Cedar and Holmes (1989), which has good dissipative properties for use with multigrid. Velocity and temperature gradients are computed using auxiliary control volumes, an approach similar to that adopted by Kallinderis and Baron (1987). Local time stepping and multigrid are used to accelerate convergence. At present up to five levels of multigrid may be used, with a simple V cycle. Residual averaging with constant coefficients (usually 1.0) is used to stabilize solutions rather than accelerate convergence. This was found to be necessary to converge fine grid cases with features such as overtip leakage and, as it adds very little computer time, is currently used as default. For a Runge–Kutta scheme with an odd number of partial steps, the averaging is applied on the finest grid level and the odd steps only.

The k–ϵ turbulence model is discretized about the same flux balance control volumes used by the explicit flow solver, with k and ϵ stored at cell centers. The resulting equations are solved implicitly using an ADI scheme on a crossflow plane. Alternatively, the algebraic equations used in Baldwin–Lomax are solved on a crossflow plane with reference to the nearest wall. Although the number of explicit time steps per turbulent viscosity update (solving of the turbulence model) can be varied, in practice the viscosity is updated every time step. All runs presented in this paper use the k–ϵ model with wall functions.

Developing a code with this "building block" approach results in a very flexible tool with many attractive features. Those that have not been mentioned so far are listed below:

- An option to use tip leakage has always been available in the code and is now being exercised with the viscous version.
- Solid bodies, e.g., part-span shrouds and engine splitters, are now modeled as viscous and can be rotating or stationary. As we are using an implicit ADI solver for the k and ϵ equations this had to be modified to account for the triple grid lines, which are used to define solid bodies in the code.
- Source terms are used to account for the average effects of adjacent blade rows. These source terms usually come from a throughflow analysis but could come from a separate three dimensional calculation in a manner similar to that used by Celestina et al. (1986).
- The radial equilibrium exit boundary condition has been supplemented by the addition of an exit condition, which allows no change in the cross-stream pressure gradient between the next to last and the last streamwise cell center values. This boundary condition, although not totally nonreflective, allows vortices and shock waves to escape from the solution domain without causing spurious reflections.

Quality solutions depend on the control of numerical viscosity, i.e., an accurate differencing scheme, and a good grid. Because the Navier–Stokes solver is an extension of an Euler solver, the amount of numerical viscosity produced by the code for inviscid applications has been monitored extensively and gridding requirements have been established. The extension to quality viscous solutions can therefore be made knowing the underlying errors associated with a purely inviscid solution.

Preprocessing and Postprocessing

The three dimensional system of codes—preprocessing, solvers, and postprocessing—is built around the use of binary files that separately contain the grid and flow information. These binary files permit storage of large amounts of data in a relatively small space. Conversion routines for transfer of files between computers (principally to and from the GE CRAY YMP 464), all of which are unseen by a designer, permit easy use of this format.

The preprocessing part of the system consists of the following main steps, the exact number used depending on the complexity of the geometry to be modeled:

- Convert the quasi-three-dimensional design system files obtained from throughflow and blade-to-blade codes into a three-dimensional blade passage description of the geometry. The meridional grid distribution on both suction and pressure surfaces is set in this code, which allows

for the setting of lines along which solid bodies may appear.

- The passage wall distribution is then taken and a blade-to-blade grid is produced by solving a sequence of two dimensional grid sections from hub to casing. The blade-to-blade grid is generated by an elliptic grid generator, which is loosely based on that of Sorenson (1980). At this point we have a full three dimensional grid, which for a stator would be complete.
- Tip clearance is accommodated by placing grid lines in the tip gap region and restretching the grid locally in order to obtain acceptable stretchings in the spanwise direction.
- Internal solid bodies are grown from an existing grid line that has been placed to run through the center of the body. Extra lines are placed to describe the upper and lower surfaces of the body, these lines being coincident with the central line upstream and downstream of the body. Leading and trailing edges are then matched to the real geometry and the grid relaxed in the neighborhood of these bodies to produce lines that blend in smoothly with the surrounding grid.
- The flow conditions from the throughflow are mapped onto the grid to give a starting flow file for the three dimensional Navier–Stokes solver.

The grids produced by the above sequence are checked for near-wall proximity in order that calculations are not performed outside the range of validity of the wall functions being used. Likewise, in all of the above gridding steps, multigrid requirements are adhered to. This amounts to areas with like boundary conditions, not crossing a triple line, being grouped together for multigrid purposes. Sometimes this poses a problem, but grid numbering is quickly established for a new configuration and used in similar future designs.

Postprocessing is mainly performed using an in-house code, which runs in both interactive and batch modes on a number of different platforms, including the CRAY. The code principally deals with line or contour plots and for designer use runs in a batch mode with input dictating the plots to be produced. In this fashion the solver and postprocessor can be run together, plots of convergence history and engineering variables of interest being returned to the designer in order that the next design decision can be made. Third party postprocessors are available on high-end workstations and their use in rendering complex three-dimensional information in a meaningful way is growing rapidly.

In the overall cycle time of producing a solution, a majority of the time is spent in creating good grids. The initial grid can take some time to produce, especially if new features (e.g., island splitters) have to be accommodated. However, once a gridding procedure is established, future design iterations are regularly accomplished within a working day. We are currently working on reducing the overall time to produce an initial grid and foresee that a three dimensional grid generator would be extremely useful.

Simple Test Cases

As was stated previously, the quality of a numerical technique should be evaluated with regard to analytical or simple test cases as well as real (engine) simulations. The code has been validated using the following simple cases:

- Boundary layer flow on a flat plate—laminar and turbulent.
- Low Reynolds number flow around a cylinder (Re = 20).
- Fully developed flow in a channel.

For these simple runs, effects of grid sizing and wall functions

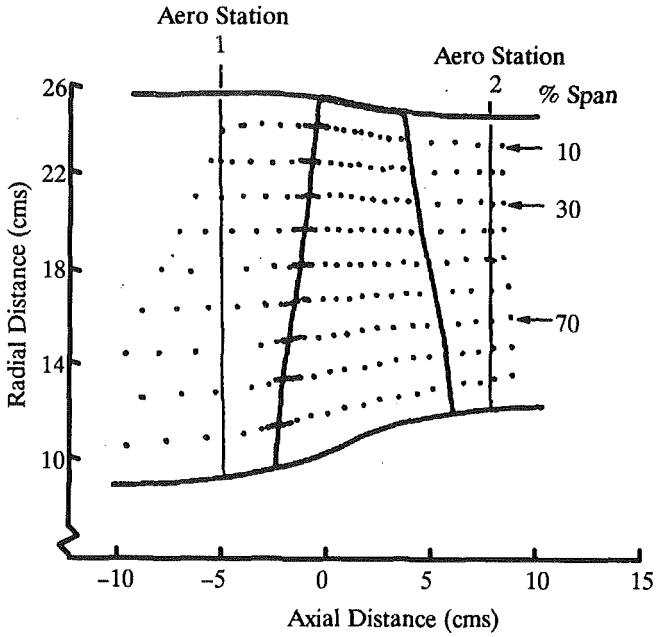

Fig. 1 Meridional view of rotor 67 showing laser anemometer and aerodynamic survey locations

were ascertained and used as starting points for gridding the more complex engine cases. It should be noted that while these cases are simple, they can be manipulated so as to check the operation of most of the coding. For example, although we may compute a boundary layer flow along a plate aligned with the axial direction and hence test the cross-stream gradient and turbulence model calculation, if the plate is rotated to be inclined to all three axes a much more severe test of the code is devised.

Fan Simulations

While the code has been applied to axial stators and rotors, radial diffusers, impellers, and unducted fans, only its transonic fan capability will be shown here. The simulations presented are chosen to demonstrate three successively more complex calculations. The first case is that of an isolated rotor (NASA Rotor 67). The next case demonstrates a design point multirow capability by including the downstream stator in the computation (GE/Wennerstrom Rotor 4). Lastly, we examine the real engine case of the NASA/GE E^3 fan in which solid bodies (part-span shroud and engine splitter) are accounted for, along with core engine adjacent blade row effects. In all three cases, only the normal design system has been employed to generate the grid and process the fan results. Grid clustering and number are typical of those used in day-to-day operation by designers and are very similar for each case.

NASA Rotor 67. Rotor 67 was designed and tested at NASA Lewis and is shown schematically in Fig. 1. It has 22 blades with a design pressure ratio of 1.63 and mass flow of 33.25 kg/s at 100 percent speed, corresponding to 16,043 rpm with a tip relative Mach number of 1.38. The extensive test data available both from laser measurements and static probes are given by Strasizar et al. (1989). The rotor has also been tested as a stage with a following stator, but this configuration will not be addressed here. Instead we investigated the operating map for three values of tip clearance: nominal (0.024 in., the observed running clearance), half nominal, and twice nominal. In particular, the data reported here concentrate on the near peak efficiency and near stall conditions where most experimental data are available. These cases are also interesting as a number of other researchers have recently computed the flow through this fan (Chima, 1991; Hah and Reid, 1992;

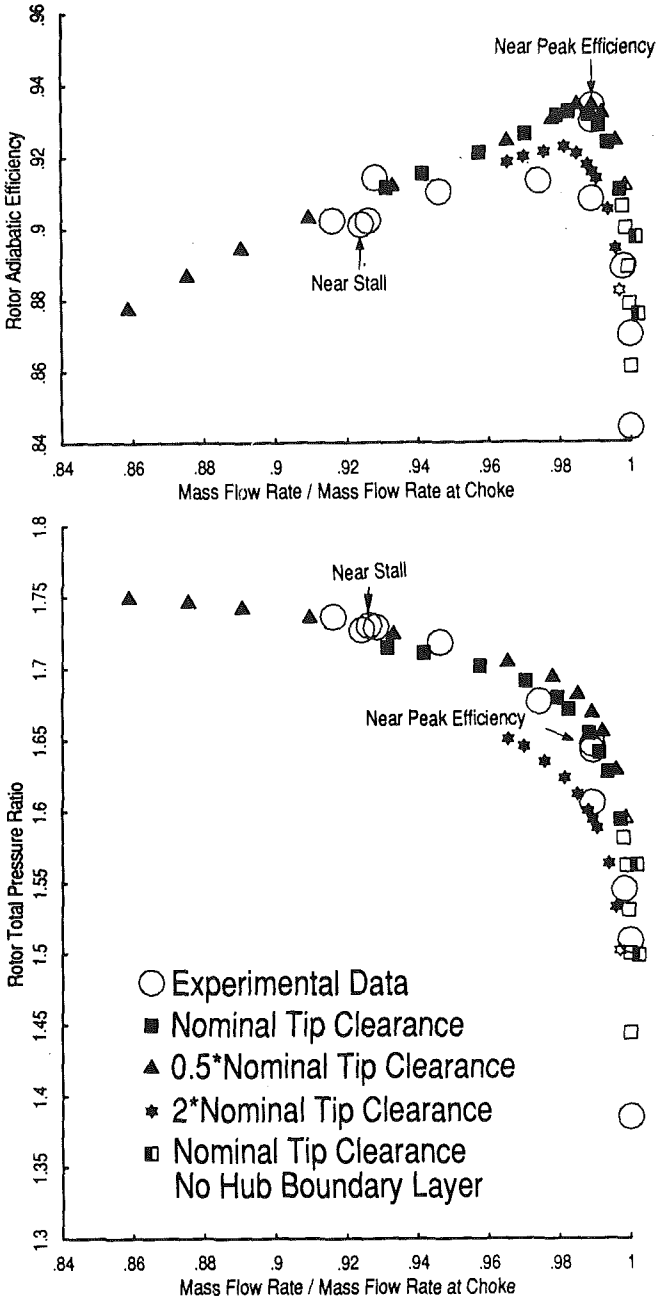

Fig. 2 Rotor 67 design speed operating characteristics

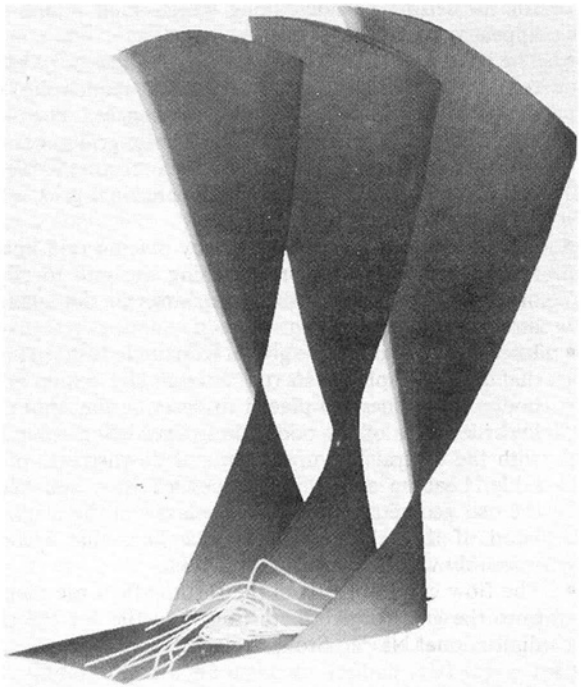

Fig. 3 View aft looking forward of rotor 67 at near peak efficiency showing the separated region found in the hub/suction surface trailing edge corner

Weber and Delaney, 1991; Adamczyk et al., 1993) thus facilitating comparison with other published computed results.

The simulations employed 328,937 grid points; 49 points in the blade-to-blade direction, 49 in the spanwise direction (4 being in the tip gap), and 137 in the axial direction. The inlet was positioned at Aero Station 1 and the exit just downstream of Aero Station 2. The code took 1 to 1.5 hours on the GE CRAY YMP to produce results for one point on the performance map. Other points can take less time, being restarted from previous solutions.

Computed and experimental performance maps are shown in Fig. 2. Three individually computed tip clearance cases are shown, with higher pressure rise, greater peak adiabatic efficiency, and greater flow range being obtained as the clearance is reduced. The computed mass flows are nondimensionalized with respect to the choked mass flow for the nominal tip clearance case. This mass flow was found to be 1.2 percent lower than the experimentally observed value. The leftmost point on each of the computed characteristics represents the highest downstream static pressure at which the code would converge. Raising the static pressure further produced reverse flow near the tip through the inlet and hence no solution was possible. This is not what would happen in practice as the rotor would probably experience rotating stall before being pushed to its ultimate stall point, but as only a single passage is being modeled it is the closest the simulation can come to the stall point. It should be noted in passing that although inlet total pressure profiles at near peak efficiency and near stall are available from experimental data, the near peak efficiency profile has been used throughout these runs. The two profiles only marginally different near the tip and the mechanism for transitioning between profiles is not easy to define.

As the exit pressure was lowered from stall past the peak efficiency point, a separated region observed near the hub/suction surface trailing edge (Fig. 3) at all operating conditions began to grow and become unsteady. This behavior manifests itself in the solution neither converging nor diverging, with slowly fluctuating errors in the solution domain being encountered only in the separated region. These solutions are marked with open symbols. As local time stepping is being used to accelerate convergence, the true unsteady solution is not found, but rather a pseudo-unsteady solution. Such solutions are not uncommon with fine grids and have been observed around part-span shrouds at off-design conditions and on turbine blade trailing edges where vortex shedding can occur. The present results do, however, fall at reasonable positions on the performance map, because the separated region is affecting such a small region of the flow, and are considered realistic.

There are a number of ways to produce a steady-state result, such as increasing the smoothing to damp out the unsteadiness. In Fig. 2 we show the sensitivity of the solutions by removing the small inlet hub boundary layer (Fig. 5) and hence produce the converged points shown at a (consistently) slightly higher mass flow. While no other inlet boundary layer profiles have been investigated, it is clear that reasonably fine grids are needed for an accurate definition of this profile.

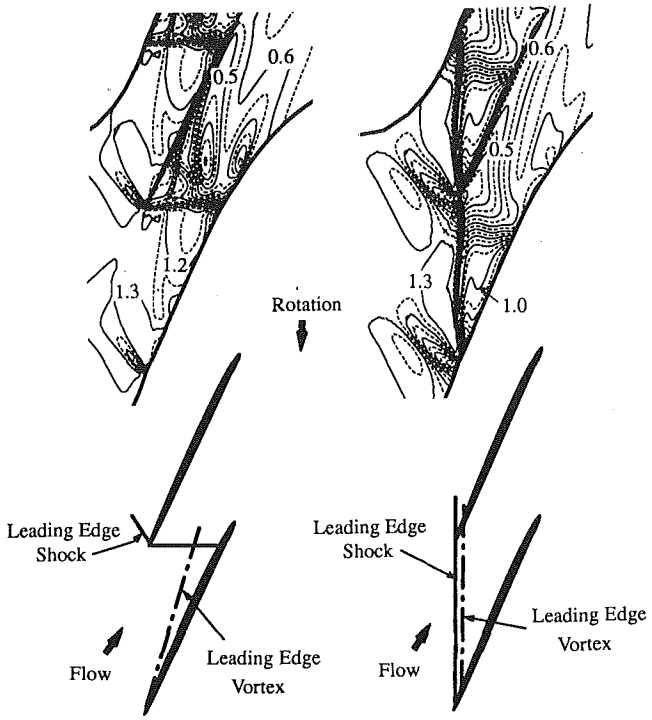

Fig. 4 Computed relative Mach number contours midway between tip and casing showing tip vortex shock interaction for near peak efficiency (left) and near stall (right) cases; contours at intervals of 0.05; schematics shown for clarification

The presence of this separation region near the hub has been observed by Chima (1991) but it is interesting to note that other researchers (e.g., Hah and Reid, 1992) do not seem to have found this feature in their computations. When experimental data were being taken on the rotor, it was found to be very difficult to seed, and hence take data, in this hub corner region. While this does not confirm the presence of the separated region, it lends some weight to its possible existence.

Efficiencies seem to be reasonably well predicted with the nominal clearance except that the dramatic fall off from 93.4 to 91.3 percent as the mass flow changes from 0.989 to 0.974 is not seen in the calculations. Instead a smooth curve extending out toward stall is predicted. It is not understood what phenomena cause the sudden efficiency loss in the experiment (hysteresis effects have been proposed) and so it is difficult to explain the behavior of the computations, which, on an isolated basis, look reasonable.

Three tip clearance cases were run to test the sensitivity of the results to the modeled clearance and hence aid with future tip clearance modeling. The tip of the blade is formed by simply closing the crossflow plane grid at this location, resulting in a roof type structure on the top of the blade. The clearance is then the distance from the roof apex to the casing, modeled as the true tip clearance for the nominal case. What this distance should actually be set to is the subject of some debate. If the flow perpendicular to the chord over the tip is likened to the flow through a sharp two-dimensional slot, then it can be argued that in shaping the tip of the blade is this manner we have in some way modeled the limiting streamline emanating from the upstream blade corner and the tip gap should be reduced according to a coefficient of discharge for such a geometry. Alternately, the current results show a 14.4 percent peak pressure loss for a 1 percent increase in tip gap. Existing experimental data could be correlated and the modeled tip gap sized to produce the correct pressure loss effect. At present these data are viewed as a first attempt to understand tip clearance effects and no definite conclusions regarding the tip gap sizing have been drawn.

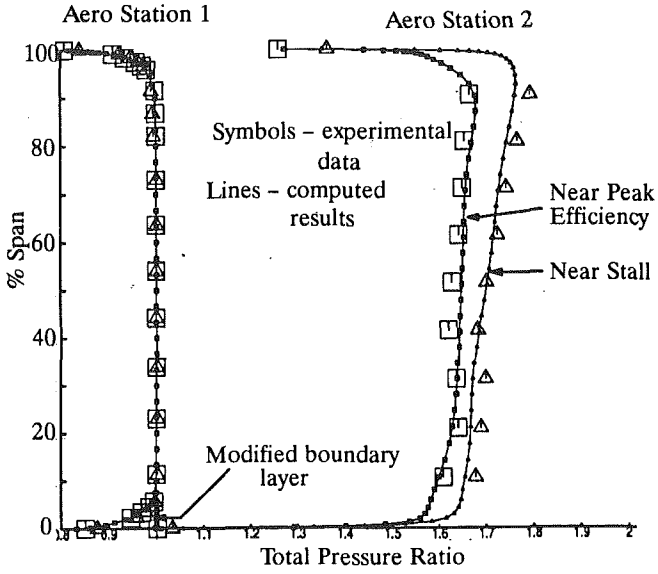

Fig. 5 Rotor 67 total pressure profiles

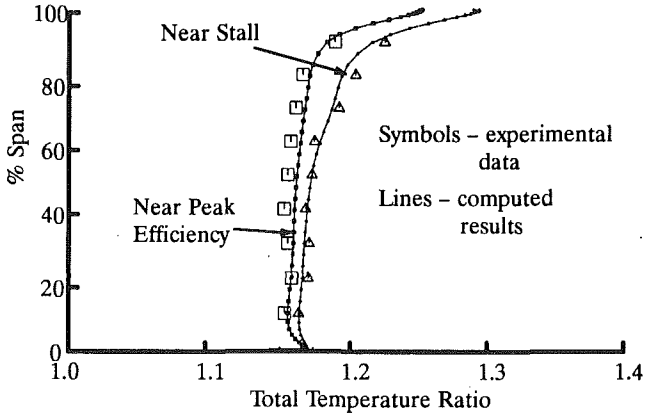

Fig. 6 Rotor 67 total temperature profiles at Aero Station 2

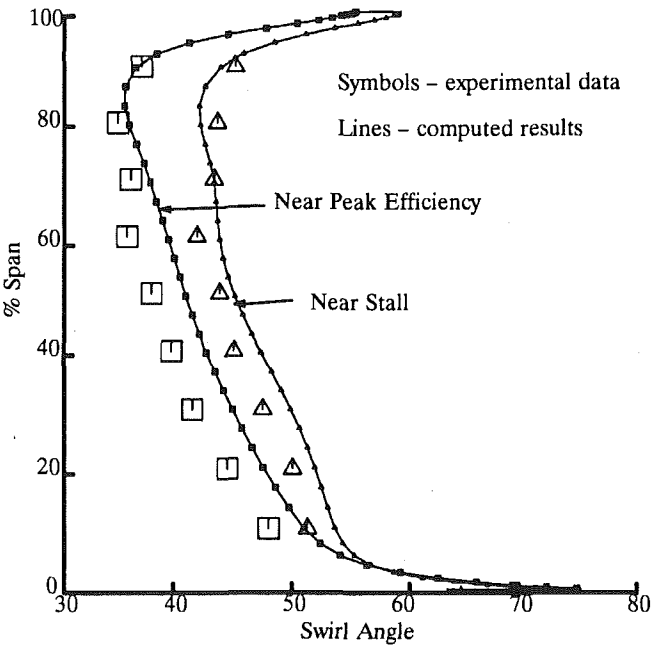

Fig. 7 Rotor 67 swirl angle profiles at Aero Station 2

The interaction between the tip vortex and the shock is very complex, especially near stall. At near peak efficiency it appears that a tip vortex is formed from the blade leading edge and intersects the shock inside the blade passage (Fig. 4). It has been found that the tip vortex is tighter and more discrete as the clearance is reduced, affecting some 2 percent of the blade span for the smallest clearance and 8 percent of the blade for the largest case (an increase of a factor of 4 on clearance). Near stall the shock is detached (Fig. 4) with traces of the tip vortex appearing from the leading edge just behind the shock system. Viewed in terms of casing separation, a three-dimensional line appears inside the passage for the near peak efficiency case and is moved to the leading edge as the back pressure is increased to near stall. Further increase of the exit pressure causes the shock and vortex to be pushed upstream and eventually intersect the inlet boundary, the condition we are describing here as numerical stall. It is believed that these observations are consistent with, and serve to support, those found by Adamczyk et al. (1993).

Experimental and computed Aero Station 2 total pressures, temperatures, and angles are shown in Figs. 5, 6, and 7, respectively. The present results agree reasonably well with the experimental data. They have also been compared with Chima's (1991) results and show remarkably good agreement for both the profiles and the Mach number contours (not shown). Finally, Figs. 8 and 9 present a comparison of the computed and experimental relative Mach number contours at 10, 30, and 70 percent span from the casing, both at near peak efficiency and near stall cases. The experimental data are taken using laser anemometry in which a laser system measures the speed of particles assumed to be moving with the flow. As the flow passes through a shock the particle response lags behind that of the flow, i.e., particles do not decelerate as quickly as the flow. It is therefore believed that the beginning of the shock is correctly captured by the laser measurements, but the shock itself is somewhat smeared. Taking this into account, Pierzga and Wood (1984) estimated the location of the experimental shocks, shown by the dashed lines on the experi-

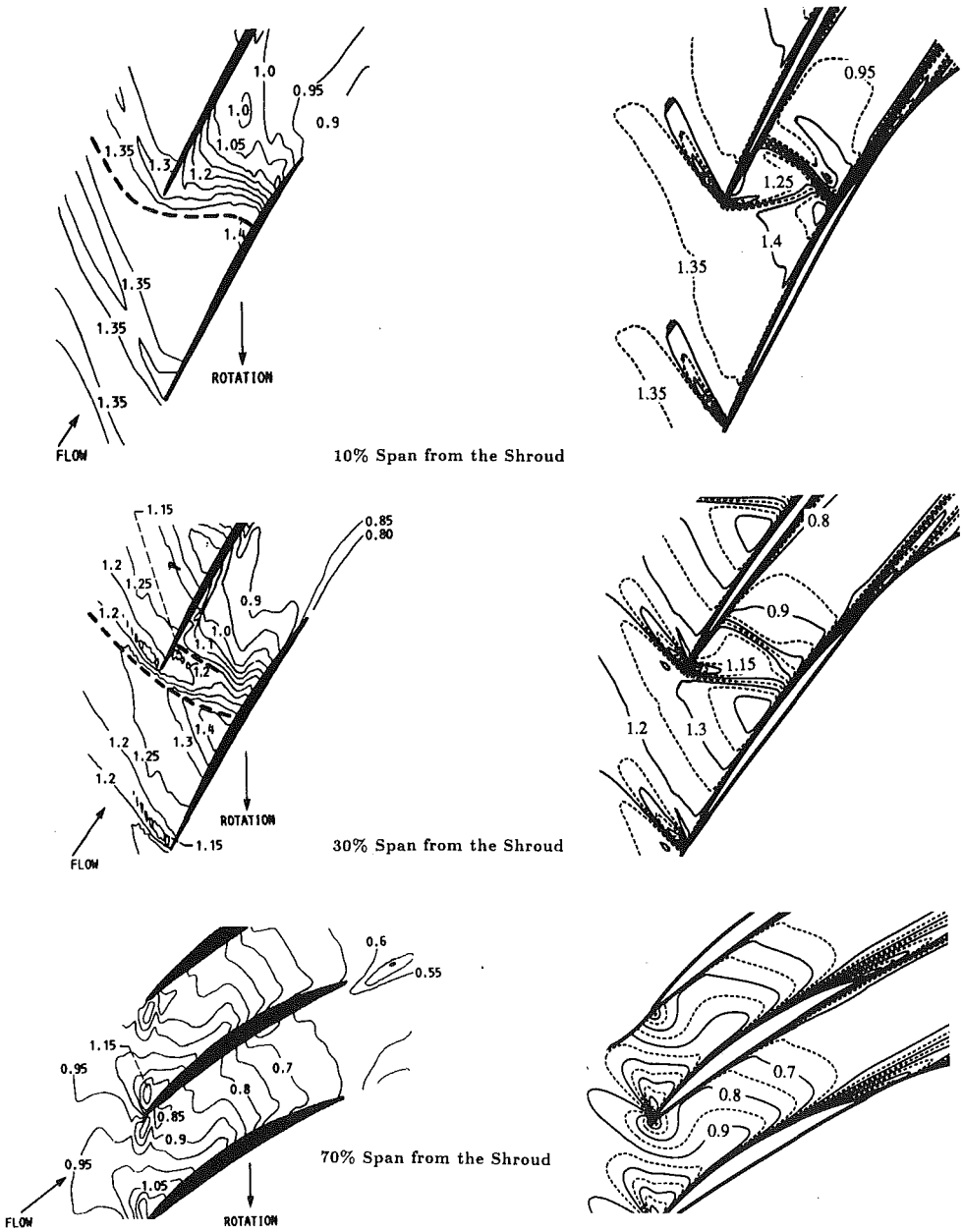

Fig. 8 Experimental (left) and computed (right) contours of relative Mach number near peak efficiency for Rotor 67; contours at intervals of 0.05; dashed lines are estimated shock positions from Pierzga and Wood (1985)

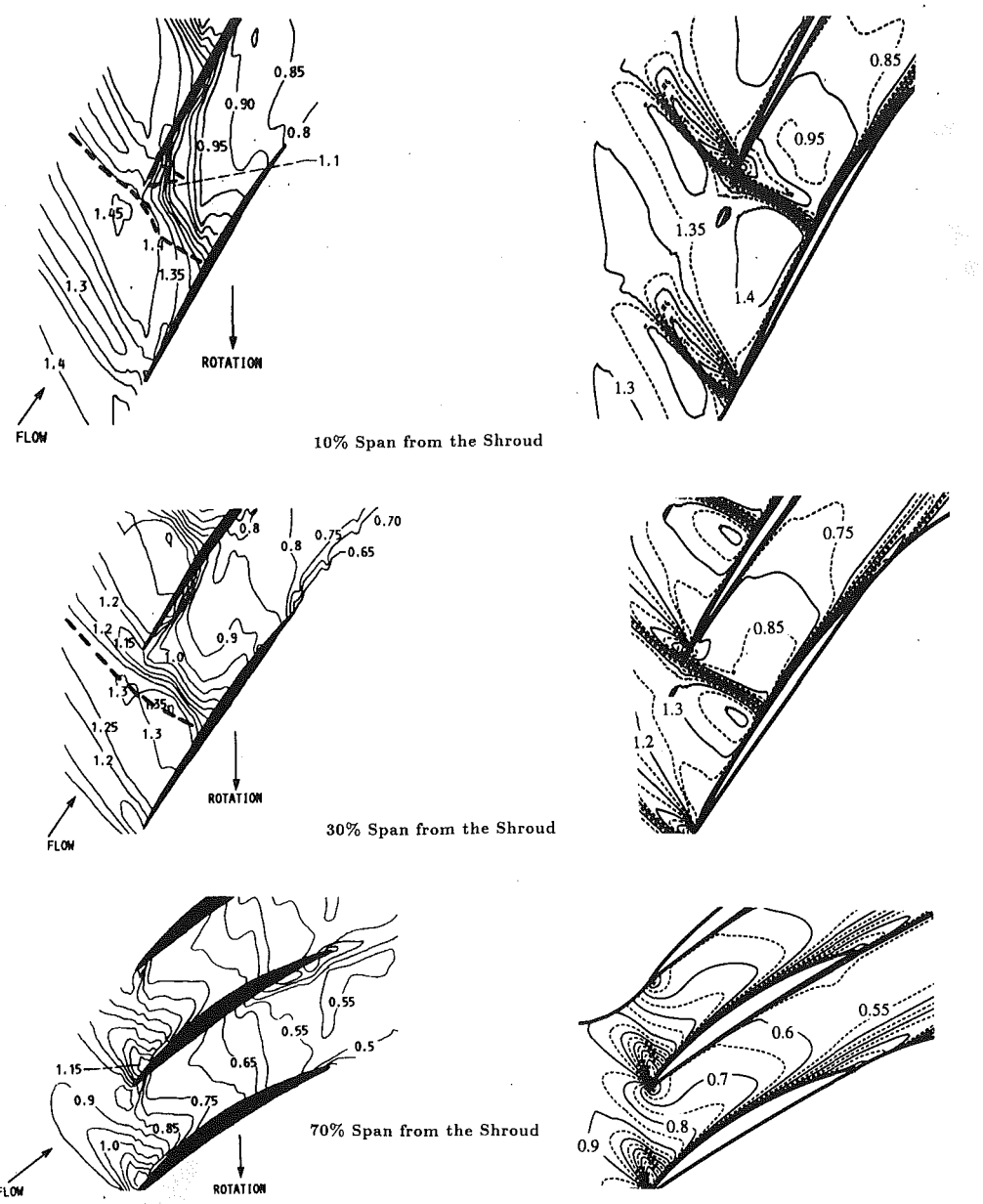

Fig. 9 Experimental (left) and computed (right) contours of relative Mach number near stall for Rotor 67; contours at intervals of 0.05; dashed lines are estimated shock positions from Pierzga and Wood (1985)

mental plots. With this in mind the experimental and computed results at the two operating points appear to be in reasonable agreement. Again, when the present calculations are compared to those of other researchers, agreement in terms of overall shock structure and position is more obvious. It seems to us that most of these computations are producing very similar results; indeed, they correspond better to each other than to the experimental data.

GE/Wennerstrom Rotor 4. For a number of years a collaborative effort has existed between WPAFB (Wennerstrom) and GEAE aimed at the design and testing of transonic rotors. This case presents the fourth rotor in the series, simulated with its accompanying stator to demonstrate a full-stage calculation. The rotor has 20 blades rotating at 20,222 rpm, with a design stage pressure ratio of 2.0 and a tip speed of 1500 ft/sec. The rotor alone configuration,with an investigation of turbulence modeling, appears in an accompanying paper (Turner and Jennions, 1993).

The total grid for this case consists of 49 points in the blade-to-blade direction, 37 in the spanwise direction (4 in the tip gap), and 117 in the axial direction; 212,121 grid points in all. The stator lies between axial grid lines 89 and 111 as shown in Fig. 10. A full simulation of the stage would be unsteady and extremely computer intensive. Here we do not attempt to model this unsteady flow but rather produce a solution in which the time-averaged effects of the stator have been included via the use of axisymmetric source terms in this region (Cedar and Holmes, 1989). The steady simulation run in this manner took 45 CPU minutes on the GE CRAY YMP.

The casing endwall static pressures are shown against experimental data in Fig. 11. Agreement is good and the presence of the stator on the endwall pressure is clearly visible. Figure 12 shows the more detailed kulite pressure measurements on the casing. An oblique leading edge shock followed by a passage diffusion to the trailing edge is seen in both cases. The numerical solution shows the tip leakage vortex emanating from the leading edge region of the blade and intersecting the shock. While the experimental data do not pick out the details of the tip vortex, it is possible to detect its interaction with the passage shock.

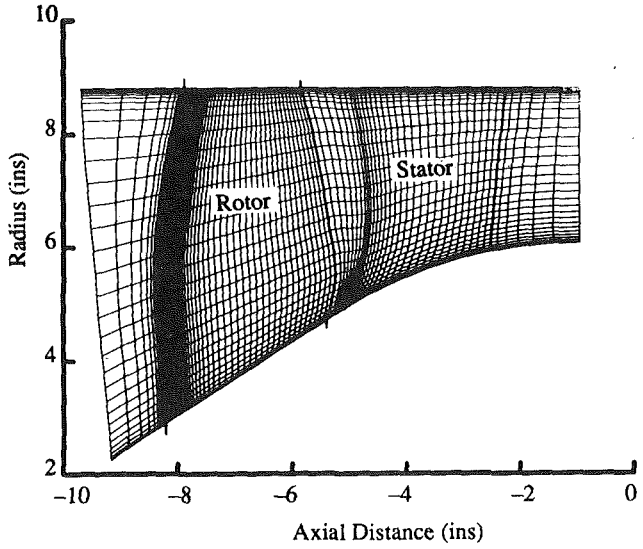

Fig. 10 Wennerstrom Rotor 4 grid showing rotor and stator locations

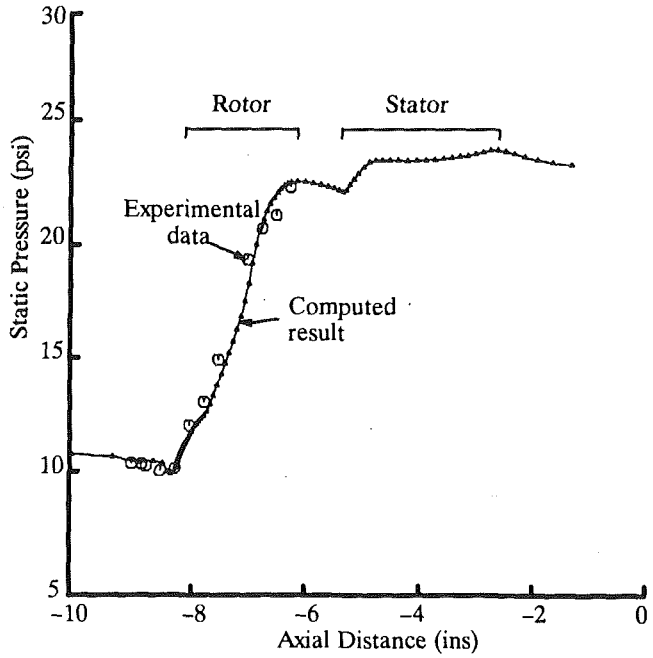

Fig. 11 Wennerstrom Rotor 4 casing static pressure comparison

Finally, Fig. 13 presents a passage-averaged contour plot of the product of radius and absolute tangential velocity (RCu). This product is considered constant along a streamline in duct regions for most throughflow calculations and changes through blade rows depending on the turning of the flow. From Fig. 13 the turning of the rotor can be observed, the almost horizontal contours between the trailing edge of the rotor and the leading edge of the stator and then the turning back to axial imposed by the source terms used to model the stator. This type of simulation with an adjacent blade row modeled by source terms provides more flexibility when dealing with boundary condition location and effect on the solution.

GE/NASA E^3 Fan. The last, and most complex, simulation is that of the GE/NASA E^3 fan (Sullivan and Hager, 1983). This fan was chosen because it is one of the few high-efficiency, high-bypass-ratio fans typical of modern aero-engines for which test data are available and because it had previously been simulated by Cedar and Holmes (1989). Figure 14 is taken from their paper and shows the fan configuration,

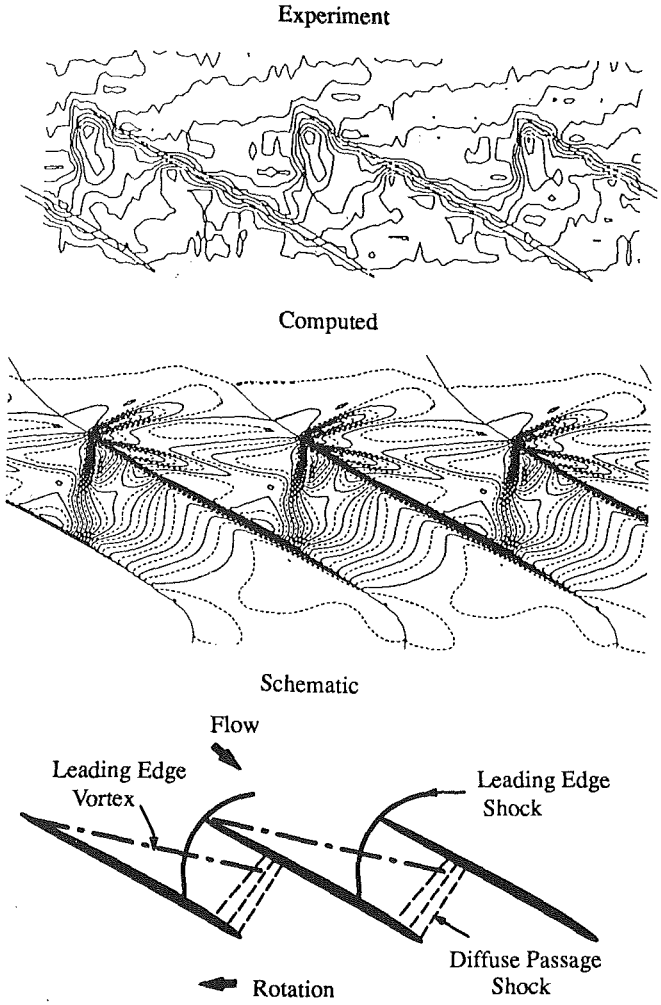

Fig. 12 Wennerstrom Rotor 4 casing static pressure contours and explanatory schematic

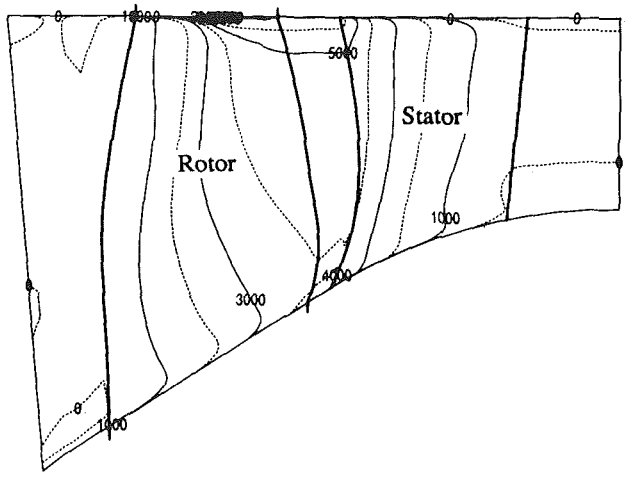

Fig. 13 Passage-averaged contour plot of RCu for Wennerstrom Rotor 4; contour interval of 1000

part-span shroud, island splitter, and quarter stage booster. The meridional grid is shown in Fig. 15 and has 81 points in the spanwise direction, including 4 points in the tip gap. Such a high number is needed in order to model viscous effects on the endwalls and solid bodies. There are 157 points in the axial direction to enable an accurate description of all the geometry present, an enlargement of the part-span shroud and blade leading edge region being shown in Fig. 15. Finally, 49 points

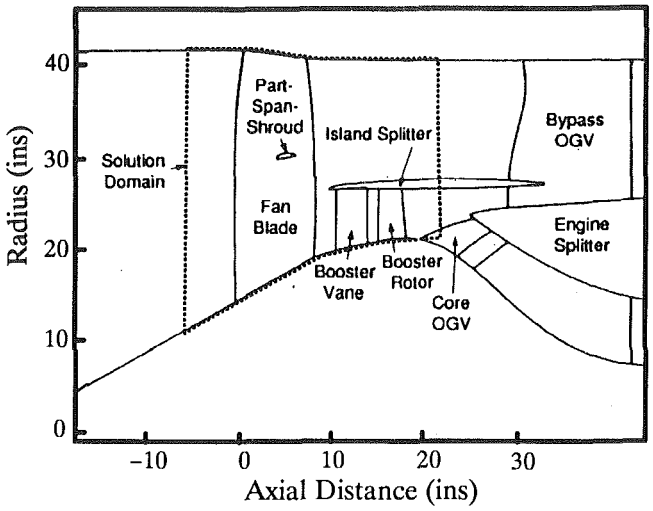

Fig. 14 E^3 fan configuration

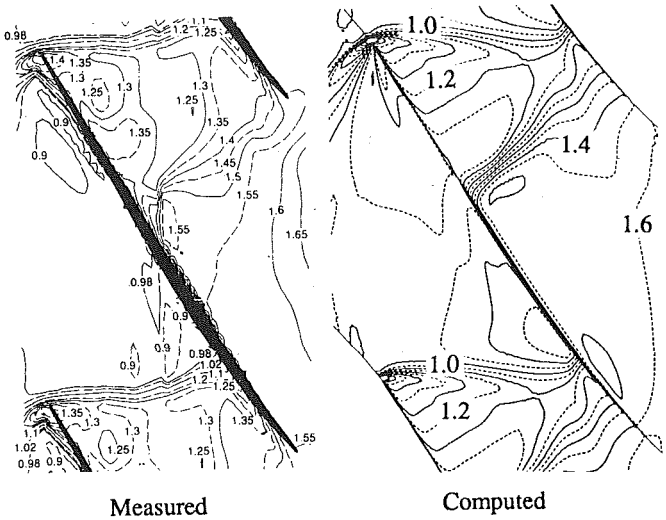

Fig. 16 E^3 Casing normalized static pressure contours

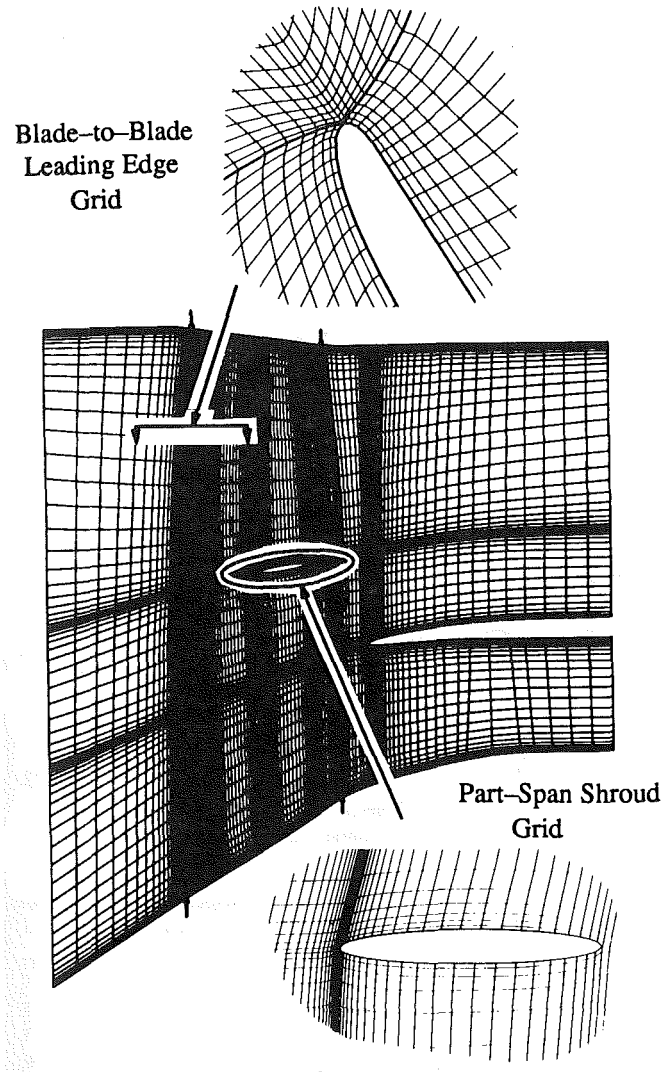

Fig. 15 E^3 fan grid details

are used in the blade-to-blade direction, giving a total grid of 623,133 points.

An initial estimate of the flow field is made by mapping the throughflow datamatch onto the three dimensional grid. Even so, starting a calculation as complex as this can be difficult with a five-stage Runge–Kutta scheme and usually a two-stage scheme, which has been found to be more robust, is run for the first 100 time steps, after which the five-stage scheme is run as normal. For the present case, including the effects of the booster blade rows as source terms, a converged solution was obtained in a total of 500 time steps, taking some 3.6 hours on the GE CRAY YMP. Of course, in the normal design process, changes of back pressure will have to be made to obtain the correct bypass ratio, such runs typically taking a further 300–400 iterations to converge depending on the severity of the change that is made.

The current simulation models a 97.2 percent speed case. The datamatch throughflow analysis that was performed subsequent to the fan being tested gave a bypass ratio of 3.52. The current calculation, which was essentially run to the datamatch bypass exit and booster vane leading edge static pressures, predicted a bypass ratio of 3.51 with the individual mass flows being predicted to better than 1 percent.

Figure 16 shows contours of static pressure on the casing from kulite measurements and from the calculation. Agreement is reasonable with both showing a two-shock system, the calculation predicting a more noticeable tip clearance vortex from the leading edge. This vortex is also evident in the relative Mach number contours, plotted midway between the tip and casing in Fig. 17. It is accompanied by a second stronger vortex, driven by the pressure difference created across the tip by the in-passage shock. This second vortex interacts more strongly with the in-passage shock than does the leading edge vortex.

The measured pressures show an almost constant pressure on the "pressure" surface behind the first shock (static pressure ratios around 1.3) whereas the computation shows a rapid acceleration into the second shock. This is further seen in the average endwall statics shown in Fig. 18 where the higher pressure from experiment is again evident. This discrepancy is not fully understood at the present time but a combination of probe error and tip clearance gap sizing might be the cause. Possible probe error was investigated by Weyer and Schodl (1971) where they concluded that a pneumatic measuring system such as that used here could record up to five percent high at the frequencies and pressure ratios encountered in this rotor. For the other two rotors simulated in this paper, probe error would be much lower, as their rotational speeds and hence their excitation frequencies are much higher. Studies of the effect of tip clearance gap are underway.

Total pressure and temperature measurements were available at the booster vane leading edge and on the bypass OGV. These are compared with the prediction in Figs. 19 and 20 and show remarkably good agreement. Island static pressure taps were also taken and are shown in Fig. 21. As the main interest of this simulation was with the fan, matching the booster

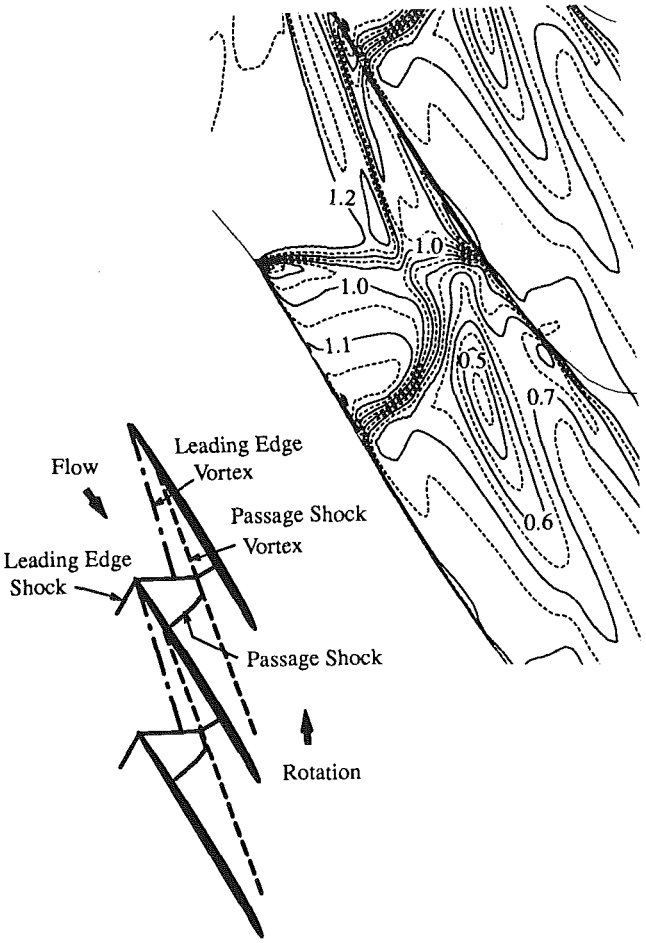

Fig. 17 Computed E^3 relative Mach number contours between tip and casing and schematic showing tip vortex/shock interaction; contour interval of 0.05

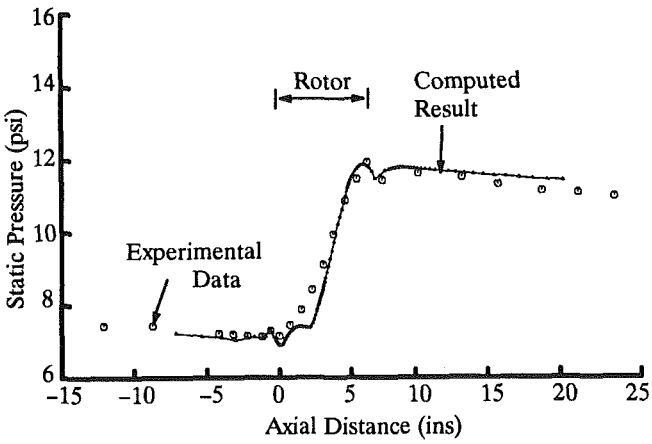

Fig. 18 E^3 casing static pressure comparison

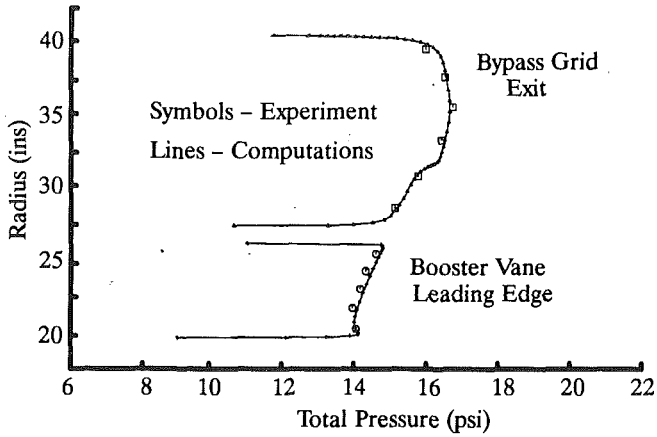

Fig. 19 E^3 downstream total pressure profiles

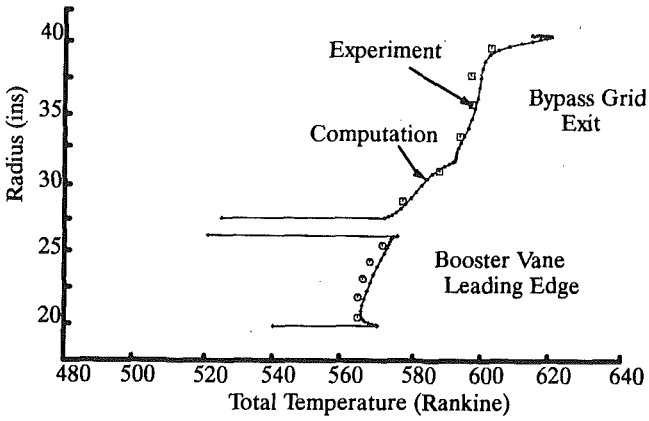

Fig. 20 E^3 downstream total temperature profiles

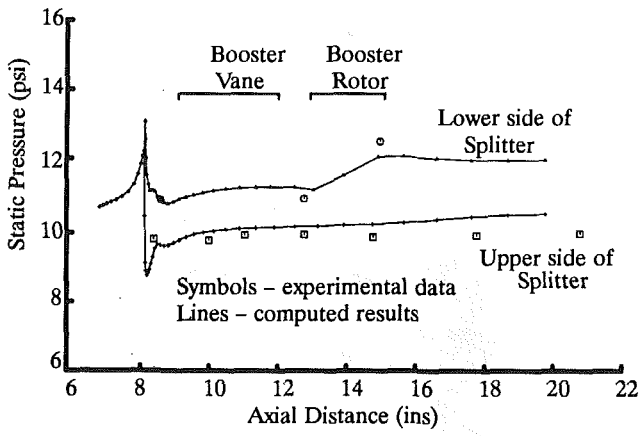

Fig. 21 E^3 island static pressure distribution

leading edge pressure was judged to be important; the other pressures on the island inner side depending critically on the source term modeling.

Recent design interest in cases like this has focused on the part-span shroud as being an area for possible performance improvement. Ideally, this body would be nonlifting to cause minimal disturbance to the surrounding flow, a situation that cannot be fully achieved due to the presence of the fan's shock system. The loading on the part-span shroud is shown in Fig. 22, the near suction surface velocity vectors in Fig. 23, and the local velocity vectors around the part-span shroud at three locations across the passage in Fig. 24. Near the suction surface, the pressure inbalance between the upper and lower part-span shroud surfaces causes flow around the trailing edge and a small separation to form on the upper surface. This radial flow then joins the radial flow produced by the action of the passage shock on the suction surface boundary layer as it is centrifuged out toward the tip, action that is confined to a region very close to the blade surface. At midpassage the flow appears healthy, the loading being mostly from the interaction of the part-span shroud with the passage shock. Over near the pressure surface an overspeed is observed near the leading edge on the upper surface and the flow in the trailing edge region behaves in a more orderly manner than that near the suction surface. Design improvements aimed at better aligning the part-span shroud with the flow, to remove the leading edge overspeed and trailing edge flow migration, would improve the efficiency of the part-span shroud.

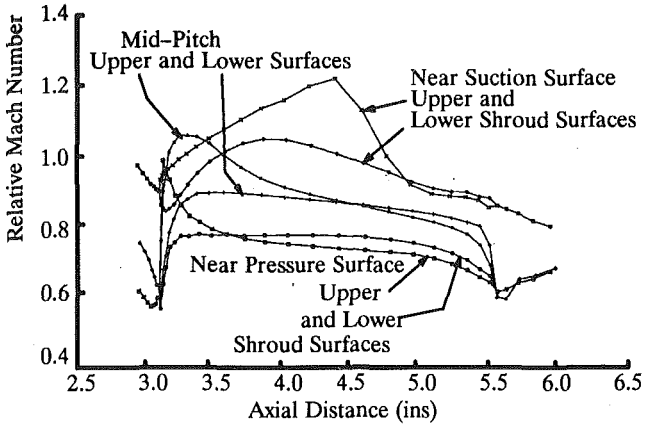

Fig. 22 E^3 part-span shroud loading distributions

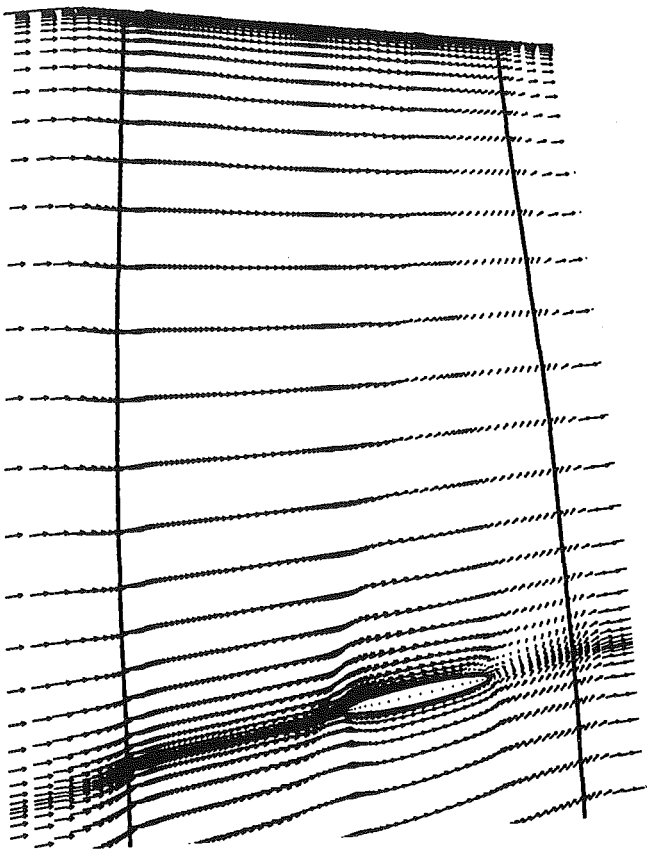

Fig. 23 E^3 near suction surface velocity vectors

Concluding Remarks

This paper has demonstrated the ability of a three-dimensional Navier–Stokes solver, used on a daily basis in industry, to predict the experimental data on three fans typical of those found in modern commercial engines. All simulations yielded good results and show that CFD has matured into a technology useful for industrial design. Progress still needs to be made in a number of areas, principally gridding and turbulence modeling, but the results shown here give real encouragment and purpose to work in these areas.

Acknowledgments

The authors would like to thank their many colleagues at General Electric Aircraft Engines (GEAE) for their helpful suggestions during the course of this work. In particular, we are indebted to Chung Shin and Te Liang, who performed the gridding and calculations for the Rotor 67 and E^3 cases, respectively. From NASA Lewis, Jerry Wood gave us valuable assistance with the Rotor 67 geometry and John Adamczyk provided many useful discussions during the course of the work. A majority of the computing for the Rotor 67 simulations was performed using NASA Numerical Aerodynamic Simulator (NAS) computers. The authors also wish to thank GEAE for permission to publish this paper.

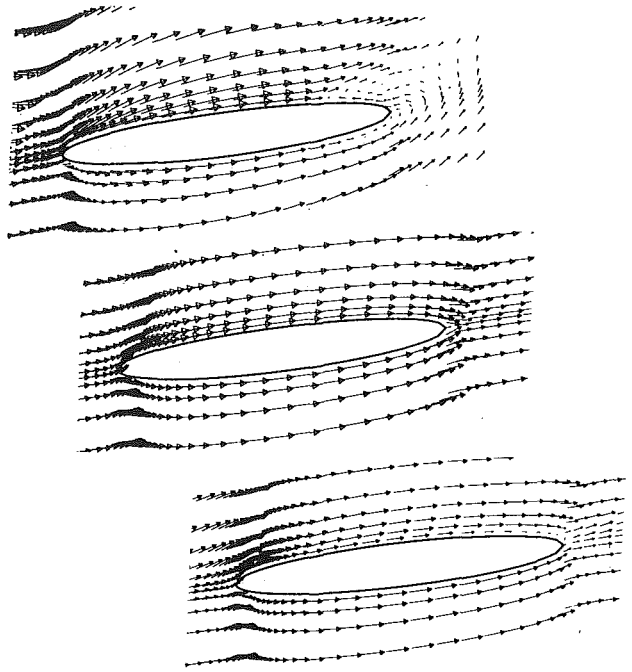

Fig. 24 Velocity vectors around the part-span shroud near the suction surface (left), at midpassage, and near the pressure surface (right) for E^3

References

Adamczyk, J. J., Celestina, M. L., and Greitzer, E. M., 1993, "The Role of Tip Clearance in High-Speed Fan Stall," ASME JOURNAL OF TURBOMACHINERY, Vol. 115, pp. 28–39.

Baldwin, B., and Lomax, H., 1978, "Thin Layer Approximation and Algebraic Model for Separated Turbulent Flow," AIAA Paper No. 78–257.

Calvert, W. J., and Ginder, R. B., 1985, "A Quasi-Three-Dimensional Calculation System for the Flow Within Transonic Compressor Blade Rows," ASME Paper No. 85-GT-22.

Cedar, R. D., and Holmes, D. G., 1989, "The Calculation of the Three-Dimensional Flow Through a Transonic Fan Including the Effects of Blade Surface Boundary Layers, Part-Span Shroud, Engine Splitter and Adjacent Blade Rows," ASME Paper No. 89-GT-325.

Celestina, M. L., Mulac, R. A., and Adamczyk, J. J., 1986, "A Numerical Simulation of the Inviscid Flow Through a Counterrotating Propeller," ASME JOURNAL OF TURBOMACHINERY, Vol. 108, p. 187.

Chima, R. V., 1991, "Viscous Three-Dimensional Calculations of Transonic Fan Performance," presented at the AGARD 77th Symposium on CFD Techniques for Propulsion Applications, Paper No. 21.

Dawes, W. N., 1987, "A Numerical Analysis of the Three-Dimensional Viscous Flow in a Transonic Compressor Rotor and Comparison With Experiment," ASME JOURNAL OF TURBOMACHINERY, Vol. 109, pp. 83–90.

Dawes, W. N., 1990, "A Comparison of Zero and One Equation Turbulence Modelling for Turbomachinery Calculations," ASME Paper No. 90-GT-303.

Denton, J. D., 1983, Lecture Notes, ASME Turbomachinery Institute Course on Fluid Dynamics of Turbomachinery, July 18–27.

Hah, C., and Reid, L., 1992, "A Viscous Flow Study of Shock-Boundary Layer Interaction, Radial Transport, and Wake Development in a Transonic Compressor," ASME JOURNAL OF TURBOMACHINERY, Vol. 114, pp. 538–547.

Holmes, D. G., and Tong, S. S., 1985, "A Three-Dimensional Euler Solver for Turbomachinery Blade Rows," ASME *Journal of Engineering for Gas Turbines and Power*, Vol. 107, p. 258.

Jameson, A., Schmidt, W., and Turkel, E., 1981, "Numerical Solutions of the Euler Equations by Finite Volume Methods Using Runge–Kutta Time-Stepping Schemes," AIAA Paper No. 81-1259.

Kallinderis, J. G., and Baron, J. R., 1987, "Adaptation Methods for a New Navier–Stokes Algorithm," AIAA Paper No. 87-1167.

Launder, B. E., and Spalding, D. B., 1974, "The Numerical Computation of Turbulent Flows," in: *Computer Methods in Applied Mechanics and Engineering 3*, North-Holland Publishing Company, p. 269.

Miranda, L. R., 1982, "A Perspective of Computational Aerodynamics From the Viewpoint of Airplane Design Applications," AIAA Paper No. 82-0018.

Pierzga, M. J., and Wood, J. R., 1985, "Investigation of the Three-Dimensional Flow Field Within a Transonic Fan Rotor: Experiment and Analysis," ASME JOURNAL OF TURBOMACHINERY, Vol. 107, pp. 436–449.

Singh, U. K., 1982, "A Computation and Comparison With Measurements of Transonic Flow in an Axial Compressor Stage with Shock and Boundary Layer Interaction," ASME *Journal of Engineering for Power*, Vol. 104, No. 2.

Sorenson, R. L., 1980, "A Computer Program to Generate Two-Dimensional Grids About Airfoils and Other Shapes by the Use of Poisson's Equation," NASA Technical Memorandum 81198.

Smith, L. H., Jr., 1987, "Unducted Fan Aerodynamic Design," ASME JOURNAL OF TURBOMACHINERY, Vol. 109, p. 313.

Strazisar, A. J., Wood, J. R., Hathaway, M. D., and Suder, K. L., 1989, "Laser Anemometer Measurements in a Transonic Axial-Flow Fan Rotor," NASA Technical Paper 2879.

Sullivan, T. J., and Hager, R. D., 1983, "The Aerodynamic Design and Performance of the General Electric/NASA E^3 Fan," Paper No. AIAA-83-1160.

Turner, M. G., and Jennions, I. K., 1993, "An Investigation of Turbulence Modeling in Transonic Fans Including a Novel Implementation of an Implicit k–ϵ Turbulence Model," ASME JOURNAL OF TURBOMACHINERY, Vol. 115, this issue, pp. 249–260.

Von Backstrom, T. W., 1990, "Dawes and Denton Codes Applied to a Transonic Compressor Rotor," ASME Paper No. 90-GT-304.

Wadia, A. R., and Law, C. H., 1993, "Low Aspect Ratio Transonic Rotors, Part 2: Influence of Location of Maximum Thickness on Transonic Compressor Performance," ASME JOURNAL OF TURBOMACHINERY, Vol. 115, this issue, pp. 226–239.

Weber, K. F., and Delaney, R. A., 1991, "Viscous Analysis of Three-Dimensional Turbomachinery Flows on Body Conforming Grids Using an Implicit Solver," ASME Paper No. 91-GT-205.

Weyer, H., and Schodl, R., 1971, "Development and Testing of Techniques for Oscillating Pressure Measurements Especially Suitable for Experimental Work in Turbomachinery," ASME Paper No. 71-GT-28.

Wood, J. R., Schmidt, J. F., Steinke, R. J., Chima, R. V., and Kunik, W. G., 1988, "Application of Advanced Computational Codes in the Design of an Experiment for a Supersonic Through-flow Fan Rotor," ASME JOURNAL OF TURBOMACHINERY, Vol. 110, p. 270.

A Comparison of the Measured and Predicted Flow Field in a Modern Fan-Bypass Configuration

R. K. Goyal
Allison Turbine Division,
General Motors Corporation,
Indianapolis, IN 46206-0420

W. N. Dawes
Whittle Laboratory,
University Engineering Department,
Cambridge, United Kingdom

A three-dimensional viscous Navier-Stokes flow solver was used to predict core and bypass rotor performance and radial flow characteristics of a 4.6:1 bypass ratio, single-stage fan. The three-dimensional flow solver can handle several blade rows simultaneously and has the capability to include a downstream splitter. Results of the analysis are compared with experimental data obtained during rig testing of a modern high bypass single-stage turbofan in which rotor performance for both bypass and core streams was measured.

Introduction

The design of the transonic fan in a modern bypass engine is of considerable interest. Any improvement in its efficiency has a strong influence on engine thermal efficiency, while any shortfall in capacity is detrimental to the overall propulsion system efficiency. The design and analysis of the fan blade in this environment must include consideration of its interaction with the downstream flow splitter. Moreover, core stream performance and bypass duct losses are strongly impacted by fan/splitter flow interactions. It is extremely important to account for these effects in an analytical simulation of the fan system.

The simulation of the flow in multistage turbomachinery has become a topic of intense research activity in recent years. Truly unsteady simulations, while feasible technically, are far too expensive to consider for design use. Attention is therefore being given to simplified approaches and the efforts of Dawes (1991), Adamczyk et al. (1990), and Cedar and Holmes (1989) are representative of this trend. Reported herein is a comparison of experimental test data for a single-stage transonic rotor with predictions using the three-dimensional viscous code of Dawes (1988, 1991). Calculations were made with and without the presence of a down-stream flow splitter and core vane typical of a modern turbofan compression system. The experimental program was designed to provide detailed aerodynamic measurements needed for comparison with the analytical effort.

Equations of Motion and Solution Algorithm

The basic equations of motion are the fully three-dimensional Reynolds-averaged Navier-Stokes equations expressed in cylindrical coordinates in integral conservation form:

$$\frac{\partial}{\partial t}\oint_{\text{VOL}} \overline{U} d\,\text{VOL} = \oint \overline{H} \cdot d\overline{\text{AREA}} + \oint \rho \overline{S} d\,\text{VOL} \qquad (1)$$

where

$$\overline{U} = \begin{bmatrix} \rho \\ \rho V_x \\ r\rho V_\theta \\ \rho V_r \\ \rho E \end{bmatrix} \quad \overline{H} = \begin{bmatrix} \rho\overline{q} \\ \rho V_x \overline{q} + \overline{\overline{\tau}}\hat{i}_x \\ r\rho V_\theta \overline{q} + \overline{\overline{\tau}}\hat{i}_\theta \\ \rho V_r \overline{q} + \overline{\overline{\tau}}\hat{i}_r \\ \rho I \overline{q} \end{bmatrix} \quad \overline{S} = \begin{bmatrix} 0 \\ 0 \\ -2\Omega r V_r \\ \dfrac{V_\theta^2}{r} + r\Omega^2 - 2\Omega V_\theta \\ 0 \end{bmatrix}$$

with $\overline{q} = V_x\hat{i}_x + V_r\hat{i}_r + V_\theta\hat{i}_\theta$, the relative velocity, and V_x, V_r, V_θ are the axial, radial, and tangential relative velocities; Ω = rotational speed of rotor; $\overline{\overline{\tau}}$ = the stress tensor containing both the static pressure and the viscous stresses; and $I = c_\rho T_{0_{\text{rel}}} - 0.5\,(\Omega r)^2$, the rothalpy. The system is closed by an equation of state $p = \rho(\gamma - 1)(E - 0.5^*(\overline{q}\cdot\overline{q} - (\Omega r)^2))$.

The turbulent viscous stresses are computed from the Baldwin-Lomax (1978) mixing length model. The implementations of the Baldwin-Lomax (BL) model in a three-dimensional code is described by Dawes (1987). The main point algorithmically is how to determine the velocity and length scales in the blade endwall corners. (We cannot quantify the likely errors associated with a strongly three-dimensional boundary layer on the fan blade with perhaps strong radial outward migration of boundary layer fluid downstream of the shock suction surface interaction.) Rather than use weighted averaging of the scales in the corners as recommended by some authors (e.g., $l = N(1/l^2_{\text{suction side}} + 1/l^2_{\text{hub}})$), which gives rise to too much diffusion, the crossflow plane is divided into such zones simply on the basis of the closest wetted surface. Within each of these "triangular" zones, BL is applied along the crossflow plane. This approach was subsequently adopted and recommended by Adamczyk et al. (1991). Transition remains a substantial uncertainty and for the present work transition was fixed at the blade leading edges.

The equations are discretized on a set of six-faced control values, formed by a simple, structured H-mesh construction. Flow variables are stored at cell centers and values on the cell

Contributed by the International Gas Turbine Institute and presented at the 37th International Gas Turbine and Aeroengine Congress and Exposition, Cologne, Germany, June 1-4, 1992. Manuscript received by the International Gas Turbine Institute February 27, 1992. Paper No. 92-GT-298. Associate Technical Editor: L. S. Langston.

face for flux evaluation are found by simple linear interpolation conferring second-order accuracy on smoothly varying meshes. The code solves the equations of motion using a simple and robust time-marching algorithm. The basic solution algorithm has been described in detail elsewhere (for example, Dawes, 1988), and consists of a two-step explicit, one-step implicit scheme similar in implementation to a two-step Runge–Kutta method plus residual smoothing.

The Dawes code uses the "industry standard" artificial smoothing model, first introduced by Jameson, consisting of a solution-adaptive combination of second and fourth derivatives. The fourth derivative term provides background smoothing and has the form $\epsilon^4|\lambda|\Delta x^3\nabla^4 u$ and so does not disrupt the formal second-order accuracy of the algorithm ($|\lambda|$ is related to the spectral radius of the equation of motion). For the current application ϵ^4 was set to 0.01. Near shocks, a pressure gradient switch (based on the undivided Laplacian of static pressure) turns off the fourth derivative smoothing and turns on second derivative smoothing to obtain crisp shock capture over (3)–(4) cells. In tests (Dawes, 1987), the overall impact of smoothing and truncation error on predicted loss coefficient was estimated to be such that 10–20 percent of the loss level is spurious (i.e., a predicted loss coefficient of 5 percent is 5 ± 1 percent).

The basic single row analysis has recently been extended to allow simultaneous solution of several blade rows (Dawes, 1991). To permit multirow analysis in reasonable computer times, the assumption is made that the flow is steady relative to each individual blade row. Clearly, some sort of circumferential averaging must then be employed to model the relative motion of the blade rows and this averaging is implemented via interrow "mixing planes." Any model adopted for the mixing planes represents an approximation; nevertheless, it is important to note that although the circumferential information is smeared, the radial variation is not.

In the present version of the multiblade code, the mixing plane model is based on performing a classical mixing analysis at each spanwise station on either side of the mixing plane. Dring and Spear (1991) have shown in the context of throughflow analysis, that such mixing analyses are much better able to produce an "equivalent steady inlet condition" to subsequent blade rows than other forms of averaging. For compressible flow this mixing is expressed as shown below (expressed for simplicity in a mixing plane normal to the axial direction):

$$\Sigma \rho v_x \Delta A = \dot{m} = \tilde{\rho}\tilde{v}_x \overline{A}$$

$$\Sigma (p + \rho v_x^2)\Delta A = (\tilde{\rho} + \tilde{\rho}\tilde{v}_x^2)\overline{A}$$

$$\Sigma (\rho V_x v_t)\Delta A = \tilde{\rho}\tilde{v}_x\tilde{v}_t\overline{A}$$

$$\Sigma (\rho v_x v_r)\Delta A = \tilde{\rho}\tilde{v}_x\tilde{v}_r\overline{A}$$

$$\Sigma \rho v_x T_{o_{\text{abs}}} \Delta A = \dot{m}\tilde{T}_{o_{\text{abs}}}$$

$$\Sigma \Delta A = \overline{A}$$

where $\Sigma \ldots \Delta A$ represents a circumferential summation of area for each radial station and m is the mass flow. These five equations are solved for the five uniform mixed-out flow variables (denoted by the superscript $\sim$ to be imposed on either side of the mixing plane).

If the mixing is carried out in this way, then all the loss implicit in the nonuniform circumferential flow is mixed out explicitly into loss. Obviously not all of the nonuniformity may actually become a loss in practice as the following blade may interact favorably with its inflow. The point is that no spurious losses (or mass flow or total temperature) are introduced by the circumferential averaging process. In practice, this mixing plane formulation performs well even if the flow is separated and is coded in a more general manner than described above to permit the mixing plane to be inclined to the purely axial direction.

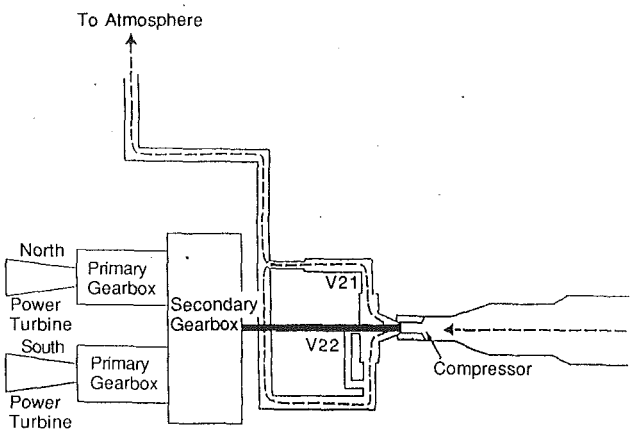

Fig. 1 Large compressor facility

The governing equations are completed by specification of boundary conditions, At inflow, total pressure and temperature are fixed and either flow angle or absolute swirl velocity are held constant. At the outflow, the hub or tip static pressure is fixed and the radial variation is derived from the simple radial equilibrium equation. For cells adjacent to solid boundaries, zero fluxes of mass, momentum, and energy are imposed through the cell face aligned with the solid boundary. Wall static pressure is calculated by setting the derivatives of pressure normal to the wall equal to zero. To prescribe the wall shear stress, the velocities stored at cell centers adjacent to the wall and the known zero value of velocity on the wall are used to compute the velocity gradients at the wall. These gradients, together with the wall viscosity, are used with a locally defined curvilinear coordinate system to compute the wall shear. If appropriate, the wall shear stress is computed from a universal logarithmic skin friction law; the code itself decides when.

Test Rig and Instrumentation

A single-stage fan rig arrangement (Fig. 1) was used for the experimental portion of the program. Ambient air enters the inlet plenum after being metered through an adjustable orifice located in the upstream ducting. Fan drive power is provided by two J71 power turbines, which drive through two primary (and one secondary) gearboxes. From the fan discharge, the air is turned and exhausted to the atmosphere.

The fan stage is designed to produce a corrected airflow rate of the order of 300 lb/sec. The rotor operates transonically with an inlet tip relative Mach number of 1.55. The fan rotor inlet hub/tip diameter ratio is 0.38.

Instrumentation

Fan rotor, core, and bypass vane instrumentation used during fan rig testing and the computational domain is summarized in Fig. 2. The inlet plenum is instrumented with four five-element total pressure and four total temperature rakes and four tip static pressure taps. The case instrumentation over the fan rotor has 14 in-line static pressure taps equally spaced axially: two upstream of the blade leading edge, two downstream of the blade leading edge, one each in the plane of leading and trailing edge, and eight over the blade. No bleed was used on the casing of the fan rotor. The hub instrumentation at the fan rotor trailing edge consists of four static pressure taps 90 deg apart. The fan splitter nose was instrumented with two static pressure taps at each of six axial locations, each 180 deg apart pitchwise.

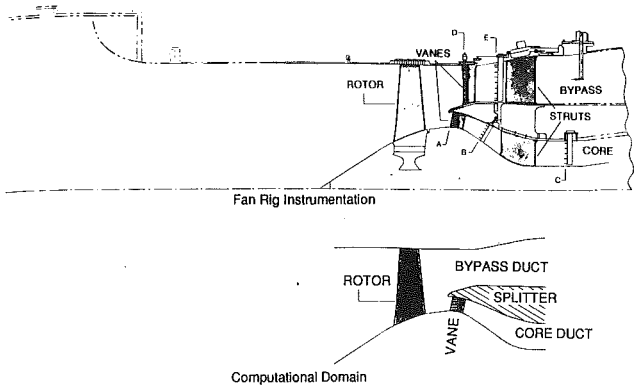

Fig. 2 Fan rig instrumentation and the computational domain

At plane A, the leading edge of the core vane was instrumented with total pressure probes at 5, 10, 30, 50, 70, 90, and 95 percent of the vane span. (Duplicate coverage was used at each depth.) Two each hub and tip wall static taps were located in the axial plane of the total instrumentation.

At the core vane midpitch, there were two static pressure taps 180 deg apart at 50 percent chord, and two static pressure taps 180 deg apart at the trailing edge of the vane. At plane B, the vane discharge was instrumented with total temperature probes at 5, 10, 30, 50, 70, 90, and 95 percent of the vane span. (Duplicate coverage was used at each depth.) There were two each hub and tip wall static taps. Additional instrumentation consisted of (1) hub and tip wall statics located axially along the duct, and (2) a tip boundary layer nine-element rake located at the strut trailing edge.

The bypass vane leading edge instrumentation at plane D consisted of total pressure probes at 5, 10, 23, 36, 50, 64, 77, 90, and 95 percent span (two at each depth). Two tip static pressure taps are located 180 deg apart in the plane of the total pressure probes. Similarly, the bypass vane discharge instrumentation at plane E consisted of total temperature probes at 5, 10, 23, 36, 50, 64, 77, 90, and 95 percent span (two at each depth). Two tip static pressure taps were positioned 180 deg apart in the plane of the total pressure probes.

Conservation of angular momentum was enforced in an axisymmetric throughflow analysis to project measured temperatures and pressures from planes A, B, D, and E to the rotor blade trailing edge. This analysis uses the method of Stratford (1978) to assess endwall boundary layers. No allowance is made for mixing of either the total temperature or pressure distribution across axisymmetric streamsurfaces.

Results and Discussion

The results computed without the presence of a downstream splitter (Case A) and with splitter and core vane (Case B) as shown in Fig. 3 are presented. The geometry of the fan rotor is the same for both cases. All the flow parameters are presented in normalized form. The corrected flow, total pressure ratio, and efficiency are normalized with respect to overall design values of these parameters for fan rotor Type II. A discussion in each case including fan rotor Type II is presented in the following paragraphs.

Case A. Downstream Splitter Not Included in Computations. Two fan rotors with different blade designs were fabricated and experimentally tested. The baseline configuration, designated as Type I utilized conventionally designed MCA (multicircular-arc) blading in the supersonic region of the blade. The second fan (Type II) was designed incorporating precompression airfoils in the supersonic region of the blade span. Both rotors employed double circular arc blading (DCA) in the hub region.

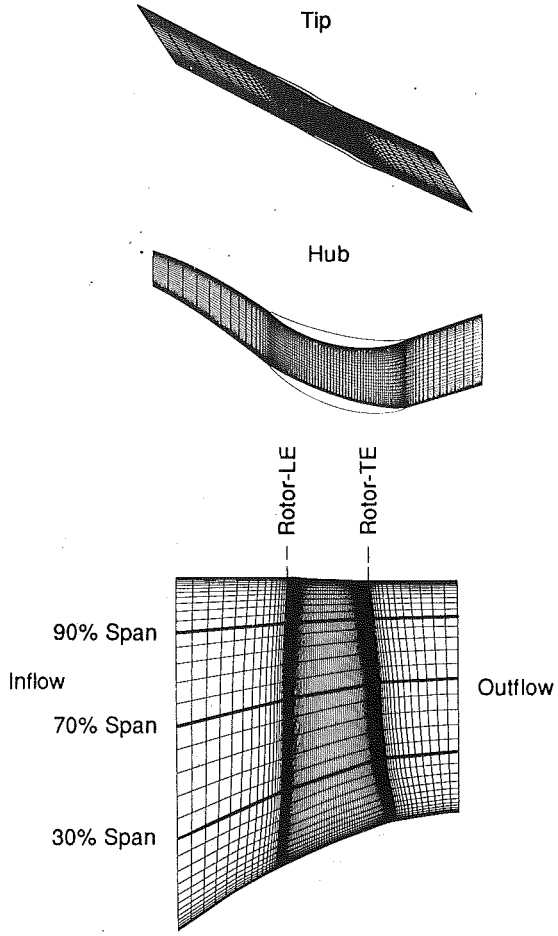

Fig. 3 Meridional and blade-to-blade plane mesh for a fan rotor configuration (Case A, Type II)

Dawes' three-dimensional code was used for designing both rotors. An H-grid comprised of 37, 95, and 37 mesh points in the circumferential, axial, and radial directions, respectively, was used for the rotor analysis. The grid sections in the midpitch meridional and hub and near-tip blade-to-blade planes are shown in Fig. 3. The mesh was clustered exponentially near the blade suction and pressure surfaces. In the radial direction, cells were concentrated near the casing and hub.

The fan rotor blade tip clearance was modeled rather approximately in the calculations. The present blade tip model used in the code (Dawes, 1988) is the so-called "pinched-tip" H-mesh model wherein the blade thickness is rapidly pinched to zero just near the tip and the casing. This is obviously a poor model for thick turbine blades but, in fact, surprisingly good for thin compressor blades. Stores and Cumpsty (1991) published a validation of the present pinched-tip model and showed good agreement with detailed experimental measurements for a compressor cascade. Basson et al. (1991) published a comparison of measured compressor cascade flow with predictions using a pinched-type H-mesh model and a H-mesh with an embedded mesh over the actual square blade tip. They showed little difference between the pinched-tip and embedded mesh predictions except very near the tip. In particular, global features of the clearance flow were similarly resolved by other clearance models. In terms of the number of nodes used in the clearance gap in the present study (3), Stores and Cumpsty (1991) showed, for a thin compressor blade, that even three nodes in the gap allowed remarkably accurate predictions of global features of the clearance flow like, for example, the axial validation of the integrated clearance leakage flow. These studies guided our engineering choice of the mesh. As stated

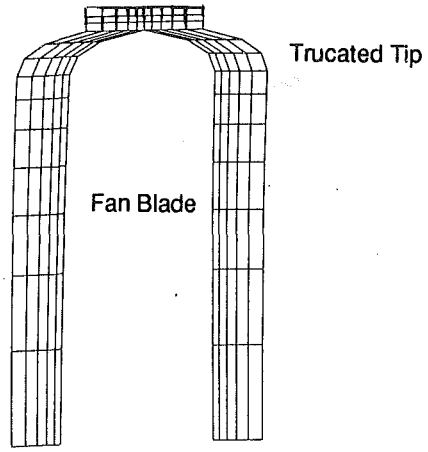

Fig. 4 Near-tip blade section at constant axial plane

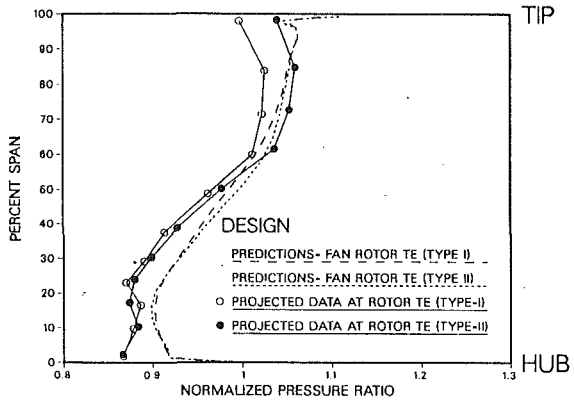

Fig. 5 Predicted and measured spanwise variations of pitchwise mass-averaged total pressure ratio (fan rotor Type I and Type II)

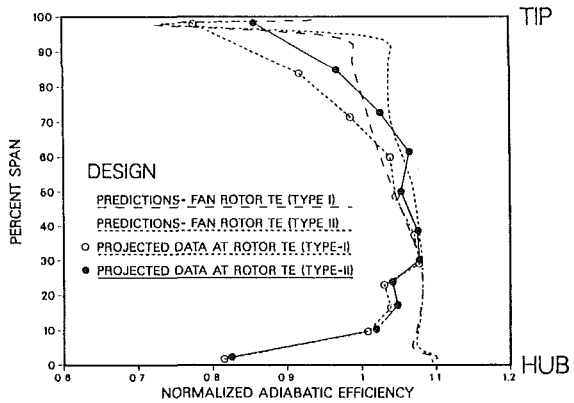

Fig. 6 Predicted and measured spanwise variations of pitchwise mass-averaged adiabatic efficiency (fan rotor Type I and Type II)

earlier, the blade is treated in the code by simply reducing the blade thickness smoothly to zero and then applying periodic boundary conditions between the tip and the casing. A view of both fan rotors in the axial plane at 40 percent axial chord is shown in Fig. 4. As shown in Fig. 4, the blade is truncated near the tip in three nodes. In the hot run conditions, the tip clearance was taken to be 0.04 in., which is equal to 0.37 percent of the average blade span. Only three nodes were used in the tip clearance region.

A mesh of 37 points was used in the blade-to-blade and hub-to-tip plane to simulate the boundary layers. To characterize the meshes in terms of boundary layer resolution, the mesh resolve the airfoil boundary layers down to $Y+$ values in the range 15–25 and the hub and casing boundary layers to 30–50. The numbers of nodes in the boundary layer region were 4 and 3 for the blade suction surface and blade pressure surface and 3 and 4 for the hub and tip endwalls, respectively.

Regarding the dependency of the solution on the grid, it is difficult to establish mesh independence in three-dimensional flows. Ritually halving the mesh in each direction increases the CPU cost by at least a factor of 8 each time. Dawes (1988) reported a mesh refinement study for a transonic compressor cascade representative of the midspan of a fan. Three meshes containing 17*35, 29*68 and 57*133 nodes in the blade-blade plane were used. $Y+$ values for the blade boundary layers were determined to be of the order of 30, 15, and 5 respectively. The predicted exit loss coefficients were shown to be essentially identical for the medium and fine meshes. This guided our current choice of meshes with 37*95 points in the blade-to-blade planes of the fan.

Design point calculations were made for both rotors. Measured values of fan inlet total pressure and total temperature were the inlet boundary conditions for the calculations. Inlet swirl was assumed to be negligible. Although the presence of an inlet tip boundary layer was detected from a boundary layer rake located 9 in. upstream of the rotor, this effect has not been included in the calculations. However, it should be noted that it is our intention to include inlet boundary layer effects into the calculations during future efforts. Cold-to-hot airfoil coordinate transformations were made using a finite element analysis as a means to account for blade untwist and shape change.

The solution was assumed to be converged when the mass flow error was within 0.4 percent of fan inlet flow, and the peak suction surface pressure at certain reference locations became fairly constant during the time iterations. This generally occurred after 3000 iterations. To eliminate the effect of iteration count on the accuracy of the solution, the computations were continued for another 4000 iterations. (The flow, pressure ratio, and efficiency changed by -0.13 percent, -0.4 percent, and -0.2 percent, respectively.) From this study, it was concluded that 3000 iterations were adequate to obtain an acceptable solution. The computations were made on an IBM RS-6000 work station (Model-550) and the code processed at about 0.00022 sec/node/time step. The processing speed of a CRAY-YMP for comparison purposes is about six times faster than the Model-550.

Figures 5 and 6 show the predicted spanwise variation of pitchwise mass-averaged normalized total pressure ratio and adiabatic efficiency at the trailing edges of Type I and Type II fan rotors. The predictions are compared with the data as projected to the trailing edge of the fan rotor. As previously described, the data at the rotor trailing edge were deduced from measured total pressures and temperatures at planes A, B, D, and E by enforcing conservation of angular momentum in an axisymmetric throughflow analysis. No allowance is made for mixing across axisymmetric streamsurfaces. It is interesting to see in Fig. 5 that the predicted radial variations in pressure ratio agree with the projected data to 75 percent of the span, even though the absolute levels are slightly different. Between 75 and 100 percent of the blade span, the computed pressure ratio for the Type I rotor did not show any improvement over that of the Type II rotor. The projected data showed higher pressure ratios for the Type II blade from 75 to 98 percent of the span but the computations did not show such differences. The rate of change of slopes of pressure ratio near the hub and at 20 percent span agrees with the design intent. The overprediction of the pressure ratio in the hub region is not clearly understood at this time. This may be due to inadequacies in the turbulence model or in the numerics. Overall, the predictions and the projected data confirmed the Type II fan design as being better than the Type I fan design.

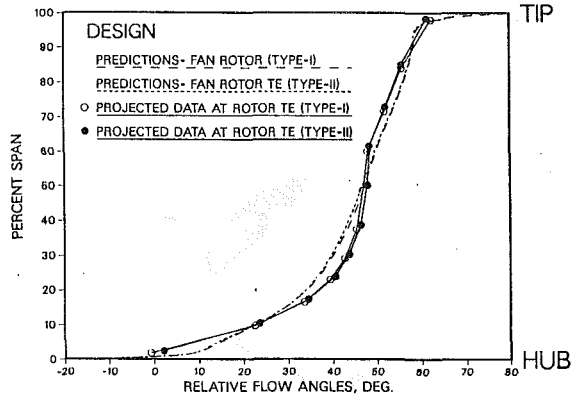

Fig. 7 Predicted and measured spanwise variations of pitchwise mass-averaged relative flow angles (fan rotor Type I and Type II)

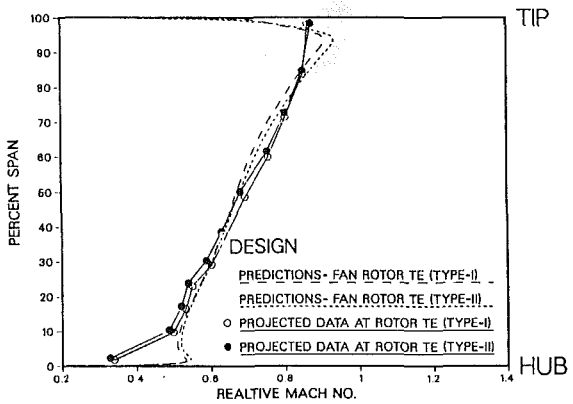

Fig. 8 Predicted and measured spanwise variations of pitchwise mass-averaged relative Mach numbers (fan rotor Type I and Type II)

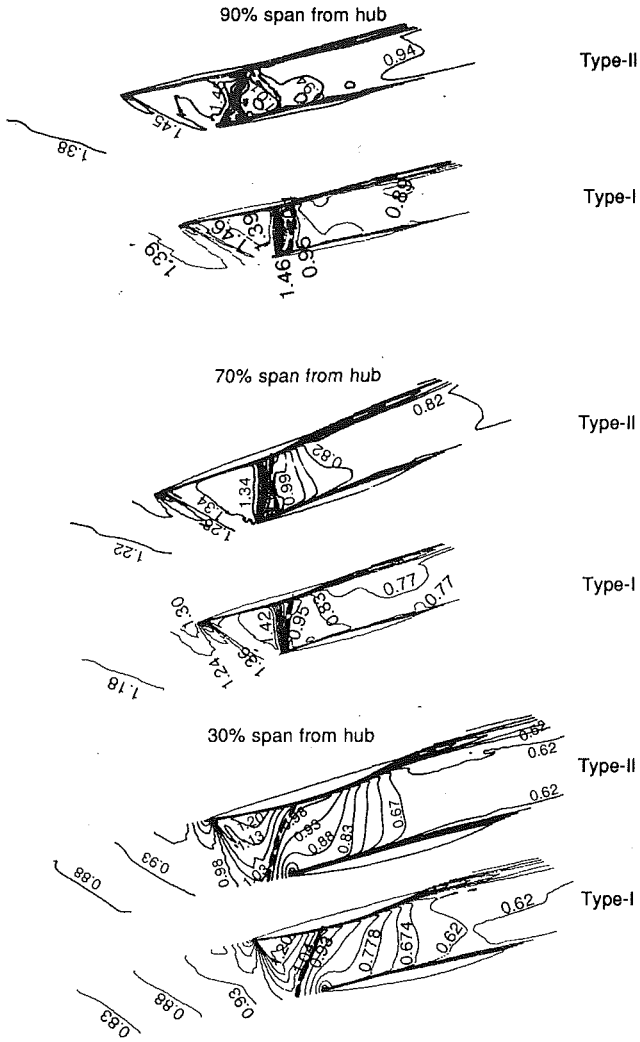

Fig. 9 Comparison of predicted relative Mach number contours at 30, 70, and 90 percent span for fan rotor Type I and Type II

The spanwise variations of efficiency shown in Fig. 6 indicate that the Type II fan rotor (designed using precompression) is more efficient than the Type I rotor. The main improvement in efficiency in the Type II rotor design occurs outboard of 50 percent span when compared to the Type I fan rotor. Such behavior is confirmed by the data. As shown in Fig. 6, even though the level of spanwise variation of predicted efficiency differs from the projected data, the differences in efficiency between the Type I and Type II rotors are in good agreement with the data. Efficiency is a very sensitive parameter to predict accurately, because a small error in temperature or pressure (either numerics or measurements) can produce a big difference in efficiency. From Fig. 6, it is clear that the absolute level of predicted efficiency, if integrated radially, is higher overall than that calculated from the measurements.

Figure 7 compares the predicted spanwise variation of pitchwise mass-averaged relative flow angles and the projected data at the trailing edges of both fan rotors. The projected flow angle data showed similar behavior in both fan rotors. The computations overpredicted flow angles for both rotors compared to the projected data near 30 percent span. The computed flow angles were lower than the projected data near 75 percent span. The predicted variations of relative flow angles are consistent with the spanwise variation of total pressure ratio shown in Fig. 5.

Figure 8 compares the predicted spanwise variation of pitchwise mass-averaged relative Mach numbers and the projected data at the design point. The comparison is shown at the rotor trailing edge for both fan rotors. The predicted Mach numbers compare reasonably well with the projected data except near the hub and tip. The overshoot of predicted Mach numbers near the hub and tip region is not clearly understood. The source of this discrepancy is being investigated.

Figure 9 shows the predicted relative Mach number contours in the blade-to-blade plane at the design point. The contours are shown for the Type I and Type II fan rotors at 30, 70, and 90 percent span (approximate grid lines; see Fig. 3 for clarification). In Fig. 9, the sonic line is shown by the dashed lines. At 90 percent span, the inlet Mach numbers to the Type I and Type II fan rotors are 1.39 and 1.38, respectively, and exit Mach numbers are 0.89 and 0.94. It is interesting to see in Fig. 9 that at 90 percent span, the Type I rotor has a different shock structure than the Type II rotor. The Type I blade has a strong normal shock located slightly upstream of the blade trailing edge. The shock is followed by subsonic flow at the rotor exit. For the Type II blade, a bow shock is followed by a weaker lambda shock. The shock in the Type II blade is closer to the trailing edge than the shock in the Type I blade. As shown in Fig. 9, at 70 percent span from the hub, the inlet relative Mach number is 1.18 and 1.22 in the Type I and II fan rotors, respectively. At 70 percent span, the Type I rotor has a stronger normal shock than the Type II rotor. The exit Mach numbers for Type I and Type II rotors are 0.77 and 0.82, respectively. At 30 percent span, the inlet Mach number is subsonic for both the rotors. A local supersonic bubble occurs on the suction surface downstream of the leading edge and this flow decelerates to a subsonic conditions after a weak

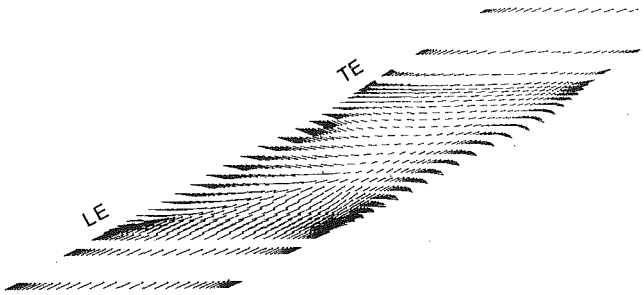

Fig. 10 Predicted velocity vectors in the tip clearance region of the fan rotor Type II

Table 1 Comparison of predicted and test performance: conventional MCA blading versus precompression blading (Type I and Type II)

	Percent change (Type II − Type I)/Type I)*100.	
	Test Data	Predictions
Rotor pressure ratio	1.285	0.470
Rotor efficiency	2.5	2.800
Corrected fan flow	1.20	1.60

shock. As anticipated (blades were redesigned in the supersonic region only), both the fan rotors did not show significant Mach number differences at 30 percent span.

A view of the predicted velocity vectors in the tip clearance region of the fan rotor is shown in Fig. 10 for the Type II rotor. The migration of fluid from one surface to the other is seen in the tip region.

Table 1 shows predicted results and the deduced data for both rotors. It is significant to note that about two and one-half percentage points improvement in fan efficiency were achieved using the unconventional blade design method. Both fan rotor designs were guided by the results of the three-dimensional viscous analysis. The predictions and the deduced data indicated that fan rotor Type II performed better than the Type I fan rotor in terms of pressure ratio, efficiency, and flow.

Comparisons between predicted and measured data given in the remaining text refer to the Type II fan design configuration (with and without the presence of the downstream splitter).

Case B. Inclusion of Downstream Splitter/Core Vane. For this case, a downstream flow splitter was modeled in the computation. The splitter divides the fan flow into the bypass and core streams as is typical for bypass engines. (Also modeled in the calculation were the stator vanes in the core stream.)

The grid for the fan blade and downstream components (i.e., ducting, splitter, and core vane) was generated by combining grid systems for individual components. This was accomplished by appropriately shifting individual elements axially and tangentially to form the composite grid. The geometry of the fan rotors was identical to those of case A (Type II) as described previously. For both cases, the fan operating tip clearance was assumed to be 0.04 in. (0.37 percent of the total span), which is the average value as measured during rig testing.

A structured H-mesh was constructed for the rotor as well as for the core vane and bypass duct. This was done by interpolating the input blade sections onto the desired radial set of blade-to-blade surfaces. The mesh used in the analysis was composed of 31*143*37 points. Figure 11 shows the grid in the meridional and blade-to-blade planes at hub and near-tip sections. The discontinuity between the fan grid and the grid for the downstream system components serves as a "dummy" boundary across which flow properties were pitchwise averaged. This was accomplished by letting the last plane of cells for the upstream domain and the first plane of cells for the downstream grid system serve as dummy storage locations for interrow mixing calculations. The tip portion of the core vane flowpath was made to coincide with the lower boundary of the splitter, while the bypass duct was free of blading. The zero flux condition was applied on the upper and lower surfaces of the splitter and the splitter leading edge.

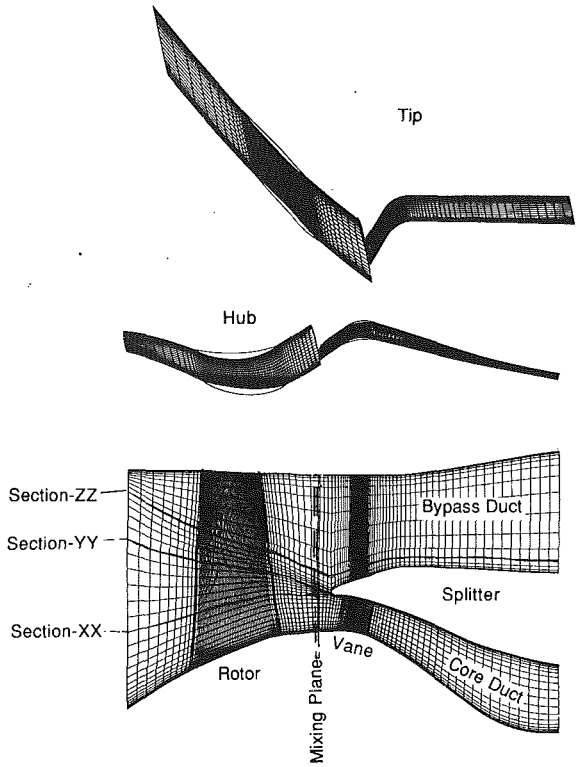

Fig. 11 Meridional and blade-to-blade plane mesh for a fan bypass configuration (Case B)

The three-dimensional computations were made for the fan bypass configuration at 100 percent speed from the fan operating point to near stall. For Case A, the computations were also made at the choke point. The exit static pressures at the tip of the core and bypass ducts were adjusted to define the fan speed characteristics. Because of the complex nature of this flow, the convergence for the fan bypass configuration was slower than for an isolated fan rotor. The maximum mass flow error for Case B did not go below 1.4 percent of the inlet mass flow as compared to 0.4 percent for the isolated rotor. The flow properties across the mixing plane were approximately satisfied. For Case B, the numerical calculations diverged if the initial guess of the pressure was not reasonable. To avoid numerical divergence, it was very important to specify a reasonably accurate guess of pressures at the fan rotor leading and trailing edges, the inlet to core and bypass vanes, and the exit of the fan bypass ducts. In the present calculations, the initial estimates for static pressures were obtained from the axisymmetric design code. The inlet flow conditions, including those for the blade tip treatment, were the same as described in the earlier section.

Figures 12 and 13 show normalized total pressure ratio/airflow and efficiency/airflow characteristics as computed for Cases A and B. Also shown are data from the experimental rig test. As shown in Figs. 12 and 13, the predicted fan characteristics agree well with data. In general, the predicted pressure ratios and efficiencies for Case B are slightly higher than that for Case A for all the fan operating points. The computed pressure ratio at a given airflow is greater than the data by 0.7

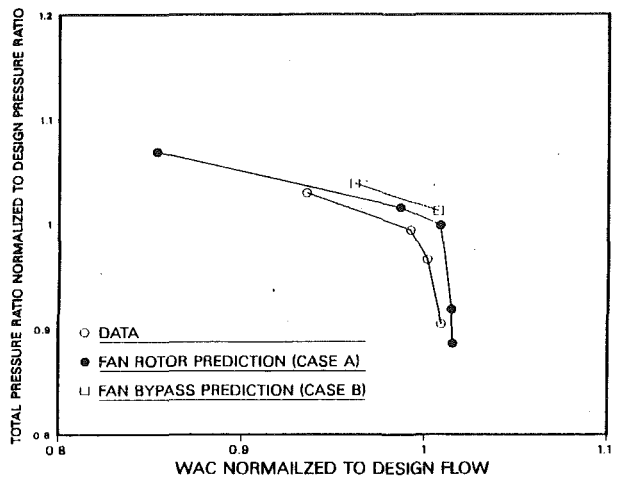

Fig. 12 Comparison of measured and predicted mass-averaged total pressure ratio versus flow (Cases A and B)

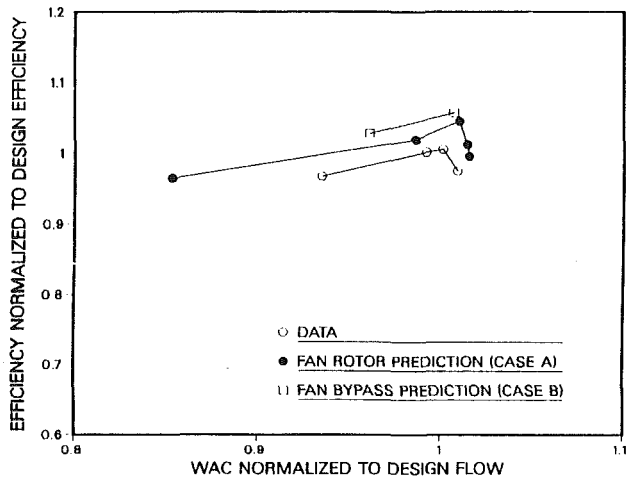

Fig. 13 Comparison of measured and predicted mass-averaged adiabatic efficiency versus flow (Cases A and B)

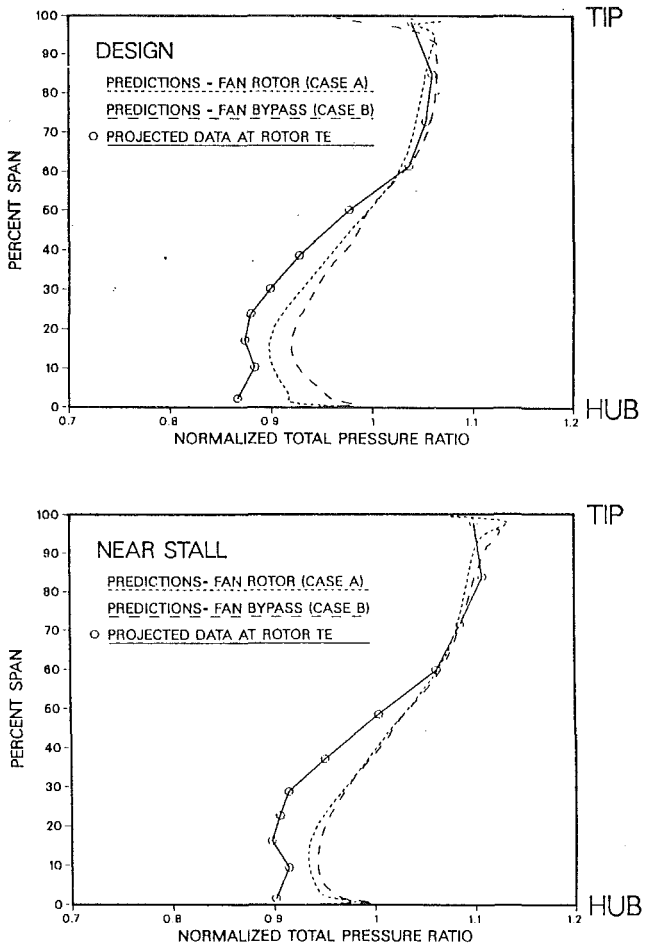

Fig. 14 Predicted and measured spanwise variations of pitchwise mass-averaged pressure ratio (Cases A and B)

and 1.8 percent for Cases A and B, respectively. Likewise, the predicted efficiency values are higher than the measured data by 3.6 percent for Case A and 4.5 percent for Case B.

Figure 14 shows the predicted and measured spanwise variations of pitchwise mass-averaged normalized total pressure ratio at the trailing edge of the rotor for Cases A and B. Figure 14 presents results for the fan design point and the near-stall conditions. The variation in slope of total pressure ratio near hub and 20 percent span agrees well with the design intent. For Case B, the predicted pressure ratio deviated more than the projected data near the hub region. At the design point, the predicted total pressure ratio for Case B showed maximum difference of 2.6 percent from predicted values for Case A at the 10 percent streamline (from hub). Outboard of 55 percent span, the computed total pressure ratios compared well with data. For the near-stall case, the predicted pressure ratio for Case A is closer to that of Case B. However, deduced data and the prediction differ from the hub to 50 percent span. As stated earlier, these discrepancies could possibly be due to numerics, turbulence model, or data transformation and need further investigation.

The spanwise variations of pitchwise-mass averaged relative flow angle at the rotor exit are shown for both fan cases in Fig. 15. Also shown are angles deduced from test measurements at the design and and near-stall points. For the fan design point, relative to Case A, Case B predictions show the flow to be about 3 deg closer to the axial direction at approximately 15 percent span. Between 50 to 70 percent span, the predicted flow angles for Case B show less turning (relative to Case A) by approximately 3 deg. Similar behavior is predicted for the near-stall conditions. In general, the predicted flow angles are in fair agreement with the data.

The spanwise variations of normalized pitchwise mass-averaged efficiencies are compared with projected data at the rotor trailing edge in Fig. 16 for Cases A and B at the fan design and near-stall points. For both the flow conditions, the predicted efficiencies were above the data in the inboard 15 percent of the span and outboard of 70 percent span. At other spanwise locations, the predicted efficiencies compared reasonably well with the data.

The predicted normalized static pressure contours for Cases A and B are shown in Fig. 17 at the midpitch meridional plane (at fan operating point and near stall). The static pressures are normalized with respect to total pressure at the trailing edge of the fan rotor. The predicted pressures show some spatial oscillations (design point and near stall). These oscillations are caused by using minimum smoothing in the code to reduce the numerical loss. The solution is converged and oscillations are not due to flow unsteadiness. At midpitch, the predicted pressures for Case A are slightly higher near the hub and lower in the tip regions as compared to Case B (for design point). The same is true for the near-stall conditions. It is observed that the large static pressure gradient shown in the plane of the splitter nose does not appreciably affect the static pressure distribution in the plane of the rotor blade trailing edge.

Figure 18 compares spanwise variations of pitchwise mass-

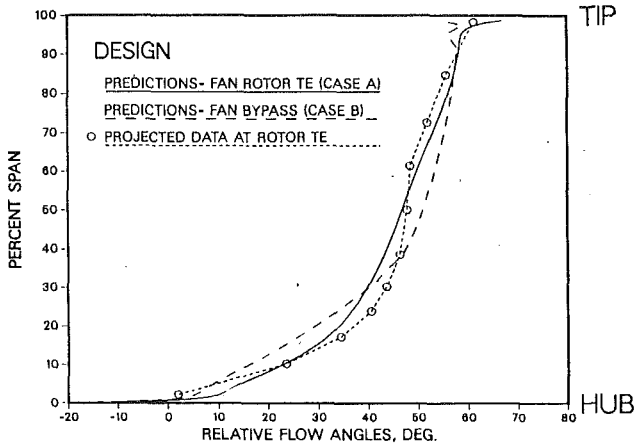

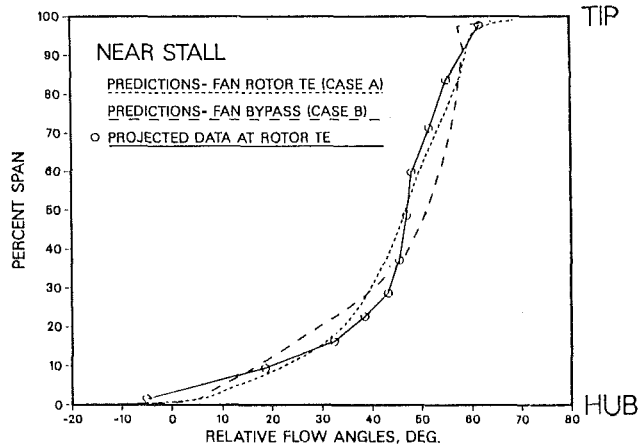

Fig. 15 Predicted and measured spanwise variations of pitchwise mass-averaged relative flow angles (Cases A and B)

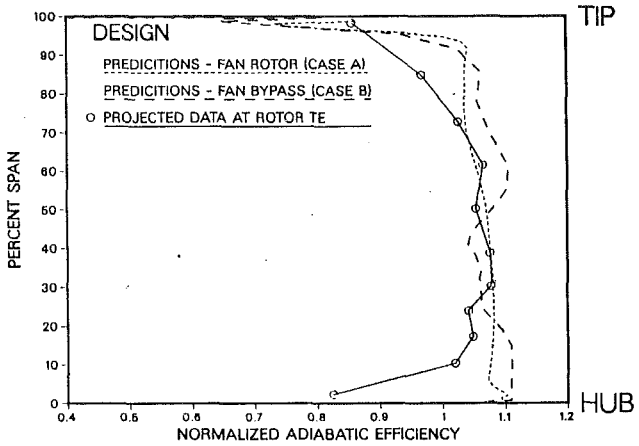

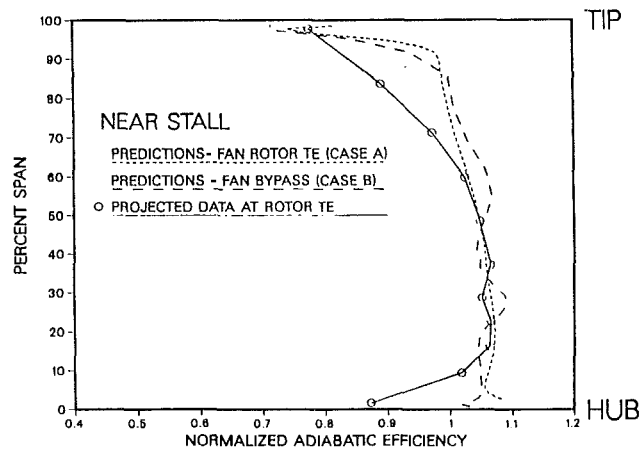

Fig. 16 Predicted and measured spanwise variations of pitchwise mass-averaged adiabatic efficiency (Cases A and B)

averaged static pressure (normalized) at the rotor trailing edge for Case A, Case B, and as deduced from the test data. Distributions for the fan design point and at near stall are shown. The predicted static pressures are within ±1.8 percent of those obtained from the data.

Predicted normalized static pressure contours in the blade-to-blade plane of the fan bypass configuration is shown in Fig. 19(*a*, *b*, *c*). The contours are shown for the fan design point and near-stall condition at three spanwise grid locations (XX, YY, and ZZ shown in Fig. 11). For the design point, the predicted static pressures at spanwise stations ZZ and YY show a bow shock followed by normal shock slightly upstream of the rotor trailing edge. There seems to be a slight difference in the shock pattern at 70 percent span between Case A (Fig. 9) and Case B (section YY). In Case B a bow shock is followed by a normal shock, while in Case A the bow shock is not seen noticeably (note that Fig. 9 is presented in terms of relative Mach numbers). For the near-stall condition, the predicted static pressures at sections ZZ and YY show normal shock sitting near the leading edge of the rotor. For the fan design and near-stall conditions (section XX), a local supersonic bubble occurs at the suction surface downstream of the rotor leading edge and terminates to subsonic flow after a weak shock (sonic Mach number at normalized pressure of 0.415).

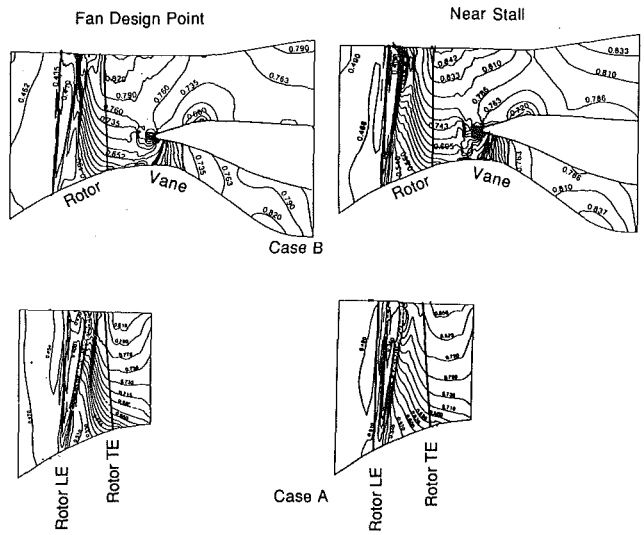

Fig. 17 Predicted normalized static pressure contours in the meridional plane at midpitch (Cases A and B)

Blade Tip Clearance Sensitivity. Table 2 show results of the three-dimensional analysis at two levels of blade tip clearances, 0.04 in. and 0.08 in. In the computations, only three nodes were used in the rotor tip clearance region of 0.04 in. and 0.08 in. Again, the study was very approximate and the purpose of the study was to predict the first-order effects in the tip clearance region of the fan rotor. These values of clearance were selected to be representative of the two levels of clearance, which were experimentally investigated during rig tests of the fan. Predicted sensitivity to blade tip clearance generally tracks well with observed results for the clearances investigated.

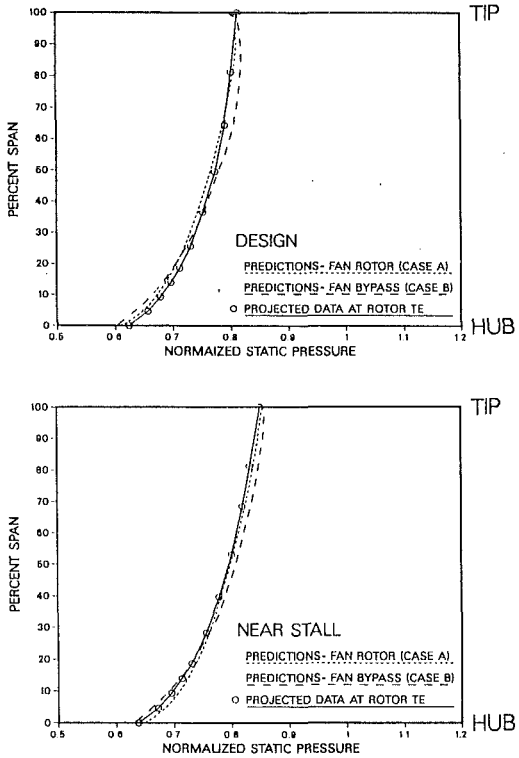

Fig. 18 Predicted and measured spanwise variations of pitchwise mass-averaged normalized static pressures at the rotor trailing edge (Cases A and B)

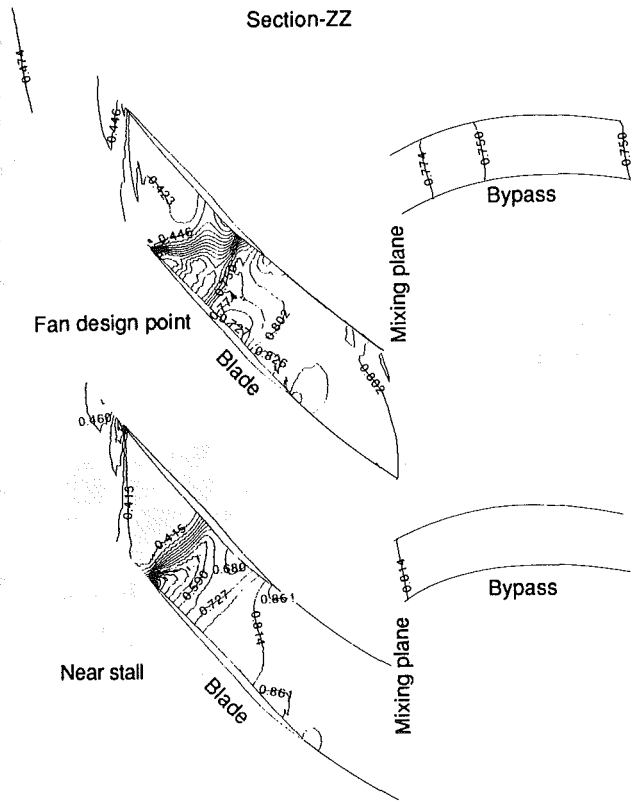

Fig. 19(*a*) Normalized static pressure contours in blade-to-blade plane (Case B; design and near stall; at section XX, YY, ZZ)

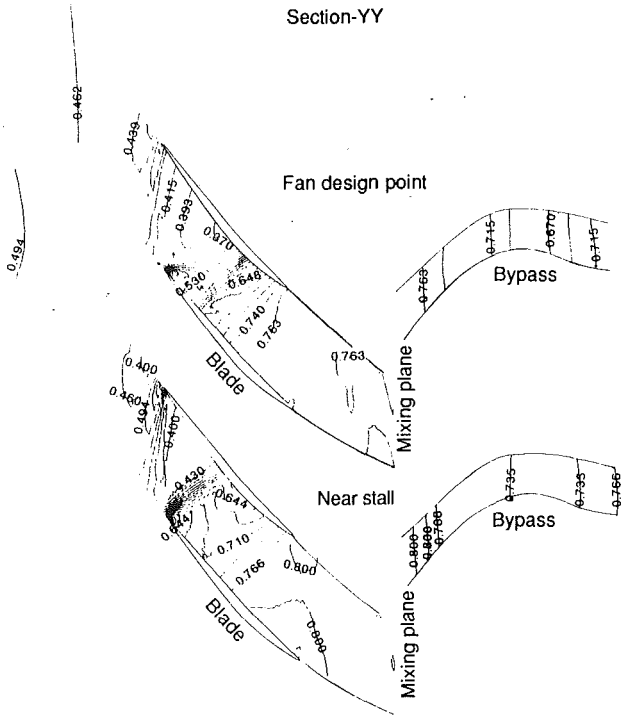

Fig. 19(*b*) Normalized static pressure contours in blade to blade plane (Case B; design and near stall; at section XX, YY, ZZ)

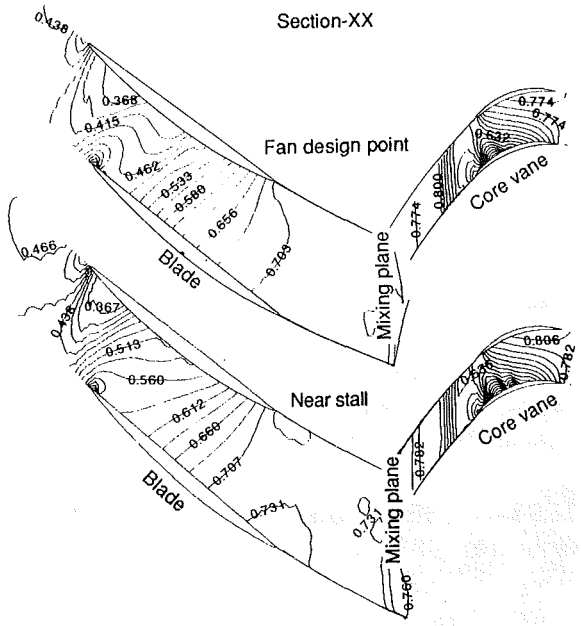

Fig. 19(*c*) Normalized static pressure contours in blade to blade

Table 2 Results of three-dimensional analysis at two levels of blade tip clearance

	Percent change in flow parameters for rotor tip clearances of 0.04 in. and 0.08 in. (reference 0.04 in. clearance)	
	Data (percent)	Predictions (percent)
Rotor pressure ratio	1.21	0.962
Rotor efficiency	1.68	1.940
Corrected fan flow	1.25	1.56

The flow field through the core vane as predicted with the three-dimensional solver compared favorably with measured data, although these comparisons are not given here in an effort to confine the scope of this paper to the fan rotor.

Concluding Discussion

The generality and robustness of the Dawes three-dimensional Navier–Stokes solver has been demonstrated by application to an advanced fan bypass configuration. The detailed

flow predictions were compared with the data in terms of design parameters at design and off-design conditions. An advanced engine fan design has been analyzed within reasonable computer resources. The analysis was used as a guide to modify the hardware, which resulted in improving the fan efficiency by 2.5 percent.

In general, the predicted efficiency exceeded the measured value by about two and a half percentage points. The shapes of efficiency, flow, and pressure ratio flow characteristics were in good agreement with test data trends.

Even with the relatively simple tip clearance model used in the calculations, the predicted tip clearance effects agreed well with those observed in the data. The predicted pressures and efficiencies were higher than the data in the near hub and tip regions. The source of these discrepancies is currently under investigation.

Due to the large axial gap between fan rotor and splitter, the splitter did not affect the performance of the rotor. However, the calculations are very important for the fan bypass configuration: First, the smaller axial gap may impact the performance of the fan rotor due to the presence of the splitter. Second, the core vanes are more affected by the performance of the upstream rotor.

References

Adamczyk, J. J., Celestina, M. L., Beach, T. A., and Barnett, M., 1990, "Simulation of Three-Dimensional Viscous Flow Within a Multistage Turbine," ASME JOURNAL OF TURBOMACHINERY, Vol. 112, pp. 370–376.

Baldwin, B., and Lomax, H., 1978, "Thin Layer Approximation and Algebraic Model for Separated Turbulent Flows," AIAA Paper No. 78–257.

Basson, A H., Kunz, R. F., and Lakshminarayan, B., 1991, "Grid Generation for Three-Dimensional Turbomachinery Geometries Including Tip Clearance," AIAA Paper No. 91–2360.

Cedar, R. D., and Holmes, D. G., 1989, "The Calculation of the Three-Dimensional Flow Through Fan Including the Effects of Blade Surface Boundary Layers, Engine Splitter and Adjacent Blade Rows," ASME Paper No. 89-GT-325.

Dawes, W. N., 1987, "Analysis of Three-Dimensional Viscous Flows in Transonic VKI Compressors," VKI Lecture Series 3 Transonic Compressors, Feb. 1–4.

Dawes, W. N., 1988, "Development of a Three-Dimensional Navier–Stokes Solver for Application to All Types of Turbomachinery," ASME Paper No. 88-GT-70.

Dawes, W. N., 1991, "Multiblade Row Navier–Stokes Simulations of Fan Bypass Configuration," ASME Paper No. 91-GT-148.

Dring, R. P., and Spear, D. A., 1991, "The Effects of Wake Mixing on Compressor Aerodynamics," ASME JOURNAL OF TURBOMACHINERY, Vol. 113, pp. 600–607.

Storer, J. A., and Cumpsty, N. A., 1991, "Tip Leakage Flow in Axial Compressor," ASME JOURNAL OF TURBOMACHINERY, Vol. 113, pp. 252–259.

Stratford, B. S., 1959, "Prediction of Separation of the Turbulent Boundary Layer," *Journal of Fluid Mechanics*, Vol. 5, pp. 1–6.

The Extension of a Solution-Adaptive Three-Dimensional Navier-Stokes Solver Toward Geometries of Arbitrary Complexity

W. N. Dawes
Whittle Laboratory,
Cambridge University,
Cambridge, United Kingdom

This paper describes recent developments to a three-dimensional, unstructured mesh, solution-adaptive Navier–Stokes solver. By adopting a simple, pragmatic but systematic approach to mesh generation, the range of simulations that can be attempted is extended toward arbitrary geometries. The combined benefits of the approach result in a powerful analytical ability. Solutions for a wide range of flows are presented, including a transonic compressor rotor, a centrifugal impeller, a steam turbine nozzle guide vane with casing extraction belt, the internal coolant passage of a radial inflow turbine, and a turbine disk cavity flow.

Introduction

It is now a matter of routine to solve the three-dimensional Navier–Stokes equations for single turbomachinery blade rows. The solutions are of course limited (and will remain limited for the foreseeable future) by the modeling of transition and turbulence in the particularly difficult environment of a turbomachine. Nevertheless, the predictions are now very usable by design engineers to interpret the reasons for the successes and failures of existing designs and to produce new designs systematically (and based on flow physics), which display genuine performance improvements. However, this improved certainty has largely been confined to clean, primary flow paths unencumbered by the additional but realistic geometric complexity of casing steps, slots and bleeds, of extraction belts, and of shrouds, lacing wires, splitters, etc. The intrinsic complexity of secondary gas paths (seals, casing treatments, internal coolant passages and their discharges, etc.) means that they have not received the attention they merit in terms of their overall aerodynamic and thermal impact on the performance of the turbomachine.

There is no technical difficulty in computing the flow field in a very complex geometry (with of course the caveat that turbulence modeling remains out of control) and simple, reliable time-marching algorithms are very suitable. Nor is there any particular problem in visualizing the simulated flow field—this is simply a matter of three-dimensional trigonometry and efficient data structures (see, for example, Giles and Haimes, 1990). The key pacing items are our ability to generate and discretize the geometry in the first place and the ease of use of the generation system by nonspecialist designers. Inevitably such a mesh is "unstructured" for complete generality and best formed from elements that stack well in three-dimensions, like tetrahedrons. Once a reasonable mesh is in place, a solution-adaptive capability allows mesh to be concentrated better where it is really needed and this can be used to help overcome any disadvantages in the initial mesh, but an initial mesh must still be produced.

Currently research is in progress toward developing the capability to generate a three-dimensional unstructured mesh for a completely general geometry. These approaches typically require the specification of a set of patches representing a set of surfaces that link together to define and confine a computational volume. This volume is then filled with tetrahedra by one of a number of approaches. At the moment the two popular approaches are "moving front" (Peraire et al., 1988; Lohner, 1987) and "Delaunay triangulation" (see, for example, Jameson et al., 1987) and very impressive results have been published. However, this "filling" of the overall volume is far from trivial and rather time consuming (and may in fact consume more computer resources than the flow solution itself) and the very generality of their bounding surface definition is a strong disincentive for the hard-pressed turbomachinery designer to make use of them. To illustrate this: The relatively straightforward geometry of a single turbine blade with overtip leakage might need at least eight surface patches to define it (inflow, outflow, hub and casing, suction and pressure side, tip and up- and downstream periodic surfaces); a more complex geometry like the radial inflow turbine internal coolant passage shown later on might need 31 surface patches [inflow, outflow, suction and pressure side, hub and casing (both of which would require three patches because of discontinuities in their slopes), three baffles (which would need three patches to define them as they are an awkward combination of two flat surfaces and

Contributed by the International Gas Turbine Institute and presented at the 37th International Gas Turbine and Aeroengine Congress and Exposition, Cologne, Germany, June 1–4, 1992. Manuscript received by the International Gas Turbine Institute February 4, 1992. Paper No. 92-GT-363. Associate Technical Editor: L. S. Langston.

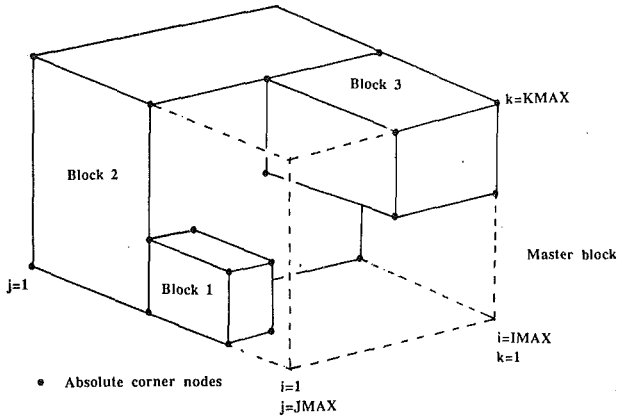

Fig. 1 The topologically cuboidal master block containing a number of individually generated blocks

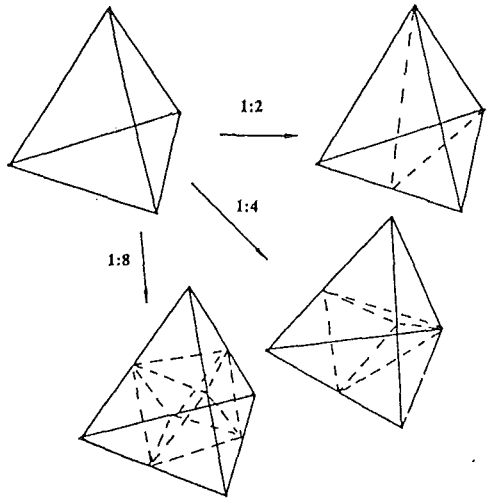

Fig. 2 Sketch of the three permitted cell divisions

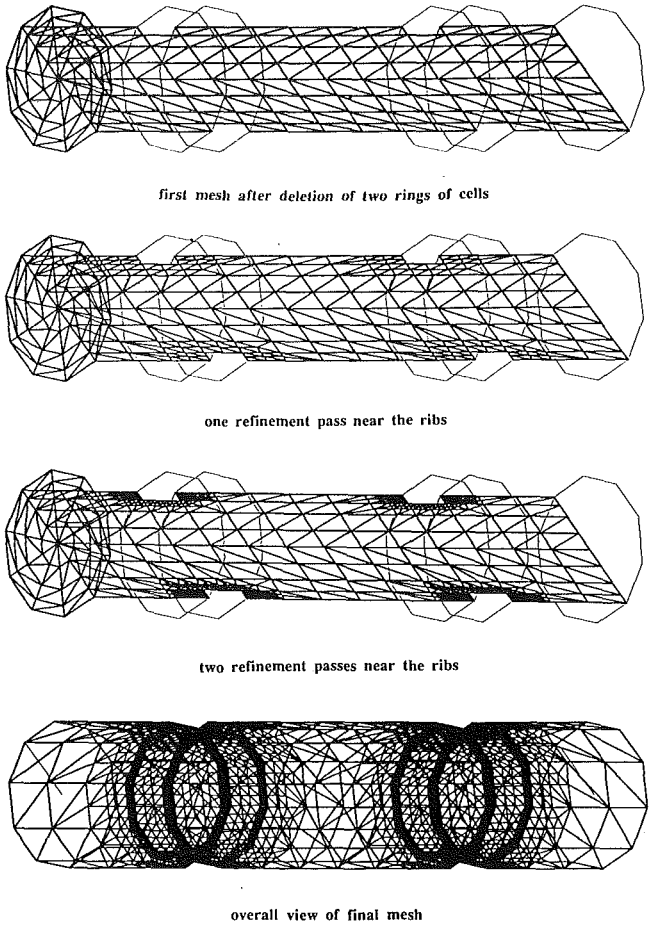

Fig. 3 Stages in the development of a mesh for a multiribbed cylindrical duct

a small radius tip) and 12 cylindrical pin fins]; if this passage was also multiribbed then the potential input surface patch specification is mind-boggling.

The objective of this paper is to describe recent work of the author attempting to produce a much more straightforward, "user-friendly" mesh-generating system, which aims to combine simplicity of data input with the ability to create complex combinations of geometry. As such the approach mimics CAD/FE stress analysis systems, which permit basic, easily input objects (which in the case of the present work includes turbomachinery blade rows) to be combined into complex configurations under the control of a master program. The key philosophy is to aim for a "connectivity" to describe a complex geometry and then use this to derive a geometric set of tetrahedrons to fill the geometry. This contrasts with the "moving front" and "Delaunay" philosophies of starting with the geometry, generating a node distribution to describe it and only then iteratively deriving a connectivity to bind the nodes into cells.

It is not yet clear how arbitrarily general a geometry can be handled by the current approach. To give some indication, solutions are presented for a range of increasingly complex geometries including a transonic compressor rotor, a splittered radial diffuser, a centrifugal impeller, a steam turbine nozzle row with casing extraction belt, the internal coolant passage in a radial inflow turbine (including the baffles and pin fins), and a turbine disk cavity seal configuration. No geometry took more than a man-day to build (several much less) but they nevertheless display a range of geometric complexity that cannot be handled in such a routine manner by other published approaches.

Mesh Generation and Adaptive Refinement

Multiblock Mesh Construction. The overall strategy of mesh generation is illustrated in Fig. 1. The concept is to define a topologically cuboidal "master" block, which runs in a structured manner over three space indices with any given node having coordinates X, T, R (1:JMAX, 1:IMAX, 1:KMAX). Within this master block are placed any number of blocks whose relative locations are determined by the values of the space indices assigned to each block's eight vertices. The mesh within each block is generated internally relative to that block and the only requirement is that intersections between blocks must be compatible both in terms of their number of nodes and spatial location of these nodes. The six faces of each block are flagged with their boundary types (inflow, blade, etc.) and when the control program links the blocks together intersections between blocks are converted to penetrations.

A variety of types of block are currently available to the control program and more are being added. They include the simple input of an externally generated X, T, R (j, i, k), obvious building blocks like a user-defined cylinder, and the data input and mesh generation of the author's standard, structured three-dimensional Navier–Stokes solvers. The basic mesh generation within each block is of simple, foolproof, "H-mesh" type with geometric stretching.

All cells in the master block not present in the various input blocks are flagged for eventual deletion. Then any of the individual cells (j, i, k) can also be flagged for deletion so that

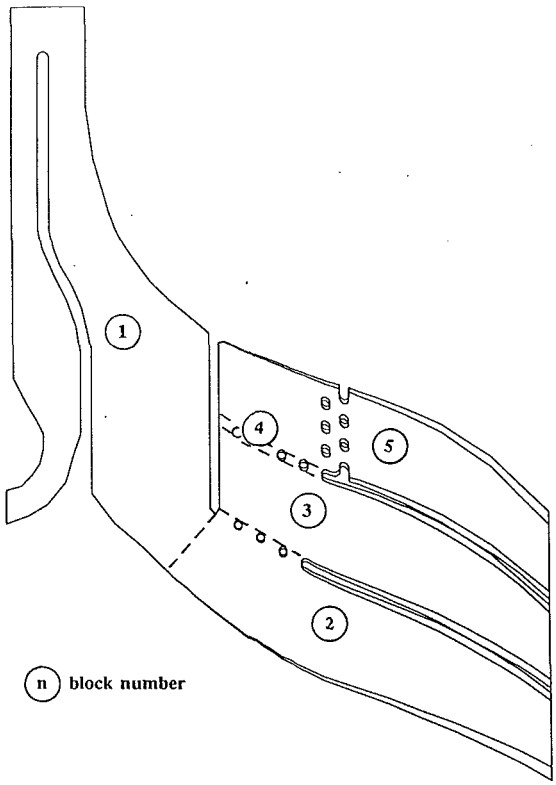

Fig. 4 The division of the passage into five blocks for the mesh generator

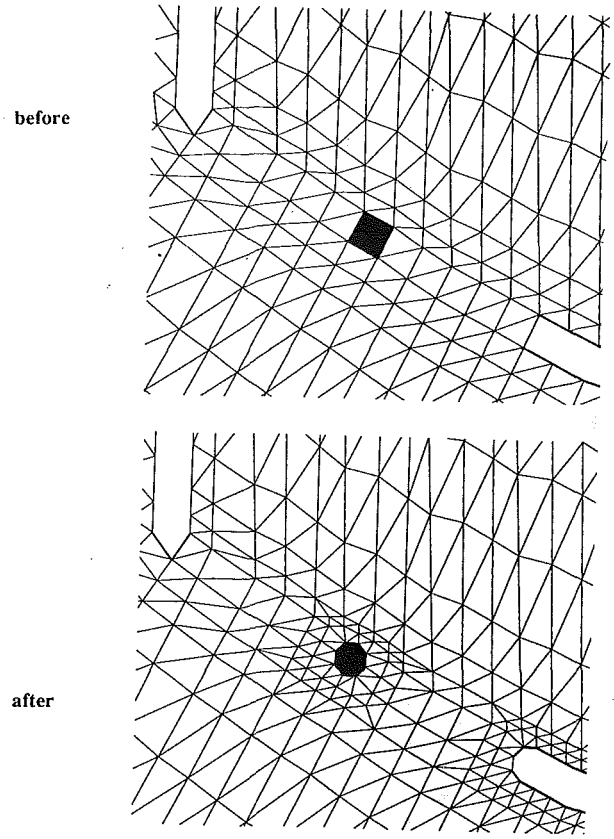

Fig. 5 The "growth" of a pin fin upon refinement

steps, internal obstacles, etc., can be generated "on-line" with minimal data input. The new boundaries so created are then flagged with appropriate type marks. At this stage also sets of nodes can be flagged for future, minor geometric adjustment so that corners can be rounded and square pins can become cylindrical, etc. Surface geometry patches can be automatically extracted and stored for each of the boundaries to the computational domain to support any subsequent geometric refinement.

Unstructuring. An "unstructuring" subroutine deletes all cells flagged as not present and numbers the nodes. Then it divides each individual cuboidal cell (j, i, k) into six tetrahedra and a connectivity table constructed associating cell numbers with the four nodes making up the cell. In dividing the quadrilateral faces of the cells, "diagonal swapping" can be used to improve mesh quality but care does need to be taken because, unlike in two dimensions, the consequences are global. Faces of cells lying on boundaries to the computational domain are then stored in a list together with their boundary types and adjacent cell information. Periodic boundaries are flagged together with their mutual correspondences.

Once a completely unstructured mesh has been formed, there is great freedom to modify it to suit particular objectives. This is carried out by selective mesh refinement.

Mesh Refinement. The refinement process is deliberately limited to a restricted number of possibilities with respect to the underlying, basic mesh; this confers great economy on the refinement process at the expense of some generality. The tetrahedal volumes are flagged to divide into 2, 4, or 8, depending on a variety of geometric or flow-based criteria. These three types of allowable division are sketched in Fig. 2. For a given tetrahedron there are three possible orientations of the division into 4 and six orientations for a division into 2. These orientations must be compatible on a cell face-to-face basis with the divisions in neighboring cells.

Those tetrahedra divided into 8 have identical aspect ratios to their parents, but repeated division into 2 or 4 does impact on local mesh quality (although in practice only two or three sequences of refinements will be performed and this has not proved a particular problem). To counter this the layer of cells surrounding those flagged for refinement can themselves be flagged. These "blanket cells" help to maintain good mesh quality in the near region of the flow feature that actually triggered the refinement.

Presolution Refinement. Presolution refinement can be undertaken to advantage near regions where large gradients are expected in the solution; these regions include near-blade surfaces and near-rapid changes in blade surface curvature (like corners and leading and trailing edges). This results in a highly unstructured mesh of tetrahedral control volumes. If the surface is not flat then the full curvature of the surface must be maintained during the refinement process. This rather complicated three-dimensional surface fit problem is handled using the basic geometric patches stored for each surface and the three-dimensional, unstructured, "multiquadratic surface interpolation" algorithm referenced by Kansa (1988). However, if the cells lying on the surface have high aspect ratio, then negative cell volumes can result from the local surface refinement. For the solutions in the present paper, this has been monitored by the refining subroutine and if necessary the surface assumed locally flat to prevent negative volumes; in current work the mesh is smoothed locally to avoid the problem.

Examples. It is easiest to illustrate the power and simplicity of the present approach with some examples.

Internal Ribs. Multiribbed ducts are a common feature of the secondary gas path, especially in the context of internal coolant passages but, despite their apparent simplicity, rather irritating to handle with traditional CFD codes without producing a "special version" of the flow solver. The stages in

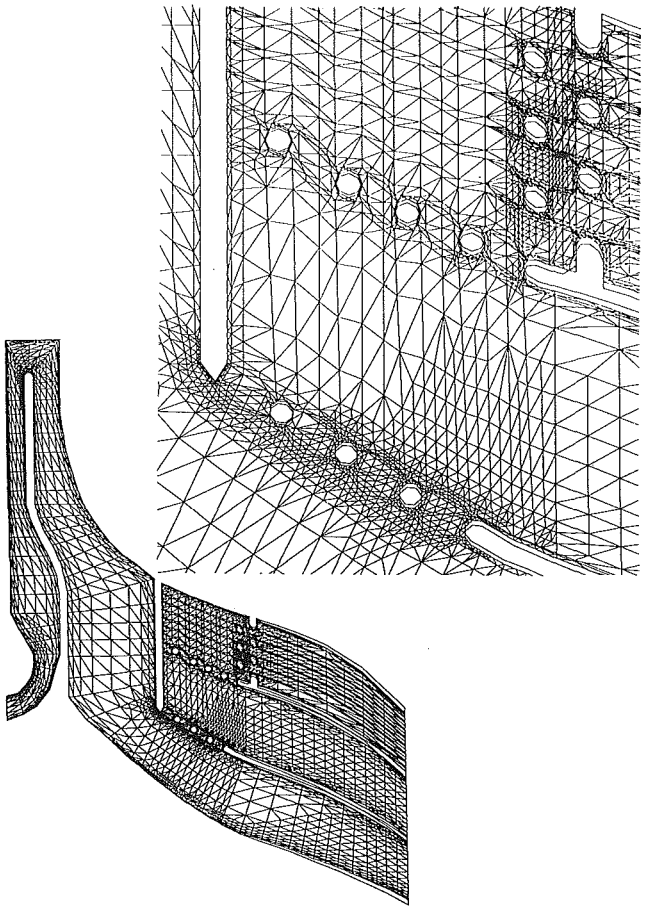

Fig. 6 The final mesh in the center plane of the coolant passage after adaptive refinement and containing a total of 75,626 nodes

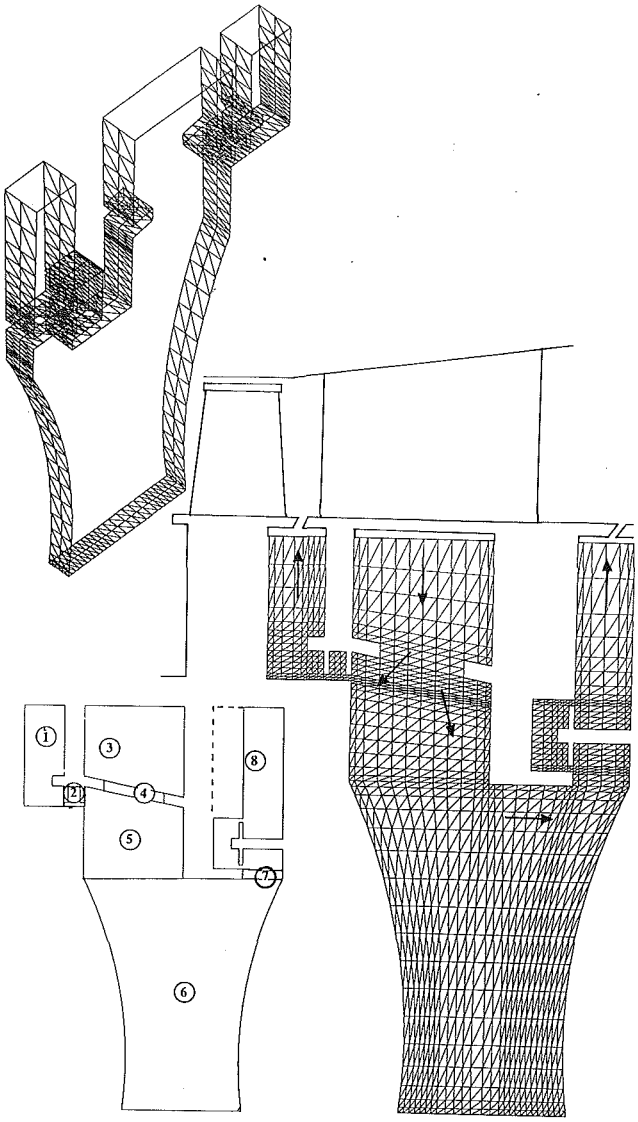

Fig. 7 Basic unstructured mesh for the generic disk cavity-seal configuration generated from eight input blocks

the development of an unstructured mesh are shown in Fig. 3. First a cylinder is generated "on-line" by specifying the radius and length of the basic cylinder and the number of nodes and then, again "on-line," circumferential rings of cells are deleted to form the ribs. To improve the mesh quality near the ribs two presolution refinement passes were then made to produce the final mesh shown in Fig. 3. The whole process takes about five man-minutes. The predicted flow field for a similar geometry, including the predicted Nusselt number distribution, is described by Dawes (1992b).

Internal Coolant Passage in a Radial Inflow Turbine. Internal coolant passages have complex geometries including baffles to split the flow and pin fins to control the flow. Figure 4 shows the internal coolant passage in a radial inflow turbine designed by Snyder and Roelke (1988). The passage was divided into five blocks for input to the present mesh generator; in fact each block used the data input format of the author's standard, structured three-dimensional flow codes. Within each block a simple topologically cuboidal mesh was generated. The three baffles and 12 pin fins were formed "on-line" by deletion of the sets of cells. Because of the scale of the input mesh, the pin fins are initially represented by a circumferential block of deleted cells with square cross section. The four edges of each pin fin were flagged as they were generated so that after a prerefinement pass the cross section of each fin may be automatically converted into something more cylindrical as illustrated in Fig. 5. The final mesh after some more refinement (in response to the solution as well as the geometry) is shown in Fig. 6. The predicted flow will be summarized later (extensive details are given by Dawes, 1992b). These and other figures have double lines plotted at the geometry boundaries. This is because the plotting software always plots the set of edges confining the computational volume so that the individual mesh (or contour or vector) plot is located. Thus the pin fins in Fig. 6, for example, are located by two edge plots, one on the suction side of the passage and one on the pressure side giving rise to two close edge lines in the particular projection selected.

Disk Cavity-Seal Geometry. Continuing in the theme of the complex geometries typical of the secondary gas path in a turbomachine, Fig. 7 shows an unstructured mesh generated for a generic disk cavity-seal configuration. The mesh generator used eight input blocks and, from start to finish, required about half a man-day of work. The seals themselves were generated on-line by deletion and so different numbers of seals and different locations could in fact be generated with minimum effort. The mesh is then prerefined in the vicinity of the seals.

The flow solver requires an initial guess for the flow field and this is achieved, even for such a complex geometry, by on-line input of guessed values of the primary flow variables at each vertex of each block. The complete flow field is then automatically specified by trilinear interpolation within each block.

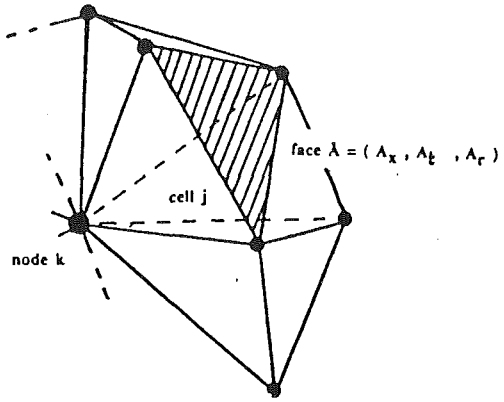

Fig. 8 A typical cell *j* contributing to node *k*

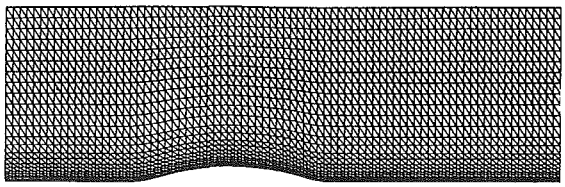

finest mesh : 2025 nodes per plane

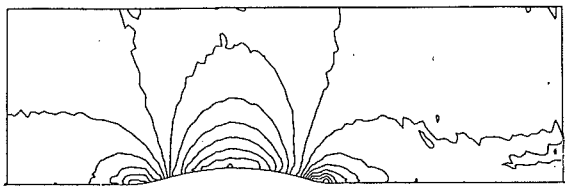

Mach number : inlet 0.30 ; interval 0.01

Total pressure : interval 0.20% of the inlet value

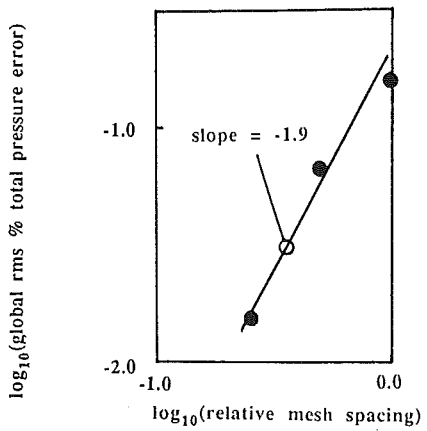

Fig. 9 Inviscid, subsonic channel hump computed using a viscous, stretched mesh showing numerical error and accuracy order of the solver

Solution-Adaptive Refinement. Once a suitable unstructured mesh has been produced it is sent to the flow solver. After a specified number of time steps the solution is examined and the mesh refined in sympathy with the developing flow field. Currently, static pressure, Mach number, and entropy are used as indicators for the need for refinement but there are a wide range of possible indicators that could be used.

The indicators are deployed in two ways: A cell face is flagged to divide either if the fractional variation of the indicator over the face exceeds a certain value or if the average value of the indicator falls within a given range. Several indicators may be chained together along with purely geometric criteria and refinement carried out simultaneously or the refinement can be built up in a sequential manner. So far the refinement strategy has been based on rather subjective judgments ("more mesh in the boundary layer," etc.) and work is needed in making the refinement process more objective and user-independent. As in the prerefinement stage, any new nodes on curved surfaces are located using the basic geometric patches stored for each surface and the three-dimensional unstructured surface interpolation algorithm.

Equations of Motion

The equations solved are the fully three-dimensional Reynolds-averaged Navier–Stokes equations expressed in strong conservation form and retaining the full stress tensor including the full viscous energy equation. Turbulence is modeled via k–ϵ transport equations (Patel et al., 1985) together with appropriate low Reynolds number terms (Lam and Bremhorst, 1981) to handle smoothly the approach to the blade surfaces. In a right-handed Cartesian (X, T, R) coordinate system rotating with speed Ω about the X axis the equations of motion are:

$$\frac{\partial}{\partial t}\oint_{\mathrm{VOL}} \overline{U} d\mathrm{VOL} = \oint \overline{H} \cdot d\overline{\mathrm{AREA}} + \oint_{\mathrm{VOL}} \rho \overline{S} d\mathrm{VOL} \quad (1)$$

where

$$\overline{U} = \begin{bmatrix} \rho \\ \rho V_x \\ \rho V_t \\ \rho V_r \\ \rho E \\ \rho k \\ \rho \epsilon \end{bmatrix}$$

$$\overline{H} = \begin{bmatrix} \rho \overline{q} \\ \rho V_x \overline{q} + \overline{\overline{\sigma}} \hat{i}_x \\ \rho V_t \overline{q} + \overline{\overline{\sigma}} \hat{i}_t \\ \rho V_r \overline{q} + \overline{\overline{\sigma}} \hat{i}_r \\ \rho I \overline{q} + \overline{q} \cdot \overline{\overline{\sigma}} + \lambda \nabla T \\ \rho k \overline{q} + (c_2 \mu / \rho) \nabla k \\ \rho \epsilon \overline{q} + (c_3 \mu / \rho) \nabla \epsilon \end{bmatrix} \qquad \overline{S} = \begin{bmatrix} 0 \\ 0 \\ t\Omega^2 - 2\Omega V_r \\ r\Omega_2 + 2\Omega V_t \\ 0 \\ G - \rho\epsilon \\ f_1 \dfrac{c_4 \epsilon G}{k} - f_2 \dfrac{c_5 \rho \epsilon^2}{k} \end{bmatrix}$$

with

$\overline{q}$ = $V_x \hat{i}_x + V_t \hat{i}_t + V_r \hat{i}_r$, the relative velocity
Ω = rotation speed
I = $c_p T_{o_{\mathrm{rel}}} - 1/2(\Omega r)^2$, the rothalpy
$\overline{\overline{\sigma}}$ = the stress tensor, $-p\overline{\overline{I}} + \overline{\overline{\tau}}$, $\overline{\overline{\tau}} = 2\mu \mathrm{def}(\overline{q}) - 2/3\mu(\nabla \overline{q})\overline{\overline{I}}$

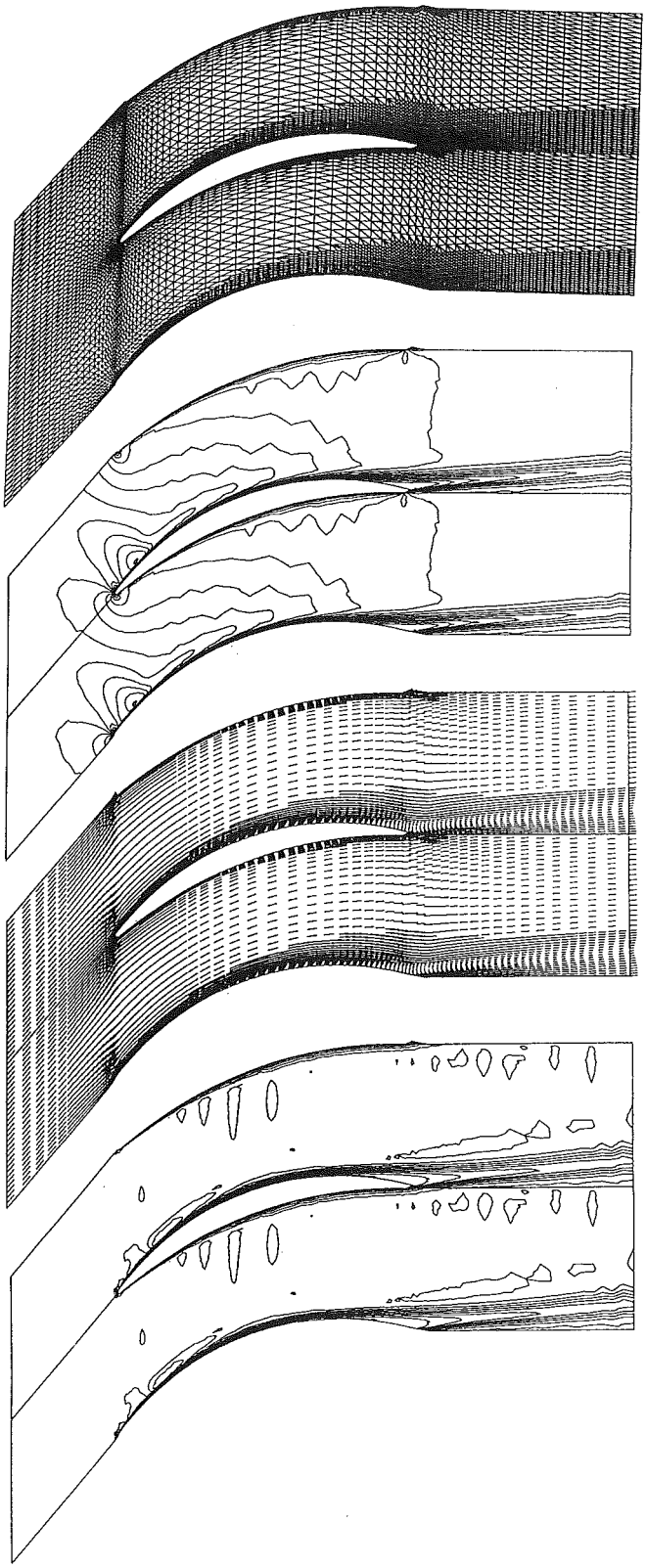

Fig. 10 V2 compressor cascade: midspan mesh containing 4755 nodes; Mach numbers (interval 0.05); velocity vectors; and total pressures (interval 2 percent PO1)

$$\text{def}(\bar{q}) = 1/2(\nabla\bar{q} + (\nabla\bar{q})^T)$$
$$\mu = \mu_{\text{lam}} + \mu_T$$
$$\mu_T = \rho f_\mu c_1 k^2/\epsilon$$
$$G = 2\mu(\text{def}(\bar{q}))^2 - 2/3\mu(\nabla\bar{q})^2$$
$$\lambda = c_p(\mu_{\text{lam}}/\text{Pr} + \mu_T/\text{Pr}_T)$$

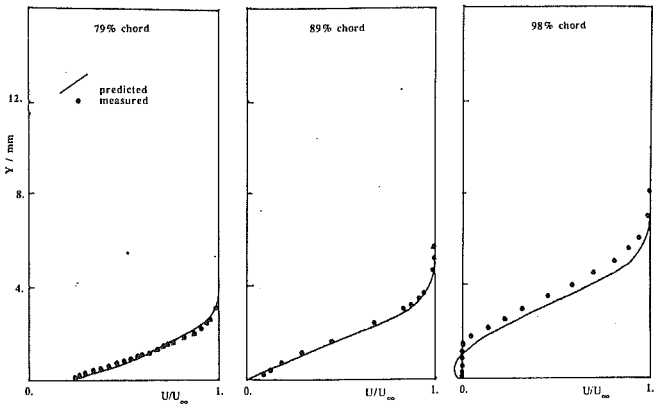

Fig. 11 V2 cascade: comparison between measured and predicted boundary layer profiles on the suction surface

and the low Reynolds number damping terms are

$$f_\mu = 1. - \exp(-0.008\text{Re}_T)$$
$$f_1 = 1. - (0.06/f_\mu)^3$$
$$f_2 = 1. - \exp(-\text{Re}_T^2)$$

where $\text{Re}_T = \rho k^2/\mu_{\text{lam}}\epsilon$, the turbulent Reynolds number.

The various constants in the k–ϵ model take their standard values:

$$c_1 = 0.09, \quad c_2 = 1.0, \quad c_3 = 0.769, \quad c_4 = 1.44, \quad c_5 = 1.92,$$

and the turbulent Prandtl number is taken as 0.9. Note that the original Lam and Bremhorst function f_μ contains a Reynolds number based on the distance from the nearest wall $\text{Re}_y = \rho\sqrt{k}y/\mu_{\text{lam}}$ but for the present work this has been replaced for convenience by $\text{Re}_y = 0.40\ \text{Re}_T$, which is valid near the wall (Patel et al., 1985).

Solution Algorithm

The solution algorithm will be described here only in outline; for further details see Dawes (1991, 1992a). The seven equations of motion are discretized in finite volume form on each of the tetrahedral control volumes with vertex variable storage. Figure 8 illustrates a typical set of tetrahedral cells, j, surrounding and influencing a node, k. The primary variables ρ, p, $\rho\bar{q}$, ρk, and $\rho\epsilon$ are assumed to have a piecewise linear variation over cell faces between the vertices so that the flux sum for a given cell is evaluated to second-order accuracy in space. The derivative terms in the viscous stresses are piecewise constant over the cell (since the primary variables are piecewise linear) and are computed by simple application of the Gauss divergence theorem. Using all the cells surrounding the node, k, as a control volume then allows the evaluation of the viscous stress terms at k. Assembling for convenience all the viscous terms into a vector D_k allows the definition of a residue, R_k, at each node as:

$$R_k = \frac{1}{\text{VOL}_k}\sum_{\text{cell}j}\text{fluxes}_j + D_k \qquad (2)$$

The net flux imbalance into each cell is used to update the flow variables themselves via a two-step Runge–Kutta time-marching algorithm with residual smoothing (see Jameson, 1987, for an excellent description).

Artificial diffusion is added to control shock capture and solution decoupling and is controlled in magnitude by the local strength of the pressure gradient. It is particularly important to construct the artificial smoothing carefully in the unstructured environment to guarantee that the smoothing involves no derivatives of flow variables normal to viscous surfaces and to scale the smoothing in accordance with the highly non-

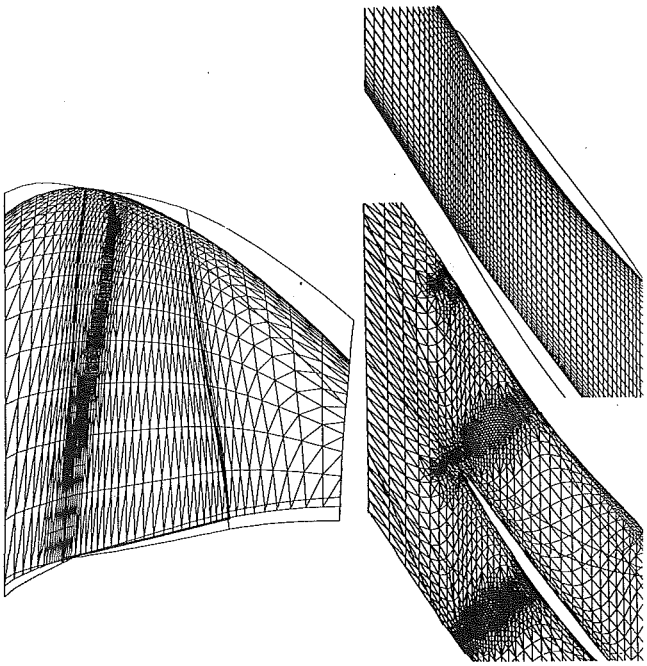

Fig. 12 Solution-adapted mesh for a transonic compressor rotor containing 71,945 nodes and midspan of the conventional structured mesh containing a total of 90,136 nodes

uniform mesh. In the present work the smoothing is computed as:

$$D_k = \left[\text{AV2} + \text{AVA} \cdot \text{VOL}^{2/3} \left| \frac{\nabla^2 p}{4p} \right| \right] A_o \Delta\bar{l} \nabla^2(W) \quad (3)$$

where W represents any of the *seven* basic flow variables (ρ, $\rho\bar{q}$, ρE, ρk, or $\rho\epsilon$), $\Delta\bar{l}$ is a representative mesh spacing over the cell, A_o is a velocity scale (taken here as the stagnation speed of sound), and $\text{VOL}^{2/3} \mid \nabla^2 p/4p \mid$ is a pressure switch of order 1 near a shock wave but $\Delta\bar{l}^2$ elsewhere. In application AV2 is set to 0.001 and AVA to between 0.50 and 2.0.

Since W is assumed to be piecewise linear over the cells, the first derivatives are piecewise constant; this guarantees that there are no smoothing second derivatives normal to the surfaces for those nodes on the surface that could interfere with the physical viscous terms. The Laplacian of W returns a zero for a trilinearly varying W even on a nonuniform mesh. This simple and economical smoother was chosen in preference to the more conventional combination of second–fourth derivative smoothing partly because of its compactness but mainly to avoid the severe problems associated with fourth-derivative smoothing on meshes with widely varying cell aspect ratios when the smoothing coefficient must be scaled highly, and expensively, anisotropically (Martinelli, 1987) to follow closely the spatial variations of the spectral radii of the flow equations.

To demonstrate the level of accuracy of the flow solver, some classic mesh refinement tests were carried out for a simple channel hump for inviscid, subsonic flow (inlet Mach number 0.30). The predicted flow should of course be loss free and so any discrepancy between the total pressure and that at the inlet represents a measure of the numerical error. Even though the flow is inviscid, a stretched viscous mesh was used, the finest of which is shown in Fig. 9. Three meshes were used with each one containing twice as many nodes as the previous one. The error was quantified by computing a mass-averaged total pressure at each of ten crossflow planes and then defining a global error as the root mean square of the discrepancy between each of these planes and the inlet. The table below summarizes the results:

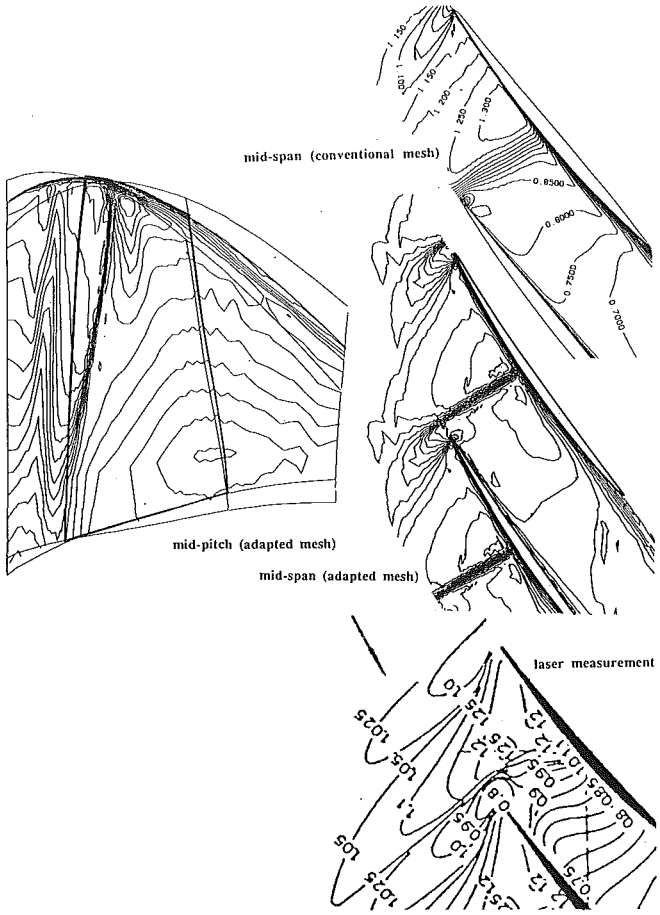

Fig. 13 Predicted Mach numbers

Number of nodes in the plane	Global rms total pressure error, percent
147	0.16
533	0.067
2025	0.015

The predicted Mach numbers and total pressures for the finest mesh case are shown in Fig. 9. The total pressure errors are near the two wall boundaries and related to the first-order accurate boundary conditions as much as to the smoothing. Some unsightly wiggles appear in the Mach number contours; these apparently arise because not all of the unstable modes are sufficiently damped by the smoothing and further work is underway in this area. Finally, Fig. 9 shows a plot of the log of the global error versus the log of the relative mesh spacing. The slope is -1.9, suggesting that the scheme as implemented is indeed second-order accurate. Overall the performance is considered acceptable.

Boundary Conditions

Various boundary conditions must be imposed for the Navier–Stokes solution presented hereafter. At inflows (of which there may be several) the total pressure, total temperature, turbulent kinetic energy and dissipation rate, and two flow angles are fixed and the derivative of static pressure in the streamwise direction set to zero. At the outflow boundaries the static pressure is held constant and the other variables extrapolated from the interior. On solid surfaces zero normal fluxes of mass, momentum, and energy are imposed. The wall shear stress is computed either from the laminar sublayer or log law equations depending on whether the local value of the

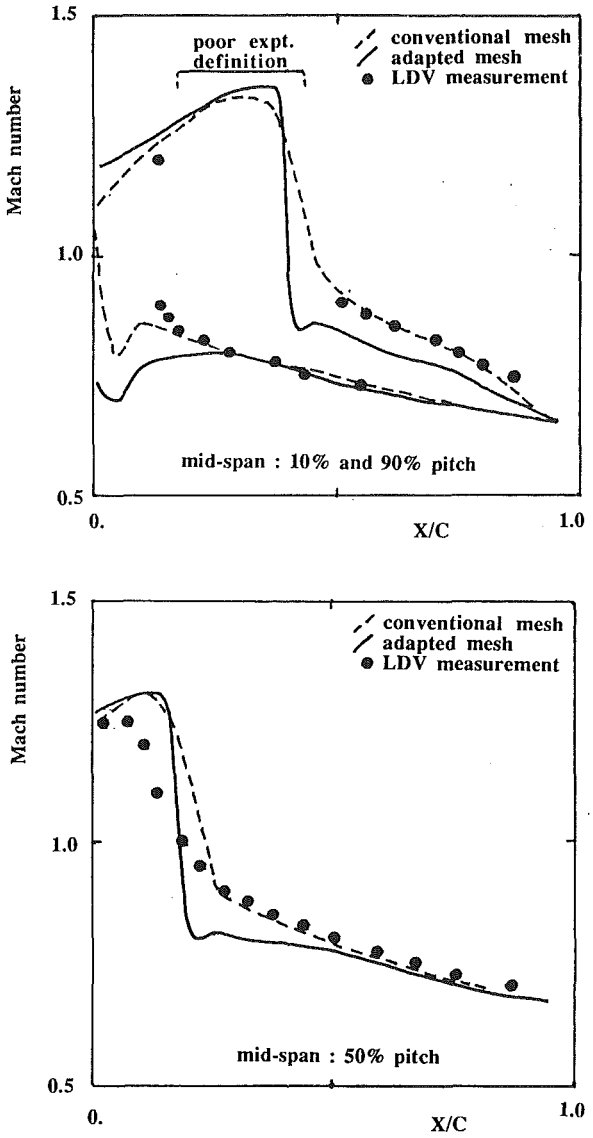

Fig. 14 Comparison of measured (LDV) and predicted Mach number variations in midspan along lines at 10, 50, and 90 percent pitch

wall coordinate Y^+ is less than or greater than 10, respectively. In a similar spirit, if Y^+ is less than 10 the turbulent kinetic energy and the normal gradient of dissipation rate are set to zero on the surface; otherwise k and ϵ are set to be consistent with the assumed log law at values of $u_\tau^2/\sqrt{c_1}$ and $u_\tau^3 / \kappa Y_w$, respectively, where κ is the von Karman constant, 0.41, and Y_w the normal distance to the wall.

Presentation of Results

In this section a selection of results will be presented to demonstrate the simplicity, versatility, and power of the present approach. The examples are divided into two sections: In the first, the solution quality in "simple" geometries is shown to benefit from the solution-adaptive capability; and in the second section solutions are presented for very complex configurations to show the benefit of the unstructured approach.

All the simulations presented here were run on an inexpensive desktop workstation, a SUN SPARCstation 2, consuming 4.2E-03 seconds per node per time step and 1 Mbyte of memory per 1000 nodes. The cpu time required is around a factor of 3 more than the author's structured code (Dawes, 1988) partly as a result of the indirect addressing used but mainly because there are five times more cells than nodes with a tetrahedral mesh (in a cuboidal mesh there are the same number of nodes as cells).

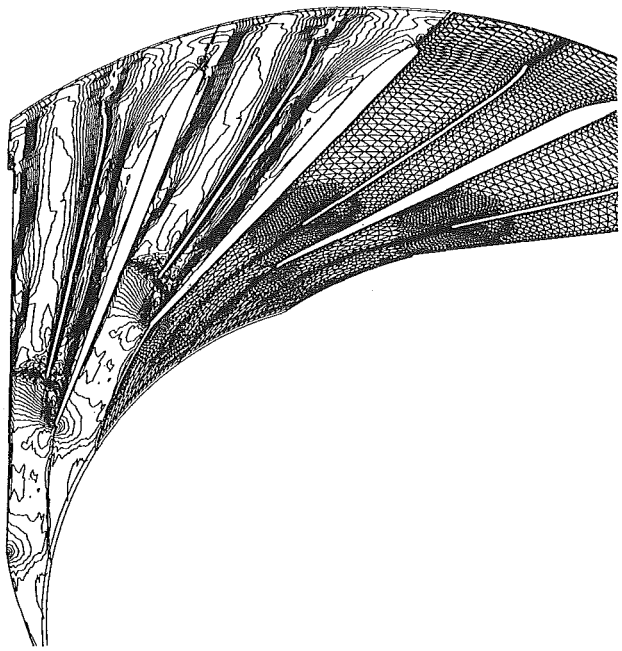

Fig. 15 Adapted mesh and predicted Mach numbers for a generic, highly loaded, splittered radial diffuser

• Simple Geometry; Improved Resolution

V2 Compressor Cascade. The first set of simulations is for a transonic, linear cascade, designated V2, representing the midheight of a highly loaded transonic fan with the following nominal operating point:

Pitch-chord ratio	=	0.45
Inlet Mach number	=	0.80
Inlet flow angle	=	49.5 deg
Exit flow angle	=	6 deg
Axial velocity density ratio	=	1.146
Reynolds number	=	5.5×10^5
Upstream turbulence level	=	3 percent

Experimental measurements (made originally at the DFVLR in Gottingen) have been widely published, for example by Calvert and Herbert (1980). The simulations were performed with inviscid hub and casing surfaces so that in effect a two-dimensional solution is obtained but using the fully three-dimensional code. This is rather wasteful but a good initial test nevertheless.

Figure 10 shows the midspan mesh used. The mesh was derived from an initial mesh with 29×67 (1943) nodes in each of three blade-blade planes. After 2000 time steps the mesh was refined by dividing every cell within which the total pressure was less than 95 percent of free stream. This results in a mesh well adapted to resolve the boundary layer and wake flow but containing only 4755 nodes (i.e., only a factor 2.4 more than in the initial mesh rather than the factor 4 that a structured code would use for the same increase in local refinement). The refined mesh was then run on for another 2000 steps to produce the solution illustrated in Fig. 10 in terms of Mach number and total pressure contours and velocity vectors. The final solution has a global residue (defined as the rms derivative of density) of 0.7 E-08 and a global mass continuity error of 0.15 percent.

Figure 11 compares predicted and measured boundary layer profiles on the suction surface at three stations toward the trailing edge. The level of agreement is considered to be satisfactory.

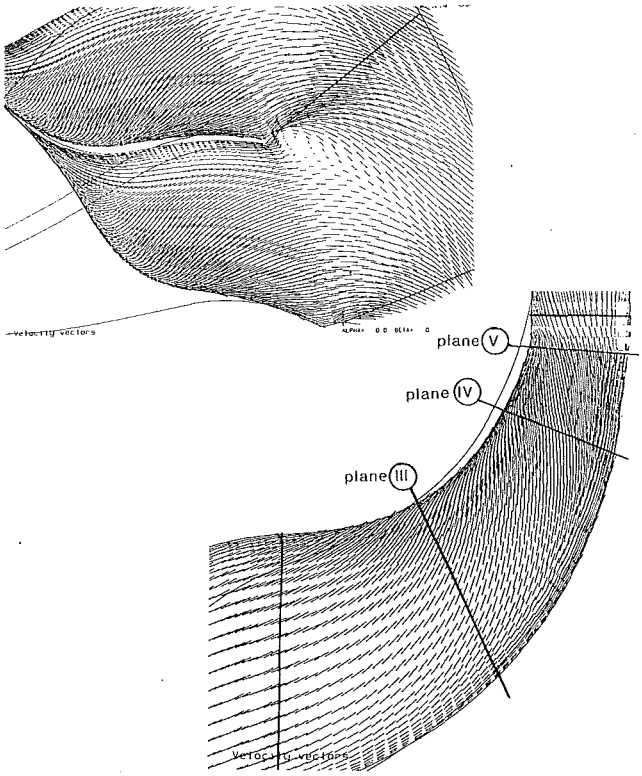

Fig. 16 Predicted velocity vectors near the shroud and near the suction surface of the Eckardt impeller

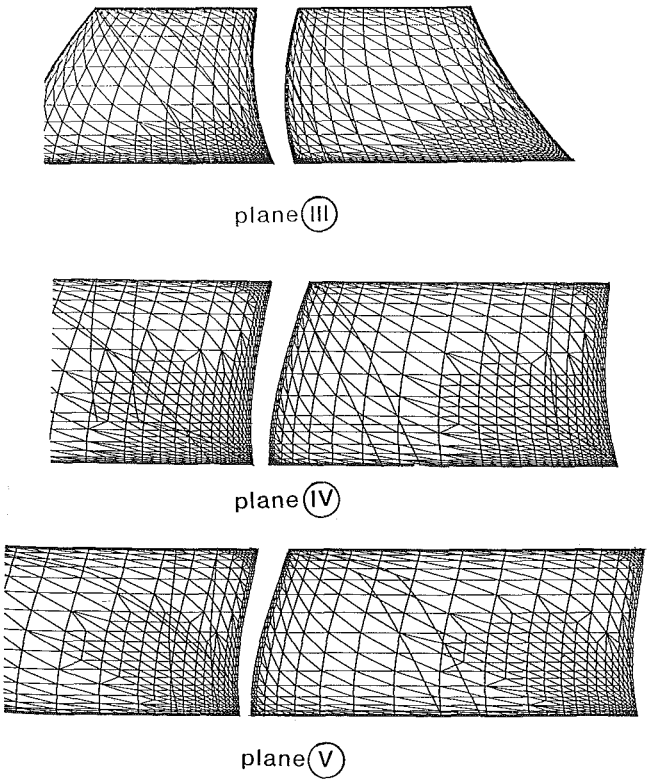

Fig. 17 The adapted mesh in the three crossflow planes

Transonic Compressor Rotor. Next, the code is applied to the study of the three-dimensional flow field in the axial flow single-stage transonic compressor rotor tested using laser-two-focus velocimetry at the DFVLR (Dunker et al., 1977). The main parameters are:

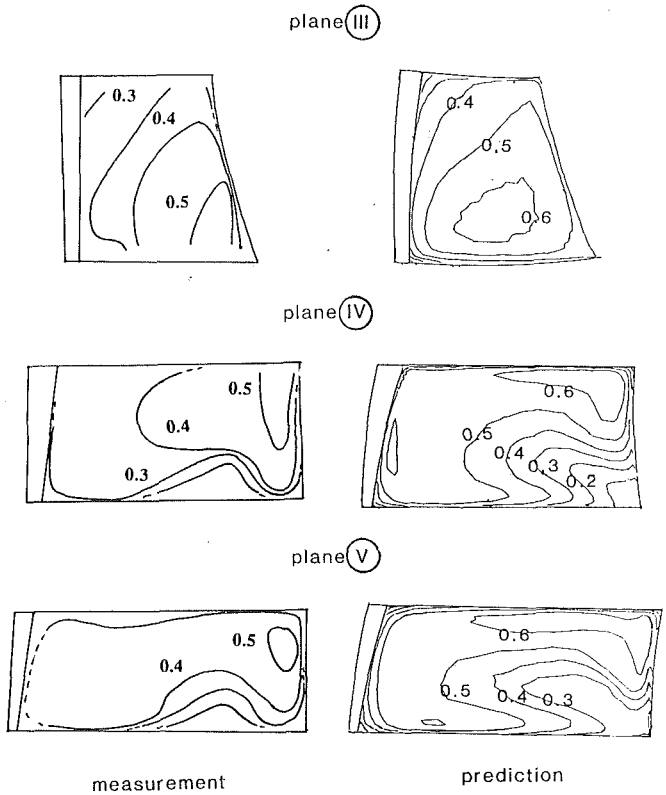

Fig. 18 Comparison of measured and predicted velocity in the three crossflow planes (made dimensionless with the wheel tip speed)

Inlet tip diameter	=	0.4 m
Hub-tip ratio	=	0.5
Tip solidity	=	1.34
100 percent speed	=	20,260 rpm
Max. η total pressure ratio	=	1.626
Max. η mass flow rate	=	17.1 kg/s

Numerical simulations have been published in the past for this rotor using the author's conventional three-dimensional Navier-Stokes solver (Dawes, 1988) and the objective here is to show the improved resolution, particularly of the bow shock, which can be obtained using the present solution-adaptive approach, and using about the same number of nodes. Figure 12 shows the final mesh used for the present study after two refinements and containing a total of 71,945 nodes. For comparison is shown (for midspan) the mesh from the earlier conventional simulation, which contained a total of 90,136 nodes. The current simulations are carried out in a Cartesian coordinate system and so the view toward the blade suction surface is a true view rather than the developed meridional view conventionally presented.

Figure 13 compares the predicted Mach numbers from the present simulation with the earlier conventional one and the laser velocimeter measurements (Dunker et al., 1977). The improved resolution of the bow shock is striking and this is achieved because the mesh can be concentrated where it is needed without having to be wasted elsewhere.

In an attempt to provide a more quantitative comparison, Fig. 14 shows measured (LDV) and predicted Mach number variations in midspan along lines at 10, 50, and 90 percent pitch. The present preprocessor cannot produce line plots and so Fig. 14 was constructed graphically from a much-enlarged contour plot. This will tend to smooth any contour-to-contour wiggles with amplitude less than the chosen contour interval but nevertheless will represent the level variations faithfully; the experimental results were processed in the same way. As noted above, the adapted mesh results give a shock prediction that is much superior to the structured code. Paradoxically,

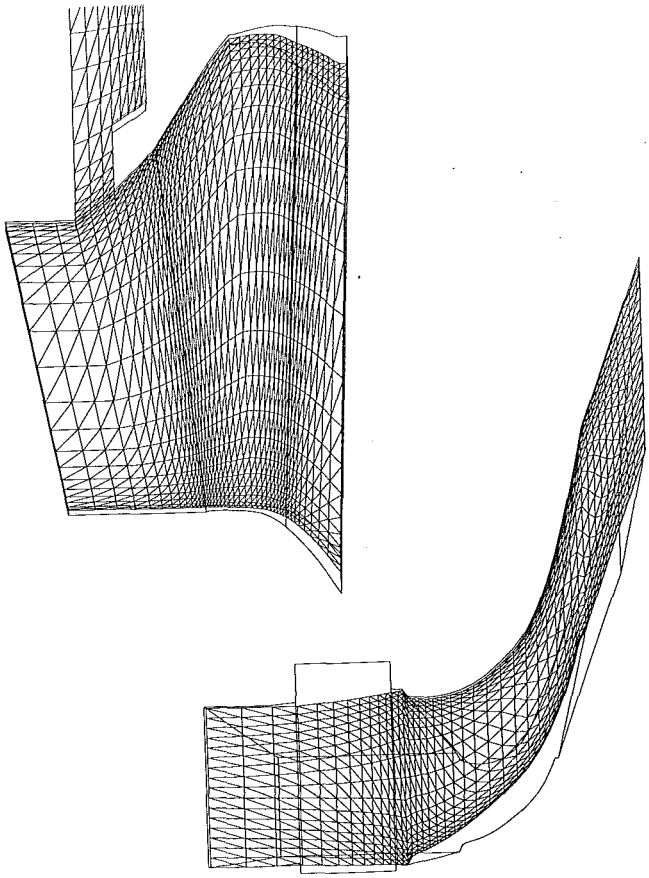

Fig. 19 Unstructured mesh for the generic steam turbine nozzle row with extraction belt

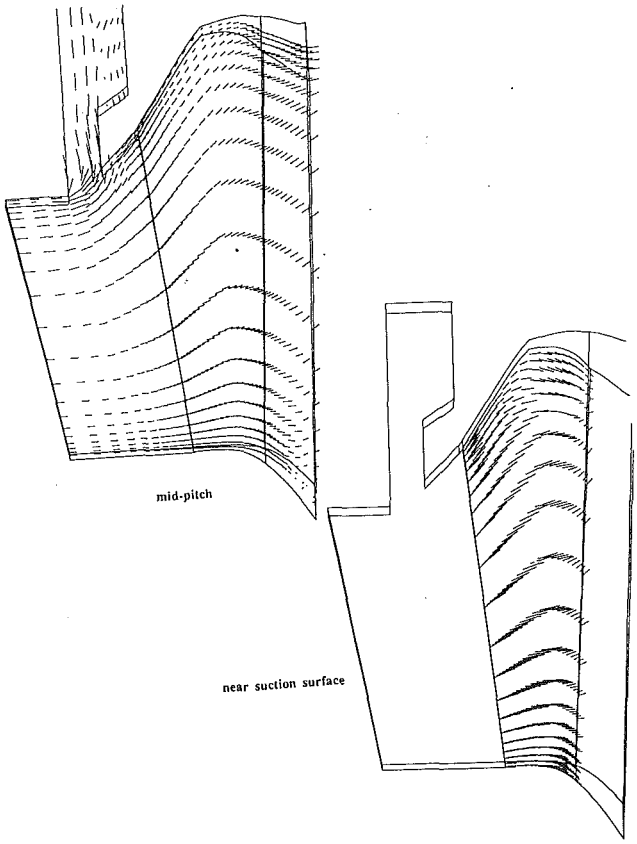

Fig. 21 Predicted velocity vectors in midpitch and near the blade suction surface

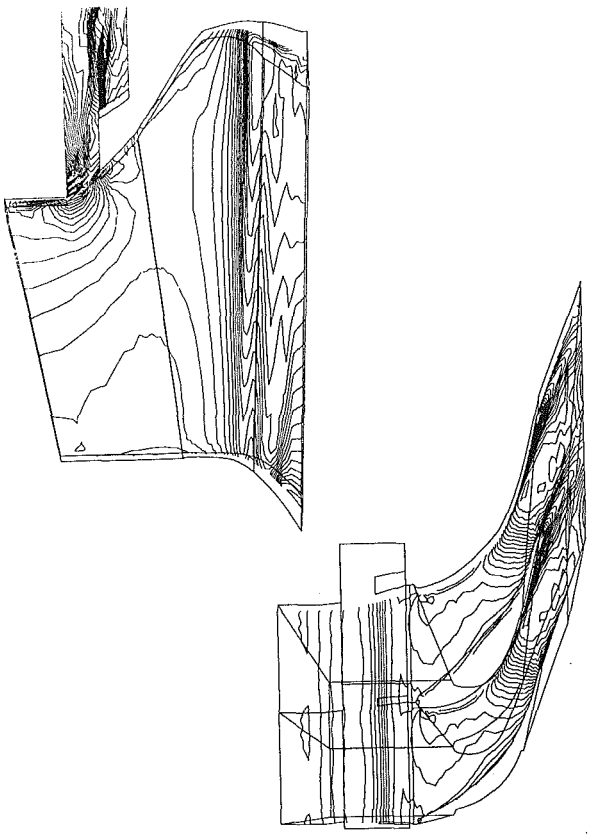

Fig. 20 Predicted Mach numbers in midpitch and in a blade-blade plane at 90 percent of the span

the smeared, structured code results are in better agreement with the smeared LDV results over the shock zone! The LDV seeding particle lag through the shock is unknown and represents a significant problem in comparison with CFD; perhaps the motion of suitable seeding particles should be simulated through the numerical solution for more relevant comparisons. On a more positive note, the structured and adapted solutions show very similar levels of Mach number up- and far downstream of the shock zone.

Splittered Radial Diffuser. The next example is a generic, splittered, highly loaded (exit static–inlet total pressure ratio around 0.75) radial diffuser. The very high entry angle (around 70 deg) and rapid turning thereafter give conventional, structured solvers (at least those using an H-mesh) severe difficulties because of the very sheared and skewed mesh. This is much less of a problem for the present solver; tetrahedralizing the underlying H-mesh in fact gives better quality individual control volumes. The midspan mesh and predicted Mach numbers are shown in Fig. 15. The flow is characterized by a strong entry shock, which induces strong separations on both the suction and pressure sides of the passage.

Centrifugal Impeller. The next example is the classic test case of the Eckardt (1976) backswept centrifugal impeller. The basic parameters are:

Impeller LE radius at hub	=	90 mm
Impeller LE radius at casing	=	280 mm
Impeller TE radius	=	400 mm
Impeller axial width	=	130 mm
Blade backsweep angle	=	30 deg
Rotational speed	=	1400 rpm
Nominal mass flow rate	=	4.54 kg/s
Stage total pressure ratio	=	1.61

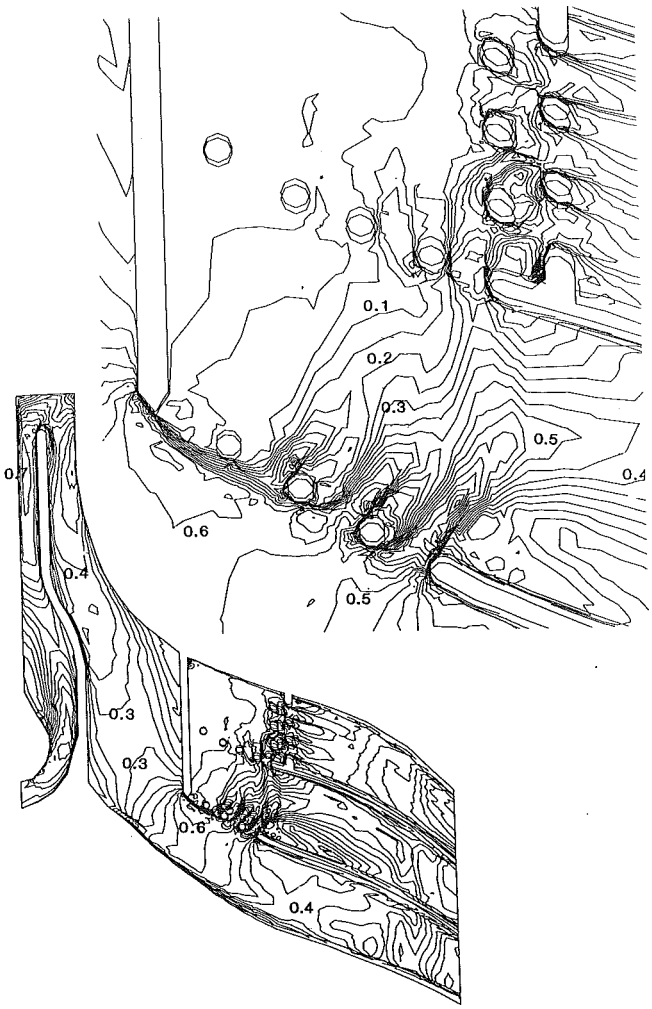

Fig. 22 Predicted midpassage Mach number contours

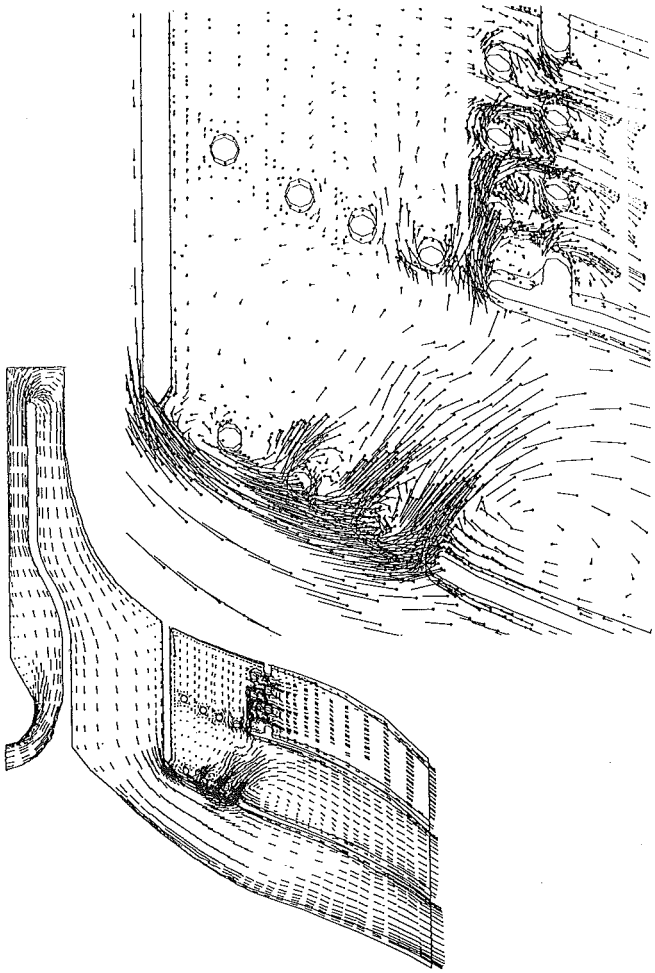

Fig. 23 Predicted midpassage velocity vectors

The flow field is characterized by strong secondary flows leading to development of a jet-wake structure in the exit of the impeller. Figure 16 shows predicted velocity vectors near the shroud and the suction surface of the impeller. The strong radial outward secondary flows near the blade surfaces coupled with the strong blade–blade flow near the shroud lead to the formation of a deep wake in the shroud–suction surface corner. Accordingly, the adapted mesh was refined along the development path of the wake (by using entropy as a refinement indicator) resulting in the crossflow meshes shown in Fig. 17; the overall mesh contained a total of 68,386 nodes. Note how the refinement occupies varying proportions of the passage in sympathy with the wake.

This simulation is included primarily to demonstrate how three-dimensional the solution adaption can be in practice. The simulation was run without overtip leakage (as it was not available in the mesh generator when this paper was prepared) and thus the wheel mass flow is predicted about 9 percent high (for the same pressure ratio). Nevertheless, in an attempt to assess the accuracy of the predictions, Fig. 18 compares the predicted velocity distributions in the three crossflow planes with Eckardt's laser velocimeter measurements. There are two main discrepancies, both partly associated with the lack of overtip leakage in the simulation. First, the velocity levels are somewhat higher than in the measurements, scaling with the mass flow. Second, although the depth of the predicted wake is similar to that measured, the spatial extent is about 50 percent larger than in the test and located rather more in the suction surface–casing corner; in the test the overtip leakage flow pushes the wake region rather more toward midpitch.

- **Complex Geometry**

Steam Turbine Nozzle With Extraction Belt. The next case consists of a generic steam turbine nozzle row, typical of the late stages in an LP cylinder, with an extraction belt in the casing (which would lead to a feed heater). The unstructured mesh is shown in Fig. 19 and was generated from two input blocks (one a "standard" dataset for the blade row and the second containing the geometrically simple casing slot) and contains 16,456 nodes. This geometry is representative of a class of problems that includes casing treatments like "map width enhancer slots," passage branching for air take-offs, etc., but which are very difficult to handle with conventional solvers without time-consuming special coding. Figure 20 shows the Mach numbers predicted in the midpitch plane and in a blade–blade plane at 90 percent of the span. Figure 21 shows the velocity vectors predicted in midpitch and near the suction surface. As expected, the extraction introduces a strong perturbation to the casing flow field, which then contributes to the radially inward secondary flow seen near the suction side of the nozzles.

Radial Inflow Turbine Coolant Pressure. It is a design imperative to minimize the mass flow rate of coolant air (which is unavailable to the cycle), which must be deployed to achieve a desired blade cooling. To do this requires an understanding of and an ability to predict the complex aerodynamics in the very complex geometries of blade internal coolant passages. Up until now designers have relied on one-dimensional analyses

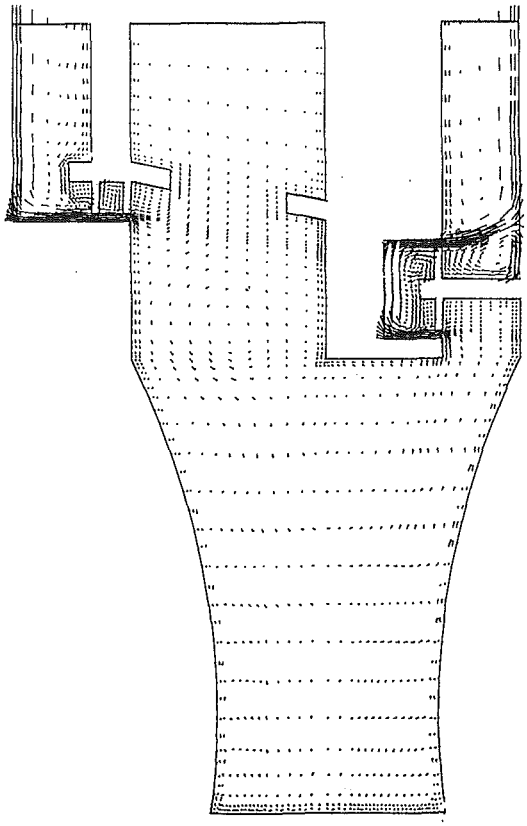

Fig. 24 Predicted velocity vectors in the generic disk cavity-seal configuration

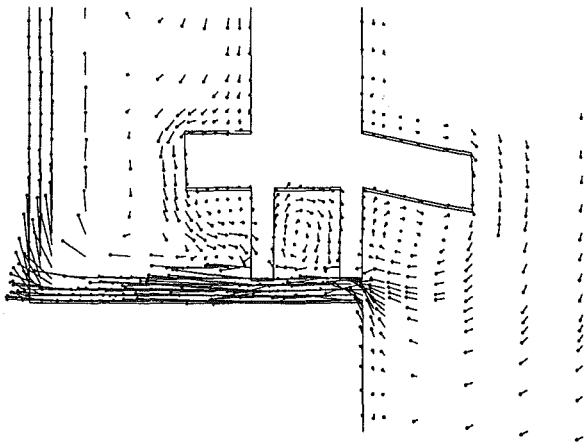

Fig. 25 Zoom view near the left seal

of these passages (e.g., Snyder and Roelke, 1988) with simple models for the head losses associated with bends, pin fins, etc., allowances for heat transfer and for rotational effects. The present methodology can readily cope with such geometries and in an earlier section (and in Figs. 4-6) the development of an unstructured mesh for the internal coolant passage in a radial inflow turbine was described.

It is believed that the solution obtained by the present solver is the first fully three-dimensional Navier-Stokes solution to be published for such a configuration; complete details (including predicted heat transfer coefficients) are presented by Dawes (1992b). To illustrate the degree of resolution obtained in the present simulation, Figs. 22 and 23 show the Mach numbers and velocity vectors predicted on the midpitch plane of this three-dimensional prediction (with zoom views into the neighborhood of the pin fins). As noted before, the post-

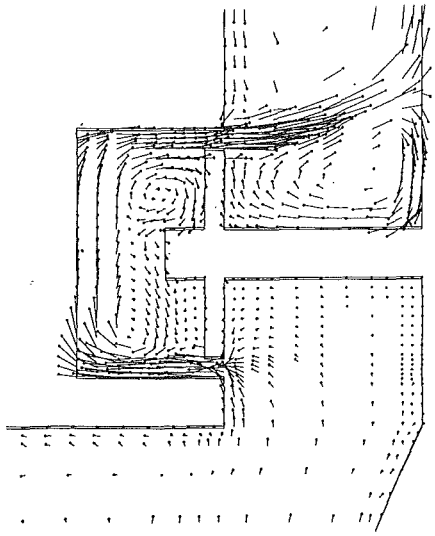

Fig. 26 Zoom view near the right seal

processor locates the chosen plots by plotting all the edges to the computational domain and in certain projections some of these edges nearly coincide, giving rise to the double lines seen in, for example, the neighborhood of the pin fins.

The serpentine passage contains, as expected, three separated flow zones: one near the entrance in the initial diffuser, one just after the 180 deg bend, and one in the corner between the casing and the radial baffle. Once past the radial baffle, the flow starts to centrifuge outward and in passing between the pin fins the simulation has clearly resolved the individual wake structures of each fin (even the vortex structure downstream of each one). These wake structures are responsible for large variations in the passage sidewall heat transfer coefficients and may contribute to unexpected hot spots.

Disk Cavity-Seal Configuration. The final example is the complex geometry associated with disk cavity-seal configurations. It is important to prevent the ingestion of hot mainstream gases through the interstage gaps into the turbine disk cavities as this can cause overheating, thermal expansion, and fatigue. To prevent this ingestion, cooling and sealing air is supplied into the disk cavities to oppose the inward flow of the hot gases. The flow rate and pressure of the cooling gases are controlled by the interstage seals. A generic geometry was generated for the present study as described earlier and shown in Fig. 7. A fully three-dimensional Navier-Stokes simulation was performed even though the geometry is in fact axisymmetric.

Predicted velocity vectors are shown in Fig. 24 and in two zoomed views near the two sets of seals in Figs. 25 and 26. A zoomed view of the predicted Mach numbers near the right-hand seal is shown in Fig. 27. The area ratios in the geometry are such that the seals are choked (this is how the flow rate is controlled) and the inlet Mach number is of the order of 0.05. The seals have associated with them a strong and strikingly crisply resolved jet-vortex structure, especially the right-hand seals as shown in Figs. 26 and 27. The form of this structure is of significance to the heat transfer characteristics of the configuration and allows the location of potential hot spots to be identified.

Concluding Remarks

• This paper has attempted to show that by adopting a simple but systematic approach toward mesh generation the applicability of three-dimensional Navier-Stokes simulations can be extended toward arbitrary geometries.

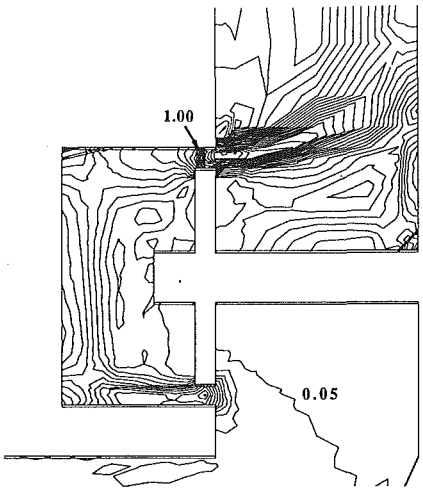

Fig. 27 Zoom view of the predicted Mach numbers near the right seal (interval 0.05)

- The simulations presented here demonstrated a very wide range of the type of simulation now possible.
- An inviscid solution for the classic channel hump but on a viscous mesh showed that the flow solver was capable of second-order accurate solutions and with low integrated total pressure error.
- For several of the more complex simulations no experimental data are yet available. In three of the "simpler" cases, comparisons were possible with data and satisfactory levels of agreement were achieved for the V2 compressor cascade and the transonic fan, but rather less so for the centrifugal impeller.
- All the simulations were performed on an inexpensive and relatively slow workstation. Typically between 2000 and 4000 time steps were used to converge the solution. The mesh adaption acts as a multiple-grid convergence accelerator in the sense that solutions are cheap and rapid to converge on the initial, coarse meshes; each refined mesh then has a good initial guess and again converges quickly and by the time a fine mesh is reached only local details are changing.
- The benefits of unstructured meshing, solution adaption, and a general purpose flow solver combine to produce a very powerful analytical ability.

References

Calvert, W. J., and Herbert, M. V., 1980, "An Inviscid-Viscous Interaction Method to Predict the Blade-Blade Performance of Axial Compressors," *Aero Quarterly*, Vol. XXXI.

Dawes, W. N., 1988, "Analysis of 3D Viscous Flows in Transonic Compressors," VKI-LS-03, Transonic Compressors.

Dawes, W. N., 1991, "The Development of a Solution-Adaptive 3D Navier-Stokes Solver for Turbomachinery," Paper No. AIAA-91-2469.

Dawes, W. N., 1992a, "The Simulation of Three-Dimensional Viscous Flow in Turbomachinery Geometries Using a Solution-Adaptive Unstructured Mesh Methodology," ASME JOURNAL OF TURBOMACHINERY, Vol. 114, pp. 528–537.

Dawes, W. N., 1992b, "The Solution-Adaptive Numerical Simulation of the 3D Viscous Flow in the Serpentine Coolant Passage of a Radial Inflow Turbine," ASME Paper No. 92-GT-193; ASME JOURNAL OF TURBOMACHINERY, in press.

Dunker, R., Strinning, P. E., and Weyer, H. B., 1977, "Experimental Study of the Flowfield Within a Transonic Axial Compressor Rotor by Laser Velocimetry and Comparison With Throughflow Calculations," ASME Paper No. 77-GT-28.

Eckardt, D., 1976, "Detailed Flow Investigations Within a High Speed Centrifugal Compressor Impeller," ASME Paper No. 76-FE-14.

Giles, M. J., and Haimes, R., 1990, "Advanced Interactive Visualisation for CFD," *Computing Systems in Engineering*, Vol. 1, No. 1, pp. 51–62.

Jameson, A., and Baker, T. J., 1987, "Improvements to the Aircraft Euler Method," AIAA Paper No. 87-0452.

Kansa, E. J., 1988, "A Comparative Study of Finite Difference and Multiquadratic Schemes for the Euler Equations," *Simulation*, Nov., pp. 180–183.

Lam, C. K. G., and Bremhorst, K. A., 1981, "Modified Form of the k-ϵ Model for Predicting Wall Turbulence," ASME *Journal of Fluids Engineering*, Vol. 103.

Lohner, R., 1987, "Three-Dimensional Grid Generation by the Advancing Front Method," in: *Numerical Methods in Laminar and Turbulent Flow*, Pineridge Press, United Kingdom.

Martinelli, L., 1987, "Calculations of Viscous Flows With a Multigrid Method," PhD Dissertation, Princeton University, Oct.

Patel, V. C., Rodi, W., and Scheuerer, G., 1985, "Turbulence Models for Near-Wall Flows and Low Reynolds Numbers: a Review," *AIAA Journal*, Vol. 23, No. 9.

Peraire, J., Peiro, J., Formaggia, L., Morgan, K., and Zienkiewicz, O., 1988, "Finite Element Euler Computations in Three Dimensions," *Int. Journal for Numerical Methods in Engineering*, Vol. 26.

Snyder, P. H., and Roelke, R. J., 1988, "The Design of an Air-Cooled Metallic High Temperature Radial Turbine," Paper No. AIAA-88-2872.

Viscous Throughflow Modeling for Multistage Compressor Design

M. A. Howard

S. J. Gallimore

Rolls-Royce plc,
Derby DE2 8BJ, United Kingdom

An existing throughflow method for axial compressors, which accounts for the effects of spanwise mixing using a turbulent diffusion model, has been extended to include the viscous shear force on the endwall. The use of a shear force, consistent with a no-slip condition, on the annulus walls in the throughflow calculations allows realistic predictions of the velocity and flow angle profiles near the endwalls. The annulus wall boundary layers are therefore incorporated directly into the throughflow prediction. This eliminates the need for empirical blockage factors or independent annulus boundary layer calculations. The axisymmetric prediction can be further refined by specifying realistic spanwise variations of loss coefficient and deviation to model the three-dimensional endwall effects. The resulting throughflow calculation gives realistic predictions of flow properties across the whole span of a compressor. This is confirmed by comparison with measured data from both low and high-speed multistage machines. The viscous throughflow method has been incorporated into an axial compressor design system. The method predicts the meridional velocity defects in the endwall region and consequently blading can be designed that allows for the increased incidence, and low dynamic head, near the annulus walls.

Introduction

An axisymmetric throughflow calculation is an essential part of the design process for multistage axial flow compressors and any improvement in its ability to model the three-dimensional unsteady viscous flow in real machines should lead to improved designs.

Ultimately it can be imagined that three-dimensional viscous calculations can be linked together to give a complete definition of the flow field for multistage machines (for example based on the work of Adamczyk, 1985; Dawes, 1990; Denton, 1992). It is likely, however, that these methods will require significant computer resources, and so a requirement remains for a simpler method that incorporates the most important aspects of the complex flow field, yet can be used quickly and often in the design process. The most appropriate method of achieving this is by further development of axisymmetric throughflow calculations. This approach is also attractive in that it retains the basic structure of the existing design procedure, an important consideration when a large amount of effort has been expended in setting up current design systems.

One of the most obvious deficiencies in current throughflow methods is the inviscid modeling of the flow near the endwalls. This limitation is usually dealt with by adding the viscous effects onto the basic throughflow solution by using separate annulus wall boundary layer or secondary flow calculations, or by including empirical blockage factors.

The problems associated with this approach are well known and it is not appropriate to go into more detail here, as the current situation has recently been reviewed by Cumpsty (1989). It is clear that existing techniques have not yet produced a satisfactory solution to the problem of modeling the endwall flows in an axisymmetric throughflow model of a multistage compressor.

Objective and Approach

The aim of the work described in this paper was to develop a method that overcomes the most serious shortcomings of the conventional inviscid throughflow approach while retaining short computational time. The method should thus be suitable for routine use in axial compressor design systems.

The approach adopted is to include a viscous shear force, consistent with a no-slip condition, on the annulus walls in a streamline curvature throughflow code that contains the turbulent diffusion model for spanwise mixing effects. In this way the velocity defects close to the annulus walls are included in the basic formulation of the numerical scheme.

It is recognized that a steady axisymmetric calculation cannot predict the complete three-dimensional unsteady flow field in a multistage compressor. However, the philosophy followed here has been to incorporate the dominant effects not currently included in throughflow calculations such as the endwall shear force.

The three-dimensional effects due to the interaction between the aerofoils and the endwall boundary layer are not part of the axisymmetric formulation but can be added empirically by specification of physically realistic loss and deviation in the endwall regions.

Contributed by the International Gas Turbine Institute and presented at the 37th International Gas Turbine and Aeroengine Congress and Exposition, Cologne, Germany, June 1–4, 1992. Manuscript received by the International Gas Turbine Institute February 24, 1992. Paper No. 92-GT-302. Associate Technical Editor: L. S. Langston.

Advantages of the Viscous Throughflow Method

Realistic velocity profiles near the annulus walls are predicted by this new approach, which eliminates the need for empirical factors such as blockage or independent annulus wall boundary layer calculations. The increased blading incidence associated with the near-wall velocity defects is therefore also predicted, and this allows improved blade design in the endwall region.

Despite this advantage over conventional throughflow methods, the required computational time is small compared to three-dimensional methods.

The viscous throughflow method also has improved compatibility with three-dimensional methods, allowing them to be used on selected blade rows, since it predicts the realistic variation of all flow parameters across the whole span. These are required as inlet conditions for three-dimensional calculations.

Mathematical Model and Discretization

The basic mathematical model for spanwise mixing, used in the throughflow method, is unchanged from that described by Gallimore (1985, 1986). The throughflow method differs from a conventional streamline curvature approach in the calculation of changes in entropy, tangential momentum, and stagnation enthalpy along a streamline. These are evaluated using forms of the energy, tangential momentum, and meridional momentum equations, which include viscous terms to model spanwise mixing. Full details are available from Gallimore (1985, 1986).

The use of viscous terms in the turbulent diffusion model of spanwise mixing makes it a relatively simple matter to specify an endwall shear stress. The high shear stresses close to the wall were, however, found to increase discretization error. With some numerical schemes this leads to significant errors in stagnation enthalpy. These errors have been avoided by developing a finite difference method, which, for the special case of unity Prandtl number, mirrors exactly the canceling out of heat transfer, dissipation, and shear work terms that occurs in the governing differential equations. This leads to conservation of mass-averaged stagnation enthalpy in the stationary frame and mass average rothalpy in the rotating frame.

This improved model has been incorporated in a design system based on the streamline curvature throughflow method described by Jennions and Stow (1985). This method utilizes a fixed grid on each quasi-orthogonal.

The concept of the finite difference scheme can be outlined by considering axial flow in a duct. The following equation for the meridional gradient of stagnation enthalpy can be obtained by combining the momentum and energy equations (Appendix):

$$r\rho V_z \frac{\partial H_o}{\partial m} = \frac{\partial}{\partial r}\left(\frac{r\mu_t}{\mathrm{Pr}_t}\frac{\partial H_o}{\partial r}\right) - \frac{\partial}{\partial r}\left(\frac{\mu_t r}{\mathrm{Pr}_t} V_z \frac{\partial V_z}{\partial r}\right) + r\mu_t\left(\frac{\partial V_z}{\partial r}\right)^2 + V_z\frac{\partial}{\partial r}\left(\mu_t r\frac{\partial V_z}{\partial r}\right) \quad (1)$$

dissipation shear work

This equation obeys the first law with global conservation of stagnation enthalpy when integrated from hub to tip with appropriate boundary conditions. For the special case of unity Prandtl number the last three terms of Eq. (1) cancel out, leaving a diffusion equation for stagnation enthalpy change along a streamline. (This special case with Prandtl number of unity provides a check on the finite difference scheme although a Prandtl number of 0.9 was used in the compressor calculations described in this paper.) If we further specify that stagnation enthalpy is uniform across the span at duct inlet the equation tells us that there is no change in stagnation enthalpy along any of the streamlines.

The finite differencing scheme has been formulated so that the latter terms in the equation above still cancel out when they are written in their finite difference form. To illustrate this we again consider axial flow in a duct with the further simplification that the duct is at a large radius to avoid the analysis becoming overly long. The combination of the energy and momentum equations for this special case yields:

$$\rho V_z \frac{\partial H_o}{\partial m} = \frac{\partial}{\partial r}\left(k_t\frac{\partial T}{\partial r}\right) + \mu_t\left(\frac{\partial V_z}{\partial r}\right)^2 + V_z\frac{\partial}{\partial r}\left(\mu_t\frac{\partial V_z}{\partial r}\right) \quad (2)$$

The computational mesh is shown diagrammatically in Fig. 1. Suffixed values of parameters are those at the junction of streamlines and quasi-orthogonals, e.g., V_{z3}. To evaluate radial derivatives, flow properties are assumed to vary linearly between streamlines. The derivatives are calculated on the faces of the computational element, which extends halfway between adjacent streamlines, shown by dashed lines in Fig. 1.

Considering first a calculation box away from the endwall, we can write for streamline 2 on any quasi-orthogonal:

$$\mu_t\left(\frac{\partial V_z}{\partial r}\right)^2 = \left(\frac{\Delta r_{\mathrm{top}}}{\Delta r_{\mathrm{bot}}+\Delta r_{\mathrm{top}}}\right)\mu_{t\mathrm{top}}\left(\frac{V_{z3}-V_{z2}}{\Delta r_{\mathrm{top}}}\right)^2 + \left(\frac{\Delta r_{\mathrm{bot}}}{\Delta r_{\mathrm{bot}}+\Delta r_{\mathrm{top}}}\right)\mu_{t\mathrm{bot}}\left(\frac{V_{z2}-V_{z1}}{\Delta r_{\mathrm{bot}}}\right)^2 \quad (3)$$

This represents an average value of dissipation function made up from area-weighted values of the derivative calculated on the top and bottom of the box. This area weighting allows

Nomenclature

r, θ, z = cylindrical coordinate system
m = meridional direction
c_p = specific heat at constant pressure
E_z = axial shear force (Eq. (12))
h = distance from inner wall
H_o = stagnation enthalpy
k_t = eddy thermal conductivity
l = mixing length
P = static pressure
P_o = total pressure
Pr_t = turbulent Prandtl number = $\mu_t C_p/K_t$
s = entropy
T = static temperature
V = flow velocity
V_τ = friction velocity
U_{mid} = mid height blade speed
y = distance from the wall
y^+ = yV_τ/ν
y_{sub} = laminar sublayer thickness
δ = deviation
κ = Von Karman constant
μ_t = eddy viscosity
ν = kinematic viscosity
ν_t = kinematic eddy viscosity
ρ = density
ϕ = dissipation function (Eq. (10))
ψ = pressure rise coefficient = $(P_o - \overline{P}_o^{\mathrm{in}})/1/2\rho U_{\mathrm{mid}}^2$
ω = pressure loss coefficient = $(P'_{o2\mathrm{is}} - P'_{o2})/(P'_{o1} - P_1)$
$\partial s_e/\partial m$ = meridional entropy gradient from empirically specified aerofoil loss coefficients

Subscripts

1 = aerofoil inlet, or first streamline away from wall
2 = aerofoil exit, or second streamline away from wall
is = isentropic process value

Superscripts

in = inlet to compressor (upstream of inlet guide vane)
$\bar{}$ = mass average value
$'$ = relative value

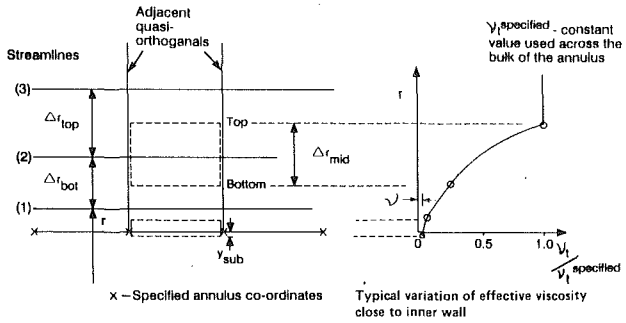

Fig. 1 Computational mesh and variation of effective viscosity

terms that cancel out in the differential equation similarly to cancel in the finite difference equation.

The third term on the right-hand side of Eq. (2) is written as:

$$V_z \frac{\partial}{\partial r}\left(\mu_t \frac{\partial V_z}{\partial r}\right) = \frac{V_{z2}}{\Delta r_{\text{mid}}}\left[\mu_{t\text{top}}\left(\frac{V_{z3}-V_{z2}}{\Delta r_{\text{top}}}\right) - \mu_{t\text{bot}}\left(\frac{V_{z2}-V_{z1}}{\Delta r_{\text{bot}}}\right)\right] \quad (4)$$

A similar form is used for the heat transfer term.

By substituting for static temperature in terms of stagnation enthalpy and velocity, along with substitution of unity Prandtl number, the resulting finite difference equation shows that the velocity dissipation term is canceled out by terms arising from heat transfer and shear work. This achieves the objective of giving a numerical scheme that conserves stagnation enthalpy in a manner required by the governing differential equations for both idealized (e.g., uniform) and practical compressor flows.

The flow on the streamlines adjacent to the wall can be calculated in a similar manner to that shown above except that the calculation box is artificially extended beyond the specified annulus coordinates by a sublayer thickness y_{sub}, as shown in Fig. 1. The specified annulus coordinates are used to define a "streamline adjacent to the wall," which is taken to be the edge of the laminar sublayer. The axial and tangential velocities are assumed to vary linearly from their levels on this streamline to zero at the edge of the extended calculation box (the "real endwall"). Heat transfer is assumed to be zero through the outer face of the extended calculation box (i.e., on the "real endwall"). The value of y_{sub} can be calculated from a knowledge of the velocities on the wall streamline and a specified value of the Reynolds number based on friction velocity and distance from the wall (y^+). Typical values of y_{sub} used in the calculations are of the order of 0.1 percent span, so that they can be ignored in the rest of the throughflow calculation with a negligible loss in accuracy.

Model for Mixing and Endwall Shear

Much work has been carried out to understand the phenomena of spanwise mixing and the relative contributions of deterministic time-averaged radial flow and turbulent mixing. Wennerstrom (1991), in his review of spanwise mixing, has observed that an advantage of the turbulent diffusion model is that it is simpler to code and easier to understand. This paper will not seek to clarify further the physics of spanwise mixing but retains the earlier (Gallimore, 1986) approach where the turbulent diffusion model for spanwise mixing is used. Further refinement of the throughflow model for spanwise mixing seems unnecessary since a more complete and rigorous mathematical approach such as that derived by Adamczyk (1985) is required to treat deterministic and random diffusion separately.

Consistent with the earlier work by Gallimore (1986), a numerical value of turbulent viscosity is specified to model the spanwise mixing phenomena. The same value is used in the outer part of the wall boundary layer and in the middle portion of the annulus; the specified value applies between about 5 and 95 percent heights. The discretization utilizes a laminar sublayer model and some formulation for turbulent viscosity is required from the edge of the sublayer to the outer portion of the wall boundary layer. The standard near-wall mixing length model of linear increase from the wall using a Von-Karman constant of 0.41 is utilized, i.e.,

$$l = \kappa y \quad (5)$$

The buffer layer is not modeled so the laminar sublayer is taken to extend to a Reynolds number based on friction velocity and distance from the wall (y^+) of 12.5.

The aim of this formulation is to provide a simulation of the near-wall passage-averaged velocities that gives sensible velocity defects and hence implicitly models radial blockage. A more sophisticated model seems unwarranted since the real flow is extremely nonaxisymmetric (Moore and Richardson, 1957) and the use of the streamline curvature method limits the cross-stream grid resolution near the endwall (Gallimore, 1985).

In the computation of turbulent viscosity from mixing length and velocity gradient a minimum value of velocity gradient is assumed to ensure that the turbulent viscosity rises to the specified level at some distance from the wall (a finite turbulent viscosity is required over the whole span to model spanwise mixing), i.e.,

$$\nu_t = l^2 \frac{\partial V}{\partial y} \quad (6)$$

$$\frac{\partial V}{\partial y} = \max\left(\left(\frac{\partial V}{\partial y}\right)_{\text{calculated}}, \text{limit}\right) \quad (7)$$

An example of the turbulent viscosity rising through the annulus wall boundary layer to the specified value is shown in Fig. 1.

Different values of the velocity gradient limit have been tried and the results are not overly sensitive. A higher limit forces the viscosity to rise to the specified level closer to the wall. The velocity gradient is computed using the velocity relative to the wall. For example, the velocity in the relative frame is used to calculate the velocity gradient for the hub underneath a cantilevered stator.

It is recognized that this formulation is rather simple compared to the complex skewed nature of the three-dimensional endwall flow, but the objective is to produce a simulation that gives satisfactory results in the framework of a streamline curvature throughflow method. Another standard assumption in common with boundary layer methods is to take the turbulent Prandtl number as 0.9 across the whole span in the absence of better information.

The coding has been checked by performing calculations in an annular duct with one-seventh power law velocity profiles specified at hub and tip at the inlet plane. The growth of displacement thickness agreed favorably with expectation, confirming that the near-wall velocity defects implicitly contain the blockage of the endwall boundary layer in this simple case.

Effect of Including Endwall Shear in the Throughflow Method

The improvement to the throughflow solution due to the modeling of endwall shear alone is demonstrated in Fig. 2. A viscous throughflow calculation using the mathematical and physical models described in the previous two sections is compared with a conventional solution, and with measurements, for the third stage exit of a high-speed compressor (which is

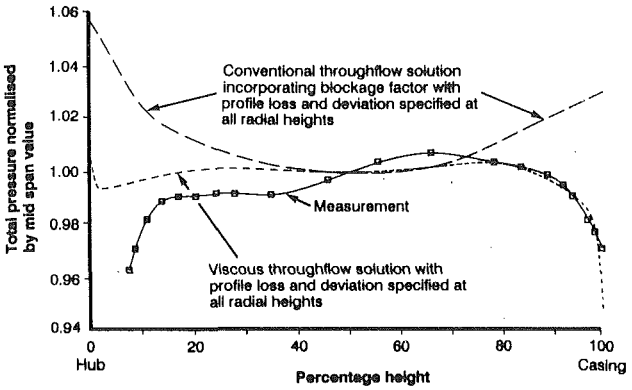

Fig. 2 "Two-dimensional" predictions of total pressure profiles, downstream of Stage 3, high-speed compressor, compared to measurement

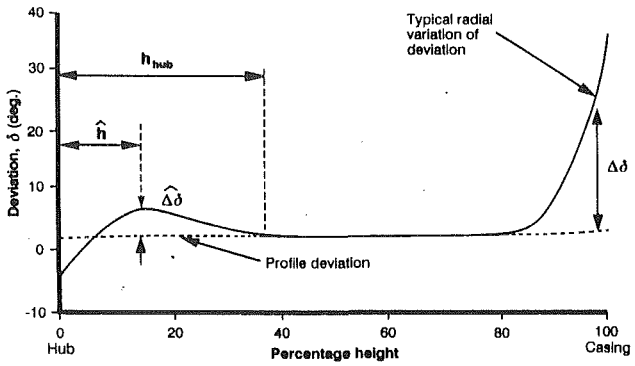

Fig. 3 Typical form of rotor deviation

described in a later section of this paper). For both the viscous and conventional throughflow solutions, the specified aerofoil loss and deviation are profile ("two-dimensional") values across the entire span, with no empirical adjustment for three-dimensional effects. Some endwall losses are calculated as part of the viscous solution, but these do not account for three-dimensional effects due to the interaction between the endwall flow and the aerofoils. The addition of endwall shear has enabled the reduction of total pressure close to the endwalls to be calculated by the viscous throughflow solution. By contrast the conventional throughflow method gives a gradient of total pressure toward the annulus wall of opposite sign to that measured. The viscous throughflow solution gives sensible reductions of total pressure, and hence meridional velocity, close to the endwalls. This removes the need to specify blockage factors for viscous throughflow solutions.

The viscous solution shown in Fig. 2 is a "two-dimensional" (actually quasi-three-dimensional) prediction obtained by the combination of a blade-to-blade method and the viscous throughflow method. While this clearly demonstrates the marked benefits due to including endwall shear, further modeling is required to obtain a viscous throughflow method suitable for design calculations. This is because only profile losses, and annulus losses arising from shear flow in the wall boundary layer, are included in this prediction. This results in the calculated efficiency being too high. The additional modeling required is outlined in the following section.

Empirical Model for Aerofoil Loss and Deviation

The viscous throughflow method can be further refined by specifying appropriate spanwise variations of loss and deviation to model the complex three-dimensional flow effects due to the aerofoil and endwall boundary layer interaction, such as tip clearance flows and corner separations. These effects cannot be predicted by the throughflow model because of its assumption of axisymmetric flow.

The spanwise distributions of loss and deviation required for the viscous throughflow method are different from those needed in a standard throughflow calculation, because both spanwise mixing and endwall shear contribute to loss and deviation. In particular, the inclusion of mixing allows realistic, rather than artificially smoothed, loss distributions to be specified across the span as discussed by Gallimore (1986).

The approach taken is in two parts. Firstly, spanwise distributions of profile loss and deviation are calculated using a quasi-three-dimensional ("two-dimensional") blade-to-blade method with a coupled boundary layer solution (following Calvert, 1982; Newman and Stow, 1985). For these calculations the inlet conditions near the annulus walls are estimates of those that would exist if the fluid were inviscid in the sense that it could slip along the annulus wall. This gives a consistent estimate of profile ("two-dimensional") loss and deviation across the whole span. The low dynamic heads and high incidences predicted near the endwalls by the viscous throughflow method are not compatible with a two-dimensional blade-to-blade calculation since the flow parameters vary rapidly normal to the calculation plane and there are significant radial flows. Wadia and Beacher (1990) showed that two-dimensional methods give misleading results close to the endwall when realistic inlet conditions are used.

These basic distributions of loss and deviation, which may be thought of as defining the primary flow field, are then modified to take into account tip clearances and other three-dimensional effects caused by the interaction of the blading with the endwall boundary layer. These modifications are based on correlations derived from a variety of multistage compressor measurements available to the authors, as well as from data published in the open literature.

The same form of loss and deviation in the endwall regions, in addition to profile levels, has been observed for a large number of compressors. This form for rotor deviation is shown in Fig. 3. The changes in loss and deviation in the endwall regions, $\Delta\omega$ and $\Delta\delta$, which are functions of radius, are termed three-dimensional loss and deviation for convenience in this paper. Additional evidence of the generality of the correlations for three-dimensional loss and deviation is that they have a similar form to those published by Roberts et al. (1986, 1988) for stators and blade ends with clearance. They have a different form, however, in the hub region of the rotor where a combination of secondary flow and corner stall leads to both underturning and overturning as shown in Fig. 3. Several measured examples of both underturning and overturning at rotor hubs are given by Robinson (1991). The author's correlation includes a term in the rotor hub three-dimensional loss and deviation to account for centrifuging of the corner stall (and therefore the extent of three-dimensional loss and deviation, h_{hub}) dependent upon the degree of profile separation and the lack of radial equilibrium of fluid moving at blade speed. An example of this is shown in Fig. 4, where for a separated double circular arc rotor the three-dimensional effects associated with the hub extend over a large proportion of the annulus height.

Figure 4 also shows that the losses from the converged viscous throughflow solution are not the same as those specified in the endwall regions. The difference is due to viscous dissipation and energy exchange between streamlines, which are part of the viscous throughflow solution. Further explanation is possible by examining the following equation for entropy along meridional streamlines, which is used within the viscous throughflow method:

$$\frac{\partial s}{\partial m} = \underbrace{\frac{1}{r\rho TV_m}\frac{\partial}{\partial r}\left(rk_t\frac{\partial T}{\partial r}\right)+\frac{\phi}{\rho TV_m}}_{\text{loss computed directly}} + \underbrace{\frac{\partial s_e}{\partial m}}_{\text{loss specified}} \tag{8}$$

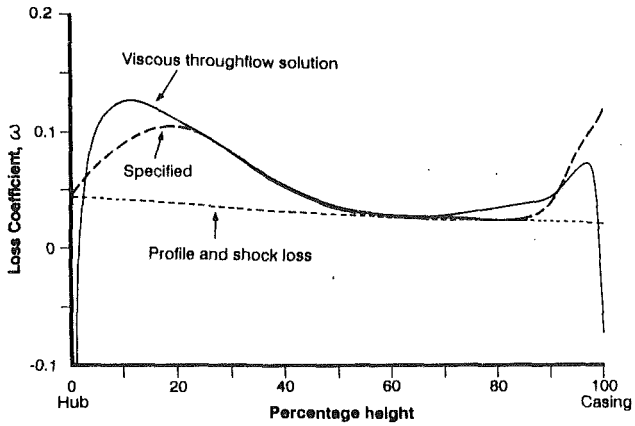

Fig. 4 Example of loss coefficient for DCA rotor

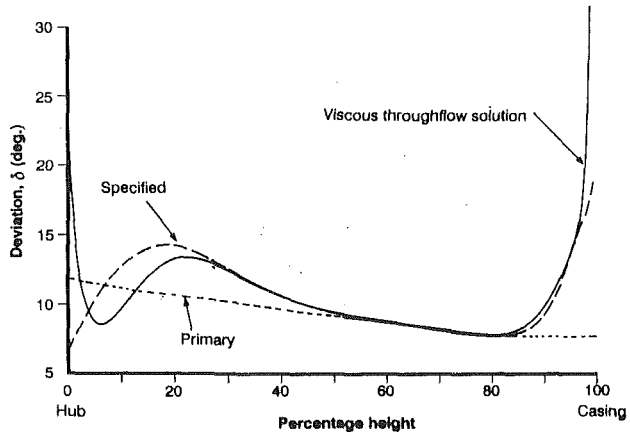

Fig. 5 Example of deviation for DCA rotor

This equation, integrated between leading and trailing edge, will give entropy change across a blade row. The first two terms give the entropy change (i.e., loss), which will be calculated as part of the viscous throughflow solution. The latter term represents entropy increases due to specified empirical loss coefficients, i.e., the curve labeled "specified" in Fig. 4. The endwall loss computed by the viscous throughflow method is the difference between the specified losses and those derived from the viscous solution.

The energy exchange between streamlines reduces the requirement to specify the three-dimensional loss coefficient accurately near the endwall where the blades are attached (i.e., where there is no leakage). This is because the endwall shear and energy exchange will dominate the entropy change adjacent to the annulus walls. The near-wall detail shown in Fig. 4 highlights the viscous nature of the calculation by showing negative loss when there is no relative motion between aerofoil and wall. A negative loss along a streamline is a standard feature of a viscous diffusing flow near to a wall. It is caused by energy addition to the near-wall fluid by that farther from the wall, which enables attached flow in adverse pressure gradients.

The associated radial variation of deviation for the double circular arc aerofoil is shown in Fig. 5. A feature of the correlations developed is that the radial extent of the three-dimensional deviation is consistent with the variation in three-dimensional loss, Fig. 4. In a manner analogous with the entropy, some of the change to tangential velocity is due to viscous forces, and this causes the generally small variations between the specified deviation and that in the solution between 20 percent height and the casing (Gallimore, 1986). Close to the endwall where the blade is attached the secondary flow overturning is derived by holding the tangential blade force constant. This reduces the need for empirical input. The region over which the tangential blade force is constant is derived from the specified radial variation of pressure loss coefficient. For the example presented in Fig. 5 the tangential blade force is constant between the hub and 20 percent height. This explains the difference in this region between the specified deviation and that of the viscous throughflow solution.

The models for three-dimensional aerofoil loss and deviation outlined above are utilized by the viscous throughflow method for two purposes. First the method must give realistic efficiency predictions to be of value as a design method, and, secondly, they allow three-dimensional features, such as corner stall to be included in the throughflow solution. However, as shown in the previous section the viscous throughflow method radically improved the predictive capability by the modeling of endwall shear alone. The detailed form of empirical adjustments to aerofoil loss and deviation are therefore of secondary importance. The novel feature of the viscous throughflow method is that a shear force, consistent with a no-slip condition, is part of the solution. The sensitivity of the viscous throughflow method to the empirical adjustments of aerofoil three-dimensional loss and deviation has been assessed. Changes to the solution caused by alternative empirical adjustments of aerofoil loss and deviation are small compared to the radical improvement caused by modeling endwall shear.

Evaluation of the Viscous Throughflow Method

Two compressor cases are presented comparing results from the viscous throughflow method, outlined in the previous sections of this paper, with measurements. The viscous throughflow results are predictions insofar as a fixed method is used for the two cases. It is, however, true that the method, particularly the model for blade three-dimensional loss and deviation, has been refined by comparison with a range of compressor cases, including those presented here. The need for consistency in the viscous throughflow modeling across a range of cases constrains markedly the ability to match measured data. Differences between prediction and measurement can be partially attributed to this.

The objective of comparing viscous throughflow predictions with measurement is to show the radical improvement possible by including endwall shear. The role of further empirical modeling is also shown where three-dimensional features, such as corner stall, can be included.

Four-Stage Low-Speed Compressor. An objective of the low-speed investigation is to compare the predictions with total pressure measurements close to the annulus walls in order to validate the model for endwall shear and turbulent viscosity. Measurements close to the endwalls are available from low-speed rigs due to their large physical size.

The measurements for this case are from a build of the low reaction compressor described by Robinson (1991) but with larger clearances. Each stage of this compressor has twisted controlled diffusion blading with a midspan preswirl angle of 19.2 deg. The low-speed blading is thickened to model the surface pressure distribution of a high speed compressor. The stators are cantilevered. Other details are given in Table 1.

The third stage of the machine achieved the repeating stage flow condition when measured, and only this stage is predicted. The throughflow solution was performed several times using the computed exit conditions to respecify the inlet plane data. This process was continued until the desired accuracy in the repeating stage condition is achieved in the viscous throughflow solution. The throughflow calculation is carried out using 28 axial planes with four axial planes inside both rotor and stator. This refinement of the axial mesh is necessary to retain numerical stability when a refined radial mesh is used. A total

Table 1 Details of four-stage low-speed compressor

		Rotor	Stator
Tip Diameter (mm)		1220	
Hub/Tip Ratio		0.85	
Rotational Speed (rpm)		850	
No. of Blades		79	72
Chord (mm)		57.2	58.2
Aspect Ratio		1.6	1.57
Space/Chord Ratio	Mid	.785	.846
Inlet Metal Angle (deg.)	Height	54.6	47.8
Camber (deg.)		33.6	31.6
Thickness/Chord Ratio		.117	.094
Clearances/Chord		.049	.045

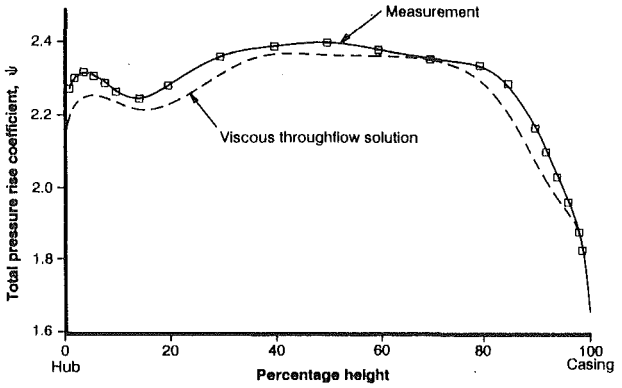

Fig. 6 Total pressure profiles downstream of the third rotor of the four-stage low-speed compressor

of 21 points are used radially with near-wall grid points 1, 3, 6, and 10 percent of height from each endwall.

The free-stream mixing level is taken to be the value measured on the same facility with an earlier set of blading (Gallimore and Cumpsty, 1986). The measured value of mass flow is specified for the throughflow solution.

The predicted and measured profiles of total pressure are shown downstream of the third rotor in Fig. 6. The stagnation pressure gradients close to the endwalls are well predicted at both hub and tip, which indicates that the model for endwall shear and turbulent viscosity is performing well. Since the static pressure gradient will be small, compared to the velocity gradient close to the walls, this comparison suggests that the near-wall velocity gradient is well predicted. There is a local minimum in total pressure rise at 15 percent height due to some form of corner stall. The viscous throughflow solution predicts this feature since the correlations in the rotor hub region give both the underturning and overturning associated with this three-dimensional effect.

The predicted and measured swirl angles are shown in Fig. 7. The measured trends are reproduced by the predictions. However, at stator exit the correlation for three-dimensional deviation appears to have overestimated the hub clearance deviation at around 10 percent height. The radial integrations of profile and endwall losses in the solution are fairly accurate since the predicted efficiency is within 1/2 percent of the measured value.

The comparison of measured and predicted yaw angles at the stator exit shown in Fig. 7 also indicates that the constant tangential blade force model gives excessive overturning at the stator casing. This would suggest that a significant corner stall is occurring here and that the stator is unloading closer to the casing. This stator flow has been predicted using a three-dimensional Navier-Stokes code by Robinson et al. (1989). These predictions are for the same blading but at smaller hub and tip clearances. This three-dimensional prediction also showed greater overturning than measurement.

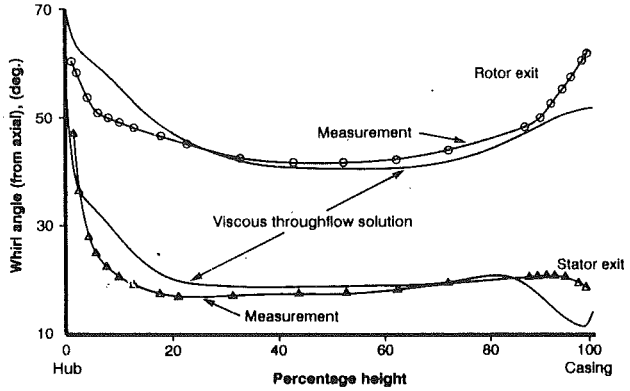

Fig. 7 Absolute whirl angles in third stage of the low-speed four-stage compressor

Four-Stage High-Speed Compressor. Details of the high-speed test case, designated C147, have been published by Calvert et al. (1989). The machine is a highly loaded reaction compressor with a design pressure ratio of 4.0, and double row outlet guide vanes. The exit hub/tip ratio is 0.912. The first three stators are cantilevered. Hub and tip clearances are low; the measured average rotor tip clearance is about 1 percent of annulus height.

For the viscous throughflow calculation 96 axial stations are used with typically four inside each blade row. The inlet guide vane and double row outlet guide vane are included in the calculation. The free-stream mixing coefficient is estimated using the method given by Gallimore and Cumpsty (1986). A refined radial mesh is used close to the annulus walls with points at 1, 3, 6, and 10 percent of annulus height from each endwall. The refinement in the calculation mesh, as well as the additional computation required for the viscous aspects of the method, imply increased computational time. The viscous throughflow solution took 6 minutes on an IBM 3090. While this time is high compared to a conventional inviscid throughflow calculation (8 seconds) it is small enough to allow the method to be used routinely. The time for the viscous throughflow solution is, however, very small compared to that required for three-dimensional solutions for similar aerofoils. It is estimated that a minimum of 50 hours on an IBM 3090 would be required for a three-dimensional calculation of the 10 blade rows of the C147 compressor using sensible grids of about 100,000 points per blade.

The advantage of the new method compared to an inviscid throughflow method utilizing blockage factors (i.e., a conventional throughflow solution) is highlighted in Fig. 8. This shows a viscous throughflow prediction of meridional velocity profile at stator 4 exit compared to a conventional throughflow solution. The distributions of velocity close to the walls predicted by the viscous throughflow method are typical turbulent boundary layer profiles giving confidence in the near-wall modeling of shear force and turbulent viscosity. All of the velocities shown are from the solution of the radial equilibrium equation: the first and last represent values at the edge of the laminar sublayer. The blockage in the viscous throughflow result is clearly shown with hub and tip displacement thicknesses of 2.1 and 3.0 percent of height, respectively.

The measured stator 3 exit total pressure profile is compared with both the viscous and conventional throughflow solutions in Fig. 9. The conventional inviscid throughflow method has to use unrealistic radial variations of loss coefficient that are too high at midspan and too low at the endwalls in order to

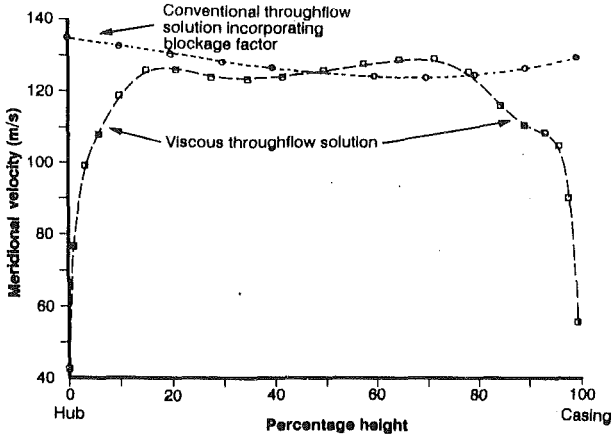

Fig. 8 Exit meridional velocity profiles from the four-stage high-speed compressor

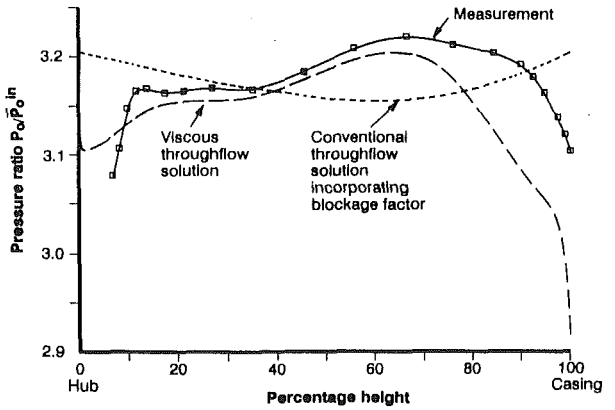

Fig. 9 Total pressure profiles downstream of Stage 3 of the high-speed four-stage compressor

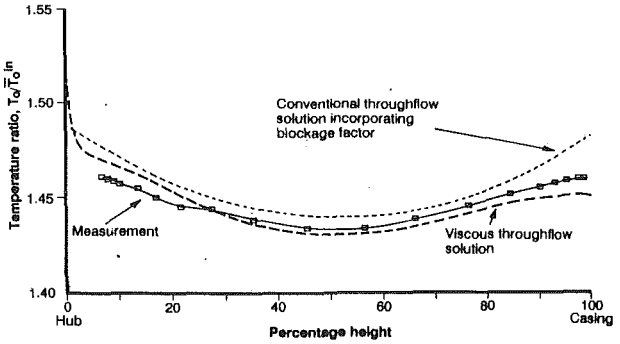

Fig. 10 Total temperature profiles downstream of Stage 3 of the high-speed four-stage compressor

achieve realistic temperature profiles (Gallimore, 1986). This, combined with the inviscid assumption, results in a poor prediction of the radial variation of total pressure. In contrast the viscous throughflow prediction is realistic across the whole span and quite good up to 70 percent span. Outboard of this the result is not as good, which is surprising given that the earlier "two-dimensional" prediction, without any empirical adjustment of loss and deviation (profile loss and deviation were specified over the whole span), was rather good in the tip region, Fig. 2. It would appear that the correlations have overestimated the three-dimensional effects close to the casing for this low tip clearance case.

The measured radial variation of total pressure has a "plateau" between 10 and 35 percent span and then rises rapidly with increasing radius. The contour plots of stator exit stagnation pressure, showing both the radial and blade to blade variations, presented by Calvert et al. (1989), allow this complex radial profile to be understood. The low total pressure in the region of the "plateau" is not associated with the stator wake but extends across the whole passage. This suggests that the low total pressure in this region is associated with some form of corner stall in the rotor. The correlations described in an earlier section give the underturning associated with this corner stall and the radial location (e.g., $\hat{h}$, Figs. 3 and 5) accounting for centrifuging of separated flow. Specification of three-dimensional deviation and loss from the correlations improves the viscous throughflow prediction from the standard shown in Fig. 2 to that shown in Fig. 9 from the hub to 70 percent height.

At the casing the three-dimensional effects are less important and a "two-dimensional" prediction with profile loss and deviation specified across the whole span yields a casing boundary layer that achieves a large proportion of the measured thickness, Fig. 2. This demonstrates the large improvement in the solution possible by the inclusion of endwall shear.

The specified loss and deviation for the second rotor are shown in Figs. 4 and 5 along with profile (or primary) loss and deviation. Also shown are the deviation and loss coefficient from the converged viscous throughflow solution. It is interesting that despite the high losses shown between the hub and midspan (Fig. 4), the machine has a high measured efficiency, as reported by Calvert et al. (1989). This suggests that this behavior is not untypical and shows the large potential for efficiency improvement by reduction of three-dimensional losses due to aerofoil and endwall boundary layer interaction. These large endwall losses contained in the viscous throughflow solution are felt to be realistic since the predicted efficiency is only 0.3 percent above the measured value.

The radial profile of stagnation temperature measured at the third stator's exit is compared with both conventional and viscous throughflow solutions in Fig. 10. The viscous throughflow prediction is very good and successfully captures the measured trend of reducing temperature gradient close to the casing. The conventional throughflow solution, despite the use of smoothed radial profiles of loss coefficient, is less good close to the casing. In contrast to this the viscous throughflow solution has simultaneously realistic radial variations of loss coefficient, Fig. 4, and temperature, Fig. 10. This is a fundamental advantage allowing regions of high loss to be accurately located. The energy input from the running hub can be observed in the viscous throughflow prediction from the hub to 3 percent annulus height, Fig. 10.

Discussion

The results of the calculations just presented have demonstrated the important effects of spanwise mixing and endwall shear on the radial distributions of total pressure, total temperature, and velocity in multistage axial flow compressors.

The benefits of including spanwise mixing have already been discussed in an earlier paper (Gallimore, 1986). One of these is the ability to predict realistic radial distributions of total temperature without artificially smearing the specified loss profiles over the span. However, an acknowledged simplification in the earlier work was the assumption of zero endwall shear and dissipation, which led to unrealistic predictions of total pressure profiles near the endwalls. Introducing endwall shear directly into the throughflow calculation allows a better prediction of the measured fall-off in total pressure near the annulus walls (Fig. 6). These are now combined with the prediction of realistic temperature profiles mentioned earlier.

To include the effects of aerofoil/endwall flow interactions, some form of correlation for three-dimensional blade loss and

turning is required. However, the details of these are not crucial because the viscous modeling provides loss generation near the endwalls. Some work is still required, particularly at blade ends with clearance. The complete model produces good agreement with measured efficiencies and has been used in recent high-pressure compressor designs. Work continues on improving the empirical aspects of the correlations.

The throughflow calculation can predict the complex shapes of the radial profiles measured in multistage axial flow compressors, as illustrated in Fig. 9. This example shows how it can be quite difficult to identify the edge of an annulus wall boundary layer a conclusion reached earlier by Cumpsty (1986) and Gallimore and Cumpsty (1986). The viscous throughflow method removes this difficulty because the same equations are being solved across the whole span and it is no longer necessary to discriminate between annulus wall boundary layer and free-stream flow. This is particularly important toward the rear of multistage compressors where the endwall effects can be seen across the entire span.

The calculations for the high-speed four-stage compressor have illustrated that realistic radial variations in total pressure and temperature can be achieved by the current model, unlike a conventional throughflow calculation (Figs. 9 and 10). This has important implications for the compressor designer because the resulting radial profiles of flow angle show different trends from those usually seen in standard throughflow solutions.

To illustrate this, Fig. 11 compares the relative inlet flow angles predicted by the conventional and viscous throughflow methods for rotor 4 of the high-speed compressor. The results from the two calculations have quite different radial distributions. In the hub region the conventional throughflow predicts a decrease in flow angle as the wall is approached while the viscous throughflow solution has a more constant value with some increase close to the wall. The difference between the predictions at the hub is about 5 deg. At the casing the conventional throughflow again predicts a decrease in flow angle as the wall is approached. The viscous prediction, however, predicts a large increase in flow angle due to the rapid drop in total pressure in this region. It is reasonable to suggest that the improved shapes of the radial distribution of total pressure and temperature described earlier (Figs. 9 and 10) have produced a more realistic prediction of flow angle from the viscous throughflow method. The calculation has therefore predicted the inlet skew near the endwalls leading to higher incidences there. The compressor designer is now able to take this variation in air angle into account when designing the ends of blades and use the viscous throughflow solution as realistic inlet conditions to three-dimensional viscous flow calculations for that blade row. This should lead to reductions in the losses associated with the blade ends.

Conclusions

A streamline curvature throughflow code that included the effects of spanwise mixing has been modified to include directly the viscous effects of endwall shear. This allows the velocity profiles close to the annulus walls to be modeled within the throughflow calculation itself, removing the need for empirical blockage factors or separate calculations of the annulus wall boundary layers. The only assumptions required to achieve this are a conventional estimate for the boundary layer laminar sublayer thickness and a near-wall turbulence model. Further refinement to model the fine detail of the complex three-dimensional endwall flows can be obtained by specifying physically realistic radial variations of blade deviation and loss.

The viscous throughflow calculations have been compared to multistage compressor measurements and shown to give realistic spanwise distributions of velocity, flow angle, pressure, and temperature across the whole annulus. This allows blading near the endwall to be designed to match the real flow conditions in those regions better.

The viscous throughflow method retains a sufficiently short computational time for routine use during the design process.

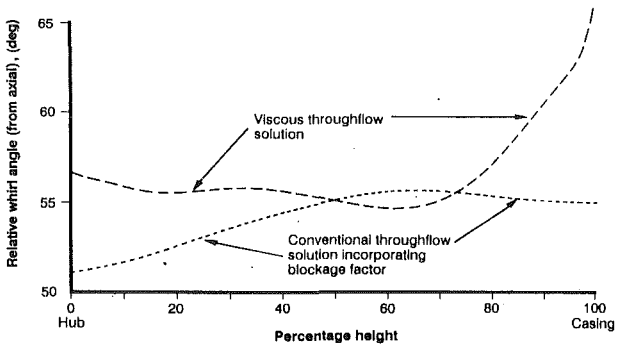

Fig. 11 Relative inlet whirl angles for the fourth rotor of the high-speed compressor

Acknowledgments

The authors would like to thank Rolls-Royce plc for permission to publish this work. Thanks are also due to the Department of Trade and Industry and the Defense Research Agency, Pyestock for permission to publish the test data for the C147 compressor.

Thanks are due to Mr. A. G. Wilson for providing analyzed low-speed data and his assistance in the viscous throughflow calculations. Finally the authors would like to thank Dr. M. V. Casey for his support and encouragement.

References

Adamczyk, J. J., 1985, "Model Equation for Simulating Flows in Multistage Turbomachinery," ASME Paper No. 85-GT-226.

Calvert, W. J., 1982, "An Inviscid-Viscous Interaction Treatment to Predict the Blade-to-Blade Performance of Axial Compressors With Leading Edge Normal Shock Waves," ASME Paper No. 82-GT-135.

Calvert, W. J., Ginder, R. B., McKenzie, I. R. I., and Way, D. J., 1989, "Performance of a Highly Loaded HP Compressor," ASME Paper No. 89-GT-24.

Cumpsty, N. A., 1986, "Annulus Wall Boundary Layer Measurement in a Four Stage Compressor," ASME *Journal of Engineering for Gas Turbines and Power*, Vol. 108, pp. 2–6.

Cumpsty, N. A., 1989, "Compressor Aerodynamics," Longman Group UK Ltd.

Dawes, W. N., 1992, "Toward Improved Throughflow Capability: The Use of Three-Dimensional Viscous Flow Solvers in a Multistage Environment," ASME JOURNAL OF TURBOMACHINERY, Vol. 114, pp. 8–17.

Denton, J. D., 1992, "The Calculation of Three-Dimensional, Viscous Flow Through Multistage Turbomachines," ASME JOURNAL OF TURBOMACHINERY, Vol. 114, pp. 18–26.

Gallimore, S. J., 1985, "Spanwise Mixing in Multi-stage Axial Compressors," PhD Thesis, University of Cambridge, United Kingdom.

Gallimore, S. J., and Cumpsty, N. A., 1986, "Spanwise Mixing in Multistage Axial Flow Compressors: Part I—Experimental Investigations," ASME JOURNAL OF TURBOMACHINERY, Vol. 108, pp. 2–9.

Gallimore, S. J., 1986, "Spanwise Mixing in Multistage Axial Flow Compressors: Part II—Throughflow Calculations Including Mixing," ASME JOURNAL OF TURBOMACHINERY, Vol. 108, pp. 10–16.

Jennions, I. K., and Stow, P., 1985, "A Quasi-Three-Dimensional Turbomachinery Blade Design System. Parts I and II," ASME *Journal of Engineering for Gas Turbines and Power*, Vol. 107, pp. 301–306.

Moore, R. W., Jr., and Richardson, D. L., 1957, "Skewed Boundary Layer Flow Near the Endwalls of a Compressor Cascade," *Transactions ASME*, Vol. 79, pp. 1789–1800.

Newman, S. P., and Stow, P., 1985, "Semi-inverse Mode Boundary Layer Coupling," presented at the IMA Conference on Numerical Methods for Fluid Dynamics, University of Reading, United Kingdom, Apr.

Roberts, W. B., Serovy, G. K., and Sandercock, D. M., 1986, "Modeling the Three-Dimensional Flow Effects on Deviation Angle for Axial Compressor Middle Stages," ASME *Journal of Engineering for Gas Turbines and Power*, Vol. 108, pp. 131–137.

Roberts, W. B., Serovy, G. K., and Sandercock, D. M., 1988, "Design Point Variation of Three-Dimensional Loss and Deviation for Axial Compressor Middle Stages," ASME JOURNAL OF TURBOMACHINERY, Vol. 110, pp. 426–433.

Robinson, C. J., 1991, "Endwall Flows and Blading Design for Axial Flow Compressors," PhD Thesis, Cranfield Institute of Technology, United Kingdom.

Robinson, C. J., Northall, J. D., and McFarlane, C. W. R., 1989, "Measurement and Calculation of the Three-Dimensional Flow in Axial Compressor Stators, With and Without End-Bends," ASME Paper No. 89-GT-6.

Wadia, A., and Beacher, B., 1990, "Three-Dimensional Relief in Turbomachinery Blading," ASME JOURNAL OF TURBOMACHINERY, Vol. 112, pp. 587–598.

Wennerstrom, A., 1991, "A Review of Predictive Efforts for Transport Phenomena in Axial Flow Compressors," ASME JOURNAL OF TURBOMACHINERY, Vol. 113, pp. 175–179.

APPENDIX

Starting from the equations given by Gallimore (1986) the energy equation for duct flow becomes:

$$\frac{\partial s}{\partial m}=\frac{1}{r\rho TV_m}\frac{\partial}{\partial r}\left(rk_t\frac{\partial T}{\partial r}\right)+\frac{\phi}{\rho TV_m}, \tag{9}$$

where ϕ is the dissipation function given by

$$\phi=\mu_t\left(\frac{\partial V_z}{\partial r}\right)^2 \tag{10}$$

for axial flow. The momentum equation as given by Gallimore (1986) simplified for axial flow is:

$$\frac{\partial H_o}{\partial m}=T\frac{\partial s}{\partial m}+\frac{E_z}{\rho} \tag{11}$$

where E_z is the axial shear force given by

$$E_z=\frac{1}{r}\frac{\partial}{\partial r}\left(\mu_t r\frac{\partial V_z}{\partial r}\right). \tag{12}$$

For axial flow the meridional and axial velocities are the same so that $V_m = V_z$. We can then use Eqs. (9), (10), (11), and (12) to substitute for the terms on the right-hand side of Eq. (11) to give:

$$r\rho V_z\frac{\partial H_o}{\partial m}=\frac{\partial}{\partial r}\left(rk_t\frac{\partial T}{\partial r}\right)+\mu_t r\left(\frac{\partial V_z}{\partial r}\right)^2+V_z\frac{\partial}{\partial r}\left(\mu_t r\frac{\partial V_z}{\partial r}\right) \tag{13}$$

The static temperature is related to the stagnation enthalpy by:

$$H_o=C_pT+V_z^2/2 \tag{14}$$

We can use this to substitute for the temperature gradient term in Eq. (A1.5) to give

$$r\rho V_z\frac{\partial H_o}{\partial m}=\frac{\partial}{\partial r}\left(\frac{r\mu_t}{\mathrm{Pr}_t}\frac{\partial H_o}{\partial r}\right)-\frac{\partial}{\partial r}\left(\frac{\mu_t r}{\mathrm{Pr}_t}V_z\frac{\partial V_z}{\partial r}\right)+\mu_t r\left(\frac{\partial V_z}{\partial r}\right)^2+V_z\frac{\partial}{\partial r}\left(\mu_t r\frac{\partial V_z}{\partial r}\right) \tag{15}$$

where we have introduced the turbulent Prandtl number Pr_t.

A. Arnone
Research Scientist,
Institute for Computer Applications in Engineering and Science (ICASE).

R. C. Swanson
Research Scientist.

NASA Langley Research Center,
Hampton, VA 23665

A Navier-Stokes Solver for Turbomachinery Applications

A computer code for solving the Reynolds-averaged full Navier-Stokes equations has been developed and applied using H- and C-type grids. The Baldwin-Lomax eddy-viscosity model is used for turbulence closure. The integration in time is based on an explicit four-stage Runge-Kutta scheme. Local time stepping, variable coefficient implicit residual smoothing, and a full multigrid method have been implemented to accelerate steady-state calculations. A grid independence analysis is presented for a transonic rotor blade. Comparisons with experimental data show that the code is an accurate viscous solver and can give very good blade-to-blade predictions for engineering applications.

Introduction

In order to realize the optimum design for modern turbomachinery, a reliable and efficient capability to predict correctly the various flow conditions that can occur in such devices is essential. As indicated by the research of the past few years, flow solutions can be obtained rapidly by solving the potential equation, but this equation does not allow for vorticity and entropy changes related to shock waves. Recently, many numerical methods have been developed to solve the Euler equations. However, an inviscid analysis requires some assumption about the circulation to get an unique solution, and the problem may become ambiguous when dealing with a rounded trailing edge. In addition, heat transfer and boundary-layer thickening, which can lead to separation and hot spots, cannot be represented in an inviscid solution.

By coupling a boundary-layer model with an inviscid procedure, one can remove some of the previous limitations, but such an approach is difficult to extend to three-dimensional flows. The improvement in the numerical schemes and in the performance of modern computers suggests investigating the solution of the Reynolds-averaged Navier-Stokes equations. Although significant progress has been made in the development of Navier-Stokes solvers for cascade flows, as evident from [1-4], much work remains before computer codes capable of efficiently solving the wide range of blade geometries and flow conditions that can be encountered in the design process are available.

The objective of the present work is to develop a fast and accurate method for the computation of viscous cascade flows. A four-stage Runge-Kutta scheme with acceleration techniques for steady-state solutions is used to advance in time the Reynolds-averaged Navier-Stokes equations. Numerical efficiency has been achieved through local time stepping, variable coefficient implicit residual smoothing, and a full multigrid method.

In this paper, numerical results are presented for a bicircular arc cascade and for a typical gas turbine high-loaded cascade with a thick, rounded trailing edge. The bicircular profile is studied for the case of subsonic laminar separated flow and for the case of transonic turbulent flow with separation after the shock. For the gas turbine blade, subsonic and transonic conditions are considered, and solutions are compared to experimental data. To validate the proposed computational method for turbomachinery applications, a grid independence analysis is carried out for the case of the turbine cascade flow.

Contributed by the International Gas Turbine Institute for publication in the JOURNAL OF TURBOMACHINERY. Manuscript received by the International Gas Turbine Institute March 16, 1992. Associate Technical Editor: L. S. Langston.

Governing Equations

Let ρ, u, v, p, T, E, and H denote, respectively, the density, velocity components in the x and y Cartesian directions, pressure, temperature, specific total internal energy, and specific total enthalpy. The two-dimensional unsteady Navier-Stokes equations, neglecting body forces and heat sources, can be written in conservative form in a Cartesian coordinate system as

$$\frac{\partial U}{\partial t}+\frac{\partial F}{\partial x}+\frac{\partial G}{\partial y}=\frac{\partial R}{\partial x}+\frac{\partial S}{\partial y} \tag{1}$$

where

$$U=\begin{bmatrix}\rho\\ \rho u\\ \rho v\\ \rho E\end{bmatrix},\quad F=\begin{bmatrix}\rho u\\ \rho u^2+p\\ \rho uv\\ \rho uH\end{bmatrix},\quad G=\begin{bmatrix}\rho v\\ \rho uv\\ \rho v^2+p\\ \rho vH\end{bmatrix} \tag{2}$$

$$R=\begin{bmatrix}0\\ \tau_{xx}\\ \tau_{xy}\\ r_4\end{bmatrix},\quad S=\begin{bmatrix}0\\ \tau_{yx}\\ \tau_{yy}\\ s_4\end{bmatrix} \tag{3}$$

and

$$\begin{aligned}\tau_{xx}&=(\lambda+2\mu)u_x+\lambda v_y\\ \tau_{yy}&=(\lambda+2\mu)v_y+\lambda u_x\\ \tau_{xy}&=\tau_{yx}=\mu(u_y+v_x)\\ r_4&=u\tau_{xx}+v\tau_{xy}+kT_x\\ s_4&=u\tau_{yx}+v\tau_{yy}+kT_y\end{aligned} \tag{4}$$

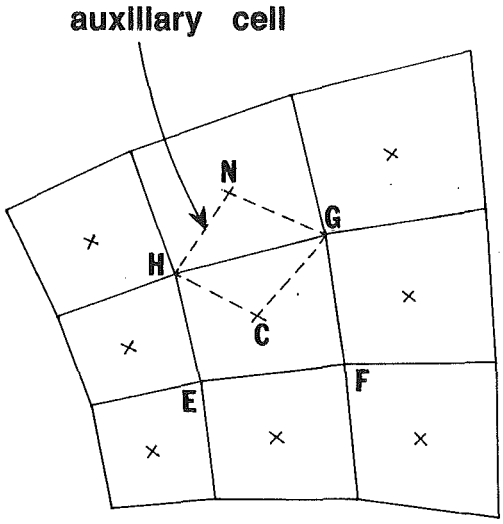

Fig. 1 Auxiliary cell for computation of viscous terms

The pressure is obtained from the equation of state,

$$p = \rho RT \tag{5}$$

According to the Stokes hypothesis λ is taken to be $-2/3\mu$, and a power law is used to determine the molecular coefficient of viscosity μ. The effect of turbulence is taken into account by using the eddy-viscosity hypothesis. That is, the molecular viscosity μ and the molecular thermal conductivity k are replaced with

$$\mu = \mu_l + \mu_t \tag{6}$$

$$k = c_p\left[\left(\frac{\mu}{\mathrm{Pr}}\right)_l + \left(\frac{\mu}{\mathrm{Pr}}\right)_t\right] \tag{7}$$

where c_p is the specific heat at constant pressure, Pr is the Prandtl number, and the subscripts l and t refer to laminar and turbulent. The turbulence quantities μ_t and Pr_t are computed using the two-layer algebraic model of Baldwin and Lomax [5].

The Euler equations can be easily obtained by neglecting the right-hand side of Eq. (1).

Spatial Discretization

A finite-volume approach is applied to discretize the equations of motion. The computational domain is divided into quadrilateral cells, fixed in time, and for each cell the governing equations are written in integral form as follows:

$$\frac{\partial}{\partial t}\int\int_{\Omega} U dxdy + \int_{\partial\Omega}(Fdy - Gdx) = \int_{\partial\Omega}(Rdy - Sdx) \tag{8}$$

where Ω is a generic cell, and $\partial\Omega$ is its boundary.

A cell-centered discretization is used, and the line integral of Eq. (8) is approximated with the midpoint rule. The convective fluxes at the cell faces are obtained by simple averaging of adjacent cell-center values of the dependent variables (see [6]). The spatial derivatives necessary to compute the viscous terms are evaluated by means of Green's theorem. For example, consider the arbitrary cell Ω (EFGH) in Fig. 1. The contributions u_x and u_y to the viscous flux across each cell face (i.e., GH) are determined using

$$\int_{\Omega'} u_x d\Omega' = \int_{\partial\Omega'} u dy$$

$$\int_{\Omega'} u_y d\Omega' = -\int_{\partial\Omega'} u dx \tag{9}$$

where Ω' is an auxiliary cell (CGNH for face GH in Fig. 1). In a similar manner, v_x and v_y are computed. Additional details for finite-volume treatment of viscous stresses and heat conduction terms are found in [6, 7].

Boundary Conditions

It is well known that the reflective behavior of numerical boundary conditions can significantly influence the convergence rate of a marching scheme. Thus, boundary conditions must be chosen carefully. According to the theory of characteristics, three quantities are specified at a subsonic inflow boundary. In the present work, the total enthalpy, the total pressure, and flow angle are specified if the axial flow is subsonic; the outcoming Riemann invariant R^- is taken from the interior. For supersonic axial inlet all the flow variables are computed from the prescribed inlet conditions. At a subsonic axial outlet, the average static pressure corresponding to the desired isentropic Mach number is prescribed, while the outgoing Riemann invariant R^+, the total enthalpy, and the component of the velocity parallel to the boundary are extrapolated from the interior. If the axial outlet is supersonic all the variables are extrapolated. On the solid wall, the only contribution to the convective fluxes is the pressure, which is obtained by extrapolation from the interior of the flow field. For viscous flow calculations, the velocity is set to zero on the solid surface, which is taken to be adiabatic in the present work.

Artificial Dissipation

For inviscid flows, the finite-volume scheme does not contain any dissipative terms. In order to prevent odd-even point decoupling and oscillations near shock waves or stagnation points, artificial dissipation terms are added to the governing discrete equations. Moreover, the introduction of appropriate dissipation in the vicinity of shocks allows an entropy condition to be satisfied, and thus guarantees the uniqueness of weak solutions. For viscous flows, dissipative properties are present because of diffusive terms; however, due to nonlinear effects the physical dissipation may not be sufficient to guarantee stability, especially in the case of the highly stretched meshes generally used to resolve the steep gradients in shear layers. Thus, to maintain the stability and robustness of the numerical procedure, artificial dissipation is also included in viscous calculations. A semidiscrete form of Eq. (8) is then given by

$$\frac{\partial}{\partial t}(V \cdot U) + Q(U) - D(U) = 0 \tag{10}$$

where V is the volume of the mesh cell being considered, $Q(U)$ is the discrete approximation of the convective and physical diffusive terms, and $D(U)$ denotes the artificial dissipation terms.

The artificial dissipation model considered in this paper is basically the one developed by Jameson et al. [8]. This nonlinear model is a blending of second and fourth differences. The quantity $D(U)$ in Eq. (10) is defined as

$$D(U) = (D_\xi^2 - D_\xi^4 + D_\eta^2 - D_\eta^4)U \tag{11}$$

where (ξ, η) are arbitrary curvilinear coordinates,

$$D_\xi^2 U = \nabla_\xi(\lambda_{i+1/2,j} \cdot \epsilon^{(2)}_{i+1/2,j})\Delta_\xi U_{i,j} \tag{12}$$

$$D_\xi^4 U = \nabla_\xi(\lambda_{i+1/2,j} \cdot \epsilon^{(4)}_{i+1/2,j})\Delta_\xi \nabla_\xi \Delta_\xi U_{i,j} \tag{13}$$

and i, j are indices (for a cell center) associated with the ξ and η directions. The operators Δ_ξ, ∇_ξ are forward and backward difference operators in the ξ direction. Following [7, 9] the variable scaling factor is defined as

$$\lambda_{i+1/2,j} = \frac{1}{2}[(\bar{\lambda}_\xi)_{i,j} + (\bar{\lambda}_\xi)_{i+1,j}] \tag{14}$$

where

$$(\bar{\lambda}_\xi)_{i,j} = \phi_{i,j}(r) \cdot (\lambda_\xi)_{i,j}$$

$$\phi_{i,j}(r) = 1 + r_{i,j}^{\zeta} \tag{15}$$

and r is the ratio λ_η/λ_ξ, with λ_ξ and λ_η denoting the scaled spectral radii of the flux Jacobian matrices (associated with the ξ and η directions) for the Euler equations. The exponent ζ is generally defined by $2/3 \le \zeta \le 1$. The spectral radii for the ξ and η directions are given by

$$\lambda_\xi = |uy_\eta - vx_\eta| + c(y_\eta^2 + x_\eta^2)^{1/2} \tag{16}$$

$$\lambda_\eta = |vx_\xi - uy_\xi| + c(x_\xi^2 + y_\xi^2)^{1/2} \tag{17}$$

and c is the speed of sound. The coefficients $\epsilon^{(2)}$ and $\epsilon^{(4)}$ use the pressure as a sensor for shocks and stagnation points, and they are defined as

$$\epsilon^{(2)}_{i+1/2,\,j} = K^{(2)} \max(\nu_{i-1,\,j},\ \nu_{i,j},\ \nu_{i+1,\,j},\ \nu_{i+2,\,j}) \tag{18}$$

$$\nu_{i,j} = \left| \frac{p_{i-1,\,j} - 2p_{i,j} + p_{i+1,\,j}}{p_{i-1,\,j} + 2p_{i,j} + p_{i+1,\,j}} \right| \tag{19}$$

$$\epsilon^{(4)}_{i+1/2,\,j} = \max[0,\ (K^{(4)} - \epsilon^{(2)}_{i+1/2,\,j})] \tag{20}$$

where typical values for the constants $K^{(2)}$ and $K^{(4)}$ are 1/4 and 1/64, respectively.

For the normal direction (η), the dissipation contributions are defined in a similar way, except

$$(\bar{\lambda}_\eta)_{i,j} = \phi_{i,j}(r^{-1}) \cdot (\lambda_\eta)_{i,j} \tag{21}$$

Care must be taken, especially for internal flows, in defining the smoothing fluxes on the boundary. If the computation of the dissipative terms is carred out in each coordinate direction as the difference between first and third difference operators, conditions on those terms can be imposed at the boundary such that no errors in the conservation property are introduced, globally, by the numerical dissipation [10]. Moreover, such a scheme reduces the presence of undamped modes and guarantees a dissipative behavior for the dissipative terms $D(U)$.

Time-Stepping Scheme

The system of differential equations, Eqs. (10), are advanced in time toward the steady-state solution with a four-stage Runge–Kutta scheme. This scheme is fourth-order accurate in time for the linear problem and second-order accurate for the nonlinear problem. It can be written for the time level n in the form

$$\begin{aligned}
U^{(0)} &= U^n \\
U^{(1)} &= U^{(0)} - \alpha_1 \Delta t R(U^{(0)}) \\
U^{(2)} &= U^{(0)} - \alpha_2 \Delta t R(U^{(1)}) \\
U^{(3)} &= U^{(0)} - \alpha_3 \Delta t R(U^{(2)}) \\
U^{(4)} &= U^{(0)} - \alpha_4 \Delta t R(U^{(3)}) \\
U^{n+1} &= U^{(4)}
\end{aligned} \tag{22}$$

where at the $(q + 1)$st stage we have in the case of a single evaluation of the dissipation

$$R(U^{(q+1)}) = \frac{1}{V}\left(Q(U^{(q)}) - D(U^{(0)})\right) \tag{23}$$

and a good set for the coefficients α_m ($m = 1, 4$) is

$$\alpha_1 = \frac{1}{4},\quad \alpha_2 = \frac{1}{3},\quad \alpha_3 = \frac{1}{2},\quad \alpha_4 = 1 \tag{24}$$

For economy the viscous terms are computed at the first stage and then frozen for the remaining stages. In multigrid computations, the driving scheme must be designed to damp out high-frequency modes rapidly. Good high-frequency damping properties are obtained with this scheme by evaluating the artificial dissipation terms on the first and second stages and freezing them for the remaining stages [11].

It is also important to note that the Runge–Kutta scheme has the desirable property that the steady-state solution is independent of the time step; therefore, the scheme is particularly amenable to convergence acceleration techniques.

Acceleration Techniques

Three methods are employed to accelerate convergence of the basic explicit time-stepping scheme. These techniques are as follows: (1) local time stepping; (2) residual smoothing; (3) multigrid. They are discussed in the subsequent subsections.

Local Time Stepping. When the interest is only in the steady-state solution, a faster expulsion of disturbances can be achieved by locally varying the time step. In the present work the actual time step limit Δt is computed using

$$\Delta t = c_0 \left(\frac{\Delta t_c \cdot \Delta t_d}{\Delta t_c + \Delta t_d} \right) \tag{25}$$

where Δt_c is the limit due to the convective terms, Δt_d is the limit due to the diffusive terms, and c_0 is a constant usually taken to be the Courant–Friedrichs–Lewy (CFL) number. In particular,

$$\Delta t_c = \frac{V}{\lambda_\xi + \lambda_\eta} \tag{26}$$

$$\Delta t_d = \frac{V^2}{K_t \mu [(x_\xi^2 + y_\xi^2) + (x_\eta^2 + y_\eta^2)]} \tag{27}$$

where λ_ξ, λ_η are defined in Eqs. (16) and (17), respectively, and K_t is a constant that has been set equal to 2.5 based on numerical experiments.

Residual Smoothing. The stability range of the basic time-stepping scheme can be extended using implicit smoothing of the residuals. This technique was first introduced by Lerat [12] for the Lax–Wendroff scheme, and later devised by Jameson [13] for the Runge–Kutta scheme. For two-dimensional flows the residual smoothing can be applied in the form

$$(1 - \beta_\xi \nabla_\xi \Delta_\xi)(1 - \beta_\eta \nabla_\eta \Delta_\eta) \bar{\mathcal{R}}^{(m)} = \mathcal{R}^{(m)} \tag{28}$$

where the residual $\mathcal{R}^{(m)}$ is defined by

$$\mathcal{R}^{(1)} = \alpha_1 \frac{\Delta t}{V} [Q(U^{(0)}) - D(U^{(0)})]$$

$$\mathcal{R}^{(m)} = \alpha_m \frac{\Delta t}{V} [Q(U^{(m-1)}) - D(U^{(1)})]$$

$$m = 2,\ 4 \tag{29}$$

and computed in the Runge–Kutta stage m, and $\bar{\mathcal{R}}^{(m)}$ is the final residual at stage m after the sequence of smoothings in the ξ and η directions with the coefficients β_ξ and β_η.

The use of constant coefficients in the implicit treatment has proven to be satisfactory (extending the CFL number by a factor of two to three) even for highly stretched meshes, provided additional dissipative support such as enthalpy damping [6] is introduced. However, the use of enthalpy damping, which assumes constant total enthalpy throughout the flow field, precludes the solution of problems with heat transfer effects. The need for enthalpy damping can be eliminated by using variable coefficients β_ξ and β_η that account for the variation in cell aspect ratio. For the factorization of Eq. (28) effective expressions for the coefficients β_ξ, β_η can be derived by following the procedure of Martinelli in [7]. These expressions are written as

$$\beta_\xi = \max\left\{\frac{1}{4}\left[\left(\frac{\mathrm{CFL}}{\mathrm{CFL}^*}\cdot\frac{\lambda_\xi}{\lambda_\xi+\lambda_\eta}\cdot\phi(r)\right)^2 - 1\right], 0\right\}$$

$$\beta_\eta = \max\left\{\frac{1}{4}\left[\left(\frac{\mathrm{CFL}}{\mathrm{CFL}^*}\cdot\frac{\lambda_\eta}{\lambda_\xi+\lambda_\eta}\cdot\phi(r^{-1})\right)^2 - 1\right], 0\right\} \quad (30)$$

where $\phi(r)$ and $\phi(r^{-1})$ are the same quantities defined for the artificial dissipation, CFL is the local Courant number (usually taken to be 5), and the asterisk refers to the unsmoothed scheme.

Multigrid Strategy. Multigrid methods were first introduced for the solution of elliptic problems [14], and later Ni [15] and Jameson [11] applied them to the Euler equations. Actually, multigrid methods can be implemented to obtain improvement in the convergence rate in solving not only the Euler but also the Navier-Stokes equations [7, 9, 16]. The basic idea is to use coarser grids to speed up the propagation of the fine grid corrections. The Full Approximation Storage (FAS) scheme in conjunction with the Runge-Kutta time-stepping algorithm developed by Jameson [11] has proven to be an effective multigrid technique.

For the multigrid process coarser meshes are obtained by eliminating every other mesh line in each coordinate direction. On the auxiliary meshes, the solution is initialized as

$$U_{2h}^{(0)} = \frac{\Sigma V_h U_h}{V_{2h}} \quad (31)$$

where the subscript refers to the mesh spacing value, and the sum is over the four fine grid cells that compose the $2h$ grid cell. This rule conserves mass, momentum, and energy. On a coarse grid, a forcing function P is added to the governing discrete equations in order to impose the fine grid approximation. After the initialization of the coarse grid solution, this function is computed as follows:

$$P_{2h} = V_{2h}^{-1}\,\Sigma V_h R_h(U_h) - R_{2h}(U_{2h}^{(0)}) \quad (32)$$

Then, the time-stepping scheme on the $(q+1)$st stage becomes

$$U_{2h}^{(q+1)} = U_{2h}^{(0)} - \alpha_{q+1}\Delta t[R_{2h}(U_{2h}^{(q)}) + P_{2h}^{(0)}] \quad (33)$$

We can also define a new value R^* for the residual as

$$R_{2h}^* = R_{2h}(U_{2h}) + P_{2h}, \quad (34)$$

collect this value, restrict the solution U_{2h} to the next coarser grid, and repeat the process. The corrections computed on a coarse grid are transferred back to a finer grid with bilinear interpolation.

Two types of simple fixed cycle multigrid strategy are primarily used. They are the V cycle and the W cycle. At a given grid level additional time steps (i.e., coarse grid sweeps) can be performed in both cycles. Moreover, the application of two Runge-Kutta (R-K) steps on the $2h$ grid and three R-K steps on all succeeding coarser grids is an effective strategy. In the present work, results were obtained with a V-type cycle and additional coarse grid sweeps.

In viscous flow calculations the viscous terms are computed also on the coarser grids, while the turbulent viscosity is evaluated only on the finest grid and then determined on each succeeding coarser grid by a simple averaging of surrounding finer grid values. The artificial dissipation model for the finest grid is replaced on the coarser grids with a simple constant coefficient second difference dissipation model. On each grid, the boundary conditions are computed in the same manner and updated at every Runge-Kutta stage. In order to provide an improved initial solution on the finest grid of the sequence of grids in the basic multigrid procedure, the Full Multigrid (FMG) method is employed. With the FMG method the solution is initialized on a coarser grid of the basic sequence of grids and iterated a prescribed number of cycles using the FAS scheme. The solution is then interpolated to the next finer grid. The process is repeated until the finest grid is reached. In the present work, three refinement levels are generally used. The first and second levels include two and three grids, respectively, and 50 cycles are performed on each. There are up to five grids in the final level.

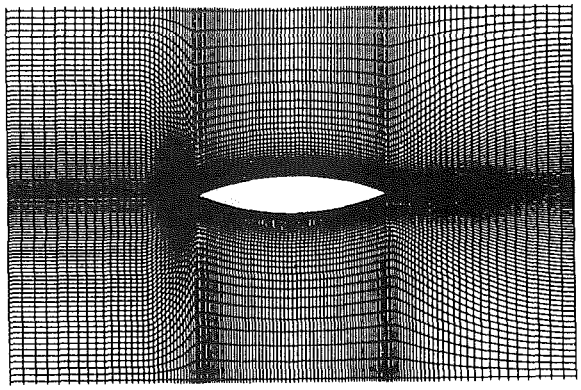

Fig. 2(*a*) 129 × 97 laminar flow grid

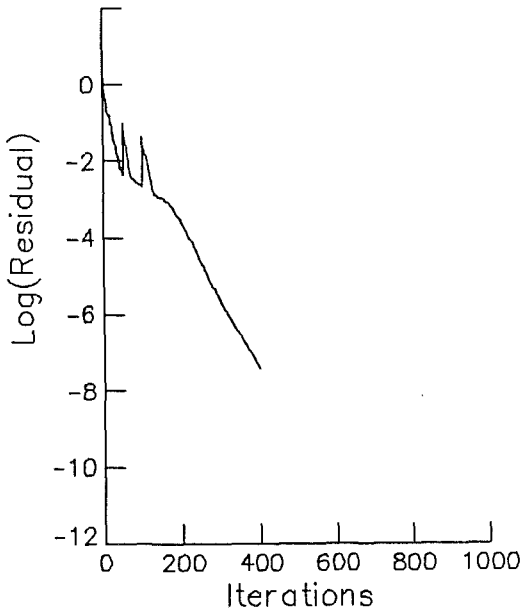

Fig. 2(*b*) Convergence history

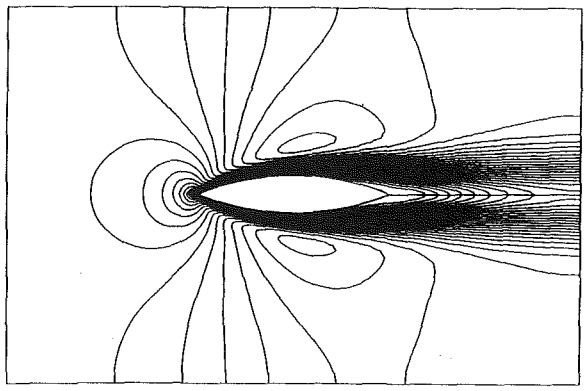

Fig. 2(*c*) Mach number contours

Fig. 2 Bicircular arc cascade (M_{2is} = 0.5; Re_2 = 500)

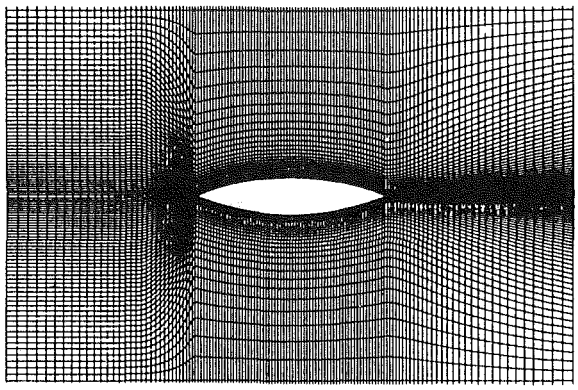

Fig. 3(*a*) 129 × 97 turbulent flow grid

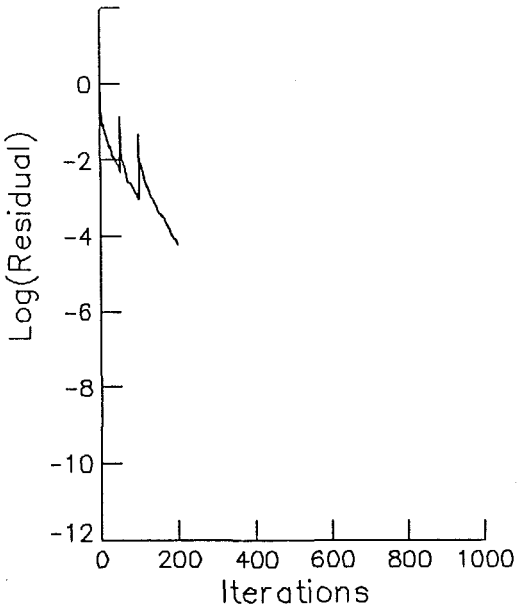

Fig. 3(*b*) Convergence history

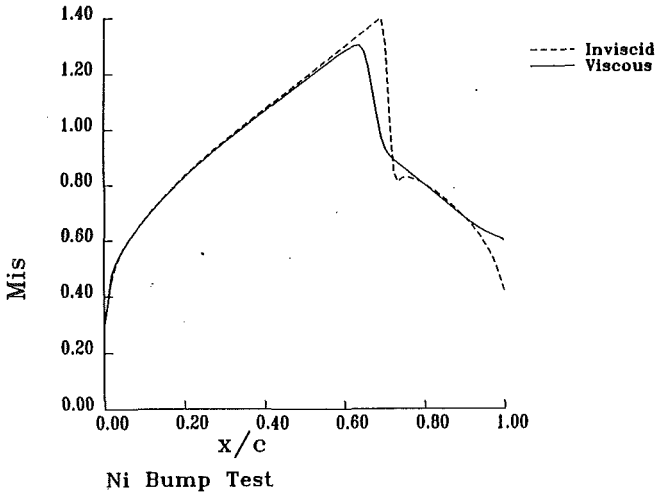

Fig. 3(*c*) Isentropic Mach number distribution

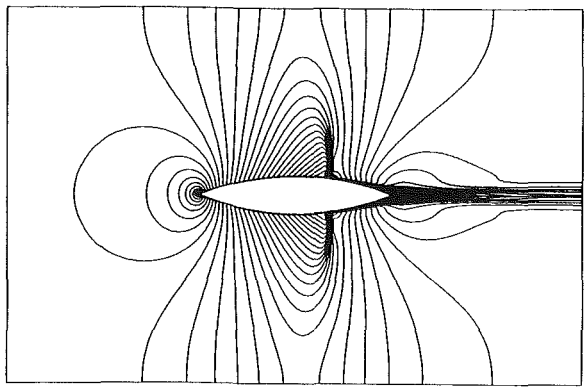

Fig. 3(*d*) Mach number contours

Fig. 3 Bicircular arc cascade (M_{2is} = .675; Re_2 = 1 × 10^6)

Results and Discussion

Bicircular Arc Cascade. In [15] Ni presented results for inviscid flow over a 20 percent bicircular arc cascade with gap/chord ratio of 2. Then, Chima and Johnson [16] studied a 10 percent bicircular arc cascade for the case of laminar flow. The present numerical method has been used to study the first cascade geometry for laminar and turbulent flow conditions with separation. In Fig. 2(*a*) the 129 × 97 *H*-type grid used for the laminar calculation is presented. The spacing between the wall and the first cell center is 3 × 10^{-4} chords, and 10^{-2} chords is the minimum spacing in the streamwise direction. For this case, the exit Reynolds number Re_2 = 500, the exit isentropic Mach number M_{2is} = 0.5, and the angle of attack is zero degrees. The isentropic Mach number is determined from the ratio of the local static pressure to the inlet total pressure. The second difference artificial dissipation is set to zero. Figure 2(*b*) shows the convergence history for the root mean square of the residual of the continuity equation scaled by the initial value. To indicate the monotone behavior of the multigrid scheme, 300 iterations were performed on the finest grid. An iteration corresponds to one multigrid cycle. Using 5 grid levels and a *V*-type cycle with additional coarse grid sweeps, there are 7.2 decades decrease in the residual. Mach number contours for this case are given in Fig. 2(*c*). The flow is separated at about the 90 percent chord location. Due to the low Reynolds number, we found that this is one of the

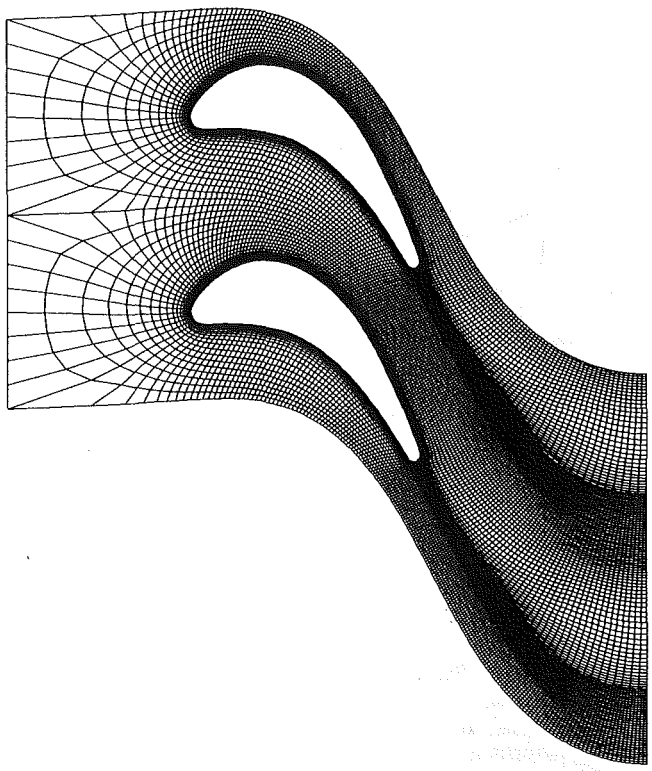

Fig. 4 A 385 × 33 nonperiodic *C*-type grid for the VKI LS59 rotor blade

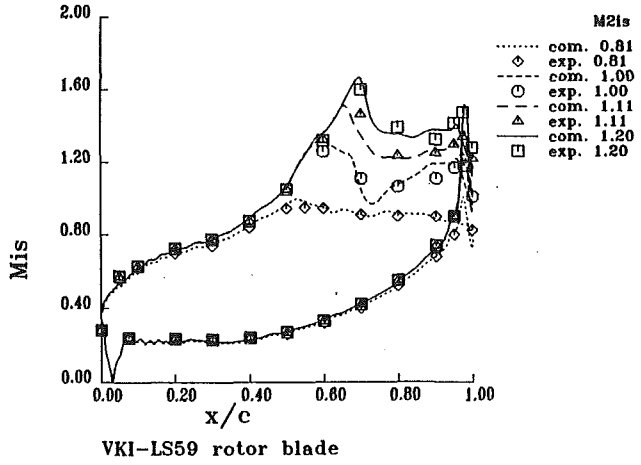

Fig. 5 Isentropic Mach number distribution for different values of M_{2is} (769 × 65 grid)

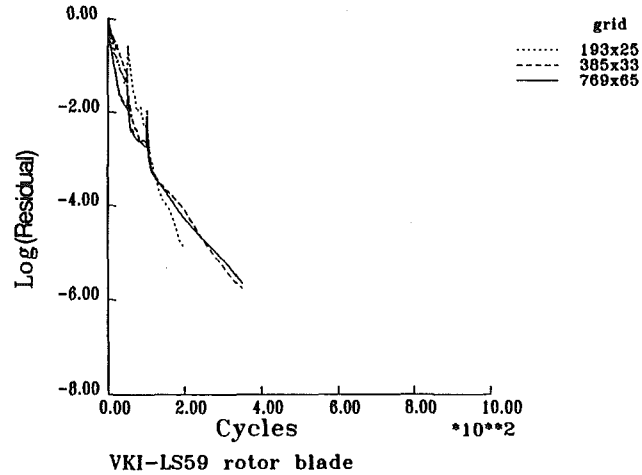

Fig. 6 Convergence histories (M_{2is} = 0.81)

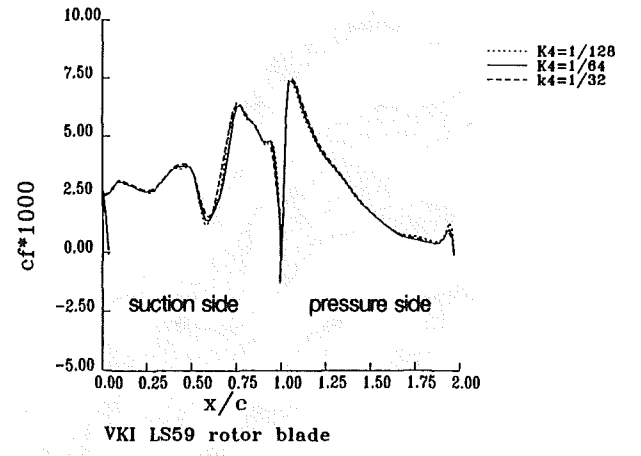

Fig. 7 Effect of dissipation on skin-friction distribution (M_{2is} = 0.81)

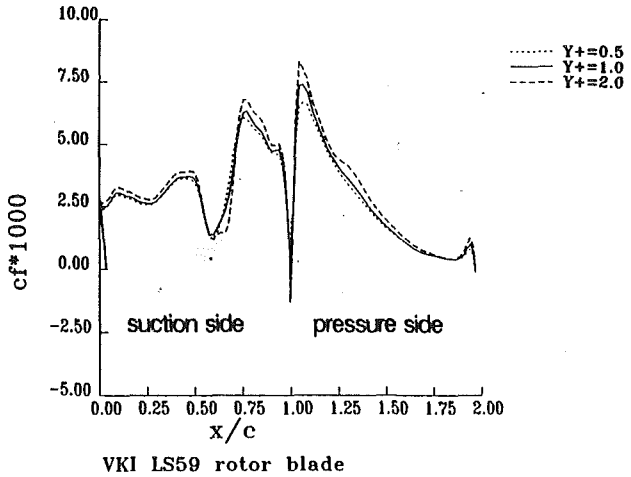

Fig. 8 Effect of Y^+ on skin-friction distribution (M_{2is} = 0.81)

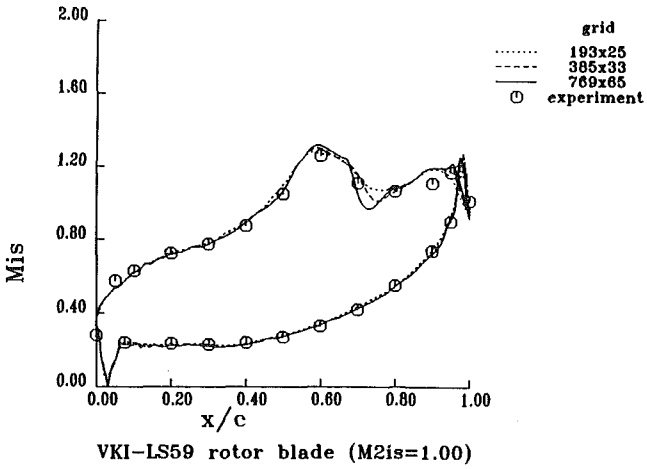

Fig. 9 Isentropic Mach number distribution with different grids (M_{2is} = 1.0)

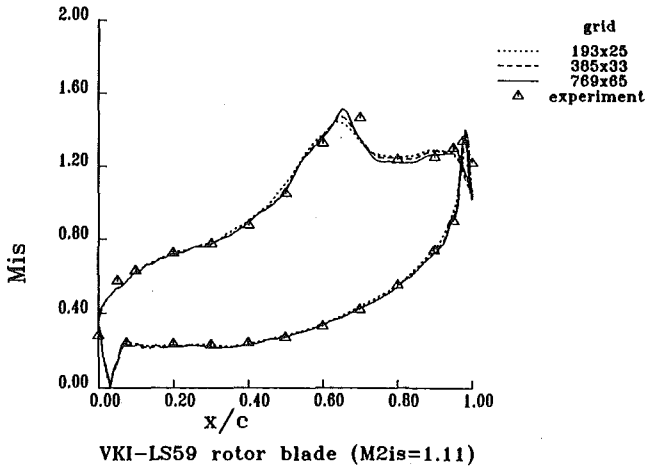

Fig. 10 Isentropic Mach number distribution with different grids (M_{2is} = 1.11)

cases where it is important to compute the viscous terms on the coarser grids.

Results for transonic turbulent flow (M_{2is} = 0.675) are presented in Fig. 3. Figure 3(*a*) displays the 129 × 97 mesh used in this test case. The minimum spacing at the wall boundary is 10^{-4} chords, and in the x direction a spacing of about 1.5 × 10^{-2} chords is used to obtain a good representation of the shock wave. For the inviscid mesh the minimum spacing at the wall is equal to the one in the x direction. Figure 3(*b*) shows the convergence history. The surface variations in the computed isentropic Mach number (M_{is}) are given in Fig. 3(*c*). In this case, the flow exhibits separation after the shock, where the Baldwin–Lomax turbulence model predicts the transition to turbulence. The flow remains turbulent for the remaining part of the body. Then, the flow reattaches and remains so

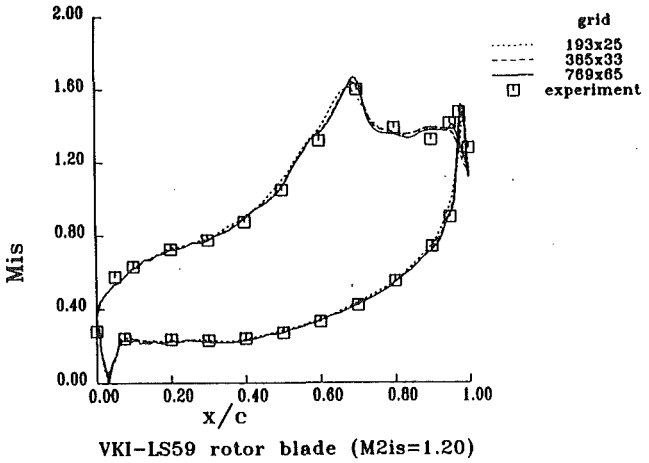

Fig. 11 Isentropic Mach number distribution with different grids (M_{2is} = 1.2)

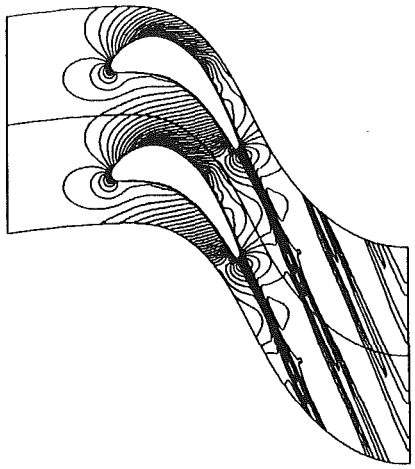

Fig. 12(*a*) M_{2is} = 0.81; Re_2 = 8.22 × 10^5

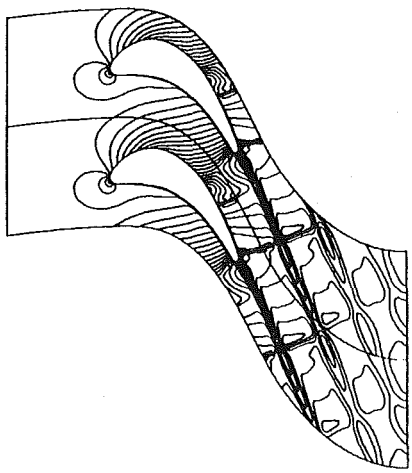

Fig. 12(*b*) M_{2is} = 1.0; Re_2 = 7.44 × 10^5

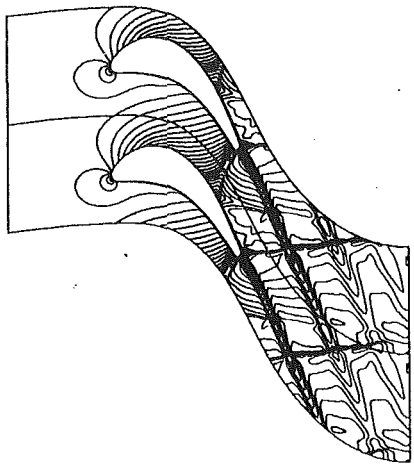

Fig. 12(*c*) M_{2is} = 1.11; Re_2 = 7.01 × 10^5

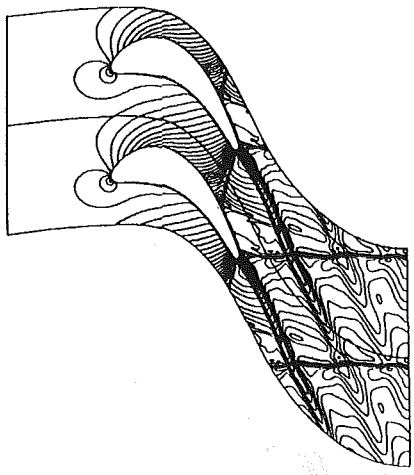

Fig. 12(*d*) M_{2is} = 1.2; Re_2 = 6.63 × 10^5

Fig. 12 Mach number contours for turbine blade cascade (769 × 65 grid)

until the 78 percent chord position. The Mach number contours for this flow (Fig. 3(*d*)) reveal a clean capturing of the shock.

Gas Turbine Rotor Blade. The present numerical method has been tested on several internal flow cases. In order to validate the method for turbomachinery applications, computations were performed for a Von Karman Institute (VKI) gas turbine rotor blade. This blade was tested extensively, as seen in [17, 18]. At the inlet the flow angle with respect to the turbine axes is 30 deg. The flow is turned about 96 deg by the blade. For the solutions included herein the inlet Mach number is about 0.27 and the outlet isentropic Mach number (M_{2is}) varies from 0.81 to 1.20. This blade represents a challenging test for a transonic flow solver. The blade passage is convergent and originally designed to work up to the sonic condition. In fact, the suction side is curved also after the trough region, which can produce a strong trailing edge shock. Losses rapidly increase in the transonic regime. Moreover, for this blade, the experimental data of [17, 18] include loss coefficients and exit flow angles. Due to the blunt leading edge and the flow deviation, computations were carried out on nonperiodic *C*-type grids. These grids were recently introduced by Arnone et al. [19]. In order to validate the computational procedure for turbomachinery applications, we performed a grid convergence analysis. Meshes consisting of 193 × 25, 385 × 33, and 769 × 65 grid points were considered. On the suction side of the blade we distributed respectively 65, 129, and 257 points. The medium grid, 385 × 33, is depicted in Fig. 4. The spacing between the blade and the first cell center in the direction normal to the blade is set to 5 × 10^{-5} chords, which for an exit Reynolds number of about one million ensures an average Y^+ (having the standard boundary-layer definition) of roughly one. A fine mesh is maintained after the blade in order to

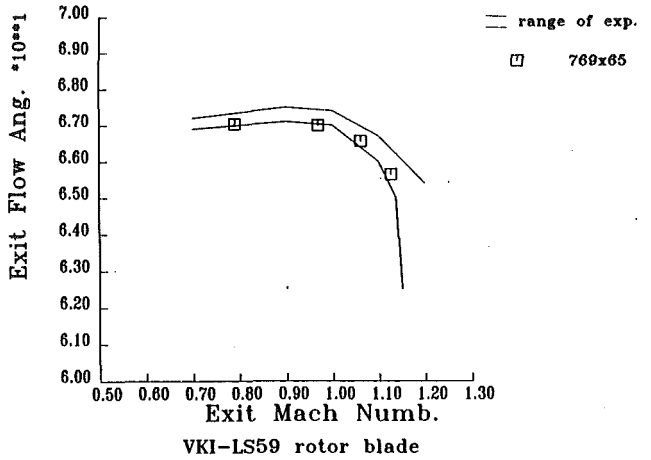

VKI-LS59 rotor blade

Fig. 13 Variation of exit flow angle with exit Mach number

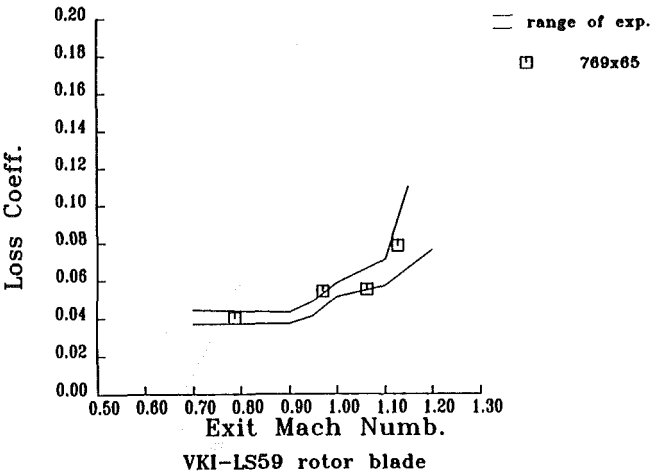

VKI-LS59 rotor blade

Fig. 14 Variation of loss coefficient with exit Mach number

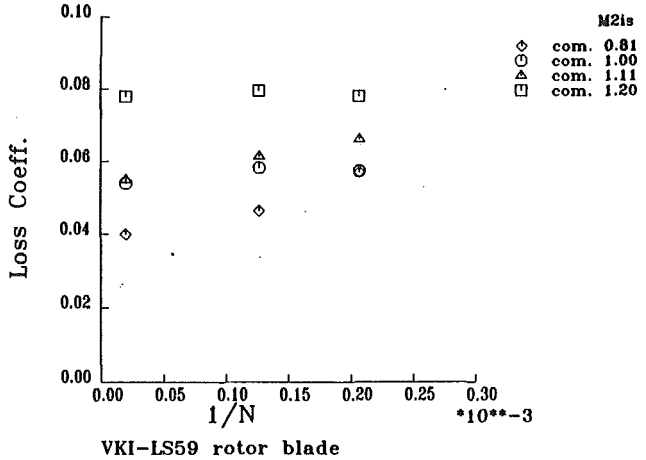

VKI-LS59 rotor blade

Fig. 15 Variation of loss coefficient with reciprocal of number of mesh points

obtain good resolution of the shock system in the case with supersonic outlet flow. For the coarsest and finest grids the normal spacings at the blade surface are 1×10^{-4} and 2.5×10^{-5} chords, respectively.

In Fig. 5 the computed and experimental isentropic Mach number distributions for the four flow conditions that we studied are shown. The annotation for computation refers to fine grid solution. Convergence histories for the case of $M_{2is} = 0.81$ and for the three grid sizes are given in Fig. 6. The capability of the FMG is evident. When the grid size is increased, we can increase also the number of the auxiliary grids, and maintain an essentially constant convergence rate. The fine grid calculations took about 580 s on the NAS CRAY Y-MP. For engineering applications a four decade drop in the residuals is a commonly used criterion for convergence. This can be satisfied in less than 5 minutes on the fine grid.

When dealing with inviscid flows, the effects of the artificial dissipation can be monitored by controlling the total pressure losses. This criterion is no longer useful in viscous calculations. Figure 7 compares the wall skin-friction distribution for the subsonic case and for different weights of the artificial dissipation. The surface skin-friction coefficient (c_f) has the standard definition. Here, the shear stress is divided by the dynamic pressure based on the conditions at the center of the blade passage. In this plot, the values on the suction and pressure surfaces start at 0.0 and 2.0, respectively, and they end at 1.0 (trailing edge). The fact that the value of the coefficient $K^{(4)}$ can be increased or decreased by a factor of two without important changes in the skin friction suggests there is only a small amount of artificial damping also in the shear layer.

Figure 8 shows a spatial convergence study in the direction normal to the wall. Three different grids, which correspond to an average Y^+ of 0.5, 1, and 2 have been considered. Differences are quite small, and the skin friction is basically converged for a Y^+ of 1, which is what we would expect from the Baldwin-Lomax turbulence model. The transonic flow conditions have been analyzed on the three grids. The isentropic Mach number distribution on the blade surface is given along with experimental data in Figs. 9–11. Transonic flows through blade passages are very complicated, as evident from the Mach contours of Fig. 12. Even though the trailing edge flow can strongly influence the whole flow field, and a fine grid is needed, we can conclude that the medium grid is giving good resolution for engineering applications.

Comparisons between experimental and computed exit flow angles and loss coefficients are given in Figs. 13 and 14. The loss coefficient is defined by the expression $1 - w_2^2/w_{2is}^2$, where w_2 is the exit velocity, and w_{2is} is the isentropic exit velocity. Calculated results agree favorably with data both in behavior and absolute values. The variation of the computed loss coefficient with the reciprocal of the number of grid points is shown in Fig. 15. Once again, the medium grid size seems to be adequate for applications. Converged solutions on these grids were obtained in about 50 s on the CRAY Y-MP.

Some details of the solution with sonic outlet are given in Fig. 16. The nice shape of the 769 × 65 nonperiodic *C*-type grid is evident as well as the clean calculation of the leading edge flow and trailing edge flow, where there are significant recirculation regions.

Conclusion

The use of a Runge-Kutta scheme with acceleration techniques has proven to be fast, reliable, and accurate for the study of transonic internal flow. No problems lie in the extension of the numerical method to three-dimensional applications due to the versatility of the procedure. In addition, the very good convergence of the full multigrid process indicates the value of the method in turbomachinery component design.

Acknowledgments

The first author would like to express his gratitude to ICASE, ICOMP, and NASA for providing facilities and computer time for this work. The authors want to acknowledge Dr. Meng-Sing Liou and Dr. Louis A. Povinelli of NASA Lewis Research Center for their helpful discussions.

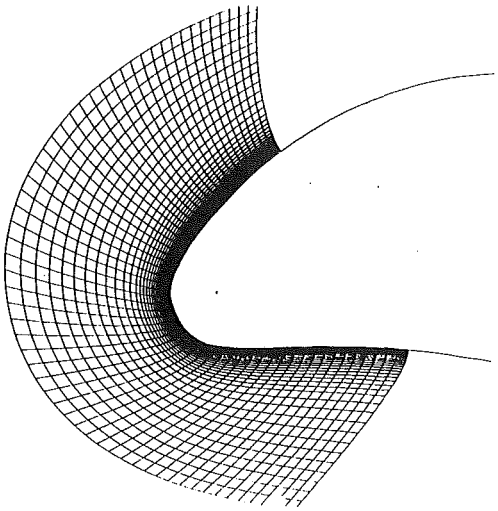

Fig. 16(*a*) Blowup of leading edge grid (769 × 65 grid)

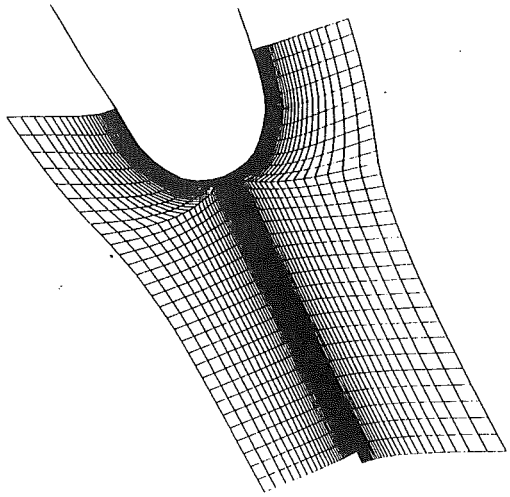

Fig. 16(*c*) Blowup of trailing edge grid (769 × 65 grid)

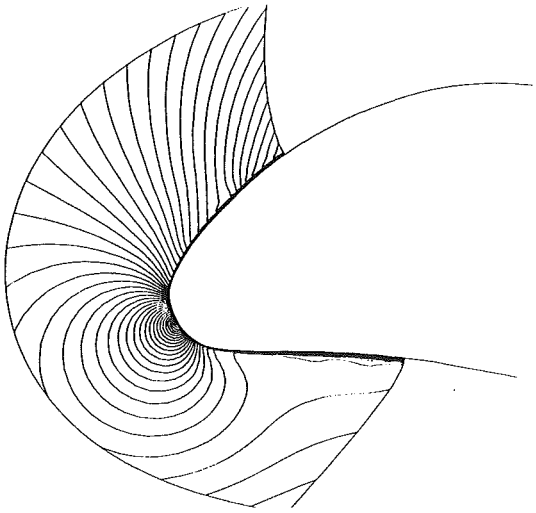

Fig. 16(*b*) Mach number contours (M_{2is} = 1.0)

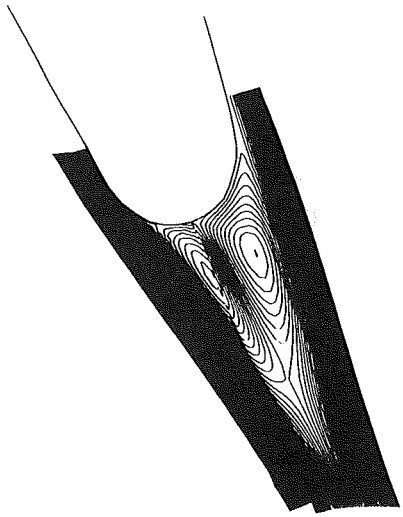

Fig. 16(*d*) Stream function contours (M_{2is} = 1.0)

Fig. 16 Flow details at leading and trailing edges

References

1 Chima, R. V., "Inviscid and Viscous Flows in Cascades With an Explicit Multiple-Grid Algorithm," *AIAA J.*, Vol. 23, No. 10, 1985, pp. 1556–1563.

2 Hah, C., and Selva, R. J., "Navier–Stokes Analysis of Flows and Heat Transfer Inside High-Pressure-Ratio Turbine Blade Rows," AIAA Paper No. 90-0343, 1990.

3 Davis, R. L., Ni, R. H., and Carter, J. E., "Cascades Viscous Flow Analysis Using the Navier–Stokes Equations," AIAA Paper No. 86-0033, 1986.

4 Chima, R. V., "Explicit Multigrid Algorithm for Quasi-Three-Dimensional Viscous Flows in Turbomachinery," *AIAA Journal of Propulsion and Power*, Vol. 3, No. 5, 1987, pp. 397–405.

5 Baldwin, B. S., and Lomax, H., "Thin Layer Approximation and Algebraic Model for Separated Turbulent Flows," AIAA Paper No. 78-257, 1978.

6 Swanson, R. C., and Turkel, E., "A Multistage Time-Stepping Scheme for the Navier–Stokes Equations," AIAA Paper No. 85-0035, 1985.

7 Martinelli, L., "Calculations of Viscous Flows With a Multigrid Method," Ph.D. Dissertation, MAE Department, Princeton University, Oct. 1987.

8 Jameson, A., Schmidt, W., and Turkel, E., "Numerical Solutions of the Euler Equations by Finite Volume Methods Using Runge–Kutta Time-Stepping Schemes," AIAA Paper No. 81-1259, 1981.

9 Swanson, R. C., and Turkel, E., "Artificial Dissipation and Central Difference Schemes for the Euler and Navier–Stokes Equations," AIAA Paper No. 87-1107.

10 Holmes, D. G., and Tong, S. S., "A Three-Dimensional Euler Solver for Turbomachinery Blade Rows," ASME *Journal of Engineering for Gas Turbines and Power*, Vol. 107, 1985, pp. 258–264.

11 Jameson, A., "Transonic Flow Calculations," MAE Report 1651, MAE Department, Princeton University, July 1983.

12 Lerat, A., "Une Classe de Schémas aux Différences Implicites Pour les Systèmes Hyperboliques de lois de Conservation," *Comptes Rendus Acad. Sciences Paris*, Vol. 288A, 1979.

13 Jameson, A., "The Evolution of Computational Methods in Aerodynamics," ASME *Journal of Applied Mechanics*, Vol. 50, 1983, pp. 1052–1070.

14 Brandt, A., "Multi-level Adaptive Computations in Fluid Dynamics," AIAA Paper No. 79-1455, 1979.

15 Ni, R.-H., "Multiple-Grid Scheme for Solving the Euler Equations," AIAA Paper No. 81-1025, 1981.

16 Chima, R. V., and Johnson, G. M., "Efficient Solution of the Euler and Navier–Stokes Equations With a Vectorized Multiple-Grid Algorithm," *AIAA J.*, Vol. 23, No. 1, 1985, pp. 23–32.

17 Sieverding, C. H., "Experimental Data on Two Transonic Turbine Blade Sections and Comparisons With Various Theoretical Methods," Von Kárman Institute for Fluid Dynamics, Report No. LS59, 1973.

18 Kiock, R., Lehthaus, F., Baines, N. C., and Sieverding, C. H., "The Transonic Flow Through a Plane Turbine Cascade as Measured in Four European Wind Tunnels," ASME *Journal of Engineering for Gas Turbines and Power*, Vol. 108, 1986, pp. 277–284.

19 Arnone, A., Liou, M.-S., and Povinelli, L. A., "Transonic Cascade Flow Calculation Using Non-periodic C-type Grids," *Proceedings of CFD Symposium on Aeropropulsion*, NASA Lewis Research Center, 1990.

Hierarchical Development of Three Direct-Design Methods for Two-Dimensional Axial-Turbomachinery Cascades

T. Korakianitis
Department of Mechanical Engineering,
Washington University,
St. Louis, MO 63130

The direct and inverse blade-design iterations for the selection of isolated airfoils and gas turbine blade cascades are enormously reduced if the initial blade shape has performance characteristics near the desirable ones. This paper presents the hierarchical development of three direct blade-design methods of increasing utility for generating two-dimensional blade shapes. The methods can be used to generate inputs to the direct- or inverse-blade-design sequences for subsonic or supersonic airfoils for compressors and turbines, or isolated airfoils. The examples included for illustration are typical modern turbine cascades, and they have been designed by the direct method exclusively. The first method specifies the airfoil shapes with analytical polynomials. It shows that continuous curvature and continuous slope of curvature are necessary conditions to minimize the possibility of flow separation, and to lead to improved blade designs. The second method specifies the airfoil shapes with parametric fourth-order polynomials, which result in continuous-slope-of-curvature airfoils, with smooth Mach number and pressure distributions. This method is time consuming. The third method specifies the airfoil shapes by using a mixture of analytical polynomials and mapping the airfoil surfaces from a desirable curvature distribution. The third method provides blade surfaces with desirable performance in very few direct-design iterations. In all methods the geometry near the leading edge is specified by a thickness distribution added to a construction line, which eliminates the leading edge overspeed and laminar-separation regions. The blade-design methods presented in this paper can be used to improve the aerodynamic and heat transfer performance of turbomachinery cascades, and they can result in high-performance airfoils in very few iterations.

Introduction

Gas turbine blades are three-dimensional objects operating in a complex flow field. Due to its complexity, the problem is usually reduced to a series of "stacked" two-dimensional problems. Blade design is partly a science and partly an art. The performance of the blades is expressed in the form of some property distribution (such as pressure, velocity, etc.) on the blade surface and in the cascade passage. Three-dimensional turbine blades are generated by "stacking" two-dimensional designs using some rules for: the flow angles from hub to tip at the leading and trailing edge, derived from radial-equilibrium flow conditions; the locus of the centers of gravity of the sections; and the three-dimensional shape of the leading edge and the trailing edge. Compromises in performance must be made to accommodate these three-dimensional constraints.

Demands for improved engine performance require sophisticated methods for blade design, because the performance of the airfoils becomes critical. Blade cascades can be designed by direct or inverse methods. Many definitions for direct and inverse design, analysis and design mode, analysis and optimization mode, are used by other investigators. For the purposes of this paper we will define the terms direct and inverse design as follows.

We define as direct the method in which the designer inputs the geometry of the blade, and the output is the performance from a flow-analysis program. The blade geometry is modified, and the analysis program is used in successive iterations until a desirable performance is obtained. We define as inverse design the various methods in which the designer specifies the performance of the cascade to obtain the geometry, or modifications to a portion of the surface velocity or pressure distribution (driven by expectations of boundary layer behavior), to obtain modifications to the geometry. The latter definition includes what other investigators define as fully inverse, semi-inverse, or simply design methods. Both methods are iterative and are based on the assumption of steady-inflow and steady-outflow conditions (although the flow around the blades during engine operation is inherently unsteady). The direct method is

Contributed by the Power Division and presented at the International Power Generation Conference, San Diego, California, October 6–10, 1991. Manuscript received by the Power Division October, 19, 1991. Associate Technical Editor: R. W. Porter.

laborious; it requires considerable insight and many iterations until an acceptable performance is obtained. On the other hand, the designer has direct control of the various geometric parameters, and structurally or dynamically infeasible blade shapes are excluded before they are analyzed. The inverse method is less laborious, but many (although not all) inverse-design programs must start from a blade geometry generated by a direct method. When inverse-design programs are used, one would like to start the inverse method with a blade shape or performance close to an acceptable design, since this will reduce the number of inverse-design iterations enormously. Therefore the designer needs a good blade shape obtained by a direct method. By the nature of inverse design, its user has less control over the blade shape and on the resulting performance. It may result in blades that are structurally inferior due to stress considerations, or impossible to manufacture. If one decides that some geometric parameters (such as stagger angle) must be changed, one must start from the beginning (direct method) again. The final design is usually obtained by a judicious combination of both methods.

Turbine-Cascade Geometry

In compressor cascades the flow diffuses; the pressure at the outlet is higher than the pressure at the inlet. In subsonic creased, and the area available to the flow should continuously increase, to a maximum area corresponding to the trailing edge of one blade and the pressure surface of the next. Traditionally compressor cascades have been designed by designing individual airfoils, in which thickness distributions are added to either side of a circular, parabolic, cubic, or other-shaped camber line (Horlock, 1958; Wilson, 1984; Moran, 1984; Cumpsty, 1989).

In turbine cascades the flow expands; the pressure at the outlet is lower than the pressure at the inlet. In subsonic cases

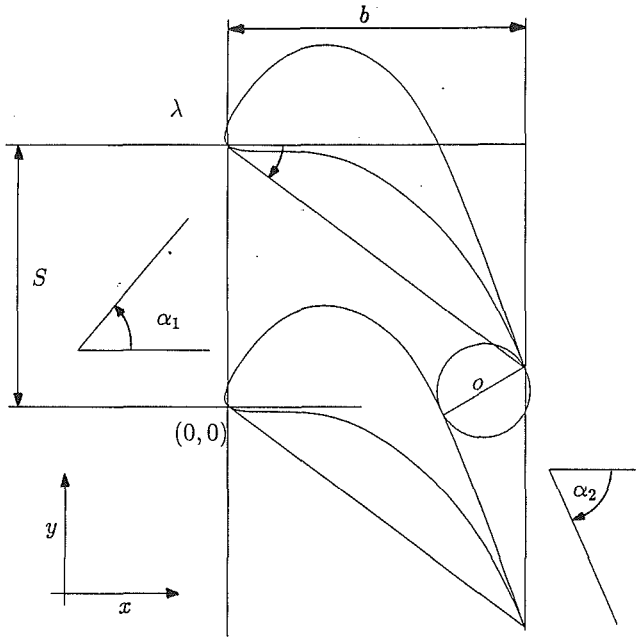

Fig. 1 Geometry of a typical turbine cascade

from cascade inlet to outlet the passage velocity is increased, and the area available to the flow should continuously decrease, to the minimum area corresponding to the circle of diameter o at the throat (see Fig. 1). Although some early turbine cascades were also designed from individual airfoils (Horlock, 1966; Dunham, 1974), traditionally turbine cascades have been designed by manipulating the shape of the passage between successive airfoils, and then closing the shape at the leading edge by specifying a leading edge circle, ellipse, or other ap-

Nomenclature

$\mathbf{A}$ = flow-area distribution along x (Fig. 7b)
a^x, a^y = spline coefficients (Eq. (9))
BC_1, BC_2 = spline derivatives (Eqs. (12), (13), (15), (20))
b = axial chord length (nondimensionally $b = 1$)
c = thickness-distribution coefficients (Eqs. (24))
$\mathbf{C}$ = $1/r$ = curvature (Eq. (7) and Fig. 7b)
$C1, \ldots, C5$ = Bezier-spline points specifying curvature (Fig. 7b)
C_L = tangential-loading coefficient (Eqs. (1), (2))
e = construction-line coefficients (Eq. (23))
fx = spline first derivative (Eqs. (11))
g = body force (Eqs. (4), (5))
K = a constant (spline arclength) (Eqs. (14), (20))
$L(\omega)$ = leading-edge construction lines
M = Mach number
p = pressure (Eqs. (4), (5))
P = points on suction and pressure surfaces
r = local radius of curvature (Eq. (7))
S = tangential spacing of the blades (Figs. 1, 2, 5, 7a)
s = spline parameter (Eq. (9))
sx = spline second derivative (Eqs. (11))
t = time (Eqs. (3), (4), (5))
T = thickness distribution (Eqs. (24))
v_i = velocity component ($i = r, \theta$)
$\mathbf{v}$ = velocity vector (Eq. (6))
(x, y) = Cartesian coordinates
$\mathbf{X}(s)$, $\mathbf{Y}(s)$ = parametric equations for (x, y) (Eq. (9))
$y1$, $y2$ = surface approximations (Eq. (22))
α = flow angle
β = angle of the blade surface
δ = root-x coefficient for T (Eqs. (24))
δ_1 = boundary layer displacement thickness (Fig. 3c)
λ = stagger angle of the blade
μ = dynamic viscosity (Eq. (6))
ρ = density (Eqs. (3), (4), (5))
τ = stress tensor (Eq. (6))
ϕ = angle of throat diameter with x axis (Fig. 7a)
ω = thickness-distribution parameters (Eqs. (23), (24))

Subscripts

1, 2 = with flow angle and Mach number, inlet and outlet, respectively
1, 2 = with blade point, leading edge, and trailing edge, respectively
a, b, c, d, m = after p or s, point on blade surface
c = construction line
f = point near the leading edge where thickness distribution joins blade surfaces
l = left side boundary condition
p = pressure side
r = right side boundary condition
s = suction side
θ = angle in polar coordinates (r, θ)
κ = construction line, with angle or point (Fig. 9)

propriate shape (Wilson, 1984; Pritchard, 1985; Korakianitis, 1987a, 1987b, 1989). The flow accelerates around both sides of the cascade, more on the suction and less on the pressure surface. These effects are shown in the performance maps of the sample turbine cascades discussed below.

In recent years the performance of both types of cascade has been improved with the use of inverse-design techniques, otherwise known as prescribed-velocity-distribution (PVD) techniques. Because the pressure is decreased along the turbine stages, any separation that may occur on turbine cascades is likely to reattach, and the fluid will continue its normal flow from turbine inlet to outlet. In compressors the pressure is increased along the stages, and any separation that may occur on compressor cascades may not reattach. This leads to compressor stall and surge. Bad turbine designs will still work, while bad compressor designs will not work. Compressors are harder to design than turbines. However, more attention has been given to compressor designs because of the deleterious effects of bad compressor performance, to the extent that many compressors are more efficient than the "corresponding" turbines (for similar mass-flow rates and pressure ratios). This is because insufficient attention has been paid to turbine-blade design. For the remainder of this paper we will concentrate on turbine cascades, although the methods developed for turbine cascades are directly applicable to compressor cascades and isolated airfoils.

The blade-design sequence depends on the application and the global constraints of the engine. The designer has many choices, but for the purposes of this paper we will refer to the axial-turbine-cascade diagram shown in Fig. 1. The flow is from left to right. One of the early design choices that must be made is the type of velocity diagram. We assume that the designer has chosen the blade row velocity diagram and its parameters such as: the inlet flow angle α_1; the outlet flow angle α_2; and the exit Mach number M_2, in the absolute frame for stators and in the relative frame for rotors. Four additional choices must be made: some specification for the nondimensional tangential spacing S/b between the blades; some specification for the stagger angle λ (the inclination of the blades with respect to the axial direction x); the nondimensional throat diameter o/b; and the trailing-edge thickness.

The stagger angle λ is defined as the angle between the axial direction and the line joining the leading edge of the cascade with the trailing edge point on the concave (pressure) surface. Some guidelines for low-speed turbine blades have been published by Kacker and Okapuu (1982), although the designer has considerable flexibility in choosing λ. The value of λ also dictates whether the cascade is front- or aft-loaded, and different philosophies and guidelines are used by different manufacturers (Korakianitis, 1993a).

The spacing between the blades (which is directly linked to the number of blades in the blade row) is a function of the tangential lift coefficient C_L, defined by:

$$C_L \equiv \frac{\text{tangential aerodynamic force}}{\text{tangential blade area} \times \text{outlet dynamic head}} \quad (1)$$

This expression can be manipulated in a number of ways (for compressible flow, for incompressible flow, accounting for variations in axial-flow velocity, etc.). Here we choose the incompressible-flow derivation (see Wilson, 1984), which reduces C_L to:

$$C_L = 2\frac{S}{b}\cos^2\alpha_2(\tan\alpha_1 - \tan\alpha_2) \quad (2)$$

where b is the axial chord and S is the tangential spacing of the blades. The actual value of C_L depends on the number of blades in the cascade, which dictates S. Typically $0.8 < C_L < 1.2$; earlier designs had lower values of C_L, and in modern cascades C_L has been gradually increasing. It is difficult to design high-efficiency cascades that have both high values of C_L and high values of flow deflection ϵ, where $\epsilon = |\alpha_1| + |\alpha_2|$.

The throat diameter is an extremely important design input, because it dictates the mass flow that can be passed through the cascade, and hence the work that can be delivered by the turbine. A good first approximation is $o/S = \cos\alpha_2$. Experimental figures linking the throat diameter o to the blade spacing S, the throat Mach number M_2, and the curvature of the convex (suction) blade surface near the trailing edge have been published by Ainley and Mathieson (1951), and are used extensively in the early stages of blade designs. The industry has for years relied on empirical relationships based on the Ainley-Mathieson data and on improvements to it (e.g., by Dunham and Came, 1970). These empirical data have been simplified by others for design applications (for example by Wilson, 1984; and Dunham, 1974). This is sufficient for preliminary design. Today's computer programs are more accurate and compute the outlet flow angle for a given geometry. Gostelow (1975) has explained how the result depends not only on the geometry, but also to some extent on the exact location of the point at which the Kutta condition is applied at the trailing edge.

The trailing-edge thickness should be as small as manufacturing considerations would allow to minimize the wake incident on the next blade row, but is also affected by geometric constraints imposed by manufacturing, strength and cooling-slot considerations. In the following figures the trailing edge is a point because we have used inviscid flow solvers to analyze the blade performance. The methods presented enable the designer to specify different trailing-edge points on the suction and pressure surfaces.

In turbine designs the flow of fluid adjacent to the convex (suction) surface is "unguided" on the suction surface downstream of the throat. In successful designs the velocity of the fluid adjacent to the suction surface accelerates from the stagnation point near the leading edge to some point near the throat, and then it decelerates. This region on the suction surface from the throat to the trailing edge is called the region of "unguided diffusion." If the flow decelerates too much then the boundary layer will become thicker and it may separate, the blade wake will be thick, and the resulting cascade will have poor performance (low efficiency). Therefore for high performance we would like the velocity to be continuously and smoothly increasing, from the stagnation point to the trailing edge, along both surfaces. On the suction surface designers like continuously and smoothly increasing velocity from the stagnation point to the point of maximum velocity that occurs near the throat, and minimum and smooth diffusion from the point of maximum velocity to the trailing edge. The Reynolds number of typical production turbine blades is of the order of 5×10^5 based on chord. The flow will probably become turbulent at some point along the surfaces. The smooth condition ensures that the boundary layer is not energized into turbulence unintentionally (although this can be done intentionally by designing a curvature discontinuity at the point where one wants the flow to become turbulent).

Theoretical Dependence on Curvature

Typically the flow in turbomachinery cascades is analyzed by considering Cartesian coordinates (x, y, z), or coordinate transformations in Cartesian systems of coordinates. But the flow needs to *curve* around the blades. The dependence of flow on curvature is seen if one writes the compressible-flow Navier-Stokes equations in the limiting case of cylindrical coordinates (r, θ, z). In particular, since we are interested in "stacking" two-dimensional solutions and geometries, we present here the equations of conservation of mass and momenta in polar coordinates (r, θ), taken from the text by Bird et al. (1960):

$$\frac{\partial \rho}{\partial t}+\frac{1}{r}\frac{\partial}{\partial r}(\rho r v_r)+\frac{1}{r}\frac{\partial}{\partial \theta}(\rho v_\theta)=0 \tag{3}$$

$$\rho\left(\frac{\partial v_r}{\partial t}+v_r\frac{\partial v_r}{\partial r}+\frac{v_\theta}{r}\frac{\partial v_r}{\partial \theta}-\frac{v_\theta^2}{r}\right)$$

$$=-\frac{\partial p}{\partial r}-\left(\frac{1}{r}\frac{\partial}{\partial r}(r\tau_{rr})+\frac{1}{r}\frac{\partial \tau_{r\theta}}{\partial \theta}-\frac{\tau_{\theta\theta}}{r}\right)+\rho g_r \tag{4}$$

$$\rho\left(\frac{\partial v_\theta}{\partial t}+v_r\frac{\partial v_\theta}{\partial r}+\frac{v_\theta}{r}\frac{\partial v_\theta}{\partial \theta}+\frac{v_r v_\theta}{r}\right)$$

$$=-\frac{1}{r}\frac{\partial p}{\partial \theta}-\left(\frac{1}{r^2}\frac{\partial}{\partial r}(r^2\tau_{r\theta})+\frac{1}{r}\frac{\partial \tau_{\theta\theta}}{\partial \theta}\right)+\rho g_\theta \tag{5}$$

where in the above equations p is the static pressure, and for Newtonian fluids the stress components τ_{rr}, $\tau_{\theta\theta}$, and $\tau_{r\theta}$ are related to the dynamic viscosity μ by the equations:

$$\tau_{rr}=-\mu\left[2\frac{\partial v_r}{\partial r}-\frac{2}{3}(\nabla\cdot\mathbf{v})\right]$$

$$\tau_{\theta\theta}=-\mu\left[2\left(\frac{1}{r}\frac{\partial v_\theta}{\partial \theta}+\frac{v_r}{r}\right)-\frac{2}{3}(\nabla\cdot\mathbf{v})\right]$$

$$\tau_{r\theta}=\tau_{\theta r}=-\mu\left[r\frac{\partial}{\partial r}\left(\frac{v_\theta}{r}\right)+\frac{1}{r}\frac{\partial v_r}{\partial \theta}\right]$$

$$(\nabla\cdot\mathbf{v})=\frac{1}{r}\frac{\partial}{\partial r}(rv_r)+\frac{1}{r}\frac{\partial v_\theta}{\partial \theta} \tag{6}$$

A similar dependence of incompressible flow on curvature is also shown in most fluid dynamics texts in cylindrical coordinates, and Schlichting (1968, p. 112) attributes a set of similar equations for incompressible flow in curvilinear coordinates (x, r, y) to W. Tollmien. The $1/r$ and $1/r^2$ terms in these equations suggest a strong dependence of local velocity on curvature. Once the flow passage has been manipulated until the turbine cascade looks like a turbine cascade, the performance depends on the behavior of the boundary layer, where Eqs. (6) also indicate that the boundary layer is affected by the local radius. Since we require smooth velocity distributions along the blade surfaces (continuous slope of velocity with respect to surface length), the above equations require smooth curvature distributions along the blade surfaces (continuous slope of curvature). Continuous slope of the curvature requires continuous third derivatives, as illustrated in the following two equations for curvature and slope of curvature for $y = f(x)$, $y' = df(x)/dx$, $y'' = d^2f(x)/dx^2$ and $y''' = d^3f(x)/dx^3$.

$$\mathbf{C}=\frac{1}{r}=\frac{y''}{[1+y'^2]^{(3/2)}} \tag{7}$$

$$\mathbf{C}'=\frac{y'''[1+y'^2]-3y'y''^2}{[1+y'^2]^{(5/2)}} \tag{8}$$

The First Blade-Design Method

In the first blade-design method (Korakianitis, 1989) the cascade geometry is specified by five points (excluding the trailing-edge points and the origin) and two slopes on each surface, as shown in Fig. 2. The leading-edge region is generated with two thickness distributions added perpendicularly to two parabolic construction lines. The leading edge geometry is similar in all methods and is described in detail below.

The points on the suction surface are P_{sf}, P_{sa}, P_{sb}, P_{sc}, and P_{sd}. The trailing-edge point P_{s2} (specified by the stagger angle λ and the trailing edge thickness), the angle of the suction surface at the trailing edge β_{s2}, and points P_{sc} and P_{sd} are used to evaluate a third-order analytic polynomial $y_1 = f(x)$ for the blade surface between points P_{sc} and P_{s2}. The value of β_{s2} is 3 to 6 deg smaller (negative values) than the outlet flow angle α_2. Point P_{sf} (user input), β_{sf}, the angle of the suction surface at P_{sf}, and points P_{sa} and P_{sb} are used to evaluate a third-order analytic polynomial $y_2 = f(x)$ for the blade surface between points P_{sf} and P_{sb}. The value of β_{sf} is smaller (positive values) than the inlet flow angle α_1. The segment from P_{sb} to P_{sc} is a fifth-order analytic polynomial $y_3 = f(x)$ evaluated from the six conditions of matching point, first and second derivatives with y_1 and y_2 at P_{sc} and P_{sb}, respectively. This segment could also be a seventh-order polynomial by adding the two additional conditions of matching third derivatives at P_{sb} and P_{sc}, but the seventh-order polynomials frequently result in undesirable inflections on the surfaces. The development of the pressure surface is exactly analogous, using points P_{pf}, P_{pa}, P_{pb}, P_{pc}, P_{pd}, and P_{p2} and angles β_{pf} and β_{p2} (a few degrees larger than the outlet flow angle α_2). The resulting trailing-edge wedge angle is given by the difference of the two slopes of the suction and pressure surfaces at the trailing edge, β_{s2} and β_{p2}, respectively, and it should be between 8 and 14 deg. A disadvantage of this method is that the throat diameter o is an output of the other design inputs.

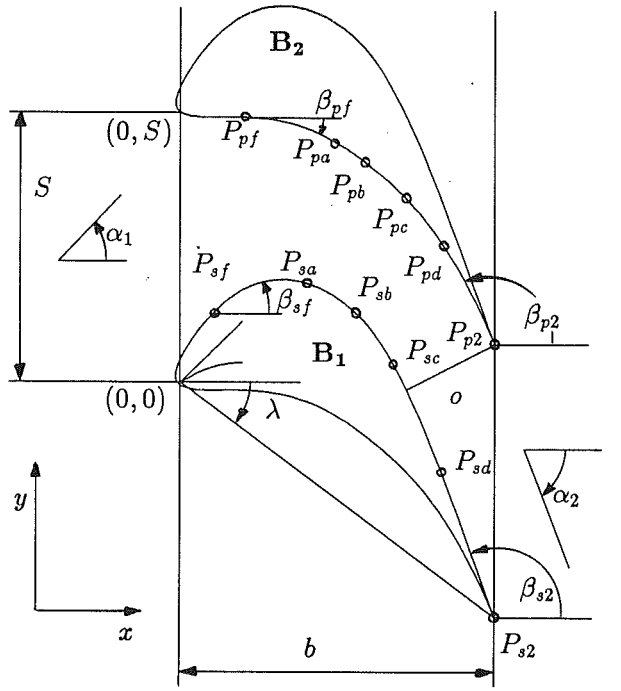

Fig. 2 Parameters used to specify the cascade surfaces in the first blade-design method

Using this method we have designed over 20 turbine cascades of various tangential loadings and deflections. Thirteen of those cascades were used to study unsteady forcing functions in turbomachinery stator–rotor interactions (Korakianitis, 1987a, 1988a, 1988b, 1992a, 1992b). Figure 3 shows the performance of four sample cascades with design inputs very close to each other, as shown in Appendix A (Table 1). The corresponding Mach number contours for cascades B4-0 and B4-3 are shown in Fig. 4. The flows (for all the Mach number distributions in this paper) have been calculated with the steady-flow calculation option of UNSFLO (Giles, 1988). The accuracy of the computations is very high, as shown in tests by Giles (1988) and Korakianitis (1992a, 1993a, 1993b) for numerous steady and unsteady flows in turbomachinery. The boundary layer behavior has been calculated with Rotta's (1971) integral method for compressible two-dimensional flows. In the latter we assumed a Reynolds number based on axial chord of 5.24×10^5, and in all cases transition on both surfaces occurred very near the leading edge. The different inputs result in very small slope-of-curvature discontinuities, which are reflected in both the Mach number distributions and the bound-

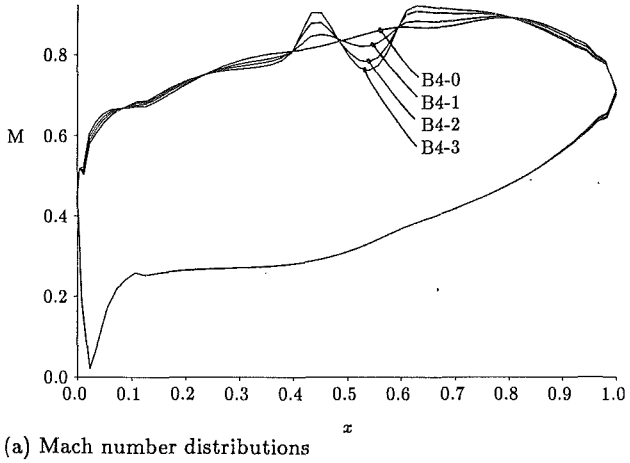

(a) Mach number distributions

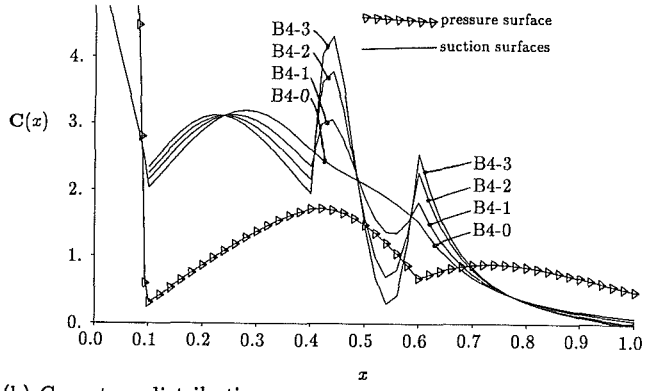

(b) Curvature distributions

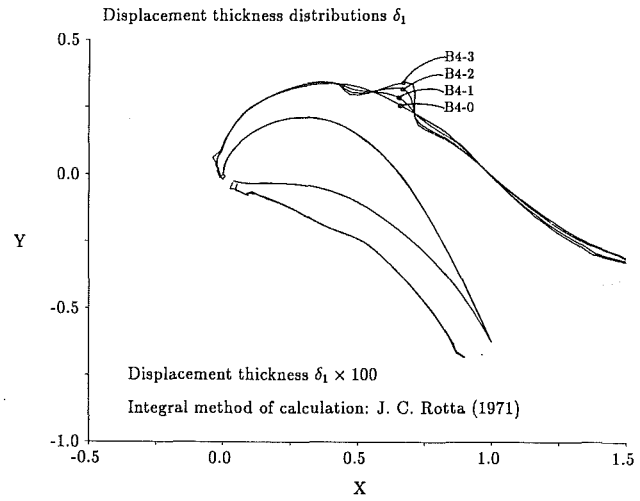

(c) Effect on boundary layers

Fig. 3 Surface distributions for cascades B4-0, B4-1, B4-2, B4-3; α_1 = 40 deg, α_2 = −60 deg, C_L = 1.00, λ = −32 deg

ary layer displacement thicknesses. The suction-surface wake from cascade B4-3 (largest slope-of-curvature discontinuity) is thicker than that of cascade B4-0 (no slope-of-curvature discontinuity). The differences in the blade surfaces are so small that they are very hard to see in either Fig. 3(*c*) (where all four blades have been plotted on top of each other), or in Fig. 4.

The first method indicates that even small slope-of-curvature discontinuities may result in unusually loaded cascades (larger curvature spikes have resulted in correspondingly larger Mach number and loading spikes) and thicker wakes. Most techniques for line and surface generation (cubic splines, B splines, Bezier curves, etc.) have continuous first and second derivatives, but not third derivative (slope of curvature) continuity.

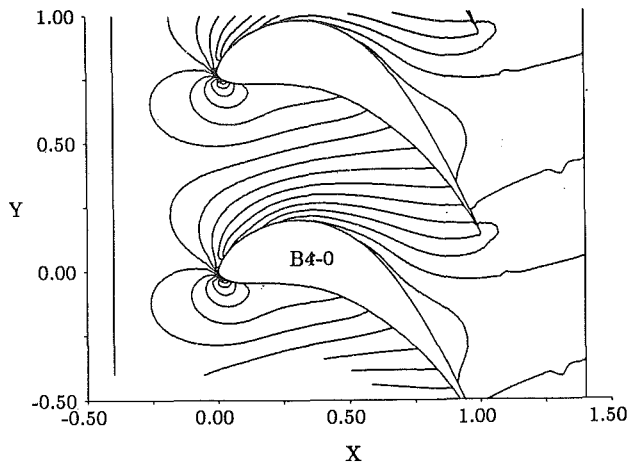

(a) For cascade B4-0 (contour increment 0.05)

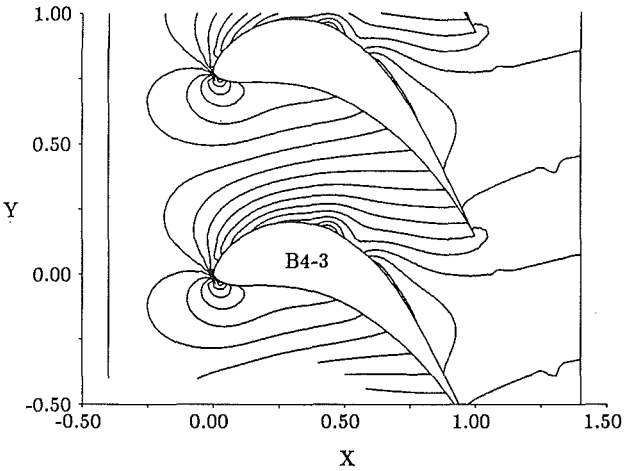

(b) For cascade B4-3 (contour increment 0.05)

Fig. 4 Mach number contours for cascades B4-0 and B4-3; contour increment 0.05

A slope-of-curvature discontinuity also occurs when a leading-edge circle or ellipse is used to join the leading-edge region. This has resulted in many test and production airfoils (isolated and in turbomachine cascades) that exhibit Mach number and pressure coefficient distribution spikes, dips, and humps of various magnitudes. These occasionally result in unexpected loading distributions along the blade length and in local separation bubbles. Some of these effects are visible in the computational and experimental data published, for example, by: Okapuu (1974), Gostelow (1976), Wagner et al. (1985), Hourmouziadis et al. (1987) (with separation bubble), Baines et al. (1986), Sharma et al. (1992), and possibly Mee et al. (1992a, 1992b) (with separation bubble).

The Second Blade-Design Method

In this method we developed a set of fourth-order parametric splines with third-derivative (slope-of-curvature) continuity at the spline junctions. The nodes of the parametric splines along the suction and pressure surfaces are illustrated in Fig. 5. On the suction surface the nodes are points $\{P_{sf}, P_{sa}, P_{sm}, P_{s2}\}$, and on the pressure surface the nodes are points $\{P_{pf}, P_{pa}, P_{pm}, P_{p2}\}$, although more nodes could be used for each surface. In the following we show the fourth-order parametric splines for n number of nodes $\{P1, P2, \ldots Pn\}$ corresponding to $(n-1)$ spline segments on either surface, where the parameter is s. Let (x_i, y_i) be the Cartesian coordinates of any point P_i on the surface and $(\mathbf{X}_j(s), \mathbf{Y}_j(s))$ be the algebraic description of any spline segment j. The splines take the form:

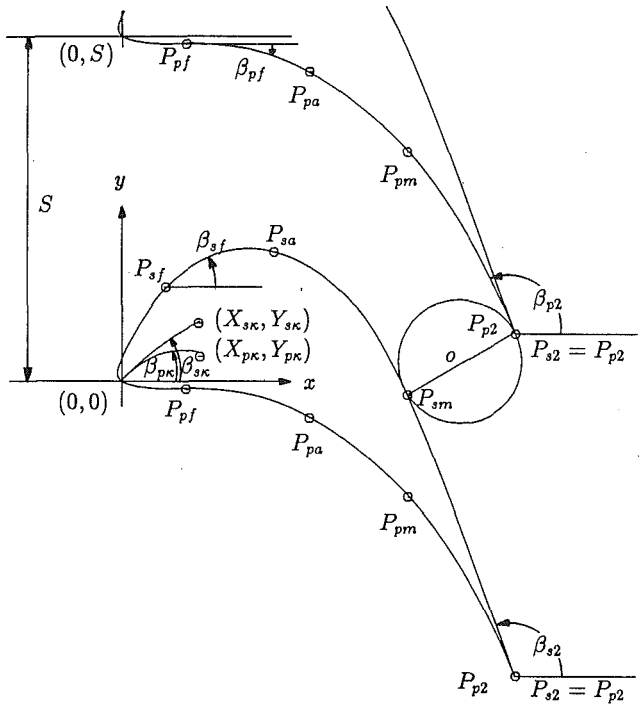

Fig. 5 Parameters used to specify the cascade surfaces in the second blade-design method

$$\begin{aligned}\mathbf{X}_j(s) &= a^x_{j0} + a^x_{j1}s + a^x_{j2}s^2 + a^x_{j3}s^3 + a^x_{j4}s^4 \\ \mathbf{Y}_j(s) &= a^y_{j0} + a^y_{j1}s + a^y_{j2}s^2 + a^y_{j3}s^3 + a^y_{j4}s^4\end{aligned} \tag{9}$$

where $0 \le s \le 1$ in each of the $(n-1)$ segments j, and a are the spline coefficients for $\mathbf{X}(s)$ and $\mathbf{Y}(s)$. In the following we show the derivations applicable to $\mathbf{X}(s)$; the derivation for $\mathbf{Y}(s)$ is exactly analogous. If fx_i and sx_i are the first and second derivatives of $\mathbf{X}(s)$ with respect to s at each of the n nodes i, requiring

$$\begin{aligned}\mathbf{X}_i|_{s=0} &= x_i \\ \mathbf{X}_i|_{s=1} &= x_{i+1} \\ \left.\frac{d\mathbf{X}_i}{ds}\right|_{s=0} &= fx_i \\ \left.\frac{d\mathbf{X}_i}{ds}\right|_{s=1} &= fx_{i+1} \\ \left.\frac{d^2\mathbf{X}_i}{ds^2}\right|_{s=0} &= sx_i\end{aligned} \tag{10}$$

Equation (11) gives the solution for the spline coefficients of the spline segment i in terms of the first and second derivatives at the nodes:

$$\begin{aligned}a^x_{i0} &= x_i \\ a^x_{i1} &= fx_i \\ a^x_{i2} &= sx_i/2 \\ a^x_{i3} &= 4(x_{i+1} - x_i) - fx_{i+1} - 3fx_i - sx_i \\ a^x_{i4} &= 3(x_i - x_{i+1}) + fx_{i+1} + 2fx_i + sx_i/2\end{aligned} \tag{11}$$

The solution for the first and second derivatives at the nodes is found by requiring second- and third-derivative continuity:

$$\left.\frac{d^2\mathbf{X}_i}{ds^2}\right|_{s=1} = \left.\frac{d^2\mathbf{X}_{i+1}}{ds^2}\right|_{s=0}$$

$$\left.\frac{d^3\mathbf{X}_i}{ds^3}\right|_{s=1} = \left.\frac{d^3\mathbf{X}_{i+1}}{ds^3}\right|_{s=0}$$

which for $i = 2, 3, \ldots, n-1$ lead to

$$6fx_{i-1} + sx_{i-1} + 6fx_i - sx_i = 12(x_i - x_{i-1})$$

$$5fx_{i-1} + sx_{i-1} + 6fx_i + sx_i + fx_{i+1} = 4(x_{i+1} + x_i - 2x_{i-1})$$

The last two equations can be manipulated into the matrix form shown in Eq. (12),

$$\begin{bmatrix}
1 & 0 & 0 & 0 & 0 & 0 & 0 & 0 & \cdot & \cdot & \cdot & \cdot & \cdot \\
0 & 1 & 0 & 0 & 0 & 0 & 0 & 0 & \cdot & \cdot & \cdot & \cdot & \cdot \\
5 & 1 & 6 & -1 & 1 & 0 & 0 & 0 & \cdot & \cdot & \cdot & \cdot & \cdot \\
6 & 1 & 6 & -1 & 0 & 0 & 0 & 0 & \cdot & \cdot & \cdot & \cdot & \cdot \\
0 & 0 & 5 & 1 & 6 & 1 & 1 & 0 & \cdot & \cdot & \cdot & \cdot & \cdot \\
0 & 0 & 6 & 1 & 6 & -1 & 0 & 0 & \cdot & \cdot & \cdot & \cdot & \cdot \\
\cdot & \cdot & \cdot & \cdot & \cdot & \cdot & \cdot & \cdot & \cdot & \cdot & \cdot & \cdot & \cdot \\
\cdot & \cdot & \cdot & \cdot & \cdot & \cdot & \cdot & \cdot & \cdot & \cdot & \cdot & \cdot & \cdot \\
\cdot & \cdot & \cdot & \cdot & \cdot & \cdot & \cdot & \cdot & \cdot & \cdot & \cdot & \cdot & \cdot \\
\cdot & \cdot & \cdot & \cdot & \cdot & 0 & 0 & 5 & 1 & 6 & 1 & 1 & 0 \\
\cdot & \cdot & \cdot & \cdot & \cdot & 0 & 0 & 6 & 1 & 6 & -1 & 0 & 0 \\
\cdot & \cdot & \cdot & \cdot & \cdot & 0 & 0 & 0 & 0 & 0 & 0 & 1 & 0 \\
\cdot & \cdot & \cdot & \cdot & \cdot & 0 & 0 & 0 & 0 & 6 & 1 & 6 & -1
\end{bmatrix}$$

$$\begin{bmatrix} fx_1 \\ sx_1 \\ fx_2 \\ sx_2 \\ fx_3 \\ sx_3 \\ \cdot \\ \cdot \\ \cdot \\ fx_{n-1} \\ sx_{n-1} \\ fx_n \\ sx_n \end{bmatrix} = \begin{bmatrix} BC_{x,1}(P_f) \\ BC_{x,2}(P_f) \\ 4(x_3 + x_2 - 2x_1) \\ 12(x_2 - x_1) \\ 4(x_4 + x_3 - 2x_2) \\ 12(x_3 - x_2) \\ \cdot \\ \cdot \\ \cdot \\ 4(x_n + x_{n-1} - 2x_{n-2}) \\ 12(x_{n-1} - x_{n-2}) \\ BC_{x,1}(P_2) \\ 12(x_n - x_{n-1}) \end{bmatrix} \tag{12}$$

from which the values of the first and second derivatives at the nodes can be found. The only remaining unknowns are the right- and left-side boundary conditions

$$\begin{aligned}BC_{lx,1} &= \left.\frac{d\mathbf{X}_1}{dx}\right|_{s=0} \\ BC_{lx,2} &= \left.\frac{d^2\mathbf{X}_1}{ds^2}\right|_{s=0} \\ BC_{rx,1} &= \left.\frac{d\mathbf{X}_{n-1}}{ds}\right|_{s=1}\end{aligned} \tag{13}$$

which are evaluated below.

The first-derivative boundary conditions at the right and left sides of each spline set are related to the angles of the blades at the leading and trailing edge β_{sr}, β_{sl}, β_{pr}, and β_{pl} shown in Fig. 5. These in turn are related to the flow angles α_1 and α_2, and the effect the designer expects that the blade-surface angles will have on the flow angles.

For the first-derivative boundary conditions we can write:

$$\tan\beta = \frac{dy}{dx} = \frac{dy/ds}{dx/ds} = \frac{\sin\beta}{\cos\beta} = \frac{K\sin\beta}{K\cos\beta} \tag{14}$$

so that an obvious choice for the first derivatives of the splines in $\mathbf{X}(s)$ and $\mathbf{Y}(s)$ at the first and last points of the spline sets of the suction or the pressure surfaces is

$$\begin{aligned}BC_{y,1} &= \frac{dy}{ds} = K\sin\beta \\ BC_{x,1} &= \frac{dx}{ds} = K\cos\beta\end{aligned} \tag{15}$$

where K is an arbitrary length chosen to be equal to the arc-length of the appropriate spline segment, and β is the corre-

sponding blade-surface angle (right for points P_{p2} and P_{s2} and left for points P_{pf} and P_{sf}) from Fig. 5.

Similarly the second derivatives can be expressed as:

$$\frac{d^2y}{ds^2} = K \cos \beta$$

$$\frac{d^2x}{ds^2} = -K \sin \beta \tag{16}$$

Equations (15) and (16) give:

$$\left(\frac{d^2y}{ds^2}\right)\left(\frac{dy}{ds}\right) = -\left(\frac{d^2x}{ds^2}\right)\left(\frac{dx}{ds}\right) \tag{17}$$

The curvature and second derivatives are also related by:

$$\frac{d^2y}{dx^2} = \mathbf{C}\left[1 + \left(\frac{dy/ds}{dx/ds}\right)^2\right]^{3/2} = \frac{(d^2y/ds^2)(dx/ds) - (d^2x/ds^2)(dy/ds)}{(dx/ds)^3} \tag{18}$$

Equations (17) and (18) are solved for the second derivatives with respect to s.

$$\frac{d^2x}{ds^2} = -\mathbf{C}\left(\frac{dy}{ds}\right)\left[\left(\frac{dx}{ds}\right)^2 + \left(\frac{dy}{ds}\right)^2\right]^{1/2}$$

$$\frac{d^2y}{ds^2} = \mathbf{C}\left(\frac{dx}{ds}\right)\left[\left(\frac{dx}{ds}\right)^2 + \left(\frac{dy}{ds}\right)^2\right]^{1/2} \tag{19}$$

which finally give the second-derivative boundary conditions at points $P1$, where $P1$ in Eqs. (20) denotes the "left" points P_{pf} and P_{sf}:

$$BC_{x,2}(P1) = \left.\frac{d^2x}{ds^2}\right|_{P1} = -K^2 \left|\mathbf{C}\right|_{P1} \sin \beta|_{P1}$$

$$BC_{y,2}(P1) = \left.\frac{d^2y}{ds^2}\right|_{P1} = -K^2 \left|\mathbf{C}\right|_{P1} \cos \beta|_{P1} \tag{20}$$

The above procedure is applied for the splines in x and y for the suction and the pressure surfaces. Point P_{sm} is special, and it is instrumental for the suction-surface design. It is constrained to move on a circle with center the trailing edge of the top blade and radius o. Out of all the points that lie on the circle we choose the ones that correspond to splines with slopes perpendicular to line $P_{p2}P_{sm}$ at point P_{sm}.

Using this method, we constructed a program that varies the locations of the nodes while searching for curvature distributions with desirable characteristics and continuously decreasing area distributions (Korakianitis and Pantazopoulos, 1993c). The performance of a sample cascade with inlet flow angle of 0 deg, outlet flow angle of -60 deg, and tangential-loading coefficient $C_L = 1.00$ is shown in Fig. 6, and the corresponding blade-design parameters are included in Appendix B (Table 2).

These fourth-order parametric splines may have additional applications, such as smooth automobile surface generation for aesthetically pleasing reflections. Designing new turbine blades with the second blade-design method was a CPU-intensive proposition. After designing six different cascades we developed the third-design method.

The Third Blade-Design Method

In the third design method part of the blade surface is an analytic polynomial, and part of the blade surface is evaluated by mapping a desirable curvature distribution on the (x, y) plane, as shown in Figs. 7(*a*) and 7(*b*).

The trailing edge region of the suction surface is specified by a third-order polynomial $y = f(x)$, evaluated using four conditions: the location of P_{s2}; the blade angle β_{s2} at the trailing

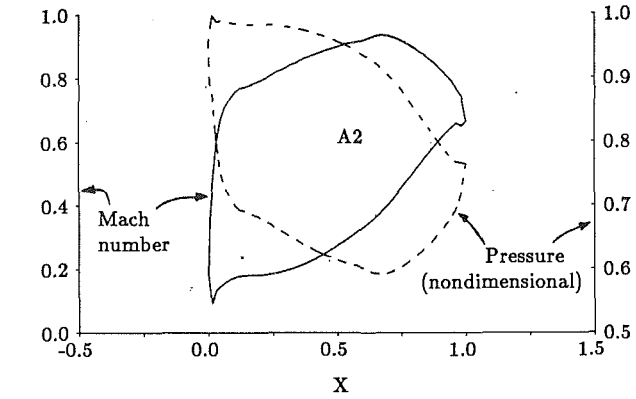

(a) Surface Mach number distributions

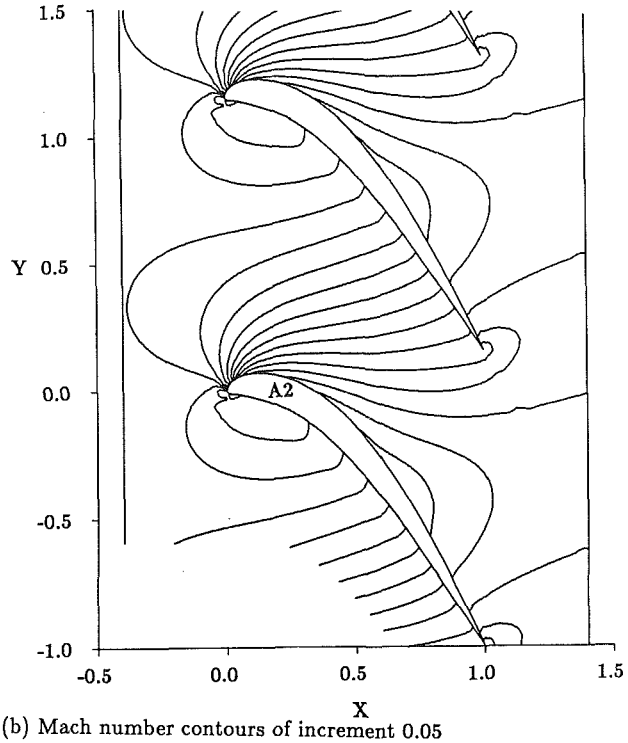

(b) Mach number contours of increment 0.05

Fig. 6 Performance of a cascade design with the second blade-design method; surface Mach number distribution and Mach number contours of increment 0.05

edge; and the angle ϕ of the throat-circle diameter with the x axis. The latter specifies two conditions: the location of point P_{sm}, and the tangent of the third-order polynomial at that point, equal to $(\pi/2 + \phi)$. The analytic polynomial has continuous first and second derivatives. With these we compute the curvature of the resulting blade surface $\mathbf{C}_s(x)$ (using Eq. (7)) between points P_{sm} and P_{s2}, and plot it between points $C4_s$ and $C5_s$ in Fig. 7(*b*).

The trailing edge region of the pressure surface is specified by a third-order polynomial $y = f(x)$, evaluated using four conditions: the location of P_{p2}; the blade angle β_{p2} at the trailing edge; the (x, y) coordinates of a point P_{pm} on the surface; and the angle β_{pm} of the blade surface at point P_{pm} with the x axis. With the first and second derivatives of this polynomial we compute the curvature of the resulting blade surface $\mathbf{C}_p(x)$ (using Eq. (7)) between points P_{pm} and P_{p2}, and plot it between points $C4_p$ and $C5_p$ in Fig. 7(*b*).

The slopes of the curvatures $\mathbf{C}_s(x)$ and $\mathbf{C}_p(x)$ at points $C4_s$ and $C4_p$, respectively, are computed and become inputs for the rest of the design. A gradually increasing curvature distribution in the trailing edge regions results in mechanically and aerodynamically feasible blade shapes.

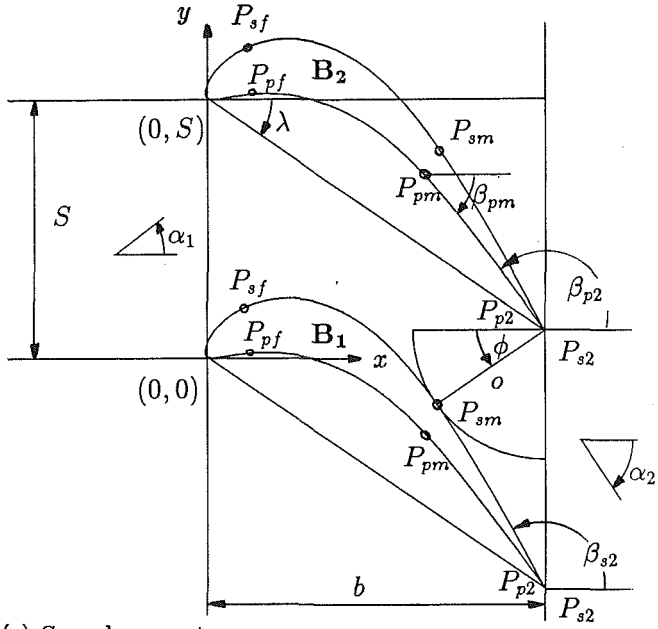

(a) Cascade geometry

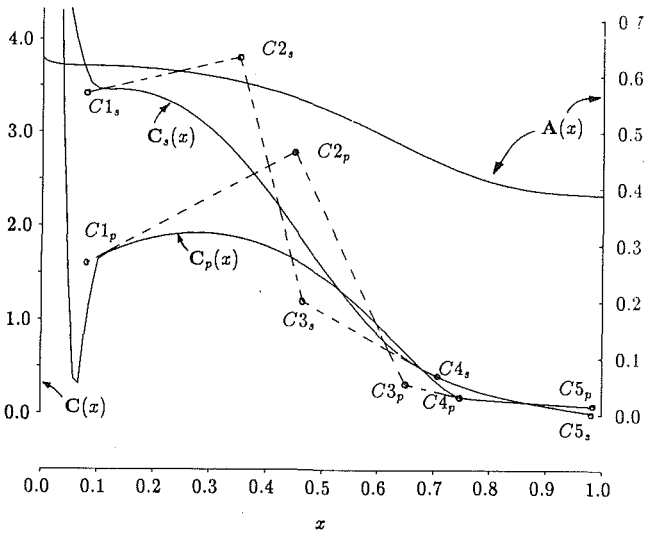

(b) Corresponding curvature distribution

Fig. 7 Parameters used to specify the cascade surfaces in the third blade-design method

The design is converted into an effort of specifying a curvature distribution for the shape of the blade surfaces $\mathbf{C}_s(x)$ and $\mathbf{C}_p(x)$. In order to ensure slope-of-curvature continuity, the curvature from points P_f to points P_m is specified using a Bezier spline in curvatures using the following conditions (see Fig. 7(*b*)). On the curvature of the suction surface we specify points $C1_s$, $C2_s$, $C3_s$, and $C4_s$. Point $C4_s$ is already specified from the corresponding value of curvature evaluated from the trailing-edge third-order polynomial. The x location of point $C3_s$ is variable, but the value of curvature there is evaluated such that line $C3_sC4_s$ is tangent to the line of curvature at point $C4_s$. Point $C2_s$ is user specified. Point $C1_s$ is specified at an x location corresponding to P_f, or at an x location just ahead of P_f. Since the slope of the Bezier curve is tangent to the line of knots at its ends, the tangency condition at point $C4_s$ ensures slope-of-curvature continuity from $C1_s$ to $C5_s$ (from P_{sf} to P_{s2}). Similarly points $C1_p$, $C2_p$, and $C3_p$ are specified on $\mathbf{C}_p(x)$. $\mathbf{A}(x)$ in Fig. 7(*b*) is the area distribution between blades $\mathbf{B}_1$ and $\mathbf{B}_2$, measured from the pressure surface of blade $\mathbf{B}_2$ to the suction surface of blade $\mathbf{B}_1$.

Using central differences, Eq. (7) is written as:

$$\mathbf{C}_i = \frac{CF1/CF2}{CF3}$$

$$CF1 = 2\left(\frac{y_{i+1}-y_i}{x_{i+1}-x_i} - \frac{y_i-y_{i-1}}{x_i-x_{i-1}}\right)$$

$$CF2 = (x_{i+1}-x_{i-1})$$

$$CF3 = \left\{\left[\frac{1}{2}\left(\frac{y_{i+1}-y_i}{x_{i+1}-x_i} + \frac{y_i-y_{i-1}}{x_i-x_{i-1}}\right)\right]^2 + 1\right\}^{3/2} \quad (21)$$

From the above equation given (x_{i-1}, y_{i-1}), (x_i, y_i), x_{i+1} and $\mathbf{C}_i$ we can compute y_{i+1}. This can be done by manipulating Eq. (21) into a sixth-order linear algebraic equation in y_{i+1}, or by a numerical solution. We have implemented a regular-falsi solution for y_{i+1} using Eq. (21). This is solved starting from points P_m and progressing explicitly to points P_f. The Bezier spline is iteratively manipulated until the slope and the y location of the blade surfaces at points P_f, and the shape of the curvature distributions are acceptable.

In some cases trying to make the blade surfaces pass with desirable slopes through desirable P_f points become tedious for the inexperienced in the method. For those cases we provide an alternative solution. The designer specifies the (x, y) location of point P_f. A parabola passing through points P_f, P_m and the next point on the blade surface in the trailing edge region is used as a first approximation $y1(x)$ to the blade surface. Equation (21) is manipulated into:

$$[y2_{i+1} - 2y2_i + y2_{i-1}] = \Delta x^2 \mathbf{C}_i \left[\left(\frac{y1_{i+1}-y1_{i-1}}{2\Delta x}\right)^2 + 1\right]^{3/2} \quad (22)$$

Equation (22) is written as a tridiagonal matrix of the form $[A]\{y2\} = \{B(y1)\}$. Points P_m and the input points for P_f are incorporated as boundary conditions in the first and last rows of the right-hand side. The system of equations is solved for $y2_i$ with an LU decomposition. The values of $y1_i$ on the right-hand side are set equal to the previous solution for $y2_i$, and the process is repeated until the values of $y1_i$ and $y2_i$ converge to the same solution (after about twelve iterations). The converged blade surface in the final $y2_i$ ($y2(x)$) passes through points P_f and P_m, but in the general case results in a spike in curvature at point P_m. The curvature-input points $C1$, $C2$, and $C3$ are iteratively manipulated until the spike is minimized, and then having found the curvature-inputs that will make the blade surface pass through point P_f, the designer returns to specifying the blade surface by solving Eq. (21).

Using this method we can produce the geometry of a continuous-slope-of-curvature turbine cascade in a few seconds, and compute its expected flow performance on a relatively coarse grid (40 by 10 grid points in one passage) in about ten DECstation-3100 CPU minutes. Successive direct-design iterations result in changes in the blade shape, curvature, and loading distributions, which we can direct towards front-loaded, midloaded, or aft-loaded performance. The final blade-shape and performance changes are computed on finer grids (100 by 40 grid points in one passage). These design iterations result in about one high-performance cascade per day (Korakianitis, 1993a). High performance means smoother Mach number and pressure distributions than typical ones published in current literature (such as the examples in (Sharma et al., 1992)). These turbine geometries have been used to study the effects of stagger angle on the type of loading distribution (front- versus aft-loaded), and time-dependent stator-rotor interactions in turbomachinery flow fields (Korakianitis, 1992c, 1993a, 1993d). The performance of a high-deflection highly loaded sample cascade with inlet flow angle of 50 deg, outlet flow angle of -60 deg, and tangential-loading coefficient $C_L = 1.20$ is shown in Fig. 8, and the corresponding blade-design parameters are included in Appendix C (Table 3).

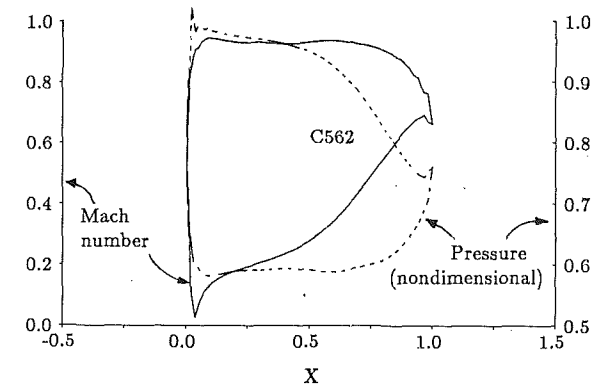

(a) Surface Mach number distributions

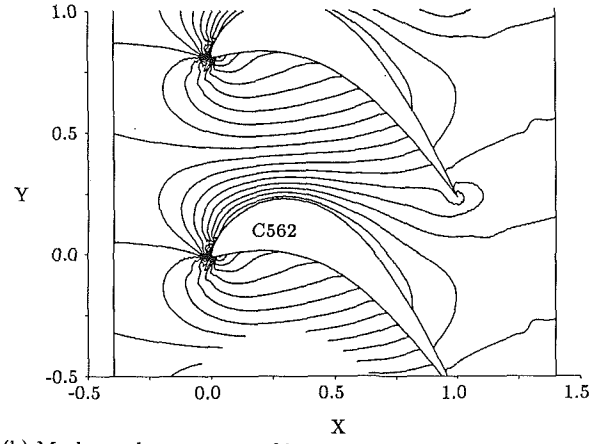

(b) Mach number contours of increment 0.05

Fig. 8 Performance of a cascade designed with the third blade-design method

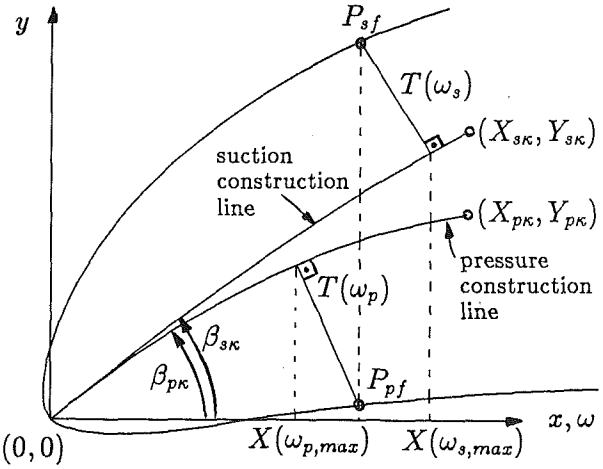

Fig. 9 Parameters used to specify the leading edge geometry

Leading Edge Geometry

The leading edge geometry is designed by specifying thickness distributions added perpendicularly to parabolic construction lines that pass through the leading edge, as shown in Fig. 9. The parabolic construction lines are specified by the angle of the construction line at the origin β_κ and the (x, y) location of the origin (0, 0), and of one additional point (X_κ, Y_κ) on the corresponding (suction and pressure) construction line. Other similarly smooth forms of construction lines could also be used. The perpendiculars from points P_f on the parabolic construction lines $L(\omega)$ define a parameter ω along x as follows (see Fig. 9):

$$\omega = x$$

$$L(\omega) = e_0 + e_1\omega + e_2\omega^2 \tag{23}$$

where the constants e_0, e_1, and e_2 are evaluated from the conditions of the parabolic construction lines. For the suction line we add a thickness distribution above the suction-side parabolic construction line, and for the pressure line we add a thickness distribution below the pressure-side parabolic construction line. The thickness distributions are of the form:

$$T_s(\omega) = \delta_s\sqrt{\omega} + c_{s1}\omega + c_{s2}\omega^2 + c_{s3}\omega^3 + c_{s4}\omega^4$$

$$T_p(\omega) = \delta_p\sqrt{\omega} + c_{p1}\omega + c_{p2}\omega^2 + c_{p3}\omega^3 + c_{p4}\omega^4 \tag{24}$$

where δ are specified by the designer. The coefficients c_1, c_2, c_3, and c_4 are derived with the conditions that the absolute values, first, second, and third derivatives of the thickness distribution and of the blade surface to the right of point P_f *with respect to the parabolic construction line* are equal. This ensures curvature and slope-of-curvature continuity at points P_f. The value of the parameter δ can be used to specify thicker or thinner leading edges, which would affect the thickness of the blade in the vicinity of the leading edge, and therefore its design-point and off-design point operating performance. The origin (0, 0) itself is a singular point. In order to achieve first-derivative continuity at that point, the angle of the parabolic construction lines should be equal for the suction and pressure surfaces ($\beta_{s\kappa} = \beta_{p\kappa}$, and approximately equal to the inlet flow angle α_1).

This type of thickness distribution has been used in the second and third blade-design methods. In the first blade-design method the thickness distributions had point, first, and second derivative continuity with the blade surface, but not third derivative continuity ($c_{s4} = c_{p4} = 0$). The effect of the resulting curvature discontinuity is seen at $x = 0.10$ in Fig. 3(*a*). These small discontinuities are not evident in the performance of the cascades designed with the second and third blade-design methods.

Conclusions

The hierarchical development of three blade-design methods has been presented. Small slope-of-curvature discontinuities result in Mach-number or pressure-coefficient distribution spikes or humps. These may introduce regions of local acceleration and deceleration, separation, or undesirable loading distributions along the length of the blades. Fourth-order parametric splines have been introduced and used to design high-performance cascades, but their use proved CPU intensive. The third blade design method uses a mixture of analytic polynomials and a mapping of a desired curvature distribution on the (x, y) plane to specify the geometry of the cascades. The third method has been used with success to design highly loaded high-performance cascades. These methods, and particularly the third, can be used to design subsonic or supersonic blades for compressors or turbines, or isolated airfoils, but the discussion in this paper is limited to high-Mach-number subsonic-exit turbine blades. The methods permit the user to specify the leading edge by two thickness distributions around two independent construction lines, in a manner that avoids the overspeed regions near the leading edge (because it does not employ the usual blending in of the curvatures near the "leading-edge circle or ellipse"). It is found that the blade performance, judged by the shape of the surface Mach number distribution, is extremely sensitive to small changes of the surface geometry and of the curvature distribution of the airfoils. These methods ensure that the boundary layer, which is usually turbulent along the blade surfaces, is not excited unintentionally. The smooth curvature and Mach number distributions also enable the user to design lower-loss higher-loaded cascades for modern applications in airborne transportion. Continuous-slope-of-curvature surfaces should be

used wherever the aerodynamic, heat transfer, hydrodynamic, or aesthetic performance, appropriately defined in each case, is critical.

Acknowledgments

The author thanks Professor Michael Giles and Rolls Royce plc. for their permission to use UNSFLO to compute the performance of the sample cascades, and the Department of Mechanical Engineering at Washington University for providing the computational resources for this program. He also thanks Mr. P. Papagiannidis for his assistance to produce the results shown in Fig. 3(*c*), and Mr. G. Pantazopoulos for his assistance in developing the second blade-design method.

References

Ainley, D. G., and Mathieson, G. C. R., 1951, "A Method of Performance Estimation for Axial-Flow Turbines," British ARC, R & M 2974.

Baines, N. C., Oldfield, M. L. G., Simons, J. P., and Wright, J. M., 1986, "The Aerodynamic Development of a Highly Loaded Nozzle Guide Vane," ASME JOURNAL OF TURBOMACHINERY, Vol. 108, pp. 261–268.

Bird, R. B., Stewart, W. E., and Lightfoot, E. N., 1960, *Transport Phenomena*, Wiley, New York.

Cumpsty, N. A., 1989, *Compressor Aerodynamics*, Longman Scientific and Technical, Essex, United Kingdom.

Dunham, J., and Came, P. M., 1970, "Improvements to the Ainley–Mathieson Method of Turbine Performance Prediction," ASME *Journal of Engineering for Power*, Vol. 92, pp. 252–256.

Dunham, J., 1974, "A Parametric Method of Turbine Blade Profile Design," ASME Paper No. 74-GT-119.

Giles, M. B., 1988, "Calculation of Unsteady Wake/Rotor Interactions," *AIAA Journal of Propulsion and Power*, Vol. 4, No. 4, July/Aug.

Gostelow, J. P., 1975, "Trailing Edge Flows Over Turbomachine Blades and the Kutta–Joukowsky Condition," ASME Paper No. 75-GT-94.

Gostelow, J. P., 1976, "A New Approach to the Experimental Study of Turbomachinery Flow Phenomena," ASME Paper No. 76-GT-47.

Horlock, J. H., 1958, *Axial-Flow Compressors*, Butterworth (reprinted 1985 by Krieger).

Horlock, J. H., 1966, *Axial-Flow Turbines*, Butterworth (reprinted 1985 by Krieger).

Hourmouziadis, J., Buckl, F., and Bergmann, P., 1987, "The Development of the Profile Boundary Layer in a Turbine Environment," ASME JOURNAL OF TURBOMACHINERY, Vol. 109, No. 2, pp. 286–295.

Kacker, S. C., and Okapuu, U., 1982, "A Mean-Line Prediction Method for Axial-Flow Turbine Efficiency," ASME *Journal of Engineering for Power*, Vol. 104, pp. 111–119.

Korakianitis, T., 1987a, "A Design Method for the Prediction of Unsteady Forces on Subsonic, Axial Gas-Turbine Blades," Doctoral thesis (Sc.D.) in Mechanical Engineering, Massachusetts Institute of Technology, Cambridge, MA.

Korakianitis, T., 1987b, "A Parametric Method for Direct Gas-Turbine-Blade Design," AIAA Paper No. 87-2171.

Korakianitis, T., 1988a, "On the Prediction of Unsteady Forces on Gas Turbine Blades. Part 1: Typical Results and Potential-Flow-Interaction Effects," ASME Paper No. 88-GT-89.

Korakianitis, T., 1988b, "On the Prediction of Unsteady Forces on Gas Turbine Blades. Part 2: Viscous-Wake-Interaction and Axial-Gap Effects," ASME Paper No. 88-GT-90.

Korakianitis, T., 1989, "Design of Airfoils and Cascades of Airfoils," *AIAA Journal*, Vol. 27, No. 4, pp. 455–461.

Korakianitis, T., 1992a, "On the Prediction of Unsteady Forces on Gas Turbine Blades: Part 1—Description of the Approach," ASME JOURNAL OF TURBOMACHINERY, Vol. 114, pp. 114–122.

Korakianitis, T., 1992b, "On the Prediction of Unsteady Forces on Gas Turbine Blades: Part 2—Analysis of the Results," ASME JOURNAL OF TURBOMACHINERY, Vol. 114, pp. 123–131.

Korakianitis, T., 1992c, "Blade-Loading Effects on the Propagation of Unsteady Flow and on Forcing Functions in Axial-Turbine Cascades," *Journal de Physique III*, Vol. 2, No. 4, pp. 507–525.

Korakianitis, T., 1993a, "Prescribed-Curvature-Distribution Airfoils for the Preliminary Geometric Design of Axial-Turbomachinery Cascades," ASME Journal of Turbomachinery, Vol. 115, No. 2, pp. 325–333.

Korakianitis, T., and Papagiannidis, P., 1993b, "Surface-Curvature-Distribution Effects on Turbine-Cascade Performance," ASME JOURNAL OF TURBOMACHINERY, Vol. 115, pp. 334–341.

Korakianitis, T., and Pantazopoulos, G. I., 1993c, "Improved Turbine-Blade Design Techniques Using 4th-Order Parametric-Spline Segments," *Computer-Aided Design*, Vol. 25, No. 5, pp. 289–299.

Korakianitis, T., 1993d, "On the Propagation of Viscous Wakes and Potential Flow in Axial-Turbine Cascades," ASME JOURNAL OF TURBOMACHINERY, Vol. 115, pp. 118–127.

Mee, D. J., Baines, N. C., and Oldfield, M. L. G., 1992a, "Detailed Boundary Layer Measurements on a Transonic Turbine Cascade," ASME JOURNAL OF TURBOMACHINERY, Vol. 114, pp. 163–172.

Mee, D. J., Baines, N. C., Oldfield, M. L. G., and Dickens, T. E., 1992b, "An Examination of the Contributions to Loss on a Transonic Turbine Blade in Cascade," ASME JOURNAL OF TURBOMACHINERY, Vol. 114, pp. 155–162.

Moran, J., 1984, *An Introduction to Theoretical and Computational Aerodynamics*, Wiley, New York.

Okapuu, U., 1974, "Some Results From Tests on a High Work Axial Gas Generator Turbine," ASME Paper No. 74-GT-81.

Pritchard, L. J., 1985, "An Eleven Parameter Axial Turbine Airfoil Geometry Model," ASME Paper No. 85-GT-219.

Rotta, J. C., 1971, "Fortran IV—Rechenprogramm für Grenzschichten bei Kompressiblen ebenen und achensymmetrichen strömungen," DLR FB report No. 71-51, 1–82.

Schlichting, H., 1968, *Boundary-Layer Theory*, 6th ed., McGraw-Hill, New York.

Sharma, O. P., Pickett, G. F., and Ni, R. H., 1992, "Assessment of Unsteady Flows in Turbines," ASME JOURNAL OF TURBOMACHINERY, Vol. 114, pp. 79–90.

Wagner, J. H., Dring, R. P., and Joslyn, H. D., 1985, "Inlet Boundary Layer Effects in an Axial Compressor Rotor: Part 1—Blade-to-Blade Effects," ASME *Journal of Engineering for Gas Turbines and Power*, Vol. 107, pp. 374–380.

Wilson, D. G., 1984, *The Design of High-Efficiency Turbomachinery and Gas Turbines*, The MIT Press, Cambridge, MA.

APPENDIX A

Table 1 Parameters specifying blades B4-0, B4-1, B4-2, B4-3

Blade Parameter	B4-0	B4-1	B4-2	B4-3
α_1	40	40	40	40
α_2	-60	-60	-60	-60
C_L	1.00	1.00	1.00	1.00
λ	-32	-32	-32	-32
$\beta_{s\kappa}$	35.00	35.00	35.00	35.00
$XS_{s\kappa}$	0.1000	0.1000	0.1000	0.1000
$YS_{s\kappa}$	0.0650	0.0660	0.0660	0.0660
δ_s	0.1300	0.1300	0.1300	0.1300
β_{sf}	33.50	33.90	34.20	34.50
$x(P_{sf})$	0.1000	0.1000	0.1000	0.1000
$y(P_{sf})$	0.1476	0.1476	0.1476	0.1476
$x(P_{sa})$	0.2000	0.2000	0.2000	0.2000
$y(P_{sa})$	0.1965	0.1965	0.1965	0.1965
$x(P_{sb})$	0.4000	0.4000	0.4000	0.4000
$y(P_{sb})$	0.1956	0.1956	0.1956	0.1956
$x(P_{sc})$	0.6000	0.6000	0.6000	0.6000
$y(P_{sc})$	0.0644	0.0644	0.0644	0.0644
$x(P_{sd})$	0.8000	0.8000	0.8000	0.8000
$y(P_{sd})$	-0.2200	-0.2200	-0.2200	-0.2200
β_{s2}	-65.70	-65.33	-64.80	-64.50
$\beta_{p\kappa}$	35.00	35.00	35.00	35.00
$XS_{p\kappa}$	0.1000	0.1000	0.1000	0.1000
$YS_{p\kappa}$	0.0500	0.0500	0.0500	0.0500
δ_p	0.3000	0.3000	0.3000	0.3000
β_{pf}	2.00	2.00	2.00	2.00
$x(P_{pf})$	0.1000	0.1000	0.1000	0.1000
$y(P_{pf})$	-0.0350	-0.0350	-0.0350	-0.0350
$x(P_{pa})$	0.2000	0.2000	0.2000	0.2000
$y(P_{pa})$	-0.0340	-0.0340	-0.0340	-0.0340
$x(P_{pb})$	0.4000	0.4000	0.4000	0.4000
$y(P_{pb})$	-0.0635	-0.0635	-0.0635	-0.0635
$x(P_{pc})$	0.6000	0.6000	0.6000	0.6000
$y(P_{pc})$	-0.1660	-0.1660	-0.1660	-0.1660
$x(P_{pd})$	0.8000	0.8000	0.8000	0.8000
$y(P_{pd})$	-0.3400	-0.3400	-0.3400	-0.3400
β_{p2}	-61.00	-61.00	-61.00	-61.00

APPENDIX B

Table 2 Parameters specifying blade A2

Blade Parameter	A2
α_1	0.00
α_2	-60.00
C_L	1.00
o/S	0.5000
λ	-45.00
$\beta_{s\kappa}$	0.00
$XS_{s\kappa}$	0.2000
$YS_{s\kappa}$	0.1500
δ_s	0.1000
$\mathbf{C}(P_{sf})$	3.5319
β_{sf}	12.7050
β_{s2}	-65.0000
$x(P_{sf})$	0.1000
$y(P_{sf})$	0.0699
$x(P_{sa})$	0.2856
$y(P_{sa})$	0.0255
$x(P_{sm})$	0.5772
$y(P_{sm})$	-0.2403
$x(P_{s2})$	1.0000
$y(P_{s2})$	-1.0000
$\beta_{p\kappa}$	0.0000
$XS_{p\kappa}$	0.2000
$YS_{p\kappa}$	-0.0500
δ_p	0.1000
$\mathbf{C}(P_{pf})$	1.4700
β_{pf}	-16.4891
β_{p2}	-56.5033
$x(P_{pf})$	0.1000
$y(P_{pf})$	-0.0279
$x(P_{pa})$	0.4500
$y(P_{pa})$	-0.2471
$x(P_{pm})$	0.7000
$y(P_{pm})$	-0.5546
$x(P_{p2})$	1.0000
$y(P_{p2})$	-1.0000

APPENDIX C

Table 3 Parameters specifying blade C562

Blade Parameter	C562
α_1	50.00
α_2	-60.00
C_L	1.00
o/S	0.5000
λ	-30.00
$\beta_{s\kappa}$	50.0000
$XS_{s\kappa}$	0.2000
$YS_{s\kappa}$	0.2000
δ_s	0.1000
β_{s2}	-64.5000
ϕ	37.0000
$x(C1_s)$	0.0800
$y(C1_s)$	2.9000
$x(C2_s)$	0.3000
$y(C2_s)$	4.5000
$x(C3_s)$	0.6500
$\beta_{p\kappa}$	50.0000
$XS_{p\kappa}$	0.2000
$YS_{p\kappa}$	0.1400
δ_p	0.1000
β_{p2}	-53.0000
β_{pm}	-47.0000
$x(P_{pm})$	0.7500
$y(P_{pm})$	-0.2725
$x(C1_p)$	0.0800
$y(C1_p)$	1.3800
$x(C2_p)$	0.4000
$y(C2_p)$	2.5500
$x(C3_p)$	0.6000

Prescribed-Curvature-Distribution Airfoils for the Preliminary Geometric Design of Axial-Turbomachinery Cascades

T. Korakianitis
Department of Mechanical Engineering,
Washington University,
St. Louis, MO 63130

Blade surfaces with continuous curvature and continuous slope of curvature minimize the possibility of flow separation, lead to improved blade designs, and reduce the direct and inverse blade-design iterations for the selection of isolated airfoils and gas-turbine-blade cascades. A method for generating two-dimensional blade shapes is presented. The geometry near the trailing edge is specified by an analytic polynomial, the main portion of the blade surface is mapped using as input a prescribed surface-curvature distribution, and the leading edge is specified as a thickness distribution added to a construction line. This procedure is similar for the suction and pressure surfaces, and by specification it constructs continuous slope-of-curvature surfaces that result in smooth surface-Mach-number and surface-pressure distributions. The method can be used to generate subsonic or supersonic airfoils for compressors and turbines, or isolated airfoils. The resulting geometric shapes can be used as inputs to various blade-design sequences. It is shown that, with other cascade-design parameters being equal, increasing the stagger angle of turbine blades results in more front-loaded and thinner blades, and that there is an optimum stagger angle resulting in minimum wake thickness. The subsonic axial-turbine blade rows included for discussion in this paper have been designed by iterative modifications of the blade geometry to obtain a desirable velocity distribution. The blade-design method can be used to improve the aerodynamic and heat transfer performance of turbine cascades, and it can result in high-performance airfoils, even if using the direct method exclusively, in very few iterations.

Introduction

Gas turbine blades are three-dimensional objects operating in a complex and unsteady flow field. Due to its complexity, the blade-design problem is usually reduced to a series of "stacked" two-dimensional problems, assuming that the cascade operates in a steady two-dimensional flow field. Blade design is partly a science and partly an art. The performance of the blades is expressed in the form of some property distribution (such as pressure, velocity, etc.) on the blade surface and in the cascade passage. Three-dimensional turbine blades are generated by "stacking" two-dimensional designs using rules for the flow angles from hub to tip at the leading and trailing edge, derived from radial-equilibrium throughflow calculations; the locus of the centers of gravity of the sections; and the three-dimensional shape of the leading edge and the trailing edge. Compromises in performance must be made to accommodate these three-dimensional constraints, the location of cooling passages, and hollow sections.

Various investigators use different definitions for the terms direct method and inverse, semi-inverse, full-inverse, or full-optimization methods (Meauze, 1989), analysis and design modes (Stow, 1989), optimization and design methods (Bry, 1989), and others, for the approaches and methods used in turbine design sequences. For the purposes of this paper we *define* as direct the method in which the designer inputs the geometry of the cascade and the output is the performance (from an analysis code) in terms of surface Mach number and pressure distributions. The performance provides guidelines for where to increase or decrease the loading, and how to modify the surface geometry in successive iterations. This means iterative use of a geometric description package and of an analysis code until a desirable performance is obtained from the analysis code. Also for the purposes of this paper we *define* as inverse the various methods in which the designer specifies the performance of the cascade to obtain the geometry, or modifications to a portion of the surface velocity or pressure distribution to obtain modifications to the geometry. This latter definition includes what other investigators define as fully inverse, semi-inverse, or simply design methods.

Both direct and inverse methods are based on the assumption of steady flow conditions, and require numerous iterations until a desirable blade shape and performance are obtained.

Contributed by the International Gas Turbine Institute and presented at the 37th International Gas Turbine and Aeroengine Congress and Exposition, Cologne, Germany, June 1–4, 1992. Manuscript received by the International Gas Turbine Institute February 20, 1992. Paper No. 92-GT-366. Associate Technical Editor: L. S. Langston.

The direct method is laborious, and it requires considerable insight. On the other hand, the designer has direct control of the various geometric parameters, and structurally or dynamically infeasible blade shapes are excluded before they are analyzed. One would like to start the inverse methods with a blade shape close to an acceptable design, since this will enormously reduce the number of inverse-design iterations. Therefore the designer needs to start inverse-design iterations from a good blade shape obtained by a direct method. The inverse method is less laborious, but many (although not all) inverse-design programs must start from a blade geometry generated by a direct method. The designer has less control on the blade shape (by the very purpose of inverse design). It can result in blades that are structurally undesirable due to stress considerations or location of cooling passages, or are impossible to manufacture. If one decides that some geometric parameters (such as stagger angle) must be changed, one must start from the beginning (direct method) again. The final design is usually obtained by a judicious combination of both methods.

Surface-Curvature Effects

Both the curvature and the slope of curvature of blade surfaces affect boundary-layer development and blade performance. The slope-of-curvature effects are less obvious than the curvature effects. Theoretical and experimental evidence of their importance is presented below.

Theoretical Evidence. The flow in turbomachinery cascades *curves* around the blades. The dependence of flow on curvature is seen if one writes the compressible-flow Navier–Stokes equations in the limiting case of cylindrical coordinates (r, θ, z). In particular, since we are interested in "stacking" two-dimensional solutions and geometries, we present here the equations of conservation of mass and momenta in polar coordinates (r, θ), taken from the text by Bird et al. (1960):

$$\frac{\partial \rho}{\partial t}+\frac{1}{r}\frac{\partial}{\partial r}(\rho r v_r)+\frac{1}{r}\frac{\partial}{\partial \theta}(\rho v_\theta)=0 \tag{1}$$

$$\rho\left(\frac{\partial v_r}{\partial t}+v_r\frac{\partial v_r}{\partial r}+\frac{v_\theta}{r}\frac{\partial v_r}{\partial \theta}-\frac{v_\theta^2}{r}\right)= -\frac{\partial p}{\partial r}-\left(\frac{1}{r}\frac{\partial}{\partial r}(r\tau_{rr})+\frac{1}{r}\frac{\partial \tau_{r\theta}}{\partial \theta}-\frac{\tau_{\theta\theta}}{r}\right)+\rho g_r \tag{2}$$

$$\rho\left(\frac{\partial v_\theta}{\partial t}+v_r\frac{\partial v_\theta}{\partial r}+\frac{v_\theta}{r}\frac{\partial v_\theta}{\partial \theta}+\frac{v_r v_\theta}{r}\right)= -\frac{1}{r}\frac{\partial p}{\partial \theta}-\left(\frac{1}{r^2}\frac{\partial}{\partial r}(r^2\tau_{r\theta})+\frac{1}{r}\frac{\partial \tau_{\theta\theta}}{\partial \theta}\right)+\rho g_\theta \tag{3}$$

where in the above equations p is the static pressure, and for Newtonian fluids the stress components τ_{ij} are related to the dynamic viscosity μ by the equations:

$$\begin{aligned}
\tau_{rr}&=-\mu\left[2\frac{\partial v_r}{\partial r}-\frac{2}{3}(\nabla\cdot\mathbf{v})\right]\\
\tau_{\theta\theta}&=-\mu\left[2\left(\frac{1}{r}\frac{\partial v_\theta}{\partial \theta}+\frac{v_r}{r}\right)-\frac{2}{3}(\nabla\cdot\mathbf{v})\right]\\
\tau_{r\theta}&=\tau_{\theta r}=-\mu\left[r\frac{\partial}{\partial r}\left(\frac{v_\theta}{r}\right)+\frac{1}{r}\frac{\partial v_r}{\partial \theta}\right]
\end{aligned} \tag{4}$$

$$(\nabla\cdot\mathbf{v})=\frac{1}{r}\frac{\partial}{\partial r}(r v_r)+\frac{1}{r}\frac{\partial v_\theta}{\partial \theta}$$

A similar dependence of incompressible flow on curvature is also shown in most fluid dynamics texts in cylindrical coordinates, and Schlichting (1960, p. 112) attributes a set of similar equations for incompressible flow in curvilinear coordinates (x, r, y) to W. Tollmien. The $1/r$ and $1/r^2$ terms in these equations suggest a strong dependence of local pressure and velocity on curvature. Turbine-blade performance depends on the behavior of the boundary layer. While one expects that the boundary layer shields the core of the flow from surface discontinuities, the boundary-layer behavior depends on the slope of the velocity distribution as it approaches the solid wall, and Eqs. (4) indicate that the boundary layer and its behavior are affected by the local radius. Smooth velocity

Nomenclature

A = flow-area distribution along x or X (Fig. 4*b*)
b = axial chord length (nondimensionally $b=1$)
c = thickness-distribution coefficients (Eqs. (12))
d = root-x coefficient for T (Eqs. (12))
$\mathbf{C}=1/R$ = curvature (Eq. 5 and Figs. 4*b* and 5*b*)
C_L = tangential-loading coefficient (Eqs. (7) and (8))
e = coefficient of the construction lines (Eq. 11)
g = body force (Eqs. (2) and (3))
M = Mach number
p = pressure (Eqs. (2) and (3))
P_f, P_m, $P2$ = surface-segment nodes
R = local radius of curvature (Eq. (5))
s = blade-surface length (Fig. 10)
S = tangential spacing of the blades (Fig. 4*a*)
t = time (Eqs. (1), (2) and (3))
T = thickness distribution (Eq. (12))
v_i = velocity component ($i=r, \theta$)
$\mathbf{v}$ = velocity vector (Eq. 4)
(x, y) = Cartesian coordinates
(X, Y) = nondimensional distances ($X=x/b$, $Y=y/b$)
$y1$, $y2$ = blade-surface approximations (Eq. (10))
α = flow angle
β = angle of the blade surface
δ_1 = boundary-layer displacement thickness (Figs. 5*c* and 10)
λ = stagger angle of the blades (Fig. 4*a*)
μ = dynamic viscosity (Eq. 4)
ρ = density (Eqs. (1), (2), and (3))
τ_{ij} = shear stress components (Eq. (4), $i, j=r, \theta$)
ϕ = angle of throat diameter with x axis (Fig. 4*a*)
ω = thickness distribution parameter (Eqs. (11) and (12))

Subscripts

1, 2 = point P, flow angle or Mach number, inlet and outlet, respectively
f = segment knot near the leading edge (Figs. 4*a* and 4*c*)
m = segment knot near the trailing edge (Fig. 4*a*)
p = pressure side
r = radius in polar coordinates (r, θ)
s = suction side
θ = angle in polar coordinates (r, θ)
κ = construction line

distributions along the blade surfaces require smooth surface-curvature distributions (continuous slopes of velocity and curvature along the blade surface). Continuous slope of curvature requires continuous derivatives, as illustrated in the following two equations for curvature and slope of curvature for $y = f(x)$, $y' = df(x)/dx$, $y'' = d^2f(x)/dx^2$ and $y''' = d^3f(x)/dx^3$:

$$\mathbf{C} = \frac{1}{R} = \frac{y''}{[1+y'^2]^{(3/2)}} \tag{5}$$

$$\mathbf{C}' = \frac{d\mathbf{C}}{dx} = \frac{y'''[1+y'^2] - 3y'y''^2}{[1+y'^2]^{(5/2)}} \tag{6}$$

Experimental Evidence. Most parametric splines currently in use for direct blade design (e.g., cubic, B-splines, Bezier splines, etc.) have continuous first and second derivatives and they result in smooth-looking surfaces with continuous curvatures, but discontinuous slopes of curvature (y''' in Eq. (6)) at the spline knots. One must distinguish here between the small local slope-of-curvature discontinuities from surface roughness and fouling, with which turbines must operate, and the slope-of-curvature discontinuities in the as-designed shape at the junctions of the splines. It will be shown below that the latter are invisible to the eye, but they may produce unusually loaded cascades and thicker wakes. This has resulted in many test and production airfoils (isolated and in turbomachine cascades) that exhibit spikes or dips of various magnitudes in Mach number and pressure-coefficient distribution, which occasionally result in unexpected loading distributions along the blade length, and in local separation bubbles. These effects are visible as small local "kinks" in surface pressure or Mach number distributions in some of the computational and experimental data published, for example, by: Okapuu (1974), Gostelow (1976), Wagner et al. (1985), Hourmouziadis et al. (1987) (with separation bubble), Sharma et al. (1992) and others.

Blending a leading-edge circle or ellipse with the blade surfaces usually results in a local curvature or slope-of-curvature discontinuity, which may cause separation and substantial leading-edge surface Mach number spikes (detected only if the probes are located at the correct location). Such a local leading-edge laminar-separation bubble due to blending of a leading-edge circle with the blade surfaces occurs in the turbine geometry published by Hodson and Dominy (1987), seen in the data published in Fig. 11 of Hodson (1985). This leading-edge spike and separation region were removed by modifying the geometry of the blade in the vicinity of the slope-of-curvature discontinuity with an inverse design technique as explained in Figs. 11, 12, and 13 of Stow (1989).

The full extent of the effects of slope-of-curvature discontinuities on blade performance, losses, and boundary-layer behavior is still under investigation. While it may be possible intentionally to trip the flow into turbulence by imposing a local slope-of-curvature discontinuity, it is clear that a prescribed-curvature-distribution blade-design method is a useful tool.

Accuracy of Computations

The performance of sample turbine blades in this paper has been evaluated using the inviscid and steady-flow version of Giles' (1988) computer program UNSFLO. The accuracy of the computations was checked by comparing the results of Euler computations with three cases of known output. The first case was a comparison of computations with the (exact) theoretical solution of Gostelow's (1984) compressor cascade. For this case $M_1 = 0.200$, $M_2 = 0.135$, $\alpha_1 = 53.5$ deg and $\alpha_2 = 30.0$ deg. A fine uniform H grid of 400×100 was used to resolve the flow around the leading edge. The results, shown in Fig. 1, indicate excellent agreement. The tick marks are the analytic solution and the straight line is the calculation by UNSFLO.

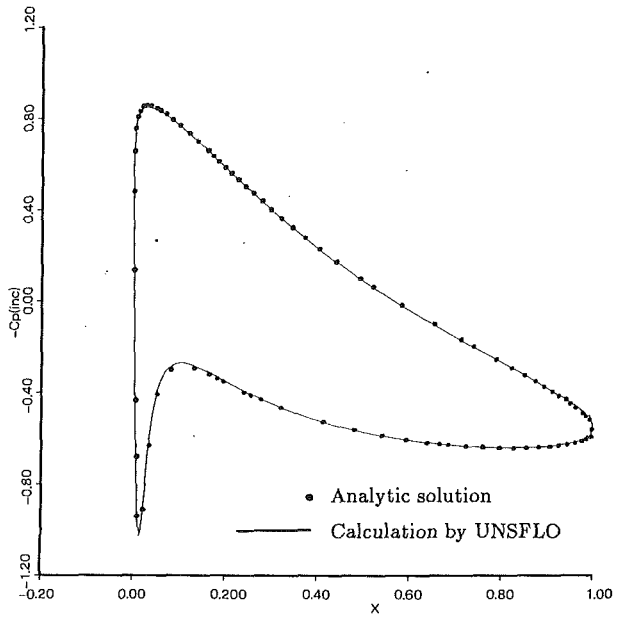

Fig. 1 Comparison of incompressible lift coefficient for Gostelow's (1984) compressor cascade

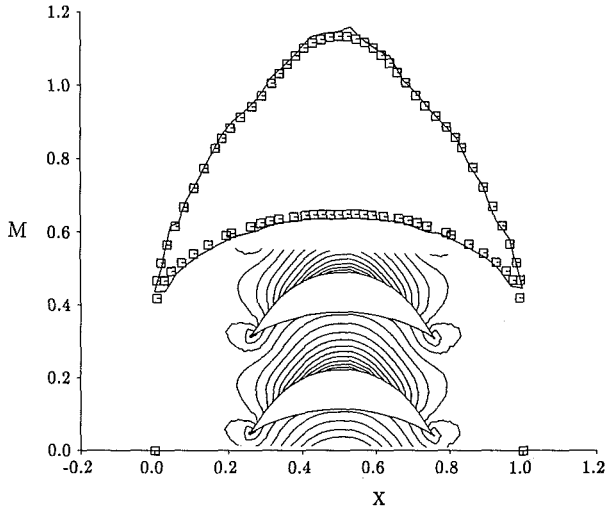

Fig. 2 Comparison of surface mach numbers for Hobson's turbine cascade No. 2 (from AGARD, 1985)

The second case was a comparison of computations on uniform H grid with the hodograph solution of Hobson's transonic turbine cascade No. 2 (taken from AGARD, 1985). This is a singular case; small perturbations result in shocks in the passage. The inlet and exit flow angle and Mach number are 46.123 deg and 0.575, respectively. A relatively coarse grid of 60×15 was used. The results, shown in Fig. 2, also indicate excellent agreement. The tick marks are the hodograph solution and the straight line is the calculation by UNSFLO.

The first two cases were suitable for inviscid-flow checks with sharp trailing edges, and indicate the accuracy of the computations. The following experimental cases, coupled with the effect of surface curvature on the performance of the sample cascades shown below, indicate the importance of surface-curvature distribution, and the need for it to be taken into account in blade-design methods.

The third case is a comparison of inviscid computations with the experimental results from the subsonic turbine cascade obtained at DFVLR Braunschweig by Kiock et al. (1986). For this case $M_1 = 0.260$, $M_2 = 0.782$, $\alpha_1 = 30.0$ deg and $\alpha_2 = -67.33$

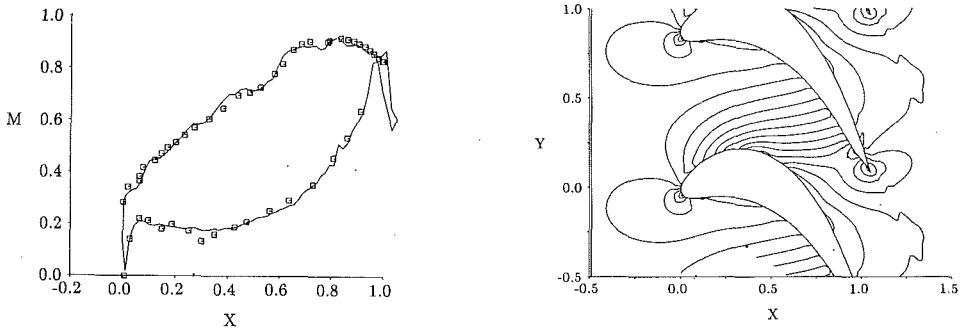

Fig. 3 Comparison of Mach number distributions for the turbine cascade investigated by Kiock et al. (1986): left, surface Mach-number distributions: Right, Mach number contours of increment 0.05

deg. A uniform H grid of 100×40 and a cusp (to close the trailing edge) were used. The results, shown in Fig. 3, indicate very good agreement with the experiments. The tick marks are the experimental results (transformed from data along percentage of chord c to data along percentage of axial chord b, along X) and the straight line is the calculation. Despite the inviscid nature of the computation, the numerical solution follows local dips in the suction-surface Mach number distribution at $X \approx 0.55$ and $X \approx 0.80$, and local accelerations at $X \approx 0.05$ and $X \approx 0.70$. Korakianitis and Papagiannidis (1993a) show an additional check with very good agreement between computation and experiment for the turbine geometry tested by Hodson and Dominy (1987). In the latter case their experiment and our computation indicate a leading-edge Mach number spike on the suction surface. The spike is caused by a curvature or slope-of-curvature discontinuity in blending the leading-edge circle with the blade surface. The comparisons with experiments and the effect of curvature discontinuities discussed below indicate the importance of curvature distribution along the blade surface on performance.

Cascade-Design Parameters

Simplified examples of geometric blade-design sequences are described in some texts such as Wilson's (1984). The designer has many choices, but for the purposes of this paper we will refer to the axial-turbine-cascade diagram shown in Fig. 4(*a*). We will assume that the designer has chosen the blade row velocity diagram and its parameters: the inlet flow angle α_1; the outlet flow angle α_2; and the exit Mach number M_2 (in the absolute frame for stators and in the relative frame for rotors). Four additional choices must be made: the nondimensional tangential spacing S/b between the blades; the stagger angle λ; the nondimensional throat diameter o/b; and the trailing-edge thickness.

Some guidelines for the stagger angle λ for low-speed turbine blades have been published by Kacker and Okapuu (1982), although the designer has considerable flexibility in choosing λ. It will be shown below that the value of λ also dictates whether the cascade is front or aft loaded.

The spacing between the blades (which is directly linked to the number of blades in the blade row) is a function of the tangential lift coefficient C_L, defined by Zweifel (1945):

$$C_L \equiv \frac{\textit{tangential aerodynamic force}}{\textit{tangential blade area} \times \textit{outlet dynamic head}} \tag{7}$$

This expression can be manipulated in a number of ways (for compressible flow, for incompressible flow, accounting for variations in axial-flow velocity, etc.). Here we chose the incompressible-flow derivation (see Wilson, 1984), which reduces C_L to:

$$C_L = 2 \frac{S}{b} \cos^2 \alpha_2 (\tan \alpha_1 - \tan \alpha_2) \tag{8}$$

The value of C_L is determined by the number of blades in the cascade, which dictates S. Typically $0.8 < C_L < 1.2$; earlier designs had lower values of C_L, and in modern cascades C_L has been gradually increasing. It is difficult to design high-efficiency cascades that have both high values of C_L and high values of deflection ϵ in the cascade, where $\epsilon = \alpha_1 - \alpha_2$.

The throat diameter is an extremely important design input because it dictates the mass flow that can be passed through the cascade, and hence the work that can be delivered by the turbine. A good first approximation is $o/S = \cos^{-1} \alpha_2$. Experimental figures linking the throat diameter o to the blade spacing S, the throat Mach number M_2, and the curvature of the convex (suction) blade surface near the trailing edge have been published by Ainley and Mathieson (1951), and are used extensively in the early stages of blade design. The industry has for years relied on empirical relationships based on the Ainley-Mathieson data and on improvements to it (e.g., by Dunham and Came, 1970) for the prediction of α_2 as function of M_2, S and o. These empirical data have been simplified by others for design applications (for example by Wilson, 1984, and Dunham, 1974). This is sufficient for preliminary design. Today's computer programs are more accurate and compute the outlet flow angle for a given geometry. Gostelow (1975) has explained how the result depends not only on the geometry, but also to some extent on the exact location of the point at which the Kutta condition is applied at the trailing edge.

The trailing-edge thickness should be as small as manufacturing and strength considerations would allow (to minimize the wake incident on the next blade row). It is also affected by geometric constraints imposed by the cooling slots in cooled blades. In the sample airfoils of this paper the trailing edge is a point, because we have used an inviscid flow solver to analyze the blade performance. But the method presented enables the designer to specify a trailing-edge thickness, which can be filled with a sharp wedge, cusp, trailing-edge circle, or other appropriate shape.

One would like the velocity of the fluid adjacent to the concave (pressure) surface to accelerate from the stagnation point near the leading edge to the trailing edge. An exception to this are the low-pressure stages of turbines, where in some cases a local decrease in velocity between the leading edge and midchord is designed to increase loading. Continuous acceleration is not as easy to accomplish for the velocity of the fluid adjacent to the convex (suction) surface, because the flow is "unguided" on the suction surface downstream of the throat in what is called the region of "unguided diffusion." The velocity of the fluid adjacent to the convex (suction) surface accelerates from the stagnation point near the leading edge to some point near the throat, and then it usually decelerates. Less deceleration (diffusion) means better designs. If the flow decelerates too much, then the boundary layer will separate, the blade wake will be thick, and the resulting cascade will have poor performance (low efficiency).

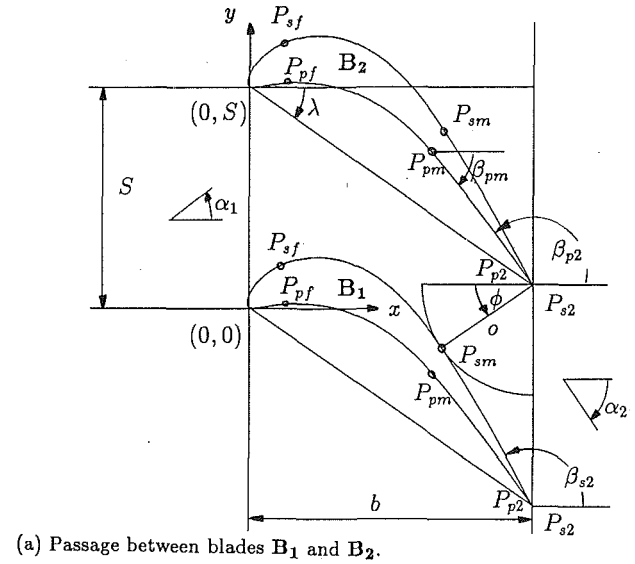

(a) Passage between blades $\mathbf{B_1}$ and $\mathbf{B_2}$.

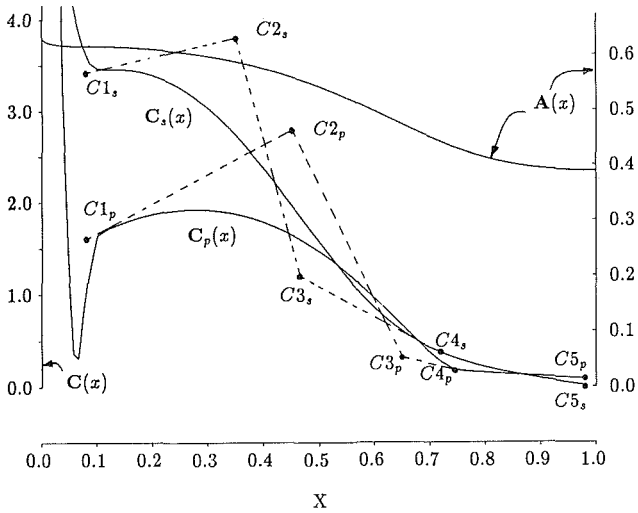

(b) Curvature $\mathbf{C}(x)$ and area $\mathbf{A}(x)$ distributions

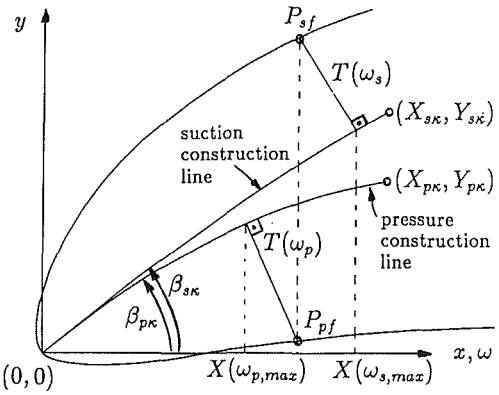

(c) Leading edge thickness distributions

Fig. 4 Geometry of a typical cascade, and parameters of the blade-design method

The Blade-Design Method

In past investigations we introduced a blade design method in which the blade surfaces were prescribed by analytic polynomials $y=f(x)$, (Korakianitis, 1989). In that method the throat diameter and its location were an output of the location of the two surfaces. The resulting blade performance exhibited a dependence on curvature, which is illustrated in Fig. 5 for a turbine cascade designed for $\alpha_1=40$ deg, $\alpha_2=-60$ deg,

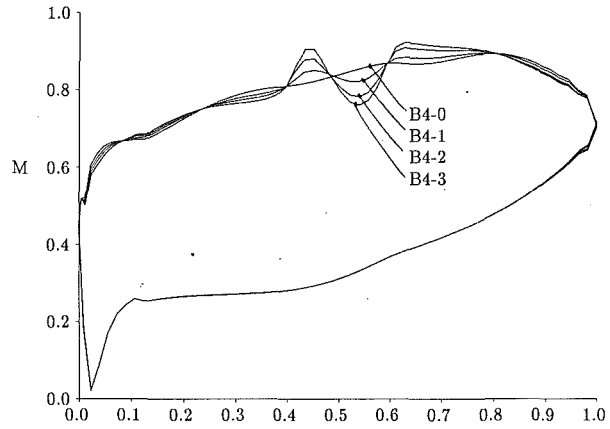

(a) Mach number distributions

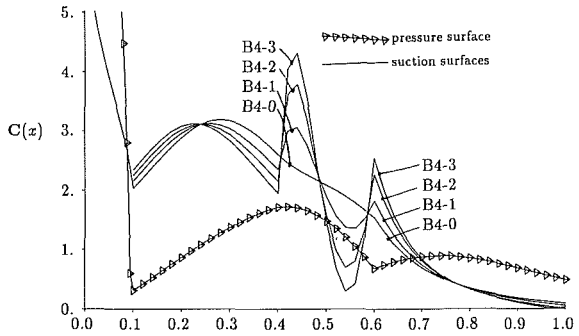

(b) Curvature $\mathbf{C}(x)$ distributions

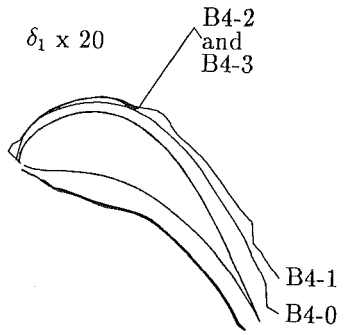

(c) Effect on boundary layers (using Albers and Gregg's (1974) program with freestream turbulence 10%)

Fig. 5 Surface distributions for cascades B4-0, B4-1, B4-2, B4-3: $\alpha_1=40$ deg, $\alpha_2=-60$ deg, $C_L=1.00$, $\lambda=-32$ deg

$M_2=0.8$, and $C_L=1.0$. Figure 5(*a*) shows the Mach number distributions of four blades of almost identical geometries, and Fig. 5(*b*) shows the corresponding surface curvature distributions. Figure 5(*c*) shows the boundary-layer displacement thickness $\delta_1\times 20$ of each blade calculated with Albers and Gregg's (1974) differential boundary layer program assuming incoming free-stream turbulence of 10 percent. All four blades have been plotted on each other in Fig. 5(*c*). The pressure surfaces are identical. The suction surfaces have differences that are small enough not to be visible in the figure. Blade B4-0 has smooth curvature and Mach number. Blade B4-1 has a small discontinuity in the slope of curvature that causes a disturbance in surface Mach number distribution, and a thicker boundary layer (and wake) at the trailing edge. Blades B4-2 and B4-3 have correspondingly larger slope-of-curvature discontinuities that cause the boundary layer to separate near the discontinuity.

A second blade design method with parametric splines in ξ ($x=f(\xi)$ and $y=f(\xi)$) resulted in a very cumbersome and time-consuming design sequence (Korakianitis and Pantazopoulos,

1993b). Through these efforts it became apparent that we wanted to control the curvature distribution as well as the location of the blade surfaces. This was accomplished by the design method presented below.

The Trailing-Edge Region. Typically the Mach number at the outlet-flow plane, M_2, will be a design specification. The values of α_1, α_2, and C_L also specify S/b; the throat diameter $o/S = \cos\alpha_2$ as described above. Choosing the value of λ and the trailing edge thickness specifies the trailing edge points P_{s2} and P_{p2} (these are shown at the same point in Fig. 4(*a*) since the designs will be analyzed with an inviscid flow program).

The trailing edge region of the suction surface is specified by a third-order polynomial $y = f(x)$ evaluated using four boundary conditions: the location of P_{s2}; the blade angle β_{s2} at the trailing edge; and the angle ϕ of the throat-circle diameter with the x axis. The latter specifies two boundary conditions: the location of point P_{sm}, and the tangent of the third-order polynomial at that point, equal to $(\pi/2 + \phi)$. The analytic polynomial has continuous first, second, and third derivatives. With these we compute the curvature of the resulting blade surface $\mathbf{C}_s(x)$ (using Eq. (5)) between points P_{sm} and P_{s2}, and plot it between points $C4_s$ and $C5_s$ in Fig. 4(*b*).

The trailing edge region of the pressure surface is specified by a third-order polynomial $y = f(x)$ evaluated using four boundary conditions: the location of P_{p2}; the blade angle β_{p2} at the trailing edge; the (x, y) coordinates of a point P_{pm} on the surface; and the angle β_{pm} of the blade surface at point P_{pm} with the x axis. With the first and second derivatives of this polynomial we compute the curvature of the resulting blade surface $\mathbf{C}_p(x)$ (using Eq. (5)) between points P_{pm} and P_{p2}, and plot it between points $C4_p$ and $C5_p$ in Fig. 4(*b*).

The slopes of the curvatures $\mathbf{C}_s(x)$ and $\mathbf{C}_p(x)$ at points $C4_s$ and $C4_p$, respectively, are computed and become inputs for the rest of the design. A gradually increasing curvature distribution in the trailing edge regions results in mechanically and aerodynamically feasible blade shapes. Different (smooth) curvature distributions would be required for supersonic blades.

The Main Part of the Blades. The design is converted into an effort to specify a curvature distribution for the shape of the blade surfaces $\mathbf{C}_s(x)$ and $\mathbf{C}_p(x)$. In order to ensure slope-of-curvature continuity, the curvature from points P_f to points P_m is specified using a Bezier spline in curvatures using the following conditions (see Fig. 4(*b*). On the curvature of the suction surface we specify points $C1_s$, $C2_s$, and $C3_s$. Point $C4_s$ is already specified from the corresponding value of curvature, evaluated from the trailing-edge third-order polynomial. The x location of point $C3_s$ is variable, but the value of curvature there is evaluated such that line $C3_sC4_s$ is tangent to the surface-curvature line at point $C4_s$. Point $C2_s$ is user specified. Point $C1_s$ is specified at an x location corresponding to P_f, or at an x location just ahead of P_f. Since the slope of the Bezier curve is tangent to the line of knots at its ends, the tangency condition at point $C4_s$ ensures slope-of-curvature continuity from $C1_s$ to $C5_s$ (from P_{sf} to P_{s2}). Similarly points $C1_p$, $C2_p$, and $C3_p$ are specified on $\mathbf{C}_p(x)$.

Using central differences Eq. (5) is written as:

$$\mathbf{C}_i = \frac{CF1/CF2}{CF3}$$

$$CF1 = 2\left(\frac{y_{i+1}-y_i}{x_{i+1}-x_i} - \frac{y_i-y_{i-1}}{x_i-x_{i-1}}\right) \tag{9}$$

$$CF2 = (x_{i+1}-x_{i-1})$$

$$CF3 = \left\{\left[\frac{1}{2}\left(\frac{y_{i+1}-y_i}{x_{i+1}-x_i} + \frac{y_i-y_{i-1}}{x_i-x_{i-1}}\right)\right]^2 + 1\right\}^{3/2}$$

From the above equation, given (x_{i-1}, y_{i-1}), (x_i, y_i), x_{i+1}, and $\mathbf{C}_i$ we can compute y_{i+1}. This can be done by manipulating Eq. (9) into a sixth-order linear algebraic equation in y_{i+1}, or by a numerical solution. We have implemented a regula-falsi solution for y_{i+1} using Eq. (9). This is solved starting from points P_m and progressing explicitly to points P_f. The Bezier spline is iteratively manipulated until the slope and the y location of the blade surfaces at points P_f, and the shapes of the curvature distributions are acceptable.

In some cases, trying to make the blade surfaces pass with desirable slopes through desirable P_f points becomes tedious. For those cases we provide an alternative solution. The designer specifies the (x, y) location of point P_f. A parabola passing through points P_f, P_m, and the next point on the blade surface in the trailing-edge region in used as a first approximation $y1(x)$ to the blade surface. Equation (9) is written as:

$$[y2_{i+1} - 2y2_i + y2_{i-1}] = \Delta x^2 \mathbf{C}_i \left[\left(\frac{y1_{i+1}-y1_{i-1}}{2\Delta x}\right)^2 + 1\right]^{3/2} \tag{10}$$

Equation (10) is written as a tridiagonal matrix in $y2_i$. Points P_m and the input points for P_f are incorporated as boundary conditions in the first and last rows of the right-hand side. The system of equations is solved with an LU decomposition. The values of $y1_i$ on the right-hand side are set equal to the previous solution for $y2_i$, and the process is repeated until the values of $y1_i$ and $y2_i$ converge to the same solution (after about twelve iterations). The converged blade surface in the final $y2_i$ passes through points P_f and P_m, but in the general case results in a spike in curvature at point P_m. The curvature input points $C1$, $C2$, and $C3$ are iteratively manipulated until the spike is minimized, and then having found the inputs that will make the blade surface pass through point P_f, the designer returns to specifying the blade surface by solving Eq. (9).

Leading-Edge Geometry. The leading edge geometry is designed by specifying thickness distributions added perpendicularly to parabolic construction lines that pass through the leading edge, as shown in Fig. 4(*c*). The parabolic construction lines are specified by the angle of the construction line at the origin β_κ, the (x, y) location of the origin (0, 0), and of one additional point (X_κ, Y_κ) on the construction line. The parabolic construction lines define a parameter ω along x, and the corresponding base line $P(\omega)$ as follows:

$$\begin{aligned} x &= \omega \\ P(\omega) &= e_0 + e_1\omega + e_2\omega^2 \end{aligned} \tag{11}$$

where the constants e_0, e_1, and e_2 are evaluated from the boundary conditions of the parabolic construction lines. For the suction line we add a thickness distribution above the parabolic construction line, and for the pressure line we add a thickness distribution below the parabolic construction line. The thickness distribution is of the form:

$$\begin{aligned} T_s(\omega) &= d_s\sqrt{\omega} + c_{s1}\omega + c_{s2}\omega^2 + c_{s3}\omega^3 + c_{s4}\omega^4 \\ T_p(\omega) &= d_p\sqrt{\omega} + c_{p1}\omega + c_{p2}\omega^2 + c_{p3}\omega^3 + c_{p4}\omega^4 \end{aligned} \tag{12}$$

where d is specified by the designer. The coefficients c_1, c_2, c_3, and c_4 are derived with the conditions that the absolute values, first, second, and third derivatives of the thickness distribution and of the downstream blade segment at point P_f with respect to the parabolic construction line are equal. This ensures curvature and slope-of-curvature continuity at point P_f, and avoids the need to blend a circle, ellipse, or other shape with the blade surfaces near the leading edge. The continuous slope of curvature at point P_f also ensures that the blade will not exhibit unexpected leading-edge separation bubbles. The value of parameter d can be used to specify thicker or thinner leading edges, which would affect the design-point and off-design-point operating performance of the cascade. These are the subject of a future investigation. The origin (0, 0) itself is

Table 1 Parameters specifying blades L25, L30, L35, and L40

Blade Parameter	L25	L30	L35	L40
α_1	40.00	40.00	40.00	40.00
α_2	-60.00	-60.00	-60.00	-60.00
C_L	1.00	1.00	1.00	1.00
o/S	0.5000	0.5000	0.5000	0.5000
λ	-25.00	-30.00	-35.00	-40.00
$\beta_{s\kappa}$	40.0000	40.0000	40.0000	40.0000
$XS_{s\kappa}$	0.1000	0.2000	0.2000	0.3300
$YS_{s\kappa}$	0.1700	0.0500	0.1300	0.0500
d_s	0.0800	0.1000	0.1500	0.1500
β_{s2}	-64.5000	-65.0000	-62.0000	-62.500
ϕ	38.5000	38.0000	34.5000	33.5000
$x(C1_s)$	0.0800	0.0800	0.08000	0.08000
$y(C1_s)$	2.9000	3.0000	3.4200	4.6000
$x(C2_s)$	0.3400	0.4000	0.3500	0.2300
$y(C2_s)$	3.7500	3.0000	3.8000	3.3000
$x(C3_s)$	0.6865	0.6000	0.4650	0.5200
$\beta_{p\kappa}$	40.0000	40.0000	40.0000	40.000
$XS_{p\kappa}$	0.2000	0.2000	0.2000	0.3000
$YS_{p\kappa}$	0.0900	0.4100	0.1000	0.0200
d_p	0.0500	0.1000	0.1500	0.2000
β_{p2}	-50.5000	-55.0000	-55.0000	-56.7000
β_{pm}	-38.7000	-47.0000	-52.0000	-52.3000
$x(P_{pm})$	0.7500	0.7500	0.7500	0.7400
$y(P_{pm})$	-0.2180	-0.2650	-0.3600	-0.4700
$x(C1_p)$	0.0800	0.0800	0.0800	0.0800
$y(C1_p)$	0.8000	0.8000	1.6000	2.0000
$x(C2_p)$	0.5600	0.5100	0.4500	0.3850
$y(C2_p)$	2.2000	2.9000	2.7900	2.3000
$x(C3_p)$	0.5500	0.6500	0.6500	0.4300

a singular point. In order to achieve first-derivative continuity at that point, the angles of the parabolic construction lines should be equal for the suction and pressure surfaces.

Some Features of the Method. This blade-design method has been used to design numerous cascades of various loading distributions. Through these design sequences it was found that the designer has a lot of freedom in specifying the curvature (and location of the blade surface) in cascades of medium and low loading (C_L) (Korakianitis and Papagiannidis, 1993a). Blades with high turning and high values of C_L require very fine adjustments in blade curvature (and location) in order to attain good performance. This is achieved by modifying the above method to use more Bezier splines to specify the curvature in Fig. 4(*b*).

In using the method we have found it useful to keep the location of points P_f at $X=0.08$. After very few geometric-design iterations, the user finds the range of values of curvatures at points $C1$ that give acceptable geometries. These values are between 2 and 6 on the suction surface, and about 1 on the pressure surface. The same leading-edge parabolas can be specified by the same angle β_κ and any of an infinite number of points (X_κ, Y_κ). We have found it useful to keep $X_\kappa=0.20$ to facilitate understanding of the effect of changing the location of Y_κ on leading-edge geometry (local curvature distribution). The design method is easy enough to master that a user improved the initial design of sample cascades L25 and L40 (see below) before he realized this intention (see Table 1).

We have also found it useful to keep the x location of point P_{pm} near the x location of point P_{sm} to control the surface angles and the wedge angle between the surfaces (inputs $\phi+\pi/2$ and β_{pm}) at that region of the airfoil. Similarly β_{s2} and β_{p2} are used to specify the trailing-edge wedge angle (it becomes an input). The curvature distribution results in (x, y) points near P_{sf} and P_{pf} that give as output the wedge angle near the leading edge. The surface-curvature distributions are manipulated until desirable wedge angles are obtained. The surface-angle distributions are part of the graphic output during use of the method.

The exact value of curvature and location of points C_1, C_2, C_3, and C_4 is not as critical as the resulting shape of the curvature distribution. In using the method we compare desired changes in Mach number distribution with changes in *curvature distribution* and location of blade surface. The alternative method (Eq. (10)) allows one to match up the leading edge position, thickness, and wedge angle in any region with the rest of the design (near the trailing edge).

After the first iteration (first geometric design and analysis), the user examines the resulting loading distribution, and appreciates where to increase and decrease local curvature (and local loading). After the second iteration the user gains an appreciation of the magnitude of the required changes in curvature to cause the desired changes in Mach number distribution. The procedure is repeated until a desirable geometry and performance is obtained (as in the case of the sample cascades below), or until the designer decides that the shape is good enough to proceed to more advanced (inverse) design methods.

Effects of Stagger Angle

The performance of four cascades designed with the prescribed-curvature distribution method is shown in Figs. 6, 7, 8, and 9. For all cases the main cascade-design variables except the stagger angle are kept constant (for example $\alpha_1=40$ deg, $\alpha_2=-60$ deg, $M_2=0.800$, $C_L=1.00$, and $o/S=0.5$). The stagger angles of cascades L25, L30, L35, and L40 are $\lambda=-25$ deg, $\lambda=-30$ deg, $\lambda=-35$ deg, and $\lambda=-40$ deg respectively. Other design inputs are shown in Table 1. In all cases the computational grid was 100×40. These figures illustrate that increasing the stagger angle, while keeping other design parameters constant, results in thinner and more front-loaded cascades. This is because as λ is increased the throat circle pushes both blade surfaces farther down, thus locating the throat farther upstream on the suction surface and thinning the blade. In order to fit the rest of the blade into the passage the designer is forced to increase the curvature of the suction surface of the blade in the vicinity of point P_{sf} (as shown in Table 1 $y(C1_s)$ is increasing with stagger angle). The increased curvature in turn increases the Mach number in that vicinity, thus loading the front part of the suction surface of the blade accordingly. While it is relatively easy to change the type of loading distribution of cascade L25 (Korakianitis and Papagiannidis, 1993a), it is harder to change the front-loaded cascade L40.

The relatively aft-loaded cascade of Fig. 6 ($\lambda=-25$ deg) has a relatively short length of relatively very adverse pressure gradient. As the stagger angle is increased, this changes until the relatively front-loaded cascade of Fig. 9 ($\lambda=-40$ deg) has a relatively long length of relatively not as adverse pressure gradient. This clearly affects the development of the pressure and suction-surface boundary layers. In a previous investigation Hoheisel et al. (1987) found that a midloaded cascade had a relatively thinner boundary layer, although their blades were designed with inverse-design methods and did not have the rest of the design parameters identical. A similar trend is shown in Fig. 10, which shows the pressure-side and suction-side boundary-layer displacement thickness $\delta_1\times20$ along the nondimensionalized blade-surface length s/b, calculated for the four cascades L25, L30, L35, and L40, using Albers and Gregg's (1974) program, for 10 percent free-stream turbulence. Blade L35 (with intermediate loading distribution) has the thin-

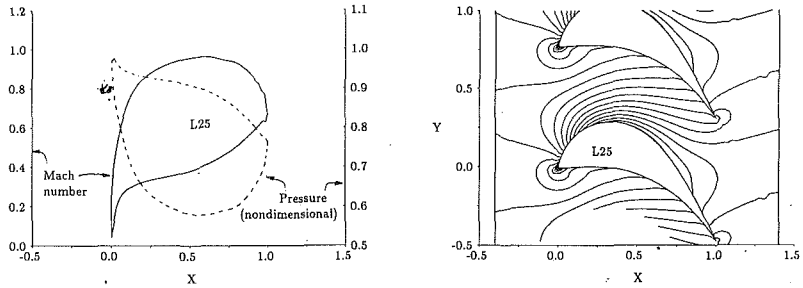

Fig. 6 Performance of cascade L25 (stagger angle λ = 25 deg); blade-design parameters shown in Table 1: left, surface Mach number and nondimensional surface pressure distributions; right, Mach number contours (increment 0.05)

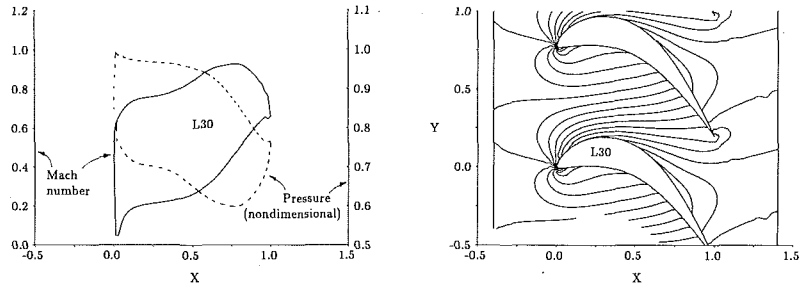

Fig. 7 Performance of cascade L30 (stagger angle λ = −30 deg); blade-design parameters *shown in Table 1: left, surface Mach number and nondimensional surface pressure distributions; right, Mach number contours (increment 0.05)*

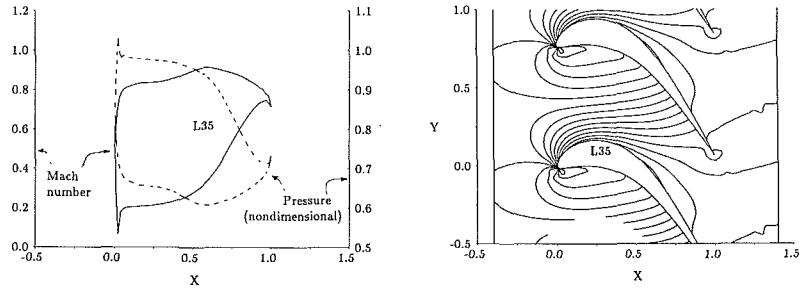

Fig. 8 Performance of cascade L35 (stagger angle λ = −35 deg); blade-design parameters shown in Table 1: left, surface Mach number and nondimensional surface pressure distributions; right, Mach number contours (increment 0.05)

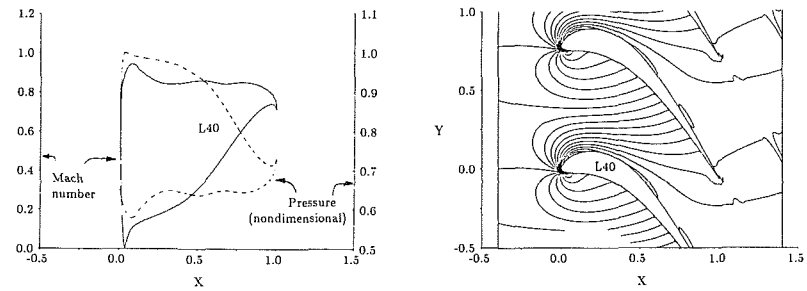

Fig. 9 Performance of cascade L40 (stagger angle λ = −40 deg); blade-design parameters shown in Table 1: left, surface Mach number and nondimensional surface pressure distributions; right, Mach number contours (increment 0.05)

nest boundary layer thicknesses on both surfaces and the thinnest wake.

Conclusions

Small slope-of-curvature discontinuities in the blade surfaces result in Mach number or pressure-coefficient surface-distribution spikes or humps, which may introduce regions of local acceleration and deceleration, separation, or undesirable loading distributions along the length of the blades. A two-dimensional direct blade-design method has been developed. It uses a mixture of analytic polynomials and a mapping of a desired curvature distribution on the (x, y) plane to specify the geometry of the cascades. By specification the blade surfaces have continuous slope of curvature throughout their length. The method permits the user to specify the leading edge by two thickness distributions around two independent construction lines, in a manner that avoids the overspeed regions near the leading edge (because it does not employ the usual blending in of the curvatures near the "leading-edge circle or ellipse"). It can be used to design subsonic or supersonic blades for

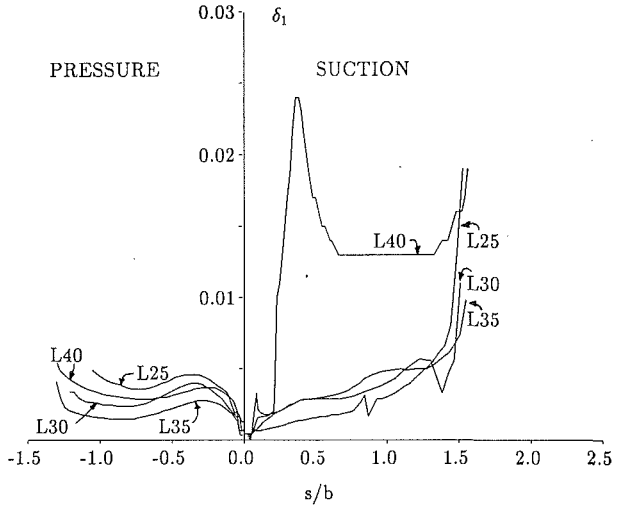

Fig. 10 Boundary layer displacement thickness δ_1 for cascades L25, L30, L35, and L40 (using Albers and Gregg's (1974) program with free-stream turbulence 10 percent)

compressors or turbines, or isolated airfoils, but the discussion in this paper is limited to high-Mach-number subsonic-exit turbine blades.

It is found that the cascade performance, judged by the shape of the surface Mach number distribution, is extremely sensitive to small changes of the surface geometry and of the curvature distribution of the airfoils. The design method presented ensures that the boundary layer, which is usually transitional and turbulent along the blade surfaces, is not perturbed unintentionally. The smooth curvature and Mach number distributions also enable the user to design lower-loss higher-loaded cascades. Continuous-slope-of-curvature surfaces should be used wherever the aerodynamic, heat transfer, hydrodynamic, or aesthetic performance, appropriately defined in each case, is critical.

The performances of four cascades of different stagger angles, but otherwise identical blade-design inputs and design criteria, have been computed, and their boundary-layer behavior has been numerically investigated. It is concluded that increasing the stagger angle results in more front-loaded cascades. An intermediate-loading philosophy (at an intermediate stagger angle) results in thinner wakes.

Acknowledgments

The author thanks Professor Michael B. Giles and Rolls Royce plc. for their permission to use UNSFLO to compute the performance of the sample cascades. He also thanks Mr. P. Papagiannidis for implementing and running Albers and Gregg's code, and for his assistance in finishing the designs of blades L25 and L40.

References

AGARD, 1985, "Test Cases for Inviscid Flow Field Methods," Advisory Report No. 211, AGARD-AR-211, May.

Ainley, D. G., and Mathieson, G. C. R., 1951, "A Method of Performance Estimation for Axial-Flow Turbines," British ARC, R&M 2974.

Albers, J. A., and Gregg, J. L., 1974, "Computer Program for Calculating Laminar, Transitional, and Turbulent Boundary Layers for a Compressible Axisymmetric Flow," NASA TN D-7521, Apr.

Bird, R. B., Stewart, W. E., and Lightfoot, E. N., 1960, *Transport Phenomena*, Wiley, New York.

Bry, P. F., 1989, "Blading Design for Cooled High-Pressure Turbines," in: *Blading Design for Axial Turbomachines*, AGARD Lecture Series 167, AGARD-LS-167.

Dunham, J., and Came, P. M., 1970, "Improvements to the Ainley-Mathieson Method of Turbine Performance Prediction," ASME *Journal of Engineering for Power*, Vol. 92, pp. 252–256.

Dunham, J., 1974, "A Parametric Method of Turbine Blade Profile Design," ASME Paper No. 74-GT-119.

Giles, M. B., 1988 "Calculation of Unsteady Wake/Rotor Interactions," *AIAA Journal of Propulsion and Power*, Vol. 4, No. 4, July/Aug.

Gostelow, J. P., 1975, "Trailing Edge Flows Over Turbomachine Blades and the Kutta-Joukowsky Condition," ASME Paper No. 75-GT-94.

Gostelow, J. P., 1976, "A New Approach to the Experimental Study of Turbomachinery Flow Phenomena," ASME Paper No. 76-GT-47.

Gostelow, J. P., 1984, *Cascade Aerodynamics*, Pergamon Press, New York.

Hodson, H. P., 1985, "Boundary-Layer Transition and Separation Near the Leading Edge of a High-Speed Turbine Blade," ASME *Journal of Engineering for Gas Turbines and Power*, Vol. 127, pp. 127–134.

Hodson, H. P., and Dominy, R. G., 1987, "Three-Dimensional Flow in a Low Pressure Turbine Cascade at Its Design Condition," ASME JOURNAL OF TURBOMACHINERY, Vol. 109, pp. 177–185.

Hoheisel, H., Kiock, R., Lichtfuss, H. J., and Fottner, L., 1987, "Influence of Free-Stream Turbulence and Blade Pressure Gradient on Boundary Layer and Loss Behavior of Turbine Cascades," ASME JOURNAL OF TURBOMACHINERY, Vol. 109, pp. 210–219.

Hourmouziadis, J., Buckl, F., and Bergmann, P., 1987, "The Development of the Profile Boundary Layer in a Turbine Environment," ASME JOURNAL OF TURBOMACHINERY, Vol. 109, pp. 286–295.

Kacker, S. C., and Okapuu, U., 1982, "A Mean-Line Prediction Method for Axial Flow Turbine Efficiency," ASME *Journal of Engineering for Power*, Vol. 104, No. 2, pp. 111–119.

Kiock, R., Lehthaus, F., Baines, N. C., and Sieverding, C. H., 1986, "The Transonic Flow Through a Turbine Cascade as Measured in Four European Wind Tunnels," ASME *Journal of Engineering for Gas Turbines and Power*, Vol. 108, pp. 277–284.

Korakianitis, T., 1989, "Design of Airfoils and Cascades of Airfoils," *AIAA Journal*, Vol. 27, No. 4, pp. 455–461.

Korakianitis, T., and Papagiannidis, G., 1993a, "Surface-Curvature-Distribution Effects on Turbine-Cascade Performance," ASME JOURNAL OF TURBOMACHINERY, Vol. 115, No. 2, pp. 334–341.

Korakianitis, T., and Pantazopoulos, G. I., 1993b, "Improved Turbine-Blade Design Techniques Using 4th-Order Parametric-Spline Segments," *Computer-Aided Design*, Vol. 25, No. 5, pp. 289–299.

Meauze, G., 1989, "Overview on Blading Design Methods," in *Blading Design for Axial Turbomachines*, AGARD Lecture Series 167, AGARD-LS-167.

Okapuu, U., 1974, "Some Results From Tests on a High Work Axial Gas Generator Turbine," ASME Paper No. 74-GT-81.

Schlichting, H., 1960, *Boundary-Layer Theory*, 4th ed., McGraw-Hill, New York.

Sharma, O. P., Pickett, G. F., and Ni, R. H., 1992, "Assessment of Unsteady Flows in Turbines," ASME JOURNAL OF TURBOMACHINERY, Vol. 114, pp. 79–90.

Stow, P., 1989, "Blading Design for Multi-Stage hp Compressors," in: *Blading Design for Axial Turbomachines*, AGARD Lecture Series 167, AGARD-LS-167.

Wagner, J. H., Dring, R. P., and Joslyn, H. D., 1985, "Inlet Boundary Layer Effects in an Axial Compressor Rotor: Part 1—Blade-to-Blade Effects," ASME JOURNAL OF TURBOMACHINERY, Vol. 107, pp. 374–380.

Wilson, D. G., 1984, *The Design of High-Efficiency Turbomachinery and Gas Turbines*, The MIT Press, Cambridge, MA.

Zweifel, O., 1945, "The Spacing of Turbomachine Blading, Especially With Large Angular Deflection," *Brown Boveri Review*, Vol. 32, No. 12, Baden, Switzerland.

Surface-Curvature-Distribution Effects on Turbine-Cascade Performance

T. Korakianitis

P. Papagiannidis

Department of Mechanical Engineering,
Washington University,
St. Louis, MO 63130

The manufacturing accuracy of turbine blades is judged by the difference between the designed and produced location of each point around the airfoils. This paper shows that the design-point and off-design-point aerodynamic and heat transfer performance of turbine cascades is affected significantly by the distribution of curvature along the suction and pressure surfaces, and less significantly by the exact location of each one point. The performances of turbine blades designed with continuous slope of curvature distribution, and with slight discontinuities in the slope of curvature, are examined using a computer program for various design and off-design flow conditions. The accuracy of the computations is checked by comparison of computational results with cascade solutions of known experimental output. It is concluded that the accuracy in local curvature is just as important as the design-location-by-manufactured-location accuracy of each point on the blade.

Introduction

Gas turbine blades are three-dimensional objects operating in a complex and unsteady flow field. Three-dimensional turbine blades are generated by "stacking" two-dimensional designs using rules for: the flow angles from hub to tip at the leading and trailing edge, derived from radial-equilibrium throughflow calculations; the locus of the centers of gravity of the sections; and the three-dimensional shape of the leading edge and the trailing edge. Compromises in performance must be made to accommodate these three-dimensional constraints, the location of cooling passages, and hollow sections. Due to its complexity the blade-design problem is usually reduced to a series of "stacked" two-dimensional problems, assuming that the cascade operates in a steady two-dimensional flow field.

Blade design is partly a science and partly an art. The performance is determined by the behavior of the boundary layers along the surfaces, and is expressed in the form of some property distribution (such as pressure, velocity, etc.) on the blade surface and in the cascade passage. Blade cascades can be designed by direct or inverse methods. In the direct method the designer inputs the geometry of the blade and the output is the performance of the airfoil. The blade geometry is modified until a desirable performance is obtained. In the inverse method the designer usually starts from some initial blade shape and performance, and inputs the desired modifications to the performance. The output is a new geometric shape and its performance, which is as close to the desired (input) one as permitted by the equations modeling the flow. Both methods are iterative and are based on the assumption of steady flow conditions.

The accuracy of the produced blade shapes is determined by comparing the intended (designed) shape with manufactured blades. The usual criterion is the allowable tolerance between design and manufactured points. The purpose of this paper is to show that comparisons of design-versus-manufactured curvature distribution at each point should be used in addition to point-to-point comparisons as a criterion for accepting an airfoil. Two sets of sample cascades are used. The cascades of the first set have similar shapes, with small local slope-of-curvature discontinuities. The latter result in small surface variations that would pass the point-for-point-tolerance tests, but introduce unacceptable cascade performance. The cascades of the second set have substantial surface variations among them, but they have been designed with continuous-slope-of-curvature surfaces. The second set is used to show that curvature distribution is what governs the shape of the surface Mach number and pressure distributions, which in turn determine boundary-layer behavior and blade performance.

Importance of Surface Curvature

Both the curvature and the slope of curvature of blade surfaces affect boundary-layer development and blade performance. The flow in turbomachinery cascades *curves* around the blades. The compressible-flow Navier–Stokes equations for Newtonian fluids in the limiting case of polar coordinates (r, θ) (taken from cylindrical-coordinate equations in the text by Bird et al., 1960) show the dependence of the core flow and the stress terms τ_{ij} on the local radius of curvature r:

$$\frac{\partial \rho}{\partial t}+\frac{1}{r}\frac{\partial}{\partial r}(\rho r v_r)+\frac{1}{r}\frac{\partial}{\partial \theta}(\rho v_\theta)=0$$

Contributed by the International Gas Turbine Institute and presented at the 37th International Gas Turbine and Aeroengine Congress and Exposition, Cologne, Germany, June 1–4, 1992. Manuscript received by the International Gas Turbine Institute February 19, 1992. Paper No. 92-GT-84. Associate Technical Editor: L. S. Langston.

$$\rho\left(\frac{\partial v_r}{\partial t}+v_r\frac{\partial v_r}{\partial r}+\frac{v_\theta}{r}\frac{\partial v_r}{\partial \theta}-\frac{v_\theta^2}{r}\right)=$$
$$-\frac{\partial p}{\partial r}-\left(\frac{1}{r}\frac{\partial}{\partial r}(r\tau_{rr})+\frac{1}{r}\frac{\partial \tau_{r\theta}}{\partial \theta}-\frac{\tau_{\theta\theta}}{r}\right)+\rho g_r$$
$$\rho\left(\frac{\partial v_\theta}{\partial t}+v_r\frac{\partial v_\theta}{\partial r}+\frac{v_\theta}{r}\frac{\partial v_\theta}{\partial \theta}+\frac{v_r v_\theta}{r}\right)=$$
$$-\frac{1}{r}\frac{\partial p}{\partial \theta}-\left(\frac{1}{r^2}\frac{\partial}{\partial r}(r^2\tau_{r\theta})+\frac{1}{r}\frac{\partial \tau_{\theta\theta}}{\partial \theta}\right)+\rho g_\theta \quad (1)$$
$$\tau_{rr}=-\mu\left[2\frac{\partial v_r}{\partial r}-\frac{2}{3}(\nabla\cdot\mathbf{v})\right]$$
$$\tau_{\theta\theta}=-\mu\left[2\left(\frac{1}{r}\frac{\partial v_\theta}{\partial \theta}+\frac{v_r}{r}\right)-\frac{2}{3}(\nabla\cdot\mathbf{v})\right]$$
$$\tau_{r\theta}=\tau_{\theta r}=-\mu\left[r\frac{\partial}{\partial r}\left(\frac{v_\theta}{r}\right)+\frac{1}{r}\frac{\partial v_r}{\partial \theta}\right]$$
$$(\nabla\cdot\mathbf{v})=\frac{1}{r}\frac{\partial}{\partial r}(rv_r)+\frac{1}{r}\frac{\partial v_\theta}{\partial \theta}$$

The stress components τ_{ij} are dominant in large-shear areas, such as the boundary layer in steady two-dimensional cascade flows. The $1/r$ and $1/r^2$ terms in these equations suggest a strong dependence of local pressure and velocity distributions on curvature. While one expects that the boundary layer shields the core of the flow from surface discontinuities, the boundary-layer behavior depends on the slope of the velocity distribution as it approaches the solid wall, and Eqs. (1) indicate that the slope of the velocity distribution, the boundary layer, and its behavior, are coupled with the local radius. Smooth velocity distributions along the blade surfaces require smooth surface-curvature distributions (continuous slopes of velocity and curvature along the blade surface). Continuous slope of curvature requires continuous third derivatives, as illustrated in the following two equations for curvature and slope of curvature for $y = f(x), y' = df(x)/dx, y'' = d^2f(x)/dx^2$ and $y''' = d^3f(x)/dx^3$.

$$\mathbf{C}(x)=\frac{1}{R(x)}=\frac{y''}{[1+y'^2]^{(3/2)}} \quad (2)$$

$$\mathbf{C}'(x)=\frac{d\mathbf{C}}{dx}=\frac{y'''[1+y'^2]-3y'y''^2}{[1+y'^2]^{(5/2)}} \quad (3)$$

Most parametric splines currently in use for direct blade design (e.g., cubic, B-splines, Bezier splines, etc.) have continuous first and second derivatives, and they result in smooth-looking surfaces with continuous curvatures, but discontinuous slopes of curvature at the spline knots. One must distinguish here between the small local slope-of-curvature discontinuities from surface roughness and fouling, with which turbines must operate, and the slope-of-curvature discontinuities in the as-designed shape at the junctions of the splines. It will be shown below that the latter are invisible to the eye, but they may produce unusually loaded cascades and thicker wakes. This has resulted in many test and production airfoils (isolated and in turbomachine cascades) that exhibit Mach number and pressure-coefficient-distribution spikes or dips and humps of various magnitudes. These occasionally result in unexpected loading distributions along the blade length, and in local separation bubbles. These effects are visible as small local "kinks" in surface pressure or Mach number distributions in some of the computational and experimental data published, for example, by: Okapuu (1974), Gostelow (1976), Wagner et al. (1983), Hourmouziadis et al. (1987) (with separation bubble), Sharma et al. (1992) and others.

Blending a leading-edge circle or ellipse with the blade surfaces usually results in a local curvature or slope-of-curvature discontinuity. This may cause separation and substantial leading-edge surface-Mach-number spikes, which are detected only if the probes are located at the correct location. Such a local leading-edge laminar-separation bubble due to blending of a leading-edge circle with the blade surfaces occurs in the turbine geometry published by Hodson and Dominy (1987), seen in the data published in Fig. 11 of Hodson (1985). This leading-edge spike and separation region were removed by modifying the geometry of the blade in the vicinity of the slope-of-curvature discontinuity with an inverse design technique as explained in Figs. 11, 12, and 13 of Stow (1989).

A direct-design method (Korakianitis, 1989) using analytic polynomials indicated that continuous-slope-of-curvature distribution was essential to avoid local surface-pressure-distribution spikes and "kinks." A subsequent direct-design method using parametric splines specified with continuous slope of curvature (Korakianitis and Pantazopoulos, 1993a) eliminated unwanted performance "kinks" but proved cumbersome and time consuming. A third direct-design method (Korakianitis, 1993b) controlled the local and global acceleration (and diffusion) by prescribing the curvature distribution along the blade length ($\mathbf{C}(x)$) such that the slope of curvature is continuous along the blade surfaces. The blade geometry was computed by mapping the input curvature in the (x, y) plane. In the last method the trailing-edge region is specified by an analytic polynomial, the main part of the blade surface is specified by its curvature distribution, and the leading-edge region is specified by a thickness distribution evaluated with respect to a construction line, such that it joins the blade surface with continuous slope of curvature. Using this method we showed

Nomenclature

b = axial chord length (nondimensionally $b = 1$)
c = blade chord
$\mathbf{C}$ = $1/R$ = curvature (Eq. (2), as shown in Fig. 3*b*)
C_L = tangential-loading coefficient = $2S\cos^2\alpha_2(\tan\alpha_1 - \tan\alpha_2)/b$
g = body force (Eqs. (1))
i = flow incidence with respect to α_1
M = Mach number
o = throat diameter of the cascade
p = pressure (Eqs. (1))
R = local radius of curvature (Eq. (2))
s = blade-surface length
S = tangential spacing (pitch) of the blades
t = time (Eqs. (1))
v_i = velocity component ($i = r, \theta$)
$\mathbf{v}$ = velocity vector (Eq. (1))
(x, y) = Cartesian coordinates
(X, Y) = nondimensional distances $(X = x/b, Y = y/b)$
α = flow angle
δ_1 = boundary-layer displacement thickness (Figs. 3*c* and 5)
λ = stagger angle of the blades
μ = dynamic viscosity (Eqs. (1))
ρ = density (Eqs. (1))
τ_{ij} = shear stress components (Eqs. (1), $i, j = r, \theta$)

Subscripts

1, 2 = cascade inlet and outlet
r = radius in polar coordinates (r, θ)
θ = angle in polar coordinates (r, θ)

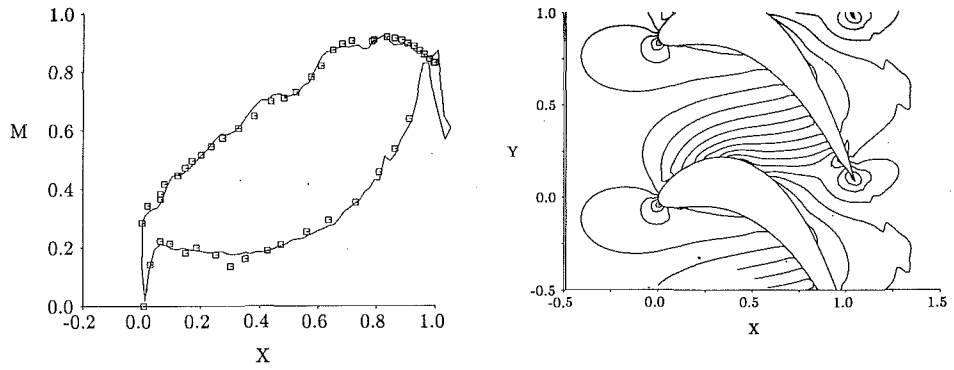

Fig. 1 Comparison of Mach number distributions for the turbine cascade investigated by Kiock et al. (1986). Left, surface Mach-number distributions. Right, cascade geometry and Mach number contours of increment 0.05.

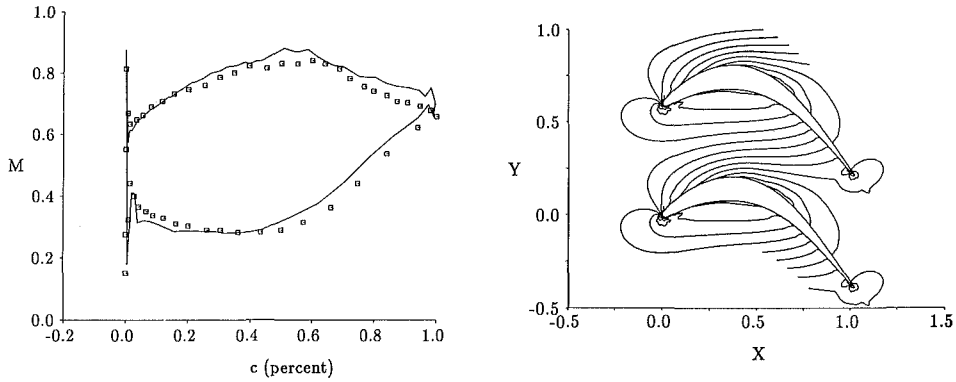

Fig. 2 Comparison of Mach number distributions for the turbine cascade investigated by Hodson and Dominy (1987). Left, surface Mach-number distributions. Right, cascade geometry and Mach number contours of increment 0.05.

that increasing the stagger angle produces more-front-loaded cascades, and that intermediate values of stagger angle promote intermediate-loading philosophy and result in thinner wakes.

Accuracy of Computations

The performance of sample turbine blades in this paper has been evaluated using the inviscid and steady-flow version of Giles' (1988) computer program UNSFLO. The accuracy of the computations has been checked by comparing the results of Euler computations with two cases of known theoretical output (Korakianitis, 1993b). The first case was a comparison of computations with the (exact) theoretical solution of Gostelow's (1984) compressor cascade. The second case was a comparison of computations with the hodograph solution of Hobson's transonic turbine cascade No. 2 (taken from AGARD, 1985). These tests were suitable for two-dimensional inviscid flow fields with sharp trailing edges, and indicated exact agreement between theory and computation. In this paper we show two comparisons with experiments.

The first case is a comparison of inviscid computations with the experimental results from the subsonic turbine cascade obtained at DFVLR Braunschweig by Kiock et al. (1986). For this case $M_1 = 0.260$, $M_2 = 0.782$, $\alpha_1 = 30.0$ deg and $\alpha_2 = -67.33$ deg. A uniform **H**-grid of 100 × 40 and a cusp (to close the trailing edge) were used. The results, shown in Fig. 1, indicate very good agreement with the experiments. The tick marks are the experimental results (transformed from data along percentage of chord c to data along percentage of axial chord b, along x), and the solid line is the calculation. Despite the absence of boundary-layer computations or corrections for it, the numerical solution follows local dips in the suction-surface Mach number distribution at $x \approx 0.55$ and $x \approx 0.80$, and local accelerations at $x \approx 0.05$ and $x \approx 0.70$.

The second case is a comparison of inviscid computations with the experimental results from the subsonic turbine cascade obtained at Cambridge University by Hodson and Dominy (1987). For this case $M_1 = 0.496$, $M_2 = 0.710$, $\alpha_1 = 38.8$ deg and $\alpha_2 = -53.5$ deg. A uniform **H**-grid of 150 × 60 and a cusp (to close the trailing edge) were used. The results, shown in Fig. 2, indicate very good agreement of computations with the experimental data (tick marks) taken from Stow (1989). Hodson (1985) has analyzed the experimental data to show leading-edge laminar-separation bubbles on both surfaces, caused by blending a leading-edge circle with the blade surfaces. The numerical solution predicts the leading-edge surface Mach number spikes. Despite the three-dimensional effects in the experiments, the effect of the trailing edge cusp in the trailing-edge region of the solution, and the absence of boundary-layer computations or corrections for it, the agreement between computation and experiment is very good.

The First Set of Sample Cascades

Figure 3 shows the geometry, surface-curvature distribution, and surface Mach number distribution of four very similar turbine cascades designed for $\alpha_1 = 40$ deg, $\alpha_2 = -60$ deg, $M_2 = 0.8$, $C_L = 1.0$, and $\lambda = -32$ deg. C_L is the tangential-loading coefficient, defined as tangential blade loading, divided by tangential blade area, divided by outlet dynamic head. For incompressible flow C_L is reduced to the function of S/b, α_1, and α_2 (Wilson, 1984) shown in the nomenclature. For these cascades $S/b = 0.7779$. These four blades have been designed using the method described by Korakianitis (1989). The pressure surfaces are identical. The suction surfaces have minute differences as described below. In that method the input was the (X, Y) points of the knots of surface segments and surface angles near the leading and trailing edges. The surface

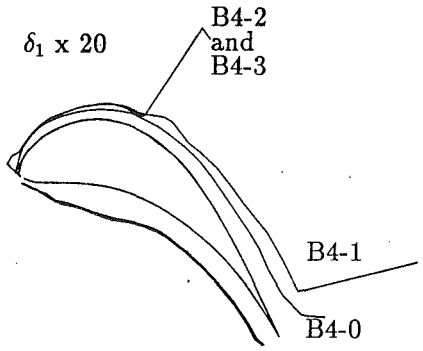

Fig. 3(*a*) Blade geometries and boundary layer displacement thickness δ_1 (free-stream turbulence 15 percent)

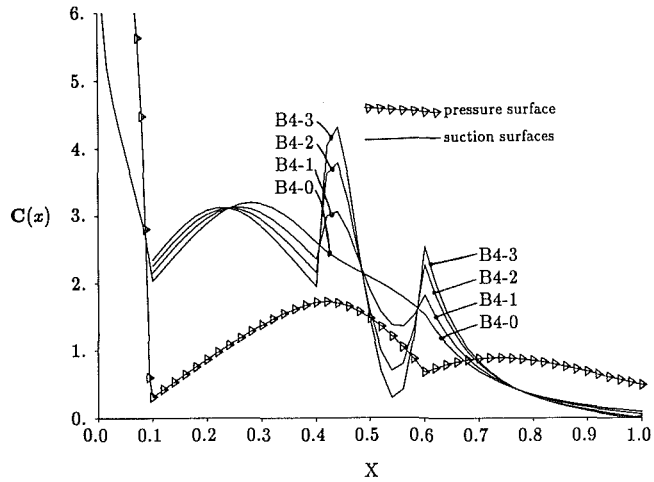

Fig. 3(*b*) Curvature distributions

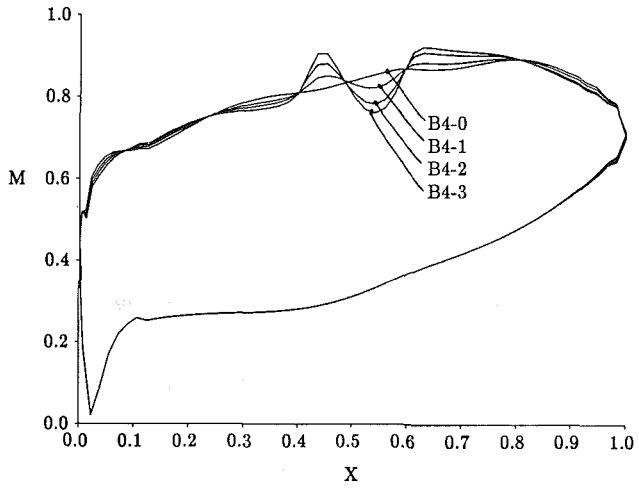

Fig. 3(*c*) Surface Mach number distributions

Fig. 3 Surface distributions for cascades B4-0, B4-1, B4-2, B4-3: α_1 = 40 deg, α_2 = −60 deg, C_L = 1.00, λ = −32 deg

segments had point, first-derivative, and second-derivative continuity at the knots. (These conditions result in continuous curvature distribution along each blade surface, but in general in slope-of-curvature discontinuity at the segment knots.) For the sample cascades shown, two consecutive knots are at X = 0.40 and X = 0.60. As shown in Fig. 3(*b*), cascade B4-0 has a smooth suction-surface curvature $\mathbf{C}(x)$ (without slope-of-curvature discontinuity at the knots at X = 0.40 and X = 0.60). Cascades B4-1, B4-2, and B4-3 have continuous suction-surface curvature ($\mathbf{C}(x)$) distributions, but they have progressively worse slope-of-curvature ($\mathbf{C}'(x)$) discontinuities at X = 0.40 and X = 0.60. These suction-surface curvature distributions result in the surface Mach-number distributions shown in Fig. 3(*c*). The smoothness in Mach-number distribution for cascade B4-0, and the spikes and dips in Mach-number distribution for cascades B4-1, B4-2, and B4-3 are "mapped" from the corresponding surface-curvature distributions.

Quantitatively the nondimensional differences in the y locations of corresponding blade points are four orders of magnitude smaller than the axial chord. Therefore, the suction-surface differences between the four blades are not visible in Fig. 3(*a*), where the four blades are plotted on top of each other. The premise of this paper is that surface-curvature distribution *along the entire blade length*, as well as point-for-point surface accuracy, are important for Mach number and pressure distributions, and the resulting boundary-layer behavior and cascade performance. Thus the differences in curvature distributions along the length of the four blades shown in Fig. 3(*b*) (which start at X = 0.1 and end at X = 1.0, but they are dominant in the sample cascades at $0.4 < X < 0.6$), result in surface-curvature and Mach number dips and spikes as shown in Fig. 3(*c*). Figure 3(*a*) shows the corresponding boundary-layer displacement-thickness distribution $\delta_1 \times 20$ of each blade, calculated with Albers and Gregg's (1974) differential boundary layer program. These calculations were performed assuming incoming free-stream turbulence of 15 percent and Reynolds number 5.5×10^5 based on chord. This program recognizes the importance of surface-curvature distribution, which is part of the input for the computations. Blade B4-0 has smooth curvature and Mach number, and results in the thinnest boundary layer. Blade B4-1 has a small discontinuity in the slope of curvature that causes a disturbance in surface Mach number distribution, and a thicker boundary layer (and wake) at the trailing edge. Blades B4-2 and B4-3 have correspondingly larger slope-of-curvature discontinuities, that cause the boundary layer to separate (similarly to the leading-edge separation shown in Fig. 2) near the discontinuity.

Boundary Layer Calculations

For Incidence i = 0 deg. Figures 4(*a*) and 4(*b*) show the Mach number distributions for cascades B4-0 and B4-1 respectively for incidences of +10, 0, and −10 deg with respect to the design inlet-flow angle α_1. Figure 4(*c*) shows the corresponding boundary-layer displacement thickness δ_1 calculated with Albers and Gregg's (1974) program, with specifications identical with those for Fig. 3(*a*). For zero incidence (i = 0 deg) the suction-surface boundary-layer displacement thickness of cascade B4-0 is smaller than that of cascade B4-1, as already expected from Fig. 3(*a*).

For Positive Incidence i = +10 deg. This increases the suction-surface Mach number and decreases the pressure-surface Mach number at $X \approx 0.05$. This front loads both cascades substantially, and at i = +10 deg the program indicates that both cascades B4-0 and B4-1 experience suction-surface laminar separation in the region of sudden deceleration at $X \approx 0.05$. This is followed by immediate turbulent reattachment, which in turn is followed by immediate turbulent separation, resulting in thick wakes at the trailing edge.

For Negative Incidence i = −10 deg. This decreases the suction-surface Mach number and increases the pressure-surface Mach number at $X \approx 0.05$. This results in substantially different behavior between cascades B4-0 and B4-1.

For blade B4-0: For i = 0 deg the boundary layer of B4-0 exhibited normal transition between $X \approx 0.65$ (onset of transition) and $X \approx 0.93$ (fully turbulent) without separation.

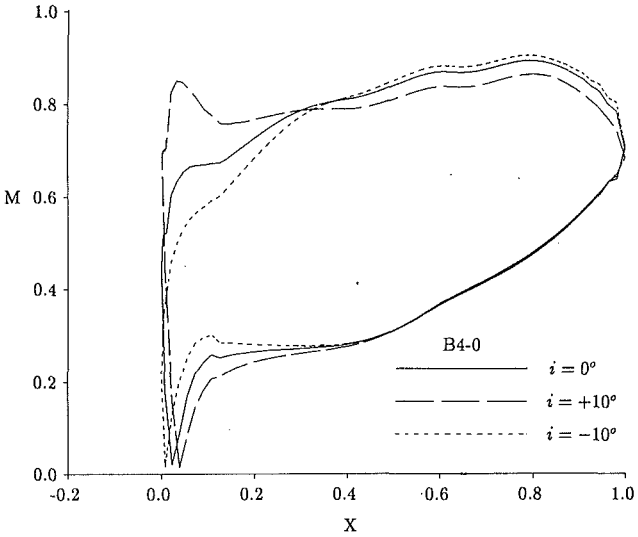

Fig. 4(*a*) Surface Mach number distributions at ±10 deg incidence for cascade B4-0

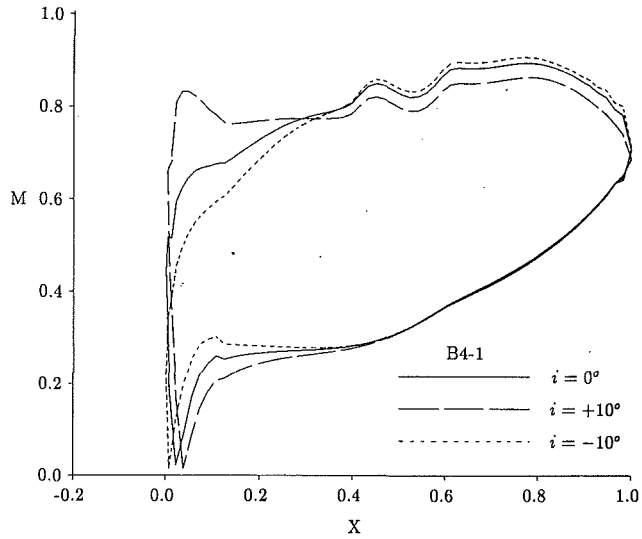

Fig. 4(*b*) Surface Mach number distributions at ±10 deg incidence for cascade B4-1

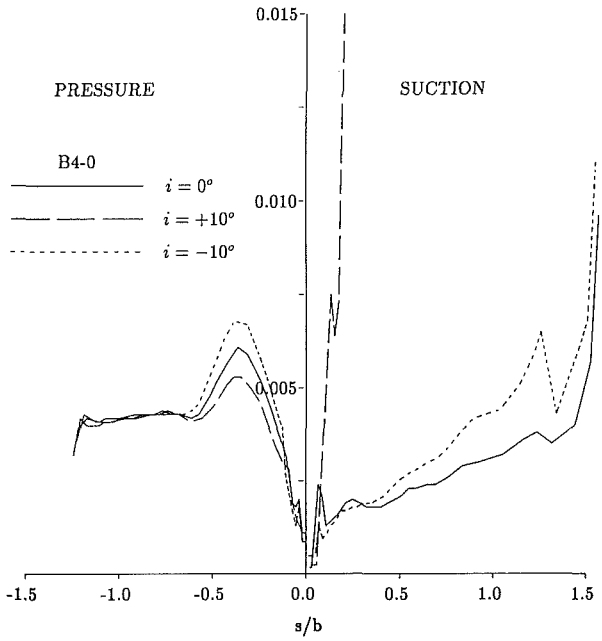

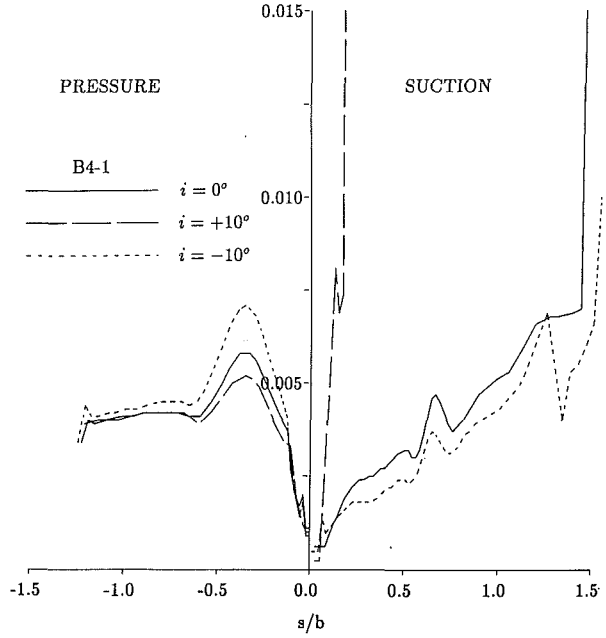

Fig. 4(*c*) Boundary layer displacement thickness δ_1 for cascades B4-0 and B4-1 at ±10 deg incidence (free-stream turbulence 15 percent)

Fig. 4 Surface Mach number distributions and boundary layer displacement thickness δ_1 for cascades B4-0 and B4-1 at ±10 deg incidence

For $i = -10$ deg the onset of transition appeared a little further downstream (at $X \approx 0.70$). At that point the boundary layer was relatively thicker compared to that at the onset of transition for $i = 0$ deg. The small delay in transition is because of the smoother and less rapid velocity acceleration near the leading edge. The thicker boundary layer could not withstand the subsequent adverse pressure gradient, and for $i = -10$ deg the code showed transitional separation at $X = 0.87$. With a turbulent restart option the program did not show any further separation, but resulted in a thicker wake compared to that for $i = 0$ deg.

For blade B4-1: For $i = 0$ deg the boundary layer of B4-1 exhibited normal transition between $X \approx 0.773$ and $X \approx 0.93$, associated with turbulent separation at $X \approx 0.98$. For $i = -10$ deg (unlike the boundary-layer behavior of blade B4-0), the considerable disturbances in Mach number distribution in the region $0.4 < X < 0.6$ caused blade B4-1 to experience earlier onset of transition, at $X \approx 0.68$. At that point the boundary layer was substantially thinner compared to that at the onset of transition for $i = 0$ deg. As a result the program indicates fully developed turbulent flow at $X \approx 0.85$ (a little earlier than in the corresponding case for blade B4-0), resulting in a thinner wake than for $i = 0$ deg for blade B4-1.

The Second Set of Sample Cascades

Figure 5 shows five continuous-slope-of-curvature cascades designed for $\alpha_1 = 40$ deg, $\alpha_2 = -60$ deg, $M_2 = 0.8$, $C_L = 1.0$, $\lambda = -25$ deg, and $o/S = 0.5$ ($\approx \cos\alpha_2$) using the prescribed-curvature-distribution direct-design method described by Korakianitis (1993b). The throat diameter is an input in this design method, and $S/b = 0.7779$. The suction surfaces of all five cascades pass from a common region at the throat. All suction surfaces must pass through the same origin at the

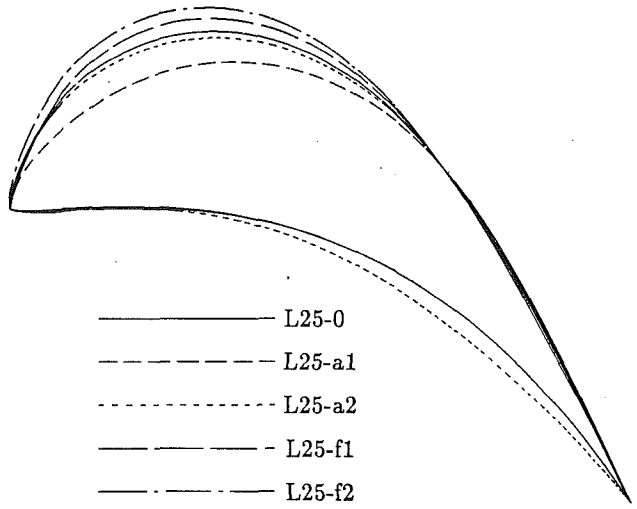

Fig. 5(*a*) Geometries of cascades L25-0, L25-f1, L25-f2, L25-a1, and L25-a2

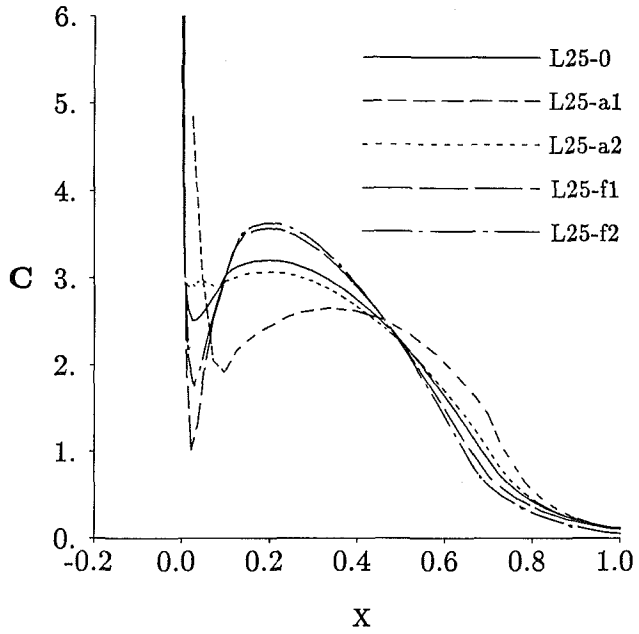

Fig. 5(*b*) Surface curvature (C(*x*)) distributions

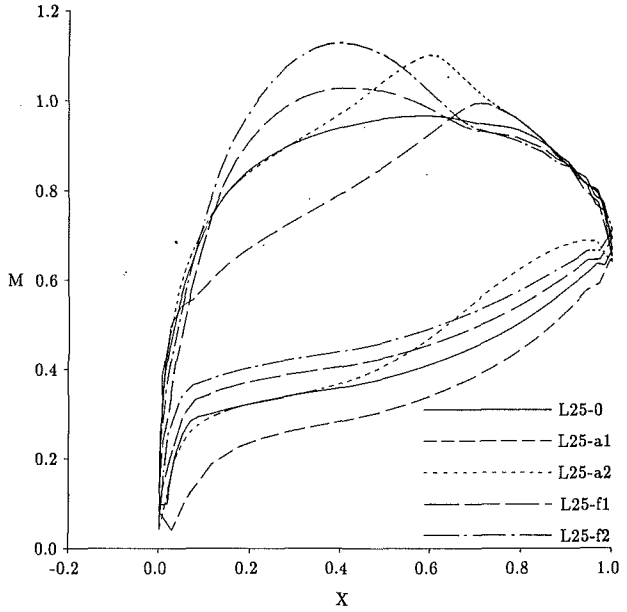

Fig. 5(*c*) Surface Mach number distributions

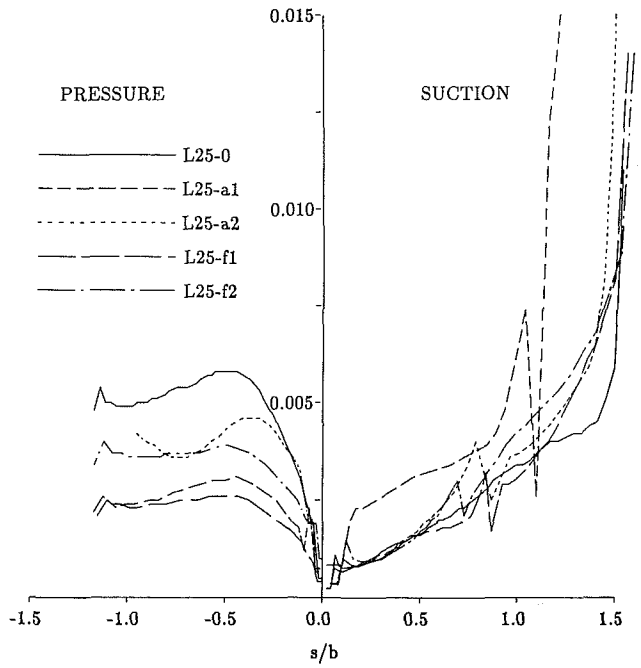

Fig. 5(*d*) Boundary layer displacement thickness δ_1

Fig. 5 Surface distributions for cascades L25-0, L25-f1, L25f2, L25-a1, L25-a2. α_1 = 40 deg, α_2 = −60 deg, C_L = 1.00, λ = −25 deg

leading edge. Those with lower curvature in the region of unguided diffusion (on the suction surface downstream of the throat) have higher suction surfaces cutting deeper into the passage. They also have higher curvatures in the corresponding suction-surface regions (in the passage) in order to reach the same origin, as indicated in Figs. 5(*a*) and 5(*b*). Thus by increasing (decreasing) the curvature distribution forward (versus aft) on the suction surface, the designer can front (versus aft) load the Mach number distribution. Cascade L25-0 has a smooth midloaded characteristic. Cascades L25-a1 and L25-a2 ("a" stands for aft loaded) are correspondingly more aft-loaded than L25-0. Cascades L25-f1 and L25-f2 ("f" stands for front loaded) are correspondingly more front-loaded than L25-0. The front versus aft loading has a direct correspondence with the suction surface curvature distribution, as indicated in Figs. 5(*b*) and 5(*c*).

Four of the cascades have identical pressure surfaces. Figure 5(*c*) shows that the pressure surface Mach numbers of the four identical pressure surfaces increase appropriately to match the suction-side loading. Comparing the pressure-surface blade shape and the pressure-side loading of cascade L25-a2 to those of the other four cascades indicates that lowering the pressure surface in the passage increases the pressure-surface Mach number (thus loading the suction-surface Mach number even more).

Figures 5(*a*), 5(*b*), and 5(*c*) illustrate that, as the curvature near the front part of the suction surface is increased, the cascade becomes front loaded; and as the curvature near the aft part of the suction surface is increased, the cascade becomes aft loaded. Curvature variations of the same magnitude have a correspondingly larger effect farther downstream on the surfaces, and they are critical in the region of unguided diffusion downstream of the throat on the suction surface. Higher values of stagger angle λ force the geometry such that the throat is located farther upstream on the suction surfaces. The trailing-

edge regions of the blades are located in lower Y values in the (X, Y) plane. Thus the blades become thinner, with less curvature near the trailing edge, and correspondingly more curvature near the leading edge. The higher curvatures near the leading edges result in more front-loaded cascades for higher λ (Korakianitis, 1993b). The designer has more flexibility in controlling the front-versus-aft loading of a cascade with lower stagger angles.

The boundary-layer calculations illustrated in Fig. 5(d) have been performed with Albers and Gregg's (1974) program, with 15 percent free-stream turbulence, and Reynolds number 5.5 $\times$ 10^5 based on chord. The aft-loaded cascades have relatively short surface lengths, with relatively more adverse pressure gradients toward the trailing edge. The front-loaded cascades have relatively long surface lengths, with relatively less adverse pressure gradients toward the trailing edge. This clearly affects the development of the pressure- and suction-surface boundary layers. The intermediate blade-loading philosophy (L25-0) results in the thinnest suction-surface wake. This agrees with the conclusions of a previous investigation by Hoheisel et al. (1987), which concluded that a midloaded cascade had a relatively thinner boundary layer, although their blades did not have the rest of the design parameters (such as throat diameter) identical. The front-loaded cascades L25-f1 and L25-f2 have thicker suction-surface wakes than that of cascade L25-0, but thinner than those of the aft-loaded cascades L25-a1 and L25-a2. The two aft-loaded cascades have lower suction-surface local Reynolds numbers, which result in larger laminar boundary-layer thicknesses, especially for cascade L25-a1. This cascade exhibits transition immediately after the peak in Mach number distribution at $X \approx 0.78$ ($s/b \approx 1.1$). The boundary layer cannot withstand the severe adverse pressure gradient and it eventually separates at $s/b \approx 1.3$. Another reason for this behavior is the relatively sudden acceleration of the flow in the leading-edge region. Although cascade L25-a2 is aft-loaded even more than cascade L25-a1, the relatively higher suction-surface Reynolds numbers, and the less sudden acceleration of the flow in the leading-edge region, result in thinner laminar boundary layers. The onset of transition is earlier, at $X \approx 0.57$ ($s/b \approx 0.85$), and the flow does not separate until the trailing edge.

Comparison of the Mach number distributions shown in Figs. 2, 3, 4, and 5 indicate that continuous-slope-of-curvature cascades can have substantial variations in geometric blade shapes that result in acceptable performance. Small slope-of-curvature discontinuities result in small surface variations, that may pass the manufacturing-tolerance tests, yet introduce unacceptable performance (and in some cases regions of undesirable separation).

Other Comments

In the early stages of axial-cascade design the geometry of airfoils is analyzed in a series of two-dimensional cuts from hub to tip. A major effort in the subsequent three-dimensional design process is to minimize the radial pressure gradients, radial flows, and other secondary flows. These three-dimensional effects always exist in actual flows, and they are particularly important in low hub-to-tip-ratio stages. Although three-dimensional design and analysis programs are widely used, much of our basic understanding of axial-turbine flows (derived from theory, computation, and experiments) is based on two-dimensional considerations. Three-dimensional investigations are enlightening, useful, and more complete, but more expensive and harder to model than two-dimensional ones. Both two-dimensional and three-dimensional approaches are necessary for the analysis of physical phenomena in different phases of turbomachinery design. This paper investigates the effects of two-dimensional surface-curvature distribution on two-dimensional flows in axial turbines. It is expected that three-dimensional curvature has similar effects to the two-dimensional ones analyzed here. Of course theoretical and computational investigations, including the present one, would benefit from experimental verification.

Curvature and slope of curvature are nonlinear functions of point-by-point geometry (expressed as (X, Y) points, or as $y(x)$, see Eqs. (2) and (3)). Therefore small variations in geometry can cause large variations in curvature, and small variations in curvature can cause large variations in geometry; see Figs. 3 and 5. Performance is a function of curvature distribution along the entire airfoil length, not just the point-by-point variation in curvature. This should not be compared with the accuracy of numerical-control cutting machines or the tolerance criteria for point-by-point quality control of manufactured blades. New tolerance criteria for surface-curvature distribution (along the chordwise blade length) must be established.

Conclusions

Small slope-of-curvature discontinuities in the blade surfaces result in Mach number or pressure surface-distribution spikes or humps, that may introduce regions of local acceleration and deceleration, separation, or undesirable loading distributions along the length of the blades. Smooth-slope-of-curvature blade surfaces avoid local kinks and spikes in surface-pressure and surface-velocity distributions, and facilitate the design of lower-loss higher-loading cascades. Continuous-slope-of-curvature surfaces should be used wherever the aerodynamic, heat transfer, hydrodynamic, or aesthetic performance, appropriately defined in each case, is critical.

Blade surfaces with continuous slope of curvature throughout their length have more desirable performance and allow the designer considerable flexibility in controlling the front versus aft loading distribution of a cascade. It is found that the cascade performance, judged by the shape of the surface Mach number distribution, is extremely sensitive to small changes in slope-of-curvature distribution of the airfoil surfaces.

The performance of two sets of turbine cascades has been presented and their boundary-layer behavior has been numerically investigated. The first set includes four near-identical blade shapes with small slope-of-curvature discontinuities (resulting in blade-surface variations that would pass the point-tolerance criteria). The small local discontinuities in the slope of curvature introduce unacceptable performance for two of the four cascades. The second set of sample cascades includes five geometries and it shows that blades designed with continuous slope-of-curvature distributions, with substantial variations in blade geometries, result in cascades of various loading distributions that are acceptable. It is concluded that in addition to point-for-point tolerance, blade designs should be checked for their point-for-point design-versus-manufactured surface-curvature distributions.

Acknowledgments

The authors thank Professor Michael B. Giles and Rolls Royce plc. for their permission to use UNSFLO to compute the performance of the sample cascades and Mr. N. Vlachopoulos for the many helpful discussions during the course of the investigation.

References

AGARD, 1985, "Test Cases for Inviscid Flow Field Methods," Advisory Report No. 211, AGARD-AR-211, May.

Albers, J. A., and Gregg, J. L., 1974, "Computer Program for Calculating Laminar, Transitional, and Turbulent Boundary Layers for a Compressible Axisymmetric Flow," NASA TN D-7521, Apr.

Bird, R. B., Stewart, W. E., and Lightfoot, E. N., 1960, *Transport Phenomena*, Wiley, New York.

Giles, M. B., 1988, "Calculation of Unsteady Wake/Rotor Interactions," *AIAA Journal of Propulsion and Power*, Vol. 4, No. 4, July/Aug.

Gostelow, J. P., 1976, "A New Approach to the Experimental Study of Turbomachinery Flow Phenomena," ASME Paper No. 76-GT-47.

Gostelow, J. P., 1984, *Cascade Aerodynamics*, Pergamon Press.

Hodson, H. P., 1985, "Boundary-Layer Transition and Separation Near the Leading Edge of a High-Speed Turbine Blade," ASME *Journal of Engineering for Gas Turbines and Power*, Vol. 127, pp. 127–134.

Hodson, H. P., and Dominy, R. G., 1987, "Three-Dimensional Flow in a Low Pressure Turbine Cascade at Its Design Condition," ASME JOURNAL OF TURBOMACHINERY, Vol. 109, pp. 177–185.

Hoheisel, H., Kiock, R., Lichtfuss, H. J., and Fottner, L., 1987, "Influence of Free-Stream Turbulence and Blade Pressure Gradient on Boundary Layer and Loss Behavior of Turbine Cascades," ASME JOURNAL OF TURBOMACHINERY, Vol. 109, pp. 210–219.

Hourmouziadis, J., Buckl, F., and Bergmann, P., 1987, "The Development of the Profile Boundary Layer in a Turbine Environment," ASME JOURNAL OF TURBOMACHINERY, Vol. 109, pp. 286–295.

Kiock, R., Lehthaus, F., Baines, N. C., and Sieverding, C. H., 1986, "The Transonic Flow Through a Turbine Cascade as Measured in Four European Wind Tunnels," ASME *Journal of Engineering for Gas Turbines and Power*, Vol. 108, pp. 277–284.

Korakianitis, T., 1989, "Design of Airfoils and Cascades of Air-foils," *AIAA Journal*, Vol. 27, No. 4, pp. 455–461.

Korakianitis, T., and Pantazopoulos, G., 1993a, "Improved Turbine-Blade Design Techniques Using 4th-Order Parametric-Spline Segments," *Computer Aided Design*, Vol. 25, No. 5, pp. 289–299.

Korakianitis, T., 1993b, "Prescribed-Curvature-Distribution Airfoils for the Preliminary Geometric Design of Axial-Turbomachinery Cascades," ASME JOURNAL OF TURBOMACHINERY, Vol. 115, pp. 325–333.

Okapuu, U., 1974, "Some Results From Tests on a High Work Axial Gas Generator Turbine," ASME Paper No. 74-GT-81.

Sharma, O. P., Pickett, G. F., and Ni, R. H., 1992, "Assessment of Unsteady Flows in Turbines," ASME JOURNAL OF TURBOMACHINERY, Vol. 114, pp. 79–90.

Stow, P., 1989, "Blading Design for Multistage HP Compressors," AGARD Lecture Series No. 167, *Blading Design for Axial Turbomachines*, May.

Wagner, J. H., Dring, R. P., and Joslyn, H. D., 1985, "Inlet Boundary Layer Effects in an Axial Compressor Rotor: Part 1—Blade-to-Blade Effects," ASME *Journal of Engineering for Gas Turbines and Power*, Vol. 107, pp. 374–380.

Wilson, D. G., 1984, *The Design of High Efficiency Turbomachinery and Gas Turbines*, The MIT Press, Cambridge, MA.

Calculation of Three-Dimensional Boundary Layers on Rotor Blades Using Integral Methods

M. T. Karimipanah

E. Olsson

Department of Thermo- and Fluid Dynamics,
Chalmers University of Technology,
412 96 Göteborg, Sweden

The important effects of rotation and compressibility on rotor blade boundary layers are theoretically investigated. The calculations are based on the momentum integral method and results from calculations of a transonic compressor rotor are presented. Influence of rotation is shown by comparing the incompressible rotating flow with the stationary one. Influence of compressibility is shown by comparing the compressible rotating flow with the incompressible rotating one. Two computer codes for three-dimensional laminar and turbulent boundary layers, originally developed by SSPA Maritime Consulting AB, have been further developed by introducing rotation and compressibility terms into the boundary layer equations. The effect of rotation and compressibility on the transition have been studied. The Coriolis and centrifugal forces that contribute to the development of the boundary layers and influence its behavior generate crosswise flow inside the blade boundary layers, the magnitude of which depends upon the angular velocity of the rotor and the rotor geometry. The calculations show the influence of rotation and compressibility on the boundary layer parameters. Momentum thickness and shape factor increase with increasing rotation and decrease when compressible flow is taken into account. For skin friction such effects have inverse influences. The different boundary layer parameters behave similarly on the suction and pressure sides with the exception of the crossflow angle, the crosswise momentum thickness, and the skin friction factor. The codes use a nearly orthogonal streamline coordinate system, which is fixed to the blade surface and rotates with the blade.

1 Introduction

1.1 Background. When Moore (1956) as well as Cooke and Hall (1962) reviewed the subject of three-dimensional boundary layers, the computational technique was still in the hand-calculating stage. The first three-dimensional computer code for boundary layer calculation, dealing with integral methods, was presented by Cumpsty and Head (1967). Later on, several other methods have been published and it is not possible to mention all the works here.

Many previous studies have dealt with boundary layers on rotating blades. Fogarty (1951) studied the compressible flow over a cylinderlike rotating blade. He derived the laminar boundary-layer equations in Cartesian coordinates, i.e., assuming developable surface. One of the authors of this paper, Olsson (1962), studied the effect of centrifugal force acting on the turbulent boundary layer of an annular compressor cascade, experimentally as well as theoretically, assuming small crossflow. Horlock and Wordsworth (1965) considered laminar boundary layers on a rotating helical blade of small chord length. Lakshminarayana et al. (1972) investigated the turbulent boundary-layer on a rotating helical blade. Lakshminarayana and Govindan (1981) predicted the three-dimensional turbulent boundary-layer development on a turbomachinery blade and used the integral momentum technique. Groves and Taylor (1981) developed a three-dimensional turbulent boundary-layer method and presented results for several rotating blades. Morris (1981) calculated the laminar boundary-layer on a rotating helical blade. Groves and Chang (1984) suggested a differential method for three-dimensional laminar and turbulent boundary layers on rotating propeller blades. Lakshminarayana et al. (1982a) measured the mean velocity profiles and annular wall boundary layer in the tip region of a compressor rotor blade, using a triaxial hot-wire probe, rotating with the rotor. Lakshminarayana et al. (1982b) measured the turbulence properties in the annular region of an axial flow compressor rotor blade, using the above instrument. Pouagare et al. (1985), i.e., again Lakshminarayana and co-workers, measured the three-dimensional turbulent boundary layer on a compressor rotor blade using a miniature "x" configuration hot-wire probe. In the above studies:

- The laminar or turbulent boundary layers are found on a helical blade with zero or very small chordwise pressure gradients,
- They determined the boundary layer characteristics only for incompressible flows,

Contributed by the International Gas Turbine Institute and presented at the 37th International Gas Turbine and Aeroengine Congress and Exposition, Cologne, Germany, June 1-4, 1992. Manuscript received by the International Gas Turbine Institute February 20, 1992. Paper No. 92-GT-210. Associate Technical Editor: L. S. Langston.

- Most of them do not describe the effects of the rotation on the transition (except for Lakshminarayana and colleagues).

Thus, it is still very difficult to determine the flow characteristics quantitatively of the boundary layer on usual rotor blades with a chordwise pressure gradient.

The aim of this study is to develop and generalize the influence of rotation and compressibility on the boundary layer parameters and the transition process on rotating blades theoretically. In this report only the boundary layer calculations are considered. Thus the free-stream conditions must be known either from tests or from computations. For the examples shown, the Euler solver by Denton (1983) has been used for the first case. Unfortunately, there are no measurements on this blade. The method was therefore also checked against Olsson's annular cascade where measurements are available.

For the calculation of three-dimensional laminar and transitional boundary layers as well as three-dimensional turbulent boundary layers, the codes developed by SSPA, see Xia et al. (1985) and Larsson (1975), have been further developed by taking into account rotation and compressibility.

The new programs have been used for calculating the boundary layer parameters for a DCA (Double Circular Arc) compressor rotor blade of Volvo Flygmotor AB, and an annular compressor cascade with NACA blades. Only the last blade calculations have been compared with experiments.

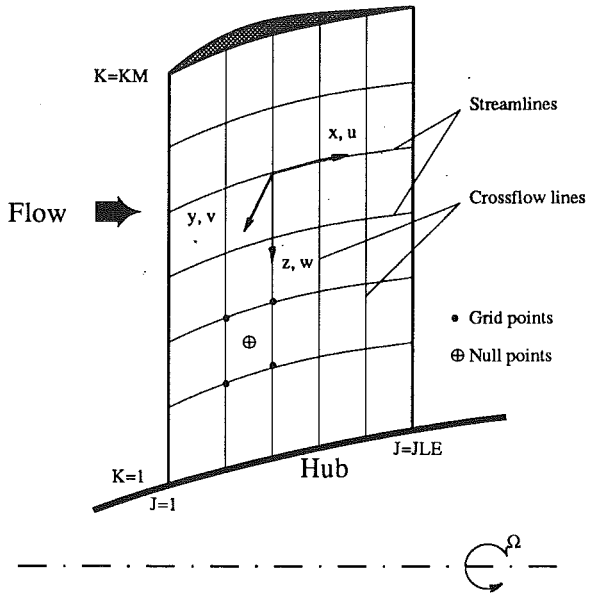

Fig. 1 Schematic of coordinate system and velocities for a rotating blade

1.2 Choice of Coordinate Systems. In the Euler solver program, the cylindrical coordinate system (x, r, θ) is used. All data obtained from the output of the Euler solver have been transformed to a curvilinear coordinate system (x, y, z), which is fixed on the blade and rotates with the blade. The coordinate system adopted in the boundary layer calculations is a so-called *streamline coordinate system* defined on the streamline just outside the boundary layer. Two parametric curves (x direction and z direction) are chosen to coincide with the streamlines and their equipotential lines (in fact the crossflow lines), respectively, and y is the direction normal to the blade surface. A nearly orthogonal curvilinear system is thus obtained. Figure 1 illustrates a typical rotor blade with such a coordinate system. The use of this coordinate system simplifies the boundary layer conditions and, hence, the governing equations, which are used in the calculation of the three-dimensional boundary layers. To get an accurate description of the flow field, a varying number of streamlines may therefore be used.

1.3 Streamline Tracing. The boundary layer equations cannot be solved without knowing the longitudinal pressure gradient, streamline curvatures, and metrics. To recognize such properties, it is necessary to trace the streamlines either from the calculated free-stream flow or from the measured one. In the following calculations, the streamlines along the three-dimensional blades have been traced by two geometry programs adopted from SSPA. In the first program (GEOM1K) the projection of streamlines are traced in the x–z plane. This program calculates "direction cosines" for the projection of the velocity vector at the null points by using the *Runge–Kutta method*. The other program (GEOM2K) obtains pressure derivatives, metrics, and their derivatives along x and z, which

Nomenclature

C_1, C_2, C_3 = constants (= transverse derivatives in Eqs. (10), (11), and (16))
c_{fx} = skin friction coefficient in x direction
c_{fz} = skin friction coefficient in z direction
c_p = pressure coefficient
D = function of G (Michel)
E, E_1, E_2 = parameters (Michel)
G = Clauser's form parameter
h_1, h_2, h_3 = metrics referred to the xyz system
H_{12} = shape parameter of the velocity profile $= \delta_1/\theta_{11}$
I_1 = integral parameter (Michel)
K_{13}, K_{31} = geodesic curvature of streamlines and crossflow lines
l_1, l_2, m_1, m_2 = crossflow parameters
M = local Mach number
Re = Reynolds number
Re_δ = boundary layer thickness Reynolds number
Re_θ = momentum thickness Reynolds number
Ro_δ = boundary layer rotation number
R_I = $1/\gamma = \sqrt{2/c_{fx}}$ in Eq. (21)
s, n = lengths of arc along streamlines and crossflow lines
P = function of G (Michel)
T = transverse pressure gradient parameter
u, v, w = velocities in the x, y, z system
u_e = velocity at the boundary layer edge
u_τ = shear velocity $= \tau_w/\rho$
U_∞ = free-stream velocity
x, y, z = local coordinates
β_w = wall crossflow angle
γ = skin friction parameter in Eq. (15)
δ = boundary layer thicknesses
δ_1, δ_2 = displacement thicknesses
$\theta_{11}, \theta_{12}, \theta_{21}, \theta_{22}$ = momentum thicknesses
λ = pressure gradient parameter
μ = dynamic viscosity
ν = kinematic viscosity
ρ = density
τ_{0x}, τ_{0z} = wall shear stresses in laminar case
τ_x, τ_z = wall shear stresses in turbulent case
ϕ_1, ϕ_2 = parameters (Michel)
Ω = rotation vector
Ω = angular velocity in x direction

are used for calculation of curvatures. The traced streamlines and other information achieved are used as input to the laminar boundary layer program (LAMBO) and the turbulent boundary layer program (TURBO).

2 Boundary Layer Integral Method

2.1 Laminar Boundary Layer Equations. By using Michel's (1972) incompressible boundary layer equations for rotational flow, and equations for compressible irrotational flow due to Lemmerman and Atta (1980), the laminar boundary layer equations with rotation and compressibility terms in the streamline coordinate system may be written

$$\frac{\rho u}{h_1}\frac{\partial u}{\partial x}+\rho v\frac{\partial u}{\partial y}+\frac{\rho w}{h_3}\frac{\partial u}{\partial z}+\rho(K_{13}u-K_{31}w)w - \frac{u_e}{h_1}\frac{\partial u_e}{\partial x}-2\Omega w-\nu\frac{\partial^2 u}{\partial y^2}=0 \quad (1)$$

$$\frac{\rho u}{h_1}\frac{\partial w}{\partial x}+\rho v\frac{\partial u}{\partial y}+\frac{\rho w}{h_3}\frac{\partial w}{\partial z}+\rho(K_{31}w-K_{13}u)u + K_{13}u_e^2+2\Omega(u-u_e)-\nu\frac{\partial^2 w}{\partial y^2}=0 \quad (2)$$

$$\frac{1}{h_1}\frac{\partial}{\partial x}(\rho u)+\frac{\partial}{\partial y}(\rho v)+\frac{1}{h_3}\frac{\partial}{\partial z}(\rho w)+\rho(K_{31}u+K_{13}w)=0 \quad (3)$$

where the curvatures K_{13} and K_{31}, see also Cumpsty and Head, are defined as

$$K_{13}=\frac{1}{h_1h_3}\frac{\partial h_1}{\partial z} \quad K_{31}=\frac{1}{h_1h_3}\frac{\partial h_3}{\partial x} \quad (4)$$

Since the boundary-layer thickness δ is assumed to be small and the y direction is assumed to measure distances along the surface normal, the metric $h_2\equiv 1$, with no loss of generality, $h_1=h_1(x, z)$ and $h_3=h_3(x, z)$. Thus, a general element of length ds in streamline coordinates may be given by

$$ds^2=h_1^2dx^2+dy^2+h_3^2dz^2 \quad (5)$$

The boundary conditions are

$$y=0, \quad u=v=w=0$$
$$y=\delta, \ u=u_e(x, z), \ w=0. \quad (6)$$

The integrated boundary layer parameters are defined as

$$\delta_1=\int_0^\delta\left(1-\frac{\rho u}{\rho_e u_e}\right)dy; \quad \delta_2=-\int_0^\delta\left(\frac{\rho w}{\rho_e u_e}\right)dy$$
$$\theta_{11}=\int_0^\delta\frac{\rho u}{\rho_e u_e}\left(1-\frac{u}{u_e}\right)dy; \quad \theta_{12}=\int_0^\delta\frac{\rho w}{\rho_e u_e}\left(1-\frac{u}{u_e}\right)dy$$
$$\theta_{21}=-\int_0^\delta\frac{\rho uw}{\rho_e u_e^2}dy; \quad \theta_{22}=-\int_0^\delta\frac{\rho w^2}{\rho_e u_e^2}dy$$
$$\tau_{0x}=\mu\left(\frac{\partial u}{\partial y}\right)_{y=0}; \quad \tau_{0z}=\mu\left(\frac{\partial w}{\partial y}\right)_{y=0}; \quad c_{fx}=\frac{\tau_{0x}}{\frac{1}{2}\rho u_e^2} \quad (7)$$

By integrating Eqs. (1)–(3), see White (1974, p. 606), and using the relations (7), the following momentum integral equations for streamwise and crosswise directions may be obtained:

$$\frac{d\theta_{11}}{ds}=\frac{c_{fx}}{2}-\frac{\theta_{11}}{u_e}\frac{du_e}{ds}(2+H-M^2)-K_{31}(\theta_{11}-\theta_{22})+2\frac{\Omega}{u_e}\delta_2. \quad (8)$$

$$\frac{d\theta_{21}}{ds}=\frac{c_{fx}}{2}\tan\beta_w-2\theta_{21}\left(\frac{1}{u_e}\frac{du_e}{ds}+K_{31}\right) + K_{13}\theta_{11}(1+H_{12}-M^2)+K_{13}\theta_{22}-\frac{2\Omega}{u_e}\delta_1 \quad (9)$$

2.2 Turbulent Boundary Layer Equations. The turbulent boundary layer equations are the laminar equations, Eqs. (1)–(3), plus additional terms due to Reynolds stresses and transverse derivatives. Thus, the momentum integral equations for compressible turbulent boundary layers may be written

$$\frac{d\theta_{11}}{ds}=\frac{c_{fx}}{2}-\frac{\theta_{11}}{u_e}\frac{du_e}{ds}(2+H_{12}-M^2) - K_{31}(\theta_{11}-\theta_{22})+2\frac{\Omega}{u_e}\delta_2-C_1 \quad (10)$$

$$\frac{d\theta_{21}}{ds}=\frac{c_{fx}}{2}\tan\beta_w-2\theta_{21}\left(\frac{1}{u_e}\frac{du_e}{ds}+K_{31}\right) + K_{13}\theta_{11}(1+H_{12}-M^2)+K_{13}\theta_{22}-2\frac{\Omega}{u_e}\delta_1-C_2 \quad (11)$$

$$\tau_{wx}=\rho\left(\nu\frac{\partial\overline{u}}{\partial y}-\overline{u'v'}\right), \quad \tau_{wz}=\rho\left(\nu\frac{\partial\overline{w}}{\partial y}-\overline{v'w'}\right)$$
$$c_{fx}=\frac{\tau_{wx}}{\frac{1}{2}\rho u_e^2}, \quad c_{fx}=\frac{\tau_{wz}}{\frac{1}{2}\rho u_e^2}$$
$$\tan\beta_w=\frac{\tau_{wz}}{\tau_{wx}}, \quad H_{12}=\frac{\delta_1}{\theta_{11}} \quad (12)$$

where τ_{wx} and τ_{wz} are components of the shear stress, c_{fx} and c_{fx} are the wall shear stresses, H_{12} is the shape factor and β_w is the crossflow angle. In Eqs. (10) and (11), the coefficients C_1 and C_2 represent derivatives with respect to z:

$$C_1=\frac{1}{h_3}\frac{\partial\theta_{12}}{\partial z}; \quad C_2=\frac{1}{h_3}\frac{\partial\theta_{22}}{\partial z}. \quad (13)$$

2.2.1 Entrainment and Skin Friction Equations. As auxiliary equation the entrainment equation, with empirical relations due to Michel et al. (1972), see also Larsson (1975, part IV), is used:

$$\frac{1}{h_3}\frac{\partial}{\partial x}[h_3u_e(\delta-\delta_1)]-\frac{1}{h_3}\frac{\partial\delta_2}{\partial z}=P\gamma \quad (14)$$

where

$$P=0.074G-\frac{1.0957}{G}; \quad \gamma=\sqrt{\frac{c_{fx}}{2}}; \quad G=\frac{H_{12}-1}{\gamma H_{12}}. \quad (15)$$

According to Larsson, by introducing C_3 and s, Eq. (14) may be written as

$$\frac{d(\delta-\delta_1)}{ds}=P\gamma-(\delta-\delta_1)\left(\frac{1}{u_e}\frac{du_e}{ds}+K_{31}\right)+C_3 \quad (16)$$

where

$$C_3=\frac{1}{h_3}\frac{\partial\delta_2}{\partial z}. \quad (17)$$

The skin friction c_{fx} is calculated from the relation

$$\frac{1}{\gamma}=\sqrt{\frac{2}{c_{fx}}}=\frac{1}{\kappa}\ln\frac{u_e\delta_1}{\nu}+D^*(G) \quad (18)$$

where

$$D^*(G)=2G-4.25G^{1/2}+2.12 \quad (G<300) \quad (19)$$

G is Clauser's form parameter for the velocity profile and is connected to H_{12} by relation (15), defined as

$$G=\frac{\int_0^1\left(\frac{u_e-\overline{u}}{u_\tau}\right)^2d\left(\frac{y}{\delta}\right)}{\int_0^1\frac{u_e-\overline{u}}{u_\tau}d\left(\frac{y}{\delta}\right)}. \quad (20)$$

Equation (18) may be expressed as

$$R_I = L + 2HR_I - 4.25\sqrt{HR_I} + 2.12 \tag{21}$$

where

$$R_I = \sqrt{\frac{2}{c_{fx}}} \tag{22}$$

$$H = \frac{H_{12}-1}{H_{12}} \tag{23}$$

$$L = \frac{1}{\kappa}\ln\frac{u_e\delta_1}{\nu} = \frac{1}{\kappa}\ln\frac{u_e\theta_{11}H_{12}}{\nu} \tag{24}$$

Equation (21) may be transformed to a second degree equation

$$R_I^2 + B_R R_I + C_R = 0 \tag{25}$$

$$B_R = -\frac{2(1-2H)(2.12+L)+4.25^2H}{(1-2H)^2} \tag{26}$$

$$C_R = \left\{\frac{2.12+L}{1-2H}\right\}^2 \tag{27}$$

Thus, c_{fx} will be obtained from Eq. (21). The constants C_1, C_2, and C_3, see Eqs. (10), (11), and (16), can be obtained from the results of a previous solution if several streamlines are solved together. Note that, by small crossflow approximation, the values of constants C_1–C_3 are zero.

Thus, by having the momentum integral equations, the entrainment equation, and the skin friction relation, the system of equations can be solved along each streamlines separately using the Runge–Kutta technique.

2.2.2 Crossflow. Because of three-dimensional effects, there is a boundary layer flow in the z direction, which results in a so-called *crossflow*. In the boundary layer, the crosswise component of flow is the component of right angles to the streamline direction. According to Geis (1961), this secondary or "transverse flow" causes the direction of the streamlines directly at the wall to deviate sometimes quite considerably from the direction of the outer potential streamlines. The direction is the same as the streamline at the outer edge of the boundary layer and agrees with the limiting streamlines at the wall. The magnitude of crossflow varies from zero on the surface to some maximum and then to zero at the edge of the boundary layer. This is a characteristic feature of three-dimensional boundary layers.

When the crossflow is small, the effect of streamline divergence is found to have an *axisymmetric analogy*. This is based on the fact that the longitudinal momentum equation, Eq. (1), takes the same form in an axisymmetric and three-dimensional case, as soon as derivatives in the crosswise direction can be neglected. This case is called *the small crossflow approximation.*

2.2.3 Crossflow Relations. The momentum thickness in crosswise direction, θ_{21}, is obtained from Eq. (11) and the displacement thickness, δ_2, is obtained from the relation (7) as

$$\delta_2 = \theta_{21} - \theta_{12} \tag{28}$$

However, Michel et al. defined the following relations for δ_2, θ_{12}, θ_{22}, and β_w

$$\delta_2 = -\theta_{12}\frac{\phi_1}{G\gamma} \approx \frac{\theta_{21}}{1-\dfrac{G\gamma}{1.1}} \tag{29}$$

$$\theta_{12} = -\delta_2\frac{G\gamma}{\phi_1} \tag{30}$$

$$\theta_{22} = -\frac{\delta_2^2}{\delta_1}\phi_2 G\gamma \tag{31}$$

$$\tan\beta_w = -\frac{\delta_2}{\delta_1\left(\dfrac{E_1 G H_{12}}{I_1(H_{12}-1)} - E_2\right)} \tag{32}$$

where G and γ are defined in relation (15), and other parameters are defined as

$$\phi_1 = 1 + \frac{3.5\left(1+\dfrac{1}{\dfrac{R_\theta}{30000}+0.6}\right)}{G^{3/2}0.35E+1.0)} \tag{33}$$

$$\phi_2 = \frac{1}{1+1.65(\phi_1-1)} \tag{34}$$

$$E = \frac{2I_1}{|T|} \tag{35}$$

$$I_1 = 0.613G - \left[3.6+76.86\left(\frac{1}{G}-0.154\right)^2\right]\frac{1}{G} \tag{36}$$

$$T = -\frac{\delta_2}{K_{13}\delta^2} \tag{37}$$

$$E_1 = \frac{1}{[A_1(A_2-1)+1]A_3} \tag{38}$$

$$A_1 = \frac{20.6I_1}{G_2} \tag{39}$$

$$A_2 = \frac{E+0.317}{2.21+0.423E} + 0.856\times 10^{(-0.1175E^{0.86})} \tag{40}$$

$$A_3 = \frac{2.28G^2-6.3G}{2I_1^2} \tag{41}$$

$$E_2 = \frac{E}{E+\dfrac{1}{I_1}} \tag{42}$$

2.3 Transitional Boundary Layer and Instability. The boundary layer on the surface of the turbomachine blade starts laminarly and mostly undergoes transition to a turbulent state before it reaches the trailing edge; see Dunham (1972). The process of transition from a known laminar flow to a turbulent one can be conceived as a problem of instability.

In a three-dimensional boundary layer, the process of transition does not occur at a certain point (as in two-dimensional layers) but appears over a finite distance, a so-called *transition region*. Thus, the details of the process of transition in a three-dimensional boundary layer appear to be entirely different from those associated with the two-dimensional flows.

Transition is known to be affected by the following parameters: the free-stream turbulence, the pressure gradient, Reynolds number, Mach number, acoustic radiation, surface roughness, surface curvature, and the history of the above parameters; see Abu-Gannam and Shaw (1980).

For the prediction of transition in stationary incompressible flow, the e^n-method, Granville's empirical relations, and Owen's crossflow transition criterion, see Xia et al. (1985), may be used.

With respect to rotation, the laminar instability criterion, which is described by Johnston (1974) has been used. The Reynolds number required for instability was found to be

$$\mathrm{Re}_\delta \geq \frac{8.8}{\sqrt{\mathrm{Ro}_\delta}}, \quad |\mathrm{Ro}_\delta| \ll 1 \tag{43}$$

Table 1 Influence of rotating and compressibility on the boundary layer parameters, in comparison with the nonrotating incompressible case; see Figs. 3-8

	pressure side		suction side	
	$\Omega > 0.$ $M = 0.$	$\Omega > 0.$ $M > 0.$	$\Omega > 0.$ $M = 0.$	$\Omega > 0.$ $M > 0.$
parameter				
θ_{11}	increases	decreases	increases	decreases
θ_{12}	increases	decreases	decreases	decreases
θ_{21}	increases	increases	increases	increases
δ	increases	decreases	increases	decreases
δ_1	increases	decreases	increases	decreases
δ_2	increases	increases	increases	increases
H_{12}	increases	decreases	increases	decreases
C_f	decreases	increases	increases	increases
β_w	increases	decreases	decreases	decreases

Table 2 Influence of rotation and compressibility on transition (DCA blade), x_{et} = end of transition, x_{ct} = transition in crossflow condition

	pressure side			suction side		
	$\Omega = 0.$ $M = 0.$	$\Omega > 0.$ $M = 0.$	$\Omega > 0.$ $M > 0.$	$\Omega = 0.$ $M = 0.$	$\Omega > 0.$ $M = 0.$	$\Omega > 0.$ $M > 0.$
x_{et}	15% chord	15.5% chord	16.5% chord	16.15% chord	16.5% chord	17.5% chord
x_{ct}	13.13% chord	12.73% chord	14% chord	15% chord	14% chord	16.15% chord

where Re_δ is the Reynolds number based on the boundary layer thickness and Ro_δ is a boundary layer rotation number, which expresses the ratio of Coriolis to inertial forces in the relative flow. They are defined as:

$$\mathrm{Re}_\delta = \frac{U_\infty \delta}{\nu}, \quad \mathrm{Ro}_\delta = \frac{2\Omega\delta}{U_\infty} \tag{44}$$

The Rosby number is defined as $1/\mathrm{Ro}_\delta$.

For compressible flow, the following criterion given by Narasimha (1985) is used. They suggest that the Reynolds number at the beginning of transition increases like

$$1 + 0.38\ \mathrm{M}^{0.6} \text{ for } 0.2 \le \mathrm{M} \le 2.4; \quad 0.1 \le q \le 3 \tag{45}$$

where M is the Mach number and q is the free-stream turbulence. The above relation is adequate for the transonic case and is used here.

Usually, one used the end of the laminar boundary layer as the start value to continue computation of the turbulent boundary layer downstreams. However, it is difficult to reach sufficient accuracy in the prediction of the position of the transition region. As mentioned previously, the transition region is influenced by many other parameters.

2.3.1 Transition Calculations on Stationary Blades. For the streamvise direction the e^n method and Granville's empirical relations give similar results. For the crossflow direction, Owen's criterion is used.

2.3.2 Effect of Rotation on Transition. For the streamvise direction Johnston's criterion is used. For the case discussed in the next section this criterion gives transition at a slightly later position than the e^n method. The two methods are, however, not consistent. Johnston's method cannot be used for stationary cases, but predicts later transition when lowering the speed of rotation, thus giving a larger discrepancy to the other method. For the crossflow direction Owen's criterion is used. This moves the region of transition from laminar

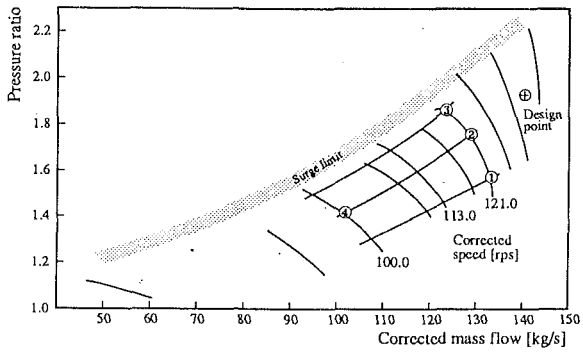

Fig. 2 Fan characteristic, from Säterskog (1990)

to turbulent flow forward (upstream) as the rotation number (or rotation parameter) increases, its position coincides with the point at which the gradient of the momentum thickness increases. Due to Coriolis effects, the boundary layer may be affected by the rotation number, see Schlichting (1979, p. 695), which is commented upon later on.

2.3.3 Effect of Compressibility on Transition. The effect of compressibility has added three complicating factors to the analysis; see White (1974):

- The density variation must be included in the definition of integral thicknesses,
- The free-stream Mach number is an important part of the pressure gradient term,
- At high speeds the pressure difference across the boundary layer may be too large to neglect.

Of course, the Mach number (say compressibility term) has certain effects on the transition as well as the boundary layer parameters.

For the case considered in the next section Johnston's criterion is used in the streamwise direction, corrected for Mach number as described above. For a stationary blade the e^n method would be used corrected in the same manner. For the crosswise direction Owen's criterion is used. As shown in Table 2, the transition position moves backward (downstream) when the Mach number increases.

3 Computational Results

3.1 Calculations for Blade 1. The compressor blade used in case 1 is of the following type:

- DCA (Double Circular Arc)
- Hub-tip radius ratio = 0.365,
- Chord at the hub = 77.98 mm; hub chord angle to tangential direction −80.10 deg
- Chord at the tip = 103.33 mm; tip chord angle to tangential direction −31.45 deg
- Blade height at leading edge = 51.15 cm.
- Blade height at trailing edge = 50.595 cm.

For all the calculations in this case, $\mathrm{Re} = 2. \times 10^6$ and $U_\infty = 363$ m/s have been used. The input quantities were found from the Euler solver. The start values for turbulent calculations have been found from the laminar calculations, except for the shape factor where $H_{12} = 1.5$ was used. Although the actual flow is rotating and compressible, the results, which have been calculated for operating point 2 and 50 percent span, see Fig. 2, are also shown for the incompressible nonrotating and rotating cases. Thus, the influence of rotation and compressibility can be separated, see Figs. 3-8. Although the calculations are done only at 50 percent span, the same procedure can be used

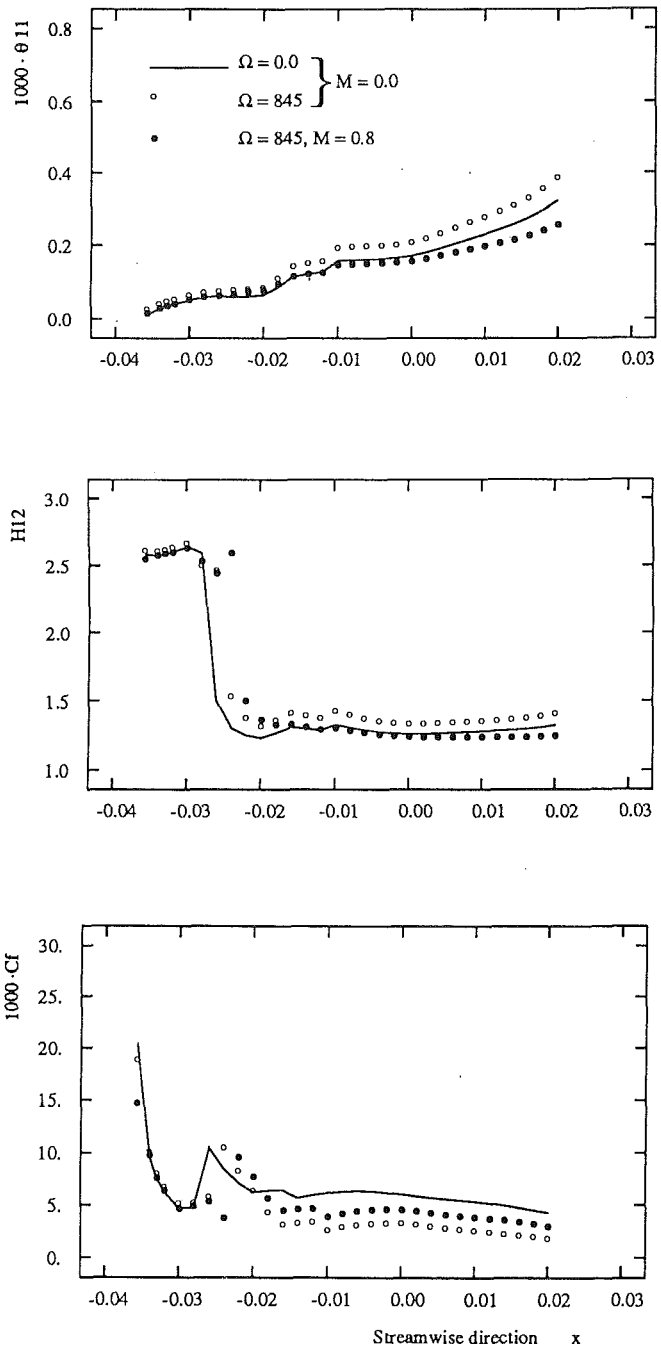

Fig. 3 Influence of rotation and compressibility on θ_{11}, H_{12}, and C_f, for DCA blade 50 percent span (pressure side)

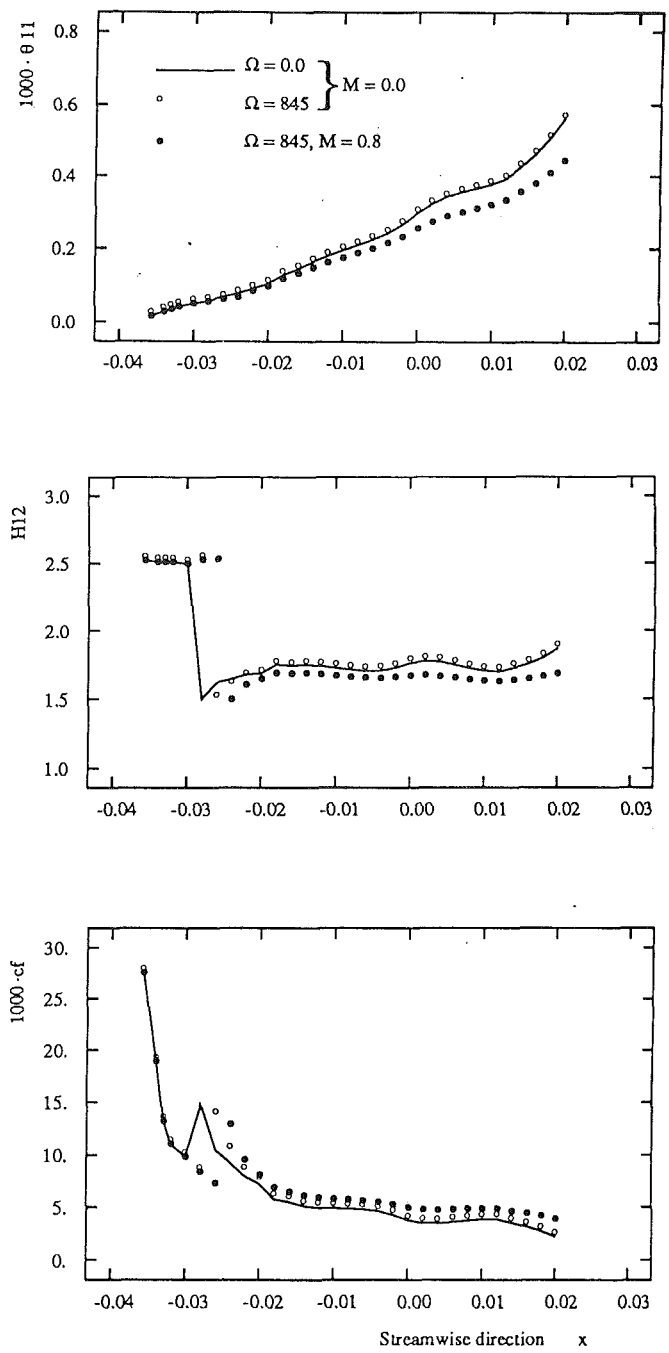

Fig. 4 Influence of rotation and compressibility on θ_{11}, H_{12}, and C_f, for DCA blade 50 percent span (suction side)

at other positions on the blade as well as on the end walls. The calculations are, of course, only useful up to the position where the turbulent boundary layer separates.

The free-stream conditions that must be given for the boundary layer computations are taken from a well-proven Euler solver as explained earlier. Unfortunately there is no experimental verification of either the pressure distribution or the boundary layer parameters.

3.1.1 Boundary Layer Parameters on Pressure and Suction Side. The boundary layer parameters on pressure and suction side are shown in Figs. 3–8. Table 1 summarizes the changes noted. It is found that the effect of rotation is small on the parameters in the flow direction θ_{11}, H_{12}, c_f, δ, and δ_1, while the effects are significant for the crossflow parameters θ_{22}, θ_{12}, θ_{21}, β_w, and δ_2. The effect of compressibility on the other hand gives significant changes in all parameters.

The parameters θ_{11}, θ_{21}, δ, δ_1, δ_2, and H_{12} show a similar behavior on both pressure and suction side of the blade, but θ_{12}, c_f, and β_w show different behaviors. Due to the streamline slope (positive β_w), the Coriolis forces in the boundary layer give rise to an additional acceleration of the flow on the suction side and a retardation on the pressure side. This may explain the more rapid growth of the pressure side boundary layer with increased rotation. On the suction side the effect is not noticed for this case, but is clearly seen on case 2 (Fig. 12).

3.2 Transition Calculations. Using the methods described in section 2.3 gives the positions of transition for the DCA blade indicated in Table 2. For the crosswise direction

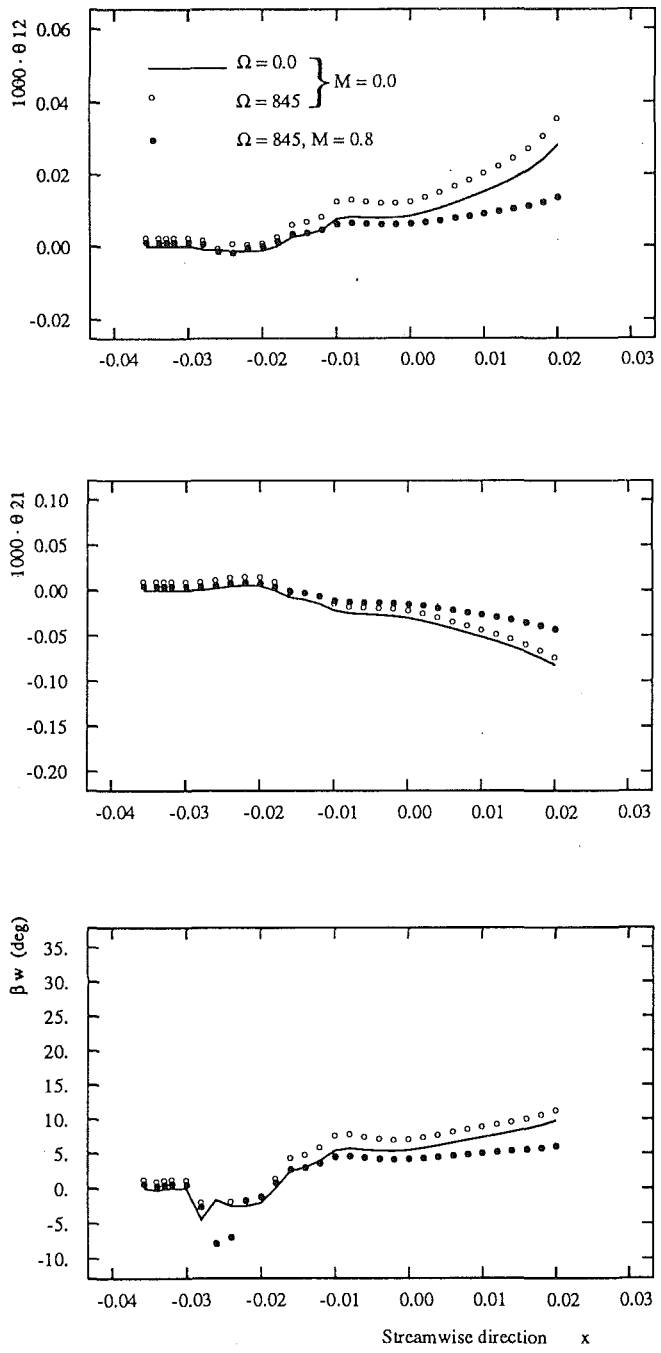

Fig. 5 Influence of rotation and compressibility on θ_{12}, θ_{21}, and β_w, for DCA blade 50 percent span (pressure side)

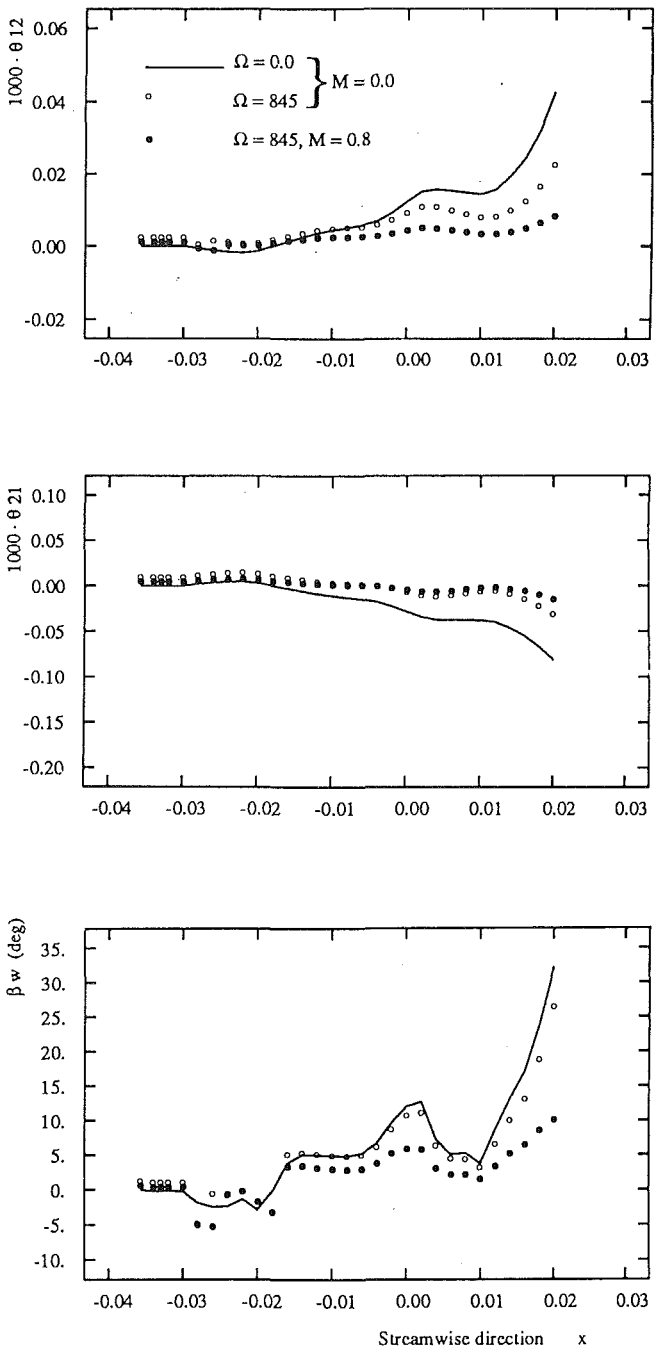

Fig. 6 Influence of rotation and compressibility on θ_{12}, θ_{21}, and β_w, for DCA blade 50 percent span (suction side)

Owen's criterion has been used without any correction for rotation or compressibility so the changes shown depend on the growth of the boundary layer only. For the streamwise direction the difference shown between the stationary and rotating case should be treated with care as different criteria are used as described previously. Prediction of transition is an important area where much more research is needed. Work is under way in our department, which we will report on in the future when more results are available.

3.3 Calculations for Blade 2 and Comparison With Experiment. The blade used in case 2 is of the following type; see Olsson (1962):

- Circular arc camber line
- NACA Four Digit Series thickness distribution with 9 percent maximum thickness
- Chord $c = 2.8$ in. (≈ 7.12 cm)
- Camber angle -35 deg
- Chord angle to tangential direction -45 deg
- Pitch-chord ratio at midspan $s/c = 1.0$
- Aspect ratio $l/c = 1.8$
- Diameter ratio $D_i/D_y = 0.65$

This blade was investigated by one of the authors in an annular stationary test facility where both the free-stream and boundary layer flow were carefully measured. An integral boundary layer method was also developed and at that time, 1962, the calculations were done without computer assistance but compared with the calculations done for this paper the agreement is almost perfect.

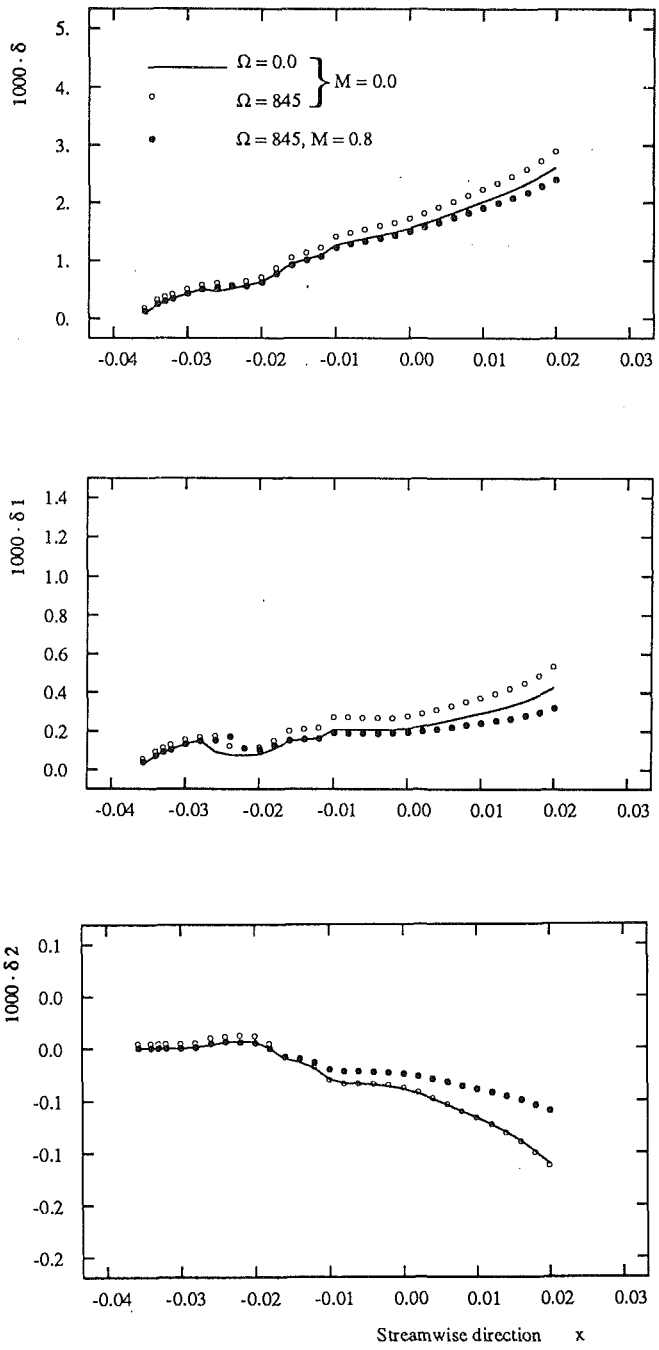

Fig. 7 Influence of rotation and compressibility on δ, δ_1, and δ_2, for DCA blade 50 percent span (pressure side)

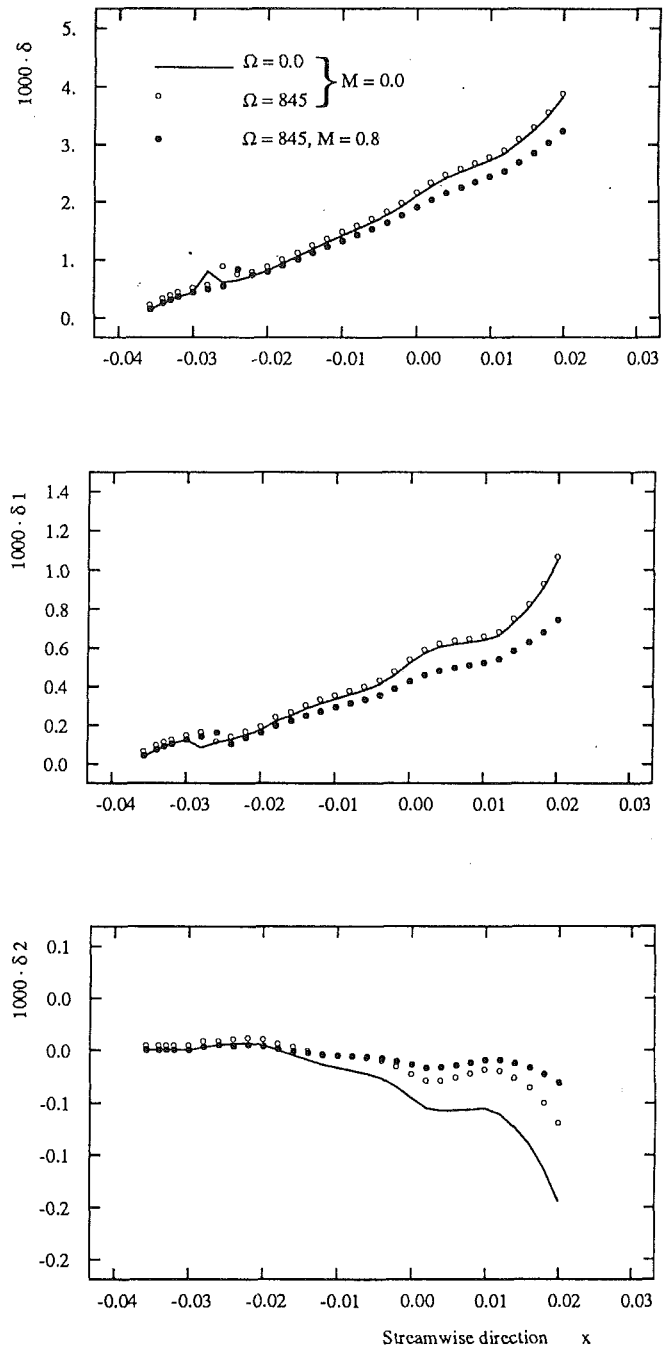

Fig. 8 Influence of rotation and compressibility on δ, δ_1, and δ_2, for DCA blade 50 percent span (suction side)

The new calculations for this blade have been done for both the pressure and suction sides. Comparison with measurements have been done for 10, 50, and 90 percent span. The calculations have also been done for a rotating case, which was chosen to be symmetric to the stator at 50 percent span position. The free-stream conditions are therefore only correct for the 50 percent span position. Thus, the values computed at 10 and 90 percent are only done to show tendencies. In the calculations done in 1962 also a corresponding two-dimensional case was computed. The same free-stream data were used, but all terms related to the three dimensionality were dropped. Those calculations indicated that the differences are mainly due to streamline convergence or divergence. When streamlines converge they will feed more fluid into the boundary layer. This is the case on the main portion of the suction side and will increase the momentum thickness as is shown in the calculations. The opposite is true for the pressure side. The difference between the two cases is rather small, of order 5–10 percent, thus in the same range as the experimental accuracy. For the two end positions, 10 and 90 percent span, on the suction side, the free streamlines are diverging while they are converging within the boundary layer. As a result these positions do not show any difference between two- and three-dimensional theory. The tested case had a constant height of the blade passage, which in general is not typical for a turbomachinery case where the passage height changes. A changing passage height would normally magnify the streamline convergence or divergence, and thus give a larger difference between the two and three-dimensional theory.

The new calculations as well as the old ones done in 1962

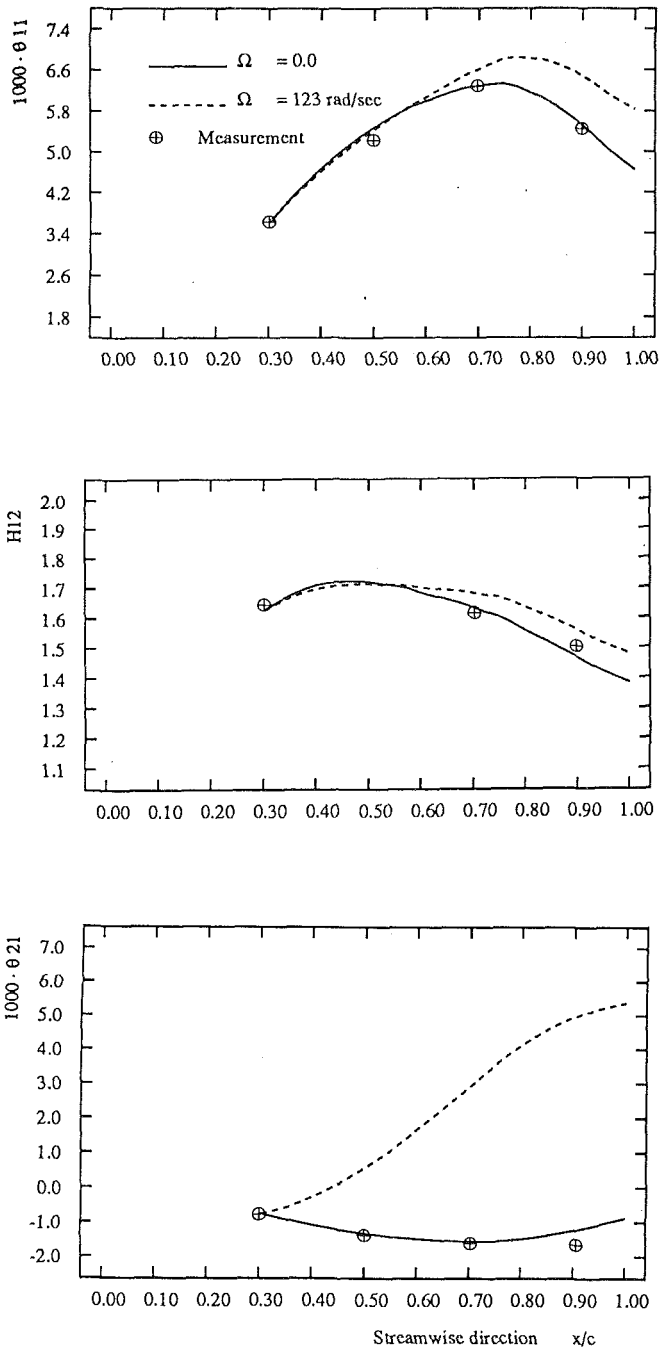

Fig. 9 Comparison of calculated and measured quantities at 10 percent span for NACA blade (pressure side)

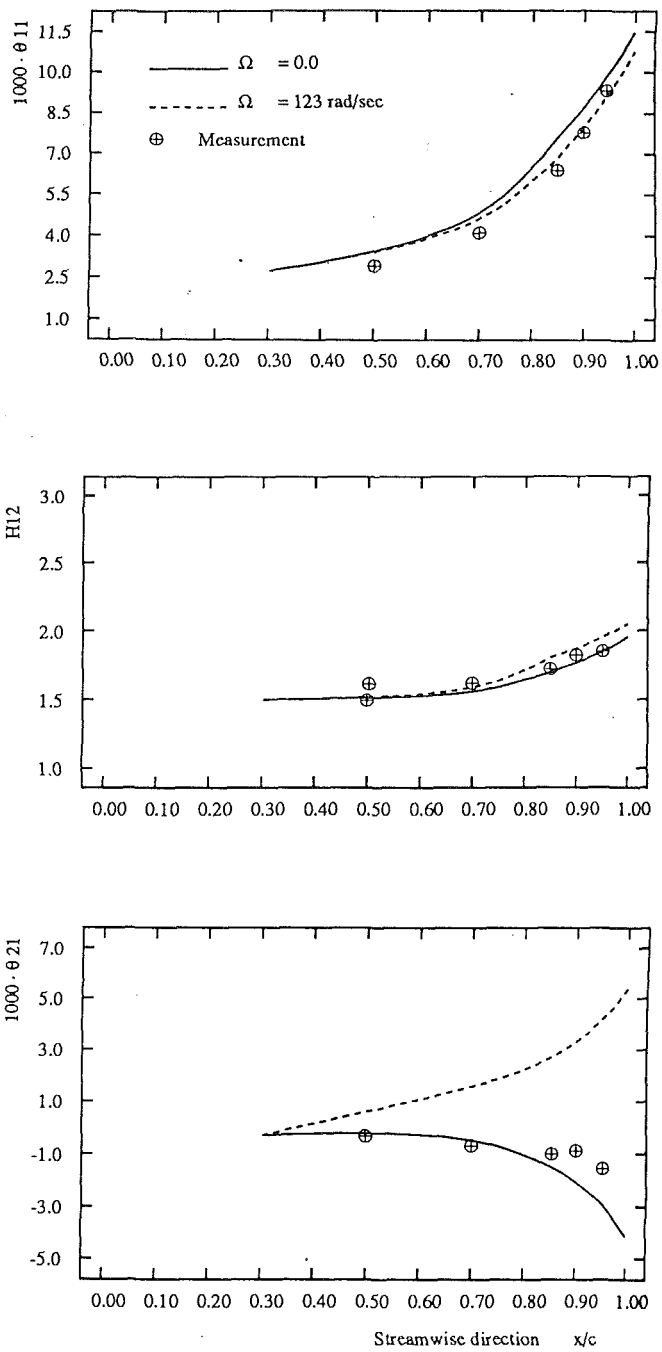

Fig. 10 Comparison of calculated and measured quantities at 10 percent span for NACA blade (suction side)

show good agreement with the measurements as seen in Figs. 11–14, the only exception being the momentum thickness in the crosswise direction in the rear part of the blade. In the 1962 calculations this particular thickness was also calculated by an inviscid theory with a quite satisfactory result. In the comparison with the experimental results one should also remember the larger uncertainty in the crossflow measurements than in the streamwise measurements.

Regarding the influence of rotation, we see first that the direction of the crossflow will be reversed and second that the magnitude of the crossflow is considerably larger than in the stationary case. Thus, secondary losses generated by the crossflow will be larger in a rotating than in a stationary cascade.

In the 1962 computations the losses were also calculated from the momentum thickness by expressing the loss as a fraction of the momentum of the free-stream flow. It was shown there that the three-dimensional case had about 10 percent higher losses than the two-dimensional case and that the rotating case showed about 10 percent higher loss than the stationary three-dimensional case. It was also suggested that the crosswise momentum thickness could be used to estimate the magnitude of the secondary losses.

3.4 Conclusions. The computer codes for calculating the compressible three-dimensional laminar and turbulent boundary layers with rotation have been tested by using two different blades and results have been presented.

Calculations for the stationary case where measured values are available show very good agreement with measurements.

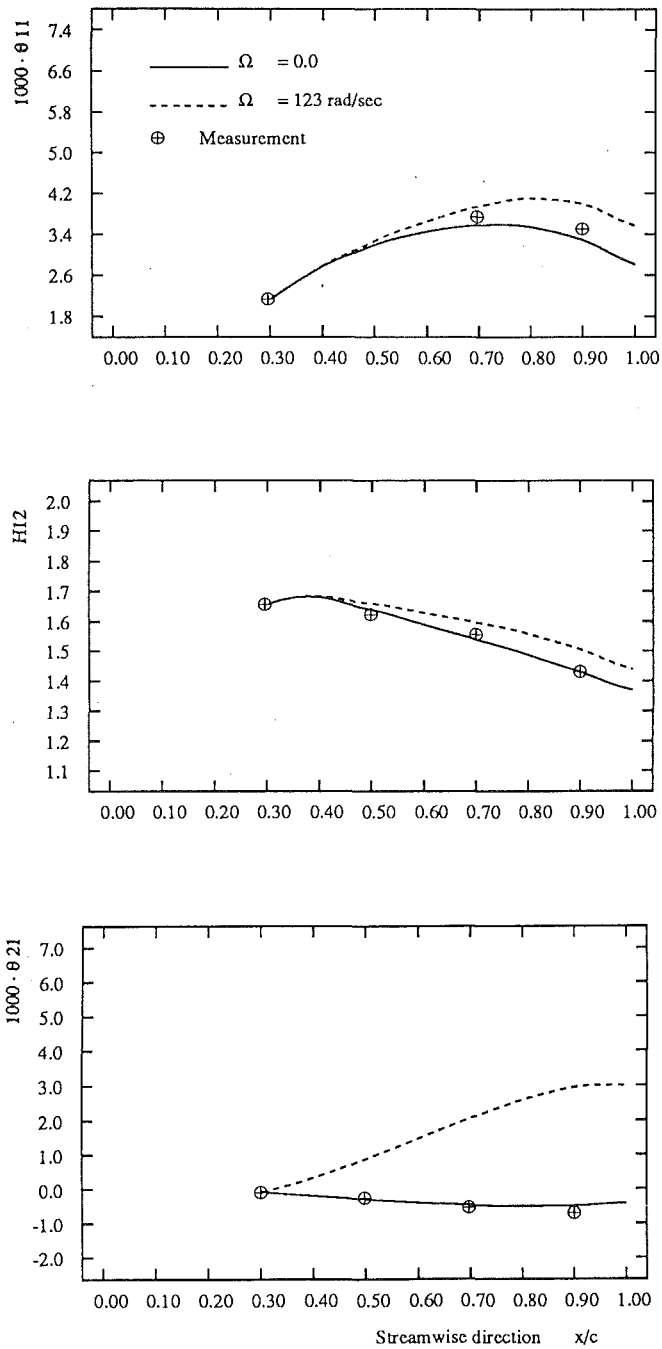

Fig. 11 Comparison of calculated and measured quantities at 50 percent span for NACA blade (pressure side)

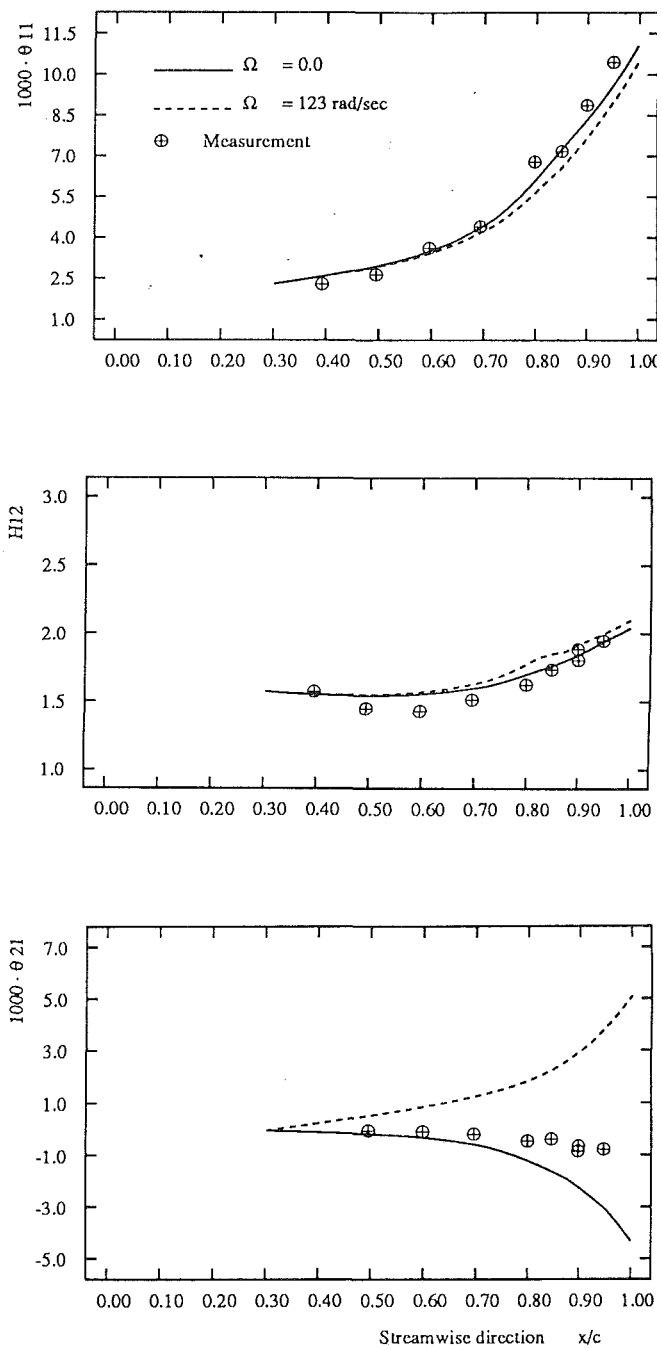

Fig. 12 Comparison of calculated and measured quantities at 50 percent span for NACA blade (suction side)

The calculations with respect to rotation and compressiblity show that those phenomena certainly have strong effects on the boundary layer parameters and transition. By using the criterion of Owen for the crossflow, the position of transition from laminar to turbulent flow moves forward (upstream) as the rotation parameter increases but backward (downstream) as the Mach number increases. Using the e^n method and the Johnston method for the stationary and rotating cases, on which the start of the turbulent calculations is based, the effect on transition as the rotation parameter increases is very uncertain and requires further investigation. The effect of compressibility more clearer and shows that as the Mach number increases the region of transition moves backward. Thus, the effects of Coriolis force and Mach number on the boundary layers of the blade have been separated.

The magnitude of the crossflow on the rotating blade is much larger than on the stationary blade. Thus, losses generated by the crossflow will be larger in a rotating cascade than in a stationary one; see Olsson (1962).

The skin factor, c_f, the crosswise momentum thickness, θ_{12}, and the crossflow angle, β_w, show different behaviors in the case with rotating and compressible flow compared with the stationary one.

For further research it is believed that the prediction of transition must be checked by experiments for rotating and compressible cases, which might lead to corrections on the present methods.

Acknowledgments

The authors would like to thank Dr. Lars Larsson and Dr. Leif Broberg at SSPA Maritime Consulting AB for their aid

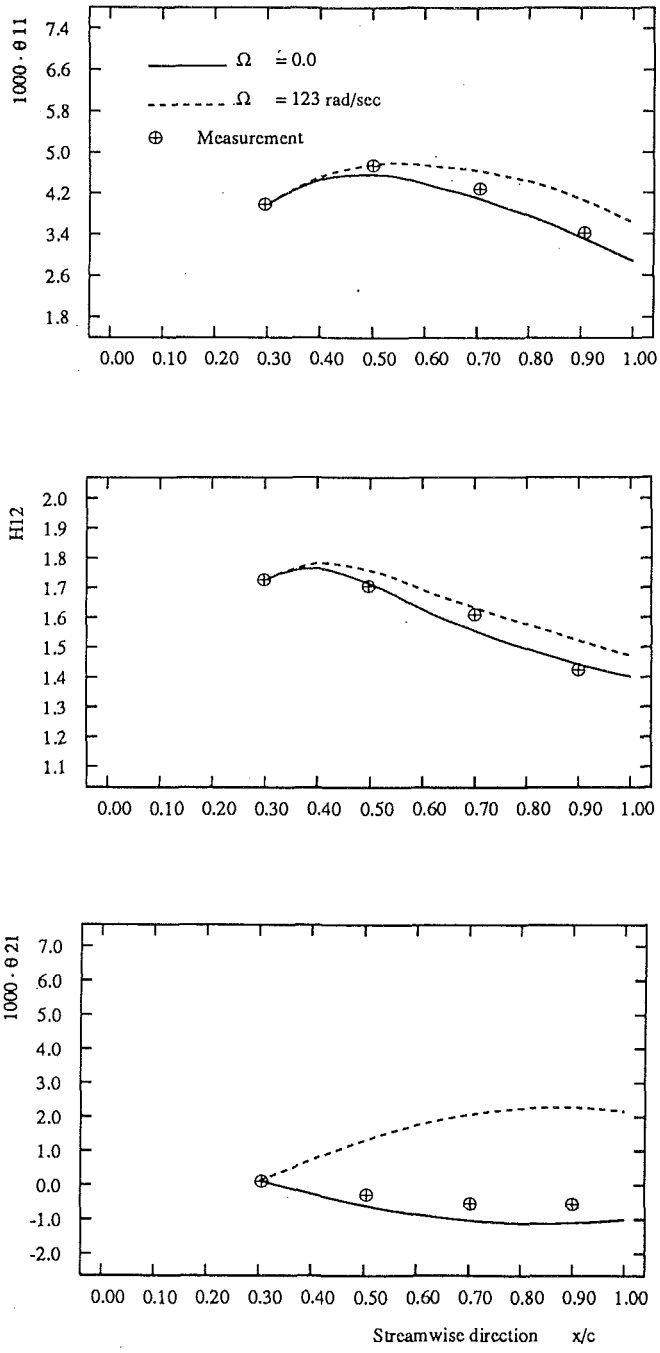

Fig. 13 Comparison of calculated and measured quantities at 90 percent span for NACA blade (pressure side)

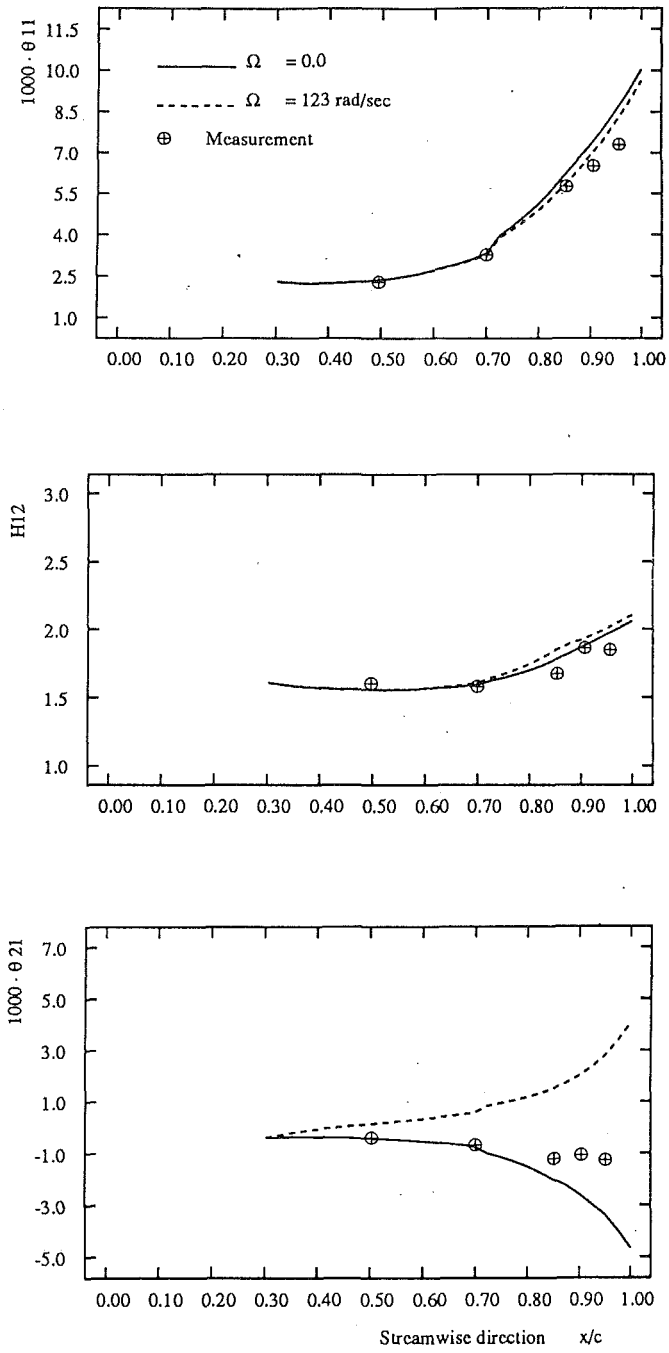

Fig. 14 Comparison of calculated and measured quantities at 90 percent span for NACA blade (suction side)

concerning the initial programs, and special thanks to Mr. Michael Säterskog with calculations from the Euler solver and plotting routines.

References

Abu-Ghannam, B. J., and Shaw, R., 1980, "Natural Transition of Boundary Layers—The Effect of Turbulence, Pressure Gradient, and Flow History," *Journal of Mechanical Engineering Science*, Vol. 22, No. 22.

Cooke, J. C., and Hall, H. G., 1962, "Boundary Layers in Three Dimensions," *Progress in Aeronautical Sciences*, Vol. 2, Pergamon Press, New York.

Cumpsty, N. A., and Head, M. R., 1967, "The Calculation of Three-Dimensional Turbulent Boundary Layers, Part I: Flow Over the Rear of an Infinite Swept Wing," *The Aeronautical Quarterly*, Feb.

Denton, J. D., 1983, "An Improved Time Marching Method for Turbomachinery Flow Calculation," ASME *Journal of Engineering for Power*, Vol. 105, pp. 514–524.

Dunham, J., 1972, "Predictions of Boundary Layer Transition on Turbomachinery Blades," AGARDograph, AG-164, Dec.

Fogarty, L. E., 1951, "The Laminar Boundary Layer on a Rotating Blade," *Journal of Aeronautical Science*, No. 18, pp. 247–252.

Geis, T., 1961, "Similar Three-Dimensional Boundary Layers," Technical Translation, NASA TT F-30, Mar.

Granville, P. S., 1953, "The Calculation of the Viscous Drag of Bodies of Revolution," DTMB Report No. 849.

Groves, N. C., and Taylor D., 1981, "An Integral Prediction Method for Three-Dimensional Boundary Layers on Rotating Blades," *The Society of Naval Architects and Marine Engineers*, No. 24.

Groves, N. C., and Chang, M. S., 1984, "A Differential Prediction Method for Three-Dimensional Laminar and Turbulent Boundary Layers of Rotating Propeller Blades," presented at the Fifteenth Symposium on Naval Hydrodynamics, Sept 6.

Horlock, J. H., and Wordsworth, J., 1965, "The Three-Dimensional Laminar Boundary Layer on a Rotating Helical Blade," *J. Fluid Mech.*, Vol. 23, pp. 305–314.

Johnston, J. P., 1974, "The Effects of Rotation on Boundary Layers in

Turbomachine Rotors," *Fluid Mechanics, Acoustics, and Design of Turbomachinery*, Part I, NASA SP-304.

Lakshminarayana, B., et al., 1972, "Turbulent Boundary Layer on a Rotating Helical Blade," *J. Fluid Mech.*, Vol. 51, Part 3, pp. 545-569.

Lakshminarayana, B., and Govindan, T. R., 1981, "Analysis of Turbulent Boundary Layer on Cascade and Rotor Blades of Turbomachinery," *AIAA Journal*, Vol. 19, pp. 1333-1341.

Lakshminarayana, B., Pouagare, M., and Davino, R., 1982a, "Three-Dimensional Flow Field in the Tip Region of a Compressor Rotor Passage—Part I: Mean Velocity Profiles and Annulus Wall Boundary Layer," ASME *Journal of Engineering for Power*, Vol. 104, pp. 760-771.

Lakshminarayana, B., Davino, R., and Pouagare, M., 1982b, "Three-Dimensional Flow Field in the Tip Region of a Compressor Rotor Passage—Part II: Turbulence Properties," ASME *Journal of Engineering for Power*, Vol. 104, pp. 772-781.

Larsson, L., 1975, "Boundary Layers of Ships, Three-Dimensional Effects," PhD thesis, Chalmers University of Technology, Department of Applied Thermo and Fluid Dynamics.

Lemmerman, L. A., and Atta, E. H., 1980, "A Comparison of Existing Three-Dimensional Boundary Layer Calculation Methods," Paper No. AIAA-80-0133.

Mayle, R. E., 1991, "The Role of Laminar-Turbulent Transition in Gas Turbine Engines," ASME JOURNAL OF TURBOMACHINERY, Vol. 113, pp. 509-537.

Michel, R., 1972, "Méthode de la couche limité turbulente tridimensionelle jusqu'a la séparation: application à un cas simple de turbomachine," AGARDograph, AG-164, Dec.

Michel, R., et al., 1972, "Méthode pratique de prevision des couches limites turbulentes bi- et tridimensionelles," *La Recheche Aerospatiale*, No. 1.

Moore, F. K., 1956, "Chapter on Three-Dimensional Boundary Layer Theory in Applied Mechanics," Vol. 4, Academic Press.

Morris, P. J., 1981, "The Three-Dimensional Boundary Layer on a Rotating Helical Blade," *J. Fluid Mech.*, Vol. 112, pp. 283-296.

Narasimha, R., 1985, "The Laminar-Turbulent Transition Zone in the Boundary Layer," *Prog. Aerospace Sci.*, Vol. 22, pp. 29-80.

Olsson, E. K. A., 1962, "Centrifugal Effect on the Boundary Layer on a Blade of an Axial Turbomachine," Gas Turbine Laboratory, MIT, Report No. 66, Apr.

Pouagare, M., Galmes, J. M., and Lakshminarayana, B., 1985, "An Experimental Study of the Compressor Rotor Blade Boundary Layer," ASME *Journal of Engineering for Power*, Vol. 107, pp. 364-373.

Schlichting, H., 1979, *Boundary Layer Theory*, McGraw-Hill, New York.

Säterskog, K. P. M., 1990, "Calculation of the Steady Three-Dimensional, Viscous and Compressible Flow Within a Fan With Tendency to Flutter," Chalmers University of Technology Dep. of Thermo- and Fluid Dynamics.

White, F. M., 1974, *Viscous Fluid Flow*, McGraw-Hill, New York.

Xia, F., Johansson, L. E., and Larsson, L., 1985, "Experimental and Theoretical Studies of Boundary Layer Transition and Ship Models," presented at the Second International Symposium on Ship Viscous Resistance, SSPA Maritime Consulting AB, Göteborg, Sweden.

A Fully Three-Dimensional Inverse Method for Turbomachinery Blading in Transonic Flows

T. Q. Dang
Department of Mechanical and Aerospace Engineering, Syracuse University, Syracuse, NY 13244

This paper presents a procedure to extend a recently developed fully three-dimensional inverse method for highly loaded turbomachine blades into the transonic-flow regime. In this inverse method, the required three-dimensional blade profile to produce a prescribed swirl schedule is determined iteratively using the blade boundary conditions. In the present implementation, the flow is assumed to be inviscid and the blades are assumed to be infinitely thin. The relevant equations are solved in the conservative forms and are discretized in all three directions using a finite-volume technique. Calculations are carried out for the design of high-pressure axial- and centrifugal-compressor rotors. These examples include prescribed swirl schedules corresponding to blade designs that are shock-free and blade designs that have rapid compression regions in the blade passage.

1 Introduction

Recently, a fully three-dimensional technique for designing the shape of turbomachine blades for large deflections was proposed (Hawthorne et al., 1984; Tan et al., 1984). In this method, the Circulation Method, the primary prescribed flow quantity is the pitch-averaged tangential velocity in the bladed region, denoted by $\overline{V}_\theta$. Note that $2\pi r\overline{V}_\theta$ is the blade circulation, hence the name given to the method. The theory is formulated in a fully inverse mode whereby the blade profile is determined iteratively from the inviscid blade boundary conditions.

What is the significance of specifying the pitch-averaged tangential velocity distribution in the bladed region? At first, it appears that the most useful choice (also the conventionally preferred choice) for the prescribed flow conditions in an inverse method is the pressure distributions along the blade pressure and suction surfaces (Dulikravich and Sobieczky, 1982; Meauze, 1982; Sanz, 1984; Tong and Thompkins, 1983). These pressure distributions are chosen to avoid flow separations on the blade surfaces at the design condition. However, this design philosophy only applies to the two-dimensional case where the streamlines along the blade surfaces are known a priori; namely they lie in the two-dimensional plane under consideration. In the general three-dimensional case, the potential presence of large radial velocities introduces excessive warping of a stream-surface across the blade passage. Thus, in a fully three-dimensional inverse method, an accurate estimation of the locations of the blade-surface streamlines prior to the design calculation is a very difficult task, and it is not clear whether there is an advantage in specifying blade-surface pressure distributions.

Conceptually, there are several advantages in choosing the pitch-averaged tangential velocity distribution as an input flow quantity. First, turbomachine devices supply work to, or extract work from, a working fluid by imposing a change in the fluid angular momentum across the rotating blades. Using the Euler Turbine equation, the input/output power of or the stagnation enthalpy rise/drop across a rotating blade row are shown to be proportional to the overall change in $r\overline{V}_\theta$ (or the average fluid angular momentum per unit mass) across the blade row.

After the overall change in $r\overline{V}_\theta$ across a blade row is chosen, the schedule of $r\overline{V}_\theta$ (or the swirl schedule) must be prescribed at all points in the bladed region. This step raises the question of how the swirl schedule in the bladed region should be specified. Novak and Haymann-Haber (1983) and Tan et al. (1984) have shown that the local rate of change of $r\overline{V}_\theta$ along the "blade streamwise" direction is related to the blade loading. Although the specification of the blade loading seems relatively arbitrary, this type of design specification is used by many design offices in their one-dimensional mean-streamline method (Holbrook and Brasz, 1984), two-dimensional inverse method (Novak and Haymann-Haber, 1983), and quasi-three-dimensional streamline curvature methods (Smith, 1987). Therefore, the present inverse method can readily be used to supplement and/or replace many existing design methods, which use the same design philosophy as the Circulation Method, but are not fully three dimensional.

In the general theory of the Circulation Method, the blades are represented by distributed bound vorticities whose strength is determined by the prescribed swirl schedule. The flow velocity is divided into pitch-averaged and periodic terms. The Stokes stream function formulation is used to determine the pitch-averaged axial and radial velocity components, while the Clebsch formulation is used to compute the periodic velocity

Contributed by the International Gas Turbine Institute and presented at the 37th International Gas Turbine and Aeroengine Congress and Exposition, Cologne, Germany, June 1-4, 1992. Manuscript received by the International Gas Turbine Institute February 20, 1992. Paper No. 92-GT-209. Associate Technical Editor: L. S. Langston.

vector. The calculation for the blade profile is initiated by the specifications of, in addition to the swirl schedule, the hub and shroud geometries, the number of blades, the blade leading- and trailing-edge locations, the blade stacking position, and the blade rotational speed. The blade profile is computed iteratively, by first assuming an initial blade shape and then computing the corresponding flow field. Next, a new estimate for the blade profile is obtained by applying the inviscid blade boundary conditions. This calculation is repeated until convergence in the blade geometry is reached. The resulting solution not only gives the blade geometry and blade-surface pressure distributions, but also the entire flow field.

The original application of the method was confined to the design of two-dimensional cascades (Hawthorne et al., 1984) and three-dimensional annular cascades (Tan et al., 1984) of infinitely thin blades in incompressible flow. Flow variables were expanded in terms of series of smooth eigenfunctions in all three directions: Bessel functions in the radial direction, Fourier series in the tangential direction, and Chebyshev polynomials in the axial direction. The method was extended to handle blades with finite thickness (Dang and McCune, 1984a) and forced-vortex blading in the presence of an incoming shear flow (Dang and McCune, 1984b). The latter study allowed for the design of three-dimensional blade profiles in the presence of secondary flows.

In the subsequent years, an intense program was carried out to apply the theory to problems of practical interest. Borges (1990a) extended the method to the design of a radial inflow turbine of arbitrary hub and shroud profiles. He retained the Fourier-series expansion technique in the tangential direction, and solved the resulting eigenvalue problems in the meridional plane using a finite-difference multigrid technique. He designed, constructed, and investigated the performance of a laboratory low-speed radial-inflow turbine consisting of a row of nozzle vanes and two impellers of identical hub and shroud profiles (Borges, 1990b). The vanes for the first impeller were designed by a method used in many design offices; those for the second impeller were designed using his program to a swirl schedule which he formulated. This work showed that the second impeller gave a definite improvement in performance over a wide range of operation. As the first complete demonstration of the value of the new technique, this was a significant step.

Using a numerical scheme based on the finite-element formulation for the eigenvalue problems in the meridional plane, Ghaly (1990) applied the method to the design of radial-inflow turbine vanes for compressible flow at subcritical Mach number. His work showed that the Circulation Method can be extended to compressible flow. Yang et al. (1991) and Zangeneh and Hawthorne (1990) used the method to design small high-speed radial-inflow turbines. To check the results given by the inverse method, the flows in the designed shapes were computed using time-marching Euler as well as viscous analysis codes. The results showed excellent agreement between the specified swirl schedules and those obtained from the direct Euler calculations. For the cases studied, even with a strong reverse flow over part of the blade pressure surface, the results for the viscous calculations do not appear to distort the prescribed swirl schedule (Yang et al., 1991).

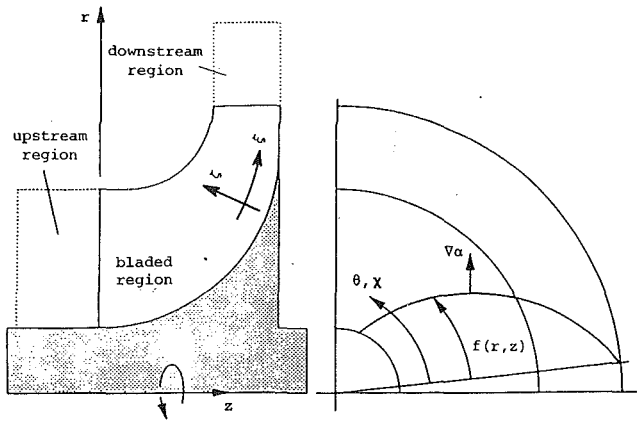

Fig. 1 Notation

In the transonic-flow regime, the appearance of shocks in the blade passage is possible for an arbitrary prescribed swirl schedule. Dang (1991) used a finite-volume technique with a shock-capturing capability to extend the Circulation Method into the transonic-flow regime for two-dimensional cascaded blades. The method can produce blade design corresponding to prescribed swirl schedules that have rapid compression regions, or possibly weak shocks, in the flow. The purpose of this paper is to demonstrate that the Circulation Method can be extended into the transonic-flow regime for three-dimensional flows.

2 Theory

The basic theory of this three-dimensional inverse method is well documented in several references (e.g., Tan et al., 1984) and is summarized in this section. In the present study, the flow is assumed to be inviscid, and the blades are assumed to be infinitely thin. Furthermore, only weak shocks will be considered so that the entropy fields generated behind these shocks are neglected.

In the Circulation Method, the classical aerodynamic approach of representing the blades as bound vortex sheets is adopted. Assuming that the approaching flow is steady and irrotational, the absolute bound vorticity can be expressed as

$$\Omega = \delta_p(\alpha) \nabla r\bar{V}_\theta \times \nabla \alpha \tag{1}$$

where $\delta_p(\alpha)$ is the periodic delta function (Lighthill, 1969). The blade surface denoted by α is defined as

$$\alpha \equiv \theta - f(r, z) = \pm m2\pi/B \tag{2}$$

where (r, θ, z) is the right-handed coordinate system (Fig. 1), f is the blade wrap angle, B is the number of blades, and m is an integer. Note that in the case of forced-vortex blading, Eqs. (1) and (2) represent the trailing vorticity and the wake surface behind the blade, respectively. The overbar denotes a pitch-averaged value defined as

Nomenclature

$\overline{A}$ = pitch-averaged value of quantity A defined in Eq. (3)
$\mathbf{A}$ = vector $\mathbf{A}$
B = number of blades
f = blade wrap angle
F_b = body-force field
(r, θ, z) = cylindrical coordinate system
$S(\alpha)$ = periodic sawtooth function
V = absolute velocity
W = relative velocity
α = blade surface defined in Eq. (2)
$\delta_p(\alpha)$ = periodic delta function
(ζ, χ, ξ) = computational space
ρ = density
$\tilde{\phi}$ = potential function
ψ = Stokes stream function
ω = blade rotational speed
Ω = absolute vorticity

Subscripts

avg = average flow
bl = at the blade
r, θ, z = r, θ, z components
∞ = inlet condition

$$\overline{A}(r, z) \equiv \frac{B}{2\pi}\int_0^{\frac{2\pi}{B}} A(r, \theta, z)\, d\theta \tag{3}$$

where A is an arbitratry flow variable, and the integral is taken over the complete blade pitch including the blade.

In the Clebsch formulation, the velocity vector is decomposed into potential and rotational parts, expressed in terms of scalar functions. On using Eq. (1), one such choice is

$$\mathbf{V} = \nabla\phi + r\overline{V}_\theta \nabla\alpha - S(\alpha)\nabla r\overline{V}_\theta \tag{4}$$

where the scalar function $\phi = \phi(r, \theta, z)$ is the potential part of the velocity vector, and the remaining terms constitute the rotational part of the velocity vector. In Eq. (4), $S(\alpha)$ is the periodic sawtooth function (Lighthill, 1969). Note that the curl of Eq. (4) gives back Eq. (1).

In the previous compressible-flow studies (Ghaly, 1990; Zangeneh and Hawthorne, 1990), as the tangential component of the pitch-averaged velocity vector was a prescribed quantity in the inverse formulation, it was convenient to divide the flow field into two parts: a two-dimensional pitch-averaged part defined in Eq. (3), and the remaining three-dimensional periodic part whose pitch-averaged value was zero. The pitch-averaged and periodic parts of the flow field were solved separately, and they were chosen to satisfy the pitch-averaged and periodic forms of the equations of motion, respectively.

In the present study, which deals with transonic flows, the equations of motion are solved in the conservative form so that (weak) shocks can be included. Thus, it is no longer useful formally to divide the flow into pitch-averaged and periodic parts. Instead, strictly for convenience (for both theoretical and numerical reasons), the velocity vector is redefined as

$$\mathbf{V} \equiv [\mathbf{V}_{\text{avg}}(r, z) + \overline{V}_\theta \hat{e}_\theta] + \nabla\tilde{\phi} - S(\alpha)\nabla r\overline{V}_\theta \tag{5}$$

where the redefined potential function $\tilde{\phi}$ is a function of (r, θ, z), and the average velocity vector $\mathbf{V}_{\text{avg}}$ has nonzero r and z components only (a meridional-like velocity vector).

On considering the θ component of the pitch-averaged integral of Eq. (5), it can be shown that the potential function $\tilde{\phi}$ must be periodic in the tangential direction, namely

$$\tilde{\phi}(r, \theta = f, z) = \tilde{\phi}(r, \theta = f + 2\pi/B, z) \tag{6}$$

Equation (6) constitutes the boundary condition for $\tilde{\phi}$ along the periodic boundaries, which include the bladed region. It is interesting to note that the use of the Clebsch formulation for the velocity vector as described by Eq. (4) does not introduce double-valued potentials along the blade camber surface and along the singularity surface leaving the blade trailing edge (for a lifting case). The reason is that, unlike in the conventional full-potential method where the circulation of a lifting surface is represented by the jump in the potential function along the lifting surface and along the singularity surface behind the trailing edge, the Clebsch approach puts all the circulation into the rotational part of the velocity vector.

Taking the curl of Eq. (5) to obtain the vorticity and compare it with Eq. (1), it can be seen that the average velocity must satisfy the following condition:

$$\nabla \times \mathbf{V}_{\text{avg}} = \nabla r\overline{V}_\theta \times \nabla\alpha = \overline{\Omega} \tag{7}$$

Equation (7) constitutes the only constraint on the average velocity $\mathbf{V}_{\text{avg}}$. It requires the curl of the average velocity to be the pitch-averaged vorticity.

2.1 Governing Equations. In the Clebsch formulation of the equations of motion, the Clebsch variables expressed in Eq. (4) are chosen to satisfy the continuity, momentum, and energy equations. Written in the rotating frame, the continuity equation is

$$\nabla \cdot (\rho\mathbf{W}) = 0 \tag{8}$$

while the momentum equation expressed in Crocco's form is

$$\mathbf{W} \times \Omega = \delta_p(\alpha) F_b \nabla\alpha \tag{9}$$

In Eq. (9), the right-hand side term is the body force representing the reaction on the fluid as a result of forces concentrated at the blades. For inviscid flow, this body force represents the force resulting from the pressure difference across the blades and acts normal to the blades. For homenthalpic and homentropic flow, the density can be computed from

$$\frac{\rho}{\rho_\infty} = \left[1 + \frac{\gamma - 1}{2}\mathrm{M}_\infty^2\left(1 + \frac{\omega^2 r^2 - W^2}{V_\infty^2}\right)\right]^{\frac{1}{\gamma - 1}} \tag{10}$$

In the above equations, M_∞ is the inlet absolute Mach number, V_∞ is the inlet absolute velocity, W is the relative velocity, γ is the ratio of the specific heats, ρ_∞ is the inlet density, and ω is the blade rotational speed. On substituting Eq. (1) into Eq. (9), along with the use of the blade boundary condition (i.e., the flow tangency condition at the blade surfaces)

$$\langle \mathbf{W} \rangle_{bl} \cdot \nabla\alpha = 0 \tag{11}$$

the following relation is obtained:

$$F_b = \langle \mathbf{W} \rangle_{bl} \cdot \nabla r\overline{V}_\theta \tag{12}$$

In Eqs. (11) and (12), the "blade" velocity $\langle \mathbf{W} \rangle_{bl}$ is defined as the average velocity at the blade pressure and suction surfaces. At the blade trailing edge and away from the bladed region, F_b must vanish and Eq. (12) reduces to

$$\langle \mathbf{W} \rangle_{bl} \cdot \nabla r\overline{V}_\theta = 0 \tag{13}$$

Physically, Eq. (13) states the Kutta condition at the blade trailing edge and, in the case of forced-vortex blading, the zero pressure jump condition across the trailing vortex sheet. The prescribed swirl distribution in the bladed region must satisfy Eq. (13) at the trailing edge, and Eq. (13) is used to compute the swirl distribution outside the bladed region.

2.2 Choice of the Average Flow. The Stokes stream function is used to determine the axisymmetric average flow. The average velocity is chosen to satisfy the actuator duct limit of the flow equations (Dang and Wang, 1992). In this limit, the continuity equation takes on the form

$$\nabla \cdot (\rho_{\text{avg}} \mathbf{V}_{avg}) = 0 \tag{14}$$

where the average density is calculated from

$$\frac{\rho_{\text{avg}}}{\rho_\infty} = \left[1 + \frac{\gamma - 1}{2} M_\infty^2\left(1 + \frac{-V_{\text{avg}}^2 - \overline{V}_\theta^2 - 2\omega r\overline{V}_\theta}{V_\infty^2}\right)\right]^{\frac{1}{\gamma - 1}} \tag{15}$$

To determine the average velocity, the Stokes stream function $\psi = \psi(r, z)$ is defined to satisfy Eq. (14), namely

$$\rho_{\text{avg}} \mathbf{V}_{\text{avg}} \equiv \nabla\psi \times \nabla\theta \tag{16}$$

The governing equation for the Stokes stream function is obtained by enforcing the constraint described by Eq. (7), leading to

$$\frac{\partial}{\partial r}\left(\frac{1}{r\rho_{\text{avg}}}\frac{\partial\psi}{\partial r}\right) + \frac{\partial}{\partial z}\left(\frac{1}{r\rho_{\text{avg}}}\frac{\partial\psi}{\partial z}\right) = \frac{\partial r\overline{V}_\theta}{\partial z}\frac{\partial f}{\partial r} - \frac{\partial r\overline{V}_\theta}{\partial r}\frac{\partial f}{\partial z} \tag{17}$$

Note that Eq. (17) represents the θ component of Eq. (7), while the other two components of Eq. (7) are identically satisfied.

In the present formulation, the average flow is not defined to satisfy the exact pitch-averaged form of the equations of motion as in the earlier compressible-flow studies (Ghaly, 1990; Zangeneh and Hawthorne, 1990). It was done so in the earlier studies so that the flow can be conveniently expressed as Fourier series in the tangential direction. In the present formulation, the average velocity is purposely defined to satisfy Eqs. (14) and (15) so that it represents the far-field flow conditions in the free-vortex limit. In this case, the potential functions $\tilde{\phi}$ defined in Eq. (5) is prevented from growing out-of-bound with streamwise distance (similar to the use of the reduced potential function in external aerodynamics). With this choice of the average flow, the pitch-averaged integral of $\nabla\tilde{\phi}$ in Eq.

(5) can have nonzero r and z components, although the θ component is always zero due to the constraint imposed on the potential function through Eq. (6).

2.3 Formulation of the Inverse Problem. In the Circulation Method, the primary prescribed flow quantity is the swirl schedule $r\overline{V}_\theta$ in the bladed region, and the primary quantity solved for is the blade wrap angle f defined in Eq. (2). The inviscid blade boundary conditions are used to compute the blade wrap angle iteratively. Substituting Eq. (2) into Eq. (11), the equation used to update the blade wrap angle is obtained

$$\langle W_r\rangle_{bl}\frac{\partial f}{\partial r}+\langle W_r\rangle_{bl}\frac{\partial f}{\partial z}=\frac{\langle W_\theta\rangle_{bl}}{r} \tag{18}$$

In Eq. (18), the blade wrap angle f can be computed given the "blade" velocity. The evaluation of the "blade" velocity using Eq. (5) requires the knowledge of the average velocity and the potential function. The choice of the average velocity is presented in Sect. 2.2, while the potential function is determined from the continuity equation. Formally, on substituting Eq. (5) into Eq. (8), the governing equation for $\tilde{\phi}$ is obtained:

$$\nabla\cdot(\rho\nabla\tilde{\phi})=-\nabla\cdot\left[\rho\left(\mathbf{V}_{\text{avg}}+\overline{V}_\theta\hat{e}_\theta-S(\alpha)\nabla r\overline{V}_\theta\right)\right] \tag{19}$$

Note that Eq. (19) is the full-potential equation with a source term. In the design problem, the unknowns in the problem are: (1) the blade wrap angle f, (2) the average velocity $\mathbf{V}_{\text{avg}}$, (3) the potential function $\tilde{\phi}$, and (4) the pitch-averaged tangential velocity component $\overline{V}_\theta$ outside the bladed region. The calculation for the blade wrap angle f is initiated by guessing a blade shape and an initial velocity field. Then, the following iterative scheme is used to update the blade profile:

1 The average velocity $\mathbf{V}_{\text{avg}}$ is computed by solving Eq. (17) for ψ.
2 The potential function $\tilde{\phi}$ is computed by solving Eq. (19).
3 The pitch-averaged tangential velocity component $\overline{V}_\theta$ outside the bladed region is computed by solving Eq. (13).
4 The blade wrap angle f is updated by solving Eq. (18).
5 Perform a convergence check on f. If convergence is not reached, then go back to step (1).

3 Numerical Technique

In this section, the numerical technique used to solve the relevant equations described in Sect. 2 will be presented. Three types of partial differential equation are encountered in the iterative scheme for the blade profile. They are: (1) the governing equation for the Stokes stream function ψ, (2) the governing equation for the potential function $\tilde{\phi}$, and (3) the governing equations for the blade wrap angle f and the pitch-averaged tangential velocity component $\overline{V}_\theta$ outside the bladed region.

3.1 Stokes Stream Function Solver. The governing equation for the Stokes stream function defining the average flow, i.e., Eq. (17), is of the elliptic type assuming that the Mach number based on the average flow is less than unity. Equation (17) is solved by first transforming it from the meridional plane (r, z) to a rectangular computational plane (ζ, ξ), then central-differencing the transformed equation using a Line-Successive-Over-Relaxation (LSOR) scheme. Written in terms of the correction in ψ between the iteration levels in the relaxation scheme, the discretized form of Eq. (17) reads

$$L_\psi\left\{\psi^{n+1}-\psi^n\right\}=\overline{\Omega}_\theta(\psi^n)-\overline{\Omega}_\theta(r\overline{V}_\theta, f) \tag{20}$$

where the superscript n denotes the LSOR iterative-level number. In the above equations, the discrete operator L_ψ is derived from Eq. (17) and is a function of the transformation metrics. Since the hub and shroud profiles do not change during the iterative process for the blade wrap angle, these transformation metrics are fixed throughout the calculations. In Eq. (20), it is important to differentiate the way $\overline{\Omega}_\theta$ appearing on the right-hand side are computed: the first term is computed using the values of the stream function ψ at the previous LSOR iterative level, while the second term is evaluated in terms of the Clebsch variables $r\overline{V}_\theta$ and f. These Clebsch variables are fixed during the LSOR iteration.

Consider the area integral of Eq. (20) about an arbitrary cell in the meridional plane. On using the theorem of Stokes applied to the first term on the right-hand side of Eq. (20), one obtains

$$L_\psi\left\{\psi^{n+1}-\psi^n\right\}=\frac{1}{A}\left[\int\overline{\mathbf{V}}(\psi^n)\cdot d\mathbf{l}-\int\int\overline{\Omega}_\theta, f)dA\right] \tag{21}$$

where A is the area of the cell, the line integral is taken counterclockwise around the sides of the cell, and the area integral is taken over the cell. In Eq. (21), the first term on the right-hand side is the circulation about the cell evaluated using the values of the stream function at the previous LSOR iterative level, while the second term is the flux of vorticity through the cell expressed in terms of the Clebsch variables. When the LSOR relaxation scheme converges, the left-hand side of Eq. (21) vanishes (i.e., the correction to the stream function between the LSOR iteration is zero), and Eq. (21) is simply a statement of circulation. It states that the stream function has been successfully adjusted to give the circulation about the cell its correct value, which is given by the flux of vorticity through the cell expressed in terms of the Clebsch variables. The right-hand side of Eq. (21) is the residual of the LSOR iterative scheme. From the numerical point of view, the convergence of the LSOR scheme is monitored through the value of this residual, not through the change of the stream function between iterations.

3.2 Potential Function Solver. Previously, to take advantage of the periodic condition in the pitchwise direction, the classical Fourier-series expansion technique was employed to solve the continuity equation for the potential function (Tan et al., 1984). This technique is numerically efficient because it reduces the three-dimensional problem to solving a set of two-dimensional Helmholtz equations. In the present study, in order to handle shocks in the transonic-flow regime, the continuity equation is solved in the conservative form and is discretized in all three directions using a finite-volume technique.

The governing equation for the potential function, Eq. (19), is of the mixed elliptic/hyperbolic type when the relative flow field is transonic. Equation (19) is solved by first transforming it from the physical space (r, θ, z) to a rectangular computational space (ζ, χ, ξ), then discretizing the transformed equation in all three directions using the Jameson's rotated scheme. This relaxation method involves the concept of adding an artificial viscosity to the central-differencing scheme in order to produce the desired directional bias in the hyperbolic region. In addition, the conservation-law form of the continuity equation is preserved in the discretized approximation so that proper jump conditions are satisfied across shocks.

Written in terms of the correction in $\tilde{\phi}$ between the iteration levels in the relaxation scheme, the discretized form of Eq. (19) takes on the form

$$L_{\tilde{\phi}}\{\tilde{\phi}^{n+1}-\tilde{\phi}^n\}=\nabla\cdot(\rho\mathbf{W}) \tag{22}$$

where the superscript n is the iterative-level number of the relaxation scheme. In the above equation, the discrete operator $L_{\tilde{\phi}}$ is derived from Eq. (19) and is the same operator as that of the full-potential equation. The details of this relaxation scheme can be found from Jameson and Caughey (1977).

Considering the volume integral of Eq. (22) about an ar-

bitrary cell and applying the theorem of Stokes to the right-hand side term, one obtains

$$L_{\tilde{\phi}}\{\tilde{\phi}^{n+1}-\tilde{\phi}^{n}\}=\frac{1}{\forall}\int\int \rho \mathbf{W}\cdot\hat{n}\,dA \tag{23}$$

where $\forall$ is the volume of the cell. In Eq. (23), the right-hand side term represents the net mass flux across the boundaries of the cell. When the relaxation scheme converges, the left-hand side of Eq. (23) vanishes (i.e., the correction to the potential function is zero), and Eq. (23) is simply a statement of the conservation of mass. The right-hand side of Eq. (23) is the residual of the iterative scheme. From the numerical point of view, the convergence of the relaxation scheme is monitored through the value of this residual, not through the change of the potential function between iterations.

The boundary conditions applied to Eq. (23) are as follows. At the inflow boundary, the potential function is set to zero since the inlet velocity vector is contained in the average flow. Along the periodic boundaries (i.e., the blade surfaces and the stream surfaces emanating from the blade leading and trailing edges), the potential function is periodic as required by Eq. (6). Along the hub and shroud surfaces, the flow-tangency condition is imposed. Finally, at the outflow boundary, the mass flux is set to be uniform and the total mass flux is set equal to the specified mass flow rate.

As the periodic boundaries change during the iteration process for the blade profile, the grid distributions in the blade-to-blade planes change at every iterative level. To alleviate the grid-generation task, an **H**-grid topology is employed. This choice of grid topology reduces to generating the grid in the (r, α, z) space. The advantage is that because α satisfies the condition $0 \le \alpha \le 2\pi/B$, the (r, α, z) space is simply an axisymmetric channel having straight vanes, and the grid-generation task reduces to generating a grid in the meridional plane and a stretching function in the pitchwise direction.

In the finite-volume method of Jameson and Caughey (1977), the solution to Eq. (23) involves the evaluation of the transformation metrics between the physical space (r, θ, z) and the computational space (ζ, χ, ξ). The metrics r_ζ, r_ξ, z_ζ, and z_ξ are calculated from the specified grid distribution in the meridional plane. These metrics are fixed during the iteration process for the blade profile since the hub and shroud profiles are given. In the present choice of the **H**-grid topology, the metrics r_χ and z_χ are zero. Finally, on using Eq. (2), the remaining three metrics θ_ζ, θ_χ, and θ_ξ are computed from

$$\theta_\zeta = f_\zeta,\ \theta_\chi = \alpha_\chi,\ \theta_\xi = f_\xi \tag{24}$$

since α_ζ, α_ξ, and f_χ are zero. During the iteration process for the blade profile, α_χ is fixed and is evaluated from the specified stretching function in the pitchwise direction, while f_ζ and f_ξ vary.

3.3 Hyperbolic Equation Solver. The governing equations for the blade wrap angle f, Eq. (18), and for the pitch-averaged tangential velocity component $\overline{V}_\theta$ outside the bladed region, Eq. (13), are hyperbolic. These equations are solved numerically using the implicit second-order accurate Crank–Nicolson scheme. For the blade wrap angle, the blade "stacking" position constitutes the initial data for Eq. (18). In the present method, the blade wrap angle is set to zero along a prescribed quasi-orthogonal grid line (constant ξ line), called the blade stacking line. For the pitch-averaged tangential velocity component outside the bladed region, the initial data for Eq. (13) are given from the prescribed swirl distribution at the blade trailing edge. For free-vortex blading, Eq. (13) is identically satisfied as $r\overline{V}_\theta$ is constant along the blade trailing edge and outside the bladed region.

4 Results and Discussions

To illustrate the method, the design of a centrifugal-compressor impeller is presented first, followed by the design of two axial-compressor rotors of the same pressure ratio; one is shock-free, while the other has a rapid compression region (possibly a weak shock) in the flow. As the purpose of these exercises is to demonstrate the capability of the method to handle transonic flow conditions, no attempt is made at choosing swirl schedules that "optimize" the blade geometry and blade-surface flow distributions.

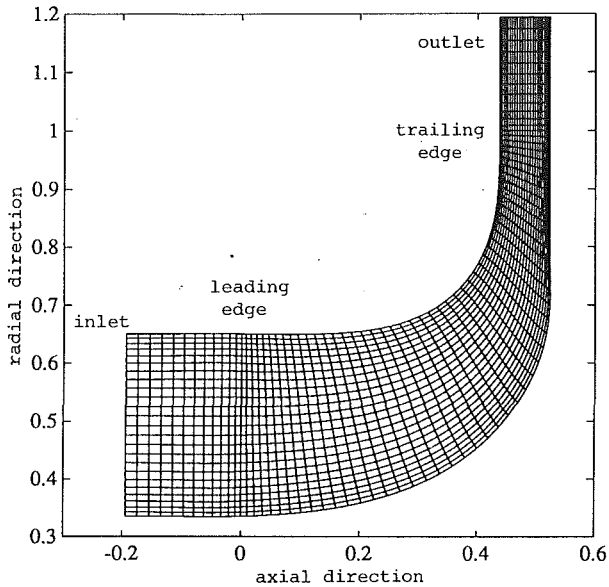

Fig. 2 Grid distribution in meridional plane

Figure 2 shows the specified hub and shroud profiles, the prescribed locations of the impeller leading and trailing edges, along with the grid distribution in the meridional plane for the centrifugal-compressor impeller. All dimensions are normalized to the trailing-edge radius (or tip radius) taken to be 0.1 m. The employed grid has 72 × 24 cells in the meridional plane and 20 cells in the circumferential direction, giving a total of 34,560 cells in the computational domain. A fully converged solution for this grid takes on the order of two hours of CPU time on a Sun Sparcstation 2 workstation (4 Mflops machine).

In this design, the specified number of blades is 14, and the blades are stacked at the trailing edge (i.e., the blade wrap angle at the trailing edge is set to zero at all spanwise stations). The impeller rotational speed is 52,000 rpm, and the incoming airflow is set at the ambient conditions with a mass flow rate of 2.0 kg/s. These prescribed conditions give inflow relative Mach numbers of 0.82 and 1.23 at the hub and shroud locations, respectively. The inflow relative angles at the hub and shroud are −43 and −59 deg, respectively. The impeller is designed to have a pressure ratio of 6.5 with a subsonic outflow relative Mach number.

Figure 3 shows the prescribed contour plot of $r\overline{V}_\theta$ in the bladed region (normalized to the impeller tip radius and tip speed). This figure indicates that the impeller is designed to increase $r\overline{V}_\theta$ from 0.0 at the leading edge to 0.7 at the trailing edge. Also shown on this figure are the loading distributions at the hub, midspan, and shroud stations used to generate this swirl schedule. They indicate that the impellers are designed to be loaded toward the trailing edge.

Figure 4 illustrates the initial (left figure) and final (right figure) grid distributions at the midspan blade-to-blade plane. This figure shows that the initial grid distribution generated on a typical blade-to-blade plane is simply for an axisymmetric channel having straight vanes. During the iteration process for the blade wrap angle f, constant ξ grid lines move circumfer-

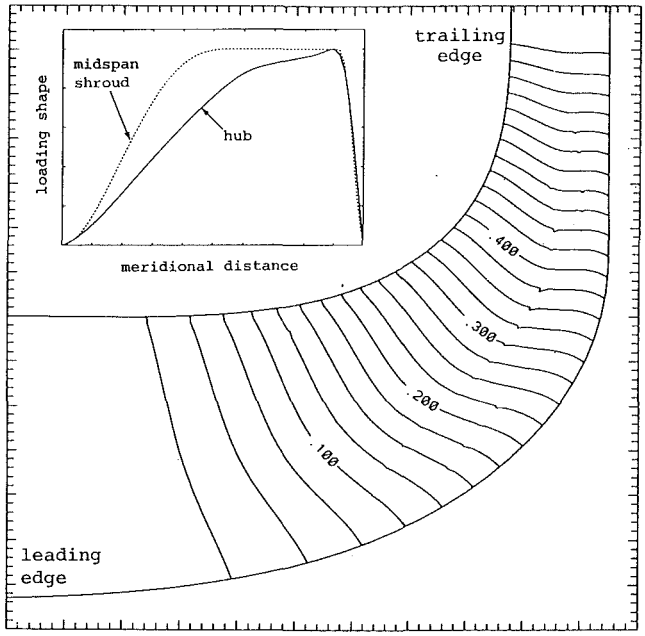

Fig. 3 Contour of prescribed $r\bar{V}_\theta$ (contour increment of 0.025)

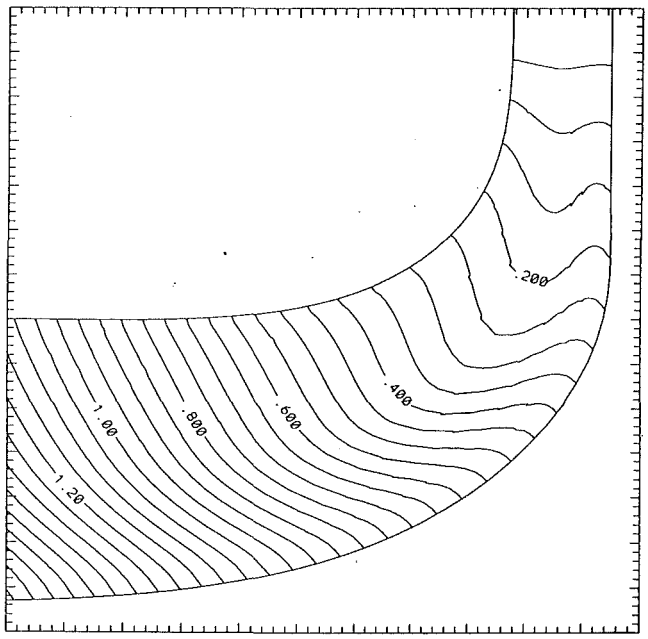

Fig. 5 Contour of blade wrap angle in radians (contour increment of 0.05)

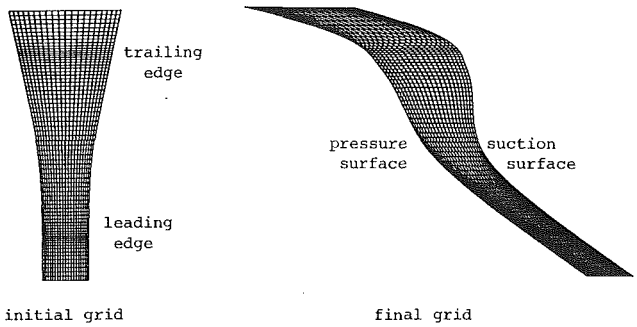

Fig. 4 Grid distribution in blade-to-blade plane at midspan

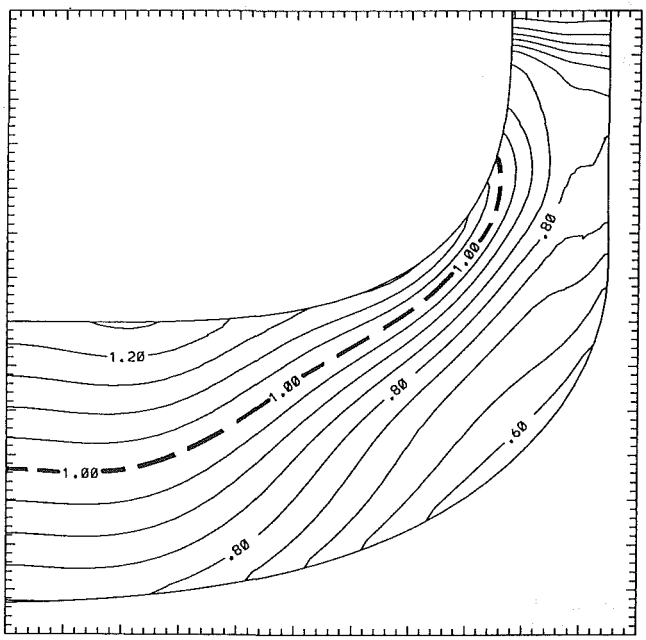

Fig. 6 Contour of relative Mach number on blade suction surface (contour increment of 0.05)

entially (i.e., horizontally in the figure) by the amount of δf varied between iterations.

Figure 5 illustrates the geometry of the designed impeller as described by contours of the blade wrap angle. The spanwise variation in the blade wrap angle at the leading edge is large and is on the order of 0.5 radian. Figure 5 also indicates that, in the region between the midchord station and the trailing edge, the blade wrap angle is larger at the hub and shroud than at midspan. Consequently, the prescribed swirl distribution shown in Fig. 3 results in a blade design that may not satisfy the structural and manufacturing constraints.

Figure 6 illustrates the contour plot of the relative Mach number at the blade suction surface (dashed line represents sonic line). This figure shows that the impeller operates in the transonic-flow regime, with a maximum relative Mach number of 1.27 on the suction surface. This figure indicates that the designed impeller is shock-free.

Next, to illustrate the capability of the present method to produce blade design corresponding to a prescribed swirl schedule that has a rapid compression region in the flow, the design of two axial-compressor rotors is presented. In these examples, the annulus has constant hub and shroud radii, and the blade axial chord is kept constant. The aspect and hub-to-tip ratios of the rotors are 0.2 and 0.8, respectively. The specified number of blades is 5, and the blades are stacked at midchord (i.e., the blade wrap angle at midchord is set to zero at all spanwise locations). The prescribed flow conditions give inflow relative Mach numbers of 0.74 and 0.78 at the hub and shroud locations, respectively. The inflow relative angles at the hub and shroud are -28 and -33 deg, respectively. These two rotors are designed to have the same pressure ratio of 1.22, but the prescribed swirl schedules are slightly different.

Figure 7 shows the loading shapes used to generate the prescribed swirl schedules for the designed rotors. Rotor A is designed to have a simple free-vortex swirl schedule of the form $r\bar{V}_\theta = r\bar{V}_\theta(z)$. The swirl schedule for rotor A is generated using a "smooth" loading shape (type A) at all spanwise stations. On the other hand, the free-vortex swirl schedule for rotor B has a spanwise variation; it is generated using the same "smooth" loading shape of rotor A at the hub station, but a

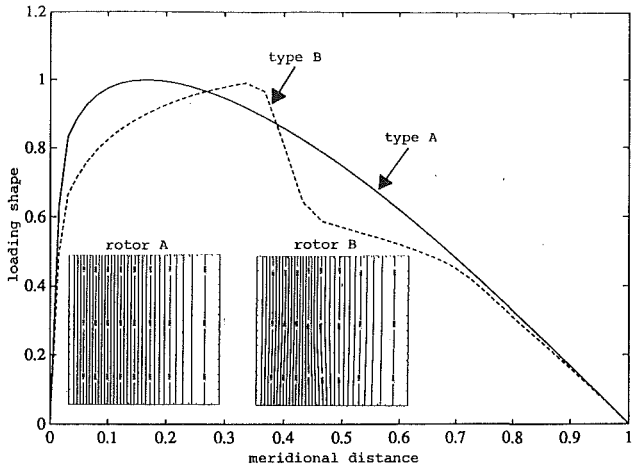

Fig. 7 Prescribed loading shapes and $r\bar{V}_\theta$ contours for rotor A and rotor B

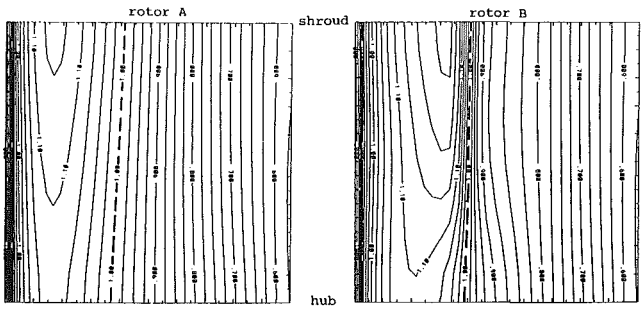

Fig. 8 Comparison of relative Mach number contours on blade suction surface (contour increment of 0.025)

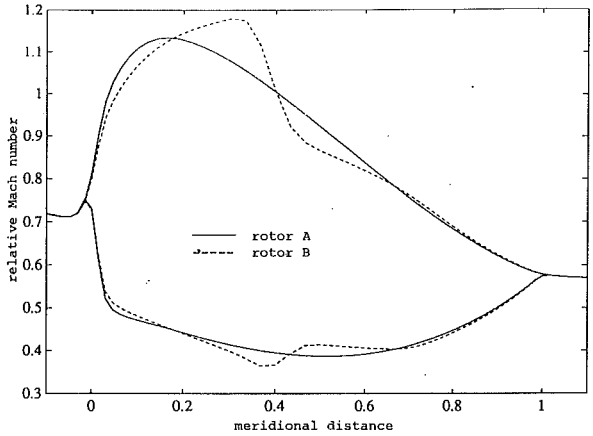

Fig. 9 Comparison of blade-surface relative Mach number distributions at shroud

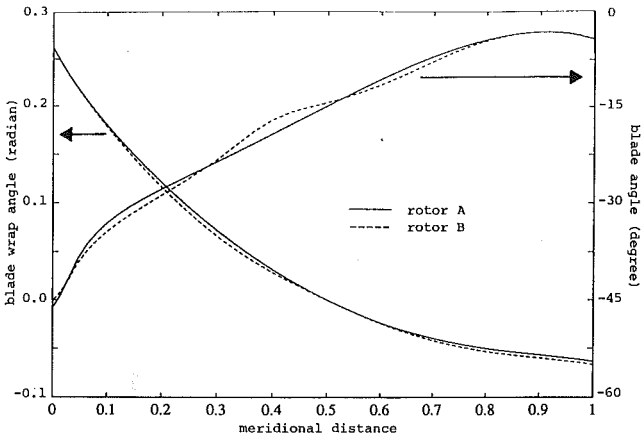

Fig. 10 Comparisons of blade wrap angle and blade angle distributions at shroud

loading shape having a "large negative gradient" at the 40 percent chord (type B) is used at the midspan and shroud stations. Also included in Fig. 7 are the resulting prescribed $r\bar{V}_\theta$ contours for the designed rotors. Note that the large difference in the loading shapes used to generate these swirl schedules is hardly noticeable in the $r\bar{V}_\theta$ contour plots.

Figure 8 shows contour plots of the relative Mach number at the blade suction surfaces for rotor A and rotor B (dashed line represents sonic line). This figure indicates that rotor A is shock-free, while rotor B has a rapid compression around the 40 percent chord station. Figure 9 illustrates a detailed comparison of the blade-surface relative Mach number at the shroud. This figure confirms the shock-free condition of rotor A and the presence of a rapid compression in rotor B, although the latter could very well be a weak shock.

Figure 10 shows detailed comparisons of the blade wrap angle and the blade angle distributions at the shroud location for the two designed rotors. This figure shows that the geometric differences in the two blade profiles are very small, even though the changes in the two flow fields were shown in Figs. 8 and 9 to be drastic.

Conclusions

In this paper, the inverse method for turbomachinery blades based on the Circulation Method has been successfully extended into the transonic-flow regime for three-dimensional flows. In the Circulation Method, the primary prescribed flow quantity is the swirl schedule in the bladed region, and the calculated geometric quantity is the blade profile. In this study, the flow is assumed to be inviscid with a uniform incoming flow, and the blades are assumed to be infinitely thin.

In the present method, the previous technique of expanding flow variables as Fourier series in the circumferential direction and solving the resulting set of eigenvalue problems in the meridional plane is replaced by a fully discretized method. The equations are solved in the conservative forms and are discretized in all three directions using a finite-volume technique. Relative to the previous mixed Fourier-series/discretized approach, the main advantage of the present formulation is its ability to handle mixed-flow conditions in the presence of weak shocks. In addition, the self-generated three-dimensional grid provided by the method can readily be used by existing Euler/Navier–Stokes analysis codes to perform off-design/loss calculations.

Calculations were carried out for the design of high-pressure centrifugal impellers and axial-compressor rotors operating in the transonic-flow regime, including design with prescribed swirl schedules that result in no shock or in the appearance of rapid compression regions (or possibly weak shocks) in the blade passage. Numerical experiments with various prescribed swirl schedules indicate that those generated using "smooth" loading shapes generally produce blade profiles that are shock-free, while those generated using loading shapes with "discontinuities" generally produce blade profiles that have rapid compression regions in the blade passage.

At the present time, little is known about how to prescribe swirl schedules corresponding to blade design that have shocks in the blade passage. The use of existing three-dimensional Euler analysis methods is recommended to examine this relationship. For example, these direct methods could be used

to calculate the swirl schedules corresponding to existing blade profiles that are known to have shocks in the blade passage. These results can provide guidelines on how to prescribe swirl schedules that produce blade design with shocks. In addition, the use of the blockage function (Yang et al., 1991) to represent blade thickness effects should be investigated as a means to produce shocks in the flow. As the purpose of this paper is to demonstrate that the Circulation Method can be extended into the transonic-flow regime for three-dimensional flows, this study is reserved for future work.

The assumption of weak shock employed in the present formulation can be relaxed by incorporating the Euler-correction method developed for strong shocks by Dang and Chen (1989). This method adds a rotational term to the velocity expression to account for the entropy field generated behind shocks. The theory can be extended to model blades with finite thickness by using two bound vortex sheets to represent the blade pressure and suction surfaces.

Acknowledgments

The author would like to thank Prof. Sir William Hawthorne of Cambridge University for bringing the problem to the author's attention and for the helpful discussions, and Prof. D. A. Caughey of Cornell University for providing the Flo-30m computer code. The work of Ms. P. R. Taft in performing the parametric studies for the design of the axial-compressor rotors is acknowledged. This work was partially supported by Hawthorne Associates.

References

Borges, J. E., 1990a, "A Three-Dimensional Inverse Method in Turbomachinery: Part 1—Theory," ASME JOURNAL OF TURBOMACHINERY, Vol. 112, pp. 364–354.

Borges, J. E., 1990b, "A Three-Dimensional Inverse Method in Turbomachinery: Part 2—Experimental Verification," ASME JOURNAL OF TURBOMACHINERY, Vol. 112, pp. 355–361.

Dang, T. Q., and McCune, J. E., 1984a, "Design Method for Highly-Loaded Blades With Blockage in Cascade," *Proceedings, ASME Conference on Computation of Internal Flows: Methods and Applications*, P. M. Sockel and K. N. Ghia, eds., pp. 129–136.

Dang, T. Q., and McCune, J. E., 1984b, "A Three-Dimensional Design Method in Rotational Flow," *Proceedings Int. Conf. on Inverse Design Concepts in Engineering Sciences (ICIDES)*, G. S. Dulikravich, ed., University of Texas, Austion, pp. 397–417.

Dang, T. Q., and Chen, L. T., 1989, "Euler Correction Method for Two- and Three-Dimensional Transonic Flows," *AIAA Journal*, Vol. 27, No. 10, pp. 1377–1386.

Dang, T. Q., 1991, "Design of Tubomachinery Blading in Transonic Flows by the Circulation Method," accepted for publication in the ASME JOURNAL OF TURBOMACHINERY.

Dang, T. Q., and Wang, T., 1992, "Design of Multi-stage Turbomachinery Blading by the Circulation Method: Actuator Duct Limit," ASME Paper No. 92-GT-286.

Dulikravich, G. S., and Sobieczky, H., 1982, "Shockless Design and Analysis of Transonic Cascade Shapes," *AIAA Journal*, Vol. 20, No. 11, pp. 1572–1578.

Ghaly, W. S. S., 1990, "A Parametric Study of Radial Turbomachinery Blade Design in Three-Dimensional Subsonic Flow," ASME JOURNAL OF TURBOMACHINERY, Vol. 112, pp. 338–345.

Hawthorne, W. R., Wang, C., Tan, C. S., and McCune, J. E., 1984, "Theory of Blade Design for Large Deflections: Part 1—Two-Dimensional Cascades," ASME *Journal of Engineering for Gas Turbines and Power*, Vol. 106, pp. 346–353.

Holbrook, G. J., and Brasz, J. J., 1984, "Experience With an Integrated Centrifugal Compressor Design Procedure," ASME Paper No. 84-GT-249.

Jameson, A., and Caughey, D. A., 1977, "A Finite-Volume Method for Transonic Potential-Flow Calculations," *Proceedings of the AIAA 3rd Computational Fluid Dynamics Conference*, Albuquerque, NM, pp. 35–54.

Lighthill, M. J., 1969, *An Introduction to Fourier Analysis and Generalized Functions*, Cambridge University Press, Cambridge, UK.

Meauze, G., 1982, "An Inverse Time Marching Method for the Definition of Cascade Geometry," ASME *Journal of Engineering for Power*, Vol. 104, pp. 650–656.

Novak, R. A., and Haymann-Haber, G., 1983, "A Mixed-Flow Cascade Passage Design Procedure Based on a Power Series Expansion," ASME *Journal of Engineering for Power*, Vol. 105, pp. 231–242.

Sanz, J. M., 1984, "Improved Design of Subcritical and Supercritical Cascades Using Complex Characteristics and Boundary-Layer Correction," *AIAA Journal*, Vol. 22, No. 7, pp. 950–956.

Smith, L. H., 1987, "Unducted Fan Aerodynamic Design," ASME JOURNAL OF TURBOMACHINERY, Vol. 109, pp. 313–324.

Tan, C. S., Hawthorne, W. R., McCune, J. E., and Wang, C., 1984, "Theory of Blade Design for Large Deflections: Part 2—Annular Cascades," ASME *Journal of Engineering for Gas Turbines and Power*, Vol. 106, pp. 354–365.

Tong, S. S., and Thompkins, W. T., 1983, "A Design Calculation Procedure for Shock-Free or Strong Passage Shock Turbomachinery Cascades," ASME *Journal of Engineering for Power*, Vol. 105, pp. 369–376.

Yang, Y. L., Tan, C. S., and Hawthorne, W. R., 1991, "Aerodynamic Design of Turbomachinery Blading in Three-Dimensional Flow: An Application to Radial Inflow Turbines," MIT Gas Turbine Laboratory Report No. 204.

Zangeneh, M., and Hawthorne, W. R., 1990, "A Fully Compressible Three-Dimensional Inverse Design Method Applicable to Radial and Mixed Flow Turbomachines," ASME Paper No. 90-GT-198.

Journal of Turbomachinery Discussion

Prediction of Unsteady Rotor-Surface Pressure and Heat Transfer From Wake Passings[1]

T. Korakianitis[2]

The authors are congratulated for their contributions to unsteady heat transfer computations. Some additional observations and questions are offered constructively. This discussion is based on previous investigations (Korakianitis, 1987a, 1988b, 1988c, 1992a, 1992b, 1993a; Korakianitis and Wilson, 1988a) on wake and potential-flow interaction propagating from upstream stators in turbine rotor cascades. (The discussion was offered in July 1991; further contributions to the unsteady flow and unsteady heat transfer phenomena on this turbine rotor are included in a recent study (Korakianitis et al., 1993b).)

The authors' Gaussian-velocity-defect wake model has amplitude $D = 0.15$ and (half) width $W = 0.04$, derived from one study on compressor wakes, presumably because no wake data on the pertinent turbine geometry were available. Our previous literature reviews (Korakianitis, 1987a, 1992a; Korakianitis and Wilson, 1988a) show experimental data on compressor and turbine-wake values of D and W as a function of distance downstream for the generating cascade. These data indicate that suction-side widths are larger than pressure-side widths, and turbine wakes have smaller amplitudes and wider widths than compressor wakes. For an axial gap of $x/C = 0.2$ from the stator cascade (as used in this study), compressor wakes would have $D_c \approx 0.25$, $W_{c,su} \approx 0.10$, and $W_{c,pr} \approx 0.05$, and turbine wakes would have $D_t \approx 0.10$, $W_{t,su} \approx 0.23$, and $W_{t,pr} \approx 0.18$ (where the subscripts c, t, su, and pr denote compressor, turbine, suction, and pressure, respectively). Based on these data, using $D_t = 0.10$, $W_{t,su} = 0.23$, and $W_{t,pr} = 0.18$ would be a better turbine wake model for the present investigation. Given the mechanisms of propagation and regions of influence of wake and potential-flow interaction (see below) the authors' wake model may have contributed to the overpredicting/underpredicting unsteady heat transfer shown in Figs. 13–16.

Our previous studies (Korakianitis, 1987a, 1988b, 1988c, 1992a, 1992b, 1993a; Korakianitis and Wilson, 1988a) have identified two important factors on the relative influence of wake and potential-flow interactions. First, for stator-to-rotor axial gaps $x/C = 0.3$ from the stator cascade: For stator-to-rotor-pitch ratio $R < 1.5$ the wake interaction dominates the unsteadiness; for $R > 2.5$ the potential-flow interaction dominates the unsteadiness; and for $1.5 < R < 2.5$ both interactions are important and they may reinforce or counteract each other. Second, as the axial gap x/C is reduced, the influence of the potential-flow interaction increases substantially. Since in the present investigation $R = 1.9024 \approx 2$ and the gap is 0.2, it is not at all clear that the wake interaction dominates the heat transfer in the geometry under investigation; it is more likely that the pressure and velocity gradients from the potential-flow interaction are dominating the flow particularly near the leading edge. Neglecting the potential-flow interaction has contributed significantly to the overpredicting/underpredicting unsteady heat transfer in Figs. 13–16.

The authors' explanation on the mechanisms of propagation of the wakes in this paper is based on previous interpretations of other investigators, which have recently been updated. For example, Meyer (1958) and Lefcort (1965) considered the cutting of wakes, and Smith (1966) introduced the idea of distinct wake segments and vorticity conservation in the rotor passages. Hodson (1983, 1985) discussed the rotation of the cut wake segments and the effects of the lower momentum fluid in the wake region, and Korakianitis (1987a, 1988c, 1992b) used the recirculating flows to show how they resulted in "suction" and "impingement" of low-momentum-fluid jets to generate unsteady-flow fields and pressure (forces) on turbine-blade surfaces.

The mechanisms of generation of unsteady flow fields by wake interaction and by potential-flow interaction were recently examined in further detail (Korakianitis, 1993a) using a cascade of low loading designed with the continuous surface-curvature distribution method described by Korakianitis (1987b, 1989). The wake effects are summarized below. Inside the cascade the cut wake segments result in recirculating-flow patterns, which in turn cause an increased unsteady-pressure region upstream of the location of the wake centerline, and a decreased unsteady-pressure region downstream of the wake centerline. Despite the shortcomings of the authors' wake model, *the above are* indeed corroborated by (and explain better) the phases of the local increases and decreases in surface pressure and velocity *upstream and downstream of the wake centerlines* shown in Figs. 4, 5, 6, and 7. The reasons are outlined below.

Figure 17 shows an example of the effect of cut wake segments (at time $t = Y/P_s = 0.12$ after the stator wake touches the leading edge of rotor 0) in a geometry corresponding to $R = .2$ and $x/C = 0.3$. The wake has amplitude $D = 0.10$, half-width $W = 0.15$ of P_s, and the stator outlet angle is 70.14 deg. The flow fields shown in Fig. 17 have been computed using Giles' (1988) computer program UNSFLO. The accuracy of the computations for steady and unsteady flow cases of known theoretical and experimental output has been checked before by Korakianitis (1987a, 1992a, 1993c), Korakianitis and Wilson (1988a), Giles (1988), and Giles and Haimes (1993). The high-turning highly loaded turbine cascade shown in Fig. 17 has been designed with a prescribed-curvature-distribution

[1]By L. T. Tran and D. B. Taulbee, published in the October 1992 issue of the ASME JOURNAL OF TURBOMACHINERY, Vol. 114, No. 4, pp. 807–817.

[2]Assistant Professor of Mechanical Engineering, Washington University, St. Louis, MO 63130.

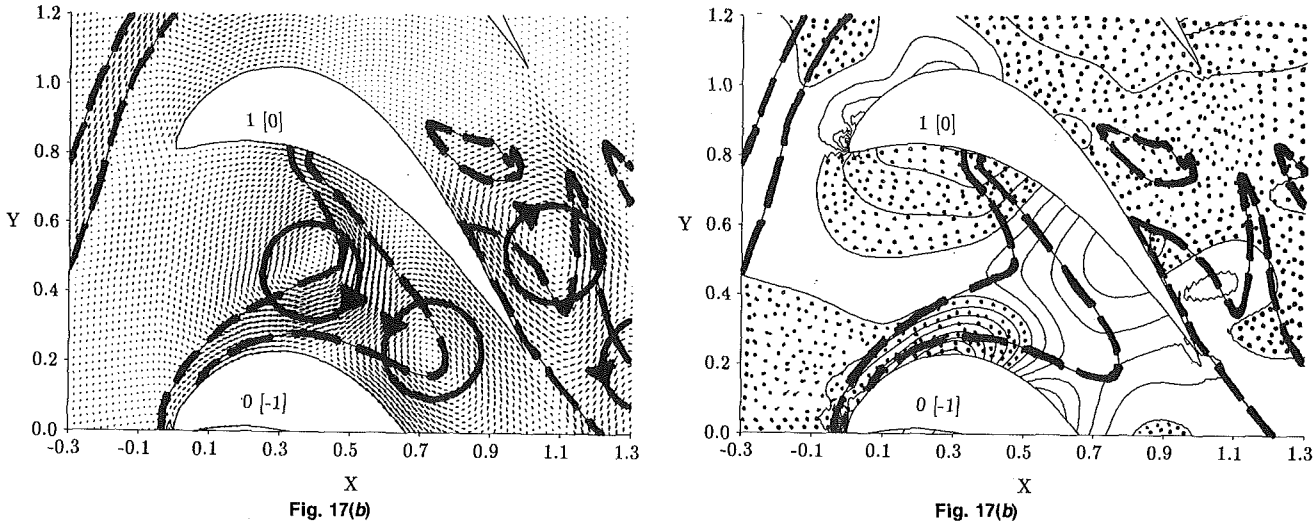

Fig. 17 Unsteady flow vectors of magnitude 0.35 (*a*) superimposed on unsteady pressure contours of increment 0.005 (*b*) and on dashed entropy contours of increment 2.0 (both) at $t = 0.12$

method (Korakianitis, 1993c) for inlet flow angle 50 deg, outlet flow angle −60 deg, and incompressible tangential-lift coefficient $C_L = 1.20$. The wake centerlines are identified by the thicker dashed lines of entropy contours. Figure 1(*a*) (left) shows unsteady flow vectors superimposed on entropy contours, and Fig. 1(*b*) (right) shows unsteady pressure contours superimposed on entropy contours for the same region. The regions of positive unsteady pressure are shown dotted, and the regions of negative unsteady pressure are shown unmarked. One can identify the magnitude of the change from the average pressure by counting the pressure contours in the dotted and unmarked regions.

As the potential-flow field of the stagnation region near the rotor leading edge interacts with the lower-momentum field in the wake, recirculating-flow patterns are established in the stagnation region of the leading edge of the rotor. These recirculating flow patterns are generated as the wake is being cut; once generated they result in a counterclockwise rotating unsteady-flow pattern downstream of the wake centerline, and a clockwise rotating unsteady-flow pattern upstream of the wake centerline. The wakes are cut by the potential-flow field of the passing rotor into individual segments acting in each passage. After the stator wake is cut to produce a segment of a wake in the rotor passage, the two ends of the wake segment travel at the local speeds; the portion attached to the pressure side moves downstream into the passage much more slowly than the portion attached to the suction side, because the local flow velocities are higher on the suction side of the cascade. At the same time lower momentum fluid moves from the wake end near the pressure side to the wake end near the suction side. The last two phenomena cause a thinner wake segment of the pressure side, a thicker wake segment on the suction side, and a counterclockwise rotation of the centerline of the wake, as it moves through the passage. The initial vorticity is conserved: Before the wake is cut there is no unsteady pressure on either side of the wake; after the wake is cut there is substantial positive unsteady pressure on the upstream side of the wake, and negative unsteady pressure on the downstream side of the wake. If the flow entering the rotor is modeled as irrotational, then the vorticity of the two counterrotating recirculating-flow patterns that flank the wake centerline must be equal and opposite. The two vortex patterns act in opposite directions. The upstream clockwise-rotating recirculating-flow pattern causes a local increase in pressure, and the downstream counterclockwise-rotating recirculating-flow pattern causes a local decrease in pressure. As the vortices move downstream and out of the rotor cascade the wake is sheared, distorted, and enlarged, while the amplitudes of the unsteady pressure maxima or minima are decreased, and their region of influence increased.

References

Giles, M. B., 1988, "Calculation of Unsteady Wake/Rotor Interaction," *AIAA Journal of Propulsion and Power*, Vol. 4, No. 4, pp. 365–362.

Giles, M. B., and Haimes, R., 1993, "Validation of a Numerical Method for Unsteady Flow Calculations," ASME JOURNAL OF TURBOMACHINERY, Vol. 115, pp. 110–117.

Hodson, H. P., 1983, "Unsteady Boundary-Layers on Axial-Flow Turbine Rotor Blades," PhD thesis, University of Cambridge, United Kingdom.

Hodson, H. P., 1985, "An Inviscid Blade-to-Blade prediction of a Wake-Generated Unsteady Flow," ASME *Journal of Engineering for Gas Turbines and Power*, Vol. 107, pp. 337–344.

Korakianitis, T., 1987a, "A Design Method for the Prediction of Unsteady Forces on Subsonic, Axial Gas-Turbine Blades," Doctoral Thesis (Sc.D.) in Mechanical Engineering, Massachusetts Institute of Technology, Cambridge, MA.

Korakianitis, T., 1987b, "A Parametric Method for Direct Gas-Turbine-Blade Design," AIAA Paper No. 87-2171.

Korakianitis, T., and Wilson, D. G., 1988a, "The Effect of the Magnitude of the Inlet-Boundary Disturbance on the Unsteady Forces on Axial Gas-Turbine Blades," *Proceedings of the Fourth International Symposium on Unsteady Aerodynamics and Aeroelasticity of Turbomachines and Propellers*, Aachen, Germany, Sept. 6–10, 1987; H. E. Gallus and S. Servaty, eds., published by RWTH Aachen, Feb. 1988, pp. 109–124.

Korakianitis, T., 1988b, "On the Prediction of Unsteady Forces on Gas Turbine Blades. Part 1: Typical Results and Potential-Flow-Interaction Effects," ASME Paper No. 88-GT-89.

Korakianitis, T., 1988c, "On the Prediction of Unsteady Forces on Gas Turbine Blades. Part 2: Viscous-Wake-Interaction and Axial-Gap Effects," ASME Paper No. 88-GT-90.

Korakianitis, T., 1989, "Design of Airfoils and Cascades of Airfoils," AIAA Journal, Vol. 27, No. 4, pp. 455–461.

Korakianitis, T., 1992a, "On the Prediction of Unsteady Forces on Gas Turbine Blades. Part 1: Description of the Approach," ASME JOURNAL OF TURBOMACHINERY, Vol. 114, pp. 114–122.

Korakianitis, T., 1992b, "On the Prediction of Unsteady Forces on Gas Turbine Blades. Part 2: Analysis of the Results," ASME JOURNAL OF TURBOMACHINERY, Vol. 114, pp. 123–131.

Korakianitis, T., 1993a, "On the Propagation of Viscous Wakes and Potential Flow in Axial-Turbine Cascades," ASME JOURNAL OF TURBOMACHINERY, Vol. 115, No. 1, pp. 118–127.

Korakianitis, T., Papagiannidis, P., and Vlachopoulos, N., 1993b, "Unsteady Flow/Quasi-Steady Heat-Transfer Computations on a Turbine Rotor and Comparison With Experiments," ASME Paper No. 93-GT-145; ASME JOURNAL OF TURBOMACHINERY in press.

Korakianitis, T., 1993c, "Prescribed-Curvature-Distribution Airfoils for the Preliminary Geometric Design of Axial-Turbomachinery Cascades," ASME JOURNAL OF TURBOMACHINERY, Vol. 115, pp. 325–333.

Lefcort, M. D., 1965, "An Investigation of Unsteady Blade Forces in Turbomachines," ASME *Journal of Engineering for Power*, Vol. 87, pp. 345–354.

Meyer, R. X., 1958, "The Effect of Wakes on the Transient Pressure and

Velocity Distributions in Turbomachines," *Transactions of the ASME*, Vol. 80, pp. 1544–1552.

Smith, L. H., 1966, "Wake Dispersion in Turbomachines," ASME *Journal of Basic Engineering*, Vol. 88, pp. 688–690.

Authors' Closure

Unsteady flows in gas turbine engines arise from the relative motion between a stationary vane row and a rotating blade row. One source of unsteadiness is the wakes, which are shed from upstream blade rows and transported to the subsequent blade rows. Although we clearly stated that our purpose was to study the effects of the wake on heat transfer to the rotor blade surface, Dr. Korakianitis instead chose to discuss the interaction between vane/rotor potential flow. Thus the bulk of his discussion is fundamentally extraneous to our investigations.

The only point Dr. Korakianitis raises that is potentially relevant to our paper concerns the wake model parameter used in our calculations. With regard to this point, we estimated the wake width W and the wake deficit D from the nozzle guide vane boundary layer calculations and from the experimental data given by Raj and Lakshminarayana (1973); we had no intention of adjusting these parameters to match the heat transfer experimental data. It is interesting to see Dr. Korakianitis suggesting the use of different values for these parameters without taking into account the vane geometry and the boundary layer developed on the vane surfaces. Finally, the equation for the Gaussian wake model defined by Dr. Korakianitis and that used in our paper are different. It should be noted that Giles (1988) used the same Gaussian wake model as ours with different values of wake width and wake deficit, yet his calculations show qualitatively the same unsteady flow phenomena as those in our calculations. This evidence suggests that moderate changes in these parameters do not change the flow phenomena substantially, which seems to be a surprise to Dr. Korakianitis.

It is not pertinent with respect to our paper to respond to other points raised by Dr. Korakianitis except to note that much of his discussion has already appeared in other works (see, e.g., Hodson, 1985; Giles, 1988; Tran and Taulbee, 1992). It is also interesting to note that his interpretation of the wake/rotor interaction using concepts such as positive unsteady pressure, negative unsteady pressure (if such a thing exists), wake cutting by a potential flow field, movement of low-momentum fluid from the pressure side to the suction side, and the conservation of initial vorticity is not supported quantitatively.

References

Giles, M. B., 1988, "Calculation of Unsteady Wake/Rotor Interaction," *AIAA Journal of Propulsion and Power*, Vol. 4, No. 4, pp. 356–362.

Hodson, H. P., 1985, "An Inviscid Blade-to-Blade Prediction of a Wake-Generated Unsteady Flow," ASME *Journal of Engineering for Gas Turbines and Power*, Vol. 107, pp. 337–344.

Raj, R., and Lakshminarayana, B., 1973, "Characteristics of the Wake Behind a Cascade of Airfoils," *Journal of Fluid Mechanics*, Vol. 61, Part 4, pp. 707–730.

Tran, L. T., and Taulbee, D. B., 1992, "Prediction of Unsteady Rotor-Surface Pressure and Heat Transfer From Wake Passings," ASME JOURNAL OF TURBOMACHINERY, Vol. 114, pp. 807–817.

Velocity Distributions in Turbomachines," *Transactions of the ASME*, Vol. 80, pp. 1544–1552.

Smith, L. H., 1966, "Wake Dispersion in Turbomachines," ASME *Journal of Basic Engineering*, Vol. 88, pp. 688–690.

Authors' Closure

Unsteady flows in gas turbine engines arise from the relative motion between a stationary vane row and a rotating blade row. One source of unsteadiness is the wakes, which are shed from upstream blade rows and transported to the subsequent blade rows. Although we clearly stated that our purpose was to study the effects of the wake on heat transfer to the rotor blade surface, Dr. Korakianitis instead chose to discuss the interaction between vane/rotor potential flow. Thus the bulk of his discussion is fundamentally extraneous to our investigations.

The only point Dr. Korakianitis raises that is potentially relevant to our paper concerns the wake model parameter used in our calculations. With regard to this point, we estimated the wake width W and the wake deficit D from the nozzle guide vane boundary layer calculations and from the experimental data given by Raj and Lakshminarayana (1973); we had no intention of adjusting these parameters to match the heat transfer experimental data. It is interesting to see Dr. Korakianitis suggesting the use of different values for these parameters without taking into account the vane geometry and the boundary layer developed on the vane surfaces. Finally, the equation for the Gaussian wake model defined by Dr. Korakianitis and that used in our paper are different. It should be noted that Giles (1988) used the same Gaussian wake model as ours with different values of wake width and wake deficit, yet his calculations show qualitatively the same unsteady flow phenomena as those in our calculations. This evidence suggests that moderate changes in these parameters do not change the flow phenomena substantially, which seems to be a surprise to Dr. Korakianitis.

It is not pertinent with respect to our paper to respond to other points raised by Dr. Korakianitis except to note that much of his discussion has already appeared in other works (see, e.g., Hodson, 1985; Giles, 1988; Tran and Taulbee, 1992). It is also interesting to note that his interpretation of the wake/rotor interaction using concepts such as positive unsteady pressure, negative unsteady pressure (if such a thing exists), wake cutting by a potential flow field, movement of low-momentum fluid from the pressure side to the suction side, and the conservation of initial vorticity is not supported quantitatively.

References

Giles, M. B., 1988, "Calculation of Unsteady Wake/Rotor Interaction," *AIAA Journal of Propulsion and Power*, Vol. 4, No. 4, pp. 356–362.

Hodson, H. P., 1985, "An Inviscid Blade-to-Blade Prediction of a Wake-Generated Unsteady Flow," ASME *Journal of Engineering for Gas Turbines and Power*, Vol. 107, pp. 337–344.

Raj, R., and Lakshminarayana, B., 1973, "Characteristics of the Wake Behind a Cascade of Airfoils," *Journal of Fluid Mechanics*, Vol. 61, Part 4, pp. 707–730.

Tran, L. T., and Taulbee, D. B., 1992, "Prediction of Unsteady Rotor-Surface Pressure and Heat Transfer From Wake Passings," ASME JOURNAL OF TURBOMACHINERY, Vol. 114, pp. 807–817.